Power and Energy Series 34

The Lightning Flash

Edited by Vernon Cooray

IET POWER AND ENERGY SERIES 34

Series Editors: Professor A.T. Johns
Professor D.F. Warne

The Lightning Flash

Other volumes in this series:

Volume 1 **Power circuit breaker theory and design** C.H. Flurscheim (Editor)
Volume 4 **Industrial microwave heating** A.C. Metaxas and R.J. Meredith
Volume 7 **Insulators for high voltages** J.S.T. Looms
Volume 8 **Variable frequency AC motor drive systems** D. Finney
Volume 10 **SF6 switchgear** H.M. Ryan and G.R. Jones
Volume 11 **Conduction and induction heating** E.J. Davies
Volume 13 **Statistical techniques for high voltage engineering** W. Hauschild and W. Mosch
Volume 14 **Uninterruptable power supplies** J. Platts and J.D. St Aubyn (Editors)
Volume 15 **Digital protection for power systems** A.T. Johns and S.K. Salman
Volume 16 **Electricity economics and planning** T.W. Berrie
Volume 18 **Vacuum switchgear** A. Greenwood
Volume 19 **Electrical safety: a guide to causes and prevention of hazards** J. Maxwell Adams
Volume 21 **Electricity distribution network design, 2nd edition** E. Lakervi and E.J. Holmes
Volume 22 **Artificial intelligence techniques in power systems** K. Warwick, A.O. Ekwue and R. Aggarwal (Editors)
Volume 24 **Power system commissioning and maintenance practice** K. Harker
Volume 25 **Engineers' handbook of industrial microwave heating** R.J. Meredith
Volume 26 **Small electric motors** H. Moczala *et al.*
Volume 27 **AC-DC power system analysis** J. Arrill and B.C. Smith
Volume 29 **High voltage direct current transmission, 2nd edition** J. Arrillaga
Volume 30 **Flexible AC Transmission Systems (FACTS)** Y-H. Song (Editor)
Volume 31 **Embedded generation** N. Jenkins *et al.*
Volume 32 **High voltage engineering and testing, 2nd edition** H.M. Ryan (Editor)
Volume 33 **Overvoltage protection of low-voltage systems, revised edition** P. Hasse
Volume 34 **The lightning flash** V. Cooray
Volume 35 **Control techniques drives and controls handbook** W. Drury (Editor)
Volume 36 **Voltage quality in electrical power systems** J. Schlabbach *et al.*
Volume 37 **Electrical steels for rotating machines** P. Beckley
Volume 38 **The electric car: development and future of battery, hybrid and fuel-cell cars** M. Westbrook
Volume 39 **Power systems electromagnetic transients simulation** J. Arrillaga and N. Watson
Volume 40 **Advances in high voltage engineering** M. Haddad and D. Warne
Volume 41 **Electrical operation of electrostatic precipitators** K. Parker
Volume 43 **Thermal power plant simulation and control** D. Flynn
Volume 44 **Economic evaluation of projects in the electricity supply industry** H. Khatib
Volume 45 **Propulsion systems for hybrid vehicles** J. Miller
Volume 46 **Distribution switchgear** S. Stewart
Volume 47 **Protection of electricity distribution networks, 2nd edition** J. Gers and E. Holmes
Volume 48 **Wood pole overhead lines** B. Wareing
Volume 49 **Electric fuses, 3rd edition** A. Wright and G. Newbery
Volume 50 **Wind power integration: connection and system operational aspects** B. Fox *et al*.
Volume 51 **Short circuit currents** J. Schlabbach
Volume 52 **Nuclear power** J. Wood
Volume 53 **Condition assessment of high voltage insulation in power system equipment** R.E. James and Q. Su
Volume 55 **Local energy: distributed generation of heat and power** J. Wood
Volume 56 **Condition monitoring of rotating electrical machines** P. Tavner, L. Ran, J. Penman and H. Sedding
Volume 905 **Power system protection, 4 volumes**

The Lightning Flash

Edited by Vernon Cooray

The Institution of Engineering and Technology

Published by The Institution of Engineering and Technology, London, United Kingdom

First published 2003

The Institution of Engineering and Technology
Michael Faraday House
Six Hills Way, Stevenage
Herts, SG1 2AY, United Kingdom

www.theiet.org

British Library Cataloguing in Publication Data
Cooray, G.V.
The lightning flash. – (IET Power and energy series no. 34)
1. Lightning 2. Lightning protection
I. Title II. Institution of Electrical Engineers
621.3'17

ISBN (10 digit) 0 85296 780 2
ISBN (13 digit) 978-0-85296-780-5

Typeset in India by Newgen Imaging Systems (P) Ltd, Chennai
First printed in the UK by MPG Books Ltd, Bodmin, Cornwall
Reprinted in the UK by Lightning Source UK Ltd, Milton Keynes

In appreciation of the work of a merciful God

Contents

Preface

Lightning research is an interdisciplinary subject where the needs of various branches of engineering and physics converge.

For power engineers, the mechanism of the lightning flash and the characteristics of electromagnetic fields generated by lightning, are vital for the design of protection measures in power lines. For the electromagnetic specialists, lightning is a long radio antenna that generates a broadband electromagnetic signal, which can be utilised to characterise the effects of the propagation path on electromagnetic fields. For the telecommunication engineer, an understanding of the interaction of these fields with overhead and underground wires is of importance in protecting electrical instruments connected to overhead power lines and underground cables from induced over voltages. For the high voltage engineer, lightning is a current and voltage generator that disrupts various components located on high voltage power lines. For the physicists, lightning is a laboratory in which one can test the fundamentals of discharge physics. Thus the researchers and students who seek information about lightning come from different backgrounds and disciplines and require tailor-made information. I hope this book will help to diffuse knowledge across such boundaries.

The topics of the chapters in this book are based on a graduate course given to the engineering students at Uppsala University. I also hope that this book may serve as a text in graduate courses on lightning, given to power engineering students.

Acknowledgements

I would like to thank late Prof. James Wait who encouraged me to take up this task. I wish to thank my fellow scientists who spend a good deal of their free time in writing the chapters of this book. I would like to thank Dr. Francisco Roman for reading and suggesting improvements of the chapter on physics of electrical discharges and my post graduate students, Mahbubur Rahman and Mose Akyuz, who read some of the chapters and provided me with inputs from a student's perspective.

I wish to express my sincere thanks to Ms. Wendy Hiles of IEE's publications department, who was at all times prepared to listen to my suggestions.

Finally, I express my gratitude to my wife Ruby and two sons, Gerald and Charith, for their encouragement and patience during the writing of this book.

Chapter 1

Charge structure and geographical variation of thunderclouds

Earle Williams

1.1 The formation of clouds

Clouds in the earth's atmosphere are composed of water droplets and ice crystals. Clouds are commonly white in appearance because these liquid and solid particles are large relative to the wavelengths of visible light, and so no selective scattering occurs to colour the cloud. Owing to the abundance of cloud condensation nuclei, clouds appear whenever the air becomes locally supersaturated in water vapour. This supersaturation condition is most often achieved by a lifting process in which air parcels subsaturated with respect to water vapour cool by adiabatic expansion. The lifting process is usually caused by the heating of air near the earth's surface, which is itself warmed by sunlight. The warmed air parcels become buoyant relative to their surroundings and rise. A second mechanism for lifting depends on the forced ascent of air by horizontal pressure gradient forces. Regardless of the lifting mechanism, the altitude at which the supersaturation condition is achieved in the rising air parcel and cloud begins to form is the lifted condensation level (LCL).

In many circumstances where clouds are frequent occurrences, the LCL is within 1000 metres of the earth's surface, and substantially lower than the altitude of the 0°C isotherm, typically 4000–5000 metres above ground. As a consequence, the great majority of clouds form at temperatures above freezing and consist entirely of liquid droplets. The weight of the evidence shows that such clouds are not strongly electrified and rarely, if ever, produce lightning.

1.2 Local conditions necessary for thunderclouds

Clouds in which lightning occurs – thunderclouds by definition – are the largest and most convectively vigorous in the atmosphere. Numerous observations in many geographical locations disclose that a cumulonimbus cloud must extend at least

2–3 kilometres into the subfreezing portion of the atmosphere before the first lightning is observed. This observation is consistent with the most favoured mechanism for electrical charge separation leading to lightning: the collisions between graupel particles and ice crystals or other smaller graupel particles. The presence of such particles requires a mixed-phase condition – the simultaneous presence of water substance in all three phases: vapour, liquid and solid. Graupel particles form when supercooled liquid droplets are accreted by large ice crystals and subsequently freeze. Continual accretion can lead to graupel growth to sizes of millimetres and, in extreme cases of high supercooled water concentrations, to centimetre-sized particles known as hail. Ice crystals grow at the expense of the supercooled water by the Bergeron process in a mixed-phase environment because the equilibrium vapour pressure with respect to ice is less than that with respect to liquid water. The selective transfer of negative electricity to the graupel particles in collisions with the smaller ice particles then provides for gravitational separation of oppositely charged particles until an electric field sufficient for dielectric breakdown is present and lightning develops. A more detailed discussion of the mechanisms for charge transfer during particle collisions may be found in Chapter 2. Charge separation by differential motions under gravity to form a positive dipole is illustrated in Figure 1.1.

A surprisingly wide variety of meteorological conditions are favourable for lightning – ordinary summer thunderstorms, severe (hail and tornadoes) thunderstorms, the hurricane eyewall and rainbands, winter snowstorms, oceanic

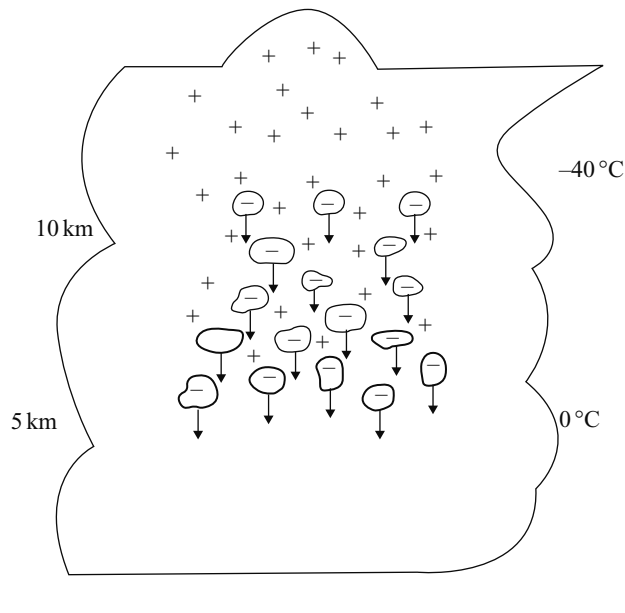

Figure 1.1 Illustration of charge separation by particle collisions and differential motions under gravity. Negative charge is selectively transferred to larger graupel particles to create the positive thunderstorm dipole

convection and mesoscale convective systems. The common ingredient in all these situations is an active mixed-phase region. Deep convection without sufficient updraft and vigorous mixed-phase process does not result in lightning. The best examples are the tropical oceanic hot towers which may attain heights of 15 km or more and not produce lightning.

1.3 The gross charge structure of thunderclouds

The electrostatic structure of thunderclouds was exposed over the course of the 20th century by remote sensing methods. Two distinct methods were pioneered independently by two British scientists who for more than two decades held opposite views on the polarity of the thunderstorm dipole moment. The two scientists were G.C. Simpson and C.T.R. Wilson. Simpson [1] measured the charge on rain beneath thunderclouds. He later designed an instrument to measure the vertical component of the electric field from a balloon released at the ground which ascended through the depth of the cloud. Wilson [2,3] measured the changes in electrostatic field accompanying lightning flashes and, with estimates of the distance to the lightning based on observations of the thunder delay, interpreted these measurements to extract the magnitude and the polarity of the charge moment for both intracloud and cloud-to-ground lightning flashes. Within the latter part of the 20th century, Simpson's method has been extended to vector electric field measurements and the use of Poisson's equation to extract estimates of space charge density [4,5]. Wilson's method has also been extended to multistation measurements of lightning field change [6,7] which enable determinations of the magnitudes and heights of the charge transferred by lightning in different phases of the lightning flash.

The longstanding disagreement between Wilson and Simpson was resolved by a series of electric field soundings by Simpson and Scrase [8] and Simpson and Robinson [9] in which a tripolar electrostatic structure for thunderclouds was identified – positive charge uppermost, main negative charge at midlevel and a region of smaller positive charge at lower levels as shown in Figure 1.2. For measurements at some distance from the cloud (a necessary condition with Wilson's method as his instruments would not have worked properly if wet by rain) the tripole structure is dominated by the upper positive dipole. For measurements directly beneath the cloud, where Simpson made numerous measurements of the electric charge carried by raindrops, the lower (inverted) dipole would be most apparent. The tripole picture brought consistency to the measurements of these two scientists.

More recent measurements with the refined methods previously described lend further support to the basic tripolar structure in isolated thunderclouds. The main negative charge is found in the cold part of the cloud where the temperature is in the range of $-10°C$ to $-20°C$, with a tendency for slightly higher altitudes (and lower temperatures) in deeper, more vigorous storms. The main negative charge is frequently vertically confined, often less than 1 km in vertical extent. The upper positive charge is more diffuse and can extend to the top of the cloud. The upper positive and main negative charge regions are often separated by a quasi-neutral zone

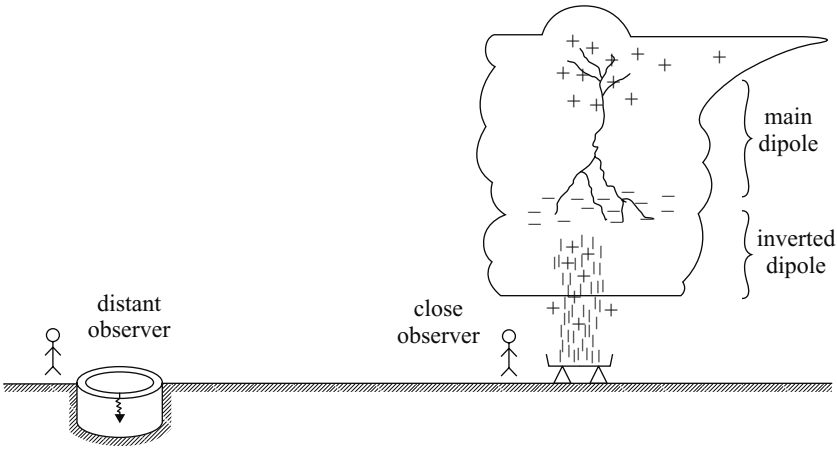

Figure 1.2 The tripole structure of the thundercloud (first identified by Simpson and Scrase [8]) and the predominant behaviour for observers at different distances from the storm. The inverted dipole dominates for the close observer and the main dipole for the distant observer.

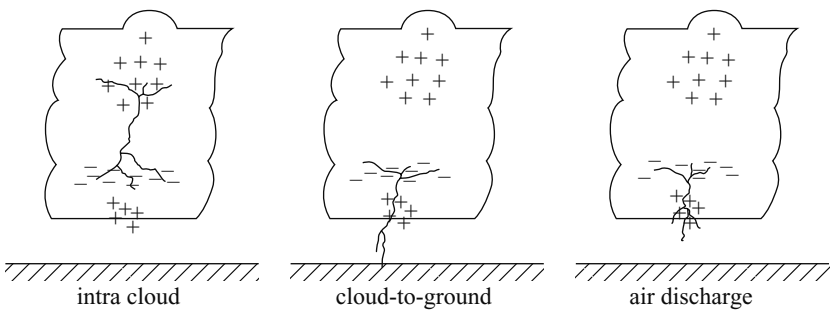

Figure 1.3 Predominant lightning types within the tripole structure of a thunderstorm: the intracloud flash, the negative ground flash and the air discharge

in the central mixed-phase region, consistent with the picture for charge separation by particle collisions illustrated in Figure 1.1. The lower positive charge is typically smaller in magnitude than the main negative charge (consistent with the common presence of upward-pointing electric fields beneath thunderclouds), and can extend below the 0°C isotherm.

The tripole structure is also broadly consistent with the dominant lightning types now recognised in isolated thunderclouds [10], as illustrated in Figure 1.3. The most common lightning type is the intracloud flash, a discharge between the upper positive charge and the main negative charge. The most common ground flash transfers negative charge from the main negative charge region to ground, but the initial discharge between the main negative charge and the lower positive charge may be an essential

aspect of the overall process. A discharge between the main negative charge and the lower positive charge which does not succeed in contacting ground is called an air discharge. Had Wilson been able to make his field-change measurements closer to the cloud, he probably would have recognised this third common lightning type in early work. A less frequent type of air discharge is the lightning that propagates upward into clear air above the cloud top. A fifth lightning type is the positive ground discharge which occurs about one tenth as frequently as does the negative ground discharge. It has not yet been established whether positive ground flashes draw on the upper positive charge or the lower positive charge, or still another positive charge reservoir. The answer may well depend on the meteorological context [11,12,22].

As previously discussed, the main charge regions in thunderclouds are often confined in the vertical in comparison with their horizontal extents. The main evidence for this behaviour has come from balloon soundings of electric field, but the various observations of lightning paths within the cloud corroborate this behavior [7,13–15]. The evidence for vertical confinement of charge contradicts earlier ideas of Malan and Schonland [16] about an extended vertical column of electric charge which originated on the basis of a misinterpretation of the electric field changes during the lightning discharge.

1.4 Sprite-producing thunderclouds: mesoscale convective systems

Although vertical confinement of charge regions characteristic of ordinary thunderclouds is depicted in Figures 1.1–1.3, this behavior is most pronounced in the stratiform region of mesoscale convective systems (MCSs) – clouds whose width-to-height ratio may be 10 or 20 to 1 instead of 1 to 1. MCSs are the result of the aggregation of isolated thunderstorms forming earlier in the diurnal cycle, and hence are most prevalent very late in the afternoon and evening. The laterally extensive layers of space charge in an MCS allow for larger and more energetic lightning than is possible in ordinary thunderclouds. Charge transfers of hundreds of coulombs are possible [17–19,42], in contrast with the few tens of coulombs in ordinary thundercloud lightning. Lightning with horizontal extents exceeding 100 km has been documented in these very broad thunderstorms [20].

The charge structure of the MCS stratiform region is often more complicated than that depicted for ordinary thunderclouds in Figure 1.1 [4], although the dominant charge layers are still found in the mixed-phase region of the storms [21]. A pronounced layer of positive space charge is often found (by balloon soundings of the electric field) near the melting level at the lower boundary of the mixed-phase zone. A negative layer is often found above this positive layer [21]. The latter positive layer appears to be an important reservoir for the very energetic positive ground flashes with laterally extensive spider lightning and long continuing currents which predominate in MCS stratiform clouds [22,23].

The discovery of sprites in the mesosphere in recent years [23–27] has intensified interest in the electrification and charge structure of the MCS stratiform region. Sprites are a luminous discharge phenomenon at 70–90 km altitude clearly caused by the large

Figure 1.4 A video camera image of a sprite in the mesosphere over a large mesoscale convective system

energetic positive ground flashes typical of this meteorological stage of convection [19,28]. A video camera image of an energetic sprite is shown in Figure 1.4. Sprites do not appear to be produced by lightning in ordinary thunderclouds, but rather require clouds with more substantial lateral extents as shown in Figure 1.5. The energetic positive discharges make sprites simultaneously excite the extremely low-frequency resonances of the earth–ionosphere cavity and thereby enable the worldwide detection of sprite locations with single station ELF measurements [19,27,28].

1.5 Geographical variability of thunderclouds

1.5.1 Environmental controls

The shape, size, intensity and prevalence of thunderstorms all exhibit geographical variations which are best understood by first considering environmental controls on thunderstorm characteristics. Thunderstorms are still notoriously difficult to predict, but this kind of information is invaluable towards that end. Important controls are the following:

Availability of water vapour: The energy made available for thunderstorms is ultimately the latent heat released when water vapour reverts to its liquid and solid phases

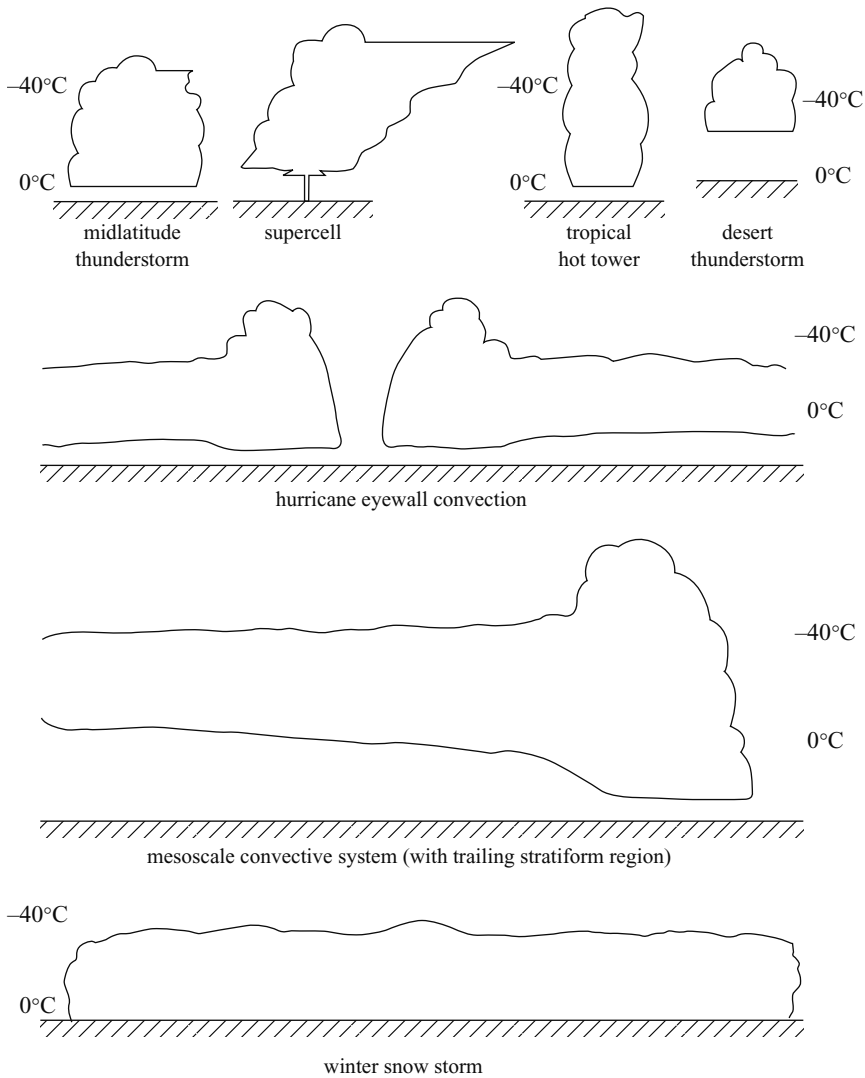

Figure 1.5 Shapes and sizes of thunderstorms in different meteorological environments and different geographical locations. A viable mixed-phase region appears to be a common feature

through the processes of condensation, vapour deposition, and freezing (riming). The most important single factor in influencing the seasonal and geographic variability of thunderstorms is the physical law governing the temperature dependence of the water vapour concentration at saturation – the Clausius–Clapeyron relation. This relationship is exponential – a rough rule-of-thumb is a doubling of water vapour concentration for each 10°C increase in temperature. For a 50°C temperature difference between

the Earth's equator and pole, this amounts roughly to a $2^5 = 32$-fold contrast in water vapour concentration.

Atmospheric instability: Vertical air motions in thunderstorms are caused primarily by cloud buoyancy forces which themselves are set up by differences in temperature, water vapour concentration and condensate between ascending and descending air parcels and their environment. One often used measure of integrated cloud buoyancy, obtained from thermodynamic soundings in the environment of a developing storm, is CAPE (convective available potential energy) [29]. In general, an atmosphere with larger CAPE is likely to produce a stronger updraft and a more vigorous and electrically active storm. The updrafts in turn will influence the vertical development of precipitation in the mixed-phase region of the cloud where the impact on charge separation appears to be greatest. Large CAPE can result from either strong surface heating and hot boundary-layer air, and/or by the presence of cold air aloft. The nature of the surface is influential here; land surfaces heat more rapidly when exposed to sunlight than water surfaces because of the rigidity, opacity and smaller heat capacity of the land surface.

The vertical extent of cloud buoyancy: Air parcels experiencing upward buoyancy forces over a greater vertical extent [30] are expected to achieve larger vertical velocities, and thereby contribute to more vigorous thunderstorms. The height at which the buoyancy force vanishes is the level of neutral buoyancy (LNB). Owing to the vertical temperature structure of the atmosphere, the LNB is in general found just beneath the local tropopause, where the temperature begins to increase into the stratosphere. The tropopause height varies considerably with geographical latitude – 17 km in the tropics to 12–13 km in midlatitude summer to about 6–7 km in midlatitude winter conditions.

Altitude of the mixed-phase region: As noted earlier and illustrated in Figure 1.5, mixed-phase microphysics appears to be essential for vigorous charge separation and lightning. The mixed-phase region is bounded by the 0°C and −40°C isotherms, which translates to a vertical extent in the atmosphere of 5–6 km. In summer this region is 4–5 km above the earth's surface. In winter, this region begins near the earth's surface and extends upward. This effect alone will obviously contribute greatly to both the seasonal and geographic variability of thunderstorms.

Boundary-layer aerosol concentration: The earth's atmosphere is polluted with submicroscopic particles whose concentration varies widely. Because the sources for many of these particles are land-based, the continental aerosol concentrations are systematically greater than those over the ocean. A subset of the aerosol particles is the cloud condensation nuclei which strongly influence the spectra of cloud droplets (both number concentrations and sizes) in developing moist convection. In this way the aerosol particles can influence the precipitation formed by the cloud. Recent speculation and observation suggest that the aerosol may also affect both lightning activity [35] and cloud-to-ground lightning polarity [31]. This issue is presently an active area of research.

Figure 1.6 *Global lightning distribution depicted by the Optical Transient Detector in space showing a predominance of lightning activity over land areas* (Dr's H. Christian and D. Boccippio, NASA/Marshall Space Flight Center.)

Land versus ocean effects: It is now well established that lightning is far more prevalent over land than over ocean, as shown in Figure 1.6. The explanation for the order-of-magnitude contrast in not well established. The traditional explanation is based on the stronger heating over land, larger CAPE, larger updraft and greater invigoration of mixed-phase microphysics. However, a large land/ocean lightning contrast is evident even at midnight [32], when the land surface is not strongly heated by the sun. It has also been pointed out that even when CAPE is large over warm ocean water, the lightning activity there is still very modest [33]. The most recent work on this issue [34] emphasises an important role in cloud basic height (low over ocean, high over land) in influencing the conversion of CAPE to updraft kinetic energy.

One alternative explanation [45] for the large lightning contrast is based on differences in continental and oceanic aerosol concentration. Over land where the air is more polluted, the available condensed liquid will be shared among a larger number of droplets, leading to smaller droplet sizes. The coalescence process to form rain is suppressed in the presence of small droplets and this may enable more liquid water to access the mixed-phase region where it is able to participate in the ice processes that promote charge separation. The results of recent field experiments cast doubt on the aerosol mechanism as the primary cause of the land–ocean lightning contrast [35].

Yet another explanation for the land–ocean lightning contrast rests on the convective theory for electrification [36] and the differences in point discharge current expected for the smooth ocean surface and the rough and irregular land surface.

Baroclinity of the atmosphere: An atmosphere whose temperature is laterally uniform is referred to in meteorology as 'barotropic'. Thunderstorms in a purely barotropic atmosphere grow vertically and frequently collapse on themselves to terminate their life cycle. The tropical atmosphere is the most barotropic region on earth. More common at midlatitude is the baroclinic atmosphere characterised by strong horizontal temperature gradients. Large-scale latitudinal temperature gradients are the direct result of differential heating of the earth by the sun – the tropics are hot and the poles are cool, with gradient regions in between. In baroclinic zones where hot and cold air masses of synoptic scale ($\sim$1000 km) interact, extraordinarily large CAPE can develop and storms can be strongly tilted from the vertical. Severe weather of all kinds (hail, wind and tornadoes) is strongly encouraged by baroclinic conditions. Recent studies have shown the severe storm to be the most electrically active in the atmosphere [37], and usually produce more than ten times more intracloud lightning than ground flashes.

1.5.2 Tropical thunderstorms

As a population of storms, the deep tropical clouds dominate the global thunderstorm category, in no small part because of the temperature dependence of the Clausius–Clapeyron relation. According to the satellite observations of Orville and Henderson [32], two of every three lightning flashes are found within the tropical belt. Tropical lightning is also dominant because, in many regions, thunderstorms develop nearly every day. Such is not the case at higher latitudes.

The flash rates of tropical thunderstorms vary widely. For storms close to and within the intertropical convergence zone (ITCZ) – the main region of synoptic scale upwelling and widespread persistent rainfall – the flash rates are quite modest, a few per minute or less. The active overturn of the troposphere on a large scale prevents the development of large CAPE (and attendant vigorous updrafts) and values here are often 1000 joule/kg or less. For storms sufficiently displaced in latitude from the ITCZ to find themselves in large-scale subsidence of the ITCZ but still close enough for adequate moisture supply, the CAPE values may be 1000–3000 joule/kg and the flash rates are substantially greater, 20–60 flashes per minute.

Owing to the high tropical tropopause (16–17 km), the cloud buoyancy is often distributed over a great range in height [29,30]. In the barotropic environment typical of the tropics, the storms grow vertically to great depth but the modest cloud buoyancy often limits the vigour of mixed-phase development (almost always in the range 4.5–10 km altitude) and the associated flash rate. The skinny nature of tropical thunderstorms [38] may well be largely responsible for the high ratio of intracloud to ground lightning which they exhibit [39]. An elevated and narrow main negative charge region (Figure 1.5) may not promote flashes to ground with the same vigour as a broader midlatitude storm.

The often modest CAPE, the high melting level (4.5–5 km) and, in particular, the lack of baroclinity, all contribute to the rarity of severe thunderstorms (hail, wind and tornadoes) in the tropical environment [40]. The hurricane and typhoon are producers of severe wind, but their vertical winds are often quite modest in comparison with ordinary thunderstorms. Lightning is often more prevalent in the outer convective rain bands of a hurricane than in the eyewall region (Figure 1.5).

1.5.3 Midlatitude thunderstorms

At the higher latitudes of the extratropics, the tropopause height is lower – $\sim$12 km in summer – and so thunderstorms are generally less tall than in the tropics. For the same total CAPE, one finds greater cloud buoyancy at midlatitude than in the tropics and larger vertical velocity on average within the mixed-phase region. The squatter clouds at midlatitude (Figure 1.5) with somewhat lower mixed-phase regions probably contribute to the tendency for smaller ratios of intracloud to cloud-to-ground lightning at midlatitude.

The clash of warm and cold synoptic scale air masses is a prevalent phenomenon at midlatitude, and the associated strong baroclinity exerts a strong influence on thunderstorms there. In North America, warm moist air flows northward at low levels from the Gulf of Mexico and cold air aloft streams eastward off the Rocky Mountains to set up extraordinary atmospheric instability, with CAPE values occasionally in the 3000–5000 J/kg range. The combination of strong baroclinity and strong instability set up conditions for giant storms with rotating updrafts called supercells (Figure 1.5). These storms exhibit the largest updrafts, most strongly developed mixed-phase regions and the largest lightning flash rates anywhere in the world. For reasons still not well understood but believed to be linked with mixed-phase microphysics, the most exceptional

of these storms also produce clusters of positive ground flashes in addition to their prodigeous intracloud lightning displays [41,42].

Dry desert regions would appear to be unfavourable for thunderstorm development, but occasionally small storms do develop there. On account of the reduced water vapour in the lower atmosphere, the LCL (and cloud base) for such storms is quite high, and the mixed-phase region dominates the depth of these clouds, as illustrated in Figure 1.5.

1.5.4 Winter thunderstorms

Snowstorms are also the product of a baroclinic atmosphere but in the winter rather than in the summer season. Now the 0°C isotherm is often very close to the Earth's surface and so storm observers are immersed in the mixed-phase region. The winter tropopause is often quite low and the lifting process is often widespread, so winter storms have aspect ratios quite distinct from those of tropical towers (Figure 1.5). On account of Clausius–Clapeyron, the available water vapour in winter is substantially less and this dilutes the mixed-phase activity relative to the usual situation in summer. Nevertheless, the available observations demonstrate that locally intensified convection and riming conditions to form small graupel particles are present when snowstorm lightning occurs. Less vigorous snowstorms which produce predominantly vapour-grown snowflakes (without appreciable riming) are only weakly electrified and rarely (if ever) become thunderstorms.

Lightning discharges are difficult to observe in winter storms because the visibility is so poor. Cloud base often coincides with the earth's surface. As a further consequence, the ratio of intracloud to ground flashes is poorly known. Based on measurements with lightning detection networks, it is well established that ground flashes of positive polarity are relatively more prevalent in the winter than in the summer. The reasons for this behaviour are not well established, and only little is known about the gross charge structure in winter storms [11,43]. These uncertainties and the direct accessibility of the mixed-phase region to ground observers indicate that winter storms are deserving of greater study.

1.6 References

1 SIMPSON, G.C.: 'On the electricity of rain and its origins in thunderstorms', *Philos. Trans. A*, 1909, **209**, pp.379–413
2 WILSON, C.T.R.: 'On some determinations of the sign and magnitude of electric discharges in lightning flashes', *Proc. R. Soc. London*, 1916, **92**, p.555
3 WILSON, C.T.R.: 'Investigations on lightning discharges and the electric field of thunderstorms', *Philos. Trans., A*, 1920, **221**, pp.73–115
4 MARSHALL, T.C., and RUST, W.D.: 'Two types of vertical electrical structures in stratiform precipitation regions of mesoscale convective systems', *Bull. Am. Meteorol. Soc.*, 1993, **74**, pp.2159–2170
5 STOLZENBURG, M., MARSHALL, T.C., RUST, W.D., and SMULL, B.F.: 'Horizontal distribution of electrical and meteorological conditions across the

stratiform region of a mesoscale convective system', *Mon. Weather Rev.*, 1994, **122**, pp.1777–1797
6 JACOBSON, E.A., and KRIDER, E.P.: 'Electrostatic field changes produced by Florida lightning', *J. Atmos. Sci.*, 1976, **33**, p.103
7 KREHBIEL, P.R., BROOK, M., and McCRORY, R.A.: 'An analysis of the charge structure of lightning discharges to ground', *J. Geophys. Res.*, 1979, **84**, p.2432
8 SIMPSON, G.C., and SCRASE, F.J.: 'The distribution of electricity in thunderclouds', *Proc. R. Soc. London*, *Ser. A*, 1937, **161**, pp.309–352
9 SIMPSON, G.C., and ROBINSON, G.D.: 'The distribution of electricity in thunderclouds II', *Proc. R. Soc. London*, *Ser. A*, 1941, **177**, pp.281–329
10 WILLIAMS, E.R., ORVILLE, R.E., and WEBER, M.E.: 'The relationship between lightning type and convective state of thunderclouds', *J. Geophy. Res.*, 1989, **94**, pp.13213–13220
11 BROOK, M., NAKANO, M., KREHBIEL, P., and TAKEUTI, T.: 'The electrical structure of the Hokuriku winter thunderstorms', *J. Geophys. Res.*, 1982, **87**, pp.1207–1215
12 WILLIAMS, E.R.: 'The tripole structure of thunderstorms', *J. Geophys. Res.*, 1989, **94**, pp.13151–13167
13 TEER, T.L., and FEW, A.A.: 'Horizontal lightning', *J. Geophys. Res.*, 1974, **79**, pp.3436–3441
14 MacGORMAN, D.R., FEW, A.A., and TEER, T.L.: 'Layered lightning activity', *J. Geophys. Res.*, 1981, **86**, pp.9900–9910
15 KREHBIEL, P.R., THOMAS, R.J., RISON, W., HAMLIN, T., HARLIN, J., and DAVIS, M.: 'GPS-based mapping system reveals lightning inside storms', *EOS Trans. Am. Geophys. Union*, 2000, **81**, p.21
16 MALAN, D.J., and SCHONLAND, B.F.J.: 'The electrical processes in the intervals between the strokes of a lightning discharge', *Proc. R. Soc. London, Ser. A*, 1951, **206**, pp.145–163
17 BURKE, C.P., and JONES, D.L.: 'On the polarity and continuous current in unusually large lightning flashes deduced from ELF events', *J. Atmos. Terr. Phys.*, 1996, **58**, pp.531–540
18 CUMMER, S.A., and INAN, U.S.: 'Measurement of charge transfer in sprite-producing lightning using ELF radio atmospherics', *Geophys. Res. Lett.*, 1997, **24**, p.1731
19 HUANG, E., WILLIAMS, E., BOLDI, R., HECKMAN, S., LYONS, W., TAYLOR, M., NELSON, T., and WONG., C.: 'Criteria for sprites and elves based on Schumann resonance measurements', *J. Geophys. Res.*, 1999, **104**, pp.16943–16964
20 LIGDA, M.G.H.: 'The radar observation of lightning', *J. Atmos. Terr. Phys.*, 1956, **9**, pp.329–346
21 SHEPHERD, T.R., RUST, W.D., and MARSHALL, T.C.: 'Electric fields and charges near 0°C in stratiform clouds, *Mon. Weather Rev.*, 1996, **920**
22 WILLIAMS, E.R.: 'The positive charge reservoir for sprite-producing lightning', *J. Atmos. Sol. Terr. Phys.*, 1998, **60**, pp.689–692
23 LYONS, W.A., NELSON, T.E., WILLIAMS, E.R., CUMMER, S.A., and STANLEY, M.A.: 'Characteristics of sprite-producing positive cloud-to-ground

lightning during 19th July 2000 STEPS Mesoscale Convective Systems,' *Mon. Weather Rev.*, 2003
24 FRANZ, R.C., NEMZEK R.J., and WINKLER, J.R.: 'Television image of a large upward electrical discharge above a thunderstorm system', *Science*, 1990, **249**, pp.48–51
25 SENTMAN, D.D., and WESCOTT, E.M.: 'Observations of upper atmosphere optical flashes recorded from an aircraft', *Geophys. Res. Lett.*, 1993, **20**, p.2857
26 LYONS, W.A.: 'Low light video observations of frequent luminous structures in the stratosphere above thunderstorms', *Mon. Weather Rev.*, 1994, **122**, pp.1940–1946
27 WILLIAMS, E.R., 'Sprites, elves and glow discharge tubes', *Physics Today*, 2001, **November**, pp.41–47
28 BOCCIPPIO, D.J., WILLIAMS, E.R., HECKMAN, S.J., LYONS, W.A., BAKER, I., and BOLDI, R.: 'Sprites, ELF transients and positive ground strokes', *Science*, 1995, **269**, pp.1088–1091
29 WILLIAMS, E.R., and RENNO, N.O.: 'An analysis of the conditional instability of the tropical atmosphere', *Mon. Weather Rev.*, 1993, **121**, pp.21–36
30 WILLIAMS, E.R.: 'Meterological aspects of thunderstorms', *in* VOLLAND, H. (Ed.): 'CRC handbook on atmospheric electrodynamics' (CRC Press, Boca Raton, Florida, 1995), vol. I, pp.27–60
31 LYONS, W.A., NELSON, T.E., WILLIAMS, E.R., CRAMER, J.A., and TURNER, T.R.: 'Enhanced positive cloud-to-ground lightning in thunderstorms ingesting smoke from fires', *Science*, 1998, **282**, pp.77–80
32 ORVILLE, R.E., and HENDERSON, R.W.: 'Global distribution of midnight lightning: September 1977 to August 1978', *Mon. Weather Rev.*, 1986, **114**, pp. 2640–2653
33 LUCAS, C., ZIPSER, E.J., and LEMONE, M.A.: 'Convective available potential energy in the environment of oceanic and continental clouds: correction and comments', *J. Atmos. Sci.*, 1994, **51**, pp.3829–3830
34 WILLIAMS, E., and STANFILL, S.: 'The physical origin of the land-ocean contrast in lightning activity', *Comptes Rendus Physique*, 2002, **3**, pp. 1277–1292
35 WILLIAMS, E.R., ROSENFELD, D., MADDEN, N., GERLACH, J., GEARS, N., ATKINSON, L., DUNNEMANN, N., FROSTROM, G., ANTONIO, M., BIAZON, B., CAMARGO, R., FRANCA, H., GOMES, A., LIMA, M., MACHADO, R., MANHAES, S., NACHTIGALL, L., PIVA, H., QUINTILIANO, W., MACHADO, L., ARTAXO, P., ROBERTS, G., RENNO, N., BLAKESLEE, R., BAILEY, J., BOCCIPPIO, D., BETTS, A., WOLFF, D., ROY, B., HALVERSON, J., RICHENBACH, T., FUENTES, J., and AVELINO, E.: 'Contrasting convective regimes over the Amazon: implications for cloud electrification', *J. Geophys. Res.*, 2002, LBA Special Issue 107 (D20), 8082, doi 1029/2001JD000380
36 VONNEGUT, B.: 'Some facts and speculations regarding the origin and role of thunderstorm electricity', *Meteorol. Monogr.* **5**, 1963, pp.224–241

37 WILLIAMS, E., BOLDI, R., MATLIN, A., WEBER, M., GOODMAN, S., BUECHLER, D., HODANISH, S., and SHARP, D.: 'The behavior of total lightning in severe Florida thunderstorms', *J. Atmos. Res.*, 1999, **51**, pp.245–265
38 WILLIAMS, E.R., RUTLEDGE, S.A., GEOTIS, S.G., RENNO, N., RASMUSSEN, E., and RICKENBACH, T.R.: 'A radar and electrical study of tropical hot towers', *J. Atmos. Sci.*, 1992, **49**, pp. 1386–1395
39 RUTLEDGE, S.A., WILLIAMS, E.R., and KEENAN, T.D.: 'The down under Doppler and electricity experiment (DUNDEE): overview and preliminary results', *Bull. Am. Meteorol. Soc.*, 1992, **73**, pp.3–16
40 BARNES, G.: 'Severe local storms in the tropics', *in* DOSWELL, C.A. III (Ed.): 'Monograph on severe convective storms', American Meteorological Society, 2001, pp. 359–432
41 MACGORMAN, D.R. and BURGESS, D.W.: 'Positive cloud-to-ground lightning in tornadic storms and hailstorms', *Mon. Weather Rev.*, 1994, **122**, pp.1671–1697
42 STOLZENBURG, M.: 'Observations of high ground flash densities of positive lightning in summer thunderstorms', *Mon. Weather Rev.*, 1994, **122**, pp.1740–1750
43 TAKAHASHI, T., TAJIRI, T., and SONOI, Y.: 'Charges on graupel and snow crystals and the electrical structure of winter thunderstorms', *J. Atmos. Sci.*, 1999, **56**, pp.1561–1578
44 WILLIAMS, E.R.: 'The electrification of severe storms', *in* DOSWELL, C.A. III (Ed.) 'Monograph on severe connective storms', American Meteorological Society, 2001, pp. 527–561
45 ROSENFELD, D.: Personal Communication, 1998

Chapter 2

Thunderstorm electrification mechanisms

Rohan Jayaratne

2.1 Introduction

The origin of thunderstorm electrification has long been an unsolved problem in atmospheric physics. Despite a number of simulated laboratory experiments, together with the vast amount of field data collected over the past few decades, our knowledge of how these convective cloud masses get charged still remains sparse at the microphysical level.

Sir John Mason in the Bakerian Lecture [48] identified thunderstorm electrification as one of the three leading unsolved problems in cloud physics. He had this to say about the problem:

> This is, for me, the most intriguing and challenging problem in cloud physics, with a strong incentive to understand one of the most spectacular of natural phenomena, but made all the more interesting by the fact that the search for a continuing solution has led us into a number of rather difficult areas of classical physics, and to a deeper study of the fundamental properties of water and ice.

A satisfactory theory must be able to explain all of the observed electrical characteristics of a typical thunderstorm. Such a list of requirements, first drawn up by Mason [47] and later extended by Moore and Vonnegut [50], is as follows:

a For lightning to occur, the cloud depth must be greater than 3–4 km. Very tall thunderclouds produce far more frequent lightning than those of ordinary height.
b Although lightning may occur in warm clouds, strong electrification is not observed unless the cloud extends above the freezing level.
c Highly electrified regions of thunderstorms almost always coincide with the coexistence of ice and supercooled water.
d Strong electrification occurs when the cloud exhibits strong convective activity with rapid vertical development.

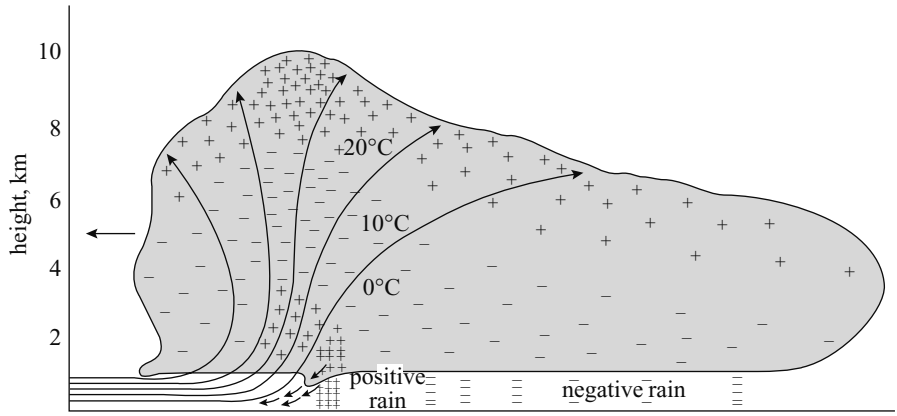

Figure 2.1 *The classical tripolar charge structure of a thunderstorm* (Simpson and Scrase [63])

e The charge generation and separation processes are closely associated with the development of precipitation, probably in the form of soft hail. Lightning generally originates in the vicinity of high-precipitation regions.

f The first lightning stroke very often occurs within 12–20 min of the appearance of precipitation particles of radar-detectable size. The initial rate of electrification has a time constant of about two minutes.

g The average duration of precipitation and electrical activity from a single thunderstorm cell is about 30 minutes.

h The location of the charge centres appear to be determined by temperature and not height above the ground. The main negative charge centre is generally located between the $-5°C$ and $-25°C$ isotherms with the main positive some km higher up. There is a small pocket of positive charge below the main negative centre, close to the freezing level, that appears to be associated with the precipitation shaft (Figure 2.1).

i In the mature stage of a storm, electric fields as high as $400\,\mathrm{kV\,m^{-1}}$ may occur, giving rise to a flash rate of several per minute requiring an average charging current of the order of 1 A. The required charging rate is about $1\,\mathrm{C\,km^{-3}\ min^{-1}}$.

j The average electric moment destroyed in a lightning flash is about 100 C km; the corresponding charge being 20–30 C.

k The dipole destroyed by the flash may depart from the vertical in some cases by as much as 90°.

These requirements suggest strongly a fundamental role for an ice-based precipitation mechanism of thunderstorm electrification. There have been reports of lightning from clouds everywhere warmer than 0°C [50,54,51] but these observations have been rare and the electrification very weak. The overwhelming observational evidence seems to favour a mechanism closely related to the presence of ice within clouds. The key

points of this evidence have been aptly summarised by Williams [72] and are essentially in line with the list of requirements above.

Over the past several decades, a number of mechanisms have been proposed to explain these observed features. Most of these have had to be discarded owing to various difficulties. In this Chapter, we shall look at each of these mechanisms in turn and discuss their merits and demerits in terms of the results from laboratory experiments and field observations.

2.2 The suggested mechanisms

2.2.1 The inductive mechanism

The inductive mechanism was one of the first theories of thunderstorm electrification and has proved to be very popular even up to the present day. It was first proposed by Elster and Geitel [18] in 1913 and has been modified by several workers since then. Figure 2.2 shows a schematic representation of their model. A water drop falling through the vertical electric field region of a thundercloud has oppositely polarised charges at its top and underside. In a downward directed electric field, that is with the positive charge above the negative in the cloud, the underside of the drop will carry a positive charge. Smaller droplets rebounding off the lower half of the drop will remove some of this positive charge which will get swept up to the top of the cloud to augment the upper positive charge centre, leaving the falling drop with a net negative charge which will be transported to the base of the cloud to enhance the lower negative charge. This provides a positive feedback mechanism that will enhance the existing electric field. The theory was later extended to ice particles by Muller-Hillebrand [52] and Latham and Mason [38]. Here, the heavier hailstones will fall with respect to the lighter ice crystals which are usually swept to the top of the

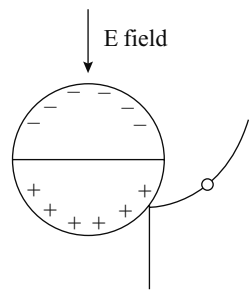

Figure 2.2 Schematic representation of the inductive charging mechanism. Charge polarisation occurs on the larger particle in the external electric field. During a rebounding collision, a smaller particle removes some of the positive charge from the lower half of the larger particle and is swept up in the air currents. The larger particle falls with a net negative charge. Both particles move in directions that reinforce the external electric field

cloud. The above workers calculated the magnitude of the charge separated when two spherical particles interacted in a given electric field in terms of their radii, time of contact and point of impact. Several workers have since shown that it is possible to account for the observed electric fields in thunderstorms within the required time intervals in terms of the inductive mechanism [57,53,77,61,14]. These models have been based on the three possible combinations of cloud particle interactions: water–water, water–ice and ice–ice. However, each of these cases has strong limitations, as we shall discuss now.

In the water–water case, a droplet colliding with a larger drop is more likely to coalesce than rebound. This is even more likely in an external electric field. Jennings [34] showed that the probability of coalescence tends to one in the presence of electric fields greater than about $25\,\mathrm{kV\,m^{-1}}$. A similar problem limits the efficiency of the water–ice case. A supercooled water droplet colliding with a falling hailstone is far more likely to freeze on impact than to rebound. Aufdermaur and Johnson [1] showed that not more than 1 in 100 droplets bounce off and these are the droplets that make grazing collisions off regions of the hailstone where there are very few polarised charges to give a significant charge separation. Further, as the hailstone acquires a net charge, the electrical equator will move down. Droplets making grazing collisions may now remove the opposite charge from the regions above the electrical equator – a process that will oppose the positive feedback to the electric field. There is also the strong possibility of a rebounding droplet subsequently coalescing with another hail pellet, placing a further limit on the amount of charge that may be transferred to the top of the cloud.

Many workers have attempted to test the ice–ice-based inductive mechanism experimentally. Latham and Mason [38] showed that two ice particles brought into contact with each other for various time intervals in an electric field separated charges in accordance with the theory. However, the bouncing collisions did not yield satisfactory results. No appreciable charge transfers were found when ice crystals were made to bounce off a cylindrical ice target at speeds up to $30\,\mathrm{m\,s^{-1}}$ in electric fields up to $70\,\mathrm{kV\,m^{-1}}$. Aufdermaur and Johnson [1] impacted frozen water drops on an ice covered target and found charges of 50 fC per collision, but this value was not affected by the electric field raising some questions as to the source of the charging process. Gaskell [21] showed that the charge separated was significantly less than that predicted under the conditions used and attributed it to the short contact times between the two particles. For a reasonable amount of charge to be transferred, the time of contact must be of the same order as the relaxation time for the redistribution of charge. Gross [24] showed that, for pure ice, the relaxation time was significantly longer than the estimated contact times in ice–ice collisions. Illingworth and Caranti [27] found that, in general, the conductivity of pure ice was too low for a complete charge transfer during the contact times available. Brooks and Saunders [7] showed that when the impacting ice particles were replaced by conducting metal spheres, the mean charge separated was appreciably larger. They attributed this to the shorter relaxation times in metals over ice. Also, most of these experiments have been conducted using radial fields around the larger particle. Experimental conditions make it difficult to produce a vertical electric field across a particle while smaller particles fall vertically to

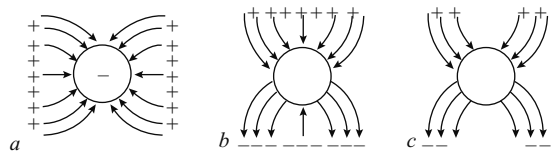

Figure 2.3 Problems encountered due to various electrode configurations in laboratory studies of the inductive charging mechanism. The smaller particle falls or is sucked by the air moving vertically downwards through a tube and is more likely to make a glancing collision at the equator of the target

- *a* the electric field is applied between the target and the walls of the tube; this leads to an unrealistically high field at the equator of the target
- *b* horizontal plate electrodes best represent natural thunderstorm fields but make it impossible to allow the particle to interact with the target
- *c* leaving gaps in the plates allows the particle to fall through but again leads to a distortion of the field, enhancing the fields at the equator

impact on it. The radial configuration creates unrealistically large electric fields near the electrical equator of the larger particle – where smaller particles are most likely to make contact. Figure 2.3 illustrates this problem schematically.

The main difficulty in accepting the inductive mechanism has been with respect to field observations of particle charges and electric fields. The theory predicts a maximum charge that a particle of a particular size may acquire in a given electric field. However, measured charges on precipitation particles are often much too large to be explicable in terms of the inductive mechanism [23,45]. The inductive mechanism requires the recovery of the electric field between lightning flashes to be exponential. However, Winn and Byerley [74] using instrumented balloons in New Mexico thunderstorms found that the recovery was linear and thus not proportional to the existing electric field. The theory also fails to explain the temperature dependence of the location of the main negative charge centre. Krehbeil *et al*. [35] showed that the temperature at the negative charge centre is restricted to a narrow range within thunderstorms forming over various climatic conditions and geographical locations (Figure 2.4).

The inductive mechanism is attractive because it is simple but in view of the above difficulties it is hard to imagine how it may operate as a viable charge generation mechanism in thunderstorms.

2.2.2 The convective mechanism

First proposed by Grenet [25] and later extended by Vonnegut [70], the convective mechanism has for many years been the foremost nonprecipitation-based theory of thunderstorm electrification. The theory is based on the vertical transport of atmospheric ions by the strong updraughts inside thunderstorms and by the compensating

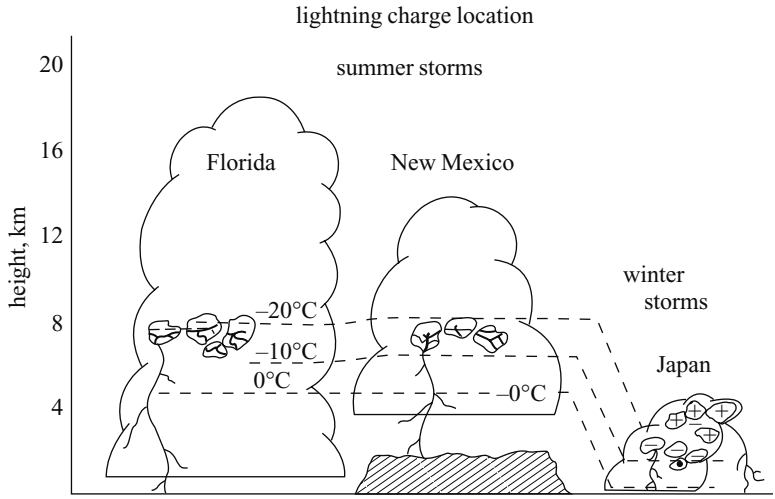

Figure 2.4 *Schematic representations of the vertical locations of charge sources giving rise to lightning in storms at three different locations – Florida, New Mexico and in wintertime in Japan. Note that the charge centres are correlated with temperature and not altitude* (Krehbeil *et al*. [35])

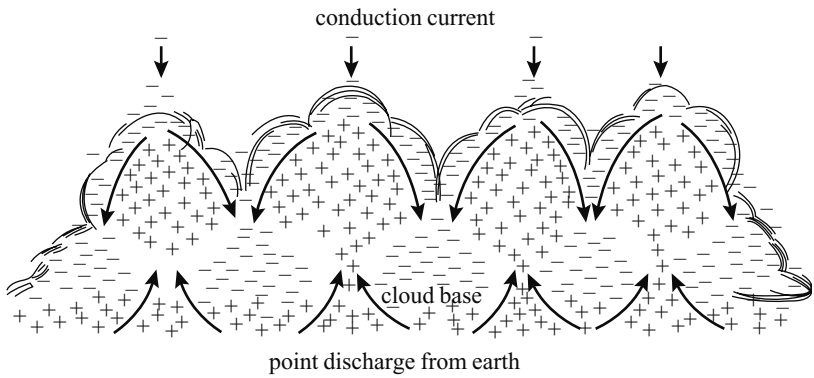

Figure 2.5 *Schematic diagram illustrating the convective charging mechanism* (Vonnegut [71])

downdraughts outside. The basic features of the theory are schematically illustrated in the idealised sketch shown in Figure 2.5 after Vonnegut [71]. It supposes that positive ions released by point discharge at the ground are carried into the cloud and towards the cloud top by the updraughts. There, these charges attract small negative ions to the cloud's upper surface from the clear upper atmosphere. The negative ions rapidly become immobilised by attachment to cloud particles which are caught up in

the downdraughts and transported to the lower part of the cloud. This causes more positive ions to be produced by point discharge at the ground, thus leading to a positive feedback mechanism.

Wormell [76] points out that the concentration of ions present around a thundercloud is insufficient to account for the observed rate of regeneration of charge within the cloud. Standler and Winn [64] showed that the total point discharge current by itself is too small to account for the observed lightning currents and that the resulting positive space charge does not form a deep vertical column from the ground up to the cloud but rather a layer of thickness 100–200 m near the ground. Chalmers [13] has questioned the validity of the theory on the grounds that the updraughts should carry not just the positive charges but also the negative charged particles that have been transported in the downdraughts. There has also been some concern regarding the time frame of the process. Point discharge currents do not occur until the electric field at the ground has built up to about 800 V m^{-1}. By this time, the electric fields within the cloud are high enough to give rise to lightning. Further, the resulting positive ions take a considerable time to reach the cloud. Thus, the theory fails to explain the initial electrification of the cloud.

2.2.3 The selective ion capture theory

Wilson [73] suggested that a raindrop polarised in a vertical electric field may acquire a net charge by a selective ion capture process. For example, a raindrop falling through a downward directed electric field would be polarised in such a way that it would attract negative ions while repelling positive ions from its lower half. The drop would, thus, gain a net negative charge and carry this down to enhance the ambient electric field. However, there is a limit to which the drop can be charged in this manner. Once it has acquired a large enough negative charge, it will begin to repel negative ions away from its vicinity. Moreover, if the mobility of the ions in the ambient electric field is too high, they will not be captured by the falling drop. This imposes a constraint on the maximum electric field at which the mechanism can be viable. For a raindrop falling at a terminal velocity of 8 m s^{-1} past small ions of mobility 1.5 cm^2 s^{-1} V^{-1}, this maximum electric field is about 50 kV m^{-1}. There is a further difficulty in that, as Wormell [76] has pointed out, the concentration of ions in the atmosphere may not be sufficiently high. Thus, although this mechanism is thought to be partly responsible for bringing down some of the ions that may have otherwise been swept up to the top of the cloud, it falls far short of accounting for the large electric fields and charge centres present in thunderstorms.

2.2.4 Drop breakup theory

An uncharged water drop suspended in a downward directed electric field will be polarised in such a way that its lower hemisphere will carry a positive charge while the upper hemisphere will be negative. If the drop were to break up along its equator, the two resulting droplets would carry roughly equal and opposite charges. It can be shown that a drop of diameter 6 mm, breaking up in an electric field of 500 V cm^{-1},

would produce two fragments with about 0.3 nC each or a charge density of about $0.3\,\mathrm{nC\,g^{-1}}$ of ruptured water. This is equivalent to a cloud charge density of about $1\,\mathrm{C\,km^{-3}}$ if the liquid water content is $5\,\mathrm{g\,m^{-3}}$ [55]. Matthews and Mason [49] show that the charge separated increases with electric field and that the larger fragment generally carries the positive charge. They conclude that the process may explain the formation of the lower positive charge centre in thunderstorms. A major problem with this theory is that large drops do not break up very easily unless they are involved in a collision with another drop. Moreover, the drops are not always likely to break up at the equator, thus reducing the expected amount of charge that may be separated.

2.2.5 Melting of ice

Dinger and Gunn [16] showed that when ice melts it acquires a net positive charge. This was later confirmed by Drake [17]. Iribarne and Mason [28] showed that the charge is separated by tiny air bubbles in the ice bursting at the surface during the melting process. The minute droplets produced by the bursting bubbles remove a negative charge leaving the ice positive. The mechanism was attributed to an electric double layer at the water/air interface which gives rise to the excess of negative ions at the surface. Electric charges up to about $2\,\mathrm{nC\,g^{-1}}$ of melted water were found depending on the bubble content of the ice. Mason [48], assuming a charge concentration of $0.7\,\mathrm{nC\,g^{-1}}$ of melted water from millimetre-sized graupel in an ice concentration of $2\,\mathrm{g\,m^{-3}}$, estimated a spatial charge concentration of approximately $1\,\mathrm{C\,km^{-3}}$ and suggested that this may explain the lower positive charge centre in a thundercloud. Indeed, the lower positive charge centre appears to be closely associated with the melting layer in many instances [62] but there are cases where it has been observed well above this level [39,45,42,65]. Moreover, the polarity of the charge separation in the melting process is the wrong way around to account for the positive charge accumulations near the freezing level that appear to be widespread in stratiform regions with radar bright bands at or below this level.

2.2.6 The Workman–Reynolds effect

Workman and Reynolds [75] observed that an electric double layer was set up across the ice–liquid interface during the freezing of dilute aqueous solutions. The sign and magnitude of the potential was found to be sensitive to the nature and concentration of the solute. Distilled water showed negligible effects. The potential appeared during the progress of the freezing front and disappeared soon after the freezing ended. The effect was attributed to the selective incorporation of ions from the liquid into the ice during freezing; the ice attained a negative potential with respect to most solutes, ammonium salts being a notable exception. During the freezing of 5×10^{-5} N solution of ammonium hydroxide the ice acquired a potential of +240 V with respect to the liquid and a 10^{-4} N solution of sodium chloride gave a corresponding potential of about −30V. The sensitivity to solute concentration was apparent when a sodium chloride solution of 5×10^{-4} N hardly showed any effect.

It is well known that hail pellets are warmer than their environment owing to the latent heat released by the accretion of supercooled water droplets. As a hail pellet

falls towards the base of the cloud, if the cloud water content is high enough, the latent heat acquired may be sufficient to raise its temperature to 0°C. The pellet will begin to melt and carry a sizable water skin at its surface. It is then said to be in a state of wet growth. Workman and Reynolds suggested that, when this water skin became thick enough, the pellet would shed some of the water as it fell through the cloud. Considering the nature and concentration of chemical impurities present in cloud water, the potential difference at the ice–water interface would ensure that the water flung off was positively charged, leaving the pellet with a net negative charge. Subsequent gravitational separation would result in the observed dipolar charge distribution within the thundercloud.

The difficulty with this mechanism is that it can occur only at temperatures close to 0°C. The cloud water content present in a typical thunderstorm at colder temperatures is insufficient to raise the temperature of graupel pellets to ensure wet growth. Reynolds *et al*. [56] showed that the mechanism was inadequate to account for negative charge centres at temperatures colder than about −16°C.

2.2.7 The thermoelectric effect

The mobility of the H^+ ions in ice is much greater than that of the OH^- ions and they both increase with temperature. In a block of ice with a temperature gradient down its length, the warmer end would acquire a net negative charge due to the faster diffusion of H^+ ions away from that end. If two pieces of ice at different temperature were brought into momentary contact they would separate with the warmer carrying a net negative charge. Latham and Mason [36] calculated that a potential difference of about $2\Delta T$ mV would be set up across the ends of a piece of ice having a steady temperature difference of ΔT°C. Several simulated laboratory experiments have been conducted with small ice particles in the form of vapour-grown ice crystals or frozen droplets made to bounce off an artificially warmed ice target [56,37,43,32,6].

In all these experiments, the warmer ice particle acquired the negative charge. However, a major drawback to the thermoelectric effect theory is that the concentration of ions in ice is grossly inadequate to explain the observed charge separation during interactions between ice particles. The magnitudes of charge transfer observed in the simulated experiments cannot be explained in terms of the Latham and Mason calculations based on the known concentrations of ions in ice.

2.2.8 Surface potential theories

Takahashi [67] used a vibrating capacitor method to determine the surface electrical potential of an ice surface under various conditions. When the ice was warmed to form a thin liquid film on its surface, it acquired a negative potential of −100 mV with respect to a dry surface. He explained the observation as follows: H^+ and OH^- ions are more concentrated in water than in ice because of their different activation energies. At the same time, H^+ ions have a greater mobility than OH^- in ice and so will diffuse more readily from the water into the ice. He calculated a potential of −150 mV for the water with respect to ice, in fair agreement with experiment.

Takahashi suggested that this mechanism may explain how hailstones in wet growth become positively charged in the lower regions of thunderstorms.

Takahashi [66] also used this technique to measure the surface potential of an ice surface rubbed with another piece of ice or with a planer. He noted a negative potential which increased to about −200 mV on the surface being rubbed. He suggested that pairs of negatively charged dislocations and positively charged D-defects were produced at the point of rubbing. D-defects diffused faster than the dislocations into the ice due to their greater mobility, leaving the surface with a net negative charge.

Using an ionisation method, Takahashi [68] observed that, in ionised air, a sublimating ice surface acquires a negative charge and a growing one becomes positively charged with a potential difference of about 200 mV between the two cases. Caranti and Illingworth [10] repeated this experiment and failed to detect any difference in surface potential between a sublimating and growing ice surface. However, they reported a very large effect during riming where the rimed surface acquired a potential of a few hundred mV with respect to an unrimed ice surface. The potential increased as the temperature decreased reaching a saturation value of about −400 mV at −15°C.

Buser and Aufdermaur [9] bounced frozen droplets off an ice target and concluded that the target charged negatively if it was sublimating and positively if it was growing from the vapour. This observation has subsequently been confirmed by several others [43,22,32,6,12]. Figure 2.6 shows a result obtained by Baker *et al*. [6] where a cloud of vapour-grown ice crystals was drawn past a stationery ice target in a wind tunnel. When the target was artificially warmed with respect to the air, it charged negatively and when it was cooled it charged positively. Caranti *et al*. [12] impacted frozen ice spheres of diameter 100 μm at a speed of 8 m s^{-1} on an ice target at various

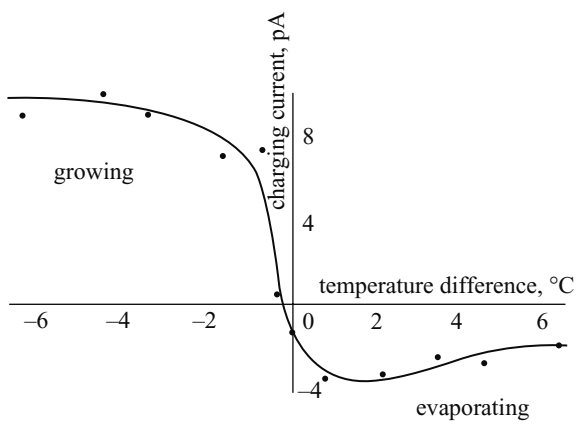

Figure 2.6 *The charging current I to an ice target as a function of temperature difference ΔT between the target and a cloud of ice crystals. Ambient temperature = −10°C; impact speed = 15 m s^{-1}. The warmer target was sublimating and charged negatively. The colder target was growing and charged positively* (Baker *et al*. [6])

air temperatures. They noted that the target charged increasingly positive as it was cooled below the environmental temperature (Figure 2.7). An ice target warmed above its ambient temperature will be in a state of sublimation. Even in a supersaturated environment it is necessary to warm it by just 1°C at −10°C and 2°C at −20°C to make it sublimate. Thus, it follows that the negative charging of a warmed ice target exposed to rebounding collisions with ice crystals may be a consequence of its surface state and not temperature. Jayaratne [29] performed a series of experiments and showed that the sign of charging was not controlled by the temperature difference between the two ice particles nor the direction of the temperature gradient in the ice on the target. Baker *et al*. [6] suggested that the sign was controlled by the relative growth rates of the two particles with the faster growing particle acquiring the positive charge.

2.2.9 The quasiliquid layer theory

Theoretical and experimental studies have shown that ice in equilibrium with the vapour has a disordered quasiliquid layer at the ice–vapour interface. The thickness of this layer increases with temperature and also with growth rate from the vapour [15]. Baker and Dash [4] proposed an explanation for the relative growth rate dependence of charge transfer between colliding ice particles based on this phenomenon. Fletcher [19] showed that it was energetically favourable for water molecules in the liquid close to the water–vapour interface to orient themselves with the H^+ ions pointing towards the vapour side. Such a preferred dipolar orientation would result in a drift of free negative ions towards the liquid–vapour interface in order to equalise the potential difference. Thus, ice would carry a net negative charge in the quasiliquid layer. Baker and Dash [5] modified their hypothesis somewhat by suggesting that segregation effects at the solid–liquid interface may be more important than the dipolar orientation effect at the liquid–vapour interface. In general, if the molecular orientations near the solid–liquid interface were such as to provide a net negative charge at this interface, this negative charge would diffuse into the more polarisable liquid. Although the origin was different, each of the hypotheses could plausibly explain the presence of a net negative charge in the quasiliquid layer on ice.

During the impact and separation of two ice particles it seems reasonable to assume that some mass would be exchanged between the quasiliquid layers of the two particles. In general, mass would flow from the thicker layer (or the layer with the higher chemical potential) to the thinner (the layer with the lower chemical potential). Since the thickness of the quasiliquid layer increases with temperature, the particle at the higher temperature would lose mass and negative charge to the colder particle and acquire a net positive charge. Further, the thickness of the layer increases with growth rate, so that the particle that was growing faster from the vapour would lose mass and negative charge to the slower-growing particle and acquire a net positive charge. In the absence of any riming, ice particles growing from the vapour are slightly warmer than the environment due to the release of latent heat from the sublimating vapour. Similarly, sublimating ice particles are slightly colder than the environment owing to the latent heat carried away by the vapour. Thus, the Baker–Dash hypothesis

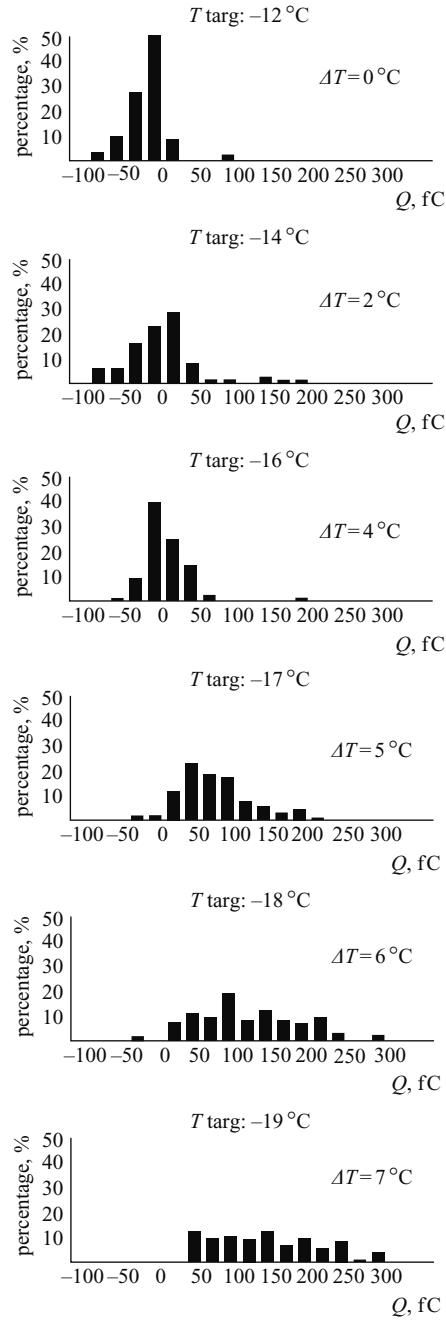
T targ: –12 °C
ΔT = 0 °C
T targ: –14 °C
ΔT = 2 °C
T targ: –16 °C
ΔT = 4 °C
T targ: –17 °C
ΔT = 5 °C
T targ: –18 °C
ΔT = 6 °C
T targ: –19 °C
ΔT = 7 °C
percentage, %
10
20
30
40
50
–100 –50 0 50 100 150 200 250 300
Q, fC

was to explain the observed sign of charge transfer in each of the possible combinations where the two interacting ice particles were growing/sublimating, fast-growing/slow-growing and fast-sublimating/slow-sublimating. However, it should be noted that when one of the ice particles was cooled with respect to the ambient temperature and the other particle, it acquired a positive charge during the interaction. Similarly, an artificially warmed target acquired a negative charge. This suggests that the surface state of the particles was having a dominant effect on the thickness of the quasiliquid layer over the temperature. Although it has not been experimentally established as yet, recent studies by Jayaratne [29] and Mason and Dash [46] indeed suggest that the sign of the charge transfer is overwhelmingly controlled by the relative growth rates between the two particles rather than temperature differences.

Supercooled water has a higher vapour pressure than ice at the same temperature. Thus the two cannot remain in equilibrium and in clouds both graupel and ice crystals will grow at the expense of the droplets. When a supercooled droplet comes into contact with and accretes on to a graupel pellet, the temperature of the droplet will initially shoot up to 0°C and then remain there until it has completely frozen, whence it will cool to the temperature of the graupel. During the time when it is at 0°C, a freezing droplet forms an intense vapour source bathing the surrounding dry graupel surface which will grow rapidly by vapour diffusion. Although ice crystals grow from the vapour supplied by the supercooled droplets in the cloud, areas around freezing droplets on the graupel surface will grow not only from the supercooled cloud droplets but also from the vapour supplied by the freezing droplets at 0°C (Figure 2.11). Baker *et al*. [6] showed that this latter term is expected to be dominant over a distance of several droplet diameters around a freezing droplet. Ice crystals bouncing off these rapidly growing areas are likely to charge the graupel positively in accordance with the Baker *et al*. hypothesis. If the cloud water content is high enough, riming may produce sufficient latent heat to warm the graupel surface sufficiently to cause sublimation. However, since droplets freeze at 0°C, whatever the surface temperature of graupel, the areas around freezing droplets would still be growing. Thus, on a graupel surface during riming, the expected picture would be many annular growing regions on an overall sublimating surface. It is interesting to note that Caranti *et al*. [12] found charging events of both signs at any given temperature (Figure 2.7). The probability of an ice crystal encountering a rapidly growing annular region around a freezing droplet is greater at higher cloud water contents because there will be more such sites. It will also be greater at higher temperatures because droplet freezing times decrease rapidly with decreasing temperature. Thus,

---

Figure 2.7 *Histograms showing the percentage of charging events of each sign and magnitude when an ice sphere of diameter 100 μm impacted at a speed of 8 m s^{-1} on an ice target that was cooled with respect to the ambi-ent temperature of $-12°C$. The target charged mostly negatively at first but became increasingly positive as it was cooled towards $-19°C$* (Caranti *et al*. [12])

the higher the temperature the better the chance of an impacting crystal finding an annular area around a still freezing droplet and charging the graupel positively. The Baker *et al*. hypothesis is therefore able to explain the dependence of charge sign on temperature and cloud water content observed by Jayaratne *et al*. [32]. There are some minor discrepancies in different studies. For example, Takahashi [69] and Saunders *et al*. [60] found positive charging of graupel at low temperatures at low cloud water contents. Saunders and Peck [58] have attempted to explain these observations in terms of the Baker *et al*. hypothesis by considering the increased growth rate of the graupel surface owing to the reduced latent heat available from fewer droplets present at lower cloud water contents. Figure 2.12 compares the results of Jayaratne *et al*. [32], Takahashi [69], Brooks *et al*. [8] and Saunders and Peck [58], and shows that in all studies using clouds of ice crystals and supercooled droplets interacting with a graupel pellet, we see an overall pattern where the graupel is more likely to charge positively when the temperature or the cloud water content is high and negatively when these parameters are low in accordance with the Baker *et al*. hypothesis.

2.2.10 Charging due to the fragmentation of ice

Caranti *et al*. [12] studied individual collisions between 100 μm diameter ice spheres and an ice target growing by vapour diffusion and showed that most charging events were accompanied by tiny frost fragments that were breaking off the target surface. The sign of charge acquired by the target was increasingly positive as its temperature was progressively decreased below ambient (Figure 2.7). The growing frost tips would be warmer than the substrate due to the latent heat generated at such points. This would give rise to an inwardly directed temperature gradient along frost fibres on the target surface. Caranti *et al*. suggested that breaking these protuberances across the temperature gradient would separate charge with the colder side, which would be the target in this case, acquiring the positive charge. They showed that reversing the temperature gradient reversed the charging sign as expected. Here, warming the target internally led to sublimation of the frost tips which cooled with respect to the substrate due to the latent heat released on sublimation. The sign of the charge transfer observed was explicable in terms of the thermoelectric theory but, as had been shown before, the observed magnitude of the charge separated was too high to be explained in terms of the theory. Caranti *et al*. proposed a modified hypothesis based on the breaking of hydrogen bonds in ice during the fracture process. It was assumed that the protons tunnelling back and forth across a double potential well in the temperature gradient had a slightly higher probability of remaining on the colder side as the fracture progressed, resulting in the observed sign of charge separation. Using a simplified calculation, they showed that the process could account for the magnitude of the charge observed.

Caranti *et al*. showed that the fragments breaking off were in fact carrying an equal and opposite charge to that acquired by the target. There seemed no doubt that their 100 μm ice spheres impacting at a speed of 8 m s^{-1} were capable of breaking frost fragments off the target. However, charge is transferred in experiments where

the impacting particles are ice crystals no larger than 10 μm. These have much lower energy than the 100 μm ice spheres used by Caranti *et al*. and are quite unlikely to break any fragments. Griggs and Choularton [26] showed experimentally that frost and rime protuberances on ice can be surprisingly strong. Glass beads of diameter 485 μm required a minimum speed of about 20 m s^{-1} to fracture even the most fragile of the rime deposits studied. Frost deposits grown on a target fractured more easily but still required beads of diameter 485 μm at speeds of 4–6 m s^{-1}. Jayaratne *et al*. [33] detected no ice fragments when they impacted frost or rime-covered targets with small ice crystals of size 10–20 μm and light lycopodium spores. However, when these particles were replaced with 250 μm grains of sand, many fragments were observed. They concluded that, although it may occur, fragmentation was not a necessary requirement for charge transfer during ice–ice collisions.

2.3 Riming experiments

The Baker *et al*. hypothesis successfully explains the sign of the charge transfer between two interacting ice particles in terms of their relative growth rates in the absence of riming. Experiments where the target was allowed to rime at the same time require further explanation.

The first simulated riming experiment was conducted by Reynolds *et al*. [56]. They whirled an ice-covered metal sphere through a cloud of supercooled droplets and ice crystals in a chest freezer which could be cooled down to −25°C. The sphere acquired an electric charge that was negative when the cloud water content was high and positive when it was low. In the latter case, the sign could be reversed to negative by heating the sphere with a lamp.

Takahashi [69] whirled a 3 mm diameter rod through a cloud of supercooled droplets and vapour-grown ice crystals at a speed of 9 m s^{-1} and showed that the sign and magnitude of the charge acquired by the rod was controlled by the temperature and the cloud water content (Figure 2.8). At temperatures higher than about −10°C the rod charged positively at all cloud water contents. At lower temperatures, the sign was positive at high and low cloud water contents but negative in an intermediate range as shown in the Figure. In a similar study, Jayaratne *et al*. [32] showed that a simulated graupel pellet subject to ice crystal interactions charged positively at higher temperatures and higher cloud water contents and negatively at lower temperatures and lower cloud water contents (Figure 2.9). At a cloud water content of 1 g m^{-3}, the charge sign reversal temperature was about −20°C. Baker *et al*. [6] extended this study down to −35°C and found a charge sign reversal temperature of −18°C (Figure 2.10). It is clear from Figure 2.9 that the reversal temperature was higher at lower cloud water contents. At 0.2 g m^{-3} the reversal temperature was close to −10°C. These observations were used to explain the existence of the classical tripolar charge structure in thunderclouds [63]. At temperatures higher than the reversal temperature, graupel would acquire a net positive charge and the rebounding crystals would carry the negative charge in the updraughts. In the upper parts of the cloud at lower temperatures, the crystals would carry a positive charge to the top of the

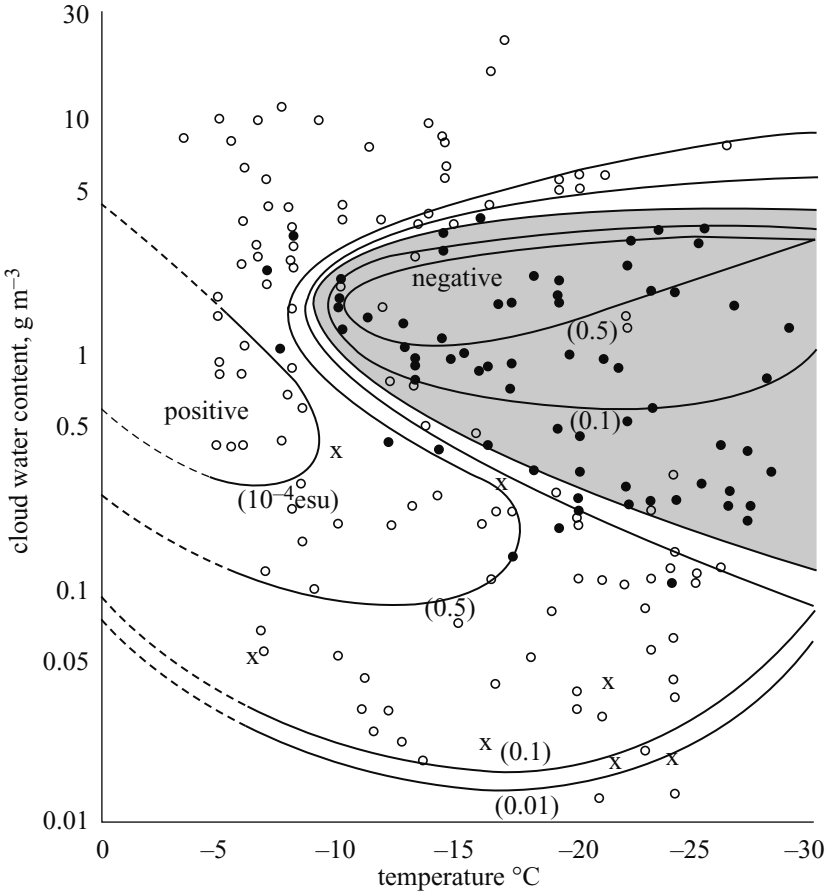

Figure 2.8 *The charge acquired per crystal rebounding event by a simulated graupel particle moving through a mixed cloud at 9 ms^{-1} shown on a cloud water content versus temperature diagram* (Takahashi [69])

cloud forming the upper positive charge centre and the falling graupel would carry a negative charge, augmented by the ice crystals from below to form the main negative charge centre at the reversal temperature.

2.4 Droplet size effect

Jayaratne and Saunders [31] showed that, in addition to the temperature and cloud water content, the droplet size spectrum played an important role in determining the sign of the charge separated during ice crystal–graupel collisions. The Jayaratne *et al*. [32] experiments were carried out with a cloud of droplets of mean diametre 10 μm extending up to about 30 μm. Jayaratne and Saunders [31] repeated this

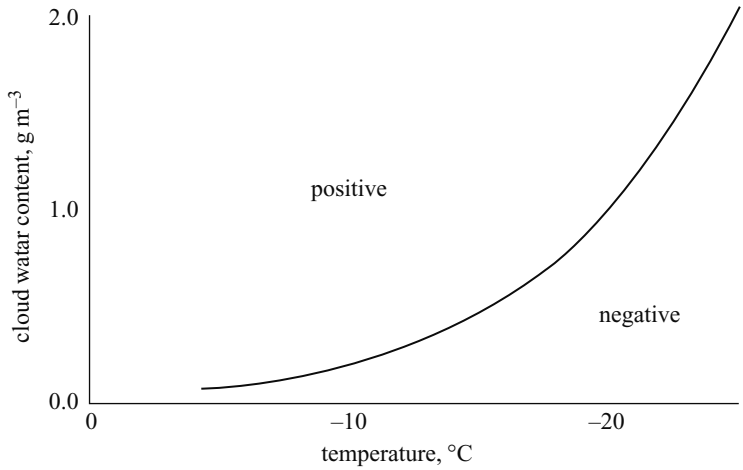

Figure 2.9 *The charge acquired per crystal rebounding event by a simulated graupel particle moving through a mixed cloud at 3 ms^{-1} shown on a cloud water content versus temperature diagram* (Jayaratne *et al*. [32])

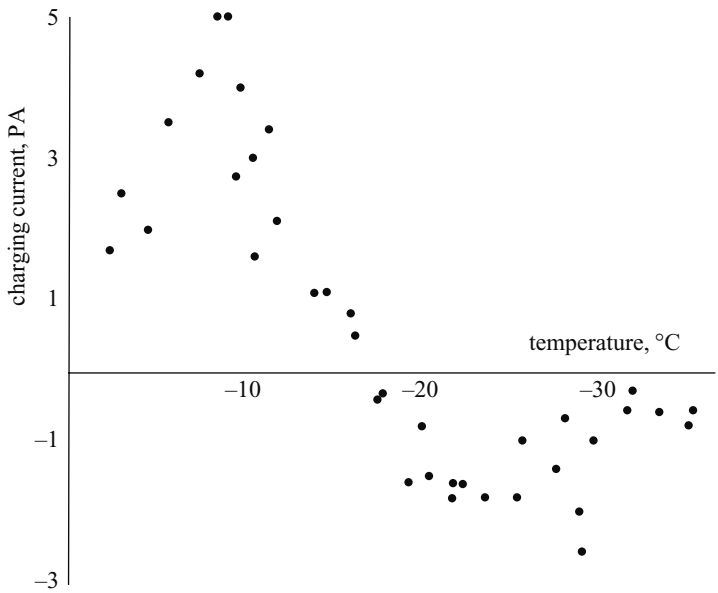

Figure 2.10 *The charging current to the graupel as a function of temperature according to Jayaratne et al. [32] extended by Baker et al. [6]. Cloud water content = 0.3 gm^{-3}, mean crystal size = 40 μm, crystal concentration = 50 ml^{-1}, impact speed = 3 ms^{-1}*

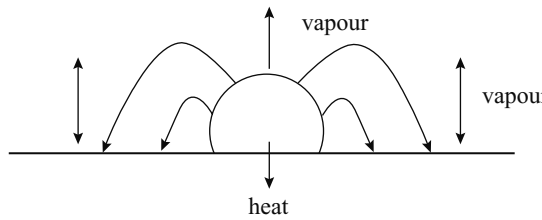

Figure 2.11 *Schematic diagram showing a droplet freezing on a graupel surface. Much of the latent heat released by riming droplets is conducted into the graupel substrate. At high cloud water contents (high riming rates) the heat absorbed may be high enough to raise the surface temperature of the graupel sufficiently above ambient to cause it to sublimate. However, the temperature of a droplet remains at 0°C while freezing and so forms an intense source of vapour to the annular area immediately surrounding a freezing droplet. Thus, a sublimating graupel surface may be scattered with many such growing spots*

study with a droplet size spectrum shifted to smaller sizes with a maximum droplet diameter of less than 4 μm. They showed that at −10°C the graupel now charged negatively. Jayaratne [30] noted that, with such a spectrum, the corresponding charge–temperature dependence was startlingly different to that observed with the normal droplet size spectrum with four charge sign reversal temperatures instead of the single reversal temperature observed by Jayaratne *et al*. [32] and Takahashi [69] using larger droplets (Figure 2.13). Saunders *et al.* [59] noted a similar trend, with smaller droplets giving negative charged graupel at −10°C and at −20°C at a comparable cloud water content of about 1 g m^{-3}. These observations do not allow us to conclude that larger/smaller droplets favour positive/negative charging of graupel. Although it may be true at −10°C and at −20°C, the opposite occurs at −15°C and at −30°C. The picture became more complicated when Avila *et al*. [2,3] reported negative charging of graupel at all temperatures when the droplet size spectrum was shifted to sizes significantly larger than that used by Jayaratne *et al*. [32] (Figure 2.14). This behaviour is puzzling but not unexpected when we consider what a change in the droplet size can do to the relative growth rate between a riming graupel and the vapour grown ice crystals in the cloud.

The droplet size affects the relative growth rates of the two particles in several ways and these are summarised in Figure 2.15. We shall consider these in turn. Some of these have been discussed in Avila *et al*. [2]:

(i) Large droplets take longer to freeze than smaller droplets and so allow the crystals a longer time to find a fast growing area on the graupel surface. Thus, according to the Baker *et al*. [6] relative growth rates hypothesis, this effect predicts positive/negative charging of the graupel with larger/smaller droplets.

(ii) During accretion, larger droplets tend to spread more than smaller droplets and freeze as hemispheres; smaller droplets freeze as spheres very often showing a buildup into a chain-like structure as shown in Figure 2.16 [40]. The contact

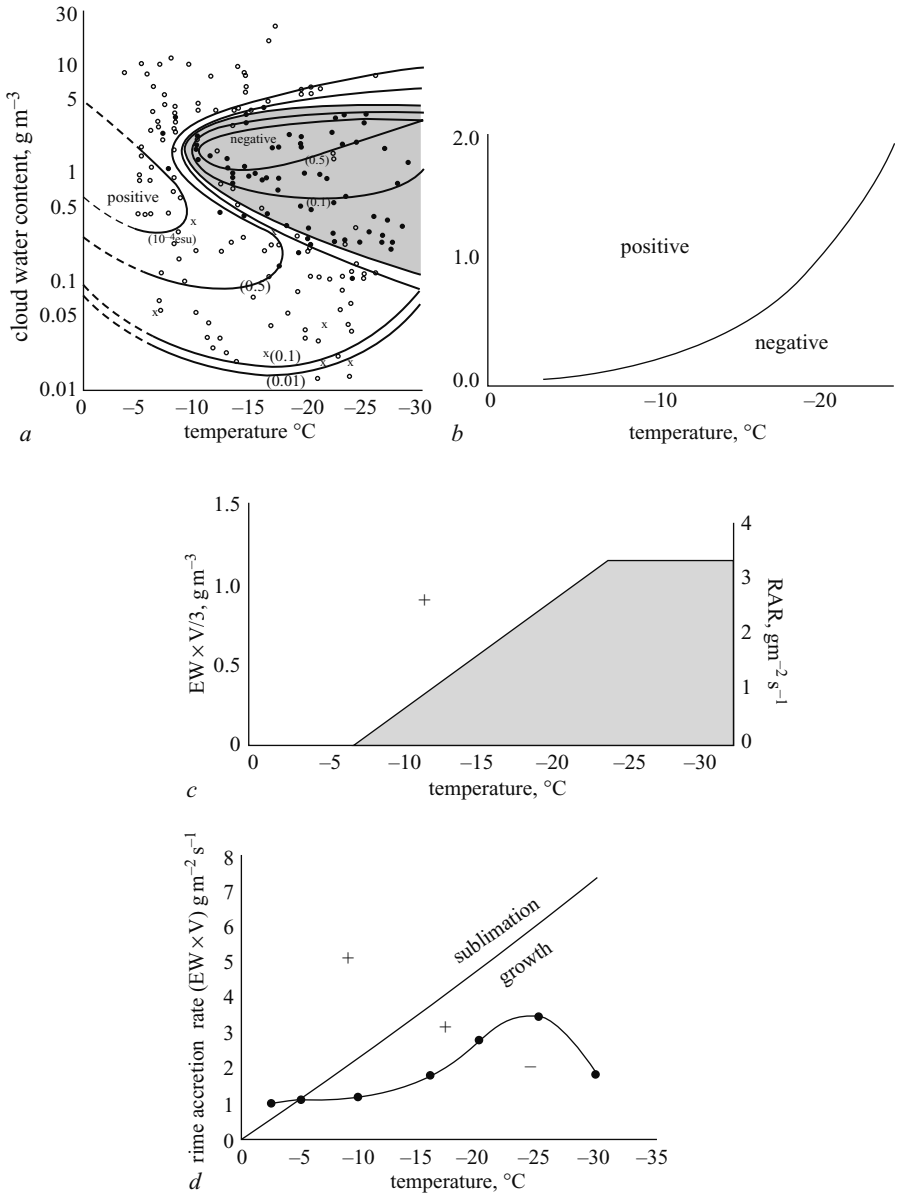

Figure 2.12 *Charge sign reversal lines according to:*

a Takahashi [69]
b Jayaratne *et al*. [32]
c Brooks *et al*. [8]
d Saunders and Peck [58]

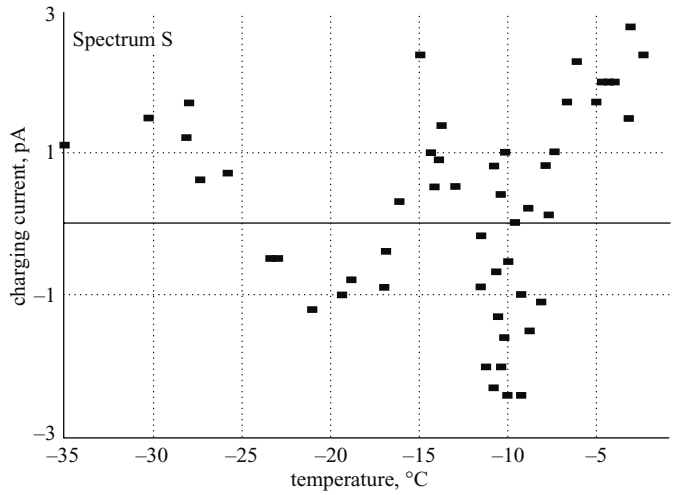

Figure 2.13 *The temperature dependence of the graupel charging current with a smaller droplet size spectrum* (Jayaratne [3])

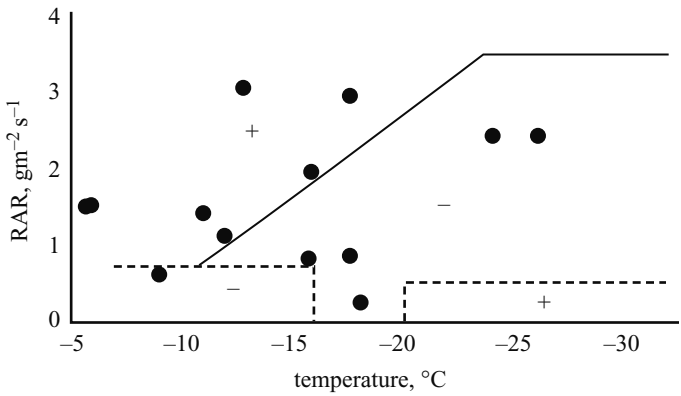

Figure 2.14 *The charge sign zones as a function of rime accretion rate (RAR) and temperature from Saunders et al. [60] and Brooks et al. [8] together with the negative charging events (solid circles) found by Avila et al. [2] using large spray droplets*

area between the droplet and the graupel will increase with droplet size. This allows a greater fraction of the latent heat to conduct into the rime substrate for larger droplets than for smaller droplets. Thus, at the same ambient temperature and rime accretion rate, larger droplets will make a graupel particle warmer and, hence, allow it to grow slower than when the droplet size was smaller. This predicts negative/positive graupel charging with larger/smaller droplets.

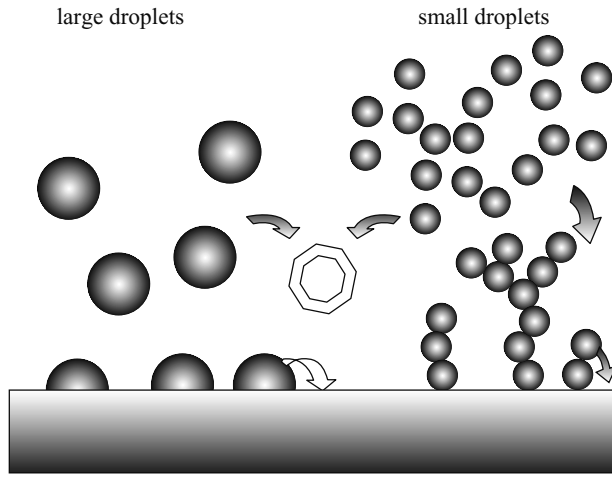

Figure 2.15 *Summary of the possible effects of droplet size on the relative growth rates of the two interacting ice particles. Cases favouring negative charging of graupel are underlined. See text for explanation*

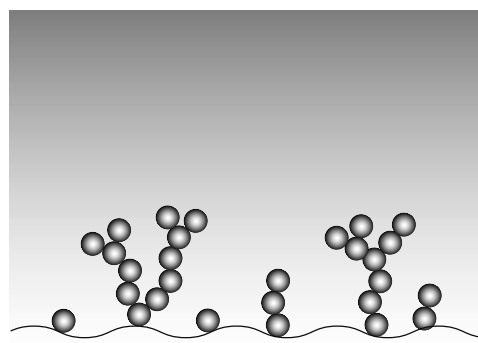

Figure 2.16 *Schematic diagram showing the structure of rime formed by small droplets. Note the chain-like growth which restricts flow of latent heat into the graupel substrate*

(iii) A number of small droplets (of the same mass as one large droplet) will present a larger fast growing area on the graupel surface than the larger droplet. Thus, at the same temperature and rime accretion rate, impacting crystals have a greater chance of finding a faster growing area when the droplets are smaller than

when they are larger. The prediction due to this effect is again negative/positive graupel with larger/smaller droplets.

(iv) A large droplet has a smaller surface area than several smaller droplets of the identical total mass. Thus, at the same temperature and rime accretion rate, the large droplet is likely to provide less vapour to the graupel surface than all the smaller droplets together. This effect predicts negative/positive graupel charging with larger/smaller droplet sizes.

(v) Finally, let us consider what effect the cloud droplet size could have on the growth rate of the crystals. Marshall and Langleben [44] showed that ice crystal growth was enhanced when there were more droplets in the cloud. At the same cloud water content, smaller droplets present a greater surface area and, thus, a greater vapour flux to the crystals than larger droplets. Crystals would grow faster in a cloud of smaller droplets than larger droplets. This would still be true if we keep the rime accretion rate the same in the presence of both droplet size clouds because smaller droplets have a lower collision efficiency than larger droplets and would need to be present in even larger numbers to maintain the same rime accretion rate. So, whether it be at the same cloud water content or the same rime accretion rate, crystals would grow faster when the droplet size was smaller. Faster growing crystals are likely to charge the graupel more negatively according to the relative growth rate hypothesis, so our prediction in this case is positive/negative graupel charging with larger/smaller droplets.

So, we see that the droplet size spectrum plays a complex role in determining the relative growth rate of the two particles. A change in any one or more of the above conditions may flip the sign of charging. Predicting the exact sign of charging under a given set of conditions becomes extremely difficult. The matter may be further complicated if it is the shape of the droplet size spectrum rather than just the mean droplet size that may be relevant in determining the sign of charging. For example, a normal size distribution and a bimodal distribution can have the same mean droplet size but the resulting charging sign could well be very different. This presents a major hurdle to numerical modellers of thunderstorm electrification. Representing the droplet size spectrum in a model requires multidimensional parameters that are very difficult to manipulate.

2.5 Effect of chemical impurities

Many laboratory workers have shown that the presence of chemical impurities has a profound effect on the sign of the charge transfer during ice–ice collisions. In general, the presence of trace quantities of NaCl in the rime made the graupel charge negatively, but most ammonium salts made it charge positively [56,41,69,32]. Jayaratne *et al*. [32] investigated the effect of temperature and showed that the magnitude of the charging generally increased sharply as the temperature was decreased (Figure 2.17). At present, there is no plausible explanation for these observations except a similarity with the Workman–Reynolds effect (Section 2.2.6) where NaCl and ammonium salts indeed produced potentials of opposite signs. However, the

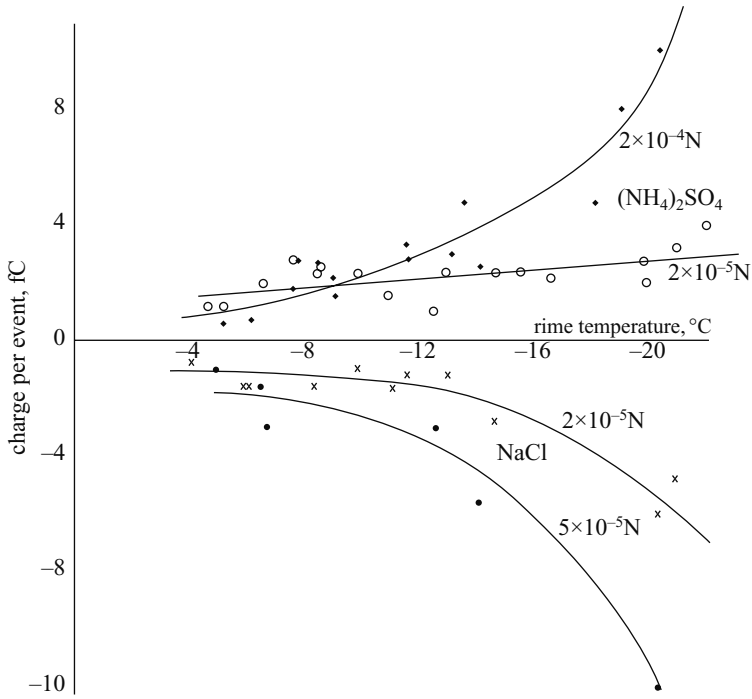

Figure 2.17 *The charge per crystal collision as a function of temperature when the droplets in the cloud contained dilute ammonium sulphate and sodium chloride solution* (Jayaratne *et al*. [32])

Workman–Reynolds potentials decayed as soon as the freezing ended. The probability of an ice crystal impacting on a still-freezing droplet on the graupel surface is negligibly small and, so, it becomes difficult to relate the sign of the charge separation to the Workman–Reynolds potentials. Caranti and Illingworth [11] attempted to measure a possible remnant potential on a rimed surface. They found no such potential once the supercooled droplets had completely frozen. Considering the resolution of their measurements in time, they concluded that, if there was such a potential, it would have disappeared within a fraction of a second – too short an interval of time to have an appreciable effect on the charge transfer due to ice crystal impacts. However, we do know that ions have different mobilities in ice and water. For example, Cl^- ions diffuse into ice more easily than Na^+ ions. Thus, an ice surface contaminated with NaCl, will have an excess positive ion concentration near its surface on the quasiliquid layer (Figure 2.18). Impacting ice crystals may remove some of this positively charged mass off the quasiliquid layer, leaving the graupel negative. Also, NH_4^+ ions are readily incorporated into the ice. Following the same argument as for NaCl we could expect a graupel particle containing impurity ammonium salts to acquire a net positive charge during ice crystal interactions (Figure 2.19).

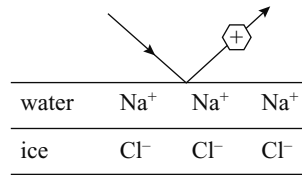

Figure 2.18 Schematic diagram showing the separation of ions near an ice surface contaminated with sodium chloride

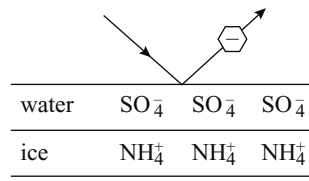

Figure 2.19 Schematic diagram showing the separation of ions near an ice surface contaminated with ammonium sulphate

The role played by chemical impurities in determining the sign and magnitude of the charge separated during rebounding collisions between ice particles remains a major mystery and so far it has not been possible to explain it in terms of any of the existing hypotheses. Furthermore, it is reasonable to imagine that thunderstorms in various geographical locations must contain cloud condensation nuclei of varying chemical content such as the excess salt nuclei found in coastal and maritime clouds. However, thunderstorms all over the world show a remarkably similar charge structure. These questions pose a major difficulty for explaining the electrification of thunderstorms in terms of the noninductive ice–ice charging mechanism.

2.6 References

1 AUFDERMAUR, A.N., and JOHNSON, D.A.: 'Charge separation due to riming in an electric field', *Q. J. R. Meteorol. Soc.*, 1972, **98**, pp.369–382
2 AVILA, E.E., CARANTI, G.M., and CASTELLANO, N.E.: 'Laboratory studies of the influence of cloud droplet size on charge transfer during crystal-graupel collisions', *J. Geophys. Res.*, 1998, **103**, pp.8985–8996
3 AVILA, E.E., CASTELLANO, N.E., and SAUNDERS, C.P.R.: 'Effects of cloud droplet spectra on the average surface temperature of ice accreted on fixed cylindrical collectors', *Q. J. R. Meteorol. Soc.*, 1999, **125**, pp.1059–1074
4 BAKER, M.B., and DASH, J.G.: 'Charge transfer in thunderstorms and the surface melting of ice', *J. Cryst. Growth*, 1989, **97**, pp.770–776
5 BAKER, M.B., and DASH, J.G.: 'Mechanism of charge transfer between colliding ice particles in thunderstorms', *J. Geophys. Res.*, 1994, **99**, pp.10621–10626

6 BAKER, B., BAKER, M.B., JAYARATNE, E.R., LATHAM, J., and SAUNDERS, C.P.R.: 'The influence of diffusional growth rate on the charge transfer accompanying rebounding collisions between ice crystals and hailstones', *Q. J. R. Meteorol. Soc.*, 1987, **113**, pp.1193–1215
7 BROOKS, I.M., and SAUNDERS, C.P.R.: 'An experimental investigation of the inductive mechanism of thunderstorm electrification'. Proceedings of ninth international conference on *Atmos. Elec.*, St Petersburg, Russia, 1992, pp.92–95
8 BROOKS, I.M., SAUNDERS, C.P.R., MITZEVA, R.P., and PECK, S.L.: 'The effect on thunderstorm charging of the rate of rime accretion by graupel', *Atmos. Res.*, 1997, **43**, pp.277–295
9 BUSER, O., and AUFDERMAUR, A.N.: 'Electrification by collisions of ice particles on ice or metal targets', *in* DOLEZALEK, H., and REITER, R. (Eds.): 'Electrical processes in atmospheres' (Steinkopff, Darmstadt, 1977) pp.294–301
10 CARANTI, J.M., and ILLINGWORTH, A.J.: 'Surface potentials of ice and thunderstorm charge separation', *Nature*, 1980, **284**, pp.44–46
11 CARANTI, J.M., and ILLINGWORTH, A.J.: 'Transient Workman–Reynolds freezing potentials', *J. Geophys. Res.*, 1983, **88**, pp.8483–8489
12 CARANTI, G.M., AVILA, E.E., and RÉ, M.A.: 'Charge transfer during individual collisions in ice growing from vapour deposition', *J. Geophys. Res.*, 1991, **96**, pp.15365–15375
13 CHALMERS, J.A.: 'Atmospheric electricity' (Pergamon Press, 1963, 2nd edn)
14 CHIU, C.S.: 'Numerical study of cloud electrification in an axisymmetric, time-dependent cloud model', *J. Geophys. Res.*, 1978, **83**, pp.5025–5049
15 DASH, J.G.: 'Surface melting', *Contemp. Phys.*, 1989, **30**, pp.89–100
16 DINGER, J.E., and GUNN, R.: 'Electrical effects associated with a change of state of water', *Terr. Magn. and Atmos. Elect.*, 1946, **51**, pp.477–494
17 DRAKE, J.C.: 'Electrification accompanying the melting of ice particles', *Q. J. R. Meteorol. Soc.*, 1968, **94**, pp.176–191
18 ELSTER, J., and GEITEL, H.: 'Zur Influenztheorie Der Niederschlagselektrizitat', *Phys. Z.*, 1913, **14**, p.1287
19 FLETCHER, N.H.: 'Surface structure of water and ice II: a revised model', *Philos. Mag.*, 1968, **18**, pp.1287–1300
20 FOSTER, H.: 'An unusual observation of lightning', *Bull. Am. Meteorol. Soc.*, 1950, **31**, pp.140–141
21 GASKELL, W.: 'A laboratory study of the inductive theory of thunderstorm electrification', *Q. J. R. Meteorol. Soc.*, 1981, **107**, pp.955–966
22 GASKELL, W., and ILLINGWORTH, A.J.: 'Charge transfer accompanying individual collisions between ice particles and its role in thunderstorm electrification', *Q. J. R. Meteorol. Soc.*, 1980, **106**, pp.841–854
23 GASKELL, W., ILLINGWORTH, A.J., LATHAM, J., and MOORE, C.B.: 'Airborne studies of electric fields and the charge and size of precipitation elements in thunderstorms', *Q. J. R. Meteorol. Soc.*, 1978, **104**, pp.447–460
24 GROSS, G.W.: 'Role of relaxation and contact times in charge separation during collision of precipitation particles with ice targets', *J. Geophys. Res.*, 1982, **87**, pp.7170–7178

25 GRENET, G.: 'Essai d'explication de la charge electrique des nuages d'orages', *Ann. Geophys.*, 1947, **3**, pp.306–307
26 GRIGGS, D.J., and CHOULARTON, T.W.: 'A laboratory study of secondary ice particle production by the fragmentation of rime and vapour-grown ice crystals', *Q. J. R. Meteorol. Soc.*, 1986, **112**, pp.149–163
27 ILLINGWORTH, A.J., and CARANTI, J.M.: 'Ice conductivity restraints on the inductive theory of thunderstorm electrification', *J. Geophys. Res.*, 1985, **90**, pp. 6033–6039
28 IRIBARNE, J.V., and MASON, B.J.: 'Electrification accompanying the bursting of bubbles in water and dilute aqueous solutions', *Trans. Faraday Soc.*, 1967, **63**, pp.2234–2245
29 JAYARATNE, E.R.: 'Temperature gradients in ice as a charge generation process in thunderstorms', *Atmos. Res.*, 1993, **29**, pp.247–260
30 JAYARATNE, E.R.: 'Possible laboratory evidence for multipole electric charge structures in thunderstorms', *J. Geophys. Res.*, 1998, **103**, pp.1871–1878
31 JAYARATNE, E.R., and SAUNDERS, C.P.R.: 'Thunderstorm electrification: the effect of cloud droplets', *J. Geophys. Res.*, 1985, **90**, pp.13063–13066
32 JAYARATNE, E.R., SAUNDERS, C.P.R., and HALLETT, J.: 'Laboratory studies of the charging of soft-hail during ice crystal interactions', *Q. J. R. Meteorol. Soc.*, 1983, **109**, pp.609–630
33 JAYARATNE, E.R., PECK, S.L., and SAUNDERS, C.P.R.: 'Comment on "a laboratory study of static charging by fracture in ice growing by riming" by AVILA, E.E., and CARANTI, G.M.', *J. Geophys. Res.*, 1996, **101**, pp.9533–9535
34 JENNINGS, S.G.: 'Charge separation due to water drop and cloud droplet interactions in an electric field', *Q. J. R. Meteorol. Soc.*, 1975, **101**, pp.227–233
35 KREHBIEL, P.R., BROOK, M., and McCRORY, R.A.: 'An analysis of the charge structure of lightning discharges to ground', *J. Geophys. Res.*, 1979, **84**, pp.2432–2456
36 LATHAM, J., and MASON, B.J.: 'Electric charge transfer associated with temperature gradients in ice', *Proc. R. Soc., Ser. A*, 1961, **260**, pp.523–536
37 LATHAM, J., and MASON, B.J.: 'Generation of electric charge associated with the formation of soft hail in thunderclouds', *Proc. R. Soc., Ser. A*, 1961, **260**, pp.537–549
38 LATHAM, J., and MASON, B.J.: 'Electrical charging of hail pellets in a polarizing electric field', *Proc. R. Soc., Ser. A*, 1962, **266**, pp.387–401
39 MacCREADY, P.B., Jr., and PROUDFIT, A.: 'Observations of hydrometeor charge evolution in thunderstorms', *Q. J. R. Meteorol. Soc.*, 1965, **91**, pp.44–53
40 MACKLIN, W.C.: 'The density and structure of ice formed by accretion', *Q. J. R. Meteorol. Soc.*, 1962, **88**, pp.30–50
41 MAGONO, C., and TAKAHASHI, T.: 'On the electrical phenomena during riming and glazing in natural supercooled clouds', *J. Meteorol. Soc. Japan*, 1963, **41**, pp.71–81
42 MARSH, S.J., and MARSHALL, T.C.: 'Charged precipitation measurements before the first lightning flash in a thunderstorm', *J. Geophys. Res.*, 1993, **98**, pp.16605–16611

43 MARSHALL, B.J.P., LATHAM, J., and SAUNDERS, C.P.R.: 'A laboratory study of charge transfer accompanying the collision of ice crystals with a simulated hailstone', *Q. J. R. Meteorol. Soc.*, 1978, **104**, pp.163–178
44 MARSHALL, J.S., and LANGLEBEN, M.P.: 'A theory of snow crystal habit and growth', *J. Meteorol.*, 1954, **11**, pp.104–120
45 MARSHALL, T.C., and WINN, W.P.: 'Measurements of charged precipitation in a New Mexico thunderstorm: lower positive charge centers', *J. Geophys. Res.*, 1982, **87**, pp.7141–7157
46 MASON, B., and DASH, J.: 'An experimental study of charge and mass transfer during ice contact interactions'. Proceedings of the 11th international conference on *Atmospheric electricity*, Guntersville, Alabama, USA, 1999, pp.264–267
47 MASON, B.J.: 'A critical examination of theories of charge generation in thunderstorms', *Tellus*, 1953, **5**, pp.446–460
48 MASON, B.J.: 'The physics of the thunderstorm', *Proc. R. Soc., Ser. A*, 1972, **327**, pp.433–466
49 MATHEWS, J.B., and MASON, B.J.: 'Electrification accompanying melting of snow and ice', *Q. J. R. Meteorol. Soc.*, 1963, **89**, pp.376–380
50 MOORE, C.B., and VONNEGUT, B.: 'The thundercloud', *in* GOLDE, R.H. (Ed.): 'Lightning, vol. 1: Physics of lightning' (Academic Press, San Diego, CA, 1977) pp.51–98
51 MOORE, C.B., VONNEGUT, B., STEIN, B.A., and SURVILAS, H.J.: 'Observations of electrification and lightning in warm clouds', *J.Geophys. Res.*, 1960, **65**, pp.1907–1910
52 MUHLER-HILLEBRAND, D.: 'Charge generation in thunderclouds by collision of ice crystals with graupel falling through a vertical electric field', *Tellus*, 1954, **6**, pp.367–381
53 PALUCH, I.R., and SARTOR, J.D.: 'Thunderstorm electrification by the inductive charging mechanism: I. Particle charges and electric fields', *J. Atmos. Sci.*, 1973, **30**, pp.1166–1173
54 PIETROWSKI, E.L.: 'An observation of lightning in warm clouds', *J. Meteorol.*, 1960, **17**, pp.562–563
55 PRUPPACHER, H.R., and KLETT, J.D.: 'Microphysics of clouds and precipitation' (D. Reidel, Dordrecht, Holland, 1997)
56 REYNOLDS, S.E., BROOK, M., and GOURLEY, M.F.: 'Thunderstorm charge separation', *J. Meteorol.*, 1957, **14**, pp.426–436
57 SARTOR, J.D.: 'The role of particle interactions in the distribution of electricity in thunderstorms', *J. Atmos. Sci.*, 1967, **24**, pp.601–615
58 SAUNDERS, C.P.R., and PECK, S.L.: 'Laboratory studies of the influence of rime accretion rate on charge transfer during crystal/graupel collisions', *J. Geophys. Res.*, 1998, **103**, pp.13949–13956
59 SAUNDERS, C.P.R., AVILA, E.E., PECK, S.L., CASTELLANO, N.E., and AGUIRRE VARELA, G.G.: 'Vapour and heat supply to riming graupel: effect on charging'. Proceedings of 11th international conference on *Atmospheric electricity*, Guntersville, Alabama, USA, 1999, pp.268–271

60 SAUNDERS, C.P.R., KEITH, W.D., and MITZEVA, R.P.: 'The effect of liquid water on thunderstorm charging', *J. Geophys. Res.*, 1991, **96**, pp.11007–11017
61 SCOTT, W.D., and LEVIN, Z.: 'A stochastic electrical model of an infinite cloud: Charge generation and precipitation development', *J. Atmos. Sci.*, 1975, **32**, pp.1814–1828
62 SHEPHERD, T.R., RUST, W.D., and MARSHALL, T.C.: 'Electric fields and charges near 0°C in stratiform clouds', *Mon. Weather Rev.*, 1996, **124**, pp.919–938
63 SIMPSON, G.C., and SCRASE, F.J.: 'The distribution of electricity in thunderclouds', *Proc. R. Soc., Ser. A*, 1937, **161**, pp.309–352
64 STANDLER, R.B., and WINN, W.P.: 'Effects of coronae on electric fields beneath thunderstorms', *Q. J. R. Meteorol. Soc.*, 1979, **105**, pp.285–302
65 STOLZENBURG, M., RUST, W.D., and MARSHALL, T.C.: 'Electrical structure in thunderstorm convective regions 2: isolated storms', *J. Geophys. Res.*, 1998, **103**, pp.14079–14096
66 TAKAHASHI, T.: 'Electric potential of a rubbed ice surface', *J. Atmos. Sci.*, 1969, **26**, pp.1259–1265
67 TAKAHASHI, T.: 'Electric potential of liquid water on an ice surface', *J. Atmos. Sci.*, 1969, **26**, pp.1253–1258
68 TAKAHASHI, T.: 'Electrification of growing ice crystals', *J. Atmos. Sci.*, 1973, **30**, pp.1220–1224
69 TAKAHASHI, T.: 'Riming electrification as a charge generation mechanism in thunderstorms', *J. Atmos. Sci.*, 1978, **35**, pp.1536–1548
70 VONNEGUT, B.: 'Possible mechanism for the formation of thunderstorm electricity', *Bull. Am. Meteorol. Soc.*, 1953, **34**, pp.378–381
71 VONNEGUT, B.: 'Some facts and speculations concerning the origin and role of thunderstorm electricity', *Meteorol. Monogr.*, 1963, **5**, pp.224–241
72 WILLIAMS, E.R.: 'The role of ice in the electrification and dynamics of thunderstorms'. Conference on *Cloud physics*, American Meteoroligol Society, San Fransisco, USA, 1990
73 WILSON, C.T.R.: 'Some thundercloud problems', *J. Franklin Inst.*, 1929, **208**, pp.1–12
74 WINN, W.P., and BYERLEY, L.G.: 'Electric field growth in thunderclouds', *Q. J. R. Meteorol. Soc.*, 1975, **101**, pp.979–994
75 WORKMAN, E.J., and REYNOLDS, S.E.: 'Electrical phenomena occurring during the freezing of dilute aqueous solutions and their possible relationship to thunderstorm electricity', *Phys. Rev.*, 1950, **78**, pp.254–259
76 WORMELL, T.W.: 'Atmospheric electricity: some recent trends and problems', *Q. J. R. Meteorol. Soc.*, 1953, **79**, p.3
77 ZIV, A., and LEVIN, Z.: 'Thundercloud electrification: cloud growth and electrical development', *J. Atmos. Sci.*, 1974, **31**, pp.1652–1661

Chapter 3

Mechanism of electrical discharges

Vernon Cooray

3.1 Introduction

The experiments performed by researchers in different countries, notably, South Africa, England, Switzerland and the USA, during the last sixty years have greatly advanced our knowledge concerning the mechanism of lightning flashes. However, many pieces of the puzzle are still missing and many of the theories put forth as explanation of its mechanism are mainly of a qualitative nature. The reason for this slow progress is the impossibility of studying lightning flashes under controlled laboratory conditions. On the other hand, the mechanism of the electric spark, which could be studied under controlled conditions, may guide the researchers in their quest for understanding the mechanism of lightning flashes and creating more advanced theories of the phenomena. After all, it is the observed similarities between the small laboratory sparks and lightning discharges that forced Benjamin Franklin to conclude that the lightning flash is a manifestation of electricity. This Chapter is devoted to a description of the mechanism of laboratory sparks.

3.2 Basic definitions

3.2.1 Mean free path and cross section

An electron moving in a medium consisting of other atoms can make either elastic or inelastic collisions. An elastic collision is one in which the total kinetic energy of the colliding particles is conserved during the collision. An inelastic collision is a collision in which part or all of the kinetic energy of the colliding particles is converted to potential energy of one or more colliding particles. An inelastic collision between an electron and an atom could lead either to the attachment of the electron to the atom, to the excitation of the atom or to the ionisation of the atom. The atomic excitations could be either electronic, vibrational or rotational.

The distance an electron travels between elastic collisions is called the free path for elastic collision. Similarly, one can define the free paths for excitation and ionisation collisions. The average values of these free paths are defined as mean free paths for respective collisions (i.e. elastic, excitation, ionisation etc.).

The mean free path for a given type of collision can be described by:

$$\lambda = \frac{1}{n\sigma} \tag{3.1}$$

where n is the atomic or molecular number density of gas and σ, which has the dimension of area, is known as the microscopic collision cross section; the quantity $n\sigma$ is known as the macroscopic collision cross section of the process under consideration.

One can define a collision cross section for elastic collisions, excitation collisions or ionisation collisions. Let σ_t and Q_t be, respectively, the gross (total) microscopic and gross (total) macroscopic cross sections for an electron to undergo some reaction regardless of type in traversing a gaseous medium. Then one can write:

$$\sigma_t = \sigma_e + \sigma_{ex} + \sigma_{ion} + \sigma_a + \sigma_{oth} \tag{3.2}$$

and the gross (total) macroscopic cross section is given by:

$$Q_t = Q_e + Q_{ex} + Q_{ion} + Q_a + Q_{oth} \tag{3.3}$$

where the subscripts stand for: e – elastic; ex – excitation; ion – ionisation; a – attachment; oth – other processes. Note that Q_{ex} refers either to electronic excitations, vibrational excitations or rotational excitations.

If p_x is the probability that a collision will result in the process x then:

$$p_x = Q_x/Q_t \tag{3.4}$$

where the subscript x stands for either *e, ex, ion, a*, or *oth*. Then eqn. 3.3 can also be written as:

$$Q_t = (p_e + p_{ex} + p_{ion} + p_a + p_{oth})Q_t \tag{3.5}$$

3.2.2 Drift velocity and mobility

If given sufficient time two types of particle in a medium will reach thermal equilibrium and their motion can be described by the Boltzman equation [6]. However, in the case of charged particles immersed in a background electric field the situation may become much more complicated. The electric field exerts a force on the charged particles in a direction parallel to the electric field. As a result, in addition to the random motion the charged particles will drift either in the direction of the electric field or opposite to it depending on the sign of their charge. In a vacuum the charged particles will continue to accelerate under the influence of the electric field but in a medium full of gas atoms the charged particles will make collisions with the atoms resulting in a loss of energy gained from the electric field. This energy dissipation to the gas atoms

Table 3.1 Mobility of singly charged positive (K^+) and negative (K^-) gaseous ions at 0°C and 760 Hg (in cm/s/V/cm)

Gas	K^-	K^+
Air (dry)	2.1	1.36
Air (very pure)	2.5	1.8
A	1.7	1.37
A (very pure)	206.0	1.31
Cl_2	0.74	0.74
CCl_4	0.31	0.30
C_2H_2	0.83	0.78
C_2H_5Cl	0.38	0.36
C_2H_5OH	0.37	0.36
CO	1.14	1.10
CO_2	0.98	0.84
H_2	8.15	5.9
H_2 (very pure)	7900.0	
HCl	0.95	1.1
H_2S	0.56	0.62
He	6.3	5.09
He (very pure)	500.0	5.09
N_2	1.84	1.27
N_2 (very pure)	145.0	1.28
NH_3	0.66	0.56
N_2O	0.90	0.82
Ne		9.9
O_2	1.80	1.31
SO_2	0.41	0.41

increases with increasing drift speed of the charged particles and as a result the charged particles will attain a certain constant speed within a certain time called the relaxation time. This constant speed is known as the drift velocity. The drift velocity depends on the applied electric field, the charge and the mass of the particle, among other parameters. The ratio of the drift velocity to the electric field is known as the mobility of the charged particles. Table 3.1 gives the mobility of common ions in air [1,9].

The drift velocity of electrons, v_e, as a function of electric field, E, in air can be calculated from the following empirical equation [2]:

$$v_e = 1.0 \times 10^6 (E/p)^{0.715}, \quad E/p \leq 100 \text{ (V/cm.torr)}^1 \tag{3.6}$$

$$v_e = 1.55 \times 10^6 (E/p)^{0.62}, \quad E/p \geq 100 \text{ (V/cm.torr)} \tag{3.7}$$

where p is the pressure in torr and the drift velocity is given in cm/s.

[1] In many of the empirical equations pertinant to electrical discharges the electric field is given in V/cm and the pressure is given in torr [1 torr (mm Hg) = $1.333.10^2$ Pa]; the same units are used in this Chapter

3.2.3 Thermal equilibrium and local thermal equilibrium

For a given type of particle in an ensemble, the concept of temperature is defined in terms of the average kinetic energy of the particles. Thus, ascribing a certain temperature to a species presupposes that its velocity distribution conforms to a definite distribution function. For example, the velocity distribution of the atoms or molecules in a gas follows the Maxwellian distribution. The requirement that the particle velocities should conform to a certain distribution imposes some restrictions on the system. For example, the mean free path of the particle must be much less than the dimension of the enclosure containing the particles, and the time between collisions should be short in comparison with other characteristic times of the system. These are the time spent by a particle within the enclosure before being lost and the time taken for a new particle to reach the energies characteristic of the ensemble. The energy of an ensemble is also present in the form of radiation and, if the mean free path for the absorption of the radiation is much less than the plasma dimensions, a radiation equilibrium is established. In this case the plasma characteristics approaches those of a black body. When all the species in the plasma including the radiation are in thermodynamic equilibrium with each other, one can say that the system is in thermal equilibrium.

Under thermal equilibrium all the particles including the radiation have the same temperature. However, in laboratory plasmas, the optical mean free path is usually longer than the dimensions of the plasma so complete radiation equilibrium is not reached. In this situation it is possible for the collisional process to be in complete thermodynamic equilibrium (excluding the radiation processes which are assumed to cause insignificant energy exchange and losses). In this case the system is said to be in local thermodynamic equilibrium. It is important to note that in some situations all the species may not be in thermodynamic equilibrium but the reactions that take place in the ensemble are dominated by one species. In this case the temperature which describes the local thermodynamic equilibrium is that which describes the distribution function of the species that dominates the reaction rates. In dense laboratory plasmas this is the electron temperature, since their cross section for collisions tend to be higher than for all other reactants.

Whenever a system is in thermal equilibrium, the system is devoid of temperature and density gradients. However, in reality they exist and the condition for the thermodynamic equilibrium in such cases can be written as [3]:

$$\lambda \frac{\partial T_g}{\partial r} \ll T_g \tag{3.8}$$

$$\lambda \frac{\partial n}{\partial r} \ll n \tag{3.9}$$

$$Ee\lambda_e \ll \frac{mc^2}{2} \tag{3.10}$$

where E is the electric field, e is the electronic charge, λ_e and λ are the mean free path of electron and gas atoms, respectively, $mc^2/2$ is the mean electron kinetic energy, T_g

is the temperature of gas, n its concentration and r is the distance. The first two conditions impose small temperature and density variation and the third condition restricts the energy fed to the electrons from the electric field. If this condition is not satisfied the behaviour of electrons would not be able to be described using an average temperature because the energy fed from the electric field will upset the thermodynamic equilibrium.

In the presence of an electric field the energy gained by the electrons from the electric field is randomised by the collisions between electrons and gas particles. Thus, one can speak of an electron temperature. However, it is important to note that the energy exchange between the electrons and gas particles is an inefficient process since in elastic collisions an electron loses only a small fraction of its energy. Thus, in the presence of an electric field, the electron temperature would be higher than that of the gas.

3.3 Ionisation processes

The electrical breakdown of air takes place when the air changes from an insulator to a conductor. This process is mediated by an increase in the electron concentration in air. The processes that lead to the increase in electron concentration in air are called ionisation processes. There are many ionisation processes in air and following is a description of them.

3.3.1 Ionisation due to electron impact

In an electric field an electron continues to gain energy but it can transfer only a quantum of its energy to atoms in the medium during an inelastic collision. Thus, when the electron energy increases by more than the excitation energy of the colliding atom, a quantum of energy is transferred during collisions leaving the atom in an excited state. If the electron energy is larger than the ionisation energy of the atom a collision may result in the ionisation of the atom. The ionisation energy of common gases is tabulated in Table 3.2 [4].

The process of ionisation due to electrons can be quantified either in terms of an ionisation cross section, coefficient of ionisation or the probability of ionisation. The coefficient of ionisation (also known as the Townsend primary ionisation coefficient) is defined as the number of ionisation collisions made by an electron in moving a unit distance along the direction of the electric field. Usually this is denoted by the symbol α. The probability of ionisation is defined as the ratio of the number of ionisation collisions to the total number of collisions. These quantities can be related to each other as follows. The mean free path for the ionisation collisions, λ_{ion}, is given by:

$$\lambda_{ion} = \frac{1}{n\sigma_{ion}} \tag{3.11}$$

Table 3.2 Some excitation and ionisation energies of atomic and molecular forms of some gases

	Gas	Excitation energy W_e(eV)	Ionisation energy W_i(eV)
Oxygen	O_2	7.9	12.5
	O	1.97, 9.15	13.61
Nitrogen	N_2	6.3	15.6
	N	2.38, 10.33	14.54
Hydrogen	H_2	7.0	15.4
	H	10.16	13.59
Mercury	Hg	4.89	10.43
	Hg_2		9.6
Water	H_2O	7.6	12.62
Nitrogen oxide	NO	5.4	9.26
	NO_2		9.59

where n is the concentration of gas atoms and σ_{ion} is the microscopic cross section for ionisation. Thus the number of ionisation collisions made by an electron in moving a unit length, α, is given by:

$$\alpha = n\sigma_{ion} \tag{3.12}$$

The probability of ionisation is given by:

$$P_{ion} = \frac{\sigma_{ion} n}{\sigma n} = \frac{\sigma_{ion}}{\sigma} \tag{3.13}$$

where σ is the total collision cross section.

The ionisation cross section of electrons in nitrogen and oxygen as a function of the electron energy is shown in Figure 3.1. It was mentioned above that the electrons will ionise when their energy is larger than the ionisation energy of the atoms. However, the curve in this Figure in combination with the data given in Table 3.2 shows that the ionisation starts even before this threshold is reached. The reason for this is the stepwise ionisation of the atoms. The first collision of the atom with an electron may cause an excitation of the atom and the next collision may remove the excited electron from the atom. This process can take place with electrons having energies of less than the ionisation threshold. Note also that even though the electron energy is larger than the ionisation energy this does not mean that the electron will ionise every time it collides with an atom. During each collision the electron has a certain probability of ionisation. This probability (which is proportional to the ionisation cross section) increases with increasing electron energy and, in N_2 and O_2, reaches its peak value around

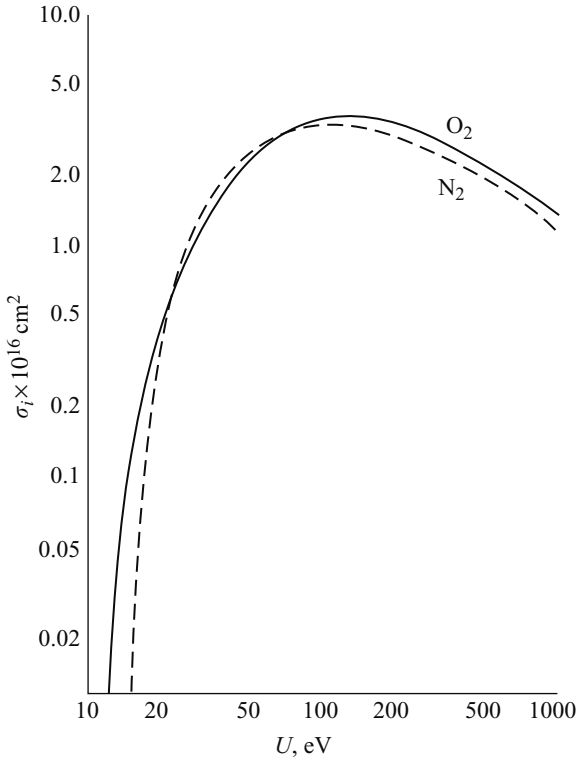

Figure 3.1 Ionisation cross section, σ_i, for electrons colliding with O_2 and N_2 molecules as a function of electron energy, U (eV) [2]

100 eV and then starts to decrease. The decline is probably caused by the fact that the time available for the interaction between a high energetic electron and an atom is small and the electron may pass near the atom without ejecting an electron from it.

The way in which the coefficient of ionisation in air varies as a function of the electric field is shown in Figure 3.2. Townsend derived an expression for the coefficient of ionisation, α, in air as a function of the electric field and this it is given by:

$$\frac{\alpha}{p} = Ae^{-B/(E/p)} \tag{3.14}$$

where p is the atmospheric pressure, E is the electric field and A and B are constants. The constants A and B depend on the gas under consideration and the atmospheric conditions. Even though the predictions of this equation are confirmed by experimental observation [5] this equation is not used in practice to evaluate the ionisation coefficient in air. It is customary to use the following set of empirical equations based

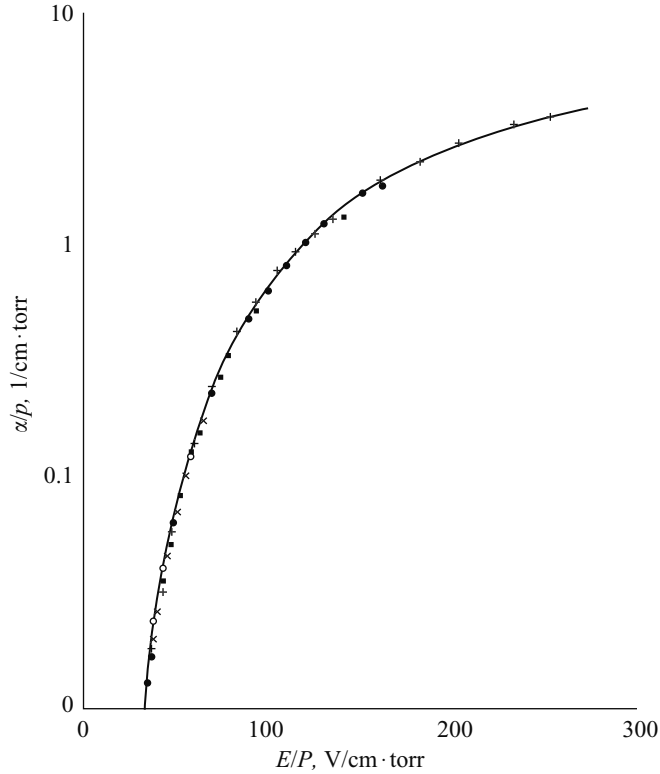

Figure 3.2 Measured ionisation coefficient α as a function of the reduced electric field E/p. Data of a number of authors are shown. The solid line represents eqn. 3.16 [2]

on experimental observations [2]:

$$\frac{\alpha}{p} = \exp\left(\frac{E/p - 58.2}{4.95}\right), \quad E/p \leq 35\,\text{V/cm/torr} \tag{3.15}$$

$$\frac{\alpha}{p} = \exp\left(\sum_{n=0}^{9} a_n \{E/p\}^n\right), \quad 35 \leq E/p \leq 250\,\text{V/cm/torr} \tag{3.16}$$

$$\frac{\alpha}{p} = 14.5\exp(-356p/E), \quad E/p \geq 250\,\text{V/cm/torr} \tag{3.17}$$

where E is in V/cm, p in torr and α is in cm^{-1}. The values of coefficients a_n are given in Table 3.3.

3.3.2 Photoionisation

Ionisation of an atom can be caused not only by energetic material particles but also by photons if the photon energy is larger than the ionisation energy of the atom. The

Table 3.3 Coefficients corresponding to eqn. 3.16

$a_0 = -0.64927 \times 10^{2}$
$a_1 = 0.52642 \times 10^{1}$
$a_2 = -0.20238 \times 10^{0}$
$a_3 = 0.45178 \times 10^{-2}$
$a_4 = -0.63081 \times 10^{-4}$
$a_5 = 0.56724 \times 10^{-6}$
$a_6 = -0.32780 \times 10^{-8}$
$a_7 = 0.11739 \times 10^{-10}$
$a_8 = -0.23661 \times 10^{-13}$
$a_9 = 0.20479 \times 10^{-16}$

process can be represented by the equation:

$$A + h\nu = A^{+} + e \tag{3.18}$$

where A is the target atom, h is Plank's constant and $h\nu$ is the energy of the incident photon. The escaping electron, e, has the energy $h\nu - h\nu_n$ where $h\nu_n$ is the ionisation energy and ν_n is the minimum frequency at which photoionisation occurs. This threshold frequency for ionisation is given by:

$$\nu_n = V_i / h \tag{3.19}$$

where V_i is the ionisation energy of the atom. Experiments show, however, that ionisation occurs even if the frequency of the incident photons is below this threshold [7]. The reason for this is the stepwise ionisation of the atoms where many photons act on the atom simultaneously. Stepwise ionisation caused by many photons is important in ionisation of gases by lasers where in many cases the energy of individual photons is less than the ionisation energy of the target atom.

3.3.3 Thermal ionisation

If a gas is heated the input heat energy will increase the translational or kinetic energy of the atoms in the gas. The velocities of the atoms are distributed according to the Boltzmann distribution and with increasing energy the atoms in the tail of the distribution may reach first energies sufficient to cause ionisation through collisions. With increasing temperature the number of atoms that have energies sufficient to cause ionisation increases and so do the number of ionisation collisions. However, in analysing the thermal ionisation it is not possible to consider only collisions between neutral atoms because once the ionisation sets in it will change the particle concentrations and the types of particle which in turn may take part in the ionisation process. For

example, ionisation in a gas at high pressure is caused by (i) ionisation by collision of atoms with atoms, (ii) photoionisation resulting from the thermal emissions and (iii) the collision of high energetic electrons produced by the above two processes. The first scientist to analyse this process in detailed was Saha [8]. In a gas volume heated to a high temperature there are electrons, neutral atoms, excited atoms, ions and radiation. In the mathematical development Saha assumed that all these species are in thermal equilibrium at the temperature of the gas volume. Then the Maxwell–Boltzmann distribution laws apply to the various components of the discharge. Using this procedure, Saha evaluated the concentration of different species in the discharge in terms of the gas temperature. For example, according to Saha the number of ionised particles in a volume of gas which is in thermodynamic equilibrium is given by:

$$\frac{\beta^2}{1-\beta^2} = \frac{2.4 \times 10^{-4}}{p} T^{2.5} e^{-V_i/kT} \tag{3.20}$$

with $\beta = n_i/n$ where n is the total number of particles and n_i is the number of ionised particles in the volume of gas under consideration, p is the pressure in torr, T is the temperature in kelvins, V_i is the ionisation energy of atoms in electron volts and k is the Boltzman constant given in units of eV/K. This expression is plotted in Figure 3.3 for several values of ionisation potential. The data shows that the thermal ionisation in air is significant only at temperatures above about 4000 K.

It is important to note that the derivation of the Saha equation does not depend on any particular ionisation process, although the thermal equilibrium implies thermal ionisation as opposed to ionisation created by the acceleration of charged particles.

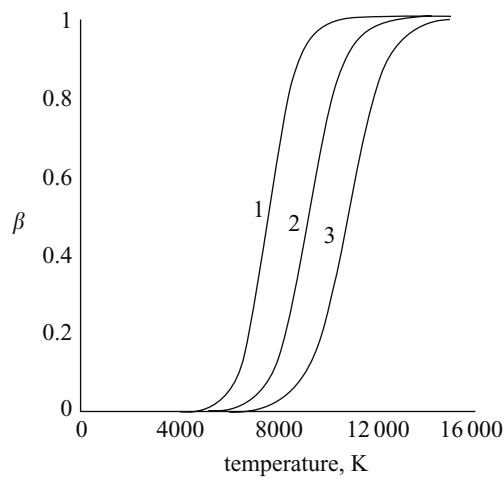

Figure 3.3 *The fraction of ionisation, β, as a function of temperature as predicted by the Saha eqn. 3.20*

(1) $V_i = 10\,\text{eV}$
(2) $V_i = 12.5\,\text{eV}$
(3) $V_i = 15\,\text{eV}$

However, the above equation is sometimes used in situations where the ionisation is known to occur through electron impacts with the temperature of the electrons at a higher level than that of the gas atoms. Then the temperature appearing in the equation is actually the electron temperature and the assumption is that the ionisation is the same if the process takes place thermally at that temperature.

3.3.4 Ionisation caused by meta-stable excited atoms

Usually, an excited atom in a gas returns from its excited state to the ground state within about 10^{-8} s, releasing the energy as one or more quanta of radiation. These are called normal excited states of the atom. The meta-stable excited states of an atom differ from these normal states in the following manner. Owing to quantum mechanical selection rule restrictions, the meta-stable level of an atom can be excited only by a direct electron impact and it can come back to its ground state only by transferring its extra energy to a third body. Thus, the duration of the meta-stable excited state could last 10–100 ms; however in the presence of other particles the life time of these states are much shorter than this time due to de-excitation by various collision processes [9]. If the meta-stable excited state has energy equal to or slightly higher than the ionisation energy of atoms in the ensemble the process leads to enhanced ionisation. This process is sometimes called the Penning ionisation. A typical collision process of this kind is given by [10]:

$$\mathrm{Ne_m} + \mathrm{A} = \mathrm{Ne} + \mathrm{A^+} + \mathrm{e} \tag{3.21}$$

where Ne_m is a meta-stable neon atom. For example, Figure 3.4 shows the breakdown voltage of neon and argon mixtures as a function of the argon content. Note the reduction of breakdown voltage of the mixture in comparison with the virgin gases. The reduction in the breakdown voltage is caused by the Penning ionisation. Normal excited states cannot take part in a similar process because, due to the short lifetime of the excited state, the atom suffers only a few collisions except when the gas pressure is very high before returning to the ground state.

It is important to note that common molecular gases have ionisation potentials below the meta-stable levels of He and Ne. Thus, small traces of (1 ppm) common molecular gases can drastically affect the electrical breakdown characteristics of inert gases.

3.3.5 Ionisation due to positive ions

Any charged particle can gain energy from an electric field and one can expect that if raised to sufficient energies through the application of an electric field, positive ions can also contribute to the ionisation process through collisions. Using the basic laws of mechanics one can easily show that a positive ion needs twice the energy needed by an electron to ionise an atom. However, the experimental data indicates that positive ions need more energy than this threshold before ionisation from them could be detected [11,44]. The reason for this could be that the collision between the ion and the atom is not so rapid so that the system can gradually adjust itself throughout the collision thus preventing kinetic to potential energy transfer leading to an elastic

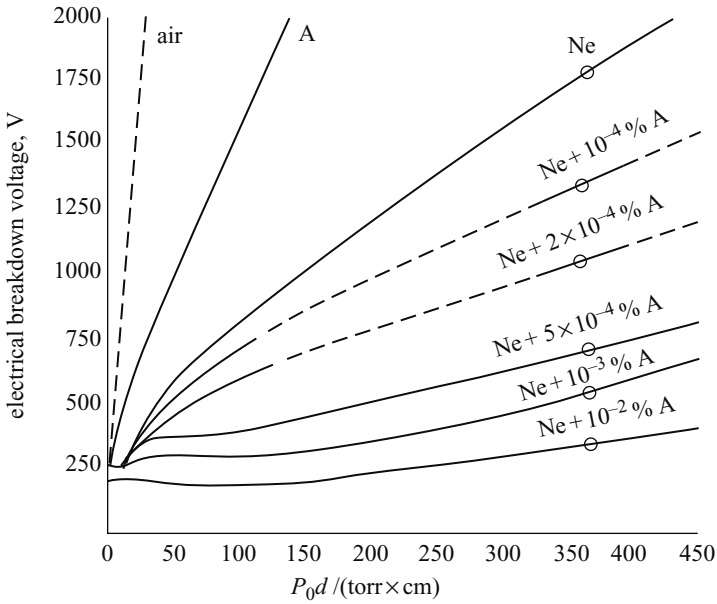

Figure 3.4 Electrical breakdown voltage, V, as a function of pd (pressure × gap length) in neon–argon mixtures between parallel plates at 2 cm spacing at 0°C (from [1])

collision. This may also depend on the fact that the collision is not point like, as in the case of electrons, and the collision energy is distributed in the electron cloud so that it is not concentrated on a single electron.

In considering the collision between the ions and molecules it is necessary to consider the collisions in which only charge transfer occurs between the colliding particles. One example is the collision of an argon atom, A, with singly ionised neon, Ne^+, where after the collision the argon is ionised leaving behind an energetic and neutral neon atom. This can be represented by:

$$A + Ne^+ = A^+ + Ne + \text{kinetic energy} \tag{3.22}$$

Such a process can produce fast neutral atoms at the expense of the kinetic energy of the ions. This is the reason why it is difficult to produce a homogeneous beam of high-speed positive ions in a gas.

3.4 Deionisation processes

3.4.1 Electron–ion recombination

In a volume of gas in which an electrical discharge takes place there is a high concentration of electrons and positive ions. Whenever these oppositely charged particles

come closer in collisions they have a tendency to recombine. The recombination between an electron and an ion can take place in several modes depending on the way in which the extra kinetic energy of the electron is removed.

3.4.1.1 Radiative recombination

In radiative recombination, as the electron combines with the ion, X^+, the extra energy of the electron is released as a quantum of radiation. During recombination the electron may be captured into a vacant orbit and the recombination energy is released as a photon, $h\nu$. The resulting neutral atom could be in an excited state which may come back to the ground state by releasing another photon. The process can be described by the following reaction:

$$X^+ + e = X^* + h\nu \tag{3.23}$$

where X^* denotes an excited state of X.

3.4.1.2 Dissociative recombination

In this mode of neutralisation the extra energy of the electron is spent in dissociating the ion, XY^+ to which it gets attached. In general, the dissociation process takes place in two steps. In the first step a negative, unstable and vibrationally excited ion, XY^* is formed. Subsequently, the relaxation of the vibrational energy causes the molecule to dissociate. This process can be visualised as follows:

$$XY^+ + e \Leftrightarrow (XY)^*_{\text{unstable}} \Leftrightarrow X^* + Y + (\text{kinetic energy}) \tag{3.24}$$

In the case of dissociative recombination the removal of energy to vibrational levels can be done very quickly (order of a vibrational period) and, therefore, high rates of recombination are realised. Due to the absence of dissociative recombination, the recombination process in monatomic gases is one or two orders of magnitude slower than that in molecular gases [12].

3.4.1.3 Three-body recombination

In this mode the extra energy of the reaction is transferred to a third body. At low pressures, however, the probability of finding a third body is rather small and three-body recombination mostly occurs at the walls of the discharge chamber, the latter acting as the third body. Thus, the probability of three-body recombination is rather low at low gas pressures and it increases with increasing pressure.

3.5 Other processes that can influence the process of ionisation

3.5.1 Electron attachment and detachment

Some molecules and atoms have an affinity to form negative ions. The ground state energy of the negative ions in these cases is slightly lower than the energy of the ground state of the neutral molecules. The difference in energy, which is released

Table 3.4 Electron affinities of some atoms and molecules

Atom or molecule	Electron affinity (eV)
O	1.461
O_2	0.451
O_3	2.103
NO_2	2.273
NO	0.026
SF_6	1.05–1.5
H	0.714

during the formation of negative ions, is called the electron affinity of the atoms or molecules. The stability of the negative ion increases with increasing electron affinity.

When electronegative molecules are present in a gas discharge they tend to attach to free electrons. This process will remove fast moving free electrons and replace them with slow moving molecules. Even though no charge is destroyed during the process, the development of the discharge can be impeded. Thus, the addition of electronegative gases into a discharge chamber may lead to the stabilisation of the medium against electrical breakdown.

The electron affinities of different molecules of interest are given in Table 3.4. Observe that the oxygen molecule is electronegative with an electron affinity of about 0.5 eV. The electron affinity of SF_6 is 1.0–1.5 eV, and this large affinity makes this gas a suitable candidate for increasing the breakdown voltage in high-voltage equipment.

The process of electron attachment can be divided into different types depending on the way in which the extra energy is released. As in the case of electron recombination, the process can be divided into radiative attachment, dissociative attachment or three-body attachment. The three processes can be described mathematically as:

$$e + XY = XY^- + h\nu \text{ (radiative attachment)} \tag{3.25}$$

$$e + XY = X + Y^- \text{ (dissociative attachment)} \tag{3.26}$$

$$e + XY + Z = XY^- + Z \text{(three-body attachment)} \tag{3.27}$$

where XY is a molecular species, $h\nu$ is the energy released as radiation and Z is an atom or molecule that acts as a third body.

The process of attachment can be defined in terms of an attachment coefficient or by an attachment frequency. The attachment coefficient η denotes the number of attachment events per electron per unit length of travel. The attachment frequency is a measure of how fast free electrons are disappearing in a given medium due to attachment. This can be represented by the equation:

$$n_e = n_0 \exp(-\nu_a t) \tag{3.28}$$

where n_0 is the density of free electrons at $t = 0$ and n_e is the density of free electrons at time t. For thermalised electrons at $T = 300\,\mathrm{K}$ the value of $\nu_a = 0.9 \times 10^8\ \mathrm{s}^{-1}$ [13]. That is, the lifetime of an free electron in air is about 10^{-8} s.

The attachment coefficient of electrons is a function of the electric field and the pressure. Its value in air can be calculated from the empirical equation [2]:

$$\frac{\eta}{p} = 1.95\frac{e^{-60p/E}}{E/p} \tag{3.29}$$

where p is in torr, η is in cm^{-1} and E/p is expressed in units of V/cm/torr.

Electron detachment is the opposite of electron attachment. Once an electron is attached to an atom or molecule it is necessary to provide the negative ion with a certain amount of energy to remove the attached electron. This amount of energy is equal to the electron affinity in the case of atoms but need not be the same as electron affinity in the case of molecular ions. Depending on the way in which this energy is supplied, the detachment process can be divided into three categories.

The first process is called photo detachment. In this case the extra electron of a negative ion can be detached by the energy of incident photons. The process can be described by the equation:

$$XY^- + h\nu = XY + e \tag{3.30}$$

where $h\nu$ is the energy of the photon.

The second process is associative detachment. This is the inverse process of dissociative attachment and can be represented by:

$$X^- + Y = XY + e \tag{3.31}$$

If the electron affinity of X^- is less than the dissociative energy of XY, the reaction is possible for zero relative kinetic energy of X^- and Y and the process can therefore be important under electrical discharge conditions.

Collisional detachment is the third process. In this case the energy necessary to release the electron from the ion is obtained from the energy released during the collision of negative ion, XY^-, with another atom or molecule, Z. This is actually the reverse of the three-body attachment, and can be represented by:

$$XY^- + Z = XY + Z + e \tag{3.32}$$

This process is important under discharge conditions and most probably the first seeding electrons necessary for the initiation of an electrical discharge in air are produced by this process. For example, the negative O_2^- ions are decomposed by collisions with molecules possessing an energy high enough to detach an electron. Especially effective in this are the excited nitrogen molecules [12,13].

The situation is little bit more complicated in the case of humid air. The detachment of electrons from negative oxygen atoms in humid air is much slower than in dry air because the negative ions become hydrated by attaching to a cluster of water

molecules i.e. $O_2^-(H_2O)_n (n = 1, 2, 3 \ldots)$. The most probable cluster type in atmospheric pressure is $O_2^-(H_2O)_3$ [13]. The detachment energy increases with cluster number and, therefore, it is more difficult to remove an electron from a hydrated ion. In order to detach an electron from a hydrated ion the latter has to be declustered first and then the electron removed from the negative ion.

3.5.2 Excitation of molecular vibrations

Low-energy electrons can actively excite molecular vibrations, and this is one of the most important processes for removing energy from free electrons in air. In nitrogen, molecular vibrations are excited by electrons in the range of energies 1.8–3.3 eV. Electrons can also excite rotational levels, but the process is not that important as an energy-draining source. In moderate values of E/p about 3–30 $\mathrm{V\,cm^{-1}\,torr^{-1}}$, electrons spend about 90–95 per cent of the gained energy in exciting molecular vibrations in air and nitrogen [12]. At higher values of E/p excitation of electronic levels and ionisation are the main energy-draining processes.

Once a molecule is excited vibrationally it will take some time for this energy to convert back to translational or kinetic energy. This process is called vibrational–translational (VT) relaxation and is denoted by the relaxation time τ. In dry air at atmospheric pressure $\tau = 1.7 \times 10^{-2}$ s. In air containing $0.8 \times 10^{-5}\,\mathrm{g\,cm^{-3}}$ of water the relaxation time decreases to $\tau = 7 \times 10^{-4}$ s. That is, water molecules can deactivate the molecular vibrations. In hot humid air $\tau = 8 \times 10^{-05}$ s at 1000 K and will decrease to 10^{-5} s at 2000 K [12]. This shows that the VT relaxation process is self accelerated, that is, the relaxation produces heat resulting in an increase of temperature of the gas which in turn decreases the relaxation time, thus accelerating the relaxation process.

3.5.3 Diffusion

Diffusion plays an important role during the initiation and decay of discharge channels because it causes charged particles to move from regions of high concentration, where they are created, to regions of low concentration. This reduces the charge density in the source region thus impeding the discharge development.

A given volume of an electrical discharge contains both electrons and positive ions. Electrons being smaller than the positive ions diffuse faster from regions of high concentration, which will lead to a charge separation and result in the creation of an electric field. This electric field will accelerate the drift of positive ions but retard the drift of electrons. However, at equilibrium, there will be an equilibrium electric field and both electrons and positive ions will diffuse at the same rate. Diffusion taking place under these circumstances is called ambipolar diffusion.

Let us consider a situation in one dimension where the concentration of particles varies in the x direction. The number of particles crossing a unit area of thickness dx placed perpendicular to the direction of x per unit time (i.e. the particle flux in the

x direction), p_f, is given by:

$$p_f = -D\frac{dn}{dx} \tag{3.33}$$

where D is the coefficient of diffusion and n is the concentration of particles (i.e. number of particles per unit length). The rate of increase of the number of particles in the element dx is:

$$\frac{\partial n}{\partial t}dx = p_f(x) - p_f(x + dx) \tag{3.34}$$

This can be written as:

$$\frac{\partial n}{\partial t}dx = p_f(x) - \left[p_f(x) + \frac{\partial p_f(x)}{\partial x}dx\right] \tag{3.35}$$

or

$$\frac{\partial n}{\partial t} = \frac{\partial p_f(x)}{\partial x} \tag{3.36}$$

Combining eqns 3.33 and 3.36 one obtains the rate of change of concentration of charged particles due to diffusion as:

$$\frac{\partial n}{\partial t} = D\frac{\partial^2 n}{\partial x^2} \tag{3.37}$$

In three dimensions this can be written as:

$$\frac{\partial n}{\partial t} = D\nabla^2 n \tag{3.38}$$

The diffusion coefficient of electrons is related to their mobility through the equation:

$$\frac{\mu}{D} = \frac{2.4 \times 10^{19} e}{\varepsilon_e} \tag{3.39}$$

where μ is the mobility (in $\mathrm{cm^2\,V^{-1}\,s^{-1}}$), e is the electronic charge (in C), ε_e is the mean energy of the electrons (in eV) and D is given in $\mathrm{cm^2 s^{-1}}$. The electronic mobility is a function of the electric field and for air it can be obtained from the equations for the drift velocity (eqns 3.5 and 3.6). The mean energy of the electrons is also a function of the background electric field. The relationship between the two parameters in air can be described by the equation [2]:

$$\eta_m = 17(E/p)^{0.71}, \quad E/p \leq 3\,(\mathrm{V/cm.torr}) \tag{3.40}$$

$$\eta_m = 21(E/p)^{0.49}, \quad E/p \geq 3\,(\mathrm{V/cm.torr}) \tag{3.41}$$

with

$$\eta_m = \varepsilon_e/\varepsilon_{gas} \tag{3.42}$$

where ε_{gas} is the mean thermal energy of the gas molecules given by $3\,kT/2$ (T is the gas temperature in kelvins and k is the Boltzman constant). In the above equation E is given in V/cm, p in torr. Using these equations one can calculate the coefficient of diffusion of electrons in air for a given value of E/p.

3.6 Cathode processes

In general, laboratory discharges are created between electrodes and these electrodes can supply the discharge with electrons through various physical processes. Under normal conditions electrons in a metal are prevented from leaving that metal by electrostatic forces between the electrons and the ions in the metal lattice. As shown in Figure 3.5*a* the electrons in the metal are trapped in a potential well. The energy necessary to remove an electron from the top of the Fermi energy levels is known as the work function of the metal. This is denoted by ϕ in Figure 3.5*a*. The work functions of typical metals are tabulated in Table 3.5 [14].

Electrons can be removed from the metal either by giving the electrons sufficient kinetic energy to surmount the potential barrier, or the work function, at the surface, by reducing the height of the barrier so that the electrons can overcome it or by reducing the thickness of the barrier so that the electrons can tunnel through it. The first can be achieved by the application of heat to the electrode, through impact of photons on the surface of the electrode or by the incidence of particles such as other electrons, positive ions, neutral molecules, meta-stable atoms on the electrode. The reduction in the potential barrier height or its thickness can be achieved by the application of an electric field in the correct direction so that the electrons will experience a force directed out of the metal surface (see figure 3.5b). Let us consider different physical processes that can cause emission of electrons from metals.

3.6.1 Photoelectric emission

When a photon is incident on a metal it can transfer all its energy to an electron in the metal so that the latter can surmount the potential barrier at the surface. Thus, an electron at the Fermi level after absorbing the energy of the quanta can escape with energy E_e given by:

$$E_e = h\nu - \phi \tag{3.43}$$

where $h\nu$ is the energy of the photon. For a clean Ag surface $\phi = 4.74$ eV (Table 3.5) and the threshold frequency corresponds to a wavelength of 2616 Å.

3.6.2 Thermionic emission

In metals at room temperature the energy of the conduction electrons is not sufficient for them to surmount the potential barrier at the surface of metals. However, heating a metal will increase the kinetic energy of its electrons. With increasing

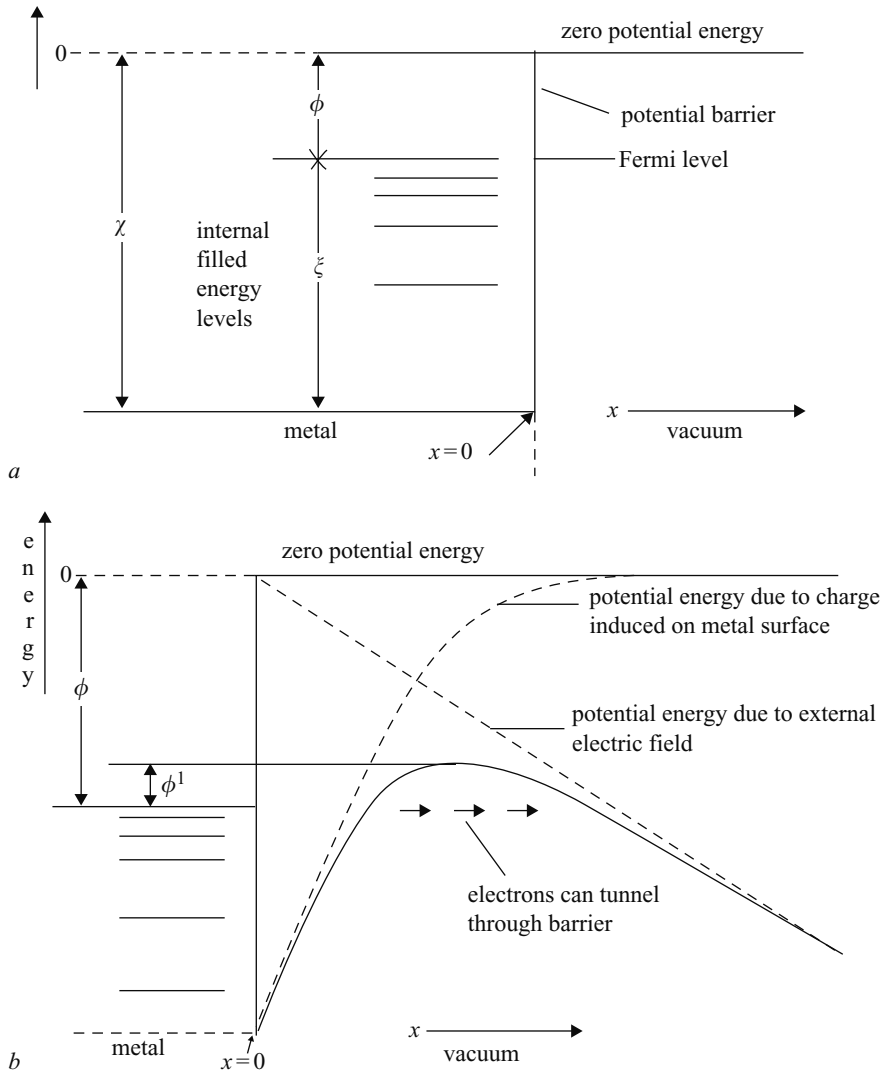

Figure 3.5 Energy diagram

a electrons in a metal

b when an electric field is applied. Note that the electric field not only reduces the height of the barrier but it also reduces the thickness of the barrier. This makes it easier for the energetic electrons to jump over the barrier (Schottky effect) and a certain percentage of the electrons to tunnel through the barrier

Table 3.5 Work function for typical elements

Element	Ag	Al	Cu	Fe	W
W_a (eV)	4.74	2.98–4.43	4.07–4.7	3.91–4.6	4.35–4.6

temperature one may expect the number of electrons surmounting the barrier to increase. Since this process is caused by the heating of the electrode it is called thermionic emission. The thermionic current density, J_t, is given by the following equation [15]:

$$J_t = AT^2 \exp(-\phi/kT) \tag{3.44}$$

where k is the Boltzman constant, ϕ is the work function of the metal, T is the absolute temperature and A is a constant equal to $120\,\mathrm{A\,cm^{-2}\,deg^{-2}}$. Actually, the experimentally obtained current densities are smaller than those predicted by this equation because this equation does not take into account the wave nature of electrons and the possibility that some of the electrons will be reflected at the barrier even if they have enough energy to overcome it.

3.6.3 Schottky effect

As one can see from the equation given in the previous section, the thermionic current depends on the height of the barrier that the electrons have to surmount in order to come out of the metal. The height of this barrier can be decreased by the application of an electric field in such a way that the electrons in the metal experience a force out of the metal. This is illustrated in Figure 3.5*b*. In the presence of such an electric field the work function is effectively reduced to [16]:

$$\phi_1 = \phi - \sqrt{\frac{e^3 E}{4\pi\varepsilon_0}} \tag{3.45}$$

This reduction in the barrier height will lead to a change in the thermionic emission current. Thus, if J_0 is the thermionic emission current density for zero electric field at temperature T then the current density at the same temperature in the presence of an electric field E is given by:

$$J_s = J_0 \exp(4.4\sqrt{E}/T) \tag{3.46}$$

where the electric field E is given in V/cm and T in kelvins. This was shown to be valid for electric fields up to about 10^6 V/cm. This process of enhancement of the thermionic emission current due to the reduction in the barrier height is called Schottky emission.

3.6.4 Field emission

Calculations done with the Schottky equation show that the thermionic emission current at $T = 293$ K for values of ϕ about 4.5 eV is negligible even when the electric field reaches values as high as 10^6 V/cm. However, experiments show that electrodes in vacuum do emit appreciable currents, in the range of μA, at such electric fields. The reason for this is the quantum nature of the elementary particles. The illustration in Figure 3.5*b* shows that the application of the electric field not only reduces the height of the barrier but will also decrease its thickness. In the absence of the electric field the barrier is infinitely thick but its thickness decreases with increasing electric field.

Electrons incident on the barrier can be represented by a wave; during the interaction part of the wave will be reflected and the other part of the wave will be transmitted. The transmitted wave attenuates rapidly when moving into the barrier, but if the thickness of the barrier is not large a small fraction of the wave may be able to penetrate it. Of course, in the case of electrons, the reflection and transmission coefficients have to be regarded as probability functions, so there is a certain probability that an electron incident on the barrier will penetrate it. If the number of electrons incident on the barrier per unit time is known, quantum mechanical calculations can be performed to evaluate the number of electrons coming out of the barrier. Fowler and Norheim [17] analysed this process in detail and obtained the following expression for the field emission current density, J_f, for pure metallic surfaces in vacuum:

$$J_f = 61.6 \times 10^{-7} \frac{\zeta^{1/2} E^2}{(\zeta + \phi)\phi^{1/2}} \exp(-6.8 \times 10^7 \phi^{3/2}/3E) \tag{3.47}$$

where $\zeta = 5$ eV (typical value for metals), ϕ is the work function in eV, E is the electric field in V/cm and the current density is given in A/cm^2. This equation indicates that measurable currents should be obtained for electric fields of the order of 10^7 V/cm. This has been found to be valid for very clean surfaces. Experiments show, however, that an appreciable electric field dependent emission current can be obtained for electric fields one to two orders of magnitude smaller than this in the presence of surface contamination. The reason for this is that surface contamination causes a reduction in the width of the barrier thus enhancing the field emission process. Moreover, if there are protrusions on the surface the electric field at the tip of these protrusions can reach very high values leading to field emission from them. The field emission process is very important in providing initiatory electrons in the creation of electrical discharges.

3.6.5 Incidence of positive ions

It was mentioned previously that photons incident on a metal can supply electrons with energy sufficient to surmount the barrier. Indeed, not only photons but also elementary particles incident on the surface can cause electrons to be ejected from the surface. This is a common situation at the surface of the cathode of an electrical discharge

where positive ions, having sufficient energy to support an electron to overcome the potential barrier, are incident on the cathode and liberate electrons from it.

3.7 Electrical breakdown

In a given environment with a background electric field there is a competition between the ionisation and deionisation processes. The ionisation processes attempt to increase the number of electrons in the environment whereas the deionisation processes attempt to reduce their number. The relative efficiency of the two competing processes depends on the magnitude of the background electric field. Figure 3.6 shows how the frequency of ionisation, ν_i, and the frequency of attachment, ν_a, vary as a function of the reduced electric field. Since $\alpha = \nu_i/v_e$ and $\eta = \nu_a/v_e$, where v_e is the electron drift velocity, one can also infer from the data how the ionisation coefficient and the electron attachment coefficient in air at atmospheric pressure vary as a function of the background electric field [18]. Note that the two curves cross (i.e. $\alpha = \eta$) around 2.6×10^4 V/cm. Since cumulative ionisation is possible only if $\alpha > \eta$, the background electric field should exceed this critical value in atmospheric air before electrical breakdown takes place. This value is called the breakdown electric field in atmospheric air and in qualitative analysis it is assumed to be 3.0×10^4 V/cm.

Figure 3.7 illustrates how the background electric field necessary to cause electrical breakdown in a plane parallel gap (i.e. the electric field is uniform) varies with the plate separation [19,29]. Note that for small gap separations the breakdown electric field is larger than the critical field given above. However, the breakdown electric field approaches this critical electric field with increasing gap distance. The data shows that in order to create electrical breakdown two conditions should be satisfied. First, the electric field in the gap should exceed a critical value. Second, depending on the

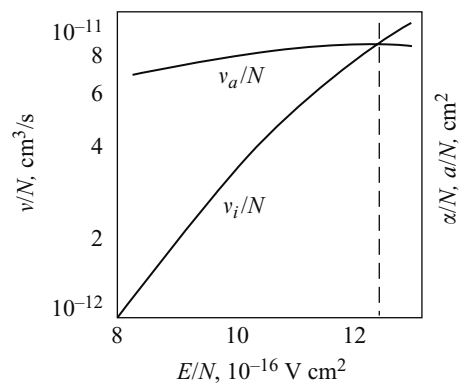

Figure 3.6 The electron ionisation frequency (per unit air density), ν_i/N, and the electron attachment frequency (per unit air density), ν_a/N, as a function of reduced electric field in air [18]. N is the density of air, at $T = 273\,k$ and $p = 760$ Torr, $N = 2.69 \times 10^{19}\,cm^{-3}$

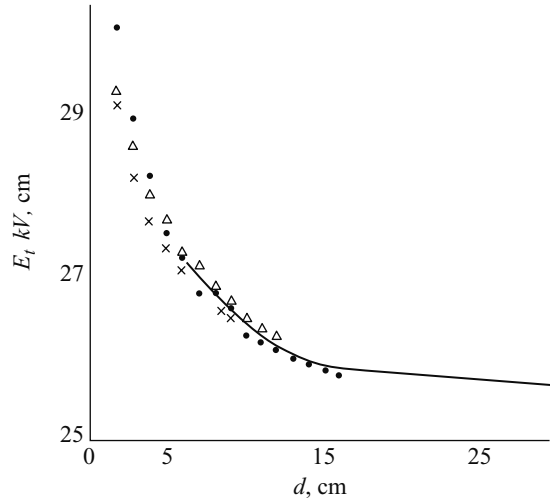

Figure 3.7 Threshold electric field, E_t, for the breakdown of air ($p = 760$ torr, water vapour pressure $= 20$ torr, temperature $= 20°C$) as a function of the gap length, d. Data of a number of authors are shown by different symbols in the Figure [19]

magnitude of the electric field there is a certain critical length over which the electric field should extend. This critical length decreases with increasing electric field.

The physical processes that take place during the formation of an electric discharge can be summarised as follows. The electrical breakdown in a gas starts with a single electron which will lead to an avalanche of electrons created through the electron collision ionisation. As the avalanche grows the electric field created by charges concentrated at the avalanche head starts to modify the electric field in the vicinity of the head of the avalanche. When this space charge electric field reaches a critical value the avalanche will convert itself to a streamer discharge. If the gap is short then the streamer discharge may bridge the gap and, after streamer to spark transition, the complete breakdown of the gap may take place. If the gap is long many streamers may start from the electrode having their origin at a common streamer stem. The heat generated by the streamer currents will increase the temperature of the streamer stem and when the temperature reaches a critical value the thermal ionisation sets in the stem, the conductivity of the stem increases and it will convert itself to a leader discharge. Since the leader channel is a good conductor the potential of the electrode is now transferred to the head of the leader channel and the resulting high electric field will cause streamers to grow from the head of the leader channel. The leader elongates in the gap through the action of streamers that forge further and further into the gap. When the leader discharge reaches the grounded electrode the current in the channel increases, and the applied voltage collapses, leading to the formation of a spark. In the following sections the processes that take place in the formation of electric sparks are described.

3.7.1 Electron avalanche

Consider a free electron originated at $x = 0$ in space and moving under the influence of a background electric field directed in the x direction. If the background electric field is larger than the critical value necessary for cumulative ionisation the electron may produce another electron through ionisation collisions and these two electrons in turn will give rise to two more electrons. In this way the number of electrons increases with increasing x. Assume that the number of electrons at a distance x from the origin is n_x. Let α be the number of ionising collisions per unit length made by an electron travelling in the direction of the electric field and η be the number of attachments over the same length. As discussed previously α is Townsend's ionisation coefficient and η is the attachment coefficient. Consider an elementary length of width dx located at a distance x from the origin. In travelling across the length dx, n_x number of electrons will give rise to dn additional electrons:

$$dn = n_x(\alpha - \eta)\, dx \tag{3.48}$$

The solution of this equation is:

$$n_x = e^{(\alpha-\eta)x} \tag{3.49}$$

This equation shows that the number of electrons increases exponentially with distance. This exponential growth of electrons with distance is called an electron avalanche. Figure 3.8 shows a photograph of an electron avalanche obtained in a cloud chamber [20]. The equation also shows that cumulative ionisation is possible only if $(\alpha - \eta) > 0$. The quantity $(\alpha - \eta)$ is known as the effective ionisation coefficient and denoted by $\bar{\alpha}$.

It is important to note, however, that the value of n_x given in eqn. 3.49 is a mean value and it is subject to considerable variations due to the statistical nature of the collision process. The probability that one electron at the origin results in an avalanche of total number n at a distance x is given by

$$P(n, x) = \frac{1}{n_{mean}}\left[1 - \frac{1}{n_{mean}}\right]^{n-1} \tag{3.50}$$

with a standard deviation given by:

$$\sigma = n_{mean}\left[1 - \frac{1}{n_{mean}}\right]^{1/2} \tag{3.51}$$

where

$$n_{mean} = e^{(\alpha-\eta)x} \tag{3.52}$$

For large values of n this becomes:

$$P(n, x) = \frac{1}{n_{mean}} e^{-n/n_{mean}} \tag{3.53}$$

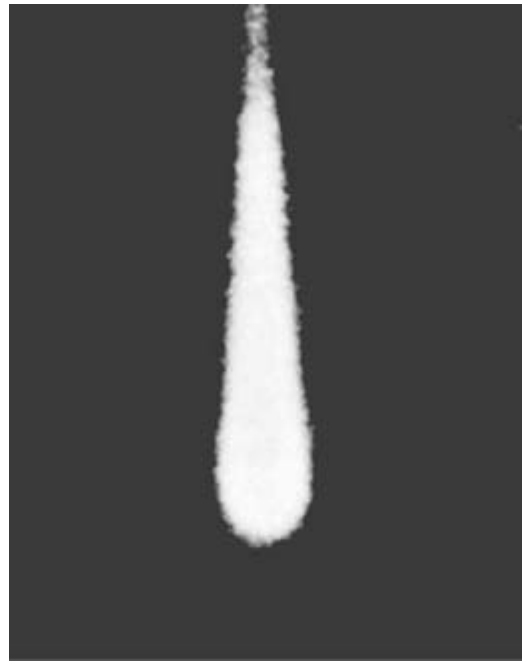

Figure 3.8 Cloud chamber photograph of a single electron avalanche (from [62])

with $\sigma = n_{mean}$. That is, the size of an electron avalanche originating from a single electron follows an exponential distribution. It is important to note that this result is based on the assumptions that the space charge of the avalanche does not have significant influence on the background electric field and the probability of an electron ionising a gas molecule is constant and is independent of the distance it has travelled in the electric field direction since the last ionising collision.

3.7.2 The space charge electric field due to an avalanche

It was shown in the previous sections that as an avalanche initiated by a single electron grows the number of electrons in the avalanche head increase according to the formula:

$$n = e^{\bar{\alpha}x} \tag{3.54}$$

where $\bar{\alpha}$ is the effective ionisation coefficient. Let us assume that these electrons at the head of the avalanche are confined to a spherical region of radius r. Then the electric field at the head of the avalanche is given by:

$$E_r = \frac{ee^{\bar{\alpha}x}}{4\pi\varepsilon_0 r^2} \tag{3.55}$$

where e is the electronic charge (not to be confused with the exponential). In fact, as the electron avalanche advances, its tip is spreading laterally by the random diffusion of the electrons. The average radial distance of diffusion can be calculated from the equation $r = \sqrt{4Dt}$ where $t = x/v_d$ is the time of advance of the avalanche, D is the coefficient of diffusion and v_d is the drift velocity of the electrons. Substituting this into eqn. 3.55 one obtains:

$$E_r = \frac{e e^{\bar{\alpha} x}}{4\pi\varepsilon_0}\left(\frac{v_d}{4Dx}\right) \tag{3.56}$$

This equation shows that with increasing avalanche length the electric field created by the space charge increases and at a certain critical length the electric field generated by the space charge becomes comparable to the background electric field. At this stage an electron avalanche will convert itself to a streamer discharge.

3.7.3 Formation of a streamer

A schematic description of the formation of a positive streamer is shown in Figure 3.9 [21]. As the electron avalanche propagates towards the anode low mobile positive space charge accumulates at the avalanche head. When the avalanche reaches the anode, the electrons will be absorbed into it leaving behind the net positive space charge. Due to the recombination of positive ions and electrons, the avalanche head is a strong source of high energetic photons. These photons will create other avalanches in the vicinity of the positive space charge. If the number of positive ions in the avalanche head is larger than a critical value the electric field created by the space charge becomes comparable to the background electric field and the secondary avalanches created by the photons will be attracted towards the positive space charge. The electrons in the secondary avalanches will be neutralised by the positive space charge of the primary avalanche leaving behind a new positive space charge, a little bit closer to the cathode. The process repeats itself and the positive space charge head travels towards the cathode as a consequence. This discharge is called a cathode directed streamer or a positive streamer. Cloud chamber photographs of the creation and propagation of streamer discharges are shown in Figure 3.10 [19].

The formation of a negative streamer or an anode directed streamer is shown in Figure 3.11. The electrons of the avalanche move into the gap leaving behind positive charge close to the cathode. When the avalanche reaches the critical size the secondary avalanches extend the positive space charge towards the cathode (as in a cathode directed streamer). When the positive channel reaches the cathode both the field enhancement associated with the proximity of positive space charge to the cathode and the collision of positive ions on the cathode lead to the emission of electrons from the latter. These electrons will neutralise the positive space charge creating a weakly conducting channel that connects the negative head of the electron avalanche to the cathode. The high electric field at the head of the avalanche pushes the negative space charge further into the gap while the positive space charge left behind is neutralised by the electrons supplied by the cathode and

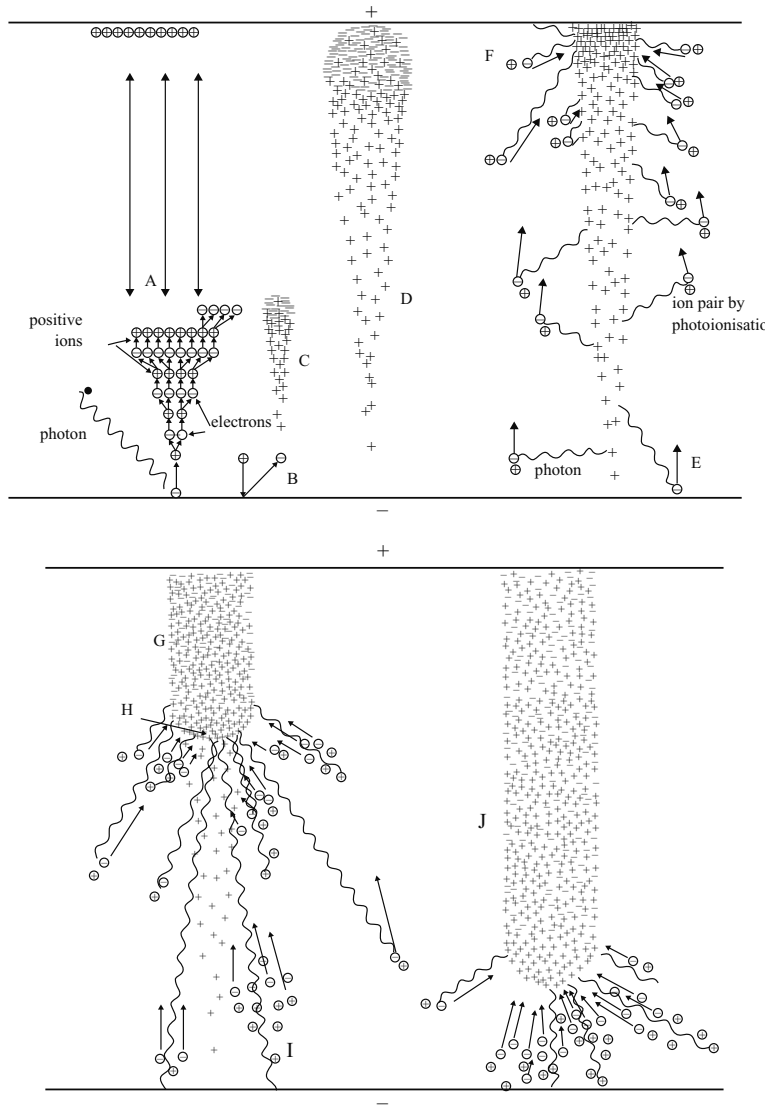

Figure 3.9 *Schematic diagram showing the formation of a positive streamer. A: an external photon triggers an avalanche. B: a positive ion strikes the cathode and starts an avalanche C. D: the avalanche tip reaches the anode. E: photons originating from the avalanche produce free electrons both from the cathode and in the gas. F: the positive space charge close to the anode increases the electric field and a streamer is just about to be formed. G: plasma of positive ions and electrons forms the streamer channel. H: streamer tip. I: production of free electrons by photons. J: streamer close to the cathode* (from [21])

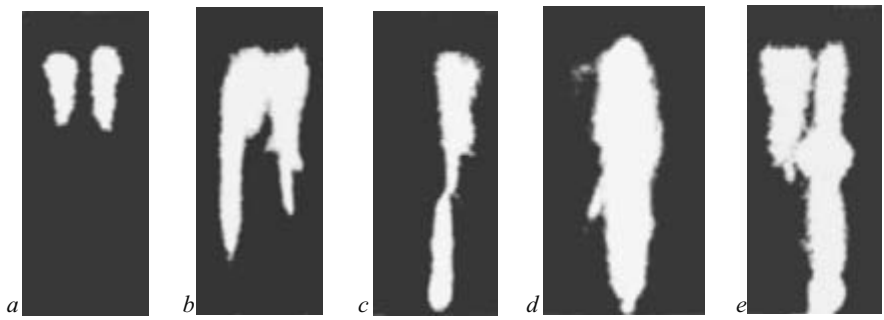

Figure 3.10 *Cloud chamber photograph showing the development of positive streamers* (from [22]).

a	avalanche near the anode
b and *c*	positive streamer starts
d and *e*	the streamer bridges the gap (from [22])

travelling along the weakly conducting channel connecting the streamer head and the cathode.

If the background electric field is very high the positive space charge of the avalanche may reach the critical size necessary for streamer formation before reaching the anode. This may lead to the formation of a bidirectional discharge the two ends of which travel towards the anode and the cathode, the former as a negative streamer and the latter as a positive streamer. Such a discharge is called a mid-gap streamer. This is illustrated in Figure 3.12.

As the streamer propagates it may lead to the formation of branches. The mechanism of streamer branching is illustrated in Figure 3.13.

The avalanche to streamer transition takes place when the number of charged particles at the avalanche head exceeds a critical value, N_c. From cloud chamber photographs of the avalanches and streamers, Raether [22] estimated that an avalanche will convert to a streamer when the number of positive ions in the avalanche head reaches a critical value of about 10^8. A similar conclusion is also reached independently by Meek [23]. Thus the critical avalanche length for transition to a streamer is given by:

$$e^{\bar{\alpha} x_c} = 10^8 \tag{3.57}$$

or

$$\bar{\alpha} x_c \approx 18 \tag{3.58}$$

Figure 3.14 shows the critical avalanche length at which an electron avalanche transforms itself to a streamer discharge as a function of the background electric field which is assumed to be uniform [24]. Note that the critical avalanche length decreases with increasing electric field.

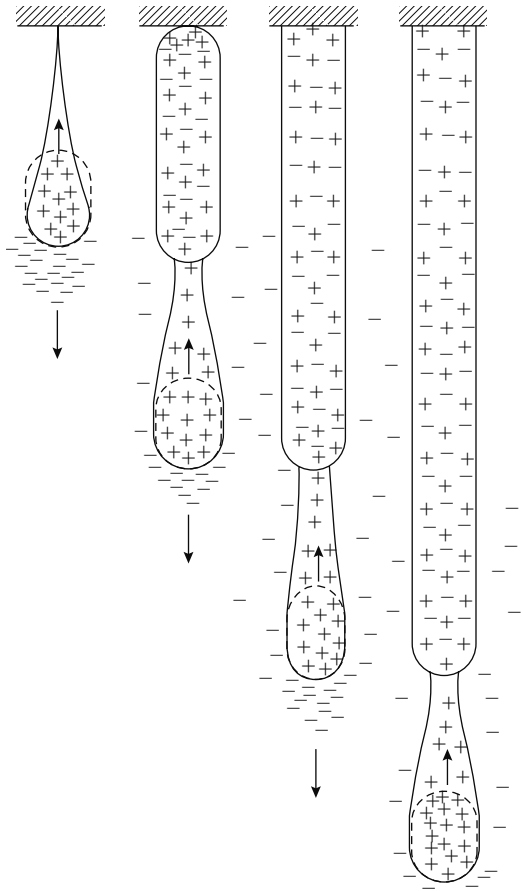

Figure 3.11 *Schematic representation of the formation of a negative streamer and the physical processes taking place at the streamer head* (adapted from [63])

3.7.4 Characteristics of the streamers

3.7.4.1 The physical processes taking place at the streamer head and its propagation

The advancement of the streamer in a given background electric field is based on the distortion of the electric field at and the enhanced production of the photons from the head. The photons create secondary electrons in front of the streamer head and these secondary electrons give rise to secondary avalanches which will move, in the case of positive streamers, towards the streamer head. Once initiated, the streamers have been observed to travel in background electric fields that themselves cannot support avalanche formation. Thus, the secondary avalanche formation in the streamer is confined to a very small region around the streamer head where the

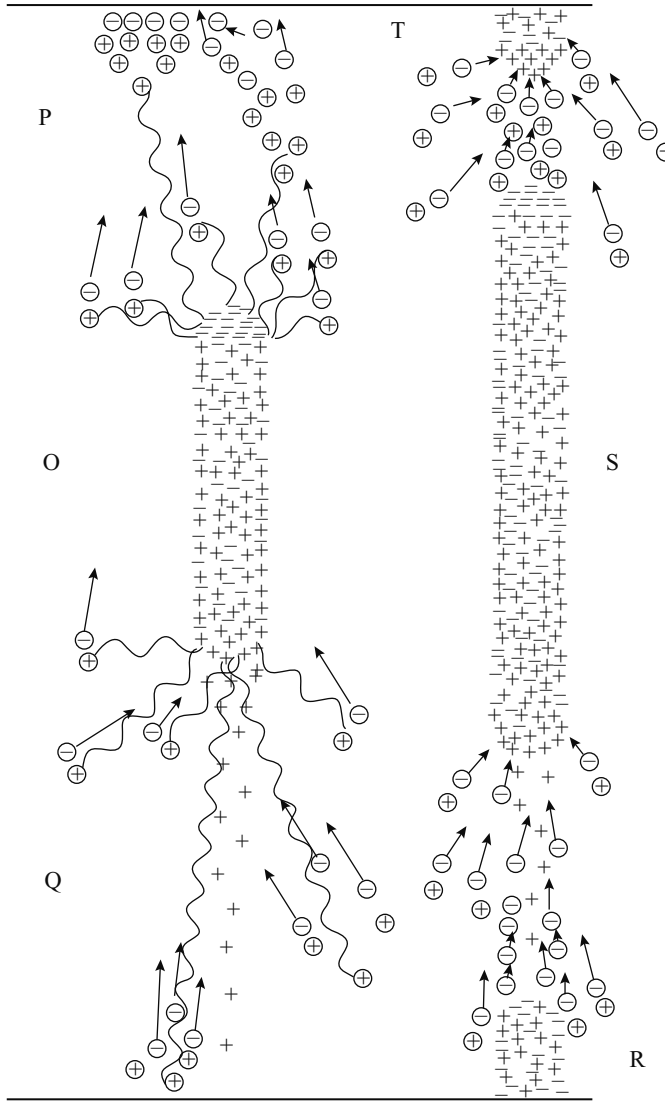

Figure 3.12 *Schematic diagram showing the formation of a mid-gap streamer. The electron avalanche coverts itself to a streamer when it has advanced two thirds of the gap (O). This may lead to the formation of a bidirectional discharge the two ends of which travel towards the anode and the cathode, the former as a negative streamer and the latter as a positive streamer. As the streamer heads approach the electrodes the electric field at the electrodes is enhanced leading to the formation of avalanches (P and Q) which may even lead to the formation of streamers from the electrodes (T and R)* (from [21])

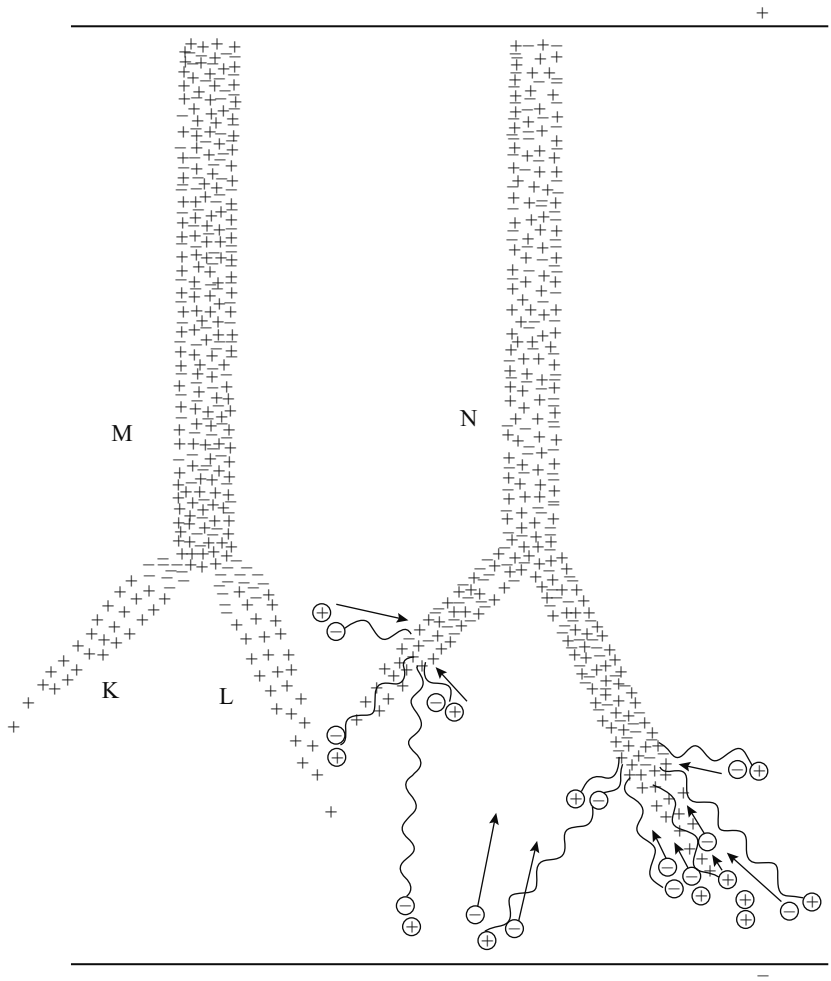

Figure 3.13 *Schematic diagram showing the branching of the streamer. The streamer channel M attracts two avalanches K and L towards its tip simultaneously leading to the formation of a branch* (from [21])

electric field exceeds 2.6×10^4 V/cm which is the minimum field required for the cumulative ionisation in air at atmospheric pressure. This region is called the active region. A schematic representation of the streamer tip and the active region is shown in Figure 3.15.

If the number of positive charges at the streamer head of radius R_s is Q_c then, assuming spherical charge distribution, the electric field at a distance r from the centre of the charge distribution is given by:

$$E(r) = \frac{Q_c}{4\pi\varepsilon_0 r^2} \quad \text{for } r > R_s \tag{3.59}$$

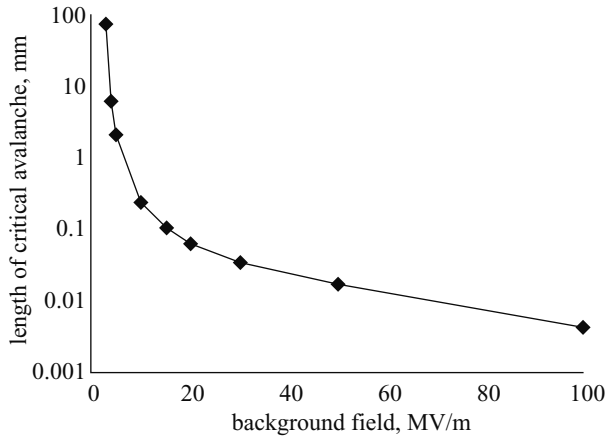

Figure 3.14 The length of the avalanche at the avalanche to streamer transition for different values of the uniform background electric field [24]

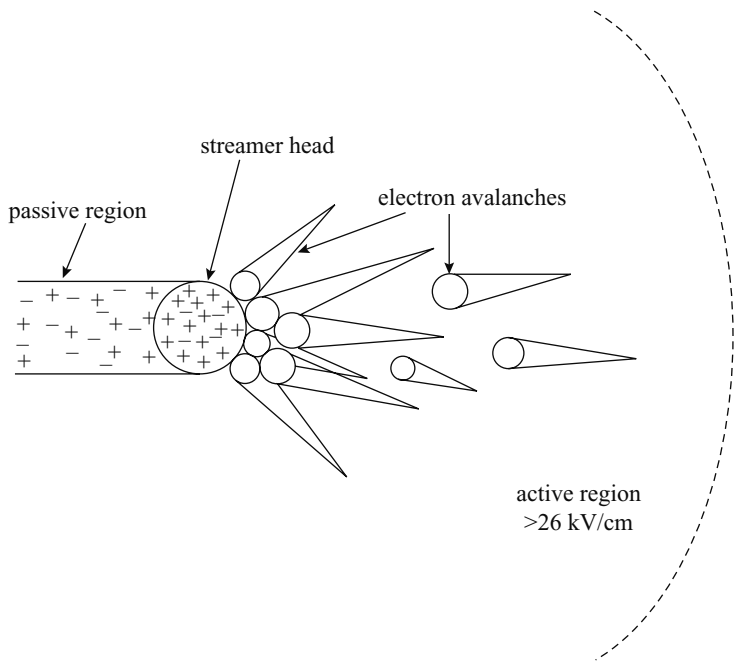

Figure 3.15 Schematic presentation of the active region of the streamer (adapted from [13])

With the number of charges at the head equal to 10^8 (i.e. $Q_c = 10^8 e$, where e is the electronic charge), the electric field will be higher than 2.6×10^4 V/cm for a radius of 0.23 mm. This shows that the radius of the active region is about 200 μm. The average electron energy in the active region is about 10–15 eV and this corresponds to an average electric field of about 1–1.5 $\times$ 10^5 V/cm [25].

3.7.4.2 Propagation of the streamer discharges

A schematic representation of the propagation of a positive streamer is shown in Figure 3.16. The local but strong electric field resulting from the concentration of positive charge at the streamer head attracts the secondary avalanches towards it. These avalanches neutralise the positive space charge of the original streamer head leaving behind an equal amount of positive space charge at a location slightly ahead of the previous head. The repetition of the process leads to an effective forward propagation of the streamer head connected to the anode by a weakly conducting channel.

Since the electron multiplication in the active region is supported by the space charge electric field of the streamer head, the streamer can propagate in electric fields which are much smaller than the critical electric field necessary for cumulative electron ionisation. Indeed, Dawson and Winn have shown that a spherical space charge containing 10^8 electrons confined within a radius of 30 μm can propagate in zero electric field for a short time [26].

The mechanism of propagation of negative streamers is a little bit more complicated than that for positive streamers. This is shown in Figure 3.17. Note that there are two main differences between the negative and positive streamers. In the negative streamer, the electrode has to supply the electrons necessary for the neutralisation of the positive space charge left behind by the avalanches whereas in the positive streamers the anode absorbs the extra electrons generated by the secondary streamers. The latter is a much easier process than the former. Second, in the positive

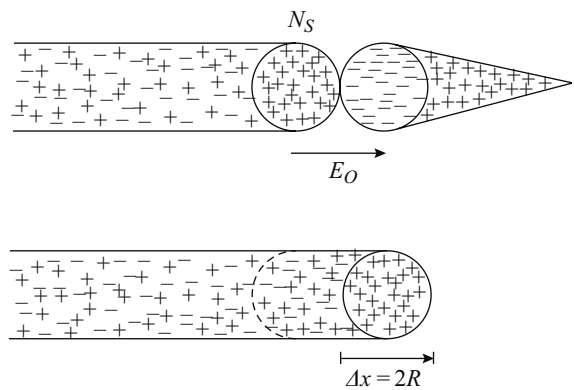

Figure 3.16 *Schematic presentation of the propagation of positive streamers* (from [57])

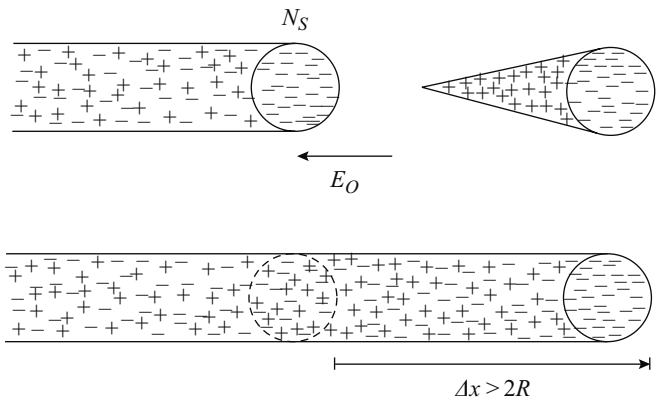

Figure 3.17 *Schematic presentation of the propagation of negative streamers* (from [57])

streamers the electrons propagate towards the positive charge head of the streamer and therefore into an increasing electric field. In the case of negative streamers the electrons move into the low electric field region and some of them will be captured by electronegative atoms which create an immobile negative space charge region that will impede the streamer propagation. Both these features make the propagation of positive streamers easier than that of negative streamers. This is reflected in the minimum background electric fields necessary for the propagation of streamers as will be described in section 3.7.4.4.

We have seen before that for the inception of a streamer the number of charged particles at the avalanche head should reach a critical value. Similarly, for the continuous propagation of a streamer the number of charged particles in the streamer head has to be larger than a critical number, N_{stab}. The value of N_{stab} partly depends on the background electric field, E_b, and can be calculated from the following equation [13]:

$$N_{stab} = 0.558 \times 10^8 - 0.231 \times 10^3 E_b \quad \text{for } E_b \leq 2 \times 10^5 \text{ V/cm} \tag{3.60}$$

$$N_{stab} = 3.34 \times 10^8 e^{-1.614 \times 10^{-5} E_b} \quad \text{for } E_b \geq 2 \times 10^5 \text{ V/cm} \tag{3.61}$$

3.7.4.3 Physical properties of the positive streamer channel

The streamer channel, although weakly ionised, provides a path for the electrons to propagate from the head of the streamer to the anode in the case of positive streamers or from the anode to the head of the streamer in the case of negative streamers. The streamer channel consists of a quasineutral plasma with an excess of positive charge and, based on rotation temperature measurements [25], one can conclude that the gas in the streamer channel is at ambient temperature.

The streamer radius was found to be of the order of 10–50 μm [27,38]. This value, however, may correspond to short streamers. The radius of long streamers could be larger than these values because of the channel expansion due to diffusion. Streamer

length in principle has no limits; it may grow as long as the gap and the voltage source permits. In laboratory conditions, cathode directed streamers as long as 10 m were observed in air at gap voltages of 5 MV. This may be even longer in the stepped leaders of lightning discharge. However, this length has not yet been measured.

The net positive charge in the streamer channel is about 0.6–3 $\times$ 10^9 ions/cm. The free electron density per unit length of the streamer channel lies in the range of (0.7–6) $\times$ 10^{12}/cm [28]. Thus the streamer can be regarded as a quasi-neutral plasma filament.

3.7.4.4 Critical background electric field necessary for streamer propagation

In air, the background electric field necessary for positive streamer propagation lies in the range of 4–6 $\times$ 10^3 V/cm [30–32]. For negative streamers it lies in the range of 1–2 $\times$ 10^4 V/cm. Any variation in the electron loss processes can change this electric field. For example, when air is saturated with water vapour, the critical electric field for positive streamer propagation grows from 4.7 $\times$ 10^3 V/cm at humidity of 3/gm^3 to 5.6 $\times$ 10^3 V/cm at 18 g/cm^3 [32–34]. The critical electric field necessary for streamer propagation not only varies with gas composition and humidity but it also changes with the temperature and density. For example, Figure 3.18 shows how this critical electric field varies both with humidity and with pressure. Note that the critical electric field decreases with decreasing pressure.

3.7.4.5 Streamer speed

Experimental data on positive streamer speed, both in air and along insulating surfaces, is shown in Figure 3.19 [35]. The results show that the streamer speed increases with increasing background electric field. When the background electric field is close to the critical electric field necessary for streamer propagation the streamer speed is close to 2 $\times$ 10^5 cm/s. For a given background electric field the speed of a streamer propagating along an insulating surface may be higher than that of the streamers propagating in air.

The minimum or critical streamer velocity seems to increase when electronegative components are removed from gas. In technical nitrogen (about one per cent oxygen) long-lived steady streamers could be observed propagating at 5 $\times$ 10^6 cm/s and in pure argon at 2 $\times$ 10^6 cm/s [36, 37].

3.7.4.6 Current in the streamer

The current flowing along the streamer channel is essentially an electron conduction current supported by the background electric field. An example of a current generated at the initiation of a streamer is shown in Figure 3.20 [32]. The peak current of the streamer may depend on the background electric field and whether or not the streamer is propagating along an insulating surface. The streamer current has a rise time of about 10–50 ns and a tail duration of about 200–500 ns [13,32]. Experiments show that the duration of the tail depends on the concentration of electronegative O_2 molecules because this will change the lifetime of free electrons due to attachment [38].

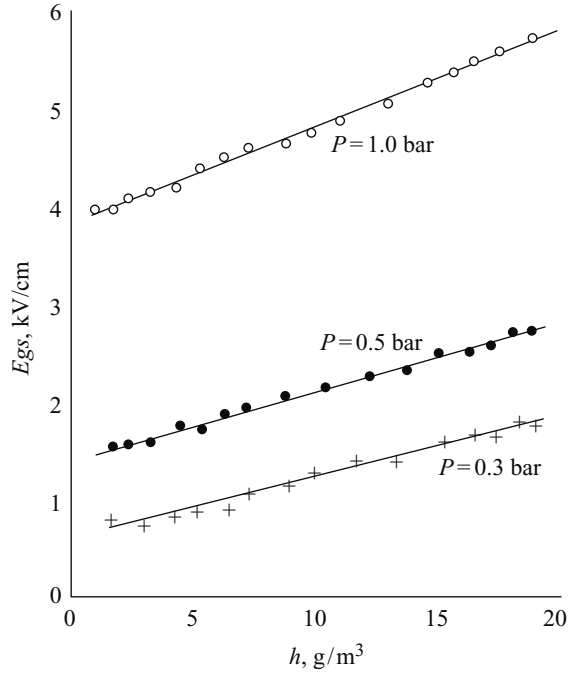

Figure 3.18 The critical streamer propagation fields as a function of absolute humidity for three values of pressure [from 33, see also 34]

3.7.4.7 Potential gradient of the streamer channel

No direct measurements are available today on the potential gradient of the streamer channels. Experiments conducted with long sparks show that the average potential gradient of the electrode gap when the positive streamers bridge the gap between the two electrodes is about 5×10^3 V/cm [39]. This indicates that the potential gradient of the positive streamer channels in air at atmospheric pressure is close to this value. Note that this value is approximately the same as the critical electric field necessary for the propagation of positive streamers.

3.7.4.8 Charge distribution along the streamer channel

The charge incorporated into a streamer channel can be evaluated from the current oscillograms, and the linear charge density along the channel can be evaluated by dividing this number by the length. However, this procedure is not very informative because the streamer charge need not be distributed uniformly along the channel. The charge distribution along the streamer channel can be evaluated theoretically but the distributions so obtained depend on the assumptions made in the theory. Actually, there is no consensus among scientists on the distribution of the charge along the

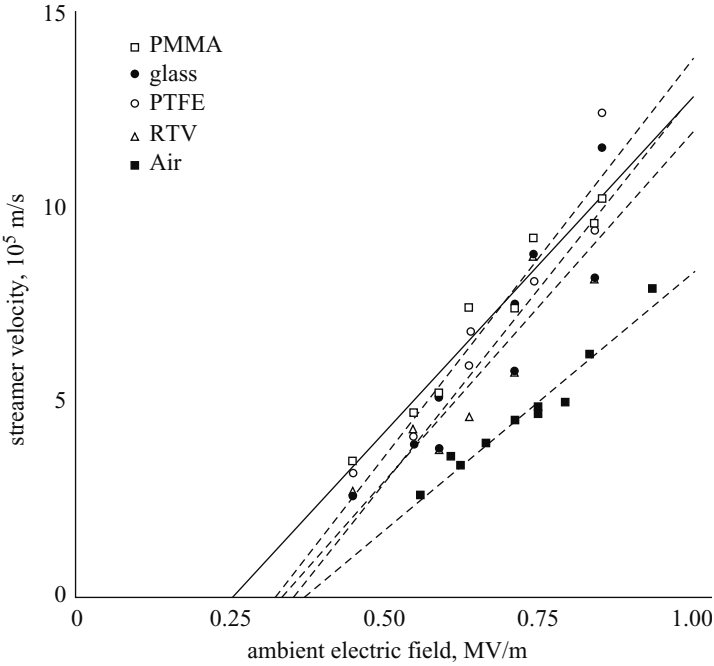

Figure 3.19 *Speed of streamers propagating along different insulator surfaces and in air as a function of the ambient electric field [35]*

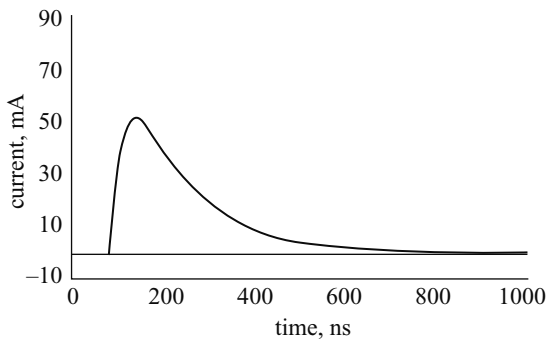

Figure 3.20 *Typical example of a streamer current measured at the point of inception. In the experiment the streamer is initiated by applying a 15 kV impulse to a needle of length 2 mm and 0.35 mm diameter located in a background electric field of 430 kV/m [40]*

streamer channel. Some scientists assume that the charge distribution in the streamer channel is such that the potential gradient is constant and equal to about 5×10^3 V/cm in the channel [40]. Some scientists assume that the charge of the streamer channel is concentrated at the head and the streamer channel is neutral [13,26]. One can also treat the streamer channel as a perfect conductor in estimating the charge distribution of the streamer in a given background field [41]. This treatment neglects the fact that the streamer channel is a weakly conducting channel and there is a potential gradient along it. The present author believes that the first assumption is the most reasonable one.

3.7.5 Streamer-to-spark transition and thermalisation

In the previous sections we have considered the conditions necessary for the initiation of streamer discharges in a given electric field configuration but not the formation of electrical breakdown in the gap. As mentioned previously, the streamer is a cold discharge (i.e. the gas temperature in the channel is close to ambient) and the conductivity of the streamer channel is rather small. Thus, the propagation of the streamer from one electrode to another is not a guarantee that it will result in electrical breakdown. Before, the electrical breakdown of the gap is realised the streamer channel has to be converted to a highly conducting channel by heating. This process is called streamer-to-spark transition and it is achieved by the heating of the channel through the process of thermalisation.

In small electrode gaps, the streamer channel can convert itself to a highly conducting spark channel leading to direct streamer-to-spark transition. Figure 3.21 shows the current and the gap voltage associated with the formation of the streamer and the subsequent increase in the current due to the streamer-to-spark transition in a 10 mm gap [42]. Observe that the streamer inception (at the time marked with the arrow) and its subsequent crossing of the gap (streamer may take about 50 ns to

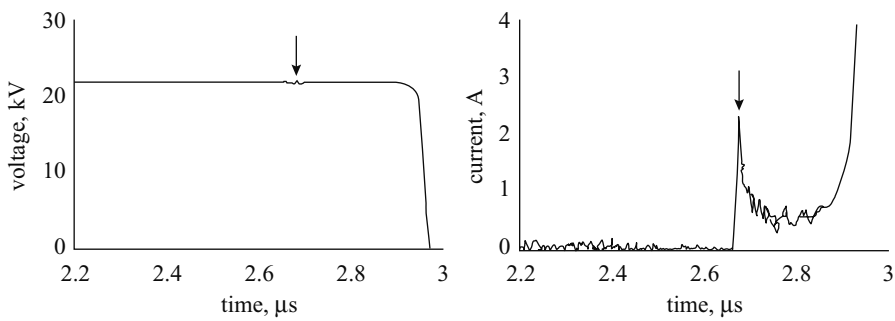

Figure 3.21 The voltage (left) and current (right) oscillogram corresponding to the streamer inception and streamer to spark transition. Data obtained for a 10 mm gap at atmospheric pressure [42]

cross the gap) do not lead to the collapse of the voltage. The streamer channel has to be heated up before full breakdown materialises in the gap. According to Marode [38] the streamer-to-spark transition takes place as follows. The streamer creates an ionised track which finally bridges the gap with the formation of a cathode fall region at the cathode (see Section 3.10). At all stages of its development the streamer channel behaves like a glow discharge with a local high electric field region (i.e. at the head) followed by a filamentary positive column. Within this positive column the small value of the electric field leads to an attachment rate higher than the ionisation rate so that the discharge current decreases. In spite of the inefficient transfer of energy from the electrons to neutrals, a weak but nonnegligible increase of the temperature of the neutrals can occur which raises the pressure in the channel. The resulting dynamics of the neutral species will lead to a reduction of this pressure causing the neutral density within the discharge channel to decrease. In turn, the ratio of electric field strength to neutral density increases, and if it reaches a critical value, where the ionisation coefficient begins to surpass the apparent attachment coefficient, a final growth of ionisation will occur leading to thermalisation and spark formation. Let us now consider how thermalisation is achieved in the discharge.

In the streamer phase of the discharge many free electrons are lost due to attachment to electronegative oxygen. Furthermore, a considerable amount of energy gained by electrons from the electric field is used in exciting molecular vibrations. Since the electrons can transfer only a small fraction of their energy to neutral atoms during elastic collisions the electrons have a higher temperature than the neutrals. That is, the gas and the electrons are not in thermal equilibrium. As the gas temperature rises to about 1600–2000 K rapid detachment of the electrons from oxygen negative ions supplies the discharge with a copious amount of electrons thus enhancing the ionisation [13]. As the temperature rises the VT relaxation time (see section 3.5.2) decreases and the vibrational energy converts back to translational energy thus accelerating the heating process. As the ionisation process continues the electron density in the channel continues to increase. When the electron density increases to about 10^{17} cm^{-3} a new process starts in the discharge channel. This is the strong interaction of electrons with positive ions through long range coulomb forces [13]. This leads to a rapid transfer of the energy of electrons to positive ions causing the electron temperature to decrease. The positive ions, having the same mass as the neutrals, transfer their energy very quickly, in a time of the order of 10^{-8} s, to neutrals. This results in a rapid heating of the gas. At this stage thermal ionisation sets in causing a rapid increase in the ionisation and the conductivity of the channel. This process is called thermalisation. During thermalisation as the electron temperature decreases the gas temperature increases and very quickly all the components of the discharge, namely, electrons, ions and neutrals, will achieve the same temperature and the discharge will reach local thermodynamic equilibrium. The rapid increase in the conductivity of the channel during thermalisation leads to an increase in the current in the discharge channel and the collapse of the applied voltage leading to a spark.

3.7.6 Electrical breakdown criterion in the presence of streamer discharges

As discussed in the previous section creation of a streamer in a discharge gap does not necessarily mean that it will always lead to electrical breakdown of the gap. However, if electrical breakdown does not materialise after the streamers have bridged the gap only a slight increase in the voltage will lead to final breakdown. Thus, the voltage necessary for the inception of a streamer and the subsequent propagation across the gap can be used as a criterion for electrical breakdown.

3.7.6.1 Plane uniform gap

Consider a plane uniform gap of separation d. In order for a streamer to be incepted in the gap the electric field in the gap (and hence the applied voltage) should be such that the critical avalanche length x_c is less than or equal to the gap length. This is illustrated in Figure 3.22. Thus the electrical breakdown criterion could be stated as:

$$x_c = d \tag{3.62}$$

If we use the Raether and Meek criterion for streamer inception, the electrical breakdown criterion in the gap would be:

$$\bar{\alpha} d \approx 18 \tag{3.63}$$

Note that in order for a streamer to be initiated in the gap the electric field should increase beyond 2.6×10^6 V/m. Since this electric field is larger than the critical

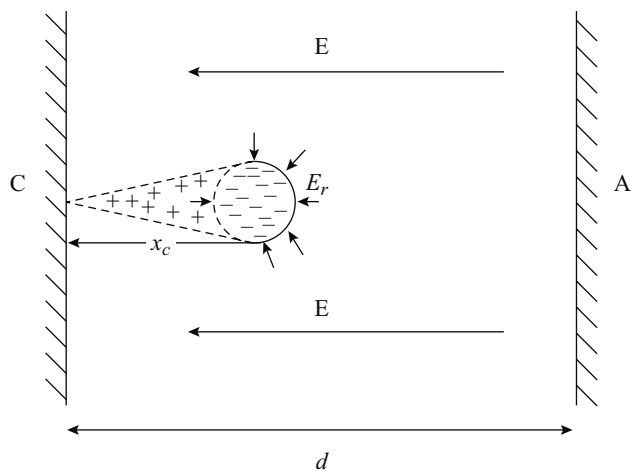

Figure 3.22 Geometry pertinent to the derivation of streamer breakdown criterion in a plane parallel gap

background electric field necessary for the propagation of streamers, once a streamer is initiated in the gap the conditions necessary for its propagation are already fulfilled in the space between the two electrodes.

3.7.6.2 Nonuniform gap

The geometry under consideration is shown in Figure 3.23. For a streamer to be initiated at the high-voltage electrode and for it to bridge the gap two conditions, one for the streamer inception and the other for the streamer propagation, have to be satisfied:

(i) Inception criterion: the criterion for the inception of the streamer can be written as

$$\int^{x_c} \bar{\alpha}(x)\, dx \geq 18 \tag{3.64}$$

where x_c is the axial length of the region within which the electric field is higher than 2.6×10^4 V/cm. Note that this is identical to the Raether and Meek streamer inception criterion, the only difference being that the electric field is not uniform and hence $\bar{\alpha}$ is not a constant but a function of x.

(ii) Propagation criterion: once the streamer is created, the background electric field must be able to sustain the streamer propagation. If the background electric field beyond the point x_c decreases below about 0.5×10^4 V/cm then neither positive nor negative streamers will reach the grounded electrode (in reality one has to consider the fact that streamers can propagate short distances in electric fields of less than this

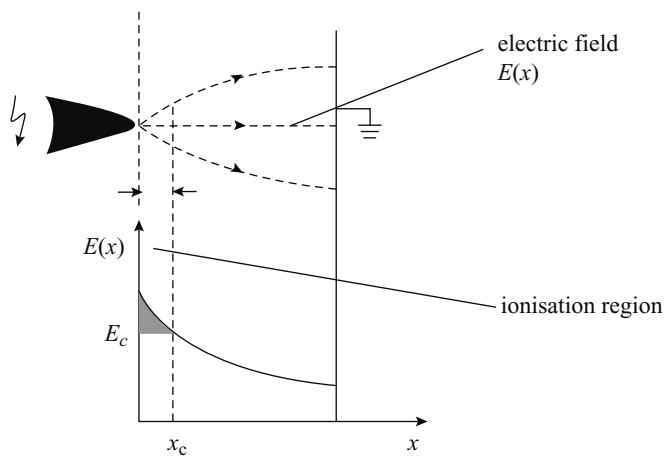

Figure 3.23 Geometry pertinent to the derivation of streamer breakdown criterion in a nonuniform gap

critical value). If this background electric field is greater than about 0.5×10^4 V/cm but is less than about $(1–2) \times 10^4$ V/cm then positive streamers will cross the gap and reach the cathode and the negative streamers may die out before reaching the anode. This last fact explains the reason why it is easier to cause breakdown in a rod–plane gap when the rod is at a positive polarity than when it is at a negative polarity.

3.8 Electrical breakdown in very small gaps – Townsend's breakdown mechanism

As described previously, avalanche to streamer transition requires that the avalanche grows to about 10^8 electrons and the space charge in the avalanche tip creates an electric field that significantly adds to the background electric field in the vicinity of the avalanche tip. This avalanche to streamer transition has been observed when the product of the pressure and the electrode spacing in plane uniform gaps exceeds about 0.5 bar.cm. Below this limit the space charge of the avalanche is not large enough to change the background field significantly. This will inhibit the avalanche to streamer transition. Under such conditions the breakdown takes place according to the Townsend mechanism.

3.8.1 Townsend's experiment

In Townsend's experiment (Figure 3.24) a plane parallel electrode gap was located in a cell, the gas pressure of which was of the order of a few torr [43]. The cathode was illuminated with a steady beam of ultraviolet radiation which led to a steady stream of electrons from it. The current flowing across the gap was measured as a function of the voltage. Townsend found that the voltage and the current vary in a manner shown in Figure 3.25.

Let us investigate the features of this curve in detail. Initially, the current in the gap increases with increasing voltage. The reason for this is that some of the electrons emitted by the cathode diffuse back into it and some of the electrons are lost to the walls. This diffusion and the losses to the walls of the tube decrease with increasing voltage. When the voltage increases to a certain level almost all the electrons emitted by the cathode are collected by the anode, thus producing the saturation in current. In reality, however, the current will only approach but not sustain a saturation level. The reason for this is that even though the back diffusion decreases with increasing voltage not all the emitted electrons will reach the anode even when the voltage is close to the sparking potential. As the voltage increases further, Townsend found that the current starts to increase exponentially with the applied voltage. This exponential growth of the current was sustained over a certain range of applied voltage but with further increase in voltage the current started to increase faster than the exponential growth. Further increase in voltage resulted in the electrical breakdown of the gap.

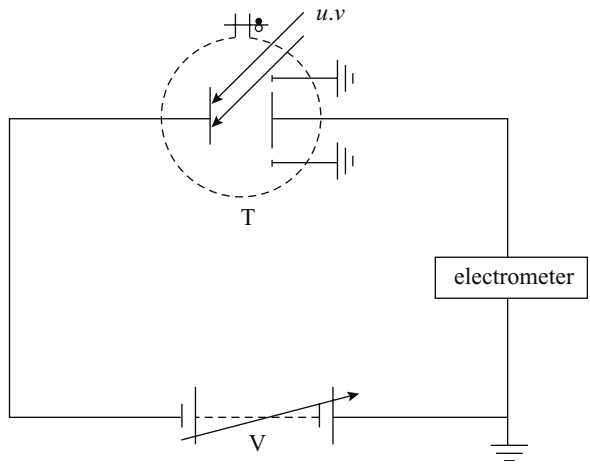

Figure 3.24 Schematic representation of the apparatus used by Townsend in his experiment. V is the voltage source and T is the vacuum tube. The discharge gap is located in the vacuum tube and the cathode is illuminated by ultraviolet radiation

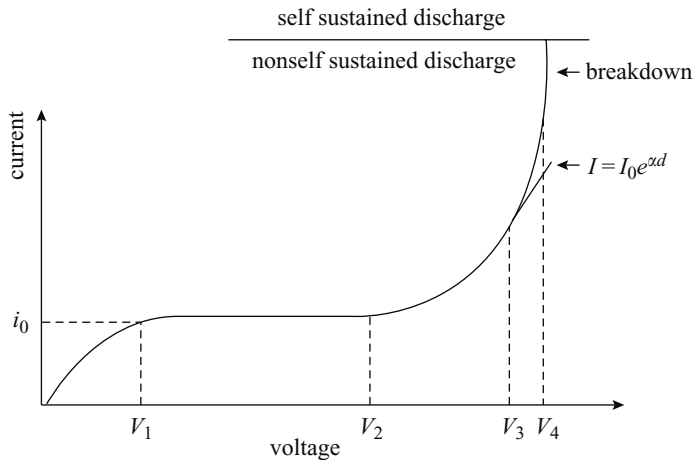

Figure 3.25 Variation of the current flowing across the discharge tube of Townsend's experiment as a function of the applied voltage.

3.8.2 Townsend's theory of electrical breakdown

Townsend assumed that the initial exponential growth of the current in the discharge tube is caused by the production of secondary electrons through the collision of primary electrons, generated from the cathode, with gas atoms. The second phase

of the discharge in which the current grows faster than exponential is assumed to be caused by the ionisation of the atoms through the collision of ions. However, today we know that the correct explanation is the additional production of electrons by the collision of positive ions with the cathode. Let us consider the mathematical treatment of the discharge process taking place in Townsend's experiment and come up with an equation which matches the experimental data.

3.8.2.1 Primary ionisation stage

If n_0 is the number of electrons emitted by the cathode per second then in steady state, neglecting the electron attachment, the number of electrons reaching the anode per second, n_d, is given by:

$$n_d = n_0 e^{\alpha d} \tag{3.65}$$

Consequently, the current inside the tube is given by:

$$I_d = I_0 e^{\alpha d} \tag{3.66}$$

where d is the gap length, $I_d = n_d e$, $I_0 = n_0 e$, α is Townsend's first ionisation coefficient and e is the electronic charge. This equation explains the exponential growth of current with increasing voltage. Note that even though the voltage does not appear explicitly in this equation it indirectly appears in α which increases with increasing electric field (and hence with increasing voltage when d is constant). Note that I_0 is the current generated by the ultraviolet radiation at the cathode. Consequently, if the source of ultraviolet radiation is removed (i.e. $I_0 = 0$) then the current in the discharge tube will go to zero. Thus, the discharge is not self sustained, that is, it needs the support of the external agency for its continuation.

3.8.2.2 Secondary ionisation stage

Townsend observed that with increasing voltage the current in the discharge tube begins to increase with voltage at a rate faster than that predicted by eqn. 3.66. This departure from eqn. 3.66 is shown in Figure 3.26 where $\log(I)$ is plotted as a function of the gap spacing, d. The upcurving occurs when the current departs from this equation. Townsend assumed that the cause of this departure of the experimental data from that predicted by eqn. 3.66 is the ionisation of the gas atoms due to the collision of positive ions. But, in reality, the energy gained by the positive ions at electric fields encountered in Townsend's experiment is not sufficient to create significant ionisation. However, one process that may cause this departure from eqn. 3.66 is the generation of electrons from the cathode by positive ion bombardment. As the voltage increases the positive ions gain more and more energy and this energy is released at the cathode. With increasing energy a stage will be reached in which these positive ions will start liberating electrons from the electrode. In order to explain the variation of current with voltage one has to take this effect into account. Let us now derive a mathematical expression for the current in the discharge tube taking into account the electron current created by the bombardment of positive ions on the cathode.

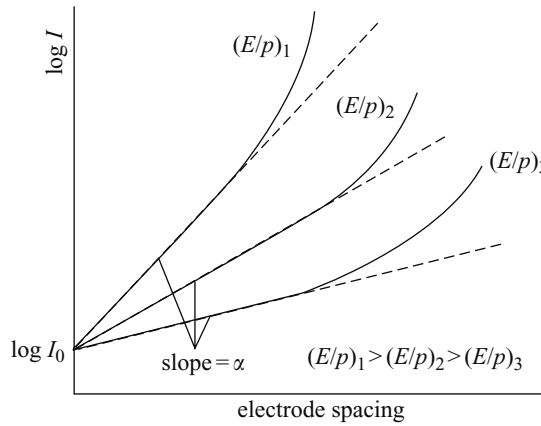

Figure 3.26 Variation of the logarithm of the current flowing across the discharge tube in Townsend's experiment as a function of the logarithm of the electrode spacing for different values of (E/p) where E is the electric field in the gap and p is the pressure

Let n_0 be the number of electrons emitted by the cathode per second due to ultraviolet illumination and n_+ be the number of electrons released from the cathode per second due to bombardment of positive ions. Then the number of electrons reaching the anode at steady state per second, n, is equal to:

$$n = (n_0 + n_+)e^{\alpha d} \tag{3.67}$$

The number of positive ions created by the electrons reaching the anode per second is equal to $n - (n_0 - n_+)$ and at steady state the number of positive ions reaching the cathode per second is equal to this number. Consequently, the number of electrons released by the positive ion bombardment at the cathode per second is given by:

$$n_+ = \{n - (n_0 - n_+)\}\gamma \tag{3.68}$$

where γ is the average number of electrons released by each positive ion striking the cathode. This parameter is called Townsend's secondary ionisation coefficient. Substituting this expression in eqn. 3.67 one obtains:

$$n = \frac{n_0 e^{\alpha d}}{1 - \gamma(e^{\alpha d} - 1)} \tag{3.69}$$

The current in the discharge tube is given by:

$$I = \frac{I_0 e^{\alpha d}}{1 - \gamma(e^{\alpha d} - 1)} \tag{3.70}$$

This equation predicts a faster current growth than eqn. 3.66 with increasing electric field (or voltage) providing an explanation for Townsend's experimental results.

In deriving the above equation we have considered the bombardment of positive ions on the cathode as the only secondary ionisation process. Let us now consider the other secondary ionisation processes.

(i) *Ionisation of gas by positive ions:* Townsend in his original derivation assumed that the secondary ionisation mechanism is due to the ionisation in the gas by positive ions. However, as mentioned above, positive ions cannot produce significant ionisation in electric fields at which electrical breakdown is observed in Townsend's experiment. Nevertheless, if we assume that the ions will contribute to the ionisation the resulting equation for the current will take the form [43]:

$$i = i_0 \frac{e^{(\alpha-\beta)d}}{(\alpha/(\alpha-\beta)) - (\beta/(\alpha-\beta))\, e^{(\alpha-\beta)d}} \tag{3.71}$$

where β is the ionisation coefficient of positive ions. Since electrons ionise more readily than positive ions one can replace $(\alpha - \beta)$ by α and the equation will reduce to:

$$i = i_0 \frac{e^{(\alpha)d}}{1 - (\beta/\alpha)\, e^{(\alpha)d}} \tag{3.72}$$

This equation has the same form as that of the expression obtained for positive ion bombardment at the cathode (i.e. eqn. 3.70).

(ii) *Photo emission from the electrode:* Another secondary emission process that one may take into account is the interaction of photons in the discharge with the electrodes. If the incident photon has an energy larger than the work function of the electrode then the interaction may lead to the liberation of an electron. If this process is taken into account as a secondary mechanism then the expression for the current will take the form [20]:

$$i = i_0 \frac{e^{(\alpha)d}}{1 - (\Delta g\theta/(\alpha-\mu))\,[e^{(\alpha-\mu)d} - 1]} \tag{3.73}$$

where g is the fraction of photons emitted in the gas that are headed towards the cathode, μ is the coefficient of absorption of photons in the gas and Δ is the probability of photoelectric emission from the photons incident on the electrode (note that only a fraction of the incident photons will have sufficient energy to cause photoionisation).

In general $\alpha \gg \mu$ and the equation will reduce to:

$$i = i_0 \frac{e^{(\alpha)d}}{1 - (\Delta g\theta/\alpha)\,[e^{(\alpha)d} - 1]} \tag{3.74}$$

This again has the same form as that of the eqn. (3.70).

(iii) *Collision of meta-stable ions on the cathode:* Collision of meta-stable atoms on the cathode can also liberate electrons from the cathode. If the meta-stable level

has a higher energy than the work function of the metal, such an interaction can lead to the emission of electrons. If this is taken into account [44]:

$$i = i_0 \frac{e^{(\alpha)d}}{1 - \gamma_m [e^{(\alpha)d} - 1]} \tag{3.75}$$

where γ_m is the number of electrons liberated by the incidence of a meta-stable atom on the cathode.

(iv) *Ionisation of the gas by photons:* Another process that may contribute to electron production in the gas is the ionisation of the gas by photons. If this is taken into account, one can show that the resulting equation will have the form [44]:

$$i = i_0 \frac{e^{(\alpha)d}}{1 - (\zeta g f \mu/(\alpha - \mu))\,[e^{(\alpha-\mu)d} - 1]} \tag{3.76}$$

where μ is the coefficient of absorption of photons, ζ is the fraction of absorbed photons that will cause ionisation, $f = \theta/\alpha$ where θ is the number of excited states or photons created per unit path in the electric field direction per electron and g is a geometrical factor that will describe the fraction of photons directed in a given direction.

(v) *Final expression for the current in the presence of secondary processes:* The results presented above show that irrespective of the secondary ionisation process under consideration the final expression for the current has the same form. Indeed one can include all of them in a single formula as follows:

$$i = i_0 \frac{e^{(\alpha)d}}{1 - (\gamma_i)[e^{(\alpha)d} - 1]} \tag{3.77}$$

where

$$\gamma_i = \gamma + (\alpha/\beta) + (\Delta g \theta/\alpha) + \gamma_m + \left(\frac{\zeta g f \mu}{\alpha - \mu}\right) \tag{3.78}$$

3.8.2.3 Townsend's electrical breakdown criterion

The final expression for the current given in eqn. 3.77 shows that the discharge is still nonself sustained. That is, the discharge current goes to zero if the UV illumination on the cathode is removed (i.e as $I_0 \to 0$). However, as the voltage continues to increase a stage will be reached at which the discharge will transform itself from a nonself sustained discharge to a self sustained discharge. At this stage the discharge will continue to burn between electrodes even after removing the background ultraviolet radiation (i.e. when $I_0 = 0$). This change of state of the discharge is accompanied by a several orders of magnitude increase in the current (provided that the voltage supply can sustain such an increase in the current) in the discharge gap. This is the stage of electrical breakdown in the gap. Townsend defined the electrical breakdown condition as the condition which makes the current in the discharge gap go to infinity.

From eqn. 3.77 one can see that $I_0 \rightarrow \infty$ when the denominator of the expression for the current goes to zero. That is when:

$$1 - \gamma_i[(e^{\alpha d} - 1)] = 0 \tag{3.79}$$

This condition is known as Townsend's breakdown criterion.

One can indeed show that this criterion has a physical significance. Assume that γ is the dominant secondary process. Assume that n_0 primary electrons leave the cathode per second. These electrons will give rise to $n_0(e^{\alpha d} - 1)$ positive ions in the gap, and these positive ions on incidence on the cathode produce $\gamma_i n_0(e^{\alpha d} - 1)$ secondary electrons. When Townsend's breakdown criterion is satisfied the number of secondary electrons is equal to the original number of electrons which has been drawn away from the cathode and later passed into the anode. Consequently, each avalanche will give rise to another avalanche through secondary processes and so cause a repetition of the avalanche process. That is, the discharge process becomes self sustained.

An alternative expression for Townsend's breakdown criterion can be obtained by rewriting the above equation as:

$$\alpha d = \ln\left(1 + \frac{1}{\gamma_i}\right) \tag{3.80}$$

The value of γ_i is greatly affected by the cathode surface and gas pressure. However, γ_i is a very small number ($<10^{-2}$–10^{-3}) so $1/\gamma_i$ is very large. Therefore, $\ln(1+(1/\gamma_i))$ does not change too much and is of the order of eight to ten in a Townsend's discharge.

3.8.2.4 Townsend's mechanism in the presence of electron attachment

In the experiments conducted by Townsend the gases under investigation were noble gases. In this case electron attachment to atoms can be neglected. However, in air, one cannot neglect the electron attachment. Let us consider the effect of electron attachment in Townsend's equation. In the presence of attachment, the number of electrons reaching the cathode per second is given by:

$$n_d = n_0 e^{(\alpha-\eta)d} \tag{3.81}$$

Consider an elementary length dx located at distance x from the cathode. Let n_x be the number of electrons reaching x in a unit time. In travelling across dx these electrons will generate dn_- number of negative ions per second. Then:

$$dn_- = n_x \eta \, dx \tag{3.82}$$

substituting for n_x one obtains:

$$dn_- = \eta n_0 e^{(\alpha-\eta)x} \, dx \tag{3.83}$$

Since the number of negative ions at the cathode is equal to zero the solution of this equation is given by:

$$n_- = \frac{\eta n_0}{\alpha - \eta}[e^{(\alpha-\eta)x} - 1] \tag{3.84}$$

where n_- is the number of negative ions crossing a plane at a distance x from the cathode per second. Thus the number of negative ions reaching the anode per second, n_{-d}, is given by:

$$n_{-d} = \frac{\eta n_0}{\alpha - \eta}[e^{(\alpha-\eta)d} - 1] \tag{3.85}$$

The total current reaching the anode, both due to the electrons and to negative ions, is given by:

$$i = \frac{i_0}{\alpha - \eta}[\alpha e^{(\alpha-\eta)d} - \eta] \tag{3.86}$$

In the presence of secondary ionisation due to bombardment of positive ions on the cathode one can show using the procedure outlined in the section 3.8.2.2

$$i = i_0 \frac{[\alpha e^{(\alpha-\eta)d} - \eta]}{\alpha - \eta - \alpha\gamma\{e^{(\alpha-\eta)d} - 1\}} \tag{3.87}$$

This reduces to eqn. 3.70 in the absence of attachment (i.e. $\eta = 0$). From this equation the breakdown condition in the presence of electron attachment is given by:

$$1 - \left\{\frac{\gamma\alpha}{(\alpha - \eta)}\right\}[(e^{(\alpha-\eta)d} - 1)] = 0 \tag{3.88}$$

This criterion shows that if $\alpha > \eta$ then electrical breakdown is possible irrespective of the values of α, η and γ provided that d is large enough. That is, for a given electric field there is a particular value of d at which the gap breaks down. For $\alpha < \eta$, with increasing d, the above equation approaches an asymptotic form:

$$\frac{\gamma\alpha}{(\alpha - \eta)} = -1 \quad \text{or} \quad \alpha = \frac{\eta}{(1 + \gamma)} \tag{3.89}$$

This defines the limiting condition at which electrical breakdown is possible in an electronegative gas. This condition depends only on E/p. Noting that the value of $\gamma \ll 1$, the limiting value of E/p which can cause electrical breakdown in electronegative gases can be obtained from the relationship $\alpha = \eta$ (see section 3.7). This point is illustrated in the plot given in Figure 3.27.

3.9 Paschen's law

If a slowly increasing voltage is applied across two plane parallel electrodes the electrical breakdown of the gap occurs at a certain critical voltage. The experimental data shows that the breakdown voltage, V_s, is only a function of the gas pressure, p (or gas density), multiplied by the gap length, d. That is:

$$V_s = f(pd) \tag{3.90}$$

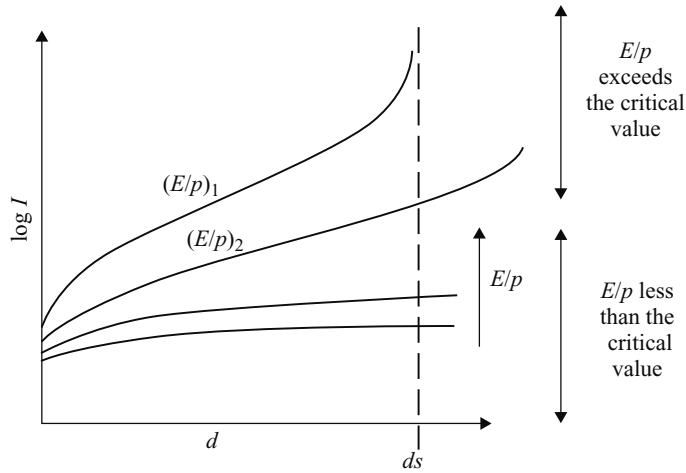

Figure 3.27 Variation of the logarithm of the current flowing across the discharge tube in Townsend's experiment as a function of the logarithm of the electrode spacing for different values of (E/p) for electronegative gases

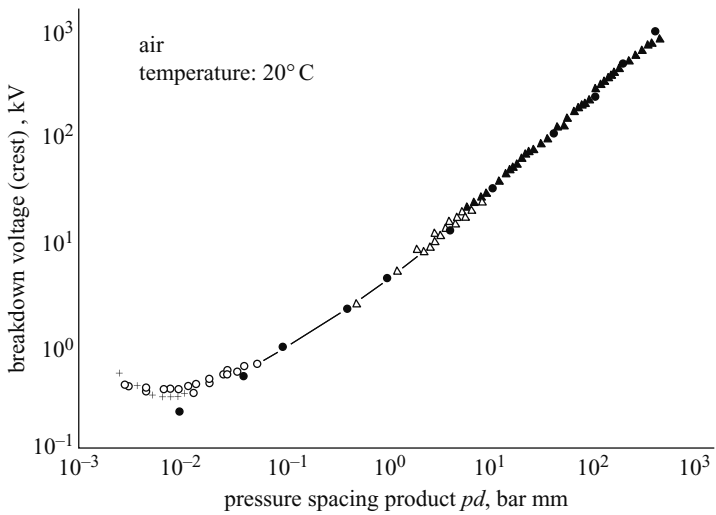

Figure 3.28 Paschen curve for air in log–log scale at temperature 20°C [45]

This is known as Paschen's law. The Paschen curve for air is shown in Figure 3.28 [45]; the data points correspond to measurements by several authors and the solid black dots are generated from the equation $V_s = 6.72\sqrt{pd} + 24.4(pd)$ (p in bar and d in mm). In this Figure the results are given in terms of pd corresponding to a temperature of 293 K. Note that the sparking potential is high both in the case of low and high values of pd but there is a minimum at a certain value of pd. This

minimum is called the Paschen minimum. The Paschen minimum in air is about $pd = 10^{-2}$ bar.mm.

One can show that the breakdown voltage estimated using either Townsend's or Raether and Meek's criterion adheres to Paschen's law. The electrical breakdown criterion of a uniform gap of length d is given by:

$$\alpha d = K \tag{3.91}$$

where K is a constant. Depending on the value of K this equation represents both Townsend's breakdown criterion and the streamer breakdown criterion. Substituting the expression for α given in eqn. 3.14 we obtain:

$$K = Apde^{-Bpd/V_s} \tag{3.92}$$

where V_s is the voltage at which electrical breakdown is observed. Note that in deriving this equation we have used $E = V_s/d$. Rearranging the above equation we find that:

$$V_s = \frac{Bpd}{\ln\{Apd/K\}} \tag{3.93}$$

This equation shows that V_s is a function of pd. The general shape of this equation is in agreement with the Paschen curve.

3.9.1 Physical interpretation of the shape of the Paschen curve

In order to give a physical interpretation for the shape of the Paschen curve let us rewrite eqn. 3.93 as follows:

$$E_s = \frac{B_1(d/\lambda)}{\ln\{A_1(d/\lambda)/K\}} \tag{3.94}$$

where A_1 and B_1 are constants, λ is the mean free path of the electrons $E_s = V_s/d$, and we have used the relationship that the mean free path is inversely proportional to the pressure. This equation has the same form as eqn. 3.93 except that pd is now replaced by d/λ. It thus predicts that the breakdown electric field has a minimum corresponding to a certain value of d/λ, say $(d/\lambda)_{min}$, and it increases when the value of d/λ moves away from this minimum. The reason for the existence of this minimum can be explained qualitatively as follows. Let E_m be the electric field in the gap corresponding to $(d/\lambda)_{min}$. At $(d/\lambda)_{min}$ an electron crossing the gap will make a certain number of ionisation collisions. Consider the case $(d/\lambda) > (d/\lambda)_{min}$. Now, the number of collisions made by an electron in crossing the gap, and hence the energy lost in collisions in crossing the gap, is higher than at $(d/\lambda)_{min}$. If the background electric field remained at E_m the total number of ionisation collisions made by an electron crossing the gap would be less than the corresponding value at $(d/\lambda)_{min}$. Consequently, the electric field should be increased in order to compensate for the losses and to increase the probability of ionisation. For $d/\lambda < (d/\lambda)_{min}$ the number of collisions, and hence the number of ionisation collisions, made by an electron in

crossing the gap is less than the corresponding value at $(d/\lambda)_{min}$. In this case the only way to increase the number of ionisation collisions is to increase the probability of ionisation in each collision. This can be achieved only by increasing the energy gained by electrons within a mean free path. This requires a higher electric field than the one which corresponds to $(d/\lambda)_{min}$.

3.9.2 Validity of Paschen's law

In section 3.9 it was shown that Paschen's law follows directly if the dominant collision processes, as is often the case, are such that the coefficients representing them, for example α, are directly proportional to p at a given value of E/p. When this is the case the processes are said to obey similarity.

In general, the experimental data obeys Paschen's law and any deviations are relatively small and arise from the existence of collision processes in the gas which do not conform to similarity. The deviations from Paschen's law can occur at high pressures and at temperatures above about 3000–4000 K. At high pressures exceeding a few atmospheres the processes such as field emission may play a significant role in the breakdown process. The role of field emission at high pressures and its influence on Paschen's law is clearly demonstrated by the observation that when very clean molybdenem electrodes are used Paschen's law holds up to very high pressures. The clean electrodes do not have oxide layers that generate field emission at low electric fields. At high temperatures experimental data departs from Paschen's law partly due to the dominant role of thermal ionisation and partly due to the gradual change of chemical composition of the gas, for example, by dissociation. Paschen's law may also break down at low pressures because the breakdown process is governed by preionisation processes caused by electrodes such as thermionic emission and the breakdown phenomena has to be described by vacuum breakdown processes.

3.10 Voltage and current (V–I) characteristics and the post breakdown stage (low pressures)

The type of discharge that appears in the gap after breakdown depends on the gas, gap length, the applied voltage and the parameters of the electric circuit. If the breakdown occurs at a pressure of the order of 1–100 torr between electrodes supplied from a d.c. source, and if the current is carefully controlled, then the V–I characteristics as shown in Figure 3.29 can be obtained [44]. The example shown in this Figure corresponds to neon gas at 1 torr. It is important to remember that what is shown is the static characteristics; the dynamic characteristics could be very different. The regions marked *B* and *C* in the diagram correspond to the Townsend discharge. During electrical breakdown, the region marked *D*, the current in the gap increases by several orders of magnitude and the rate of change of current with voltage is very high. The region marked *G* is called the normal glow discharge. Here, as the current increases the voltage remains at a constant value. As the current reaches a critical value the voltage starts to increase with increasing current and this region, marked *H* in the diagram, is

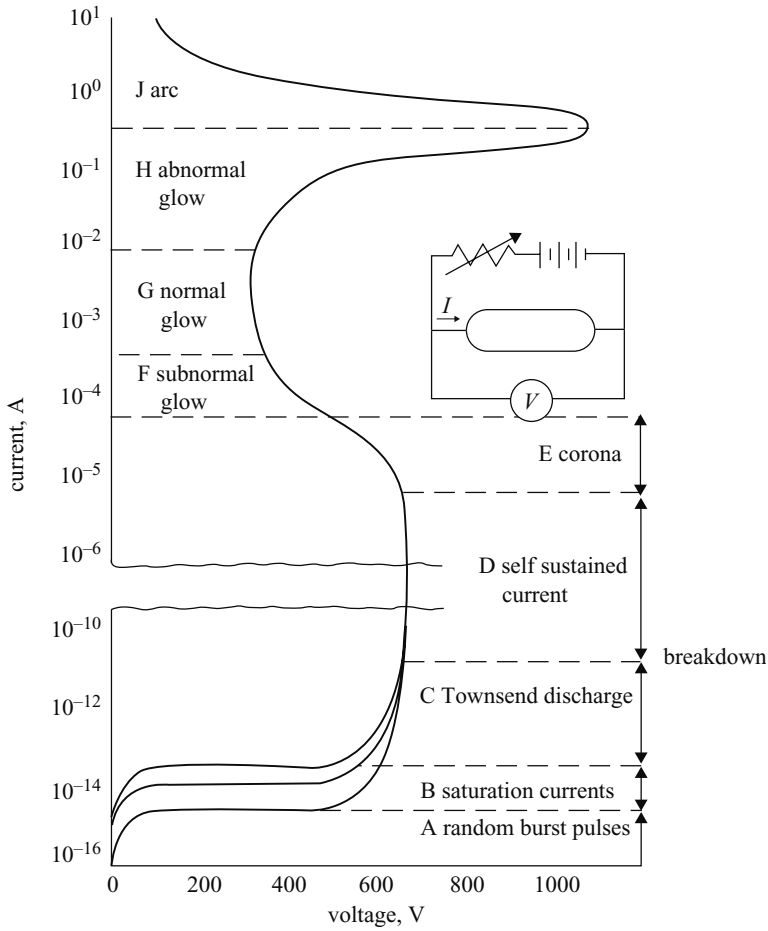

Figure 3.29 *Typical voltage–current relation of a gaseous gap. The curve given is for neon at 1 torr with disk electrodes of 2 cm diameter and 50 cm separation* (from [44]; reproduced by permission of John Wiley and Sons, Inc.)

called the abnormal glow. A further increase in current leads to a sudden change from abnormal glow to an arc discharge with a rapid drop in voltage as the current rises.

3.10.1 The glow discharge

The physical appearance of the glow discharge and the different parameters of interest as a function of length along the discharge tube are shown in Figure 3.30. It is important to point out that dark spaces marked in the diagram are not completely dark; they give less visible radiation than the other regions. One can observe that the distance marked d_c from the cathode accounts for most of the applied voltage. This rapid drop

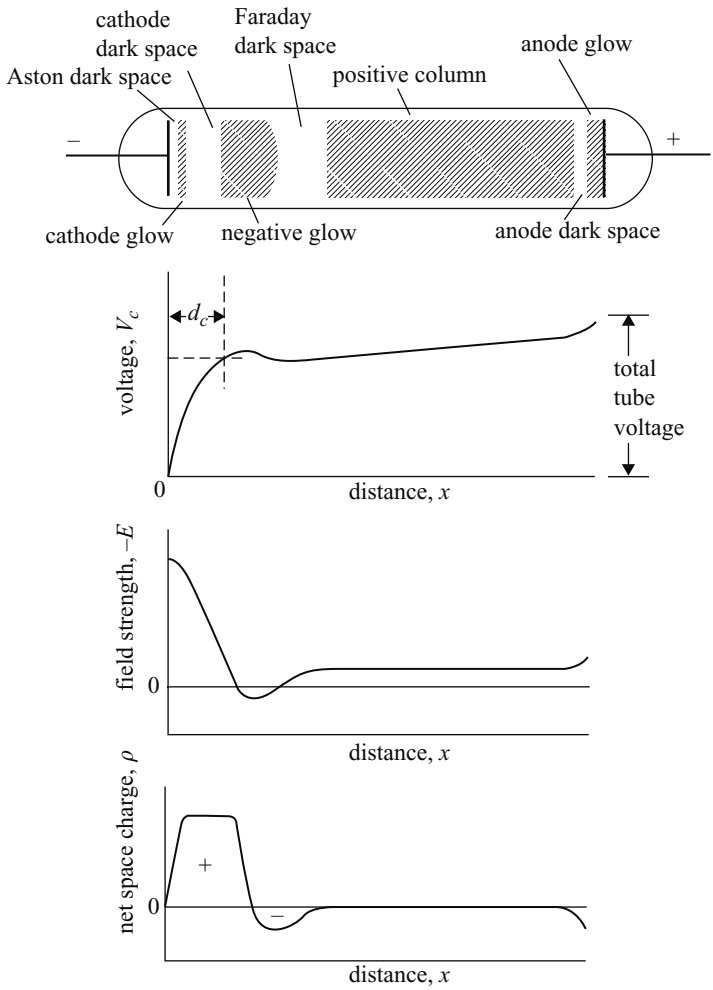

Figure 3.30 *Schematic representation of the glow discharge at low pressure together with the variation of the voltage, field strength and the space charge density along the discharge channel* (from [3])

in voltage is caused by the excessive positive charge located in the vicinity of the negative glow. This voltage drop is known as the cathode drop. Its magnitude, of the order of hundreds of volts, depends mainly on the type of gas and the material of the cathode. In the positive column there is a uniform but slow increase in the voltage and the voltage rises sharply very close to the anode. This is known as the anode fall.

3.10.1.1 Physical explanation

Electrons are emitted by positive ion bombardment and incident radiation at the cathode. Before these electrons gain appreciable velocity, they form a negative space

charge very close to the cathode. The space charge becomes positive a short distance from the cathode and remains positive throughout the cathode dark space. The cathode glow is caused by the release of ionisation energy as photons by the recombination of slow electrons with the incoming positive ions for which the recombination coefficient is high. As the electrons are accelerated in the electric field and gain energy the probability of recombination is reduced giving rise to the cathode dark space. At the end of the cathode dark space the high energetic electrons produce intense excitation and ionisation giving rise to the brightest section of the discharge, namely, the negative glow. Indeed, since the excitation and ionisation cross sections decrease at very high electron energies the maximum excitation and ionisation takes place after the electrons are slowed down somewhat. Thus the brightest part of the negative glow occurs a short distance away from the leading edge of the negative glow. As the electrons are slowed down the negative space charge reaches a maximum; the energy available for excitation and ionisation is exhausted and the Faraday dark space begins. The negative space charge increases in the Faraday dark space in comparison with the positives because only a few ions are produced here. As a result, the electric field attains a small value and electrons can gain very little energy in this region. At the end of the Faraday dark space the electric field starts to increase again leading to the acceleration of electrons. The electric field stabilises over a small distance, however, at the beginning of the positive column.

The typical values of the electric field in the positive column range from about a fraction of a V/cm to about a few tens of V/cm depending on the gas type, its pressure and the current flowing in the tube. The luminosity of the positive column is created by the excited particles and not from recombination. The colour of the positive column is characteristic of the gas in the discharge. The gas in the positive column is ionised with equal positive and negative charge densities. The length and diameter of the positive column depend on the geometry of the discharge tube. As the pressure increases the positive column contracts radially. One interesting fact is that if the length of the tube is reduced the total reduction in length is taken completely by the positive column leaving the other features of the discharge and the current the same (the voltage may fault slightly in the process). This will continue until the anode is in the negative glow region at which point the voltage required begins to rise. The conclusion is that the positive column is unimportant and unnecessary for the operation of the discharge.

One interesting fact pertinent to the discharge is that the product pd_c (where p is the pressure) is approximately equal to the Paschen minimum corresponding to the gas in the discharge tube. That is, discharge optimises itself by creating an effective anode at a distance d_c from the cathode.

3.10.1.2 The effect of changing the pressure

If the pressure in the discharge tube is increased the negative glow and the two dark spaces that surround it will shrink towards the cathode. The positive column will occupy much of the available tube length. With increasing pressure the voltage gradient of the positive column increases; the opposite happens with decreasing pressure.

At pressures so low that the cathode dark space fills the entire tube, the discharge is becoming more like an electron beam.

3.10.2 Abnormal glow

If the discharge is operating within the glow region it is observed that the cathode glow covers only part of the cathode surface. The area of the cathode glow may increase or decrease apparently in proportion to the current flowing. As the current increases the area of the cathode glow increases. It appears that the current density at the cathode remains constant during the normal glow and therefore the voltage also remains constant. This continues until the glow covers the whole area of the cathode. A further increase in current will lead to an increase in the voltage. This is the beginning of the abnormal glow.

3.10.3 The glow to arc transition

Glow to arc transition of the discharge takes place when the abnormal glow has acquired a critical voltage and when the power supply is capable of supplying a high current with a low internal resistance. The arc voltage is an order of magnitude lower than the glow discharge. This transition requires an important change in the electron emission process at the cathode. As we have seen in the case of Townsend's mechanism a self sustained discharge is created in the gap only after the secondary processes (i.e. positive ion bombardment on the cathode etc.) have generated a steady stream of electrons from the cathode by positive ion bombardment. However, these secondary processes alone are not sufficient to maintain an arc. In order to maintain an arc the supply of electrons from the cathode should be increased. This can be realised in three ways: (1) the cathode is heated by an external agent to increase the electron supply; (2) the cathode is heated by the arc itself resulting in an increase supply of electrons (hot spots created in this way are called cathode spots); (3) an increase in the electron supply caused by the field emission resulting from the very high electric fields caused by the space charge located in the vicinity of the cathode. Such arcs are called field emission arcs.

If the pressure is close to one atmosphere the formation of an arc takes place through a transient spark. All the features shown in Figure 3.29 will then be compressed into a very small time span and the current voltage characteristic shown in Figure 3.31 is observed [46].

In an arc the current density is much higher than that of the glow discharge. At atmospheric pressure the arc seems to have a very bright core surrounded by a less luminous region. The particle density of the arc may range from 10^{14}–10^{18} electrons/cm^3 depending on the pressure.

The longitudinal voltage distribution of an arc is shown in Figure 3.32. Note that except at the vicinity of the cathode and the anode the potential gradient is constant. Between pressures 10^{-3} torr to about 10 torr the potential gradient of the arc remains close to a few V/cm and it increases very rapidly to about 10–20 V/cm at atmospheric pressure. There is a sharp drop in the arc voltage at both the cathode (cathode fall) and

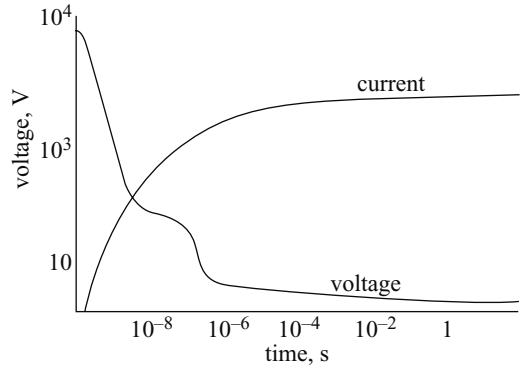

Figure 3.31 *The time variation of current and voltage at the initiation of an arc at atmospheric pressure* (from [46])

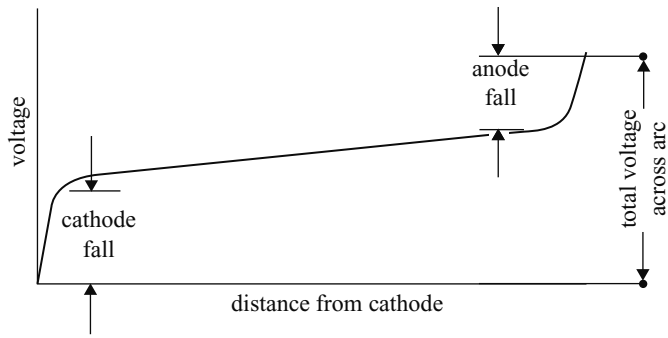

Figure 3.32 *Potential distribution along the arc channel* (from [46])

the anode (anode fall) and the cathode fall is larger than the anode fall. The cathode fall, being of the order of the ionisation potential of the gas atoms i.e. about 10 V, takes place over a very small fraction of a millimetre. Recall that in the case of glow discharge the cathode fall is of the order of hundreds of volts. Usually the cathode and anode fall remains constant and independent of the arc length, thus one requires more voltage in order to increase the arc length. This is the case since the extension of the arc leads to the extension of the linear portion of the voltage drop without affecting the end regions.

The potential gradient of atmospheric arcs as a function of current is shown in Figure 3.33 [47] and is of the order of 10–20 V/cm over a large range of current amplitudes. The potential gradient of the high-pressure arc column is considerably higher than for the low-pressure arc column, but the ratio of the potential gradient to the gas pressure is much less at high pressure.

The neutral gas temperature of the arc depends on the pressure of the discharge. This may vary from about 200 K at 10^{-3} torr to about 5000–10 000 K (axial temperature) at atmospheric pressure. The radial distribution of the temperature of a

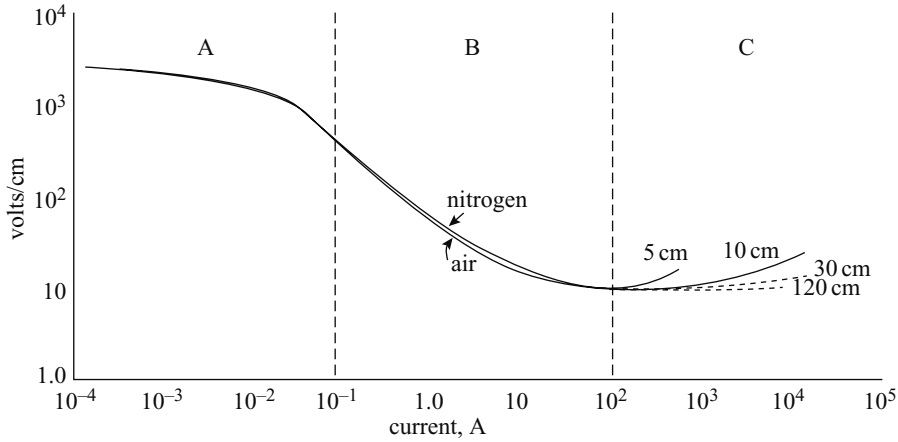

Figure 3.33 *Voltage current characteristics of free burning arcs of different lengths in nitrogen and in air at atmospheric pressure [47]*

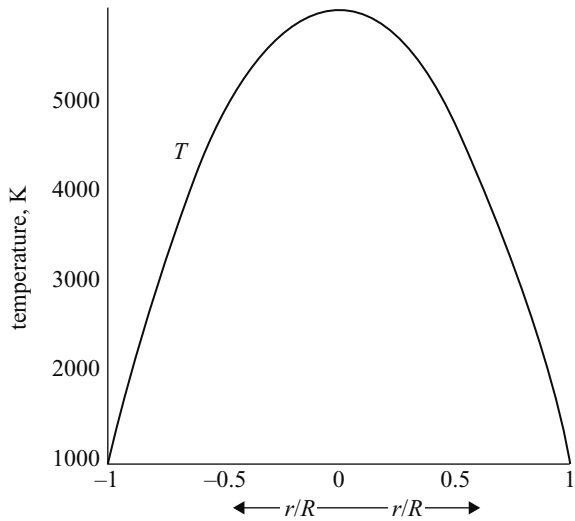

Figure 3.34 *The radial temperature distribution of a high-pressure arc* (adapted from [46])

high-pressure arc is shown in Figure 3.34. Note that the temperature of the arc has a maximum at the centre and it decreases with increasing radius.

In low-pressure arcs even though the gas temperature is low the electron temperature is very high. Figure 3.35 shows how the arc temperature and the electron temperature vary as a function of pressure. Observe that at low pressures the electron temperature is much higher than the gas temperature and the two approach each other

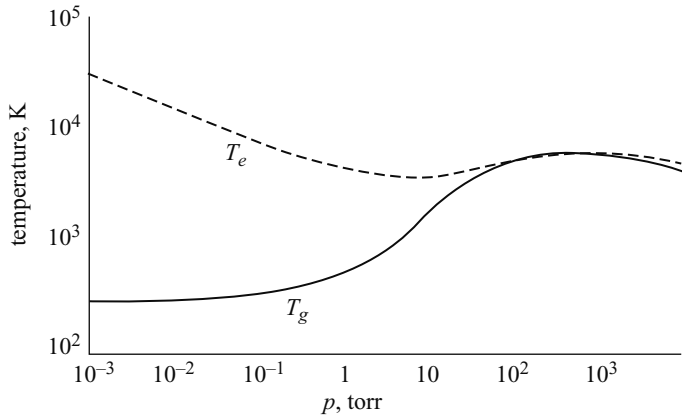

Figure 3.35 *The gas temperature T_g and the electron temperature T_e in arcs as a function of pressure* (from [64])

with increasing pressure. The ion temperature is about the same as that of the neutrals. At low pressures the electron density is not large enough for thermalisation to occur and as a result the gas and the electrons have different temperatures. With increasing pressures the electron temperature comes closer to the gas temperature partly due to the increased frequency of elastic collisions between electrons and gas atoms and partly due to the increased importance of the coulomb interactions (see section 3.7.5).

3.11 Resistance of spark channels

After the streamer-to-spark transition the thermal ionisation increases the conductivity of the channel leading to a rapid drop in the channel resistance as the current in the channel increases. There are several theoretical as well as empirical formulas that describe the time-dependent resistance of the spark channel in atmospheric pressure after the streamer–spark transition has taken place. The formula which is used frequently by electrical engineers is Toepler's formula [48]. According to this the resistance per unit length of the spark channel varies as:

$$R(t) = \frac{k_t}{\int_0^t i(t)\,dt} \tag{3.95}$$

where k_t is a constant and equal to $0.005 \pm 20\%\ \mathrm{Vsm}^{-1}$. Observe, however, that according to this equation irrespective of the shape of the spark current the resistance of the spark channel decreases monotonically with time. In reality, the resistance of the channel decreases with increasing current in the discharge channel but it will recover as the current in the spark channel decreases and finally goes to zero.

Engel *et al*. [49] compared Toepler's equation and several other published equations which predict the temporal variation of the spark resistance. According to them

the equation that predicts the resistance per unit length of the spark channel over the entire length of the current pulse is the one published by Kushner *et al*. [50] and it is given by:

$$R(t) = k_k \left\{ \frac{p_0^3}{A^2 i(t)^6} \right\}^{1/5} \tag{3.96}$$

where k_k is a constant equal to 24.7, A is the cross sectional area of the discharge in m^2, p_0 is the pressure in Pa and $i(t)$ is the current in the discharge in A. The cross section of the discharge channel varies with the current and it can be obtained from the following formula, derived by Braginskii [51], which shows how the time-dependent radius of the discharge channel, $r(t)$, varies with time:

$$r(t) = 0.93 \times 10^{-3} \rho_0^{-1/6} i^{1/3} t^{1/2} \tag{3.97}$$

where $r(t)$ is given in metres, t is the time in micro seconds, i is the instantaneous current in kiloamperes and δ_0 is the air density at atmospheric pressure (1.29×10^{-3} g/cm^3). It is important to note that Braginski's derivation is valid for a linearly increasing current, which means that the results may be applicable in the rising part of the discharge current which can be approximated by a linear ramp.

3.12 Corona discharges

In many situations the electric field in air in the vicinity of objects at higher voltages or exposed to high external electric fields may overwhelm the critical electric field necessary for the formation of electron avalanches in air. Moreover, the extent of the volume in which this high electric field exists may be confined to a very small region around the object (i.e. the electric field is strongly nonuniform) so that it would not lead to any electrical breakdown between the object under consideration and another one in its vicinity. In this case the electrical activity will be concentrated and confined to a small volume around the object. These types of discharge activity are called corona discharges. During corona discharges ionic space charges of both polarities accumulate near the highly stressed electrode, thus modifying the electric field distribution. The equilibrium between accumulation and removal of space charge causes several modes of corona discharges. Moreover, the physical nature of these corona discharges is affected by the electronegativity of the gas under consideration.

In general, the conditions necessary for the inception of negative corona discharge do not differ from Townsend's breakdown condition generalised to include the nonuniformity of the electric field. This is given by:

$$1 - \gamma \left\{ \exp\left(\int_0^{x_c} (\alpha - \eta)\, dx \right) - 1 \right\} = 0 \tag{3.98}$$

where the integral is performed over the region in which $(\alpha - \eta) > 0$. The streamer criterion, generalised to take into account the electric field nonuniformity, can be

chosen as the inception criterion for positive corona. That is:

$$\int_0^{x_c} (\alpha - \eta)\, dx \approx 18 \tag{3.99}$$

Trinch [52] has given an excellent review of DC corona modes in air. We are indebted to this work for the following brief account.

3.12.1 Negative corona modes

In negative corona, the electron avalanches are initiated at the cathode and develop towards the anode in a decreasing electric field. The situation is illustrated in Figure 3.36. Owing to their high mobility electrons will move rapidly away from the cathode into the low electric field region leaving behind the positive space charge close to the cathode. The electron avalanche will stop at the surface S_0 where the electric field is below the critical electric field necessary for ionisation. Here, the electrons are rapidly captured by the electronegative oxygen atoms creating a negative space charge. These two space charge regions, one positive and the other negative, will modify the electric field configuration in the gap in such a manner that the electric field increases near the cathode while reducing it near the anode. As one can see, the avalanches that develop later will develop in a higher electric field but propagate for a shorter distance than their predecessors. The influence of this space charge will lead to three forms of corona modes. These are, according to order of appearance with

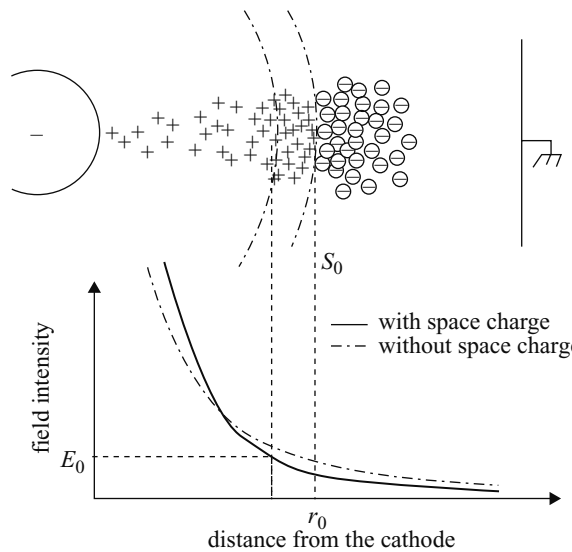

Figure 3.36 *Space charge and the electric field distribution in the gap during the formation of negative corona* (from [52]; reproduced by permission of IEEE)

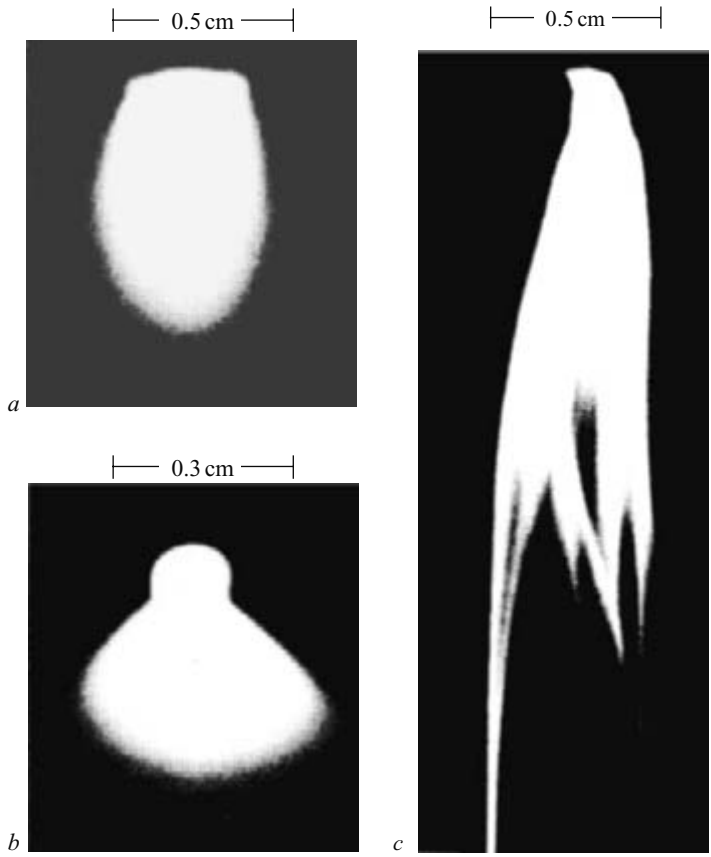

Figure 3.37 *Negative corona modes. Cathode: spherical boss ($d = 0.8$ cm) on a sphere ($D = 7$ cm); Gap length 19 cm; time exposure: 0.25 s* (from [52]; reproduced by permission of IEEE)

a trichel streamers
b negative glow
c negative streamers

increasing voltage, trichel streamers, negative pulseless glow and negative streamers. The appearance of these corona modes are shown in Figure 3.37.

3.12.1.1 Trichel streamers

In this mode the discharge activity takes place in very regular pulses with a well defined repetition frequency. The current waveform associated with a single pulse has a duration of a few tens of nanoseconds. In each event a streamer-like discharge is initiated, develops and is finally suppressed. The pulse frequency, which depends on the geometry of the electrode and pressure, increases with increasing voltage. The dead time between the pulses may vary from a few microseconds to hundreds

of microseconds. The reason for the pulsation of the discharge is the following. As the discharge develops it will give rise to a negative space charge that will reduce the electric field at the cathode leading to the choking off of the discharge. During the dead time between pulses, the space charge is removed by the electric field and this will increase the electric field at the cathode leading to the creation of another streamer.

3.12.1.2 Negative pulseless glow

This stage is characterised by a more or less uniform discharge activity without pulse bursts. The absence of the pulses indicates that the electric field is high enough to quickly transport away the negative space charge so that it will not choke the discharge activity. Moreover, positive ions gain enough energy from the electric field so that they generate a copious supply of electrons to the discharge when they collide with the cathode. The discharge behaves as a miniature glow discharge.

3.12.1.3 Negative streamers

In this regime the removal of the space charge is so efficient that the avalanches develop into streamer discharges. These streamer discharges extend far into the low electric field region of the gap with their extension increasing with increasing voltage. The streamers generate low-frequency pulses in the discharge current.

3.12.2 Positive corona modes

The important features of the positive corona are the following:

a The primary electrons initiate avalanches which grow towards the anode within the volume of gas in which the electric field is higher than the critical value necessary for electrical breakdown (see Figure 3.38).
b Since the avalanches grow in the direction of increasing electric field the drift velocity of electrons increases as the avalanche grows thus diminishing the probability of attachment to electronegative gases and giving rise to negative ions.
c The electrons reaching the anode have a high kinetic energy and they have to dispose of their energy before they can be absorbed into the anode. Thus they spend their energy in ionisation collisions leading to discharge activity at the anode surface.
d The incoming avalanches and the electrical activity at the anode leave behind a positive space charge in front of the anode. If the number density of the positive space charge within a volume of about 50 μm radius exceeds 10^8 ions the streamer inception criterion is satisfied and streamers that propagate towards the anode are generated.

The interplay between these processes give rise to different modes of corona. The visual appearance of the positive corona modes are shown in Figure 3.39.

3.12.2.1 Burst corona

The avalanches generate fast electrons which initiate ionisation and excitation at the surface of the anode as they spend their energy before they are being absorbed by the

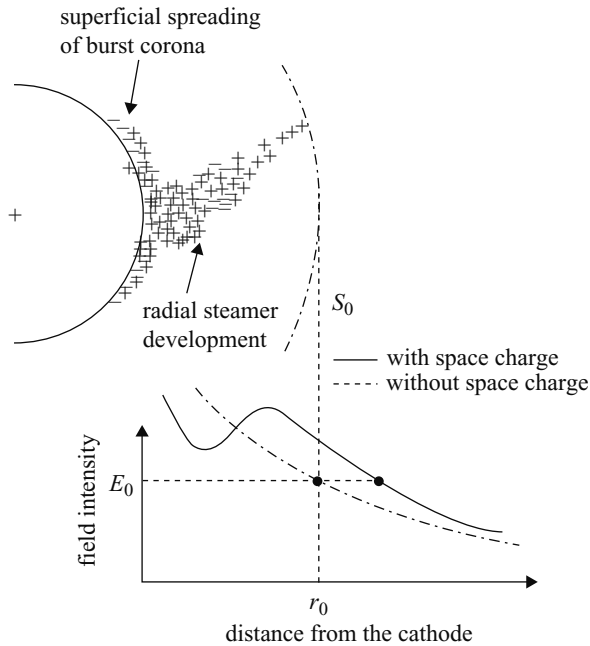

Figure 3.38 Space charge and the electric field distribution in the gap during the formation of positive corona (from [52]; reproduced by permission of IEEE)

anode. This discharge activity, which appears as a thin luminous sheath attached to the anode, gives rise to positive ions. As the concentration of the positive ions grows it will choke the discharge and the latter moves to a new location on the anode. The discharge current consists of small pulses resulting from the movement of discharge activity on the surface of the anode.

3.12.2.2 Onset streamer

As the voltage builds up the positive space charge of the avalanches reaching the anode exceeds the critical value necessary for the inception of streamers. The streamers thus generated extend into the gap. However, the streamers are short because their positive space charge will reduce the electric field at the anode thus impeding the rapid removal of electrons from the streamer channels and choking off the streamer. A dead time is required to remove the ionic space charge and restore the electric field for the formation of another streamer-like discharge. Even at this stage the electrons continue their electrical activity close to the anode so that burst corona activity occurs simultaneously with the streamer development. Some of the electrons travelling towards the anode along the streamer channels will be captured by electronegative atoms. However, when reaching the anode they shed their electrons which contribute to the electron activity at the anode. As the voltage is raised even higher, the burst corona is enhanced. The positive space charge generated by the burst corona moves away from the anode

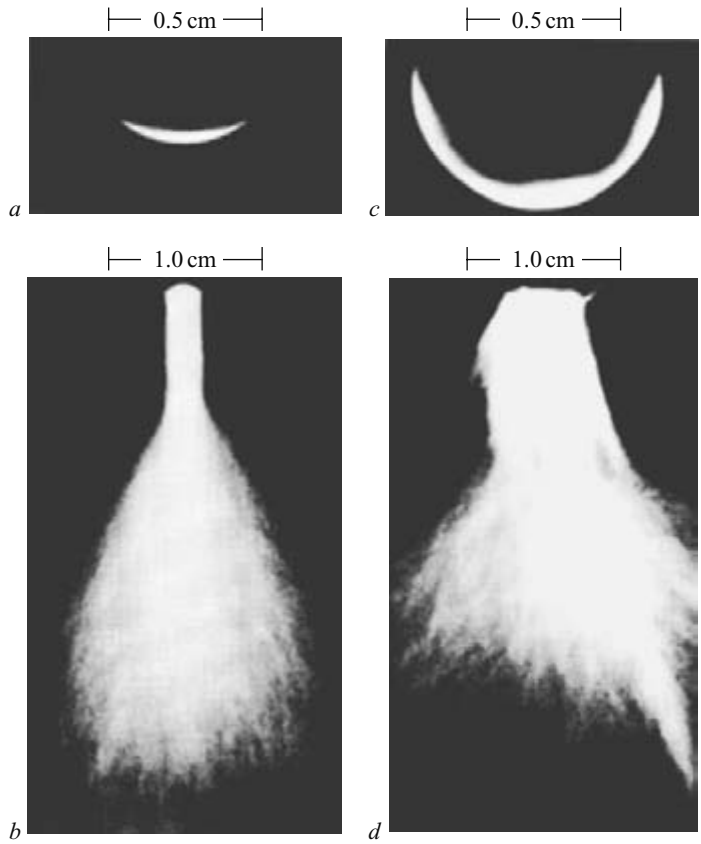

Figure 3.39 *Positive corona modes. Cathode: spherical boss ($d = 0.8\,cm$) on a sphere ($D = 7\,cm$); gap length 35 cm; time exposure: 0.25 s* (from [52]; reproduced by permission of IEEE)

- *a* burst corona
- *b* onset streamer
- *c* positive (or anode) glow
- *d* breakdown streamers

surface and forms a stable positive ionic space charge around the anode which prevents the radial development of the streamer discharge into the gap. With increasing voltage the burst corona intensifies at the expense of the onset streamers. Finally, it will completely choke off the streamer activity giving rise to a new corona mode called positive or Hermitian glow.

3.12.2.3 Positive glow

The discharge activity, which appears as a luminous layer, adheres to the surface of the anode and as in the burst corona moves around the anode from one place to another giving rise to the pulsation of the current.

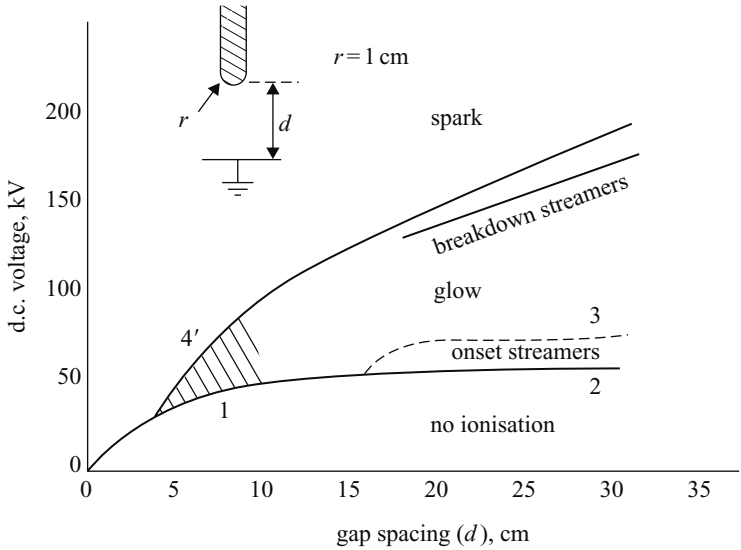

Figure 3.40 *Threshold curves in atmospheric air for various modes of positive corona and for spark breakdown for a spherically capped anode and plate cathode* (from [1])

3.12.2.4 Breakdown streamers

If the applied voltage is further increased, the electric field will be able to remove quickly the positive space charge that has blocked the streamer activity leading again to the development of radial streamers. Usually, the streamers develop from local hot spots with intense ionisation activity. As the voltage increases the streamers become more and more vigorous and extend further and further away from the anode surface.

3.12.3 Electrical breakdown and corona

Figures 3.40 and 3.41 show the threshold voltage for different corona modes of positive and negative polarity, respectively, in a rod plane gap as a function of the gap spacing in atmospheric air. Note that at very small gap spacing where the electric field is uniform direct breakdown is possible without corona inception. With increasing gap spacing the electric field in the gap becomes nonuniform and different forms of corona appears at different voltages.

3.13 Dependence of electrical breakdown conditions on atmospheric conditions

As discussed previously, the ionisation and attachment coefficients are not constants but depend on the pressure and temperature of the gas or on the density of the gas.

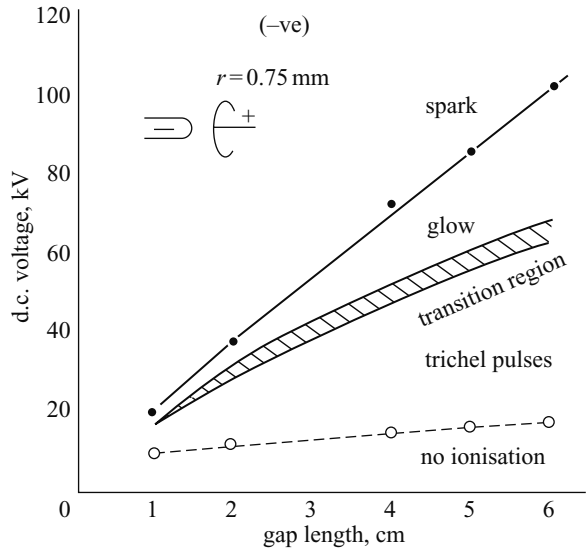

Figure 3.41 *Threshold curves in atmospheric air for various modes of negative corona and for spark breakdown for a spherically capped anode and plate cathode* (from [1])

For this reason these parameters are usually expressed as α/n or η/n where n is the density of the gas. For the same reason the critical electric field necessary for cumulative ionisation in air, and hence the breakdown voltage of air gaps, also depends on the density of air. Let E_c ($= 2.6 \times 10^4$ V/cm) be the critical electric field in air for cumulative ionisation at standard atmospheric conditions (i.e. $p_0 = 1.013$ bar, $T_0 = 293$ K). The corresponding critical electric field, E_x, at nonstandard atmospheric conditions corresponding to p and T can be obtained from:

$$E = E_c\delta \tag{3.100}$$

where δ is the relative density correction factor given by:

$$\delta = \left(\frac{pT_0}{p_0T}\right) \tag{3.101}$$

with T given in kelvins. Observe that for a given gap length this linear form of correction is valid only over a certain range of pressures. The reason for this limitation is apparent from the Paschen curve which is linear only over a certain range of pressures for a given gap length.

The atmospheric conditions influence not only the electrical breakdown electric fields but also the critical electric field necessary for corona inception. For example, the corona inception voltage in air between coaxial cylinders is given by [53]:

$$E_c = 3.15 \times 10^4\delta(1 + 0.305/\sqrt{\delta r}) \tag{3.102}$$

where E_c is given in V/cm and the radius of the inner conductor, r, is given in cm. This equation is known as Peek's formula.

3.14 Statistical nature of electrical breakdown

Consider the situation in which a step voltage is applied to a plane parallel gap (Figure 3.42). Since the electric field in the gap should be larger than the critical value of 2.6×10^6 V/m for electrical breakdown, electrical breakdown will not be observed until the applied voltage increases beyond a critical value V_s given by $V_s = d \times 2.6 \times 10^6$ where d is the gap length. However, to achieve electrical breakdown two conditions should be satisfied. First, a free electron that is capable of generating an electron avalanche should be available in the gap. Usually free electrons in air are generated by the background cosmic radiation or by the radioactivity of the ground. In general, a free electron may not be available at the instant of the application of the voltage in the volume of air under consideration. That is, there is a certain time lag between the application of the voltage and the time of creation of a free electron in the gas volume. This time lag is known as the statistical time lag. The statistical time lag could be decreased by illuminating the electrodes with UV radiation which will cause the electrode to emit free electrons. The statistical time lag also decreases with increasing applied voltage. One reason could be (in the case of a negative high-voltage electrode) the increasing probability of field emission from the cathode with increasing surface electric field. The other reason is the increase in the critical volume of gas (see section 3.15.2.3 for the definition of critical volume) with increasing applied

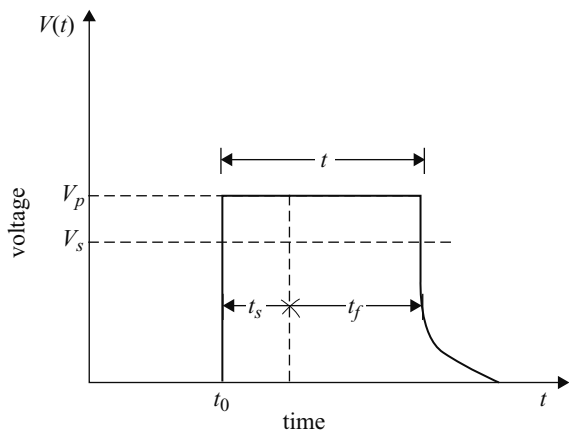

Figure 3.42 Time lag components under a step voltage. The voltage is applied at $t = t_0$. V_s minimum static breakdown voltage; V_p peak voltage; t_s statistical time lag; t_f formative time lag. The total time lag is denoted by t

voltage. Once an electron is found it should first generate a streamer and then the streamer should be converted to a spark. This process will also take some time to be completed, and this time is called the formative time lag. The total time between the application of the voltage and the final breakdown is called the time lag.

3.14.1 Electrical breakdown under the application of impulse voltages

The situation is more complicated when an impulse voltage (i.e. a voltage that reaches a peak value and then decays to zero after a certain time) is applied to a plane parallel gap (Figure 3.43). In this case two conditions have to be satisfied in order to achieve complete breakdown of the gap:

(i) The applied voltage (and hence the electric field in the gap) has to exceed the critical value V_s where cumulative ionisation is possible.

(ii) The applied voltage must remain over this critical value until the formation of the discharge is completed, which means that the voltage must remain over this critical value for a duration larger than the total time lag. Observe that since the statistical time lag and the formative time lag may change from one voltage application to another, the same voltage waveform may or may not cause breakdown in the gap depending on the length of the time lag. That is, the electrical breakdown of a gap becomes a probabilistic event.

It is important to note that for a given peak amplitude the duration over which the applied voltage exceeds the critical value depends on the shape or the time variation of the applied voltage. The narrower the impulse voltage the shorter the duration over which the voltage exceeds the critical value. Thus the breakdown voltage of a gap depends on the shape of the applied impulse voltage. The narrower the impulse voltage the higher the peak value necessary to cause electrical breakdown.

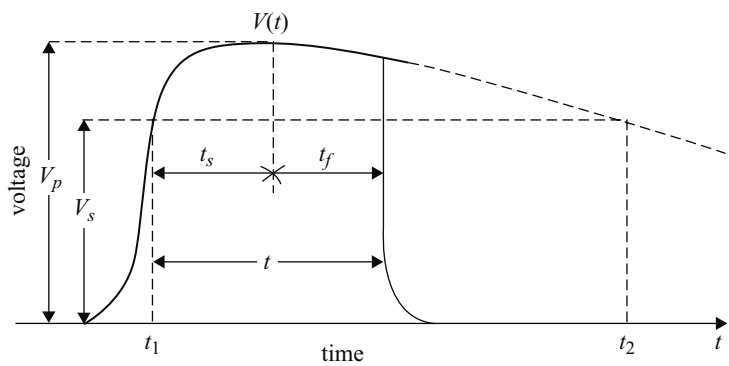

Figure 3.43 Breakdown under impulse voltage, V(t). V_s minimum static breakdown voltage; V_p peak voltage; t_s statistical time lag; t_f formative time lag. The total time lag is denoted by t

3.14.2 Statistical nature of the electrical breakdown

Owing to the statistical nature of the time lags, when a given number of identical voltage impulses with magnitude exceeding the static breakdown voltage V_s is applied to a gap, only a certain percentage will lead to breakdown. Thus, for a given voltage impulse, there is a certain probability that the gap will break down.

The breakdown probability for a given impulse voltage is obtained by applying a large number of identical impulses and taking the ratio of the number of impulses that lead to breakdown to the total number. Conventionally, V_{b-100} represents one hundred per cent breakdown voltage. That is, each voltage application of this magnitude leads to breakdown. V_{b-50} represents the peak voltage in which one half of the applied voltage impulses at this level lead to breakdown. V_{b-0} represents the largest peak impulse voltage that does not lead to breakdown. It is known as the impulse withstand level of the gap.

3.15 The long spark

In small gaps the transformation of the streamer-to-spark channel takes place directly after the streamer has crossed the gap and reached the grounded electrode. In the case of long gaps the processes that lead to the electrical breakdown are a little bit more complicated. The first phase of the discharge development is a corona discharge (called the first corona) which takes the form of a burst of filamentary channels from the high-voltage electrode. The next stage is the development of a highly conducting discharge channel called the leader from the high-voltage electrode. In the third phase the leader extends, with the aid of corona discharges emanating from its head, towards the grounded electrode. The final jump is the last stage of the leader before final breakdown. The final jump starts when the corona streamers emanating from the leader head reach the grounded electrode.

3.15.1 Streamer-to-leader transition and the initiation of the leader

Many of the streamers in the first corona have their origin in a common channel called the streamer stem. The streamers stop when the electric field decreases below the critical value necessary for their propagation. Each individual streamer is a cold discharge and the current associated with this cannot heat the air sufficiently to make it conducting. However, the combined current of all streamers flowing through the stem causes this common region to heat up increasing the conductivity of the stem. When the temperature of the stem increases to about 1000–1500 K, the rate of negative ion destruction greatly increases, retarding the drop in conductivity [13]. Furthermore, during the initial current flow through cold air, about 95 per cent of the energy gained by electrons from the electric field is transferred to vibrations of nitrogen molecules [12]. The vibrational relaxation time decreases with increasing temperature. Around 1500–2500 K, the VT relaxation of nitrogen molecules is accelerated, and the energy stored in the vibrational states of the molecules transfers to the translational energy thus raising the temperature (see also section 3.16). The increase in the temperature

causes the gas to expand making the E/n (E is the electric field and n is the gas density) ratio increase leading to an increase in ionisation and electron production. Thus the current will be concentrated into a thin channel and this in turn will produce more heating and accelerate the ionisation. Through this process the stem will be transformed into a hot and conducting channel called the leader.

Owing to its high conductivity most of the applied voltage will be transferred to the head of the leader channel resulting in a high electric field there. The production of streamer discharges now takes place from a common stem located at the head of the leader channel. With the aid of cumulative streamer currents the new stem gradually transforms itself to a newly created leader section with the streamer process now repeating at the new leader head. The streamer system located in front of the leader is the source of current which heats the air and makes possible the elongation of the leader. As the leader progresses forward through the space originally traversed by streamers, the charge of the latter forms a space charge or corona sheath around the leader channel.

The ability of the leader to propagate in the gap is determined by the electric field around the leader head and the streamer zone in front of it. At constant voltage the electric field at the leader head decreases, as the leader elongates. There are two reasons for this. One is the voltage drop along the elongated leader channel. The other is the growth of charge of opposite sign induced in the leader head by space charge in the gap, namely the streamer zone and the corona sheath. Thus, in order for the leader to propagate continuously, the voltage applied to the gap must be initially high enough or be raised during the leader development.

The leader supports a current of about 1 A at a relatively low longitudinal electric field of about 10^3 V/cm. Spectroscopic measurements show that the air in the leader channel is heated to about 5000 K [30,31].

3.15.2 General characteristics of impulse breakdown in rod–plane gaps

Extensive work on the electrical breakdown characteristics of long gaps under the application of impulse voltages was conducted by the Renardiers group [30,31]. The summary given here is based mainly on their results (see also [58]).

3.15.2.1 Positive breakdown

The breakdown voltage of a rod–plane gap depends on the rise time of the applied voltage impulse. Experiments show that there is a critical rise time at which the breakdown voltage is a minimum. This rise time is called the critical rise time or critical time to crest. The basic physical phenomena that happen when a voltage impulse of critical time to crest is applied to a rod–plane gap are shown in Figure 3.44. At time t_i, when the voltage reaches a value U_i, depending on the gap geometry, the first phase of the discharge occurs. This is a corona burst which takes the form of filamentary discharges. This corona burst is called the first corona. The corona streamers are emanating from a short bright channel located at the electrode and called the stem (Figure 3.45). At this stage the current measured at the high-voltage electrode shows an impulse with a duration of some hundreds of nanoseconds. The

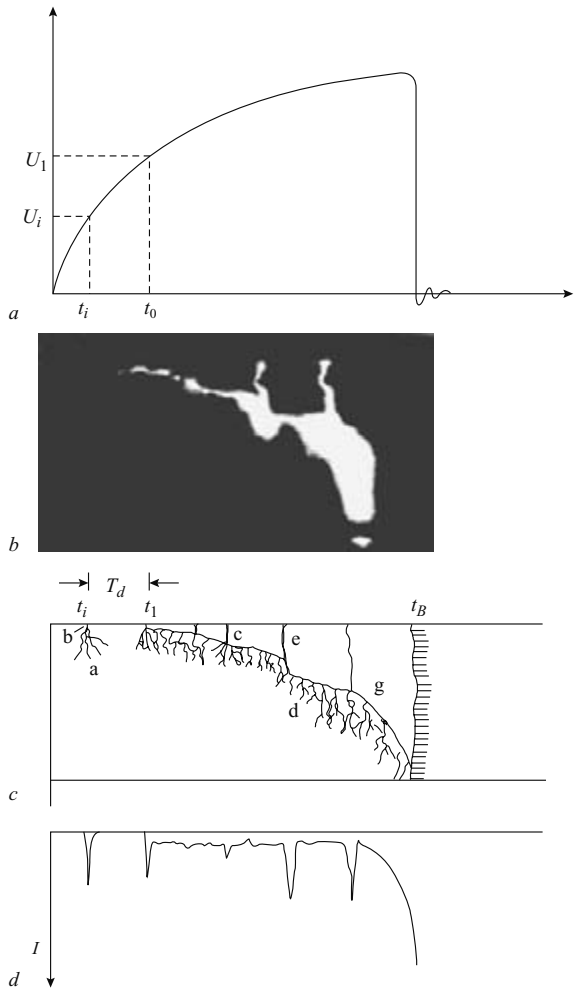

Figure 3.44 *Development of a long positive spark in air. The first corona occurs at time t_i when the voltage reaches the value U_i. The corona takes place in the form of filamentary channels (b and d). The stem is observed at the root of the corona streamers (b). After the dark period T_d the leader is initiated at time t_1 preceded by a secondary corona discharge. The leader propagates forward with the aid of corona discharges from the head (d). The leader channel luminosity is quite low except in the case of sudden elongation of the leader called restrikes (c, e). The final jump starts when the leader corona reaches the plane electrode (g). The final breakdown takes place at t_B* (adapted from [30])

- *a* applied voltage
- *b* streak photograph
- *c* schematic representation of the discharge development
- *d* the current associated with the discharge

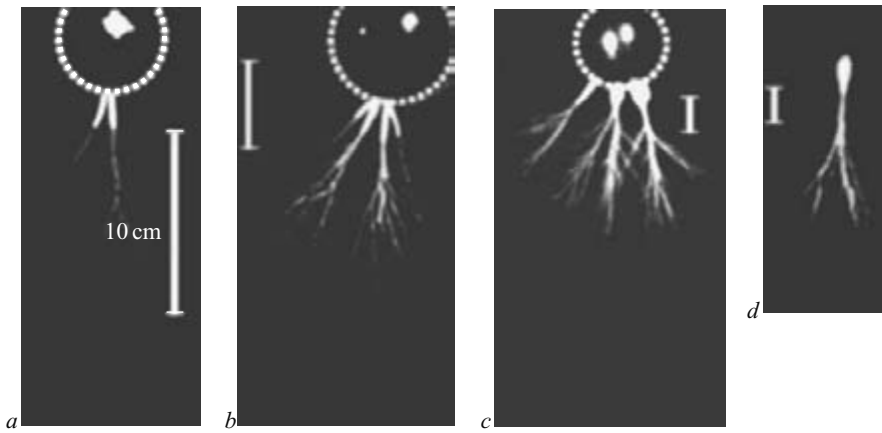

Figure 3.45 *Streamer discharges from electrodes of different dimensions* (adapted From [59])

a 6.2 cm
b 15 cm
c 25 cm
d 50 cm

space charge injected into the gap during the first corona reduces the electric field. This electric field recovers at a rate which depends on the rate of increase of the applied voltage and the dissipation of the space charge. No ionisation activity can be detectable during this period, marked T_d in the diagram and called the dark period. Depending on the geometry and the rate of rise of the applied voltage, a leader channel develops from the stem preceded by a secondary corona discharge after the dark period. If the radius of curvature of the electrode is large enough the dark period can be reduced to zero and the leader may start immediately with the first corona. The minimum radius of the electrode at which the dark period becomes zero is called the critical radius (see section 3.15.2.7).

Once initiated the leader channel propagates along a tortuous path with a corona discharge developing from its tip (Figure 3.46). Usually the leader travels more or less continuously, however, if the rate of increase of the applied voltage is too low then sudden elongations or brightening of the leader occurs. These are called restrikes. When the streamers of the leader reaches the ground plane, the final jump begins (section 3.15.2.6). At this stage the arrest of the leader is not possible and breakdown of the gap is inevitable. The leader velocity increases almost exponentially and when the leader head reaches the plane a conducting channel bridges the electrodes and the return stroke begins.

3.15.2.2 Negative breakdown

The development of the negative leader discharge is depicted schematically in Figure 3.47. The first corona and the dark period are similar to those of the positive

Figure 3.46 Successive frames of image converter picture in a 10 m gap showing the development of streamer discharges from the head of the leader channel [60]

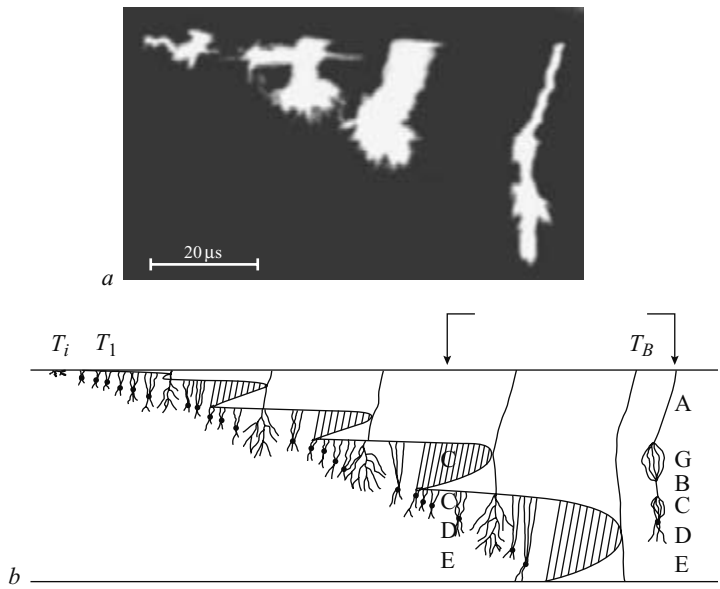

Figure 3.47 Development of long negative spark in air. The gap length was 7 m. A: negative leader; B space leader; C positive streamers, D space stem; E negative streamers; G positive streamers (adapted from [31])

a streak photograph
b schematic representation of the discharge development

breakdown. However, after the dark period a unique feature, namely a pilot system, that does not exist in the positive breakdown, is manifest in the system. The pilot system consists of a bright spot called the space stem (marked by dark spots in the Figure) of short duration, from which streamers of both polarity develop in opposite directions. The positive streamers propagate towards the high-voltage system and the negative streamers in the opposite direction. The interaction of the positive streamers generated by the space stem and the streamers of the first corona leads to the initiation of the negative leader from the cathode. During the propagation of the leader, a space stem appears in front of it at regular intervals generating positive streamers towards the leader head. The positive streamers of the space stem propagate in the region previously covered by negative streamers, connecting the space stem with the tip of the leader by a dense network of streamer channels. Once the connection is made between the positive streamers and the leader head, another section ahead of the leader head is thermalised leading to the extension of the leader. As the leader channel grows the whole system of positive and negative streamers including the space stem repeats itself in a more advanced position in the gap.

The space stem in some cases gives rise to a space leader which starts to elongate from the space stem. The space leader lengthens with a higher velocity towards the cathode (3 cm/μs) than towards the anode (1 cm/μs). As the space leader approaches the main leader, the velocity of both increases exponentially. The connection of the two leaders is accompanied by a simultaneous illumination of the whole channel starting from the meeting point. When this happens, the negative leader length increases by an amount equal to the length of the space leader. This generates an intense source of corona streamers propagating towards the ground plane ahead, at least as far as and some times exceeding the most advanced position of the space stem. The process may lead to the creation of new space stems. The space leaders may have lengths of 30–50 cm before the acceleration phase and the elongation of the negative leader after the junction could be about 1 m.

3.15.2.3 Inception and characteristics of first corona

The inception electric field for the corona can be calculated by using the streamer inception criterion. That is:

$$\int_{r_a}^{r_c} (\alpha - \eta)\, dx = K \tag{3.103}$$

where x is the coordinate parallel to the electric field and directed away from the high-voltage electrode with its origin at the centre of the spherical tip of the electrode with radius r_a, r_c is the value of x at which $E = 2.6 \times 10^4$ V/cm, and $K = 10^8$. It is important to note that the inception electric field does not depend on the gap length, the reason being that it is controlled more by the local electric field at the electrode surface which is not much influenced by the gap length. However, it is strongly influenced by the electric field inhomogeneity close to the electrode. The minimum electric field necessary for the inception of corona, E_i, is given by:

$$E_i = 6.77 \log(1.75 \times 10^3\, d_f), \quad 0.05 < d_f < 5\,\text{cm}^{-1} \tag{3.104}$$

where

$$d_f = \left[-\frac{dE_b}{dx} \cdot \frac{1}{E_b} \right]_{at\ the\ electrode\ surface} \tag{3.105}$$

is the electric field divergency factor with E_b being the background electric field. In the above equation d_f is given in cm^{-1} and the electric field is given in kV/cm.

For the initiation of the corona two conditions have to be satisfied. The first one is the availability of a free electron and the second requirement is that the free electron should be found in a volume of gas located in such a way that the electron can give rise to an avalanche that will lead to a streamer discharge. The natural production rate of electrons in air due to background radiation (both cosmic and terrestrial) is about 10 electrons/cm^3/s. These electrons will get attached to electronegative oxygen atoms forming negative ions. Since in the case of impulse voltages the times involved are in the range of microseconds, the background radiation may not contribute significantly to providing the initiatory electrons. However, this radiation leads to a copious supply of negative ions. The electrons may detach from these ions due to the influence of the electric field and this is the dominant process that provides initiatory electrons. Due to the statistical time lag involved with finding an initiatory electron there is a spread in the time of inception of first corona after the application of the impulse voltage. This time can be reduced using UV illumination of the electrode.

In order to create an avalanche that will subsequently lead to a streamer the initiatory electrons should appear in the gap in a volume of gas in which the electric field is above the critical electric field necessary for breakdown. Moreover, the location of the electron in the volume should be such that the electron can give rise to a streamer discharge. For example, if the electron is located too close to the electrode it will collide with the electrode before forming a critical avalanche. This volume is known as the critical volume. With increasing voltage the volume in which the electric field increases above the critical electric field increases. Since the probability of finding an electron in a given volume increases with its size, the probability of finding an electron that will initiate the breakdown process increases with increasing applied voltage. Figure 3.48 shows how the critical volume increases in rod–plane geometry with increasing applied voltage.

3.15.2.4 Leader velocity

The leader velocity is actually a function of the leader current. The velocity of a 1 A current leader is about 1 cm/μs and the average leader velocity may increase during the final jump. The speed of the leader may be equal to about 2–5 cm/μs at the initiation of the final jump. During the final jump its speed may increase to about 100 cm/μs.

The experimental data suggests a relationship between the leader speed, v, and the current measured at the base of the leader channel, i. The results can be approximated by the empirical equation [54]:

$$v = k_v i^a \tag{3.106}$$

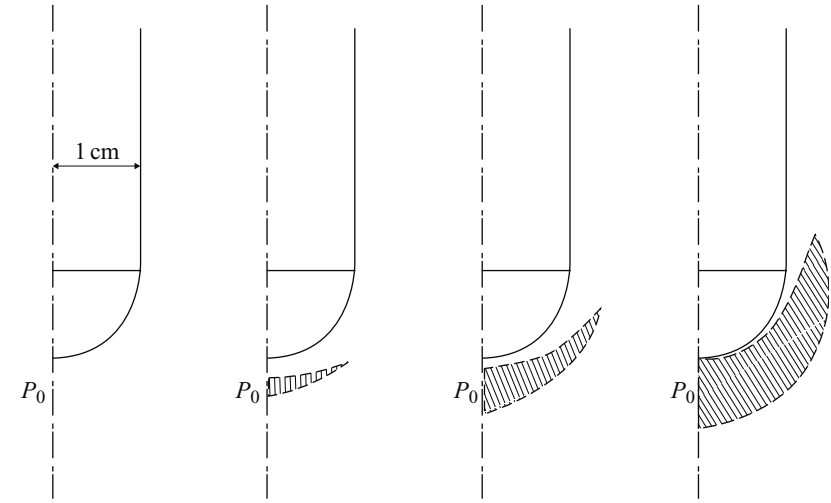

Figure 3.48 The critical volume for different applied voltages in a rod plane gap of 30 cm. U_i is the applied voltage and E_i is the electric field at the electrode [61]

with $a = 0.66$ and

$$k_v = 0.858\,\text{cm}\ (\mu\text{sA}^{\text{a}})^{-1} \quad \text{for } 1 < i < 22.6\,\text{A} \tag{3.107}$$

$$k_v = 2.65\,\text{cm}\ (\mu\text{sA}^{\text{a}})^{-1} \quad \text{for } 85 < i < 1100\,\text{A} \tag{3.108}$$

In the above equation the leader speed is given in cm/μs. On the other hand Bazelyan [55] suggests the relationship:

$$v = kI_l^{0.5}, \quad k = 4\,\text{cm}/\mu\text{sA}^{0.5} \tag{3.109}$$

3.15.2.5 The potential gradient of the leader channel

Even though the potential gradient of the leader channel cannot be measured directly, Gallimberti [13] made several calculations using a thermodynamic model of the leader. The results show that the leader potential gradient decreases with increasing length and approaches about 10^3 V/cm for lengths larger than about 10 m.

3.15.2.6 The final jump

As mentioned previously, the final jump is initiated when the leader corona reaches the anode. During the final jump the brightness and the velocity of the leader channel increases. The speed may increase to several metres per microsecond. The instantaneous velocity is an inverse exponential function of the length of the gap remaining

unabridged by the leader channel. In the case of negative leader, when the negative streamers reach the anode a positive upward going leader is initiated from the anode. Both the down coming negative leader and the positive upward going leader approach each other with an exponentially increasing velocity. When the two leaders meet the return stroke is initiated at the junction point.

3.15.2.7 The critical radius

As described in section 3.15.2.1, the critical radius is the minimum radius of a spherical electrode in a given gap length which will produce leader inception immediately with the inception of first corona. In sphere–plane geometry the critical radius, R_c in cm, is given by [30,31]:

$$R_c = 38(1 - e^{-D/500}) \tag{3.110}$$

where D is the gap length in cm. In the case of conductor–plane geometry it is given by

$$R_c = 37 \ln(1 + D/100) \tag{3.111}$$

The critical radius concept is commonly applied in lightning research in the evaluation of the background electric field necessary for the generation of a continuous leader from a grounded structure. This is done by assuming that a connecting leader is incepted when the electric field at the surface of a hypothetical metal sphere of critical radius (i.e. 38 cm) at ground potential located at the tip of the structure, exceeds the breakdown electric field in air.

Observe that the critical radius is different in sphere–plane gaps and conductor–plane gaps. However, experiments show that the length of the corona streamers at the critical radius is about 3 m and that this length is the same in both geometries (Figure 3.49) [30,31]. In other words, irrespective of the geometry the length of the streamers should exceed this critical value before the inception of the leader. Akyuz and Cooray [56] have used the critical streamer length as the criterion, instead of the critical radius, in evaluating the inception of connecting leader. One advantage of the

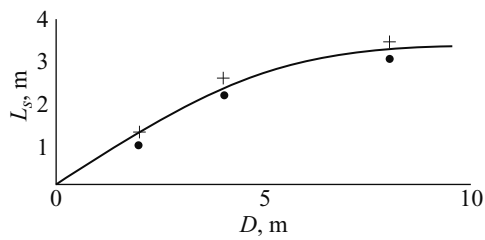

Figure 3.49 The length of streamers at leader inception from electrodes of critical radius as a function of the gap length. The dots correspond to spherical geometry and the crosses correspond to cylindrical geometry [30]

critical streamer length criterion over the critical radius criterion is that the former is independent of geometry. The second advantage is that it can be easily implemented in any complicated structure that one may encounter in practice.

3.16 Humidity effects

The increase in humidity causes an increase in the attachment coefficient and a decrease of the photoionisation efficiency. The reason for the former is the high affinity of water molecules to electrons. Thus, in a given electric field, the rate of ionisation decreases with increasing humidity. The reason for the latter is the reduction in the ultraviolet absorption length by humidity. Moreover, with increasing humidity the probability of finding a free electron in the critical volume decreases. The reason for the reduction of this probability is the increased difficulty of electron detachment from hydrated negative ions. Consequently, the electron detachment rate decreases with increasing humidity. Another interesting effect of humidity is its influence on the relaxation time of vibrational energy into translational energy. As mentioned before, in the preliminary stages of electrical discharges a large fraction of the energy of electrons goes into vibrational excitation of the molecules. The VT relaxation time is the time within which this energy is converted to thermal energy. This relaxation time depends on the temperature and the water vapour content. At $T = 910\,\mathrm{K}$, τ_{vt} varies from $32\,\mu\mathrm{s}$ with humidity $12\,\mathrm{g/m^3}$ to about $100\,\mu\mathrm{s}$ with $4\,\mathrm{gm/m^3}$. These effects can influence the characteristics of electrical discharges in several ways [13].

3.16.1 Critical electric field necessary for streamer propagation

The propagation characteristics of streamers depend on the energy balance in the active region: between the energy input from the space charge and applied electric fields and losses in electron avalanche production. The decrease in ionisation rate caused by the increased humidity in the streamer requires an increase in the minimum charge at the head which is necessary to sustain streamer propagation. Thus, the stable streamer propagation electric field increases linearly with humidity from about 4×10^3 V/cm in dry air to about 6×10^3 V/cm at $20\,\mathrm{g/m^3}$ (see Figure 3.18).

3.16.2 Influence on the corona development at the initiation of long sparks

The amount of corona produced at the initiation of the long sparks depends on the humidity. The charge associated with the first corona and the extension of the corona streamers into the gap decreases with increasing humidity. This happens because the rate of ionisation decreases with increasing humidity [13,30,31].

The duration of the dark period between the first corona and the second corona decreases with humidity. The reason for this is the following. The first corona injects a space charge into the gap and it causes a reduction in the electric field in the gap. Restart of the ionisation after the dark period is determined by the recovery of the

electric field in the stem region. The recovery of the electric field depends on the rate of increase of the applied voltage and how fast the space charge is removed from the stem region. Since the space charge injected by the first corona decreases with increasing humidity a smaller increase in voltage is needed for second corona inception [13,30,31].

3.16.3 Influence on leader propagation

At high humidity, a situation can be reached in which the streamer activity is so low that the leader current is practically reduced to zero. However, since the channel behaves like a resistive conductor, the leader tip potential approaches that of the high-voltage electrode. The local electric field is increased and vigorous new corona can start from the leader tip. This leads to the sudden elongation of the leader channel called restrikes. Another important effect of the increased humidity is that, in spite of the large current pulses associated with the restrikes, the charge per unit length of the leader decreases strongly with increasing humidity [13,30,31].

3.17 References

1 KUFFEL, E., and ZAENGL, W.S.: 'High voltage engineering fundamentals' (Pergamon Press, 1984)
2 BADALONI, S., and GALLIMBERTI, I.: 'University Di Padova, Istituto Di Elettrotecnica E Di Elettronica, Upee-72/05, 1972
3 HOWATSON, A.M.: 'An introduction to gas discharges' (Pergamon Press, 1965)
4 KNOLL, M., OLLENDORFF, F., and ROMPE, R.: Gasentladungstabellen, 'Handbuch der Physik;' Bd.23/1, pp. 141, 142, 1933
5 VON ANGEL, A.: 'Ionised gases' (Clarendon Press, 1965, 2nd edn) p.181
6 LOEB, L.B.: 'The kinetic theory of gases' (Wiley, New York, 1963)
7 TOZER, B.A.: *Phys. Rev.*, 1965, **137**, A1665
8 SAHA, M.H.: *Philos. Mag.*, 1920, **40**, p.472
9 COBINE, J.D.: 'Gaseous conductors; theory and engineering applications' (Dover Publications, Inc. New York, 1958)
10 PENNING, F.M.: *Physica*, 1934, **1**, p.1028
11 THOMSON, J.J.: *Philos. Mag.*, 1912, **23**, p.449
12 BAZELYAN, E.M., and RAIZER, Yu.P., 'Spark discharge' (CRC Press, 1998)
13 GALLIMBERTI, I.: *J. Phys.*, 1979, **40**, (7), pp.C7–193–250
14 WEISSLER, G.L.: 'Encyclopedia of Physics' (Springer, Berlin, 1956) vol. 16, p.445
15 RICHARDSON, O.W.: 'The emission of electricity from hot bodies' (Longmans Green, London, 1921)
16 SCHOTTKY, W.Z.: *Phys.*, 1923, **14**, p.63
17 FOWLER, R.H., and NORDHEIM, L.: *Proc. R. Soc. A*, **119**, p.173 (1928)
18 BORTNIK, I.M., KUSHKO, A.N., and LOBANOV, A.N.: Proceedings of second all-union conference on *Physics of electrical breakdown of gases*, Tartu, 1984, p.270

19 RAETHER, H.: 'Electron avalanches and breakdown in gases' (Butterworths, London 1964)
20 LOEB, L.B., 'Basic processes of gaseous electronics' (University of California Press 1955)
21 LOEB, L.B., and MEEK, J.M.: 'The mechanism of the electric spark' (Stanford University Press, 1940)
22 RAETHER, H.: *Z. Phys.*, 1939, **112**, p.464
23 MEEK, J.M.: *Phys. Rev.*, 1940, **57**, p.722
24 COORAY, V., BERG, M., AKYUZ, M., LARSSON, A., ZITNIK, M., and SCUKA, V.: 'Proceedings of the 24th international conference on *Lightning protection*, Birmingham, UK, 1998, paper 1c.10, pp.128–133
25 HARTMANN, G.: Doctorat d'Etat thesis, University of Paris-Sud, France, 1977
26 DAWSON, G.A., and WINN, W.P.: *Z. Phys.*, 1965, **183**, p.159
27 MARODE, E.: 'The glow to arc transition', *in* KUNHARDT, E., and LARSSEN, L. (eds): 'Electrical breakdown and discharges in gases' (Plenum Press, New York, 1983)
28 SUZUKI, T.: *J. Appl. Phys.*, 1971, **42**, pp.3766–77
29 RAIZER, Yu.P.: 'Gas discharge physics' (Springer, 1997)
30 Les Renardiéres Group: *Electra*, 1977, (53), pp.31–153
31 Les Renardiéres Group: *Electra*, 1981, (74), pp.67–216
32 GAO, L., LARSSON, A., COORAY, V., and SCUKA, V.: *IEEE Trans. Dielectr. Electr. Insul.*, 2000, **7**, (3), pp.458–460
33 GRIFFITHS, R.F., and PHELPS, C.T.: *Q. J. R. Meteorol. Soc.*, 1976, **102**, pp.419–26
34 PHELPS, C.T.: *J. Atmos. Terr. Phys.*, 1974, **15**, p. 169
35 WINDMAR, D.: 'Water drop initiated discharges in air'. Acta Universitatis Upsaliensis, Uppsala, 1994
36 BAZELYAN, E.M., GONCHAROV, V.A., and GORJUNOV, A. YU.: *Izv. Akad. Nauk SSSR Energ. Transp.*, 1985, **2**, 154
37 BAZELYAN, E.M., and GORJUNOV, A.YU.: *Izv. Akad. Nauk SSSR Energ. Transp.*, 1982, **4**, 75
38 MARODE, E.: *J. Appl. Phys.*, 1975, **46**, pp.2005–2020
39 PARIS, L., and CORTINA, R.: *IEEE Trans.*, 1968, **PAS-98**, pp.947–957
40 GAO, L., LARSSON, A., COORAY, V., and SCUKA, V.: *IEEE Trans. Dielectr. Electr. Insul.*, 1999, **6**, (1),
41 AKYUS, M., LARSSON, A., COORAY, V., and STRANDBERG, G.: UURIE 286–02, Division for electricity and lightning research, University of Uppsala, Sweden, 2002
42 LARSSON, A.: Ph.D. thesis, Acta Universitatis Upsaliensis, no. 12, Uppsala, 1997
43 TOWNSEND, J.S.: 'Electricity in gases' (Oxford, 1914)
44 NASSER, E.: 'Fundamentals of gaseous ionization and plasma electronics' (Wiley-Interscience, 1971)
45 DAKIN, T.W., LUXA, G., OPPERMANN, G., VIGREUX, J., WIND, G., and WINKELNKEMKER, H.: '*Electra*', 1974, (32), pp.61–82

46 BROWN, S.C.: 'Introduction to electrical discharges in gases' (John Wiley & Sons, Inc, 1966)
47 KING, L.A.: 'Proceedings of the 5th international conference on *Ionisation phenomena in Gases*, Munich, 1961
48 TOEPLER, M.: Arch. Electrotech (German), 1927, **18**, p.630
49 ENGEL, T.G., DONALDSON, A.L., and KRISTIANSEN, M.: *IEEE Trans. Plasma Sci.*, 1989, **17**, (2)
50 KUSHNER, M.J., *et al*.: *J. Appl. Phys.*, 1985, **58**, pp.1744–1751
51 BRAGINSKII, S.I.: *Sov. Phys.-JETP*, 1958, **34**(7), pp.1068–1074
52 GIAO TRINH, N.: *IEEE Electr. Insul. Mag.*, 1995, **11**, (2)
53 PEEK, F.W.: 'Dielectric phenomena in high voltage engineering' (McGraw-Hill, New York, 1920, 2nd edn)
54 KEKEZ, M., and SAVICH, P.: Proc. IV international symposium on *High voltage Engineering*, Athens, 1983
55 BAZELYAN, E.M.: *Zh. Tekh. Fiz.*, 1966, **36**, p.365
56 AKYUZ, M., and COORAY, V.: *J. Electrost.*, 2001, **51–52**, pp.319–325
57 GALLIMBERTI, I.J., BACCHIEGA, G.L., GAZZANI, A., BERNADI, M., and BONDIOU, A.: Proceedings of the 1994 international aerospace and ground conference on '*Lightning and static electricity*', Manheim, Germany, 1994, p. 23
58 BALDO, G., KUNHARDT, E., and LUESSEN, L.: *In* 'Electrical breakdown and discharges in Gases' (Plenum, 1983)
59 SALKA, O.: '*En översikt over urladdningar I långa gap vid stötspänningar*', Internal report of the Institute of High Voltage Research, 1966
60 LEROY, G., SIMON, M.F., and LIAO, T.W., Proceedings of IEE summer *Power* meeting, paper 74 CH 0910–0 PWR, 1974
61 BADALONI, S., and GALIMBERTI, I.: Padua University report, Upee 72/03, 1972
62 RAETHER, H.: *Z. Angew. Phys.*, 1955, **7**, p.50
63 LOEB, L.B.: 'Electrical coronas: Their basic physical mechanisms' (University of California Press, USA, 1965)
64 ELENBASS, E.: 'The high pressure mercury vapor discharge' (North-Holland Publication Company, 1951)

Chapter 4

The mechanism of the lightning flash

Vernon Cooray

4.1 Introduction

Experimental observations of the optical and electromagnetic fields generated by lightning flashes during the last 50 years have significantly advanced our knowledge concerning the mechanism of the lightning flash. Nevertheless, this knowledge is not as exhaustive as that of long laboratory sparks due to our inability to observe lightning flashes under controlled conditions. Thus, the mathematical description of the mechanism of a lightning flash is relatively poor at present even though the main features of lightning flashes themselves are well known. The main goal of this Chapter is to provide the reader with the important features of the mechanism of the lightning flash. No attempt is made to provide an exhaustive list of the literature since this can be found elsewhere.

Nomenclature: in this chapter a positive discharge is defined in such a way that the direction of motion of electrons in such a discharge is opposite to that of the discharge itself; a negative discharge is defined as one in the opposite sense. According to this definition a negative return stroke is a positive discharge and a positive return stroke is a negative discharge.

A positive field is defined in terms of a negative charge being lowered to ground or positive charge being raised. According to this definition a lightning flash that transports negative charge to ground gives rise to a positive field change.

4.2 The ground flash

As outlined in Chapter 1, a thundercloud generally contains two main charge centres, one positive and the other negative, and a small positive charge pocket located at the base of the cloud. A ground flash occurs between the charge centres of the cloud and the ground. When a ground flash brings positive charge down to earth it is called a positive ground flash and when it brings negative charge it is called a negative ground

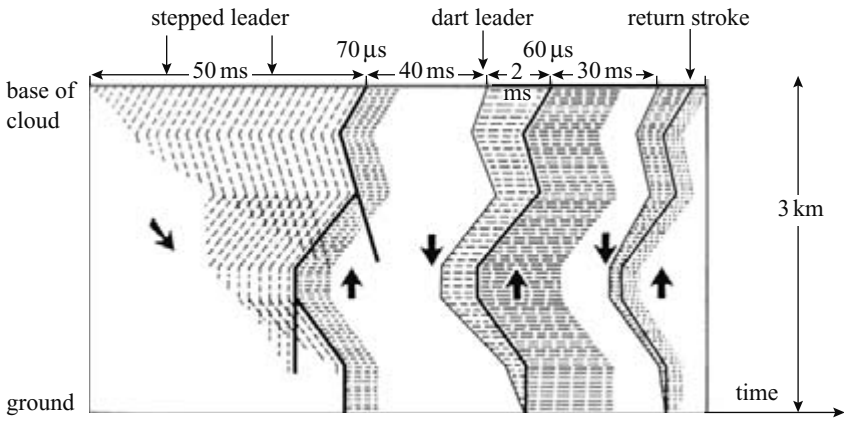

Figure 4.1 *Time resolved luminous features of a lightning flash as would be recorded by a streak camera. The time increases from left to right. The time scale has been distorted for clarity* (adapted from [10] and [169])

flash. Time-resolved luminous features of a lightning flash as would be recorded by a streak camera are shown in Figure 4.1.

Electromagnetic field measurements show that a ground flash is initiated by an electrical breakdown process in the cloud called the preliminary breakdown. This process leads to the creation of a column of charge called the stepped leader that travels from cloud to ground in a stepped manner. Some researchers use the term preliminary breakdown to refer to both the initial electrical activity inside the cloud and the subsequent stepped leader stage.

On its way towards the ground a stepped leader may give rise to several branches. As the stepped leader approaches the ground the electric field at ground level increases steadily. When the stepped leader reaches a height of about a few hundred or less metres from the ground the electric field at the tip of grounded structures increases to such a level that electrical discharges are initiated from them. These discharges, called connecting leaders, travel towards the down-coming stepped leader. One of the connecting leaders may successfully bridge the gap between the ground and the down-coming stepped leader. The object that initiated the successful connecting leader is the one that will be struck by lightning. The separation between the object struck and the tip of the stepped leader at the inception of the connecting leader is called the striking distance. Once the connection is made between the stepped leader and ground, a wave of near ground potential travels along the channel towards the cloud and the associated luminosity event that travels upwards with a speed close to that of light is called the return stroke.

Whenever the upward moving return stroke front encounters a branch, there is an immediate increase in the luminosity of the channel; such events are called branch components. Although the current associated with the return stroke tends to last for a few hundred microseconds, in certain instances the return stroke current may not go

to zero within this time, but may continue to flow at a low level for a few tens to a few hundreds of milliseconds. Such long duration currents are called continuing currents.

The arrival of the first return stroke front at the cloud end of the return stroke channel leads to a change of potential in the vicinity of this point. This change in potential may initiate a positive discharge that travels away from the end of the return stroke channel. Occasionally, a negative recoil streamer may be initiated at the outer extremity of this positive discharge channel and propagate along it towards the end of the return stroke channel. Sometimes, discharges originate at a point several kilometres away from the end of the return stroke channel and travel towards it. On some occasions these discharges may die out before they make contact with the end of the return stroke channel; such events are called K changes. If these discharges make contact with the previous return stroke channel, the events that follow may depend on the physical state of the return stroke channel. If the return stroke channel happens to be carrying a continuing current at the time of the encounter, it will result in a discharge that travels towards the ground. Such discharges are called M components. When the M components reach the ground no return strokes are initiated, but recent analyses of the electric fields generated by M components show that the current wave associated with them may reflect from the ground. If the return stroke channel happens to be in a partially conducting stage with no current flow during the encounter, it may initiate a dart leader that travels towards the ground. Sometimes, the lower part of the channel has decayed to such an extent that the dart leader stops before actually reaching the ground. These are termed attempted leaders. In other instances, the dart leader may encounter a channel section whose ionisation has decayed to such an extent that it cannot support the continuous propagation of the dart leader. In this case the dart leader may start to propagate towards the ground as a stepped leader. Such a leader is called a dart-stepped leader. If these leaders travel all the way to ground then another return stroke, called the subsequent return stroke, is initiated. In general, dart leaders travel along the residual channel of the first return strokes but it is not uncommon for the dart leader to take a different path than the first stroke. In this case it ceases to be a dart leader and travels towards the ground as a stepped leader. The point at which this leader terminates may be different from that of the original first leader. The separation between such subsequent channels was observed to be about a few kilometres, on average.

Electrical activity similar to that which occurs after the first return strokes may also take place after the subsequent return strokes. Note, however, that branch components occur mainly in the first return strokes and occasionally in the first subsequent stroke. This is the case because in general dart leaders do not give rise to branches. In the literature on lightning, the electrical activities in the cloud that takes place between the strokes and after the final stroke are called collectively junction processes or J processes. A typical ground flash may last for about 0.5 s with a mean number of strokes between four and five.

The description given above is based on the observations of negative ground flashes. Not much information is available today concerning the mechanism of positive ground flashes but their mechanism is qualitatively similar to the negatives with differences in the details. For example, the scanty evidence indicates that positive leaders propagate more or less continuously and many positive ground flashes contain

only one return stroke. In addition to these typical ground flashes, lightning flashes can also be initiated by tall structures. In this case a connecting leader is initiated at the top of a tower, for example, and propagates into the cloud. Dart leaders travel along this channel and initiate return strokes. As a consequence these flashes do not contain first return strokes initiated by stepped leaders.

4.3 The cloud flash

Cloud flashes normally occur between the main negative and upper positive charge of the cloud. Most of the information available today on the mechanism of the cloud flash is based on electric field measurements. More recently, Proctor [1–3] and Krehbiel and coworkers [4–6] made important discoveries utilising VHF radio imaging techniques (see section 4.11). The following picture of the cloud flash is based on the observations of Krehbiel and his coworkers (Figure 4.2):

1 The cloud flash commences with a movement of negative discharges from the negative charge centre towards the positive centre in a more or less vertical direction.

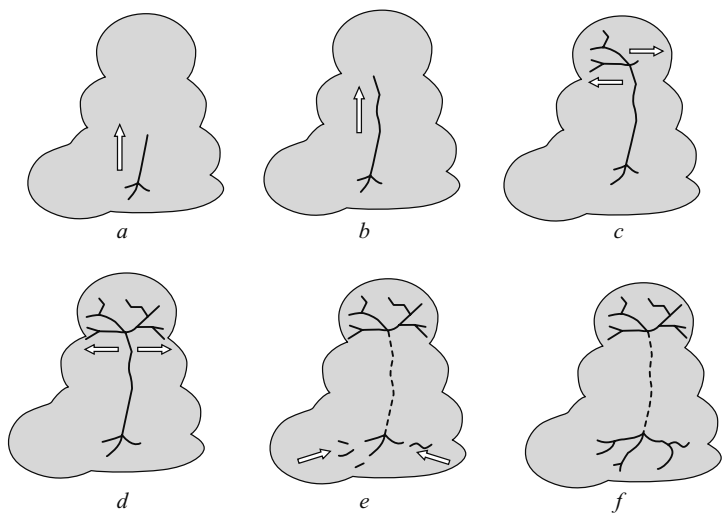

Figure 4.2 Mechanism of a cloud flash. The cloud flash commences with a movement of negative discharges from the negative charge centre towards the positive one in a more or less vertical direction. This is the initial stage (a and b). This stage is followed by an active stage in which horizontal extension of the upper level channels takes place while charge is being transported from the lower level to the upper level along the vertical channel (c and d). In the latter part of this active stage significant extensions of the lower level channels take place but the extensions take place retrogressively (e). In the final stage the conductivity of the vertical channel decreases and the upper level channels will be cut off from the low level channels (f). The arrows indicate the general direction of the discharge development

The vertical channel develops within the first 10–20 ms from the beginning of the flash. This channel is a few kilometres in length and it develops with a speed of about 1.5×10^5 m/s. Even after the vertical channel was formed, the authors could detect an increase in the electrostatic field indicative of negative charge transfer to the upper levels along the vertical channel.

2 The main activity after the development of the vertical channel is the horizontal extension of the channels in the upper level (i.e., the channels in the positive charge centre). These horizontal extensions of the upper level channels are correlated to the brief breakdowns at the lower levels, followed by discharges propagating from the lower level to the upper level along the vertical channel. Thus the upper level breakdown events are probably initiated by the electric field changes caused by the transfer of charge from the lower levels. For about 20–140 ms of the cloud flash, repeated breakdowns occur between the lower and upper levels along the vertical channel. These discharges transported negative charges to the upper levels. Breakdown events of this type can be categorised as K changes. In general, the vertical channels through which these discharges propagate do not generate any radiation in the radiofrequency range, indicating that they are conducting. This is so because, in general, conducting channels do not generate radiofrequencies as discharges propagate along them. Occasionally, however, a discharge makes the vertical channel visible at radiofrequencies and then the speed of propagation can be observed to be about $(5–7) \times 10^6$ m/s, typical of K changes. This active stage of the discharge may continue to about 200 ms.

3 In the latter part of this active stage (140–200 ms), significant extensions of the lower level channels (i.e. the channel in the negative charge centre) take place, but they occur retrogressively. That is, successive discharges, or K changes, often start just beyond the outer extremities of the existing channels and then move into and along these channels, thereby extending them further. These K changes transport negative charge from successively longer distances to the origin of the flash, and sometimes even to the upper level of the cloud flash as inferred from RF emissions from the vertical channel. Sometimes, these K changes give rise to discharges that start at the origin of the flash and move away from it towards the origin of the K changes. Such discharges can be interpreted as positive recoil events that transport positive charge away from the flash origin and towards the point of initiation of the K change.

4 At the final part of the discharge the vertical channel and the upper-level channels were cut off from the lower-level channels. This is probably caused by the decrease in the conductivity of the vertical channel.

4.4 Frequency of lightning discharges

The number of lightning flashes occurring in a given region is of interest to both power engineers and lightning protection engineers. Historically, the lightning activity was measured in terms of the number of thunder days for each region. A thunder day is a day in which thunder is heard by meteorological observers. On the basis of

this data, the World Meteorological Organisation has published a thunder-day map covering the whole world (see Chapter 1). More recently, information on lightning activity has been obtained by counting the number of lightning flashes occurring over a given region by (i) using satellites to capture the optical signals generated by lightning flashes [178,179], (ii) using lightning flash counters [180], (iii) employing magnetic direction finding systems [181] and (iv) VHF lightning mapping techniques [1,5] (see section 4.11 for a detailed description of some of these techniques). Some attempts have also been made to evaluate the number of lightning flashes occurring in the atmosphere by measuring the radio noise with an ionospheric sounding satellite [182]. Recently, advances have been made to relate the global lightning activity to the Shumann resonance [183,184]. Shumann resonances are caused by the lightning-induced excitation of the earth–ionospheric waveguide. The resonance frequencies are located at 8 Hz, 16 Hz, 32 Hz etc. Various estimates making use of these different techniques indicate that at a given time there are about 1000–2000 thunderstorms active around the globe. An isolated thundercloud may produce lightning at a rate of a few lightning flashes in a minute, but severe storms can produce lightning at a rate of several tens of flashes per minute, the maximum number recorded being about 85 flashes per minute [185]. At any one time the thunderstorms active around the globe produce lightning flashes at a rate of about 20–120 s^{-1}. The lightning activity over the oceans is about a factor three smaller than over land.

4.4.1 Cloud to ground flash ratio

A study conducted by Prentice and Mackerras [186] has summarised much of the available data on the cloud to ground flash ratio. According to them:

$$\frac{N_c}{N_g} = 1.0 + 0.063T \quad 10 \leq T \leq 84 \tag{4.1}$$

where N_c is the number of cloud flashes, N_g is the number of ground flashes and T is the number of thunderstorm days per year. They have also developed an empirical relationship between the cloud to ground flash ratio and the latitude. That relationship is given by:

$$\frac{N_c}{N_g} = (4.11 + 2.11 \cos 3\lambda) \quad 0 \leq \lambda \leq 60^\circ \tag{4.2}$$

where λ is the latitude. This equation indicates that the cloud to ground flash ratio is highest in the tropics and that it decreases with increasing latitude.

4.4.2 Ground flash density

Until the late seventies, the ground flash density, that is the number of lightning flashes striking one square kilometre on the earth in a year, was obtained by lightning flash counters. More recently it has been determined by lightning localisation systems either using the principle of magnetic direction finding or the time of arrival technique,

and sometimes both (see section 4.11). It is important to note that the sensitivity of these systems is not 100 per cent and that the sensitivity may vary in space, depending on the location of the detectors. Thus, the exact values of the ground flash density may be higher than the figures estimated from the data obtained from lightning localisation systems. Moreover, the ground flash density may vary from one geographical region to another and from one location to another within the same geographical region. In general the ground flash density will range between fewer than one ground flash $km^{-2}\ yr^{-1}$ to about 10 $km^{-2}\ yr^{-1}$. In analysing the ground flash density it is important to consider that some lightning flashes may have more than one termination to ground. The studies conducted by Rakov *et al*. [187] show that about 50 per cent of the lightning flashes evidently have multiple terminations and the average separation between individual channel terminations varies from 0.3 to 7.3 km, with a geometric mean of 1.7 km.

4.4.3 Total lightning activity

The total flash density in different regions of the world has been analysed by Mackerras and Darvaniza [188] who used the data from specially designed lightning flash counters located in 14 countries. They have found a clear tendency for the lightning flash activity to be a maximum at the equator and to decrease with increasing latitude. They have summarised their results through the equation:

$$N = \exp(3.7 - 0.07\lambda)\ \mathrm{km}^{-2}\mathrm{yr}^{-1} \tag{4.3}$$

where λ is the magnitude of the latitude in degrees.

4.5 Inception of lightning discharges in clouds

Lightning flashes are initiated in the mixed-phase region of the cloud where water drops, ice crystals, graupel and water vapour coexist. To unravel the physical processes in which these various phases of water interact with electric fields to initiate lightning flashes is one of the main challenges in atmospheric electricity. Several measurements conducted inside electrically active clouds show that they harbour electric fields of strengths typically in the range of 100–200 kV/m; the fields may occasionally reach values as high as 400 kV/m [209–213,221]. Let us consider the conditions necessary for the initiation of electrical discharges in the cloud. (The discussion given here is based on a publication of Cooray *et al*. [214].)

4.5.1 Initiation of streamer discharges from a single water drop

Since the streamer discharges are a precursor to the electrical breakdown process at atmospheric pressures which are of interest in this study, the initiation of such discharges is a necessary condition for the generation of lightning flashes.

A spherical water drop enhances the background electric field by a factor of three. Thus, the strength of the background field has to be higher than 500 kV/m so that

the maximum electric field at the surface of the water drop becomes higher than about 1.5 MV/m, the electrical breakdown field at 0.5×10^5 Pa (i.e. about half the atmospheric pressure) and at 273 K. In general, the negative charge centre of the cloud is located close to the 263 K (−10°C) isotherm, but this decrease in temperature will increase the breakdown electric field only by about four per cent. Since the electric field decreases rapidly with increasing distance from the surface of the drop, raising the surface field to 1.5 MV/m is not a sufficient condition for the generation of a streamer. The reason for this is the following. For the creation of a streamer an electric field of strength equal to or higher than the electrical breakdown value should exist over a critical volume in space. This necessarily requires an electric field higher than the breakdown field at the surface of the drop to create a streamer. Since the way in which the electric field decreases as a function of distance, measured from the surface of the drop, varies with its radius, the critical background field necessary for the creation of a streamer also varies with the drop radius. Table 4.1 summarises the background electric field necessary for the creation of streamers from different drop sizes.

Note, that although the field decreases with increasing drop radius, spherical drops need to be large, more than 3 mm in radius, to initiate streamers in background fields which are less than the electrical breakdown field. This means that it is not likely that single spherical drops will create streamers. This far we have not included the deformation of the drop due to electrical forces. According to the results of

Table 4.1 Background electric field necessary to create streamers from single water drops, both spherical ($R_p/R_e = 1$) and deformed ($R_p/R_e < 1$) according to Taylor's observations [215] (R_p = polar radius, R_e = equatorial radius)

Equivalent drop radius (mm)	Roundness R_p/R_e	Background field (MV/m)
1	1	1.41
1	1/32	1.41
2	1	1.41
2	1/32	1.27
3	1	1.41
3	1/32	1.07
4	1	1.35
4	1/32	0.95
5	1	1.29
5	1/32	0.86
6	1	1.24
6	1/32	0.80

Taylor [215], a drop will form a conical structure with an apex angle of 98.6° just before it goes into corona. The results given in Table 4.1 show that the background electric field necessary for streamer inception does not change significantly even when this change in shape is introduced into the calculations except in the case of very large drop radii. The reason for this is that, even though the field enhancement at the drop surface is drastically increased due to the conical shape, it decreases rapidly as one moves away from the surface, approaching a field strength identical to that of spherical drops within a fraction of the drop radius. The conclusion is that only very large and very deformed drops may create streamers on their own.

4.5.2 Initiation of streamer discharges by a chain of water drops

Crabb and Latham [216] analysed the generation of corona when two water drops collide and give rise to an elongated body. Cooray *et al*. [214] analysed the situation in which two water drops come close to each other in an electric field leading to an electric discharge between them. In the calculations it was assumed that the discharge takes place when the minimum electric field in the space between the drops surpasses the breakdown electric field. This is justified since the separation between the water drops just before the discharge is such that the electric field is approximately uniform in the space between them. During the discharge, the two drops will be connected by a conducting channel and this will create a complex body with a dumbbell shape. The situation just before and after the discharge is shown in Figure 4.3 together with the corresponding electric fields. In this example the background electric field was assumed to be 200 kV/m. Furthermore, in their calculations it was assumed that the electrical relaxation time of the water in the cloud is so fast that it will not impede the redistribution of charge during the discharge event. These results show that the connection of the two drops by a discharge channel enhances the electric field at the outer periphery of the two drops by much more than does the field enhancement caused by a single drop or two drops without the connecting discharge. This situation, therefore, favours the creation of streamers more than a single drop. The results in Table 4.2 show the background electric fields necessary for the creation of streamers from such an encounter.

The electric fields given in Table 4.2 are lower than those given in Table 4.1 for single drops. Of course, a similar situation may occur in the transitory region of two drops coalescing to form a complex body. In this case the two drops will be connected by a liquid column instead of a discharge channel. But, the field enhancement would be more or less similar. Note that the electric discharge between the two water drops is a transitory event, but the field enhancement achieved during the discharge phase would remain the same even after the decay of the discharge channel. However, if a streamer is created from the outer periphery of the water drops, the resulting charge redistribution may provide sufficient current to maintain the discharge channel between the two drops.

As the electric field at the outer periphery of two interacting water drops increases, an electric discharge may take place to a third drop if the latter is located at a suitable distance. Because of the field enhancement, the distance to the third water drop need

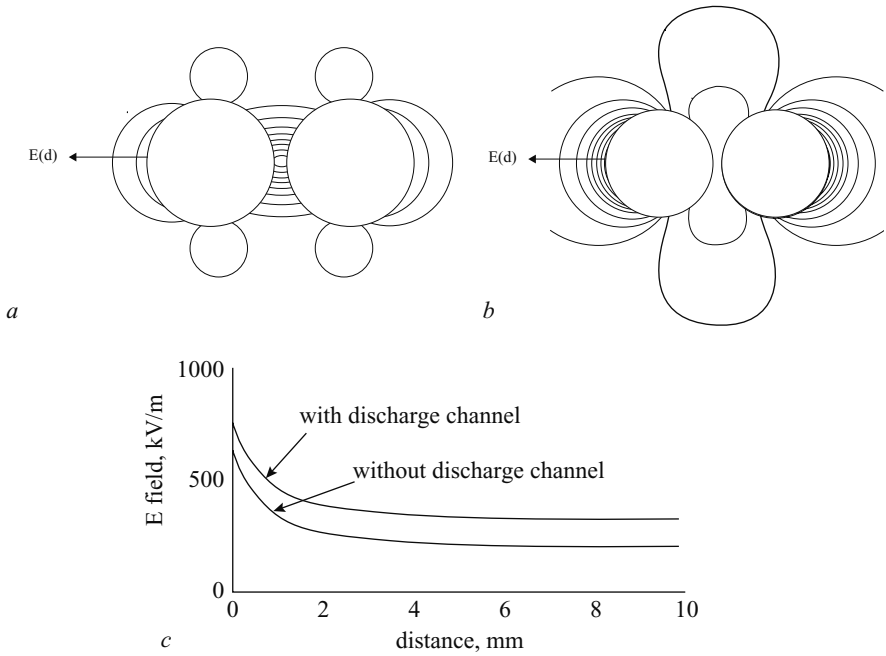

Figure 4.3 *Surfaces of constant electric field (equifield lines) for two water drops (a) before and (b) after discharge. Observe that in (b) there is a channel connecting the two drops. (c) shows the electric field as a function of distance from the outer ends of the water drops. Background electric field is 200 kV/m; drop radius is 2 mm; separation between the drops is 0.39 mm* (adapted from [214])

not be as small as the separation between the first two water drops. If a chain of drops is available, this process may continue along the drop chain and, with each succeeding discharge, the electric field at the outer periphery of the drop chain connected by the discharge channel may achieve a value higher than the one which existed during the previous discharge. If a sufficient amount of drops are available this field enhancement associated with the elongation of the drop chain may proceed until a streamer is initiated from the drops at the terminations. A mechanism somewhat similar to this is also proposed by Nguyen and Michnowski [217]. The data in Table 4.3 gives the length of the drop chain that is required to produce a streamer in a given background electric field. Calculations show that the field enhancement at the outer edge of the drop chain can be obtained without much error by replacing the drop chain with a conducting channel of hemispherical ends with radius identical to that of the water drops. This similarity was used in obtaining the data in Table 4.3. The data in this table can also be interpreted as the minimum length of the discharge channel needed

Table 4.2 Background electric field necessary to create streamers from pairs of spherical water drops with a connecting discharge channel in between (see Figure 4.3)

Drop radius (mm)	Background field (MV/m)	Gap between drops (mm)
0.1	1.41	0.62
0.5	1.20	1.52
1	1.14	2.67
2	0.97	3.83
3	0.89	4.88
4	0.83	5.94

Table 4.3 Number of drops and total length of drop chain that is required to produce a streamer for a given drop radius and background electric field

Drop radius (mm)	Background field (kV/m)	Length of drop chain (mm)
0.1	100	65
0.1	200	29
0.1	600	7
1	100	179
1	200	78
1	600	18
2	100	269
2	200	114
2	600	26
3	100	344
3	200	146
3	600	32

to create sufficient field enhancement at the channel ends to generate a streamer in the background electric field.

The analysis presented above shows that sufficiently long drop chains can give rise to streamer discharges in the cloud in background fields as low as 100 kV/m. However, the number of closely spaced water drops needed to create streamer discharges in such low fields is large, and the chances of finding such a collection of closely spaced drops in the cloud is very remote. For example, according to Latham and Dye [218], the ice particle (crystal and graupel) size distributions could be expressed roughly by the

equations:

$$N(D) = N_0 \exp(-\lambda d) \tag{4.4a}$$

where $N(D)$, the relative number of particles whose diameter (measured in mm) exceed the value d, is measured in $\mathrm{m}^{-3}\,\mathrm{mm}^{-1}$. Thus the number of particles in a unit volume having diameters between d_1 and d_2, $N_{d_1 d_2}$ (in m^{-3}), is given by:

$$N_{d_1 d_2} = \int_{d_1}^{d_2} N(D)\, dD \tag{4.4b}$$

Early in the electrical development of the storm, $N_0 = 10^4\,\mathrm{m}^{-3}$, $\lambda = 2.0\,\mathrm{mm}^{-1}$. Towards the end of the electrical life of the cloud, $N_0 = 10^5\,\mathrm{m}^{-3}$, $\lambda = 2.76\,\mathrm{mm}^{-1}$. According to this distribution, the number of particles with 0.5 mm or larger radii in an electrically active cloud is about 2000 per m^3. The relative distance, therefore, between the large (i.e. radii in the mm range) precipitation particles can be as long as a decimetre. On the other hand, cloud droplets with radii in the range of a few micrometres to a few tens of micrometres are abundant in the cloud and the number of such thundercloud droplets in a $1\,\mathrm{m}^3$ of thundercloud air is about 100×10^6 [219]. Consequently, the space between large precipitation particles is densely populated by cloud droplets; and the electric discharges may propagate in between these small droplets in exactly the same way as outlined earlier. Furthermore, under turbulent conditions the precipitation particle density may exceed the average values given above, at least in small volumes, and conditions favourable for discharge initiation may arise in there.

The calculations presented here also show that the length of the conducting channel necessary for the creation of streamer discharges in electric fields as low as 100 kV/m is in the range of a few decimetres. If the cloud has hot spots where the electric field is large enough to create electrical discharges frequently, whenever the length of these discharges exceeds a few decimetres they may act as sources of streamer discharges in the low background electric field. The volume of the hot spot need not be larger than a few cubic metres for this to happen.

4.5.3 Conditions necessary for the streamer propagation and streamer to leader transition

If clouds have hot spots where streamer discharges are frequently generated, they will culminate in lightning only if the background field exceeds the critical electric fields necessary for the propagation of streamers. This critical field decreases with decreasing pressure and it increases with increasing humidity. At sea level the critical electric field necessary for streamer propagation is about 450–500 kV/m and at the altitude of 6 km where the atmospheric pressure is about 0.5×10^5 Pa this field decreases to about 200 kV/m. However, the cloud environment is saturated with water and the stable streamer propagation requires about 250–300 kV/m.

Before a streamer system can lead to a lightning discharge it has to be converted to a leader. A system of streamers may give rise to a leader whenever the length of the streamer system exceeds about three metres (see Chapter 3). Thus if the background field exceeds the critical field necessary for streamer propagation in a region whose dimensions are a few metres, the streamer system may lead to the inception of a leader.

4.5.4 Conditions necessary for the propagation of the leader

The potential gradient of the leader in laboratory discharges is about 100 kV/m. This is approximately equal to the background electric field necessary for the continuous propagation of a leader. This is also vindicated by the fact that lightning leaders travel to ground when the background electric field in air is in the range of 60–100 kV/m. The way in which the critical electric field necessary for leader propagation changes with atmospheric pressure and relative humidity is not available, but, judging from the characteristic of streamer discharges one may expect the critical electric field to decrease with decreasing pressure. The humidity may increase the critical field but the effect of pressure may overwhelm that due to humidity. Thus, it is safe to say that in a cloud environment the background electric field required for leader propagation is less than or equal to about 100 kV/m.

4.5.5 Conditions necessary for lightning initiation – a summary

The results presented above show that the lightning can be initiated through the interaction of water drops if (a) the electric field in a volume of about 1 m^3 exceeds about 300–400 kV/m (for streamer inception), (b) the background field exceeds about 200 kV/m over a length of about a few metres (for leader inception) and (c) the background electric field remains around 100 kV/m in the bulk of the cloud (for leader propagation). Available experimental data demonstrate that the lightning is initiated in the cloud when the bulk field is about 100 kV/m. Unfortunately, the present day experimental techniques may not be able to detect the high field regions if they are confined to volumes of a few metres in radius. For example, an instrumented balloon, being several metres in diameter, could disrupt highly localised regions of strong electric fields and may not detect them even if it passed right through them.

4.5.6 The runaway electron hypothesis

Another mechanism that may lead to the initiation of lightning flashes in cloud is the acceleration of cosmic-ray-generated high energetic electrons in thunderstorm electric fields to produce an avalanche of MeV electrons [220]. The breakeven field necessary for the generation of MeV electron avalanches decreases with decreasing pressure and at 6 km level it is about 100 kV/m. This is similar in magnitude to the typical electric fields measured in active thunderclouds. Marshall *et al*. [221] claim that whenever the electric field in the cloud exceeds about 100 kV/m, an initiatory MeV electron, generated by a high energetic x-ray from cosmic radiation, may give rise to an avalanche of MeV electrons which will initiate the electric breakdown

process in the cloud. Marshal *et al*. [221] presented interesting data which confirms that whenever the electric field exceeds 100 kV/m lightning flashes are initiated in the cloud. However, the data can also be explained using conventional methods described in the last section because 100 kV/m is the limiting field necessary for the propagation of leaders.

4.6 Physical processes and the electromagnetic fields of ground flashes

4.6.1 Preliminary breakdown process

Experiments conducted in long gaps with metal electrodes under atmospheric conditions show the occurrence of several corona bursts before a self propagating leader discharge is launched from the high voltage electrode to the earthed electrode ([7], see also Chapter 3). On the basis of this experience one may expect some form of electrical activity inside the cloud before the stepped leader is launched. This electrical activity in the cloud can be much more complicated than that in the laboratory studies, mainly for the following two reasons. First, in contrast with the case of metal electrodes, the electrical charges involved in thunderclouds reside on cloud droplets and precipitation particles and an efficient mechanism is needed to accumulate the charge necessary for the initiation of the stepped leader. Second, discharges are of several hundreds of metres to several kilometres in length and they occur within a complex environment of cloud particles and reduced pressure. The best means available today to deduce the breakdown mechanism inside the cloud is to make measurements of the electromagnetic fields generated by the processes inside the cloud at several stations and to combine the information gathered with the data from VHF time of arrival and VHF imaging techniques ([1–6], see also section 4.11).

4.6.1.1 Electromagnetic fields at ground level generated by the preliminary breakdown process

4.6.1.1.1 Slow electric fields

The electromagnetic fields at ground level generated by the preliminary breakdown processes have been recorded and characterised by many researchers [8–12]. A typical electric field generated by the preliminary breakdown process is shown in Figure 4.4. Even though the main features of the electromagnetic fields obtained in different studies are similar, there are differences on a more detailed level caused probably by the meteorological conditions and the differences in the experimental techniques used in different studies. The main features of the slow electric fields generated by the preliminary breakdown process are the following. The electrostatic field starts to increase slowly and this increase may continue for some several tens to several hundreds of milliseconds. This initial phase is called the preliminary variation and it ends with a burst of pulses. This pulse burst is called the characteristic pulses or the preliminary breakdown pulses. The duration of the pulse burst is of the order of a millisecond. Sometimes this stage is followed immediately by a rapid increase in the

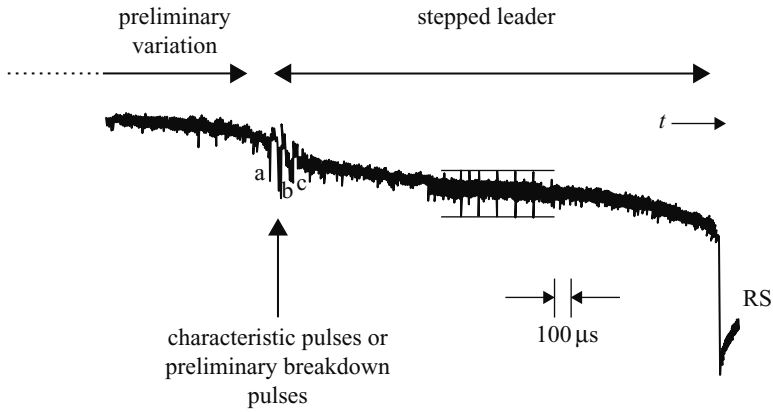

Figure 4.4 *A typical electric field preceding a cloud to ground flash at a distance of 11 km. a, b, c are the individual characteristic pulses and RS is the return stroke. A positive field corresponds to a downward deflection* (from [8]; reproduced by permission of the American geophysical union.)

electrostatic field and it culminates in a return stroke. However, sometimes the electric field may level off and continue to increase at a reduced rate before the onset of the rapid electric field change leading to the return stroke. Measurements conducted in different geographical regions may contain some or all of these features. It is likely that the channel geometry has the greatest impact on the behaviour of the electric field after the characteristic pulses, rather than the differences in the physical mechanism.

4.6.1.1.2 Characteristic pulses

According to Beasely *et al*. [8] the characteristic pulses signal the initiation of the stepped leader in the cloud. Measurements conducted in Sweden show that the HF radiation (at 3 MHz) associated with the leader stage starts immediately or with the occurrence of a characteristic pulse burst, supporting this proposition [12,13].

Beasely *et al*. [8] state that in many of the records the characteristic pulses could not be clearly identified except in six of their 79 recordings. On the other hand, the experimental data obtained from land-based thunderstorms in Sweden over the years shows very pronounced characteristic pulses and rarely can one see a return stroke without them [12,13]. However, measurements carried out in Sri Lanka using an identical experimental setup show that the characteristic pulses are weak and barely discernible in tropical storms [12,13]. It is noteworthy that the ratio of the peak of the largest characteristic pulse to the peak of the first return stroke radiation field in Sri Lanka is about 0.1 whereas in Sweden the ratio is about ten times larger. Measurements of HF radiation at 3 MHz conducted simultaneously with these broadband measurements show that as in Sweden the onset of HF radiation takes place simultaneously with the onset of characteristic pulses in Sri Lanka. In some cases where characteristic pulses were barely detectable, one can still observe the onset of the HF

radiation. It may be reasonable to assume that characteristic pulses are present, if not in all, in many of the preliminary breakdown stages, the only difference being that their amplitudes differ under different meteorological conditions.

4.6.1.2 Duration of the preliminary breakdown process

The total duration of the preliminary breakdown process can be defined as the time interval between the first detectable static field change and the return stroke. For several reasons, however, it is not easy to measure exactly the point at which the change in the static field associated with the preliminary breakdown occurs. First, inside a mature thundercloud electrical activity may take place almost continuously and any activity in the cloud that has no connection to the ground flash under study may contaminate the static field of the preliminary breakdown leading to erroneously long durations. Second, the onset of the preliminary breakdown may produce only a small static field which is difficult to detect in the background noise. Third, if the decay time constant of the measuring equipment is not long enough the equipment may not be able to reproduce the slowly increasing static field faithfully (see section 4.10). Measurements indicate that the duration of the preliminary breakdown process may range from several tens of milliseconds to several hundreds of milliseconds [8,12]. However, for the reasons mentioned above the measured durations of the preliminary breakdown process should be accepted with caution.

4.6.1.3 Location of the preliminary breakdown stage in the cloud

The location of the preliminary breakdown in the cloud can be determined by using one of three methods. The first method involves making multistation electric field measurements [15]. The preliminary breakdown is an intracloud process and the neutralisation and rearrangement of charge during this process can be modelled as a dipole. Seven variables (six space variables and the charge) describe the magnitude and location of the charge distribution and, therefore, measurements of the change in the electric field are required from at least seven stations in separate locations to estimate the unknowns. Once these are estimated the location of the preliminary breakdown process in the cloud can be obtained. The second method is based on single station measurements and utilises the fact that at ground level the vertical electric field of a dipole reverses its sign at a certain horizontal distance from the dipole. This distance depends on the height of the dipole. Thus, if the charge neutralisation or rearrangement during the preliminary breakdown stage can be represented as a dipole, the field reversal distance can provide information concerning the height of the breakdown process. This technique requires the measurement of the electric field change of the preliminary breakdown process from a number of ground flashes located at different distances from the measuring station. The method will give only a rough estimation of the height of the preliminary breakdown process in a given storm. This method was used by Clarence and Malan [9] to extract the height of the preliminary breakdown process. The third method is based on the VHF radio imaging technique ([2,5,16], see also section 4.11). These three kinds of measurement indicate that the preliminary breakdown process takes place at the same height from which the

negative charge is eventually lowered to ground by the return stroke. On the basis of these measurements, one may conclude that, in general, the preliminary break down takes place at an altitude corresponding to an ambient temperature of about −10 to −20°C.

4.6.1.4 Physical nature of the preliminary breakdown process

Clarence and Malan [9] suggested that the characteristic pulse in the preliminary breakdown process is produced by an electrical breakdown between the negative charge centre and the positive charge pocket (PCP) located below it. Ogawa [17] suggests that the preliminary breakdown starts with the positive leaders travelling from the PCP towards the negative charge centre. When the contact is established, rapid neutralisation of the positive charge by the negative charge coming down from the negative charge centre generates the characteristic pulses. This process charges the vertical channel with negative charge leading to the initiation of the stepped leader. However, the suggestion that the preliminary breakdown process involves a PCP is not accepted by all researchers, the main argument against this theory being that the heights at which the preliminary breakdown takes place appear to be somewhat larger than the base level of the cloud where the PCP is expected to be located [15].

Recent laboratory experiments and the inferences based on them show that the collision of graupel with ice crystals in the presence of super cooled liquid water could be the dominant process in charge generation inside the cloud ([18,19], see also Chapter 2). The grauple and ice crystals obtain charges of opposite polarity during the collision. The grauple particles are heavier and fall towards the base of the cloud and the miniscule ice crystals move upwards creating two charge centers. The experimental data shows that at temperatures below −10°C (according to Takahashi, [20]) or −20°C (according to Jayaratne *et al*. [21]) the graupels will receive a net negative charge during the collision but above this temperature they will be charged positively. Thus, the PCP may occur at regions in the cloud in which the temperature is higher than about −20 or −10°C, explaining why the preliminary breakdown process takes place at significantly larger heights than the height at which the cloud base is located.

The observations of Murphy and Krider [22] provide support for the involvement of a lower, positive charge in the initiation of cloud-to-ground flashes. Analyses of multistation electric field data, and the field changes produced by lightning, show that ground flashes often require the presence of positive charge below the main negative charge to obtain a satisfactory description of the field pattern. This is further supported by the observations of Krider *et al*. [194,246] which show that more than eighty per cent of the cloud-to-ground flashes were initiated by RF sources that began just below the negative charge centre and propagated downwards towards what was inferred to be a region of positive charge at lower altitude.

As described previously, in Sweden the electric field pulses generated by the preliminary breakdown process at distances of 5–10 km have peak amplitudes comparable to those of the return stroke radiation fields [12]. It is difficult to understand

how the preliminary breakdown process can generate electric field pulses of that magnitude if the breakdown is not associated with a neutralisation process.

Cooray and Jayaratne [13] argue that, since the field enhancements at cloud heights attributable to the presence of the ground could not influence breakdown processes taking place in the cloud, the necessary condition for the creation of a lightning ground flash is the generation of a vertical conducting channel below the main negative charge centre. When the electric field between the main negative charge centre and the positive charge pocket leads to electrical breakdown, one end of the discharge channel advances towards the negative charge centre and the other extends towards the positive charge pocket. The orientation of this channel will be determined by the relative location of the two charged regions. If the positive charge pocket is located below the negative charge centre the channel will grow in a more or less vertical direction. When this channel reaches the positive charge pocket, the charge in it is neutralised. After the neutralisation of the positive charge pocket, the conducting channel may continue to grow along the direction of the ambient electric field produced by the negative charge centre. If the positive charge was originally located below the negative charge centre, the channel grows downwards towards the ground leading to a ground flash.

The probability of ground flashes increases if electric breakdown events take place frequently between the negative charge centre and the PCP. Cooray and Jayaratne attribute the characteristic pulses to an electrical breakdown event between the negative charge centre and PCP and, based on the observation that the characteristic pulses are more intense in Sweden than in Sri Lanka, argue that meteorological conditions which favour the production of strong PCPs are more likely to be found at mid and high latitudes than in the tropics, thereby explaining why there is a greater probability of lightning flashes striking the ground in these regions.

If this argument is correct then any process that increases the positive charge in the cloud below the negative charge centre should promote the creation of ground flashes. One such process is the ground corona, the positive charge generated by which is transported into the base of the cloud by updrafts [14]. In this respect it is of interest to investigate whether the topographical conditions that favour corona generation, such as the presence of thick vegetation, can lead to high ground flash densities.

4.6.2 Stepped leader

4.6.2.1 Structure of the stepped leader

It is a general consensus that the stepped leader channel consists of a hot core surrounded by a cold, charged region called the corona sheath. Based on the results obtained from the spectral emissions of the stepped leader Orville [29] estimated the radius of the hot core to be between 0.1 m and 0.5 m. The corona sheath is formed partly by the charge deposited by streamers propagating ahead of the leader channel and partly by the lateral corona discharges from the hot core.

A rough estimation of the diameter of the corona sheath can be obtained by assuming that the space charge spreads out radially until the electric field at the outer boundary of the corona sheath is equal to the breakdown electric field in air. At

standard atmospheric pressure and temperature the breakdown electric field of air is about 3.0×10^6 V/m and it decreases with decreasing pressure. Since the charge per unit length of a stepped leader that gives rise to a 30 kA peak current is about 0.001 C/m, the diameter of the corona sheath of a typical leader close to ground would be about six metres.

4.6.2.2 Optically determined properties of the stepped leader

4.6.2.2.1 The stepping process

On photographs the stepped leader appears to advance in a series of rapid and discontinuous steps [10]. During their formation leader steps appear bright, whereas the channel remains dark in between the step formation. A new step generally starts a little way back up the track formed by the previous step. Usually, the leader gives rise to several branches and therefore at a given instant the stepping process may proceed in several branches simultaneously. The length of the steps ranges from 10 to 100 m. The average length of the steps in the upper portion of the channel (close to the cloud base) is about 50 m and close to ground it reduces to about 10 m [10,24]. The formation of a step takes place in about a microsecond. The interval between the steps is about 50 μs at upper levels and decreases to about 10 μs close to ground [10,23,30,33]. The available data indicates that the step length increases with increasing time interval between the steps [10].

The creation of a step probably takes place as a bidirectional discharge. As the negative discharge surges forward towards the ground creating a new step it will remove negative charge from the tip of the last leader step. The change in potential caused by the removal of negative charge leads to a positive discharge that travels upwards along the stepped leader channel transporting positive charge towards the cloud. This upward discharge appears as a luminous phenomenon propagating towards the cloud. Observations of Chen *et al*. [23] indicate that the luminosity travels upward without much degradation within the first several tens of metres to 200 m from the leader step, but with severe attenuation above. The upward speed of propagation is estimated to be about 10^8 m/s. The speed at which the luminosity of the negative discharge surges forward (i.e. the speed of the step development) has not yet been measured; however, the signature of the optical pulse generated by this process has been measured; it has a rise time of about 1.5 μs and its duration is about 3 μs [23,25]. Since the length of the step is a few tens of metres and the formation of the step is over in a few microseconds a speed of about 10^8 m/s appears to be reasonable.

According to observations made by Berger [24], one could observe faint traces of impulse corona at the tip of the newly made step. The impulse corona appears simultaneously with the step formation and the corona region extends forward by a distance of about one step length.

A time-resolved picture of the formation of a step in a stepped leader has not yet being obtained. Interestingly, Orville and Idone [26] managed to zoom in on the structure of the dart stepped leader and found that the tip of the leader step appears to be a luminous point and that the luminosity fans out upwards along a vertical direction.

4.6.2.2.2 Speed of the stepped leader

The average speed at which the stepped leader propagates differs from the speed of the step development because there is a gap in time or a pause time between the steps. Schonland [27] divided the stepped leaders into two categories. The α-type leaders have a more or less continuous speed of 10^5 m/s and have a step length and luminosity which does not vary appreciably along the channel. The β-type leaders, on the other hand, are heavily branched near the cloud base, are very bright and make long steps; they travel towards the ground with a speed of the order of 10^6 m/s. As they approach the ground they take on the characteristics of α leaders. It is debatable whether α and β leaders are two different phenomena or whether they are attributable to the same process manifested in a different way because of the presence of space charge below the cloud base. More recent measurements show stepped leader speeds of about 10^6 m/s with individual values falling in between 10^5–2×10^6 m/s [23,24,26]. Combining the results from electric field measurements with theory, Thomson [28] estimated the stepped leader speeds along 0.6–2 km of the channel to be between 1.3 and 19×10^5 m/s with a mean value of 5.7×10^5 m/s.

4.6.2.2.3 The temperature of the stepped leader

The measurements made by Orville [29] showed that the formation of the step raises the channel temperature to about 30 000 K. The channel section associated with a particular step is illuminated again and again due to the upward moving waves of current associated with the successive steps below it. Orville suggests that the temperature of the channel between these illuminations does not fall much below 15 000 K.

4.6.2.3 The electric field generated by the stepped leader

4.6.2.3.1 Duration of the stepped leader electric fields

One major problem in evaluating the duration of the stepped leader field is caused by the difficulty of pinpointing its exact beginning. Researchers have used different techniques to identify the beginning of the stepped leader field [8,11,12]. Some have utilised the occurrence of the characteristic pulses or the beginning of the HF radiation to identify the initiation of the stepped leader. Others, guided to some extent by the simulation of the stepped leader as a column of charge travelling towards the ground, have utilised the rate of change of the electric field to pinpoint the beginning of the stepped leader. The duration of stepped leader fields, summarised in Table 4.4, are based on these method.

4.6.2.3.2 The signature of the static electric fields generated by the leader

The static fields generated by stepped leaders at different distances are shown in Figure 4.5. The signature of these fields can be characterised and its main features can be described by simulating the stepped leader as a uniform line charge with one end fixed at cloud height and the other end approaching the ground with a uniform speed. Such model simulations can be compared with measurements to evaluate the approximate charge and the charge per unit length on the leader.

Table 4.4 Duration of the stepped leader (adapted from Beasely *et al*. [8])

Reference	No. of flashes	Distance, km	Minimum, ms	Maximum, ms	Mode, ms	Frequency system
Schonland *et al*. [27]	69	0–24	0–3	66	9–12	30 Hz to 20 kHz
Pierce [200]	340	40–100	0–20	525–550	20–40	1 Hz to 4 kHz
Clarence and Malan [9]	234	0–80	6	442	–	0 Hz to 300 kHz
Kitagawa [31]	41	0–15	8	89	20–30	0 Hz to 300 kHz
Kitagawa and Brook [132]	290	–	0–10	210	10–30	1 Hz to 1 MHz
Thomson [11]	53	6–40	4	36	–	0.1 Hz to 7.2 kHz
Beasely *et al*. [8]	79	0–20	2.8	120	6–20	0.03 Hz to 1.5 MHz
Gomes *et al*. [12]	41	10–100	2.0	70	8.7	1 kHz to 5 MHz

Thomson [28] showed that the time derivative of the static electric field generated by the stepped leader can be used to derive the properties of the leader. For example, he showed that the derivative of the leader field is a function of the speed of the leader tip and the measured field derivatives can be used to estimate the leader speeds. However, such an interpretation is valid only if the linear charge density at a given point on the leader does not vary as the leader extends towards the ground.

4.6.2.3.3 Signature of the radiation fields generated by the stepped leader

Broadband measurements of leader fields indicate that small field pulses with an amplitude in the range of about 0.5–1 V/m at 100 km occur in the electric fields preceding the return strokes [30–33]. Several examples of such pulses are shown in Figures 4.6 and 4.7. Simultaneous optical and electric field measurements show that these radiation field pulses are produced by the processes taking place during the formation of leader steps [25]. The separation between these pulses immediately before the return stroke is about 10–15 μs. When the propagation path of the electromagnetic fields is over salt water, which is highly conducting, one can observe that the rise time of the electric field pulses is about 0.1 μs and their duration is about a microsecond [33,160]. The leader pulses immediately preceding the return stroke are almost unipolar and their electric field derivative normalised to 100 km is about 22 V/m/μs, which is comparable to that of return strokes [99,105].

The amplitude of the last leader pulse, E_l, is about 0.1 of the return stroke amplitude, E_r, and Cooray and Lundquist [32] found that these amplitudes are correlated

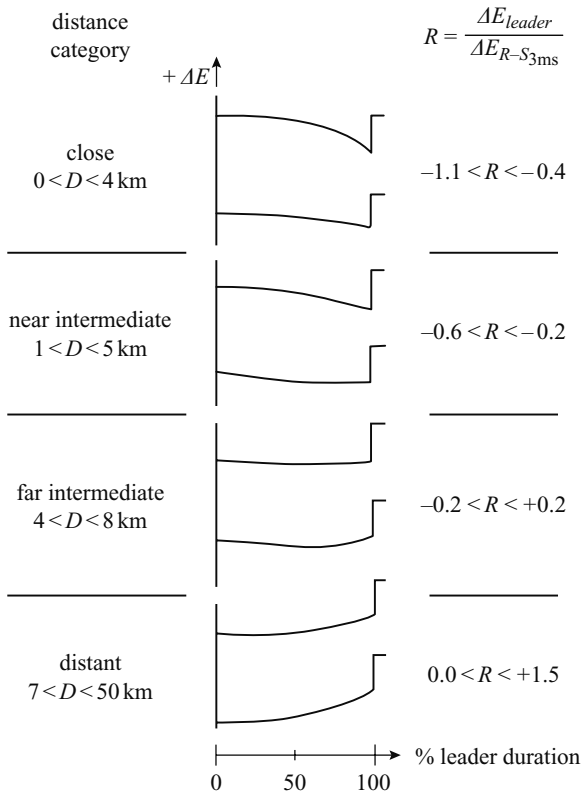

Figure 4.5 *Representative shapes of stepped leader fields in four distance categories. The ratio, R, of the leader field to the return stroke field is also given in the diagram. D denotes the distance. A positive field corresponds to an upward deflection* (from [8]; reproduced by permission of the American geophysical union)

through the relationship:

$$E_r = kE_l^{\nu} \tag{4.5}$$

where $\nu = 0.64$ and $k = 10.5$.

The amplitude spectrum of leader pulses is shown in Figure 4.8. The high-frequency end of this spectrum is almost identical to that of the return strokes. This indicates that the stepped leader pulses could play an important role in creating disturbances in telecommunication systems and low-voltage power installations.

4.6.2.4 Linear charge density and the total charge of the leader channel

From electric field measurements Schonland [34] estimated the charge density of the leader channel to be typically about 0.001 C/m. By combining theory with experiment

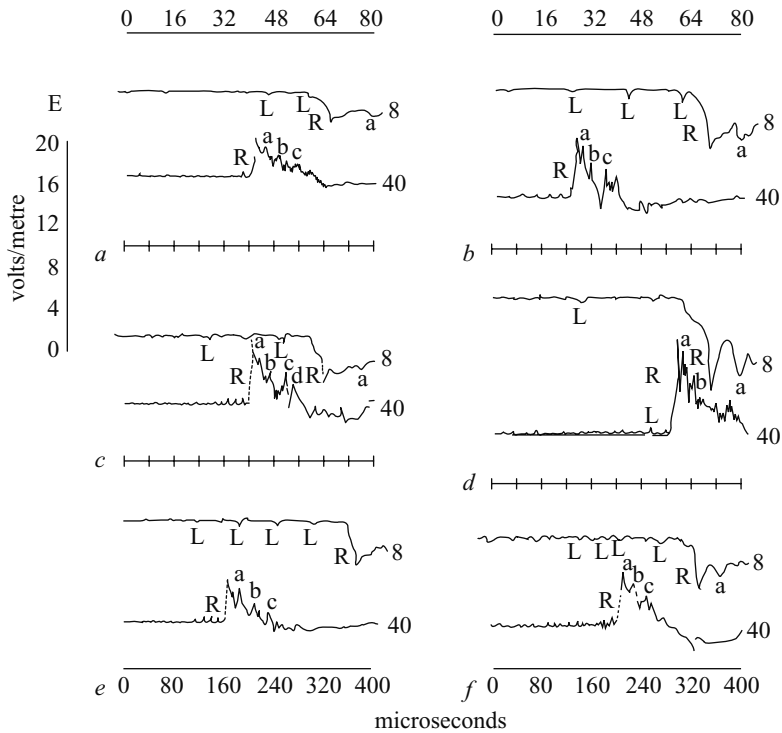

Figure 4.6 *Electric fields produced by first return strokes at distances of 100–200 km over salt water. Each record contains an abrupt return stroke transition R preceded by small pulses characteristics of leader steps. The same waveform is shown on both a slow (*40 μ*s/div) and a fast (*8 μ*s/div) time scale. A positive field corresponds to an upward deflection* (from [94]; reproduced by permission of the American geophysical union)

Thomson *et al*. [28] estimated the linear charge density of a stepped leader to vary between 0.7 to 32×10^{-3} C/m with a mean of 3.4×10^{-3} C/m. One should keep in mind however that the leader is branched and the charge density estimated through electrostatic fields is an effective value.

An estimate of the total charge on the leader channel can be obtained either by analysing the electric fields created by stepped leaders [35] or by integrating the return stroke current measured at the channel base [24]. In the first case the geometry and the assumed charge distribution in interpreting the measured data may influence the results and in the latter case one has to make an assumption that the leader charge is completely neutralised by the return stroke. Moreover, in integrating the currents measured at the channel base one must make a judgement, which may very well be subjective, concerning the time at which the current generated by the return stroke (arising from the neutralisation of the leader) ends and the continuing currents begin.

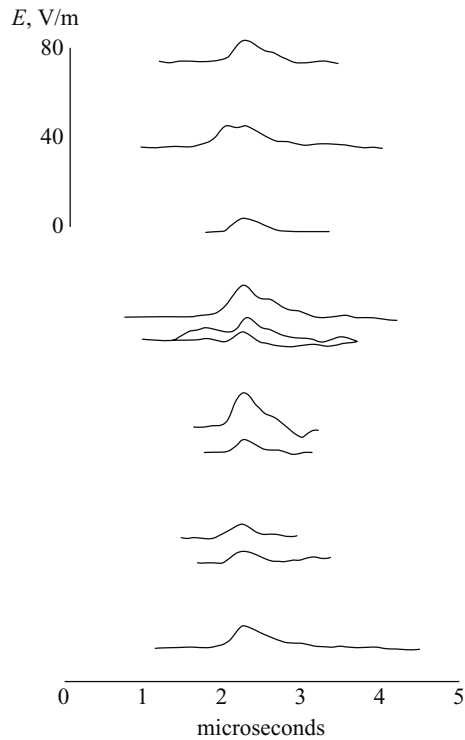

Figure 4.7 *Time resolved electric fields produced by the stepping process of stepped leaders at distances of 20–30 km or less over salt water. A positive field corresponds to an upward deflection* (from [33]; reproduced by permission of the American geophysical union)

The situation is complicated even further by the fact that the extent to which the charge deposited on the leader contributes to continuing currents is not known at present. Anyway, one can make a rough estimation of the leader charge by integrating the rapidly varying portion of the return stroke current, i.e., the impulse current [24]. The values obtained from these techniques range from a few coulombs to some several tens of coulombs with an average of about 5 C.

4.6.2.5 Charge distribution along the leader channel

After analysing electric fields produced by stepped leaders, Schonland [34] came to the conclusion that leader charge is distributed uniformly along the channel. However, on the grounds that the capacitance of the leader channel increases close to ground, Bruce and Golde [36] argue that the charge density should decrease upwards along the channel; they approximated it with an exponential distribution. If the charge density of the leader increases as the leader approaches the ground then one may expect the leader current to increase with time. According to the observations of

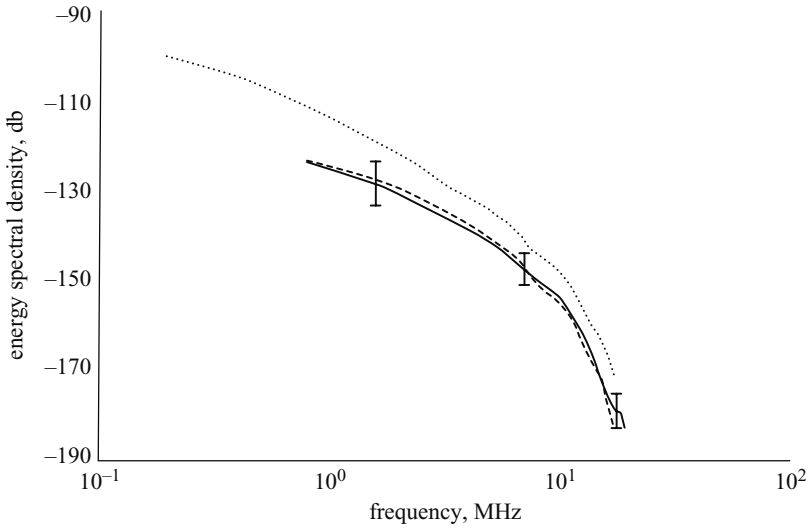

Figure 4.8 *Average frequency spectrum of stepped leader steps (solid line) and dart stepped leader steps (dashed line). The average spectrum of first return strokes is shown by a dotted line for comparison* (from [159]; reproduced by permission of the American geophysical union)

Krehbiel [39], in fewer than fifty per cent of the stepped leaders the current increased with leader propagation. This indicates at least in some cases that the assumption of uniform charge density is justified. Both uniform and exponential distributions are used frequently by return stroke modellers.

The charge distribution of the leader channel can be calculated if one can assume the leader channel to be a good conductor. For example, if the spatial extension of the charge centre in the cloud is sufficiently large for the field below to be assumed to be uniform, the linear charge density of a leader channel that develops in this uniform field will increase linearly towards ground, except in the last few tens of metres where the proximity of the ground will cause the charge density to increase more rapidly towards the ground [37].

4.6.2.6 Leader current

There are two forms of current associated with a stepped leader. The first one is the time averaged current and the second one is the impulse current associated with the formation of steps. Let us consider the former first. Since the duration of the leader is around a few tens of milliseconds and the charge on the stepped leader ranges from a few coulombs to about 20 C, the average current of the stepped leader should be of the order of a few hundred amperes. Several researchers have estimated the leader current by analysing the remote electric and magnetic fields. Williams and Brook [38] estimated the leader currents of 50 and 65 A. However, much larger currents are obtained by Krehbiel [39] and Thomson *et al*. [28]. Krehbiel found the average leader current

over the last several milliseconds of the leader to be 0.2–3.8 kA for seven leaders. For 62 leaders Thomson found leader currents within a few hundred microseconds of the return stroke in the range of 0.1–5 kA with an average current of 1.3 kA.

The peak of the impulse current associated with the stepping process can be roughly estimated from the amplitude of the electromagnetic field pulses using the transmission line model ([33] see Chapter 6). Since the radiation field amplitude of the stepped leader is about ten per cent of that of the return stroke, if similar speeds are assumed for the return stroke and step development, a peak current of about 3 kA is involved in the formation of a step in a stepped leader that gives rise to a 30 kA return stroke current. In reality, the step speed could be less than that of the return stroke and hence the step current would be larger than the 3 kA given. Using the same theory, Krider *et al*. [33] estimated the leader step current to be about 2–8 kA and the charge transported by the stepping process to be about $1\text{–}4 \times 10^{-3}$ C/m. If this estimation is correct then the step process is responsible for the bulk of charge transfer down the leader channel. This is the case since the estimated linear charge densities of the leader channel lie in this range. This is in contrast to the inferences made by Schonland [40]. According to Schonland's measurements, the electrostatic field change caused by the stepping process is less than one tenth of the static field change that takes place during the step interval. From this observation he concluded that the stepping process does not transport much charge but the bulk of it is transported by other processes such as negative streamers which travel continuously ahead of the stepped leader channel – the pilot leader of Schonland. Uman and McLain [41] question the validity of this observation since, if the bandwidth of the measuring system were large enough to resolve the electrostatic field change taking place in a few microseconds, then such a measurement would be obscured by the presence of radiation fields. However, since the durations of the step fields are about 1 μs and the intervals between the steps are about 10–50 μs, one should be able to see the static fields generated by the steps even in the presence of radiation fields.

4.6.2.7 Bidirectional and unidirectional leader concept

The bidirectional leader concept was first introduced by Sopor [42] and then independently by Kasemir [43,44]. The concept was supported and developed further by Mazur [45,46], Runke and Mazur [47], Kawasaki and Mazur [48] and Heckman and Williams [49]. The bidirectional leader concept is as follows. From the point from which the leader is initiated – probably the outer periphery of the negative charge centre – a negatively charged channel propagates downwards while a positively charged channel penetrates the negative charge centre. The net charge on the leader channel is zero with negative charges being concentrated on the lower end and positive charges on the upper branches. All the mobile charges are created in the channel and no movement of the cloud charge takes place during the leader progression. However, the positive end of the bidirectional leader brings positive charge into the charge centre, thus effectively removing negative charge from it. Laboratory experiments that support the bidirectional leader concept were performed and reported by Laroche *et al*. [50], Bondiou *et al*. [51] and Mazur [45]. However, the

VHF observations of Shao *et al*. [5] did not show any bidirectional leader activity in the cloud. Mazur [45] argued that the positive leaders do not produce strong VHF radiation and therefore the VLF mapping technique of Shao *et al*. is not sensitive to positive streamer activity (see section 4.11). Observations of the latter show that at least some positive discharge activity could be detected using the VLF techniques. One possible explanation could be that the level of VHF radiation from positive leaders is small but occasionally some of the positive leaders give rise to strong VHF activity.

The unidirectional leader model, which is frequently utilised in the calculation of leader fields, treats the leader as a charged cylindrical column extending out from the charge centre. It does not specify, however, any mechanism for the generation and transfer of charge from the main negative charge centre onto the leader channel. Nevertheless, it assumes that charge is depleted from the charge centre as the leader progresses. The two concepts are illustrated in Figure 4.9. If we assume that the upper

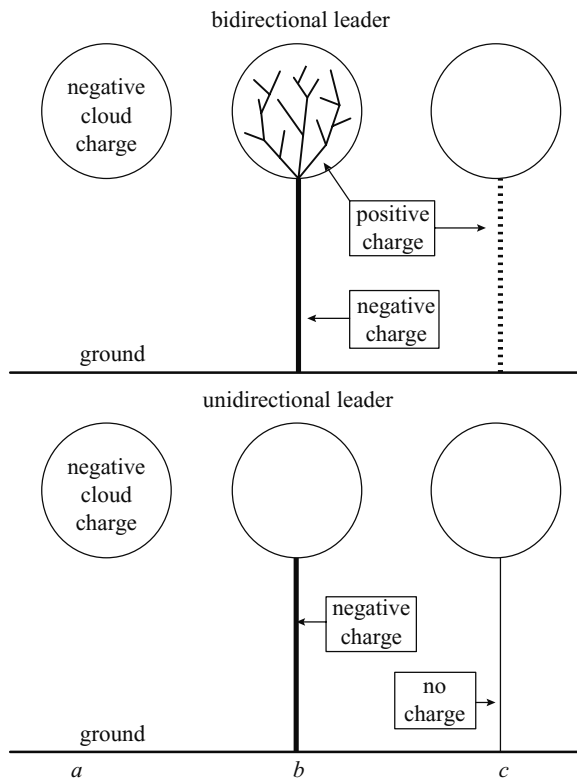

Figure 4.9 *The concept of bidirectional and unidirectional leader. The unidirectional leader does not specify any mechanism for the transfer of charge from the cloud to the leader channel. Note that in the bidirectional leader model the channel is positively charged after the return stroke* (from [52]; reproduced by permission of the IEEE)

branches of the leader channel form a dendritic network of channels then, as far as the fields generated at ground level by the leader are concerned, there is not much difference in the two concepts. The upward moving branches of the bidirectional leader bring positive charge into the charge centre, the net effect being that the net negative charge in the charge centre decreases and the negative column of charge extends towards ground. In unidirectional leaders too, one assumes that cloud charge is effectively removed and deposited on the down-coming leader channel. In this respect, the only difference between the two models is that the bidirectional leader specifies what happens and the unidirectional leader concept does not.

4.6.2.8 Energy dissipation during the leader stage

By simulating the leader as a column of charge (either uniform or with an exponential charge distribution) extending down from the cloud and assuming spherical distributions of cloud charge, Cooray [52] calculated the way in which the energy dissipation in the leader stage varies as a function of the total charge pumped into the channel. The results obtained from this study are shown in Figure 4.10. He found that the energy dissipation during the leader stage is comparable to that of return strokes. He also discovered that for a given charge density of the cloud, there is a critical charge on the leader channel that minimises the energy in the cloud–leader system. The critical charge increases with increasing charge density of the cloud and *vice versa*. For a cloud charge density of 10^{-9} C/m^3, a typical measured value, he estimated the critical charge on the leader channel to be about 5 C.

4.6.2.9 Stepped leader as a source of disturbance

Usually, the return strokes are responsible for the largest overvoltages in electrical networks and, for this reason, the majority of the studies dealing with overvoltages in electrical systems have concentrated on the effects of return strokes. The rapid development of low-voltage electronic devices and their incorporation into modern day decision-making apparatus, however, makes it necessary for engineers to consider the threats imposed by lightning events other than return strokes – for example stepped leaders.

As described previously, each step of a stepped leader gives rise to a fast electromagnetic radiation pulse, the duration of which is about a microsecond. A stepped leader can create a long train of such pulses with a time interval between individual pulses of some 10–200 μs. Given the low tolerance of modern day electronic devices there is little doubt that these bursts of pulses can create significant disturbances in digital electronic systems.

In order to characterise the features of voltages and currents induced in electrical networks by stepped leaders, it is necessary to have a mathematical model that can describe this phenomenon so that the electromagnetic fields generated by them can be calculated at any distance, especially where it is difficult to make experimental observations. Such a model was introduced recently by Cooray and Galvan [189]. The model is based to some extent on the observed features of the negative leaders in long sparks. The model parameters were selected to give a fit to the electric field

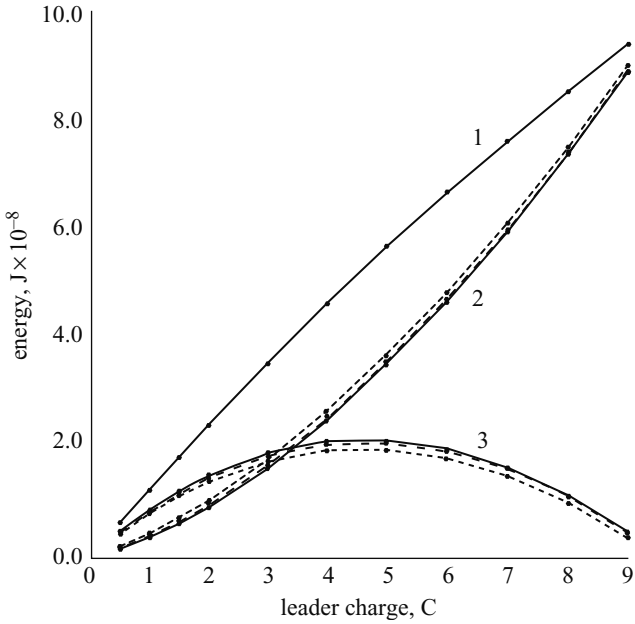

Figure 4.10 *Energy dissipation in leader return stroke process as a function of charge on the leader channel. In the simulations the charge density of the cloud is assumed to be $10^{-9}\,C/m^3$. The negative charge centre is located at 7 km height and the positive charge at 12 km. Curve 1 shows the total energy dissipation. The set of curves marked 2 shows the energy dissipation in the return stroke stage and the set of curves marked 3 shows the energy dissipation in the leader stage. The solid lines correspond to exponential charge distribution with the decay height constant equal to 3000 m, the long dashed lines correspond to exponential charge distribution with the decay height constant equal to 7000 m and the short dashed lines correspond to uniform distribution* (from [52]; reproduced by permission of the American geophysical union)

pulses of stepped leaders observed in reality. The model was used to evaluate the induced voltages caused by stepped leaders in low-voltage power installations. It is shown that the stepping process of the stepped leader could be an important source of disturbance in them.

4.6.2.10 Interception of the stepped leader and grounded structures

As the stepped leader approaches the ground, the electric field at the extremities of the grounded objects increases to such a level that they launch connecting leaders towards the down-coming stepped leader. There is direct and indirect evidence for the occurrence of connecting leaders to meet the down-coming stepped leader. A time-resolved picture of the down-coming leader and the upward moving connecting leader

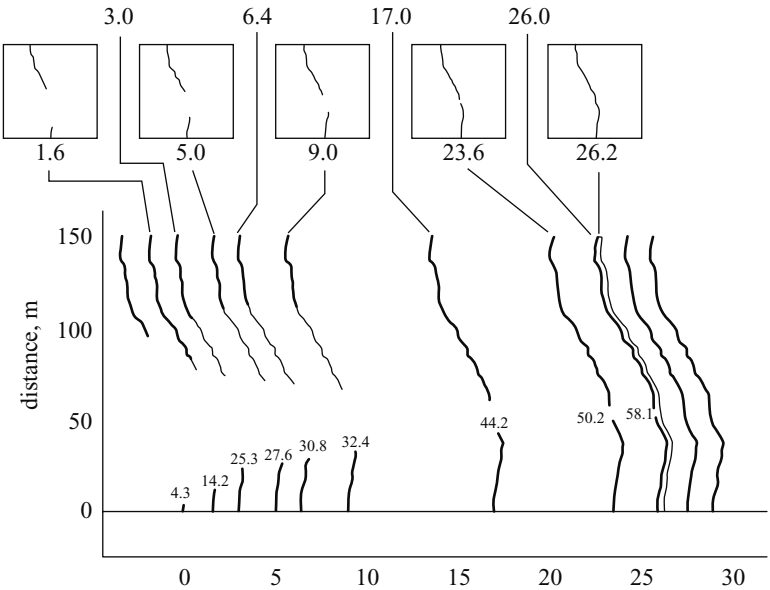

Figure 4.11 *Time-resolved photograph of a down coming leader and the upward connecting leader. The time is given in microseconds and the time zero corresponds to the instant at which a connecting leader is initiated. The height of the connecting leader at different times is indicated in the figure. The numbers on the horizontal axis and at the boxes show the time in microseconds* (by the courtesy of Prof. S. Yokoyama)

is shown in Figure 4.11. The first return stroke is initiated at the instant contact is made between the down-coming stepped leader and one of the connecting leaders. The strike point of the lightning flash is the place from which the connecting leader that made the successful connection to the stepped leader was initiated. With the knowledge available at present, derived mainly from laboratory experiments, one can specify the conditions necessary but not necessarily adequate for the launch of a successful connecting leader from a grounded object such as a Franklin conductor. These conditions are the following.

Condition 1: The inception of a streamer discharge at the tip of the grounded structure: As described in Chapter 3, the criterion for streamer inception is given by:

$$\exp\left[\int_0^{x_c} (\alpha - \eta)\, dx\right] = 10^8 \tag{4.6}$$

where α is the Townsend ionisation coefficient in air, η is the attachment coefficient in air, x is the distance measured from the tip of the grounded structure, x_c is the distance

from the tip of the grounded structure where the electric field drops to 2.6×10^6 V/m. The values of α and η are given as a function of the electric field by Badaloni and Gallimberti [191].

Condition 2: The streamer to leader transition: It is customary in lightning protection studies to use the concept of critical radius in estimating the minimum background field required for a streamer to leader transition. This concept, which is based on the information gathered from experiments conducted with long sparks, assumes that the streamer to leader transition takes place when the electric field at the surface of a hypothetical metal sphere of critical radius, R_c, at ground potential located at the tip of the structure, reaches a value of about 3.0×10^6 V/m. Unfortunately, the critical radius varies from one geometry to another and therefore depends on the shape of the structure under consideration. On the other hand, laboratory experiments conducted with long sparks and using a rod–plane configuration show that the critical length of the streamer discharge initiated from the rod at the time of leader inception is equal to about 3 m ([7], see also Chapter 3). This is the minimum streamer length required for a direct transition from streamer to leader. This critical streamer length has been observed to be independent of the electrode geometry. Thus, as pointed out by Akyuz and Cooray [192], the critical streamer length could be a better criterion for use in estimating the electric fields necessary for streamer to leader transitions. The length of the streamer system at a given electric field can be evaluated by utilising the procedure outlined by Lalande [193]. A comparison of the calculations conducted by the author with more precise results than presented by Lalande show that the above criterion can predict the inception of a leader to a reasonable accuracy.

Condition 3: The continuous propagation of the connecting leader and its successful encounter with the stepped leader: The physical process that takes place from the inception of a connecting leader to its successful connection to the down-coming stepped leader is a dynamic one. First, the background electric field needs to be larger than a critical value for the connecting leader to be able to propagate. The experimental data indicates that this field is about 100 kV/m (the value observed for leaders in long sparks). Second, when and where the two leaders will meet depends on their relative speed and orientations.

One important point to remember is that, as the stepped leader approaches the ground, these conditions may not be satisfied in the same order as given above. For example, it is possible that condition 2 is satisfied before condition 1. In this case, as soon as the streamer is incepted it will be converted to a leader. In the alternative scenario, the electric field at the tip of the Franklin rod may be high enough for the creation of streamers, but the electric field distribution ahead of the rod may not have attained the optimal value for the streamer to leader transition. In this case, streamers will be incepted repeatedly until the conditions are ripe for the inception of a leader.

4.6.2.10.1 The striking distance

The striking distance is defined as the separation between the object struck and the tip of the stepped leader at the inception of the connecting leader. In other words, the

separation between the tip of the leader and the point of strike at the instant when both conditions 1 and 2 described in the previous section are satisfied. Thus, in order to obtain the striking distance, it is necessary to quantify the electric field generated by the stepped leader at ground level and the field intensification arising from the structure. This can be done if a reasonable assumption can be made concerning the distribution of the charge along the leader channel. Frequently assumed distributions for this purpose are uniform, linear or exponential. These distributions can be represented mathematically as:

$$\rho(z) = \rho_0 \quad \text{(uniform)} \tag{4.7}$$

$$\rho(z) = \rho_0 e^{-z/\lambda} \quad \text{(exponential)} \tag{4.8}$$

$$\rho(z) = \rho_0(1 - z/H) \quad \text{(linear)} \tag{4.9}$$

where z is the vertical coordinate with origin at the ground end of the leader channel, ρ_0 is the charge per unit length at the tip of the stepped leader channel, λ is the decay height constant and H is the height of the channel.

Using these distributions one can show that the electric field generated by a stepped leader when its tip is within a few hundred metres from ground level does not depend significantly on the distribution of the charge on the leader channel. This is certainly the case if the decay height constant or the channel length is larger than about 2000 m. The electric field at ground level depends mainly on the charge per unit length at the ground end of the leader channel; that is on ρ_0. In other words, for a given charge per unit length at the tip of the stepped leader, the electric field at ground level generated by the leader does not depend significantly on the total charge on the leader channel. For example, assume that the charge per unit length at the tip of the leader is ρ_0 C/m. If the charge per unit length is assumed to decay with a decay height constant λ, then the total charge on the leader channel is $\rho_0\lambda$. Thus if $\rho_0 = 0.001$ C/m, the total charge on the leader channel may vary from 2 to 5 C as λ changes from 2 to 5 km; the electric field at ground level will remain more or less constant if the leader tip is within about a few hundred metres of ground level. The same is true for any other charge distribution. Thus the striking distance can be directly connected to the charge per unit length at the tip of the leader channel because it is this parameter which controls the electric field generated by the stepped leader at ground level.

Lightning protection engineers prefer to express the striking distance as a function of the peak of the first return stroke current that is initiated by the stepped leader. Since the first return stroke current is generated by the neutralisation of the charge deposited on the leader channel, one can expect the peak return stroke current to be correlated to the charge per unit length at the tip of the stepped leader. Unfortunately, at present experimental data is not available to find the relationship between these two parameters. However, their relationship can be extracted by utilising return stroke models. As described in Chapter 6, one such relationship is:

$$\rho_0 = 5.767 \times 10^{-5} I_p^{0.81} \tag{4.10}$$

where I_p is the peak current in kA and ρ_0 is the charge per unit length (C/m) at the ground end of the leader channel. According to this relationship, a typical 30 kA current is associated with a linear charge density of about 0.001 C/m. This is in agreement with the available experimental observations.

Recently, several attempts have been made to extend the striking distance of lightning conductors by artificial triggering of streamers at the tip of a lightning conductor. Akyuz and Cooray [192] have made a theoretical investigation of this. Their conclusions are the following. For Franklin conductors of radii less than about 0.3–0.4 m, artificial initiation of streamers at the conductor tip would not result in any increase in the attractive distance. For rods of radii larger than 0.3–0.4 m, it may be possible to launch a connecting leader by the artificial triggering of streamer discharges at the conductor tip, but the gain in the attractive distance would not be larger than about thirty per cent.

4.6.3 Return stroke

4.6.3.1 The origin of the return stroke

The front of the leader channel consists of a system of streamers, and the return stroke is initiated when this streamer front makes a connection either with the ground or with the streamer front of a connecting leader that rises to meet it. It is reasonable to assume that, starting from the meeting point between the stepped leader and the connecting leader, the neutralisation process will progress in different directions, one towards the ground and the other towards the cloud. Direct evidence for the existence of two such fronts is not available in the literature, but the data available from the measurements conducted at the CN tower in Canada indicates that this interpretation is probably correct [53].

4.6.3.2 Optically determined properties

4.6.3.2.1 Return stroke speed

Pioneering work on the development of return strokes was done by Schonland and coworkers in South Africa and McEachron in the United States. They obtained time resolved pictures of the return stroke development using Boys camera or streak cameras [10,196,197]. More recent velocity measurements have been carried out either using streak cameras [54] or detectors consisting of a series of photomultipliers [60]. The most important results from a number of studies are summarised in Tables 4.5. The data obtained from these studies indicates that (i) the return stroke velocity decreases with height in both the first and subsequent return strokes, (ii) the average velocity of subsequent return strokes over the first few hundred metres close to ground is greater than that of the first return strokes, (iii) the return stroke velocity in the vicinity of the ground may, in some cases, reach values comparable to the speed of light in free space, and (iv) the average velocity of both first (positive and negative) and subsequent return strokes over the first kilometre is about 1.0×10^8 m/s.

Table 4.5 Velocity of return strokes as obtained in different studies

Reference	Type of return stroke	Average speed, m/s	Standard deviation, m/s	Comments
Mach and Rust [60]	positive	0.8×10^8	0.4×10^8	short channel segments close to ground (average 370 m)
Mach and Rust [60]	positive	0.9×10^8	0.3×10^8	long channel segments (average length 1120 m)
Mach and Rust [55]	negative (first)	1.7×10^8	0.6×10^8	short channel segments (average length less than 500 m near ground)
Mach and Rust [55]	negative (first)	1.2×10^8	0.7×10^8	long channel segments (average length greater than 500 m near ground)
Mach and Rust [55]	negative (subsequent)	1.9×10^8	0.7×10^8	short channel segments (average length less than 500 m near ground)
Mach and Rust [55]	negative (subsequent)	1.3×10^8	0.5×10^8	long channel segments (average length greater than 500 m near ground)
Mach and Rust [55]	negative (triggered)	1.4×10^8	0.4×10^8	short channel segments (average length less than 500 m near ground)
Mach and Rust [55]	negative (triggered)	1.2×10^8	0.2×10^8	long channel segments (average length greater than 500 m near ground)
Idone and Orville [54]	negative (first and subsequent)	1.4×10^8	–	velocity near ground (<1.3 km)
Idone and Orville [54]	negative (first and subsequnt)	1.1×10^8	–	over longer channel segments (at least 0.7 km in length)
McEachron [197]	negative (subsequent)	6.1×10^7	–	
Schonland and Collens [196]		4.6×10^7	–	

The return stroke speed is an important parameter both in extracting the physical mechanism behind the return stroke development and as an input to the mathematical return stroke models. It is important to note, however, that the optically measured

speeds may differ considerably from the speed of the onset of the return stroke current along the channel for several reasons. First, the limited resolution of the optical measuring systems may make it almost impossible to obtain the exact time of the onset of the optical radiation. The situation is further complicated by the fact that the channel may remain slightly luminous, either continuously or intermittently, after the passage of the leader. Secondly, it is difficult to locate the same relative point on the optical signature at two different heights; this is further complicated by the fact that the optical pulse changes its shape and amplitude along the channel. Thirdly, there can be a delay in the onset of optical radiation with respect to the onset of the current and this delay might vary depending on the rise time of the current waveform. Fourthly, there could be a significant difference in the signatures of the optical pulse and the current waveform at a given height. The optical speed, therefore, may differ considerably from that of the speed of the onset of the return stroke current along the channel. The latter is the speed which is needed in return stroke models.

There is no information available at present concerning the spatial variation of the first return stroke velocity at the onset of the discharge. It is reasonable to assume that the first contact between the stepped leader and the grounded object is established by the streamer region of the former. Thus, the early stage of the first return stroke involves the neutralisation of the streamer region of the stepped leader. The streamers, being cold discharges, are not good conductors like the thermalised and hot portion of the stepped leader channel. One would expect, therefore, the front of the return stroke to proceed slowly until it catches up with the hot leader; at which point the speed of the return stroke front increases dramatically. Such a scenario is predicted by the models introduced by Cooray [56] and Cooray and Galvan [57] (see Chapter 6).

4.6.3.3 Characteristics of the optical radiation generated by the return stroke

4.6.3.3.1 Variation of the broadband optical pulse along the return stroke channel

Information about the variation of the return stroke current as a function of height is important in the construction and validation of return stroke models. The behaviour of the current signature along the channel can be inferred to some extent by analysing the way in which the broadband optical radiation generated by the return stroke varies as a function of height. Using a measuring system capable of 0.5 μs resolution, Jordan and Uman [58] and Jordan *et al*. [59] found that the light signal produced by a small channel section of subsequent strokes has a fast rise to peak followed by a slower decrease to a relatively constant value. The 20–80 per cent rise time of the light signal near ground is about 1.5 μs, this rise time increases to about 4.0 μs by the time the return stroke peak reaches the cloud base at about 1.4 km. The amplitude of the initial peak decreases exponentially with height with a decay height constant of about 0.6–0.8 km. The photomultiplier measurements of Mach and Rust [60] show that the rise time (10–90 per cent) of the optical pulse generated by a channel segment with

an average length of about 3 m and located within 100 m of the ground is 3.5 μs for negative first strokes and 9.4 μs for positive first strokes. They also observed that the rise time of the optical pulse increased with increasing height.

The experimental data of long laboratory sparks shows that the rise time of the current in the discharge channel is approximately equal to the rise time of the optical pulse, and the peak amplitude of the optical pulse is linearly correlated to the peak current [247]. Interestingly, Idone and Orville [61] found a strong linear correlation between the peak current and the peak optical radiation. It is reasonable to assume, therefore, that the rising part of the return stroke optical pulse follows the rising part of the current waveform, at least approximately. If this is the case, the data given earlier indicates that (i) the rise time of the return stroke current waveform increases with height, (ii) the peak return stroke current decreases with height and (iii) the rise time of the current in positive return strokes is longer than that of the negative return strokes. It is important to mention here that Idone and Orville [61] found that the 20–80 per cent rise time of the optical radiation from a channel section 50 m above the point of strike of triggered lightning flashes had an average value of 2 μs, whereas the current measured at the channel base had a rise time of about 0.5 μs. The reason for this difference could be the rapid elongation of the front of the current waveform during the first few tens of metres (see Chapter 6).

4.6.3.3.2 Energy and power released in the optical signal

The energy and power released in the optical signals of return strokes are important in the evaluation of the total energy dissipated in them. For example, the ratio between the electrical energy and the optical energy in long sparks can be obtained from experiments conducted in the laboratory. The electrical energy dissipated in lightning discharges can thus be obtained by assuming the same energy conversion ratio as in the laboratory discharges and measuring the optical energy generated by lightning flashes [62].

The most extensive investigation made to date on optical signals generated by return strokes was that conducted by Guo and Krider [63,64]. They recorded the optical signals radiated by return strokes in the 0.4–1.1 μm wavelength interval. The peak optical power radiated by the first return strokes in the range 5–35 km had a mean and standard deviation of $2.3 \pm 1.8 \times 10^9$ W. Normal subsequent strokes (i.e., those preceded by dart leaders) generated $4.8 \pm 3.6 \times 10^8$ W and subsequent strokes preceded by dart stepped leaders produced $5.4 \pm 2.2 \times 10^8$ W. From the data they estimated the average radiance over space and time to be $1.0 \pm 0.9 \times 10^6$ W/m for first return strokes, $2.5 \pm 1.8 \times 10^5$ W/m for subsequent strokes preceded by dart leaders and $4.3 \pm 3.1 \times 10^5$ W/m for subsequent strokes preceded by dart stepped leaders. The values of peak optical powers obtained by Guo and Krider are in general agreement with the results obtained by other researchers [65, 66]. From this data Krider and Guo estimated the average peak radiance of subsequent strokes near the ground to be in the range of 6×10^5 W/m to 1×10^6 W/m. By integrating the optical power they arrived at the figures of 3.7×10^5, 7.7×10^4 and 8.7×10^4 J for the mean radiant energies of first return strokes, normal subsequent strokes and

subsequent strokes preceded by dart leaders respectively. Note that this energy is produced mainly by the visible channel section, which may be about 1–2 km, located below the cloud.

Orvile and Henderson [67] measured the absolute spectral irradiance of lightning flashes from about 15 km away in the wavelength range 375–880 nm. The average spectral irradiance of the strokes observed in the study for the wavelength range 375–650 nm is 3.5×10^{-5} J/m^2 with a standard deviation of 2.0×10^{-5} J/m^2. The individual values range from 0.7 to 6.8×10^{-5} J/m^2 per stroke. The corresponding values for the range 650–880 nm were 1.2×10^{-5} J/m^2, 0.7×10^{-5} J/m^2, 0.5–3.2×10^{-5} J/m^2. The strongest emissions occurred in the visible region centred at 505 nm. One interesting observation is that strong emissions at 384 nm have been identified to be CN emissions from ground flashes with continuing currents.

4.6.3.3.3 Estimation of the channel temperature, electron density and pressure from the lightning spectrum

The measured spectral data of return strokes can be used to determine physical properties of the lightning channel such as the temperature, pressure and particle densities. For example, the ratio between two spectral lines can be related to the channel temperature through theory, provided that the following assumptions are valid: (i) the lightning discharge is optically thin for the two wavelengths under consideration, (ii) the temperature is constant across the cross section of the stroke, (iii) the discrete atomic levels responsible for the spectral lines used to determine the temperature must be populated according to Boltzman statistics and (iv) the lightning channel is in local thermodynamic equilibrium, and this is achieved within a time short compared to the time over which the temperature is evaluated (see Chapter 3). If the last assumption is not satisfied, the temperature determined is the electron temperature. Using the theory and the measured relative intensities of NII emissions at 5680 and 5942 Å, Orville [68] determined the temperature of the lightning channel as a function of time. The results are shown in Figure 4.12. Using the experimentally observed stark broadening of the H-alpha line, Orville estimated the electron density in the channel as a function of time. The results obtained are shown in Figure 4.13. Once the temperature and the electron density in the channel have been determined it is possible to use the data to obtain the other physical characteristics of the channel. For example, from the data, Orville [68] estimated that the channel pressure within the first five microseconds of the initiation of the return stroke is about eight atmospheres and that it decreased to atmospheric pressure within about 30 μs.

4.6.3.3.4 Lateral propagation of the optical radiation from return strokes

There is a general consensus that the bulk of the charge in the stepped leader channel resides in the corona sheath, which has a diameter in the range of several metres to several tens of metres (see section 4.6.2.1). The return stroke neutralises this charge and one may expect some luminosity variations in the radial direction to be associated with this process. Recently Takagi *et al*. [69] measured the radial variation in the light intensity of the return stroke as a function of time. They found that, at a height of about

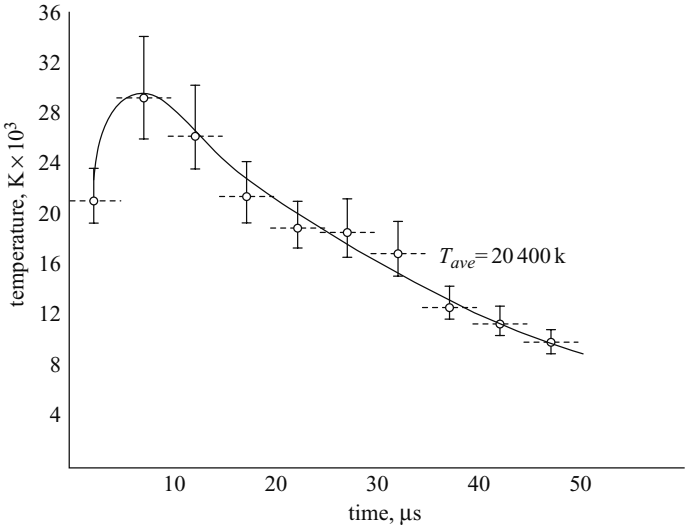

Figure 4.12 *Return stroke temperature as a function of time obtained from the analysis of NII spectral emissions. The dashed lines show the time interval over which the data points are averaged* (from [68]; reproduced by permission of the American Meteorological Society)

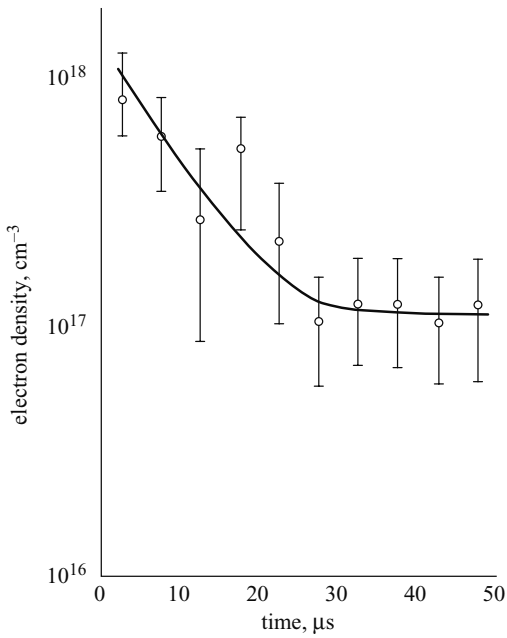

Figure 4.13 *Return stroke electron density as a function of time obtained from the analysis of H-alpha line widths. Each data point is averaged over 5 μs* (from [68]; reproduced by permission of the American Meteorological Society)

200–300 m from ground, the luminous region of the return stroke channel expands with a speed of 10^5 m/s during the initial stage and reaches a maximum diameter of several tens of metres about 100 μs after the initiation of the return stroke. The speed given above is similar to that of positive streamers and, therefore, the observations lend support to the idea of Cooray [70] that the neutralisation of the corona sheath takes place by positive streamers that travel out from the central core.

4.6.3.3.5 The thickness of the lightning channel

The lightning channel diameter can be measured by photographic observations [71–73], by measuring the diameters of fulgarites in sand and fulgamites [74,75], by measuring the dimension of holes made by lightning flashes in metal [76] or fibre glass plates [77], by analysing the lightning damage [78] and finally by using theoretical analysis [201,202,175]. The results obtained with these techniques are summarised in Table 4.6. In describing the lightning channel diameter, it is important to note that the temperature of the lightning channel varies in the radial direction. At the very centre there is a high temperature core and even within this core the temperature may decrease radially outwards. Outside this core there could be a streamer region which is at ambient temperature and very weakly luminous. Thus, it is more reasonable to discuss the radius of the lightning channel above a certain temperature. The measuring techniques used in gathering the data in Table 4.6 may provide a reasonable estimation of the high temperature core of the return strokes.

4.6.3.4 The properties of return stroke currents measured at the base of the channel

The return stroke current at the channel base can be measured in two ways. The first of these is to use the fact that tall structures are struck frequently by lightning flashes. Relatively tall structures, such as high towers, can be equipped with current measuring equipment that can record the current signatures at the channel base of

Table 4.6 Diameter of the lightning return stroke (adapted from Orville [73])

Reference	Diameter, cm	Method of determination
Schonland [71]	15–23	photographic
Schonland [74]	<5	fulgarites in sand
Evans and Walker [72]	3–12	photographic
Hill [75]	0.03–0.52	fulgamites
Uman [77]	0.2–0.5; 2–3.5	holes in fibreglass bonnets
Taylor [78]	0.05–0.3, 1–8	tree trunk damage
Jones [76]	0.1–0.3	discharge craters in aluminium
Orville [73]	6–7	photographic
Braginskii [201]	0.3–2	spark discharge model
Oetzel [202]	0.1–8	electrical circuit model
Plooster [175]	0.33–1.76	spark discharge model

lightning flashes. Since the frequency of lightning strikes to a given object increases with increasing height, a reasonable amount of information can be obtained over a time span of a few years using this technique [24,79]. The second method is to use the lightning triggering technique. In this technique a small rocket, trailing a thin metal wire attached to ground through a coaxial shunt, is launched towards a mature thundercloud. As the rocket travels upwards, the field at its tip increases and, when this field reaches a certain critical value, a connecting leader is initiated that travels towards the cloud. Lightning flashes initiated by this upward moving leader

Table 4.7 Parameters of the currents measured at the tower at San Salvarore, Switzerland (N is the number of observations) [87,203]

	Units	*N*	Percentage of cases exceeding the tabulated value		
			95%	50%	5%
Peak current	kA				
Negative first strokes		101	14	30	80
Negative subsequent strokes		135	4.6	12	30
Positive first strokes		20	4.6	35	250
Impulse charge	C				
Negative first strokes		90	1.1	4.5	20
Negative subsequent strokes		117	0.22	0.95	4.0
Positive strokes		25	2.0	16	150
Maximum current derivative	kA/μs				
Negative first strokes		92	5.5	12	32
Negative subsequent strokes		122	12	40	120
Positive first strokes		21	0.2	2.4	32
Action integral	A^2s				
Negative first strokes		91	6.0×10^3	5.5×10^4	5.5×10^5
Negative subsequent strokes		88	5.5×10^2	5.5×10^3	5.2×10^4
Positive first strokes		26	2.5×10^4	6.5×10^5	1.5×10^7
Total charge C					
Negative first strokes		93	1.1	5.2	24
Negative Subsequent strokes		122	0.2	1.4	11
Negative flashes		94	1.3	7.5	40
Positive flashes		25	20	80	350

Table 4.8 Triggered lightning current parameters; N is the number of observations, GM is the geometric mean (adapted from Rakov [86])

	Units	*N*	GM	Percentage of cases exceeding the tabulated value		
				95%	50%	5%
Peak current (Fort McClellan, Alabama, USA)	kA	45	12	4.7	13	29
Peak current (Kennedy Space Center)	kA	305	12.1	4.7	12.1	31.3
Peak current (Saint-Privat d'Allier, France)	kA	54	9.8	4.5	9.8	21.5
Peak current derivative (Kennedy Space Center)	kA/μs	134	91.4	28.1	91.4	297.7
Peak current derivative (Saint-Privat d'Allier, France)	kA/μs	47	36.8	14.9	36.8	90.9
Stroke charge (Fort McClellan, Alabama, USA)	C	65	2.5	0.38	2.1	15
Action integral* (Fort McClellan, Alabama, USA)	A^2s	65	3500	400	3800	20000

*The charge and action integrals are underestimates because part of the waveforms are saturated

will follow the trailing wire to ground. In this case, the lightning channel intercepts the instrumented launching pad and the current is measured directly to an accuracy better than ten per cent as it passes through the resistive shunt [80–86]. Parameters of lightning currents of engineering interest obtained from both tower measurements and triggered lightning techniques are summarised in Tables 4.7 and 4.8. These parameters are of interest from an engineering viewpoint because a knowledge of the peak current distribution in lightning flashes is necessary to estimate the voltages developed across resistive devices during lightning strikes and the number and the strength of lightning strikes that a given structure will intercept over a given time interval. The available data indicates that the peak current distribution can be approximated by a log–normal distribution. The distribution of the peak current derivative is necessary to evaluate the voltage drop developed across conductors as the lightning current travels along them. The action integral provides a measure of the total energy that will be dissipated when the current passes through resistive materials or protective devices such as varisters. The total charge provides an estimation of the heat generated, and hence any melting, when lightning strikes a metal object. In this case a constant voltage drop is maintained between the plasma and the metal transition and the total heat generated is given by the charge times this voltage drop.

4.6.3.4.1 Modification to the current parameters introduced by the experimental technique

It is important to note that the experimental technique used to measure the current can, itself, introduce errors into the measurements. Let us consider the tower measurements first. The striking distance of an object increases with increasing charge per unit length on the leader channel (and hence with the peak return stroke current) and with increasing height of the structure (because of the enhanced field intensification). As mentioned previously, the striking distance is defined as the separation between the tip of the stepped leader and the structure to be struck at the moment when a connecting leader is initiated from the latter. One can presume, therefore, that tall structures (typically the ones used to measure lightning currents) receive a high proportion of large currents and the current distribution is somewhat biased towards the higher end. Petterson [89] also came to a similar conclusion.

However, through a comparison of the current distributions obtained at towers of two different heights, Eriksson [90] came to the conclusion that the height of the structure does not significantly modify the current distribution.

The second problem with the tower measurements is the following. The current waveform injected by the return stroke at the top of the tower travels along the body of the tower and will be reflected at the ground end, due to the impedance mismatch, with the reflection coefficient being determined by the grounding conditions. These reflections may travel along the tower producing errors in the measured currents. Guerrieri *et al*. [91], showed that the error resulting from this could be significant even for a tower of 55 m height, similar to that of Berger's experiment. The error depends on the reflection coefficient and for higher reflection coefficients it can increase the measured current amplitude by about 30–50 per cent. However, Guerrieri and coauthors point out that the effect might be minor in the case of Berger's measurements since the towers were built on dry terrain with a low conductivity. In addition to these uncertainties, the field enhancements caused by the tower can lead to connecting leaders that are longer than their counterparts in open terrain. The length of the connecting leader may change the current parameters to some extent, but exactly how and to what degree is not known at present.

The main difference between the triggered and natural lightning flashes is the absence in the former of first return strokes initiated by stepped leaders. Furthermore, in the triggering process a leader is launched into a cloud which may not yet be ripe enough to launch a natural lightning flash to ground. This may affect the characteristics of lightning flashes, such as the time interval between strokes and the percentage of continuing current strokes. Moreover, the last few hundred metres of the lightning channel is polluted by the vapour of the metal wire used in the triggering process; this may to some extent influence the measured current parameters such as the peak current derivatives.

Whatever technique is used to measure the current parameters, the fast features of the current waveforms will be distorted if the recording system does not have a sufficiently high resolution to record them faithfully. This could very well be the case in Berger's measurements, where the measured current derivatives may have been

affected by the low time resolution of the measuring equipment, thereby leading to lower measured values than the values actually present. However, it is difficult to believe that the current derivatives of first strokes obtained in that study are significantly distorted by the measuring system because the measured values lie much below the values measured for subsequent strokes using the same measuring equipment. On the basis of the results of theoretical simulations Cooray [56] and Cooray and Galvan [57] suggest that Berger's first return stroke current derivatives have not been significantly distorted by the frequency response of the current measuring system (see also Chapter 6).

4.6.3.4.2 Experimentally observed correlation between different current parameters

Various relationships and correlations observed between different current parameters are of interest both in return stroke modelling and in improving the understanding of the physical mechanism behind lightning return strokes. The available experimental data indicates that there is a weak correlation between the peak current, I_p, and the peak current derivatives, $(dI/dt)_p$, of return strokes. This relationship can be described by the equation:

$$(dI/dt)_p = a(I_p)^b \tag{4.11}$$

where $a = 6.6$ and $b = 0.38$ for first strokes and $a = 3.4$ and $b = 0.94$ for subsequent strokes [87]. In this relationship the peak current is in kA and the peak current derivative in kA/μs. A similar relationship is also observed in triggered lightning currents (pertinent to subsequent return strokes) with constants $a = 2.6$ and $b = 1.34$ for Florida, USA, and $a = 2.0$ and $b = 1.28$ for Saint-Privat d'Allier, France [222].

The tower measurements of Garbanati and Piparo [79] show that the peak current is correlated to the action integral, A_c, calculated over the first 500 μs, through the equation:

$$A_c = a(I_p)^b \tag{4.12}$$

where $a = 12.0$ and $b = 2.4$ for first strokes and $a = 26.9$ and $b = 2.13$ for subsequent strokes. In triggered subsequent strokes $a = 50.0$ and $b = 1.89$ [222]. In the above relationship peak current is in kA and the action integral is in A^2s.

Both Berger [88] and Garbanati and Piparo [79] found a strong correlation between the peak current and the impulse charge (the charge associated with the return stroke excluding the contribution from continuing currents), Q_{im}, dissipated in the first return stroke. Both relationships can be written as:

$$Q_{im} = a(I_p)^b \tag{4.13}$$

where Garbanati and Piparo found $a = 3.16 \times 10^{-2}$ and $b = 1.3$ for the charge dissipated over the first 500 μs and Berger found $a = 3.43 \times 10^{-2}$ and $b = 1.43$ for the charge dissipated over the first 2 ms. In these relationships peak current is in kA and the charge in coulombs. In the case of subsequent strokes in triggered lightning

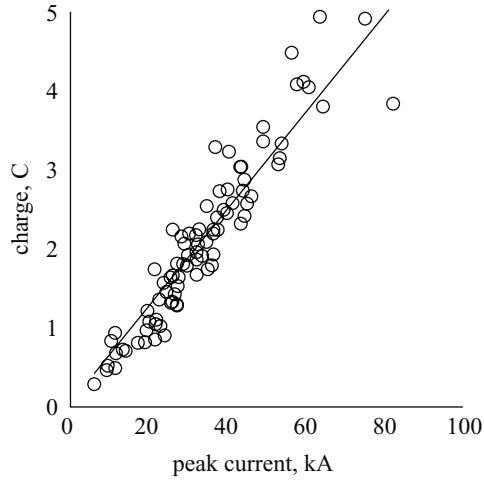

Figure 4.14 The charge brought to ground over the first 100 μs of the first return stroke currents

$a = 0.09$ and $b = 0.89$ [222]. At first glance it is difficult to understand the existence of such a correlation. For example, the peak current is determined by the charge on the first few hundred metres of the leader channel, whereas the impulse charge is the charge located on a channel section of about 3–7 km. But, if there is a strong correlation between the linear charge density of the lower sections of the channel and the peak return stroke current (which could very well be the case), one would obtain a correlation between the peak current and the total charge if the way in which the charge density varies along the channel is more or less similar in first return strokes with different current amplitudes. Recently, the author has digitised the first return stroke waveforms of Berger and the charge brought to ground by the return strokes over the first 100 μs, $Q_{100\,\mu s}$, was estimated. The results are shown in Figure 4.14. Observe the strong linear correlation between the charge and the peak return stroke current. The results could be represented by the equation:

$$Q_{100\,\mu s} = 0.061 I_p \tag{4.14}$$

where $Q_{100\,\mu s}$ is in coulombs and the peak current is in kA.

4.6.3.5 Electromagnetic fields generated by return strokes

4.6.3.5.1 General features

The overall features of the electric and magnetic fields of first and subsequent strokes at different distances are shown in Figure 4.15 [92]. The qualitative features of these waveforms are similar to those generated by a dipole excited by a nonuniform current waveform (see Chapter 5). The far fields, around 100 km, being radiation, are bipolar and electric and magnetic fields have identical signatures. As the distance to the return

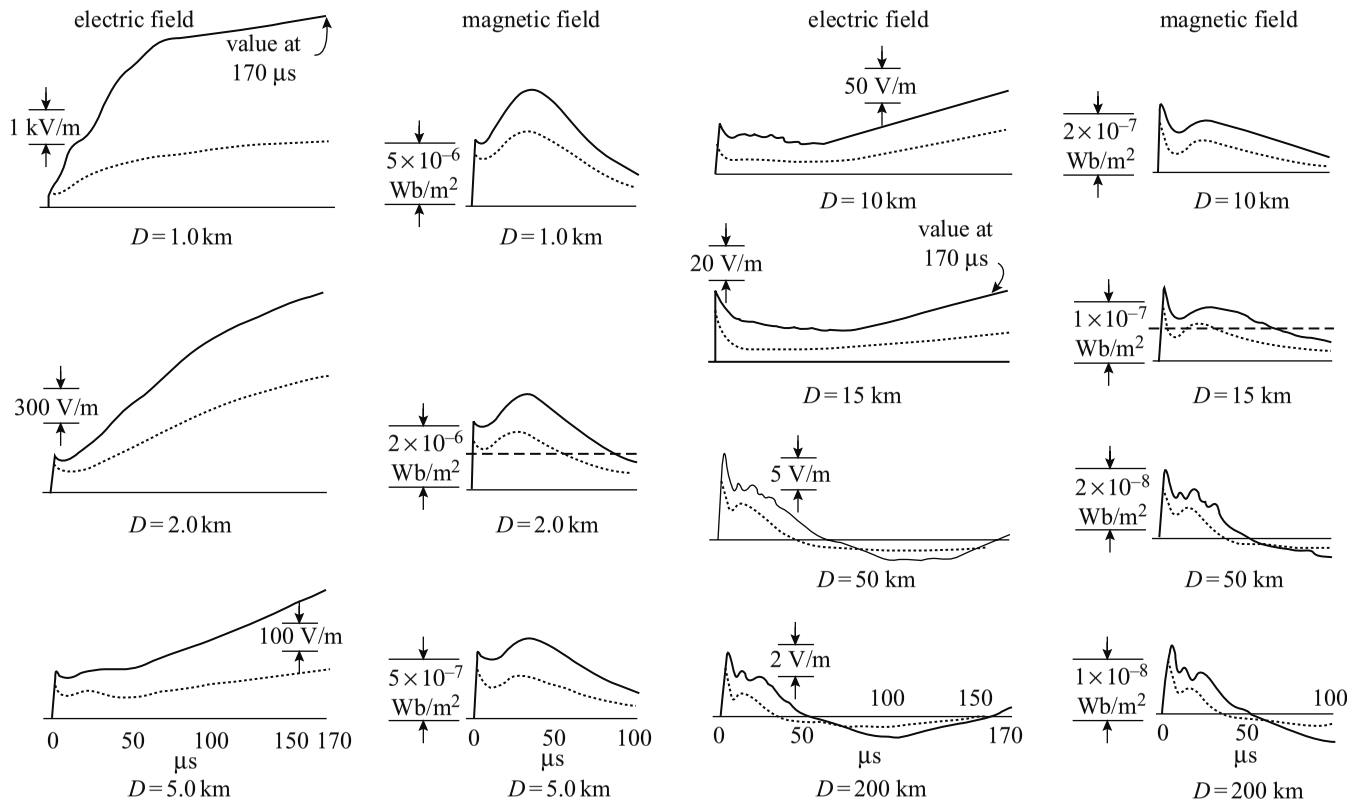

Figure 4.15 *Typical electric field intensity and magnetic flux density for first (solid line) and subsequent (dotted line) return strokes at different distances. A positive field corresponds to an upward deflection* (from [92]; reproduced by permission of the American geophysical union)

stroke decreases, the electrostatic and induction fields become dominant. The near magnetic field is mainly induction (magnetostatic) and shows a pronounced hump. It is important to observe that whether the electric field at a given point on the waveform is radiation or not depends on the distance to the return stroke, the location of the point of interest on the waveform and on the shape of the waveform. Figure 4.16*a*, based

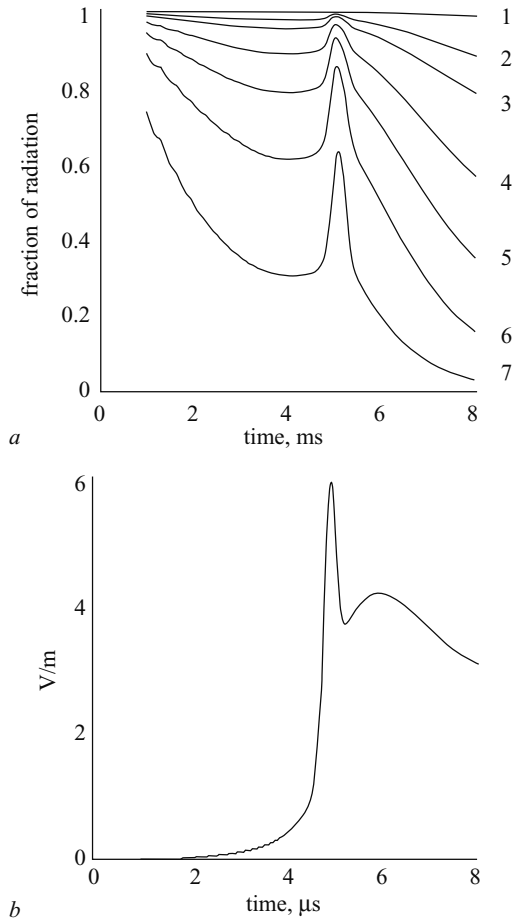

Figure 4.16 *a* the time variation of the electric radiation field as a fraction of the total field at different distances from the return stroke: (1) 100 km; (2) 10 km; (3) 5 km; (4) 2 km; (5) 1 km; (6) 500 m; (7) 200 m; the results are obtained from the negative first return stroke model described in section 6.4.2.6.3

b the model predicted electric field at 100 km, a positive field corresponds to an upward deflection

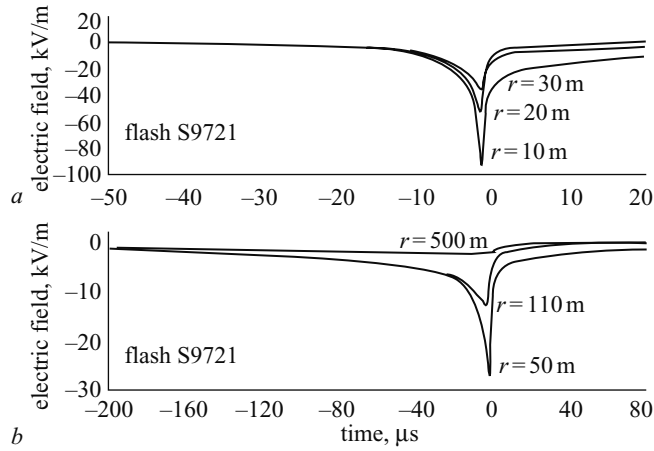

Figure 4.17 *Electric field waveforms of the dart leader/return stroke sequence as recorded at different distances, at Camp Blanding, Florida. The electric field to the left of the minimum is produced by the dart leader and the rapid recovery of the field from the minimum is produced by the return stroke. A positive field corresponds to an upward deflection* (from [86]; reproduced by permission of the author)

on the first return stroke model described in section 6.4.2.6.3 of Chapter 6, shows the relative contributions of the radiation field to the total field as a function of distance. As a reference the model predicted radiation field at 100 km is given in Figure 4.16*b*. Note that at a given distance the contribution of the radiation field increases as the point of interest comes closer to the beginning of the waveform. Observe also how the radiation field is enhanced at the fast transition that occurs at 5 μs. The reason for this is the enhancement of the high frequencies by the fast transition in the waveform.

Experimental data on electromagnetic fields very close to the channel (within about 100 m) is not available for natural lightning, but some data obtained from triggered subsequent strokes does exist. An example from such a measurement carried out at 50 m is shown in Figure 4.17. The field is U shaped with the left arm of the U being produced by the down-coming dart leader. The return stroke neutralises the charge on the dart leader which will cause a field change opposite to that of the dart leader. Note that the return stroke field saturates within a few microseconds. Measurements show that the signature of the magnetic field at these distances approaches that of the current waveform at the channel base. Several examples of the positive return stroke fields at a distance of 100–200 km are shown in Figure 4.18. There does not appear to be any experimental data in the literature showing how the electric fields from positive return strokes vary with distance. Model simulations of the positive return stroke fields at different distances are given in Chapter 6 [93].

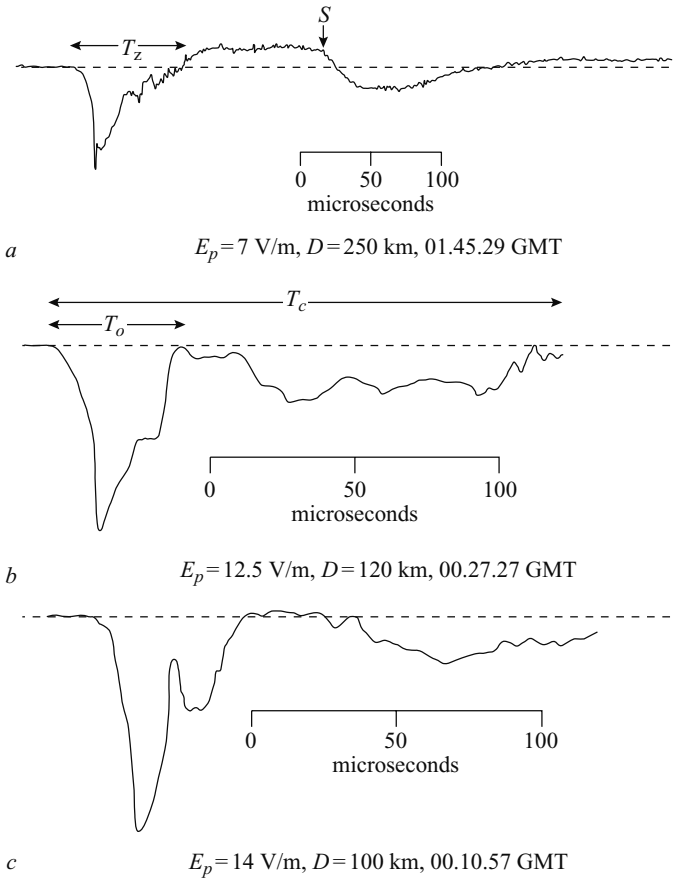

Figure 4.18 *Electric radiation fields of positive return strokes observed in Sweden. The initial peak value (E_p) and the range (D) is given below each diagram. A positive field corresponds to an upward deflection* (from [96]; reproduced by permission of the American geophysical union)

4.6.3.5.2 Characteristics of radiation fields

The fine structure of the radiation fields generated by return strokes has been analysed by many researchers [92–100]. The main features of the radiation fields generated by negative return strokes are shown in Figure 4.19.

Slow front and the fast transition: The initial rising part of the radiation field contains a slow front followed by a fast transition. The duration of the slow front is about 5 μs in negative first return strokes, about 10 μs in positive first return strokes and about 0.5 μs in the subsequent return strokes. The slow front is followed by a fast transition. The amplitude of the breakpoint is about fifty per cent of the total peak in first return strokes (both positive and negative) and is about twenty per cent in the subsequent strokes. The 10–90 per cent rise time of the fast transition is similar

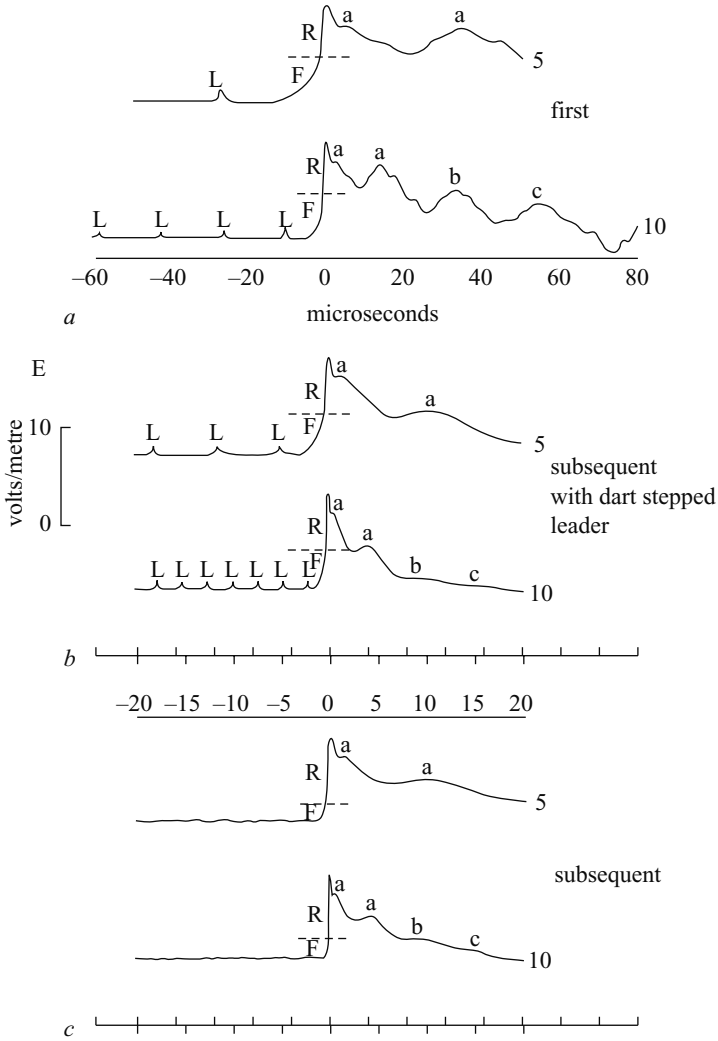

Figure 4.19 *Sketches of the shapes of the electric radiation fields produced by (a) the first return stroke, (b) a subsequent return stroke preceded by a dart stepped leader, and (c) a subsequent stroke preceded by a dart leader. The small pulses characteristic of leader steps L are followed by a slow front F and an abrupt transition to peak R. The peak amplitudes are normalised to a distance of 100 km. A positive field corresponds to an upward deflection* (from [94]; reproduced by permission of the American geophysical union)

in negative first and subsequent strokes and the average value is about 0.1 μs. In positives the corresponding rise time is about 0.25 μs.

Weidman and Krider [94] investigated the possibility that the slow front of return stroke radiation fields is generated by the connecting leader that rises up to meet the down-coming leader just before the connection between the leader and the ground is established. Their calculations show that, in order to produce field magnitudes comparable to those in slow fronts, the connecting leader has to carry a current of the order of 10 kA. However, as pointed out by Weidman and Krider, connecting leaders are quite faint and difficult to photograph, which is not consistant with currents of the order of 10 kA. Cooray (see Chapter 6) suggested a scenario that will overcome this problem. According to this, the slow front is generated by the almost exponential increase in the current in the connecting leader as it moves through the streamer region of the stepped leader. That is, after the interception of the connecting leader with the stepped leader. This stage can also be interpreted as the initial stage of the return stroke. The rapid transition in the field takes place with a rapid increase in the current that results when the connecting leader meets the hot core of the leader channel. Cooray *et al*. [97] suggested that the longer duration of the slow front in positive first return strokes is caused by the longer streamer portion associated with the positive downward leaders.

It is not clear, however, whether a streamer region can produce the conductivity gradient necessary for the creation of slow fronts in subsequent return stroke fields. The dart leader travels along a channel whose temperature may be higher than 1500–3000 K. It is not known at present whether streamer discharges in the conventional sense exist at these temperatures. However, optical observations show that the rise time (zero to peak) of the optical radiation associated with the dart leader is about 2–3 μs [59,141–142]. This indicates that the build-up of the ionisation process takes a finite time in the case of the dart leader. It is reasonable to assume, therefore, that there is a conductivity gradient along the dart leader channel with the region of lowest conductivity located at the forward end of the leader. As shown by Cooray [121], such a conductivity gradient could give rise to the slow front in the subsequent return stroke fields.

Subsidiary peaks: After the initial peak, both negative first and subsequent strokes exhibit a shoulder within about 1 μs from the initial peak. The decaying part of the first return stroke radiation field contains several subsidiary peaks whose separations are in the range of tens of microseconds. The subsequent strokes do not usually show these subsidiary peaks except in the cases in which the preceding stroke is the first stroke. Weidman and Krider [94] suggest that these subsidiary peaks are caused by rapid changes in the current and velocity when the return stroke front encounters branches of the stepped leader channel.

Zero crossing time: The negative first return stroke waveform crosses the zero line in about 50–100 μs, whereas the corresponding values for the subsequent return strokes are 30–50 μs. In positive first strokes without long tails (see Figure 4.18a and the next section), the zero crossing time is distributed over the range of 50–130 μs.

The zero crossing time of the radiation fields depends mainly on two parameters [122]. First, it depends on the rapidity at which the current generated by the

neutralisation process decreases along the channel. If the current decays rapidly along it, the zero crossing time will be shorter, and *vice versa*. The way in which the current decreases along the channel is governed to some extent by the charge distribution along the leader channel that initiated the discharge. Second, the zero crossing time depends on the vertical length of the channel. The vertical length of the channel is approximately equal to the height of the negative charge centre in the cloud. Inside the charge centre the channel may extend horizontally. A longer vertical channel can produce a longer zero crossing time and the opposite is true for shorter channels. Furthermore, even if the current does not decay along the channel, a shorter channel cannot sustain a longer radiation field because the field will decay rapidly when the return stroke front reaches the end of the vertical channel section. Thus the zero crossing time is to some extent controlled by the speed of the return stroke front. Some evidence for this conjecture is the observation that the zero crossing time of the radiation fields is significantly higher in the tropics than in temperate regions [32]. The height of the negative charge centre is higher on average in the tropics than in temperate regions.

The tail of the waveforms – differences between the negative and positive return strokes: After a comparative study of electromagnetic fields generated by positive and negative return strokes, Cooray [96] discovered that in many cases the tail of the electromagnetic radiation fields of positive return strokes, that is, the section of the field beyond about 30 μs, varies in a manner different to that of negative return strokes. After the zero crossing the negative fields continue to decrease, form a peak of opposite polarity and come back to the zero level at about 100–150 μs of the beginning of the waveform. The positive waveforms exhibit the following behaviour. After an initial peak, they also continue to decay and reach or momentarily cross the zero line at about 30–80 μs. However, at later times, instead of continuing to decrease – as does their negative counterpart – the field starts to increase again and reaches a second peak between 100 and 400 μs (see Figure 4.18). Analysis of the electric radiation fields from distant (400 km or more) positive return strokes shows that the field continues to decrease after this second peak, crossing the zero line at about 1 ms [95,101]. Several such examples measured 450 km from the return stroke channel are shown in Figure 4.20. Numerous examples show that this slowly varying phase of the positive return stroke field is associated with a burst of leader-like pulse activity.

Cooray [93,96] has suggested the following physical process as an explanation for the difference in the tail of the positive and negative return stroke radiation fields. The initial peak and the subsequent decay of the electric radiation field of both negative and positive return stroke fields within the first few tens of microseconds are features associated with the neutralisation of the leader channel as the return stroke surges upwards through it. Since there is no qualitative difference in the distribution of the leader charge and the way in which this charge is neutralised in negative and positive return strokes, there is not much difference in the electric radiation fields generated by them during this time. But what then happens when the return stroke front reaches the cloud differs between negative and positive return strokes. When the front of the negative return stroke reaches the cloud end of the leader, the current flowing into the vertical channel of the negative return stroke is quenched and, as a result, the radiation field makes an excursion to the other side of the zero field line, returning to the line

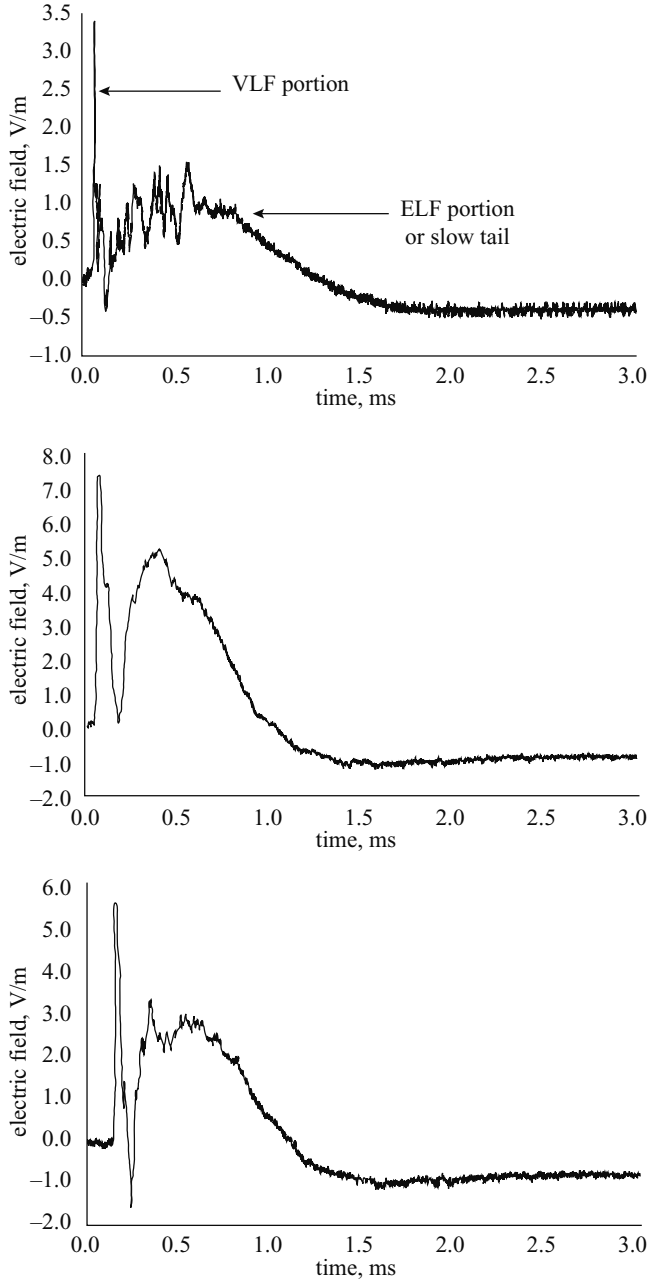

Figure 4.20 *Examples of electric radiation fields from positive return strokes measured at 450 km from the flash origin. A positive field corresponds to a downward deflection* (adapted from [101])

at a rate which is determined by the rapidity at which the current is quenched in the channel. On the other hand, when the positive return stroke front reaches the cloud end of the leader channel, it encounters a large source of positive charge, probably located on an extensive dendritic pattern of mainly horizontal branches in the cloud. Some of the recent observations do indeed show extensive horizontal branching in the cloud portion of the positive return strokes [123]. This source of charge enhances the current flowing into the vertical channel, thereby producing a second surge in the electromagnetic radiation. The high frequency activity superimposed on the tail of the fields, as observed by Cooray [96], is probably connected with the processes that make this charge available to the return stroke. In fact, the experimental data available on negative and positive return stroke currents strengthens the above hypothesis. In the first 50–100 μs, the temporal variation of the positive return stroke current is qualitatively similar to that of the negative one. After this time, however, while the negative current continues to decay, the positive current starts to increase again, reaches a second peak and then decays to zero level within about a millisecond.

Distribution of the peak radiation fields of return strokes: Several studies in which an estimation of the initial peak of the radiation field is made are available in the literature [63,92,95,97,102–104]. The peak of the radiation field of negative first return strokes normalised to 100 km lies in the range of 3 – 30 V/m, with a mean value lying somewhere between 5 and 10 V/m. The mean of the initial peak of positive return strokes is about a factor of two larger than that of negative first return strokes. The initial peak of the subsequent return strokes normalised to 100 km lies in the range 2–15 V/m with a mean value around 3–4 V/m. Many of the observations of peak electric fields are made over land and, therefore, depending on the conductivity, these peak values could to some extent be distorted by propagation effects (see Chapter 7). Indeed, the mean values of the peak radiation fields of lightning flashes striking the sea are somewhat larger than those observed from lightning flashes striking the land. Whether this difference is caused by less severe propagation effects on radiation fields from lightning flashes striking the sea or by the presence of higher current amplitudes in these flashes is not known at present. Some of the most recent data on the initial peak amplitudes is summarised in Table 4.9. Since the peak of the radiation field occurs within a few microseconds of the beginning of the electric field and since the first microseconds of the electric field are approximately radiation down to about 1 km, it is possible to extrapolate these values to calculate the peak fields at any other distance by using the fact that the radiation field decreases inversely with distance (see section 4.6.3.5.1).

Time derivative of the radiation field: The radiation field time derivative is a parameter which is difficult to measure accurately in land-based measurements owing to the strong impact propagation has on it (see Chapter 7). In order to obtain accurate results, the fields have to be measured very close to the lightning channel, or the propagation path should be over the sea so that the propagation effects are negligible. The data available today on the characteristics of the time derivatives of the radiation field are obtained from measurements conducted with the latter approach [97,99,100,103,105]. The typical shape of the time derivatives of the radiation fields of several processes are shown in Figure 4.21 with parameters of interest marked on it. Note that the signature

Table 4.9 Peak radiation fields in V/m, normalised to 100 km assuming inverse distance dependence, generated by return strokes (GM – geometric mean, SD – standard deviation)

Author	First strokes			Subsequent strokes		
	number of observations	mean	SD	number of observations	mean	SD
Master *et al*. [102]	112	6.2	3.4	237	3.8	2.2
Guo and Krider [63]	69	11.2	5.6	84	4.6	2.6
Lin *et al*. [92] (KSC)	51	6.7	3.8	83	5.0	2.2
Lin *et al*. [92] (Ocala)	29	5.8	2.5	59	4.3	1.5
Willett *et al*. [103]	125	8.6	4.4			
Rakov and Uman [104]	76	5.9 (GM)		270	2.9 (GM)	

of the time derivative is similar in all the cases. Table 4.10 and Table 4.11 provide a summary of the various parameters of the time derivative of the electric field as observed by different researchers.

4.6.3.5.3 Radiofrequency (RF) radiation generated by first return strokes

RF emission from return strokes has been analysed by several researchers [105–110,208]. Brook and Kitagawa [107] observed that the onset of the RF radiation during the first return stroke stage is delayed by 50–150 μs from the beginning of the return stroke. Since the observed delay in the RF radiation from the onset of the return stroke is larger than the time necessary for the return stroke front to reach the cloud, Brook and Kitagawa concluded that the return stroke is not a strong source of RF radiation. LeVine and Krider [108] also observed a delay in the onset of RF radiation, but the delay they measured was about 10–30 μs. However, since this delay is not large enough to let the return stroke reach the cloud end of the leader before the commencement of the RF, this observation indicates that the first return stroke itself is a source of RF radiation. This inference is also supported by the observations of Shao *et al*. [5] who found that the strength of the RF radiation increases several fold upon the initiation of the first return stroke. They could also detect RF radiation sources travelling upwards during the first return stroke phase. Cooray [111] and LeVine *et al*. [112] suggest that the delay in the onset of RF radiation following the first return strokes is probably caused by propagation effects. Furthermore, Cooray [111] could not detect any delay in 3 MHz radiation when the electromagnetic fields are propagating over the sea.

Cooray and Perez [109] and Jayaratne and Cooray [113] measured the HF radiation associated with first return strokes. According to their observations, the duration of the burst of RF radiation at 3 MHz associated with the first return stroke is 130 and 170 μs in Sweden and Sri Lanka, respectively.

Shao *et al*. [5] have found that the dart leader is a strong source of RF radiation and the radiation intensity decreases at the onset of the subsequent return stroke and

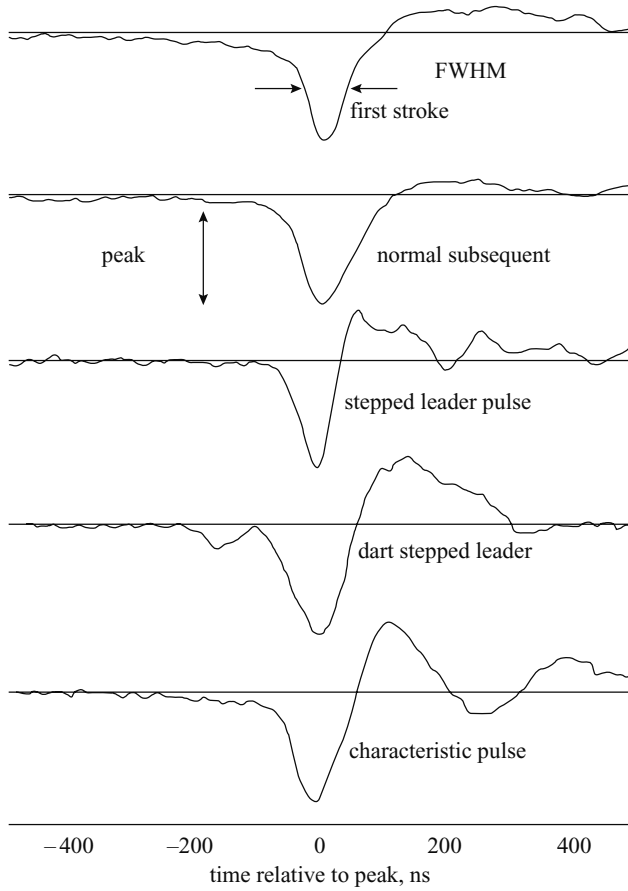

Figure 4.21 *Examples of observed dE/dt signatures from first and subsequent return strokes, stepped and dart stepped leader steps, and pulses from cloud flashes (marked characteristic pulses). The FWHM is marked on the first return stroke field. The vertical scale is arbitrary. A positive field corresponds to a downward deflection* (from [100]; reproduced by permission of the IEEE)

remains at a low level until the return stroke front reaches the cloud end of the leader. Bursts of RF pulses may appear after the return stroke front has travelled into the cloud. This also agrees with the findings of Brook and Kitagawa [107] and LeVine and Krider [108] who also observed that the subsequent return strokes are not strong sources of RF. The latter study found that the HF starts about 265 μs prior to the onset of the subsequent return strokes and ceases before the onset of the return strokes. However, the 3 MHz radiation frequently persists up to and during the return stroke. Examples of the broadband electric fields are shown in Figures 4.22 and 4.23 together with the HF radiation at several frequencies. Note, however, that the subsequent return strokes radiate somewhat in the HF region.

Table 4.10 Full width at half maximum (FWHM) of the radiation field derivative of lightning return strokes (SD – standard deviation)

Reference	Number of observations	Mean (ns)	SD (ns)	Comments
Willett and Krider [100]	133	77	20	first strokes
Willett and Krider [100]	85	79	20	subsequent strokes
Weidman and Krider [160]	18	73		first and subsequent
Krider *et al*. [99]	61	75	15	first strokes
Cooray *et al*. [97]	40	170	90	positive

Table 4.11 Peak values of electric field derivative (SD – standard deviation)

Reference	Number of observations	Mean (V/m/μs)	SD (V/m/μs)	Comments
Willett *et al*. [103]	131	37 (42)*	12	first
Krider *et al*. [99]	63	39 (46)*	11 (13)*	first
Weidman and Krider [105]	97	29	12	first and subsequent
Cooray *et al*. [97]	40	25	11.6	positive

*After correction for propagation effects

The data available concerning the RF generation by positive return strokes is scanty. Kawasaki and Mazur [110] observed UHF (at 327 MHz) radiation during the return stroke stage, but the resolution given in the data plots is not high enough to conclude whether the radiation starts immediately at the onset of the return strokes (i.e., within microseconds) or if it is delayed (and starts within tens of microseconds). Their data shows that the UHF radiation peaks at a time close to the initiation of the return stroke and tails off within about 10 or 20 ms. The observations of Cooray and Perez [109] show that there is an enhancement of the HF at 3 MHz immediately after the onset of the positive return stroke and the radiation continues for at least several milliseconds.

The mechanism whereby lightning produces HF and VHF radiation is not completely understood [124,125]. LeVine and Krider [108] suggested that branched breakdown processes could be an important source of HF, and LeVine and Meneghini [126] showed that the effects of channel tortuosity could produce HF radiation during return strokes. However, the channel tortuosity may not be solely responsible for the HF radiation for the following reason. The available photographic observations show that many of the subsequent strokes in a lightning flash also travel along the path traversed by the first return stroke. If channel tortuosity is mainly responsible for the HF radiation, one can expect comparable HF radiation from both the first and subsequent return strokes. However, the data available at present shows that subsequent strokes

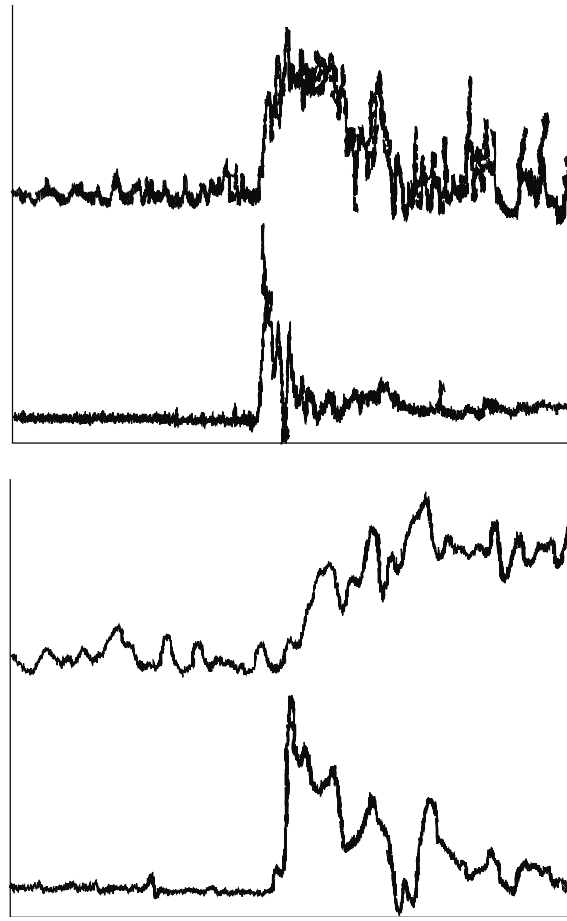

Figure 4.22 *Simultaneous records of the 3 MHz RF signal (top trace) and the electric field (lower trace) due to a first return stroke. The total length of the record is 865 μs for the upper two traces and 173 μs for the lower two traces. A positive field corresponds to an upward deflection* (from [108]; reproduced by permission of the American geophysical union)

generate much less HF radiation than do first return strokes [107,108]. This shows that channel tortuosity is not the main source of HF radiation associated with return strokes. The negative return strokes are capable of generating HF radiation almost immediately with the onset of the return strokes. Usually, the lower portion of the leader channel is free of branches and therefore it is doubtful that the branches alone are responsible for the HF emission just after the return stroke.

The observations of Shao *et al*. [6] indicate that the VHF radiation from the stepped leader is mainly generated by the downward propagating tip of the leader. The source of the VHF radiation could be this streamer system of the stepped leader.

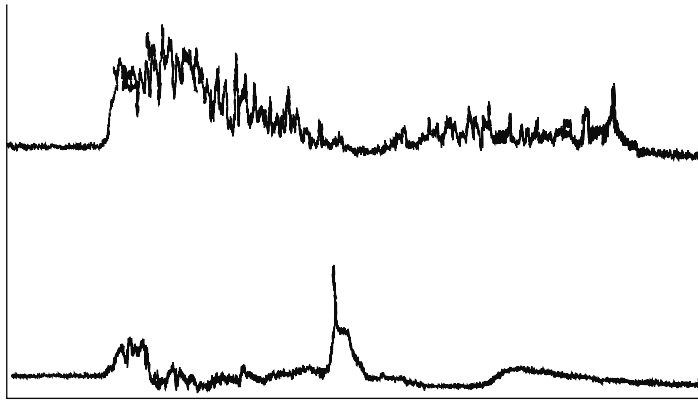

Figure 4.23 *Simultaneous records of the 3 MHz RF signal (top trace) and the electric field (lower trace) due to a subsequent return stroke. The total length of the record is 900 μs. A positive field corresponds to an upward deflection* (from [108]; reproduced by permission of the American geophysical union)

Streamers could also be responsible for the generation of RF radiation during the first return stroke stage. The charge on the leader channel resides mainly on the corona sheath, whose radius is of the order of several metres to several tens of metres. On the other hand, the radius of the highly conducting return stroke channel is of the order of a few centimetres. During the return stroke stage the funnelling of the charge from the corona sheath into the highly conducting return stroke channel may be accompanied by the ionisation of virgin air or the reionisation of old channels that have decayed to a nonconducting stage. As mentioned previously, Takagi *et al*. [69] have observed luminous discharge phenomena propagating radially from the central channel during the return stroke stage. The speed of propagation of the discharges is similar to that of streamer discharges observed in long laboratory sparks. This neutralisation process could be a source of RF radiation.

As mentioned in section 4.6.2.1 the corona sheath is created partly by the charge deposited in space by the corona streamers travelling ahead of the stepped leader channel. This charge may not be distributed uniformly along the leader channel because the streamers are created mainly in bursts from the tip of the newly created leader steps. This non uniform charge distribution in the corona sheath may give rise to an amplitude modulation of the return stroke current leading to the generation of RF radiation. This fact may also explain why subsequent return strokes do not radiate strongly in the RF region. The dart leader propagates continuously down the defunct return stroke channel and, therefore, one may presume the charge distribution on the corona sheath is more or less uniform leading to a diminishing of the RF radiation during the neutralisation. Moreover, it is also possible that the corona sheath produced by the dart leader remains conducting until the charge on it is neutralised by the return stroke.

4.6.3.5.4 Frequency spectrum of lightning generated electromagnetic fields

Frequency spectra of the electromagnetic fields generated by lightning flashes have been made either by monitoring the power received at individual frequencies using narrowband recording systems or by recording the transient with a broadband device and performing the Fourier transformation. The problem with narrowband systems is the difficulty of identifying the radiation produced by different components of the lightning flash. The problem is the conflict between two desirable attributes. The first of these is to have a narrow bandwidth so the measurements are truly representative of a particular frequency and the second is to have a large bandwidth so that the individual events can be distinguished. However, as pointed out by LeVine [114], both techniques have yielded similar spectra; these spectra agree reasonably well below 1 MHz, but even at high frequencies there is an overlap of data points.

The return stroke spectrum in the VLF region was studied, among others, by Taylor [115] and Serhan *et al*. [116]. The spectrum that extends from the VLF to the HF region was analysed by Weidman and Krider [117], Weidman *et al*. [117] and Willett *et al*. [158]. The spectrum of first and subsequent return strokes, which actually is a combination of the results from several of these studies, is shown in Figure 4.24. Note that the shape of the subsequent return stroke spectrum is identical to that of the first return strokes, with the exception that its amplitude is somewhat lower in the low frequency region. The fact that the high frequency ends of the two spectra are identical indicates that the submicrosecond structures of the first and subsequent return strokes are identical. It is important to note here that the spectrum

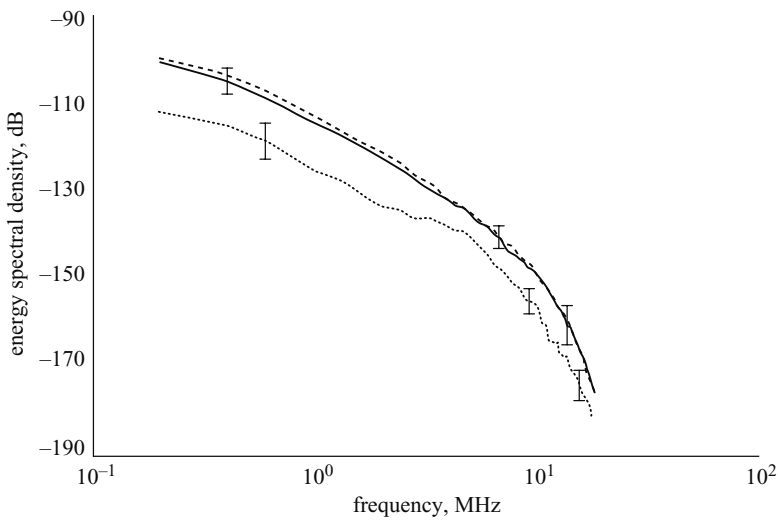

Figure 4.24 Average spectra of 74 first return strokes (solid line) and 55 subsequent strokes (dashed line). The dotted line shows the average spectrum of 18 pulses generated by cloud flashes (from [158]; reproduced by permission of the American geophysical union)

of the return stroke at the high-frequency end is remarkably similar to those obtained for stepped leaders and cloud pulses (see also Figure 4.8). LeVine [115] suggests that this could be because there is some physical process which is common to all these events.

In the spectrum shown in Figure 4.24, the spectral amplitudes decrease like $1/f^2$ over the range from 1 MHz to about 10 MHz. Beyond that frequency the spectral amplitudes decay much faster. Ye and V. Cooray [119] show that this rapid decrease in spectral amplitudes is probably caused by the impact of propagation on the radiation fields as they travel over a rough ocean surface. They point out that the return stroke spectrum measured at high altitudes, where the propagation effects are not involved, shows $1/f^2$ dependency in the region of 10 MHz and above. The spectrum obtained by applying narrowband techniques does not show this rapid decrease at high frequencies. Recall, however, that the narrowband spectrum is generated by the composite event including the activities inside the cloud. If the lightning flashes are located within about 20 km of the point of observation, the cloud portion of the ground flash can produce signals that do not attenuate significantly owing to propagation effects [120].

4.6.4 Continuing current

About fifty per cent of lightning flashes with multiple strokes are found to involve at least one stroke that is followed by a long continuing current. There is no exact definition as to the duration of the current that should be regarded as a continuing current, but a duration longer than about 1 ms is a reasonable value. Most of the inferences made about the presence of a continuing current are based on electric field measurements [127], but a significant amount of data has already been obtained from triggered lightning flashes [84]. Figure 4.25 shows an electric field generated by a lightning flash with a continuing current and Figure 4.26 shows an example of a channel base current of a return stroke which supported a continuing current.

The analysis of the electric fields indicates that the geometric mean of the peak electric fields of return strokes that precede strokes initiating continuing currents was 1.5 times larger than for regular strokes; a similar tendency is found for the charge lowered by strokes [104].

The reason for the presence of continuing currents in some of the return strokes is not known at present. Krehbiel *et al*. [15] speculate that a continuing current will flow if the charge sources in the cloud or on the channel to ground can provide a sufficient level of current to keep the channel from decaying. Otherwise, the channel will be cut off and a new leader and a return stroke will be initiated.

4.6.5 M components

Malan and Collens [128] coined the term M components to refer to the temporal increase in luminosity of the channel observed after some ground return strokes. For example, the sudden increases in the current in Figure 4.26 are caused by M components. The wealth of information available today on the M components was derived

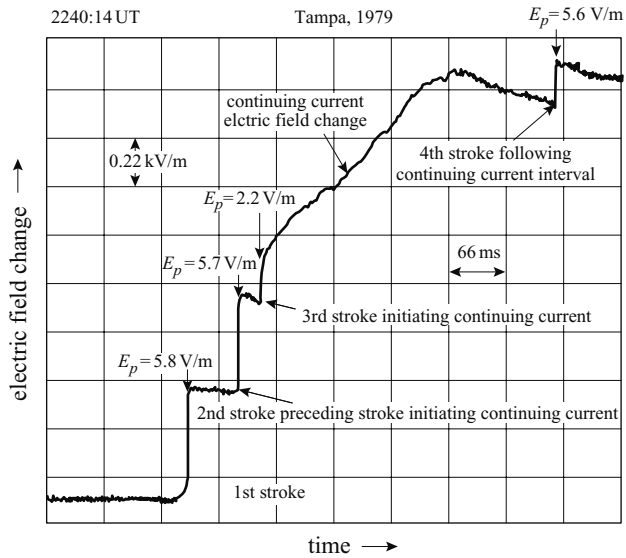

Figure 4.25 *Overall electric field change for a four stroke flash (at a distance of 6.5 km) with a long continuing current following the third stroke. Initial electric field peaks (not resolved in the figure) normalised to 100 km are labelled E_p. A positive field corresponds to an upward deflection* (from [104]; reproduced by permission of the American geophysical union)

by analysing the channel base currents and the luminosity changes in triggered lightning flashes [84,129]. The M component is a current impulse that initially travels from cloud to ground with a speed of about 10^7–10^8 m/s [5,130] and occurs during the continuing current phase of the return stroke. The light pulse associated with the M component exhibits a more or less symmetrical waveshape with a rise time and decay time of the order of many tens of microseconds. The shape of the light pulse does not change much within the bottom 1 km or so of the channel, whereas its amplitude varies somewhat with height. The statistics on M components are given in the Table 4.12.

An example of the electric field change generated by an M component is shown in Figure 4.27. Note that the M component generates a hook shape change in an otherwise ramp-like electric field change caused by the continuing current. By analysing the way in which the electric fields of M components vary with distance, Rakov *et al*. [131] established that the M component involves a downward progressing incident current wave followed by an upward progressing reflected wave. This provides an explanation for why the M component was sometimes observed to travel down and sometimes travel up [128]. Rakov *et al*. [131] treated the M component as a current wave travelling along a transmission line that is short circuited at the ground end. They explained that the observed uniformity of the pulse shape along the channel was the result of two opposing effects. The first one being that the high-frequency

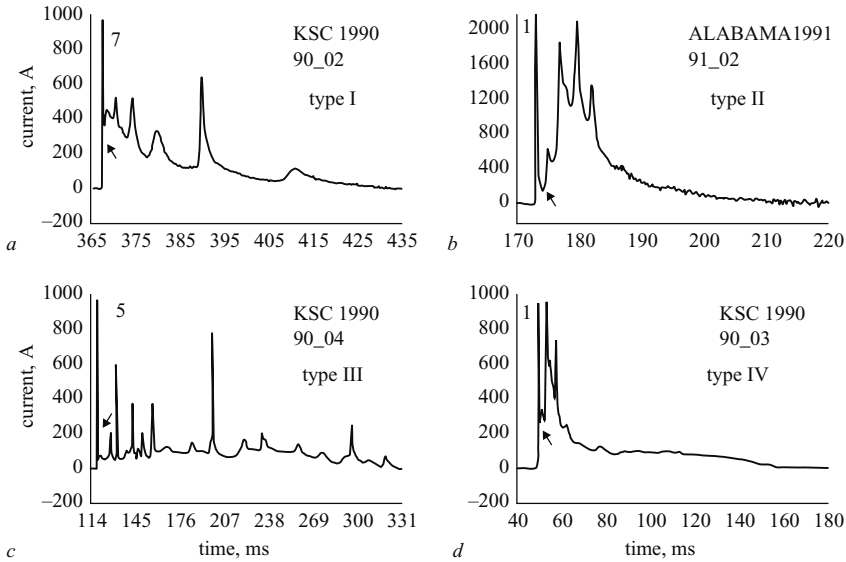

Figure 4.26 *Typical examples of continuing current wave shapes measured in triggered lightning flashes. The arrow indicates the assumed beginning of the continuing current. The subsidiary peaks in the current waveform are generated by M-components* (from [84]; reproduced by permission of the American geophysical union)

Table 4.12 *Parameters of M components; N is the number of observations, GM is the geometric mean* (from [129]; reproduced by permission of the American geophysical union)

	Units	*N*	GM	Percentage of cases exceeding the tabulated value		
				95%	50%	5%
Peak current	A	124	117	20	121	757
Rise time	μs	124	422	102	415	1785
Duration	ms	114	2.1	0.6	2.0	7.6
Half peak width	μs	113	816	192	800	3580
Charge	mC	104	129	33	131	377

components travel faster than the slow ones due to the inherent nature of the R–C line. The second one being that the M current pulse heats the channel so that the pulse tail encounters a lower resistance, thus accelerating the low-frequency components.

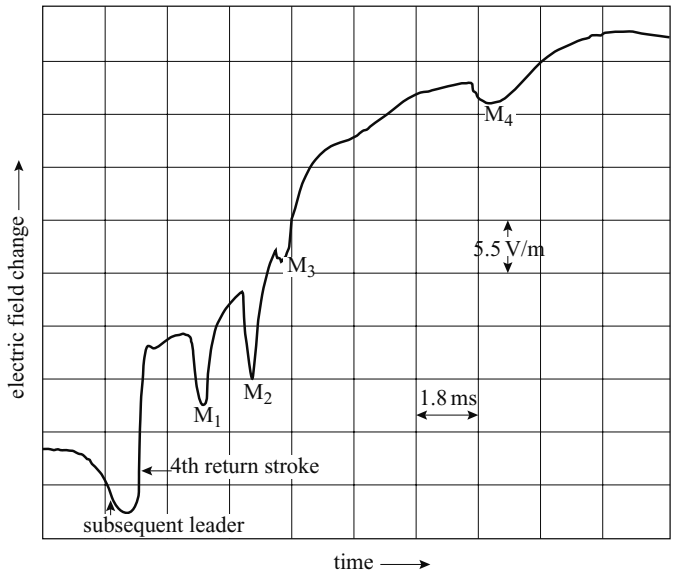

Figure 4.27 *Hooked shape M-field changes (marked M_1, M_2, M_3 and M_4) in the continuing current phase generated by the fourth return stroke in the electric field record of a lightning flash. A positive field corresponds to an upward deflection* (from [134]; reproduced by permission of the American geophysical union)

4.6.5.1 Origin inside the cloud

The observations of Shao *et al*. [6] show that M components are initiated in two ways inside the cloud. Some of the M components are initiated by a negative breakdown starting some distance from the cloud end of the return stroke channel (or the flash origin) and propagating towards it. When this discharge makes contact with the return stroke channel carrying the continuing current, an M component is initiated. The other M components are initiated as follows: immediately after the return stroke front has reached the end of the channel, a positive breakdown event propagates away from it. This generates a negative recoil event (i.e., in effect, like a return stroke travelling along the leader channel) which travels along it and towards the end of the return stroke channel. When it arrives there and makes contact with the return stroke channel it gives rise to an M component. The first type of initiation usually happens in the later stages of the continuing current phase, whereas the latter is initiated immediately after the return stroke. M components do not usually radiate in the VHF range when they are travelling along the return stroke channel.

4.6.6 K changes

K changes refer to small, millisecond duration electric field changes that occur during the interstroke intervals of cloud to ground flashes and also during intracloud

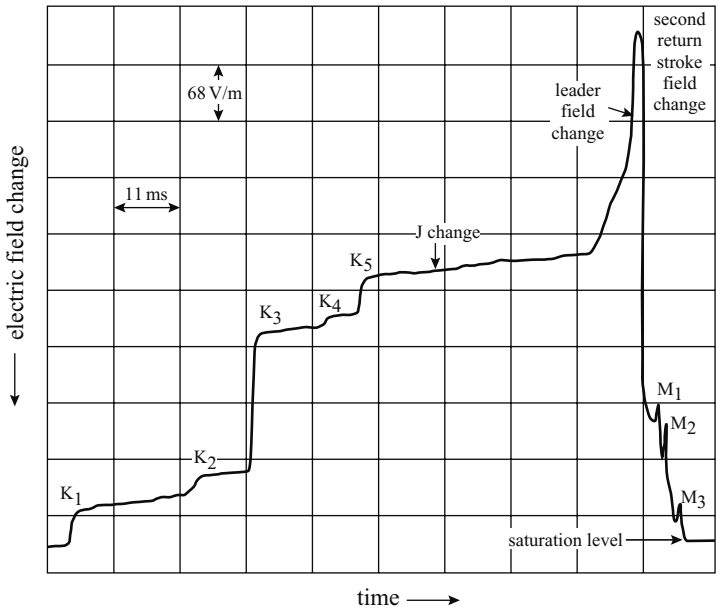

Figure 4.28 *Portion of an electric field record of a lightning flash showing the electric field changes created by K changes. A positive field corresponds to a downward deflection* (from [135]; reproduced by permission of the American geophysical union)

flashes [132,143]. Actually, the step-like field changes occurring between return strokes were first observed by Malan and Schonland [133] who interpreted them as being attributable to a leader not being able to reach ground that, instead of producing a return stroke, gave rise to a small adjustment of the charge in the cloud.

When K changes are measured with instruments having a long decay time constant (say 100 ms or more), they appear as electrostatic steps in the electric field [134,135]. Examples of K changes are shown in Figure 4.28. The polarity of the K pulses is observed to be the same as the polarity of the slow field change that occurs in between return strokes. The duration of the K pulses is distributed approximately log-normally with a geometric mean of about 0.7 ms. It is important to note that, if K pulses are measured with an antenna system with a fast decay time constant, the original step may appear as an exponentially decaying pulse ([134], see section 4.10).

The radiation field pulses associated with the K changes were analysed by Rakov *et al*. [134]. In about 23 per cent of the K changes they could detect microsecond scale pulse activity with an amplitude exceeding 50 per cent of the noise level. In many cases the beginning of the pulse activity was delayed by more than about 100 μs from the beginning of the K change. In some K changes, the initial polarity of the microsecond scale pulses was opposite to that of the K change.

4.6.6.1 Origin

Kitagawa and Brook [132] suggested that K change is a recoil event that occurs when a positive leader meets a concentration of negative charge (i.e., an event like a return stroke). This picture of a K discharge as a recoil event was disputed recently by the observations of Shao *et al*. [6]. According to these observations, K changes are negative breakdown events which often start from a point just beyond the far end of a previously active channel and move into it, thereby extending the original channel. Once the connection is made with the previously active channel, they continue to move towards the origin of the flash along this channel, but usually cease before reaching it. In some cases, when the K discharge was on its way, a burst of radiation occurred at its starting point. This was accompanied by a fast electric field change of relatively large amplitude at ground level which signals a rapid increase in current along the channel. This breakdown appears to be a process that rejuvenates the K channel at its origin, leading to an increase in the current in the channel.

The mechanism of the K change appears to be similar to that of M components, except that the latter connects to a conducting channel and transports negative charge to ground. On the basis of the differences in the distribution of time intervals between K changes and M components, Thottappillil *et al*. [135] argue that different mechanisms are responsible. Note, however, that the continuing currents, which are present during M components, may change the local conditions inside the cloud, giving rise to changes in the distribution of time interval between events.

4.6.7 Subsequent strokes

4.6.7.1 General properties

A typical ground flash may contain about four return strokes on average and, as mentioned previously, the return strokes that occur after the first return strokes are called subsequent strokes. The average separation between the subsequent strokes lies in the range 30–60 ms.

Thomson [136] investigated the characteristics of lightning flashes measured in different geographical regions to determine whether there is any systematic variation in the number of strokes per flash and the interstroke time intervals with latitude. He concluded that large differences reported in the value of the parameters in different regions are caused by the use of different measuring techniques.

A comparison between the features of return strokes in lightning flashes using the same equipment in the temperate and tropical region was conducted by Cooray and Perez [137] and Cooray and Jayaratne [138]. A summary of the statistics obtained in these studies and those obtained in Florida by Thottappillil *et al*. [139] are given in Tables 4.13 and 4.14.

In general, the peak current in the subsequent strokes is smaller than that of first return strokes. However, the tower measurements conducted by Berger [88] show that in about 15 per cent of the flashes at least one subsequent stroke may carry a peak current which is larger than that of the first stroke [139]. This fact is strengthened further by the observation that in about thirty per cent of the lightning flashes at least one subsequent stroke may generate an electric radiation field peak which is larger

Table 4.13 *Summary of interstroke interval statistics* (from [138]; reproduced by permission of the American geophysical union)

Reference	Total number of flashes	Total number of subsequent strokes	Arithmetic mean (ms)	Geometric mean (ms)
Cooray and Jayaratne [138], Sri Lanka	81	284	82.8	56.5
Cooray and Pérez [137], Sweden	271	568	65	48
Thottappillil *et al*. [139], Florida	46	199	–	57

Table 4.14 *Summary of strokes per flash and percentage of single stroke flashes* (from [138]; reproduced by permission of the American geophysical union)

Reference	Total number of flashes	Percentage of single stroke flashes, %	Mean number of strokes per flash
Cooray and Jayaratne [138], Sri Lanka	81	21	4.5
Cooray and Pérez [137], Sweden	137	18	3.4
Rakov and Uman [139], Florida	76	17	4.6

than the first. Statistics relevant to this are presented in Tables 4.15 and 4.16. Note, however, that the peak of the radiation field is not only governed by the peak current in the channel but also by the velocity of the return strokes. Thus some of the field peaks which are larger than the peak of the first return stroke are probably caused by high return stroke velocities and not by high peak currents.

4.6.8 Dart leaders

Dart leaders, which initiate subsequent return strokes, were first identified in data obtained from a series of experiments performed in South Africa in the 1930s by Schonland and coworkers [10]. The dart leader deposits negative charge along the defunct first return stroke channel and sets the stage for the subsequent return strokes. Dart leaders usually travel along the main channel of the previous return stroke and do not give rise to branches; but if the previous return stroke is the first one, then it may reenergise one or two branches. In addition to photographic techniques, the

Table 4.15 *Ratio of subsequent stroke field peak to that of the first return stroke* (from [138]; reproduced by permission of the American geophysical union)

Reference	Number of subsequent strokes	Arithmetic mean	Geometric mean
Cooray and Jayaratne [138], Sri Lanka	284	0.55	0.43
Cooray and Pérez [137], Sweden	314	0.63	0.51
Thottappillil *et al*. [139], Florida	199	–	0.42

Table 4.16 *Summary of multiple stroke flash characteristics* (from [138]; reproduced by permission of the American geophysical union)

Reference	Total number of flashes	Percentage of flashes with at least one subsequent stroke field peak larger than the first, %	Total number of subsequent strokes	Percentage of subsequent strokes with field peak larger than the first, %
Cooray and Jayaratne [138], Sri Lanka	81	35	284	12.3
Cooray and Pérez [137], Sweden	276	24	479	15
Thottappillil *et al*. [139], Florida	46	33	199	13

propagation path of the dart leader can be detected from VHF radiation that originates at the lower tip of the descending leader [6].

4.6.8.1 Optically determined properties

4.6.8.1.1 Dart leader length and speed

In optical records, the dart leader appears as a faintly luminous discharge with a bright tip of a few tens of metres long (i.e., the dart), which travels continuously along the trail of the previous return stroke. The main body of the data available concerning the speed of the dart leaders is summarised in Table 4.17. The dart leaders radiate significantly in the wavelength region 400–510 nm [140]. Thus, in evaluating the dart length it is important to take into consideration the spectral sensitivity of the film and

Table 4.17 Speed of dart leaders

Reference	Mean speed (10^6 m/s)
Schonland *et al*. [153]	5.5 (natural)
McEachron [197]	11 (natural)
Brook and Kitagawa [Winn, 204]	9.7 (natural)
Berger [24]	9.0 (natural)
Hubert and Mouget [205]	11 (triggered)
Orville and Idone [26]	11 (natural and triggered)
Idone *et al*. [206]	20 (triggered)
Jordan *et al*. [152]	14 (natural)
Shao *et al*. [6]	10 (natural)
Mach and Rust [141]	13 (triggered)
Mach and Rust [141]	19 (natural)
Wang *et al*. [198]	30–40 (triggered)
Wang *et al*. [53]	14 (natural)

any other filters used. For example, Orville and Idone [26] show examples where the differences in the measured dart leader lengths, 15 m in Florida and 42 m in New Mexico, could have been caused by the use of a red filter in the Florida measurements which excluded wavelengths below about 620 nm thereby giving a weaker image of the dart leader.

Orville and Idone found that the dart leader length and the speed are correlated with dart leader length increasing with increasing speed.

4.6.8.1.2 Spectrum and temperature of the dart leader

Orville [140] recorded the spectrum of the dart leader in the range 390 to 510 nm. All spectral lines recorded in the dart leader have been identified as singly ionised emissions which are also observed in the return stroke spectra. Combining theory with the relative intensity of NII lines at 4447 and 4630 Å, he estimated the temperature of the dart leader to be around 20 000 K, somewhat lower than the average observed for return strokes. He also estimated that the channel temperature remains around 20 000 K, at least in the channel section below the cloud base, until the arrival of the return stroke.

4.6.8.1.3 Optical signature of the dart leader

The optical signature generated by the dart leader rises to its peak value in about a microsecond [59,141,142]. After reaching a maximum**,** the pulse decays in a few microseconds to a more or less constant level. The plateau continues until it is overridden by the light waveform of the return stroke. The shape of the optical pulse of the dart leader does not change significantly with height although the pulse amplitude may increase as the leader approaches the ground. In Table 4.18 the important

Table 4.18 Rise time of dart leader optical radiation

Reference	Optical rise time (μs)
Cooray *et al*. [142]	2.9 (0 to peak rise time) (triggered)
	1.5 (20–80% rise time) (triggered)
Mach and Rust [141]	2.6 (10–90% rise time) (natural)
	1.4 (10–90% rise time) (triggered)
Wang *et al*. [199]	0.6–0.7 (10–90% rise time) (triggered)
Wang *et al*. [200]	0.5 (dart stepped leaders) (triggered)
Jordan *et al*. [59]	0.5–1 (20–80% rise time) (natural)

parameters obtained for the optical signature of the dart leader in different studies are tabulated. Since the optical radiation from long sparks shows that the rising part of the optical pulse is approximately the same as the current rise time [247], the above results indicate that the current rise time in the dart leader remains constant at around 1 μs along the channel, but the peak current may increase as the dart propagates towards the ground.

A typical dart leader is intrinsically a factor of ten less intense than return strokes [59,61]. Measurements made by Orville [140] indicate that the brighter the dart leader, the shorter the time interval between the passage of the dart leader and the return stroke, indicating that the brighter the leader, the higher the speed with which it (and also probably the ensuing return stroke) travels along the lightning channel. Idone *et al*. [206] observed a strong correlation between the dart leader speed and the peak current of the return stroke in the experiments using triggered lightning. Moreover, the light intensity of the dart leader was positively correlated with the light intensity of the return stroke [61]. That is, the brighter dart leaders have brighter return strokes. The brightness of the dart leader is a measure of the peak of the associated current. Thus, one can infer that dart leaders carrying large currents have larger speeds and that they generate return strokes with larger currents.

4.6.8.2 Origin of the dart leader in the cloud

Using VHF radiation as a tool, Shao *et al*. [6] reported that successive dart leaders in the cloud-to-ground flash tend to start further and further away from the origin of the flash. The exception was that, sometimes, successive leaders started from the same location. According to these authors, the origin of the dart leader in the cloud is no different to that of K changes and M components. The only difference in the three processes is that the dart leader makes a connection to a partially conducting return stroke channel, the M component connects to a return stroke channel which is conducting and carrying a continuing current and the K discharge stops short of reaching the return stroke channel. Sometimes the propagation of the dart leader may stop before reaching the ground; Shao *et al*. termed such events attempted leaders.

They claimed that it would be difficult to distinguish such an event from a K change solely from the electric field record.

4.6.8.3 Current and charge of dart leaders

The charge deposited on the dart leader channel has been determined by Brook *et al*. [144] to be a minimum of 0.2 C with the most frequent value between 0.5 and 1 C. These values also agree with the charge brought to ground by subsequent strokes [88]. The dart traverses the return stroke channel with a length of about 5 km in about a millisecond; the total charge of 0.5 C then corresponds to a current of about 1 kA. By using the observed correlation between the dart leader speed and the return stroke current, both Idone and Orville [61] and Cooray *et al*. [142] have estimated the dart leader current to be about a kilo ampere on average.

As in the case of the stepped leader, a rough estimation of the way in which the dart leader charge is distributed along the channel can be obtained through charge simulation methods by treating the dart leader as a conducting channel connected to a spherical electrode of several kilometres radius and raised to the cloud potential [37]. If the electric field below the cloud is uniform, then the charge density per unit length of the dart leader increases linearly towards the ground except for the last few tens of metres close to the ground. Due to the influence of the ground the charge on the last few tens of metres increases almost exponentially towards the ground. Unfortunately, no measurements are available today to pin point the distribution of the dart leader charge.

The charge per unit length on the dart leader channel located very close to the ground can be estimated from the electric field changes produced by dart leaders within about 200 m. Results obtained in this manner indicate that the charge per unit length close to the ground has a strong linear correlation to the peak current of the ensuing return stroke [86]. When interpreted using a uniformly charged leader channel, these results indicate that the value of ρ_0 lies in the range 7–12 μC/m for each kA of the peak current of the return stroke at the channel base.

4.6.8.4 Static fields generated by dart leaders

The features of slow fields produced by dart leaders in lightning flashes were originally described by Malan and Schonland [133] and, more recently, electric fields generated by dart leaders in triggered lightning flashes have been described by Rubinstein *et al*. [145] and Rakov [86] and Crawford *et al*. [207] An example from the recent studies is shown in Figure 4.17. The qualitative features of the near fields produced by dart leaders can be simulated by assuming the dart leader to be a uniformly charged channel which propagates towards ground with a constant speed.

4.6.8.5 RF radiation from dart leaders

Dart leaders produce considerable radiation in the HF, VHF and microwave regions. Shao *et al*. [6] show that the VHF radiation pulses associated with the dart leader propagate downwards along the defunct return stroke channel indicating that the dart leader head is a strong source of RF radiation. The RF radiation starts from

100 to 1000 μs before the return stroke and in some cases it ceases from 50 to 100 μs before the return stroke, whereas in other cases it may continue up to the return stroke (see Figures 4.22 and 4.23). The cessation of the RF radiation just before the return stroke could be partly attributable to propagation effects.

4.6.8.6 The parameters that control the dart leader speed

Cooray [151] modelled the dart leader as a self propagating discharge that carries a high electric field at the front which is strong enough to cause electrical breakdown in the defunct return stroke channel. The electric field at the front of the dart leader depends on both the current flowing behind it (and hence on the charge being stored on the dart leader) and the speed of the dart leader. Thus, by equating this field to the critical electric field necessary to cause electric breakdown in the defunct return stroke channel, a relationship was derived between the dart leader speed, its current and the temperature of the defunct return stroke channel through which it propagates. The results show that the speed of the dart leader increases with increasing current amplitude (and hence with increasing charge on the leader), with decreasing current rise time and with increasing temperature of the defunct return stroke channel.

If the charge on the dart leader increases as it propagates towards the ground, then its speed may also increase as it approaches the ground provided that the temperature of the defunct return stroke channel and the rise time of the dart leader current does not vary with height. The measurements show that the rise time of the optical signature generated by the dart leader does not vary significantly as the dart leader propagates towards the ground. This indicates that the rise time of the dart leader current does not vary as a function of height. On the other hand, the channel temperature may not remain constant as a function of height. If the channel sections close to ground decay faster than the rest of the channel, the dart speed may decrease as it approaches the ground, if the charge on the dart leader remains unchanged. Depending on the way in which the dart leader charge and the channel temperature vary with height, some dart leaders may show a tendency to increase their speed as they propagate towards the ground and the others may show the opposite tendency.

If the charge and the current rise time of dart leaders are independent of the interstroke time interval one may observe a tendency for the dart leader speeds to decrease with increasing time interval between return strokes. This is the case since the temperature of the defunct return stroke channel decreases with increasing interstroke time interval. However, one cannot rule out the possibility of the charge on the dart leader increasing with increasing time interval between strokes. Thus, it is difficult to predict the dependence of the dart leader speed on the interstroke time interval. Depending on the amount of charge transported down, some dart leaders may show a tendency to increase their speed with increasing interstroke interval and others may show the opposite tendency.

Unfortunately, all of the parameters that control the dart leader speed could change both spatially and temporally in an – as yet – undefined manner, and it is not easy to relate the speed of the dart leader to any one of these parameters. These facts should be kept in mind in the interpretation of the information given in the next section.

4.6.8.7 Correlation between parameters of dart leaders and return strokes

4.6.8.7.1 Dart speed and the interstroke interval

Schonland [10] reports that the higher dart leader speeds in natural lightning occur when the leaders follow the previous stroke with little delay and that low speeds are associated with longer time intervals. Such a relationship, though weak, is also found by Jordan *et al*. [152] for natural lightning. The triggered lightning data apparently exhibited the opposite tendency, however there was a clear trend for the maximum leader speed to decrease with an increasing previous return stroke interval. For successive interstroke interval ranges of 0–30, 30–70 and 70–140 ms, the maximum dart leader speed observed was 49×10^6, 34×10^6 and 12×10^6 m/s.

Schonland *et al*. [153] never found that the speed of the dart leader increased as the leader approached the ground, while Orville and Idone [26] found that in four cases out of 26 it did. Orville and Idone [26] report that the best recorded data set in their study did not only show an increase in speed, but the light output increased by a factor of two from cloud base to ground. In agreement with the observations of Schonland *et al*. [153], Orville and Idone also observed dart leaders decreasing in speed near the ground. Orville and Idone warned, however, of the possibility that the speeds determined are two dimensional and some variations could arise because of channel geometry, which cannot be identified in two-dimensional photographs.

4.6.8.7.2 Dart speed and the dart length

Orville and Idone [26] found that the length of the dart leader increases with increasing speed of the dart. This correlation is shown in Figure 4.29; the correlation coefficient was 0.72. If the duration of the luminosity of a given point on the channel caused by the current of the dart leader is τ then the length of the dart is given by τv, where v is the speed of the dart leader. The laboratory experiments show that the duration of the channel luminosity of long sparks having identical current waveshapes became longer with increasing peak current [247]. This observation suggests that the duration of the luminosity may also increase with increasing current and hence with the speed of the dart leader. The latter is likely since the experimental data hints that the larger dart speeds are associated with larger currents [61,206]. This makes the dart leader length increase more rapidly than linearly with increasing speed.

4.6.8.7.3 Dart speed and the return stroke current

As mentioned previously, Idone *et al*. [206] found a strong correlation between the speed of the dart leader and the peak return stroke current. This relationship can be understood easily if the speed of the dart leader and the return stroke are controlled by the charge density deposited by the dart leader along the lightning channel. Larger amounts of deposited charge will give rise to dart leaders with higher speeds and return strokes with larger currents. Indeed, the field measurements conducted very close to the triggered return strokes show that the peak return stroke current increases

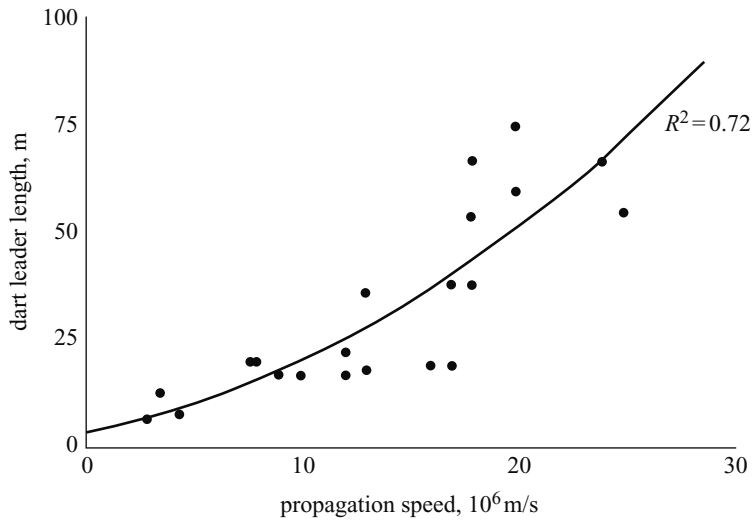

Figure 4.29 *Dart leader length versus speed of propagation along the channel* (from [26]; reproduced by permission of the American geophysical union)

approximately linearly with increasing leader charge [85] – hence, the connection between the dart leader speed and the return stroke current.

4.6.8.8 Dart stepped leaders

Schonland [10] was first to report that if the time interval to the previous return stroke is large, some of the dart leaders resume the stepping process when they approach the ground. In the literature such leaders are called dart stepped leaders. The steps in the dart stepped leaders are relatively short, about 10 m, and the time interval between the steps is about 5–10 μs. Data that confirms these observations of dart stepped leaders was obtained recently by Orville and Idone [26]. The average downward speed of dart stepped leaders, about $0.5–1.7 \times 10^6$ m/s is somewhat slower than for dart leaders. Wang *et al*. [147] found the rise time of the optical pulse created during the formation of a step of a dart stepped leader step to be about 0.5 μs and the half peak width (width of the peak at half maximum) to be about 1.3 μs. Moreover, they found that the formation of the step gives rise to an optical signature that travels upwards along the leader channel at a speed of about $(0.2–1) \times 10^8$ m/s, for a distance from several tens of metres to more than 200 m, beyond which it becomes undetectable.

In the records on electric radiation fields, one can identify the electric field pulses produced by the dart stepped leaders. Krider *et al*. [33] found that the mean time interval between the pulses of the radiation field produced by the dart stepped leaders immediately before the subsequent return strokes is about 6–8 μs, which is shorter than the 10–15 μs observed for the stepped leader pulses immediately preceding the first return strokes.

4.6.8.9 Chaotic leaders

Weidman [148] reported that some of the electric fields of subsequent return strokes were preceded by a train of pulses irregular in shape, width and separation. He named these return strokes chaotic subsequent strokes or subsequent strokes preceded by chaotic leaders. Bailey and Willett [149] illustrated one such subsequent stroke recorded about 25 km from the place of impact. Gomes *et al*. [150] analysed the characteristics of these chaotic pulse trains (CPT) in detail. One example from their study is shown in Figure 4.30. Gomes and coauthors reported that the width of the individual pulses of these pulse trains is in the range of a few microseconds, the lower limit of which may, however, extend into the submicrosecond region. The pulse separation lies in the range of 2–20 μs. The most probable duration of the CPT is 400–500 μs. Eighty four (about 25 per cent) of the CPT that these authors have observed preceded subsequent return strokes. Among these CPT, sixty five immediately preceded a subsequent stroke and continued up to the return stroke, and the rest had a delay between the end of the CPT and the return stroke. This delay varied from 0.35 to 73 ms. Gomes *et al*. [150] observed such chaotic pulse trains in ground flashes, but without any association with return strokes; they also observed them in cloud flashes. The fact that CPT occur before subsequent return strokes indicates that they are probably connected with the initiation of dart leaders. Since the initiation processes of K changes and M components are identical to that of dart leaders, it is not surprising that CPT occur in cloud flashes and in ground flashes without any association with return strokes.

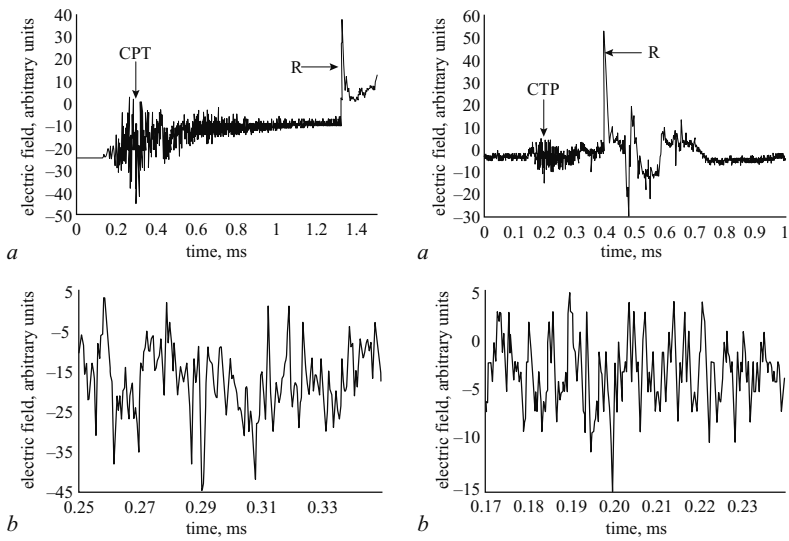

Figure 4.30 *Two examples (figures marked a) of chaotic pulse trains (marked CPT) preceding subsequent return strokes (marked R). The lower traces (marked b) show a portion of the pulse train in a faster time scale. A positive field corresponds to an upward deflection* (adapted from [150])

4.7 Electromagnetic fields generated by cloud flashes

4.7.1 General features

The average duration of the cloud flashes as measured from records of electric field changes can range from about 200 ms to about 500 ms. Typical slow electric fields generated by cloud flashes within about 10 km are shown in Figure 4.31. Note that the fields can be either unipolar or bipolar. The change in the dipole moment associated with the cloud discharges may be of the order of 100 Ckm. The charge transfers associated with the discharge as evaluated from the electric field measurements may range from 0.3 to 100 C. Several attempts were made to extract information concerning the average separation between the charge centres that take part in the discharge and values were found in the range of 0.5 km to about 3 km [154].

The most extensive study of the electric fields generated by cloud flashes was conducted by Kitagawa and Brook [132]. According to these authors, the electric field signature of cloud flashes consists of three portions which they classified as initial, very active and the final stage. The initial portion has a typical duration of 100–200 μs and is characterised by small microsecond scale pulses. During the very active portion, pulse activity is accentuated and is characterised by the pulses with

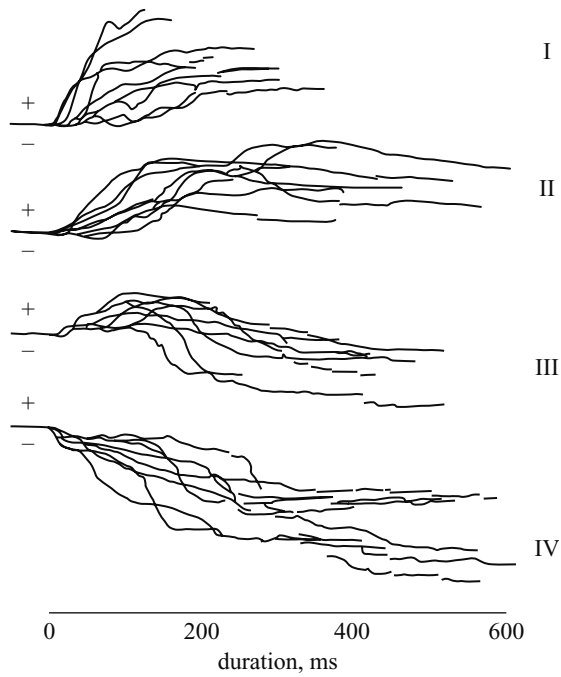

Figure 4.31 Different types of slow electric field change produced by cloud flashes (adapted from [124])

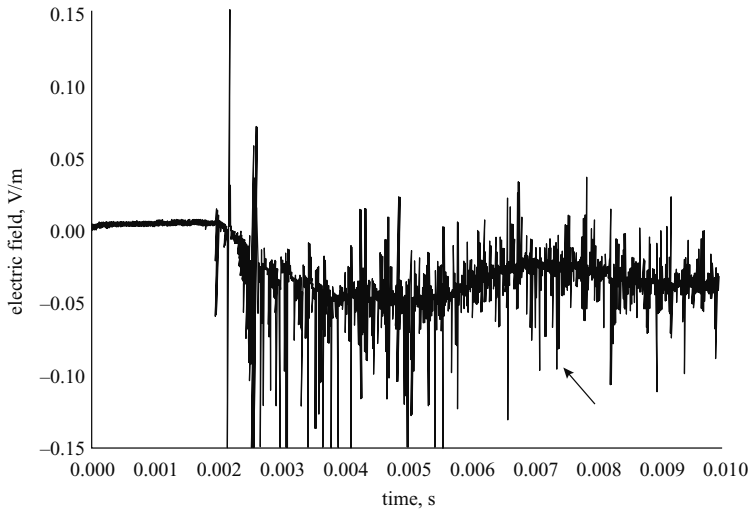

Figure 4.32 Radiation field pulses generated by cloud flashes within the first 10 ms from its beginning. The distance to the flash is about 10 km. The arrow indicates the location of the pulse shown in Figure 4.36. A positive field corresponds to an upward deflection (see [164] for the details of the experiment). The vertical scale should be multiplied by 100 to get the amplitude in V/m.

the highest amplitudes in the flash. The final stage is composed of relatively small step-like electrostatic field changes generated by the K changes. Out of about 1400 cloud discharges studies, 50 per cent contained all the three categories of electric field signature, 40 per cent exhibited both very active and final stages, and in ten per cent the final portion was not identified, but they did have either the initial or active phases or both. In contrast, Bils *et al*. [155] and Villanueva *et al*. [156] show that the largest microsecond scale pulses occur predominantly in the initial part of the cloud flash, typically in the first 20 ms. However, in agreement with Kitagawa and Brook, they find that the final portion of the flash consists of sequences of K changes. Figure 4.32 shows an example of the radiation field pulses generated by cloud flashes within the first 10 ms of flashes recorded in Sweden. The arrow indicates the location of the pulse shown in Figure 4.36. Note that, in agreement with the work presented by Bills *et al*. and Villanueva *et al*., the largest pulse amplitudes are generated within the first few milliseconds of the flash.

4.7.2 Radiation field pulse characteristics

Five categories of radiation field pulses have been observed in cloud flashes. These are:

(i) large bipolar pulses with several structures superimposed on the initial half cycle

(ii) bursts of pulses similar to the dart stepped leader pulses
(iii) narrow isolated pulses
(iv) microsecond scale pulses with a smooth rise to peak
(v) chaotic pulses as described in an earlier section.

Different types of radiation fields generated by cloud flashes are shown in Figures 4.33 to 4.36.

4.7.2.1 Large bipolar pulses

According to Weidman and Krider [157], cloud flashes generate large bipolar pulses with both positive (according to the definition of polarity adopted in this Chapter) and negative initial polarity (Figure 4.33). The pulses of positive initial polarity are very similar to the characteristic pulses in the preliminary breakdown stage of return strokes. The bipolar pulse bursts with positive initial polarity analysed by these authors did not lead to return strokes and thus could be characterised as cloud flashes. Their polarity indicated that the breakdown process transferred negative charge towards the ground. This kind of pulse activity should be distinguished from typical cloud flashes in which the initial pulse polarity tends to be negative.

The shape of the large bipolar pulses tends to be bipolar, with almost always two or three fast pulses, with submicrosecond rise times and microsecond widths, superimposed on the rising part. The time interval between these fast unipolar pulses that are superimposed on the initial portion of the bipolar waveforms averaged $7.8 \pm 5.7\,\mu s$ for 66 positive and $15 \pm 14\,\mu s$ for 78 negative waveforms. The intervals tend to increase with increasing pulse width.

The time interval between the bipolar pulses with positive initial polarity is about $130\,\mu s$ and for negative initial polarity the pulse separation is $780\,\mu s$ on average. For a total of 137 negative pulses Weidman and Krider report a mean total pulse duration of $63\,\mu s$ and a ratio of initial peak to overshoot peak of 3.6. The corresponding value for positive pulses was 2.1. The average duration they found for positive pulses was $41\,\mu s$ for 117 pulses.

The spectrum of these pulses obtained by Weidman and Krider [118] and Willett *et al*. [158] matched the return stroke spectra above 2–3 MHz. The time derivatives of the electric field associated with the pulses were analysed by Weidman and Krider [159] and an average value normalised to 100 km of about 20 V/m/μs was found. This value is slightly less but of the same order of magnitude as derivatives of the return stroke field. It is important to note that normalisation to 100 km using the inverse distance dependence is only valid if the channel is vertical, whereas some of the cloud pulses are definitely generated by channel sections which are far from vertical.

4.7.2.2 Bursts of pulses similar to the dart stepped leader pulses

Krider *et al*. [160] observed regular sequences or bursts of microsecond scale pulses with an amplitude of about an order of magnitude smaller than the return stroke pulses. Each burst had a typical duration of 100–400 μs with a mean time interval between individual pulses of about 5–6 μs. The total duration of a single pulse was typically

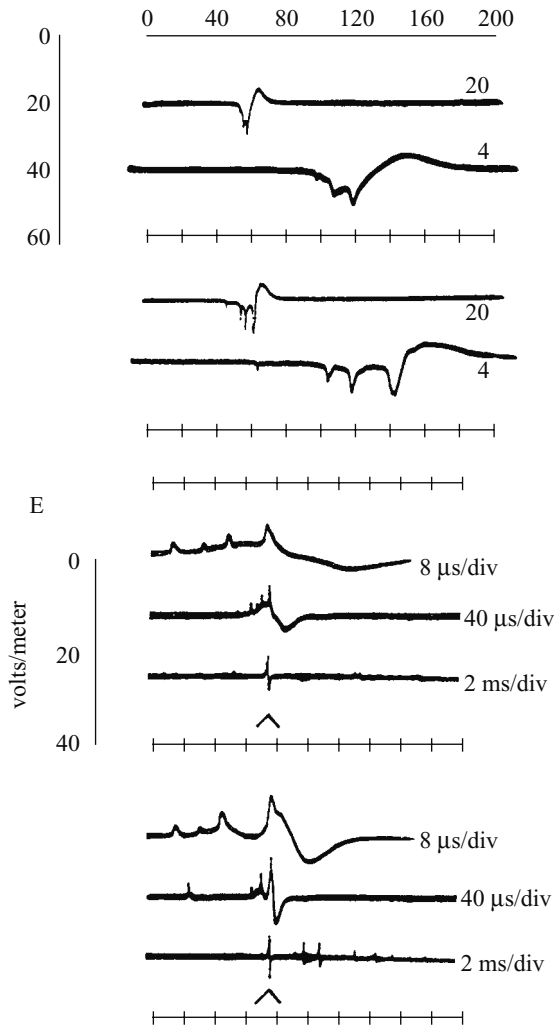

Figure 4.33 *Large bipolar pulses with positive and negative initial polarities generated by electrical activity in the cloud. Note the pulses superimposed on the initial rising part of the waveform. Each waveform is shown on two (20 μs/div or 4 μs/div) or three (8 μs/div, 40 μs/div and 2 ms/div) timescales. A positive field corresponds to a downward deflection* (from [157]; reproduced by permission of the American geophysical union)

1–2 μs with the zero crossing time at about 0.75 μs. The spectrum of the typical pulse sequence peaked around 200 kHz. The pulse bursts tends to occur towards the end of intracloud discharges and the authors suggest that the pulse burst could be due to an intracloud dart-stepped leader process. Similar pulse bursts have been observed by

Rakov *et al*. [161] both in cloud flashes and in cloud activity taking place between return strokes in ground flashes (Figure 4.34). In the latter case, the amplitudes of the individual pulses were two orders of magnitude smaller than the initial peaks of the return stroke in the same flash. There is a tendency for these bursts to occur in the latter stages of the discharge and positive and negative polarity pulses are

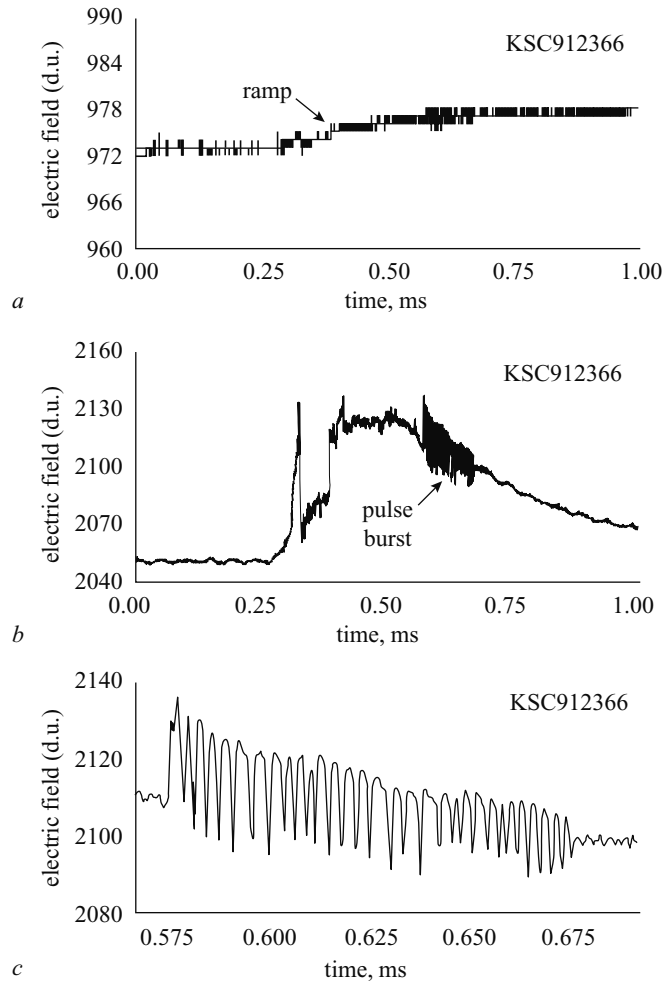

Figure 4.34 *Bursts of pulses similar to the dart stepped leader pulses generated by electrical activity in the cloud. (a) The location of the pulse burst in a ramp-like field change produced by the cloud flash. The pulse burst is shown in two time scales in (b) and (c) A positive field corresponds to a downward deflection* (from [161]; reproduced by permission of the IEEE)

equally probable. Many bursts were found to be associated with the latter part of K changes.

4.7.2.3 Narrow isolated pulses

Weidman and Krider [157] report that the first signals radiated by developing storms are single fast negative pulses with an initial half cycle of about 10 μs (judging from the waveform reproduced in their paper). Interestingly, LeVine [162] found that the source of the strongest RF radiation at 3, 139 and 295 MHz generated by lightning flashes is a short duration bipolar pulse with negative initial polarity. Most probably these pulses are identical to those reported by Weidman and Krider. Pulses similar to these are also described by Cooray and Lundquist [32], Bils *et al*. [155] and Willett *et al*. [163]. Several examples of these pulses are shown in Figure 4.35. The average duration of the negative half cycle or zero crossing of these pulses was 10 μs or less. The total duration of the pulses is about 20–70 μs and the peak amplitude is of the order of one third of the peak obtained by return strokes recorded from the same thunderstorm. In the VLF range the peak of the spectrum of the pulses occurred at

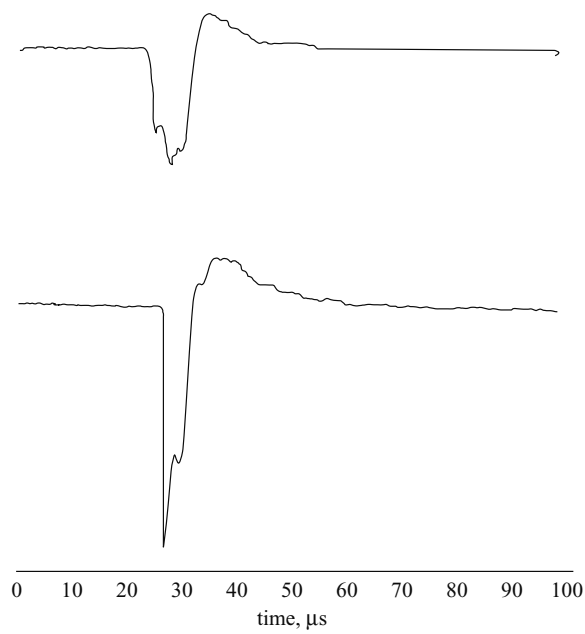

Figure 4.35 *Narrow isolated pulses generated by electrical activity in the cloud. Observations indicate that these pulses are generated by cloud activity in the growing stage of the thundercloud. The vertical scale is linear in V/m but uncalibrated. A positive field corresponds to an upward deflection* (from [162]; reproduced by permission of the American geophysical union)

10–24 kHz with 16 kHz as the average. These pulses had a higher spectral content above 1 MHz than the return stroke spectral amplitudes. However, it is possible that the difference is caused by the different propagation characteristics of these pulses and return stroke fields. These pulses occurred in isolation without detectable electrical activity before or after the pulse. They are probably produced by electrical discharges of several hundred metres in length that did not culminate in a full scale lightning discharge.

4.7.2.4 Microsecond scale pulses with a smooth rise to peak

Fernando and Cooray [164] discovered that, in addition to the bipolar pulses described previously, the pulses generated by cloud flashes within the first 10 ms (the length of their record) of its initiation contain microsecond scale pulses with a smooth rise to peak (Figure 4.36). The location of the pulse in Figure 4.36 of in the pulse burst generated by a cloud flash within the first 10 ms is shown by an arrow in Figure 4.32. Most of these pulses begin with a slow front which rises slowly for 0.05–4 μs to about 20 per cent of the peak field amplitude. At the end of the slow front the field rises rapidly to its peak value in about 0.1–0.2 μs. Even though the average duration of these pulses was more than an order of magnitude shorter than the duration of return stroke radiation fields, the characteristics of the initial rising portion of the

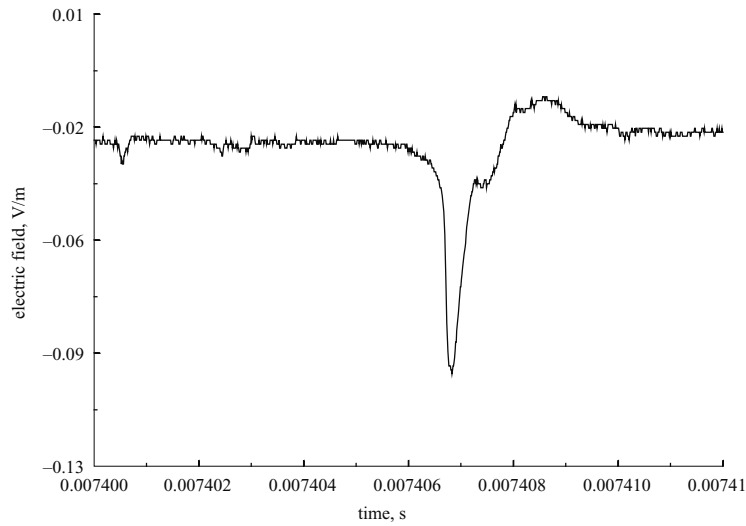

Figure 4.36 An example of microsecond scale pulses with a smooth rise to peak embedded in the electrical activity of a cloud flash. Note the slow front followed by the fast transition. The location of this pulse in the pulse burst generated by the cloud flash within the first 10 ms is shown by an arrow in Figure 4.32. A positive field corresponds to an upward deflection (see [165] for the details of the experiment). The vertical scale should be multiplied by 100 to get the amplitude in V/m.

cloud pulses show a remarkable similarity to those of the radiation fields generated by subsequent return strokes.

4.8 The difference between the ground flashes and cloud flashes

The main difference between the ground flashes and cloud flashes is that the ground flashes neutralise the charge centre in an intermittent manner in a number of high current events, that is, subsequent strokes, whereas in a cloud flash a continuous current may flow from one charge centre to the other during the initial and active part of the cloud flash. Only in the latter part of the cloud flash do intermittent breakdowns transfer charge from the negative to the positive. This difference is probably caused by the fact that in ground flashes the presence of the ground will lead to a rapid neutralisation of the leader channel, giving rise to return strokes, whereas no good conductor is involved in cloud flashes and the neutralisation process should take place slowly in comparison with the return strokes. An interesting comparison can be made between the lightning flashes and laboratory discharges. Discharge between two metal electrodes takes place in one burst of return stroke, whereas a discharge between two nonconducting materials takes place intermittently in a series of discharges with low current amplitude [165]. The reason for this is that, in the case of nonconducting electrodes, the charges transported along the discharge channel will accumulate at its extremities, thereby reducing the electric field and choking the discharge. As the charges dissipate slowly, the electric field recovers and reignites the discharge channel. In ground flashes the problem of charge dissipation is encountered only at the cloud end of the leader, whereas in cloud flashes the difficulty exists at both ends. Another difference is that in ground flashes the channels extend downwards to a high-pressure region, whereas the vertical channel of cloud flashes extends into the low-pressure region [15]. Owing to high pressure close to the ground level the ground end of the channel decays first and it will continue progressively into the upper reaches of the cloud. In the meantime negative charge continues to flow down the still conducting part of the channel. This would have the effect of filling the decaying channel with negative charge making it more difficult for the next discharge to occur. In the case of cloud flashes, the channel would be cut off first at the negative charge centre and as a result no negative charge will accumulate along the channel. Since most of the discharge events in a cloud flash travel upward from the negative to positive charge centre, this will make it easier for the subsequent discharges to reignite the upward path and maintain its conductivity.

4.9 Energy dissipation in return strokes and lightning flashes

The amount of energy dissipated during lightning flashes is an important parameter in many investigations involving lightning. It must be considered when characterising lightning flashes using their optical radiation from geostationary satellites and when quantifying the atmospheric production of ozone and nitrogen oxides etc. For

Table 4.19 Estimates of energy in lightning derived from electrical measurements

Reference	Cloud potential assumed in the calculation, MV	Channel height, km	Charge dissipated, C	Energy, J	Comment
Wilson [166]	500	2	20	10^{10}	leader + return stroke
Malan [167]	500		0.6	3×10^8	leader + return stroke
Krider *et al.* [168]	300		4.6	7×10^8	leader + return stroke
Connor [170]		1.8	9.3	1.5×10^8	return stroke
Berger [171]	30	5	5.0	1.5×10^8	leader + return stroke
Uman [169]	100	3	5	5×10^8	leader + return stroke
Cooray [52]		5–7	variable (0.5–9)	3.5×10^8	energy given is for the return stroke stage with 5 C of charge dissipation

example, the uncertainty involved in estimating the amount of NO_x produced by lightning flashes can be attributed mainly to our poor knowledge about energy dissipation in lightning flashes. Unfortunately, it is not possible to measure the energy dissipated in a lightning flash directly. Consequently, researchers have employed indirect methods for this task. These methods can be divided into four categories. In the first category the amount of energy dissipated in lightning flashes is calculated on the basis of electrostatic energy considerations [166–171]. The energy dissipation is calculated by assuming that a known amount of charge is transferred across a known potential difference during the lightning flash. The potential of the thundercloud with respect to the earth is estimated by using familiar electrostatics principles. Table 4.19 summarises the results obtained by this method. In the second category the energy dissipation in lightning flashes is derived from the measured optical radiation [170,168,172,64–66]. In the analysis, experimentally obtained relationships between the electrical and optical energy in spark discharges were extrapolated to obtain the electrical energy dissipation in lightning flashes on the basis of the measured optical radiation. Table 4.20 summarises the results obtained. In the third category the energy dissipation in lightning flashes is estimated by measuring the spectrum of thunder and relating it to the energy dissipation by applying the theory of shock waves [173,174]. Table 4.21 summarises the results obtained. In the fourth category the shape and amplitude of the return stroke current are assumed, and the energy dissipated in the channel is calculated by analysing the temporal development of the channel properties

Table 4.20 *Estimates of energy in lightning derived from optical measurements* (from [190]; reproduced by permission of the American geophysical union)

Reference	Optical band, Å	Radiant energy per unit length, J/m	Mean peak radiant power, W	Energy dissipation per unit length, J/m
Connor [170]	3800–7000	580		
Barasch [172]	visible	400	4×10^9 (stroke)	
Krider *et al*. [168]	4000–11000	870	1.1×10^{10} (stroke)	2.3×10^5
Turman [179]	4000–11000		10^9 (first stroke)	

Table 4.21 *Estimates of energy in lightning derived from acoustic measurements* (from [190]; reproduced by permission of the American geophysical union)

Reference	Energy estimate, J/m
Zhivlyuk and Mandel'shtam [173]	10^3
Newman [80]	10^2
Hill and Robb [195]	5×10^4–10^5
Few [174]	10^5

Table 4.22 *Estimates of energy in lightning derived from the theoretical analysis of the temporal development of channel properties*

Reference	Energy dissipation, J/m
Plooster [175]	2.5×10^3
Hill [176]	1.5×10^4

as a function of time [175–177]. Table 4.22 summarises the results obtained using this technique.

It is important to note that most of the estimations of the return stroke energy based on electrostatics assume that all the energy available for the leader return stroke sequence is dissipated in the return stroke (this is not true since part of this energy will be dissipated in the leader stage; see section 4.6.2.8) and only a few models

include a realistic cloud charge model. Moreover, many models presume the cloud to be at a certain potential with respect to ground but, since the cloud is an extended structure, the concept of cloud potential does not have a very strict physical meaning. For example, the potential of the cloud may change from one point in the cloud to another. Cooray [52] improved upon these results by incorporating a reasonable cloud charge model and considering different stages of the lightning flash. His results show that the total energy dissipation during the leader return stroke process, E_t, and the energy dissipation during the return stroke process, E_r, can be analytically represented as a function of the charge, q, neutralised during the return stroke process by:

$$E_r = 0.39 \times 10^8 q^{1.4} \tag{4.15}$$

$$E_t = 1.24 \times 10^8 q^{0.93} \tag{4.16}$$

where E_r and E_t are given in J and q is given in C. The difference $(E_t - E_r)$ gives the energy dissipation during the leader stage as a function of q. He also made a comparison of the energy dissipation in ground and cloud flashes as a function of the total charge neutralised. His results, depicted in Figure 4.37, show that for a given amount of charge neutralisation, a cloud flash dissipates more energy than a ground flash.

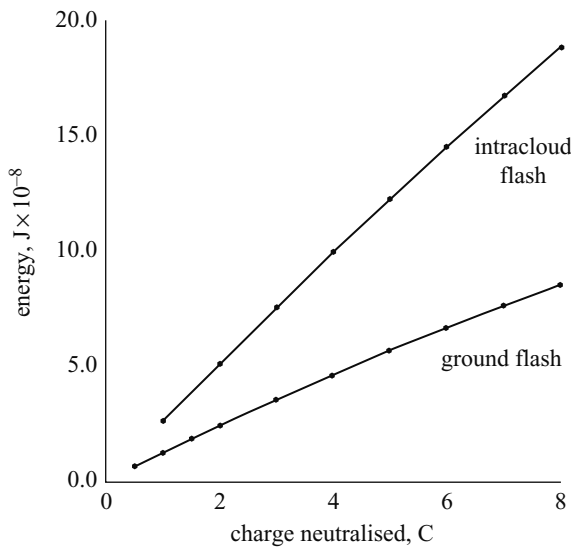

Figure 4.37 *Energy dissipation in cloud flashes as a function of the total charge neutralised. For comparison purposes the amount of energy released in return strokes (leader/stroke sequence) are also given in the figure. In the calculation it was assumed that the heights to the negative and positive charge centres are 7 km and 12 km respectively* (from [52]; reproduced by permission of the American geophysical union)

4.10 Measuring lightning-generated electric and magnetic fields

The electric fields generated by lightning flashes can be measured either using a field mill [223] or a flat plate (or a vertical whip) antenna [132,224], each method having its advantages and disadvantages. The conventional method used to measure the magnetic field is the crossed loop antenna [225,226,181]. The following is a brief description of these techniques.

4.10.1 Electric field mill or generating voltmeter

The principle of operation of the field mill is illustrated in Figure 4.38. The plate marked S is the detector which is placed in a background electric field assumed for the moment to be uniform and steady. The plate marked M is a movable electrode which is at ground potential. This electrode can be moved back and forth in front of the sensing plate either exposing it to or screening it from the background electric field. Consider the situation shown in the Figure 4.38 in which the sensing plate is completely exposed to the electric field. The electric field lines end on the plate and the total charge induced on the sensing plate is $A\varepsilon_0 E$ where A is the area of the plate. Assume that the plate M is moved back and forth in front of the sensing plate. This will change the exposed area of the sensing plate as a function of time and since the charge induced on the plate is a function of the exposed area of the sensing plate a current will flow between the sensing plate and ground. This current is given by:

$$i(t) = \epsilon_0 E \frac{\mathrm{d}_a(t)}{\mathrm{d}t} \tag{4.17}$$

where $a(t)$ is the instantaneous exposed area of the sensing plate. Thus, knowing the way in which the exposed area of the sensing plate varies in time, the background electric field can be obtained by measuring the current flowing between the sensing plate and ground.

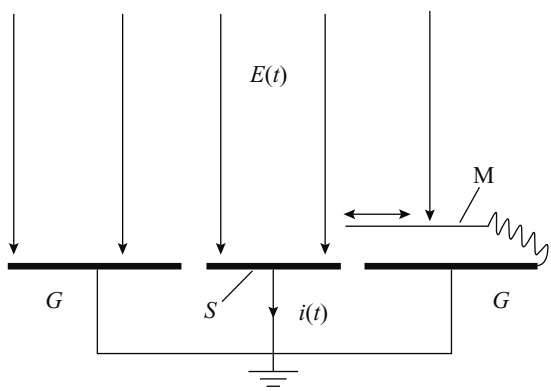

Figure 4.38 Principle of the electric field mill

Assume that M moves periodically back and forth over the sensing plate, thus alternately shielding and unshielding the sensing plate from the background electric field. If M moves back and forth n times per second then the output current oscillates with a period, T_p, equal to $1/n$ and the peak amplitude proportional to the background electric field. If the background field varies with time then the envelope of the oscillating output voltage follows the background electric field. However, any rapid variation in the background electric field faster than the period T_p cannot be measured using the field mill. In other words, the time resolution of the field mill is of the order of T_p. Thus, the rate of the periodic motion of M gives an upper limit to the resolution of the field that can be measured by a field mill. In modern field mills the time resolution is increased by utilising a rotating vaned wheel which alternatively shields or unshields the sensing electrode from the electric field as each vane rotates over it. If the rotational speed of the metal vane is n revolutions per second, and if it has m vanes then the time resolution of the field mill will decrease to $1/mn$. Such field mills can measure faster variations in the background electric field than the one described above. In general, the upper frequency limit of the modern field mills may range from 1 to 10 kHz. The main advantage of the field mill is that it can be used to measure the absolute value of the background field.

4.10.2 Plate or whip antenna

The physical configuration of the plate (or whip) antenna is shown in Figure 4.39. In principle, the antenna is a metal object connected to ground through electric circuitry. As the background electric field varies in time, the charge induced on the antenna also varies in time generating a current in the electrical circuitry.

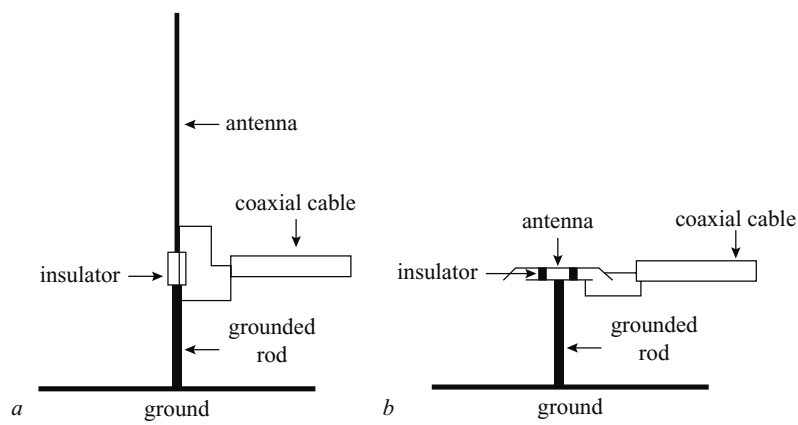

Figure 4.39 Antennas for the measurement of lightning generated fields
a whip antenna
b plate antenna
The end of the cable is connected to the electronic circuit shown in Figure 4.41

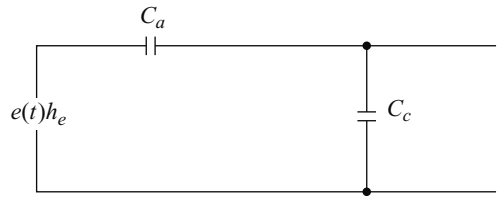

Figure 4.40 *Equivalent circuit of the electric field measuring antenna. $e(t)$ is the background electric field, h_e is the effective height of the antenna, Ca is the capacitance of the antenna and Cc is the capacitance of the cable.*

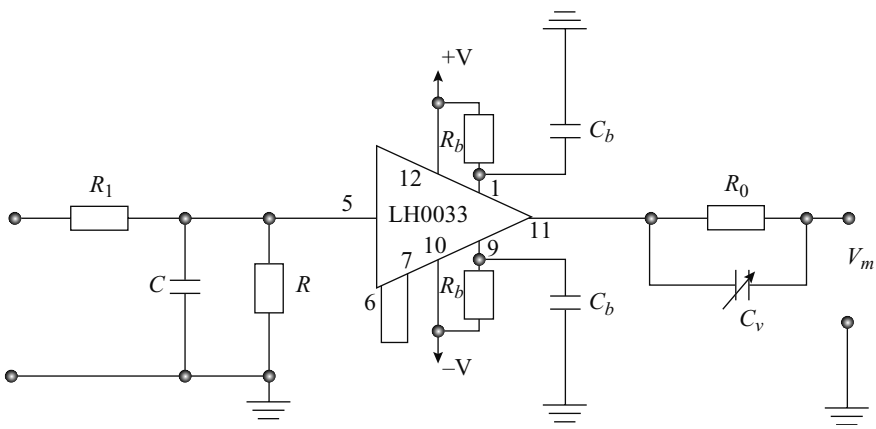

Figure 4.41 *Electronic circuit used by Uppsala researchers in the measurement of electric fields using plate antenna. $R_1 = 50\,\Omega$, $R = 99\,M\Omega$, $C = 15\,pF$–$10\,nF$, $R_b = 100\,\Omega$, $R_o = 43\,\Omega$, $C_b = 0.1\,\mu F$ and $C_v = 91\,pF$. LH0033 is an operational amplifier with an input impedance of $10^{13}\,\Omega$*

If the dimension of the antenna is much smaller than the minimum wavelength of interest in the time-varying electric field, the antenna will act as a capacitive voltage source with the voltage proportional to the background electric field, $e(t)$.

The equivalent circuit of the antenna shown in Figure 4.39 is depicted in Figure 4.40 where C_a is the capacitance of the antenna to ground and C_c is the capacitance of the cable connected to the antenna. The effective height, h_e, of the antenna can be either calculated from theory or measured by applying a known electric field to the antenna and measuring the output voltage.

The electronic circuitry that can be used to obtain the background electric field from a plate or whip antenna is given in Figure 4.41. The equivalent circuit of the electronic circuitry when connected to the antenna is given in Figure 4.42. The relationship between the output signal, V_m, of the circuit and the electric field incident

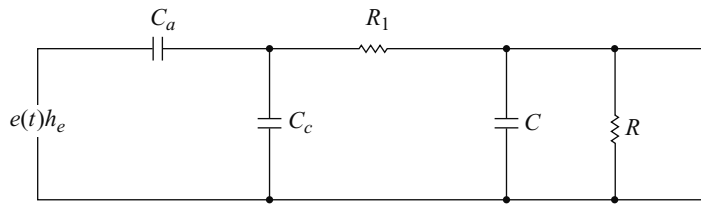

Figure 4.42 Equivalent circuit of the electric field measuring system

on the antenna is given in the frequency domain by:

$$V_m = E(s)h_e \frac{sC_aR}{1 + sF_1 + s(R_1 + R)(C_a + C_c)} \tag{4.18}$$

with

$$F_1 = RC[1 + sR_1(C_a + C_c)] \tag{4.19}$$

where s is the Laplace variable and $E(s)$ is the Laplace transform of the background electric field, $e(t)$. In general the resistance R_1 (equal to the cable impedance) can be neglected and the above equation can be simplified to:

$$V_m = E(s)h_e \frac{s}{s + 1/(R_2(C_a + C_c + C))} \frac{C_a}{C_a + C_c + C} \tag{4.20}$$

Assume for the moment that the background field incident on the antenna is a Heaviside step function of amplitude E_0. The output of the circuit in the time domain, $v_m(t)$, can be obtained by taking the inverse Laplace transformation of the above equation. The result is:

$$v_m = E_0h_e \frac{C_a}{C_a + C_c + C} e^{-\{t/\tau_d\}} \tag{4.21}$$

where

$$\tau_d = R(C_a + C_c + C) \tag{4.22}$$

This shows that the output voltage decays exponentially with a time constant τ_d. Since the applied field is a step the above results show that τ_d controls the ability of the circuit to faithfully represent the low-frequency contents of the background electric field to be measured. In other words, τ_d determines the low-frequency limit of the bandwidth of the measuring system; the lower 3 dB frequency limit of the bandwidth is given by $1/2\pi\tau_d$. To obtain an accurate measurement of the time-varying background electric field the time constant of the antenna system should be much longer than the total duration of the time-varying field. This point is illustrated further in the waveforms shown in Figure 4.43 where the effect of the time constant on the measurement of distant radiation fields generated by a subsequent return stroke is illustrated. The

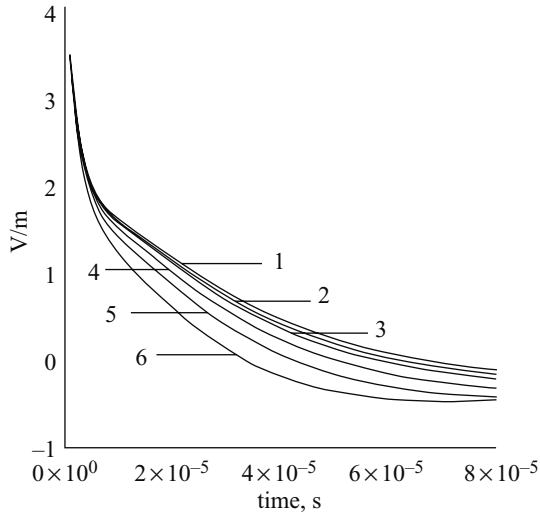

Figure 4.43 *Curve 1 shows the electric radiation field at 100 km over perfectly conducting ground as simulated by the subsequent return stroke model described in section 6.4.2.6.1 of Chapter 6. The rest of the curves show the effect of the decay time constant, τ, on the output of the electric field measuring system when excited by this electric field. (2) $\tau = 1$ ms, (3) $\tau = 500\ \mu$s, (4) $\tau = 200\ \mu$s, (5) $\tau = 100\ \mu$s and (6) $\tau = 50\ \mu$s. A positive field corresponds to an upward deflection*

data shows that in order to obtain an accurate measurement of the radiation field, the duration of which is about 100 μs, the decay time constant of the measuring system should be about 1 ms.

The upper frequency limit of the bandwidth of the measuring system is determined by the physical dimension of the antenna, the electronics components used in the circuitry and the recording system used to record the output of the measuring system. If l is the length or the diameter of the antenna it is necessary that $l \ll \lambda_m/4$ where λ_m is the minimum wavelength of interest in the electric field measurements. If this condition is not satisfied the current induced in different parts of the antenna will reach the electronic circuitry at different times thus invalidating the theory presented above. However, in many practical applications l may not exceed a few metres in the case of a whip antenna and a few tens of centimetres in the case of a plate antenna. Thus the upper frequency limit of the bandwidth is determined mainly by the electronics circuitry and the recording system. The waveforms in Figures 4.44 and 4.45 show how the upper frequency limit (3 dB limit) of the bandwidth of the measuring system affects the measurements of the subsequent stroke radiation field and its derivative. This data shows that in order to perform an accurate measurement of the peak radiation field the upper limit of the bandwidth should exceed about 5 MHz. To make an accurate measurement of the peak radiation field derivative it has to exceed about 20 MHz.

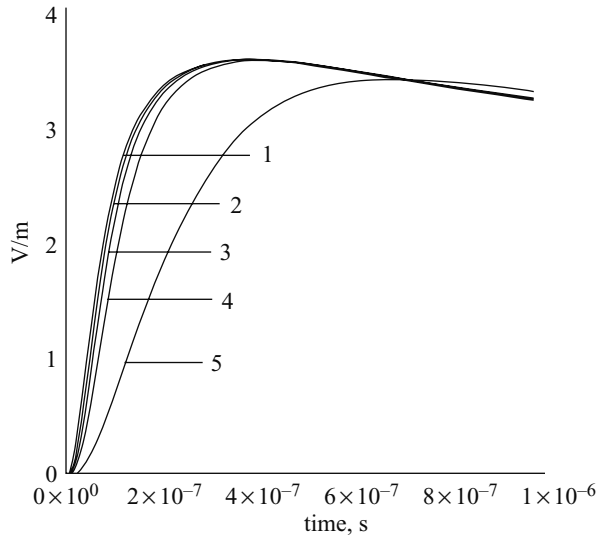

Figure 4.44 Curve 1 shows the electric radiation field at 100 km over perfectly conducting ground as simulated by the subsequent return stroke model described in section 6.4.2.6.1 of Chapter 6. The rest of the curves show the effect of the upper frequency limit (3 dB point), f_m, on the output of the electric field measuring system when excited by this electric field. (2) $f_m = 20$ MHz, (3) $f_m = 10$ MHz, (4) $f_m = 5$ MHz, and (5) $f_m = 1$ MHz. A positive field corresponds to an upward deflection

This antenna system has an advantage over the field mill in providing a higher time resolution in the measurements. However, the disadvantage of this system is that, since there is a limit to which the decay time constant could be increased, it cannot measure the low-frequency components of the electric fields including DC.

4.10.3 Crossed loop antennas to measure the magnetic field

The voltage induced in a loop antenna due to an incoming magnetic field is proportional to the area of the loop multiplied by the derivative of the magnetic field component perpendicular to the loop. By measuring the voltage induced in two magnetic loops placed orthogonal to each other the component of the magnetic field parallel to the plane containing the two axes of the loops can be obtained. The magnetic field generated by a vertical lightning channel is parallel to the ground plane and is directed perpendicular to the line joining the point of observation and the lightning channel. Therefore, the direction of the lightning flash from a given point can be obtained by measuring the ratio of the voltages induced in two orthogonal magnetic loops.

The equivalent circuit of the loop antenna is shown in Figure 4.46. Herel, L is the inductance of the loop and R is its resistance. In practice the resistance of the loop can

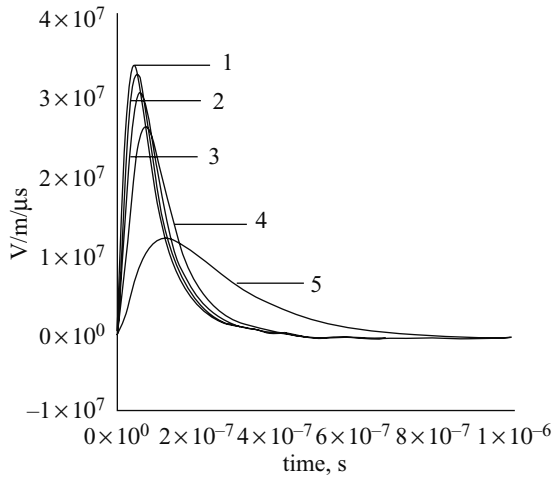

Figure 4.45 *Curve 1 shows the derivative of the electric field depicted in curve 1 of Figure 4.44. The rest of the curves show the effect of the upper frequency limit (3 dB point), f_m, on the derivative of the output of the electric field measuring system when excited by this electric field. (2) $f_m = 20$ MHz, (3) $f_m = 10$ MHz, (4) $f_m = 5$ MHz, and (5) $f_m = 1$ MHz. A positive field corresponds to an upward deflection*

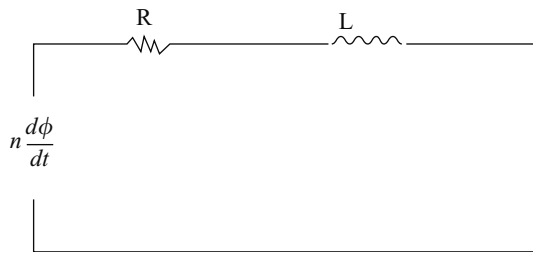

Figure 4.46 *Equivalent circuit of the magnetic loop*

be neglected. The voltage, V, induced in the loop, assumed to be electrically small, is given by:

$$V = -n\frac{d\phi}{dt} \tag{4.23}$$

where n is the number of turns in the loop and ϕ is the magnetic flux threading the loop. The flux is given by:

$$\phi = B(t)A\cos\theta \tag{4.24}$$

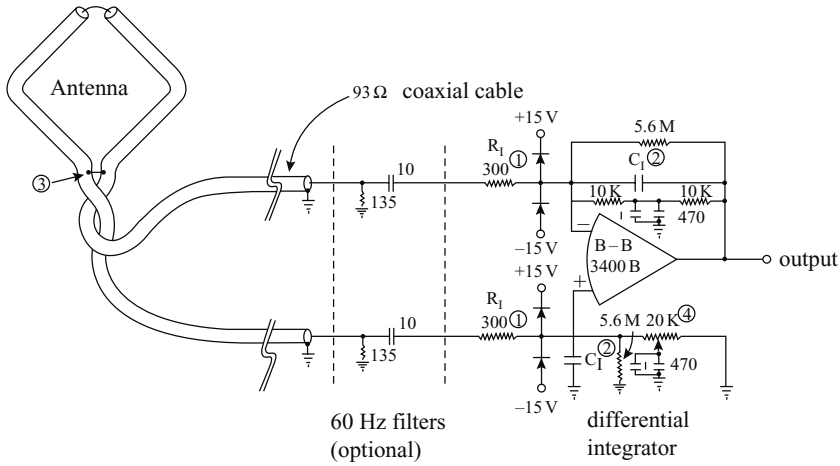

Figure 4.47 *A magnetic field antenna formed from a single loop of 93 Ω coaxial cable and associated electronics to obtain an output proportional to the field* (from [226]; reproduced by permission of the American Meteorological Society)

where $B(t)$ is the time-varying magnetic field, A is the area of the loop and θ is the angle between the axis of the loop and the magnetic vector. Since the output of the antenna is proportional to the derivative of the magnetic field it has to be integrated to obtain a signal which is proportional to the magnetic field. An antenna and the corresponding electronics suitable for this purpose, as developed by Krider and Noggle [226], are shown in Figure 4.47.

The lower limit of the bandwidth of the magnetic field measuring system is determined by the integration time constant of the integrator. Thus, the integration time constant of the system should be much longer than the duration of the waveforms of interest. In the circuit shown in Figure 4.47, with $C_1 = 1000$ pF, the time constant of the integrator was 4 ms without the 60 Hz filters and 1.3 ms when they were included. As in the electric field measuring system the upper limit of the bandwidth is determined by the electronic circuitry and the recording system.

In measuring magnetic fields it is also necessary to avoid any contamination of the measurements due to the electric fields. In the measuring system shown in Figure 4.47 this is achieved by shielding the magnetic field sensor with an outer screen which is broken at the top to avoid any circulating currents and by measuring the difference in the voltages induced at the two ends of the antenna thus cancelling out any contribution from the electric field.

4.11 Detection of lightning flashes

Lightning detection and location systems can be divided into two categories. In the detection systems belonging to the first category the number of lightning flashes

striking a given area is obtained without any specific knowledge concerning actual location of the flashes. Lightning flash counters fall into this category. Detection systems that can pin point the point of a strike or the detailed geometry of the lightning channel fall into the second category. Examples are the magnetic direction finding systems, time of arrival systems and radio interferometric systems.

4.11.1 Lightning flash counters

In lightning flash counters the lightning-generated electric field is received by a standardised electric field sensor (a vertical or a horizontal antenna) and the resulting current is passed through an electronic circuit. When the output voltage of the electronic circuit exceeds a threshold a counter is triggered. In order to avoid multiple counts due to subsequent strokes the trigger circuit has a dead time of about one second.

The first standard lightning flash counter was the one approved by the International Radio Consulative Committee (CCIR) [227]. This counter is fitted with a 7 m long vertical antenna that acts as the field sensor. The bandwidth of the electronic circuitry of this counter has 3 dB points at 3 kHz and 50 kHz with the peak at 10 kHz. CCIR counters respond mainly to the radiation field of the lightning return strokes and Pierce [228] suggested the advantages of having a counter that responds to the electrostatic field of the lightning discharges. After several modifications such a counter was adopted by CIGRE as a standard and is called the CIGRE 500 Hz counter. This counter has a bandwidth of 100 Hz–2.5 kHz with a peak at 500 Hz. It was fitted with a horizontal antenna located 5 m above ground. Tests conducted with this counter showed that a considerable fraction of its counts are due to cloud flashes and in order to achieve a better discrimination between ground and cloud flashes Anderson *et al*. [229] modified this counter to a frequency response peaked on 10 kHz with a bandwidth of 2.5–50 kHz. This modified counter is called the CIGRE 10 kHz counter.

The ability of a lightning flash to trigger the counter depends on the strength of the electric field produced by that flash at the location of the counter. Thus, strong lightning flashes could trigger a counter at long range and weak lightning flashes can do that only if they are located close to it. Thus the receiving range of a counter has to be defined in a statistical manner. The effective range of a lightning flash counter is defined as:

$$R_e = \sqrt{2\int_0^\infty P(r) r \, dr} \tag{4.25}$$

where $P(r)$ is the probability that a lightning flash located at a distance r will be detected by the counter. In general, flash counters are designed to respond to ground flashes but triggers due to cloud flashes cannot be avoided. Before one can obtain the ground flash density from the data it is necessary to correct it for triggers due to cloud flashes. If N is the total number of flashes registered by a counter within a given period of time then the total count due to ground flashes within the same period

is given by $K{\cdot}N$ where K is the correction factor. Then the ground flash density, N_g, over that period of time at the location of the lightning flash counter is given by:

$$N_g = \frac{K \cdot N}{\pi R_e^2} \tag{4.26}$$

The effective range of a counter for ground and cloud flashes can be obtained by long term observations by different methods [229] or through calculations based on the features of lightning generated electromagnetic fields [230]. More recently, Mackerras [231] has developed an advanced lightning flash counter that can separate cloud flashes, negative ground flashes and positive ground flashes. This counter is in operation in several countries.

4.11.2 Magnetic direction finding

In this technique the direction of the horizontal component of the magnetic field generated by the lightning flash is obtained at two spatially separated stations using crossed magnetic loops. Since the horizontal component of the magnetic field at a given point is perpendicular to the direction of the lightning strike as observed from that point, information obtained from two stations can be used through triangulation to obtain the point of strike of the lightning flash. Apparently, the possibility of locating lightning flashes through magnetic direction finding was first described by Watson-Watt and Herd [232] in 1926. Since then, both narrowband [233] and wide band [234] direction finding systems have been utilised. The narrowband systems were tuned to a frequency of about 5 kHz. At this frequency the attenuation of the signals propagating along the earth–ionospheric waveguide is minimum where the lightning signal is maximum.

If the lightning channel is vertical and the signal received by the loops is free of ionospheric reflections then the direction finder provides an accurate direction to the point of strike. However, in general the lightning channel is not vertical and the signal received by the direction finder may be partly due to the reflections of the lightning-generated magnetic field from the ionosphere. Both these facts can cause errors in the direction finding systems. The early magnetic direction finders had a low accuracy because of these errors. The modern broadband magnetic direction finders solve this problem by utilising the initial few microseconds of the return stroke signal which is free from ionospheric reflections [234]. Moreover, the first few microseconds of the return stroke signal is generated by the first few hundred metres of the lightning channel which is more or less straight and vertical.

The location accuracy of a direction finding system with two stations is reduced significantly when lightning flashes are located close to the baseline of the two stations and the system cannot provide a fix when a lightning flash is located on the baseline. This problem can be solved by increasing the number of direction finding stations. With a crossed loop direction finder it is impossible to determine whether a signal received by it is due to a negative ground flash in one direction or a positive ground flash in the opposite direction. This ambiguity in direction can be removed by measuring the

polarity of the electric field simultaneously with the magnetic field and determining the polarity of the flash.

Thanks to the development of decision making electronics, the modern day direction finders can discriminate between cloud and ground flashes by utilising the characteristic features of the signals generated by respective lightning flashes [234]. Today, such systems are installed worldwide.

4.11.3 Time of arrival technique: VLF range

The electromagnetic fields generated by lightning flashes propagate over the surface of the earth with the speed of light and the time of arrival of a particular feature of the electromagnetic radiation field (for example the peak of the radiation field) at several spatially separated stations can be utilised to obtain the location of the lightning flashes. Apparently Lewis *et al*. [235] were the first to describe such a lightning locating system. The time difference between the arrival of the pulse at two stations will define a hyperbola on the surface of the earth. The data from three stations defines three hyperbolas the intersection of which provides the location of the lightning flash. This method is sometimes defined as hyperbolic direction finding. With three stations two points of intersection may appear in some regions and these ambiguities can be removed by having more than three stations.

The method will work without errors if (a) the time synchronisation between different stations can be achieved with a high resolution, (b) the bandwidths of the sensing elements at different stations are identical and (c) the radiation field of the lightning flash does not change its shape in propagating from the source to the sensing stations (i.e. there are no propagation effects). Points (a) and (b) can be solved without difficulties but it is nearly impossible to realise (c). The reason for the latter is the finite ground conductivity which causes the peak of the radiation field to shift in time as it propagates from the source to the sensor. Since the length of the path of propagation and the ground conductivity may vary from one station to another the propagation effects may introduce a time delay of more than several microseconds between stations (see Chapter 7). This causes an error in the calculated point of strike.

Today, one can find lightning location systems that utilise both magnetic direction finding and time of arrival principles thus increasing the accuracy of lightning location.

4.11.4 Time of arrival technique: VHF range

During a lightning flash a large number of pulses whose rise times and durations are so short that they can excite systems tuned to HF and VHF ranges are generated. When excited by an impulse a receiving system tuned to a central frequency f_0 and bandwidth B generates an oscillating output that decays in a time which is given approximately by $1/B$. If such an antenna system is used to tag the time of arrival of the impulsive events at several spatially separated stations the information can be utilised to obtain the location of the discharge events that gave rise to

these impulses. The possibility was first suggested by Oetzel and Pierce [236]. The electrical breakdown process in air gives rise to impulses which can excite systems tuned to VHF, and by mapping the position of a large number of such pulses generated by lightning flashes an image of the lightning flash in three dimension can be obtained.

The VHF time of arrival systems can be divided into two categories, namely, long baseline systems [1–3,237,238] and short baseline systems [239–241]. In the long baseline systems the antennas are separated by distances of several kilometres. From the measured time of arrival of the same pulse at different stations hyperbolic geometry should be used to obtain the position. In short baseline systems the incoming signal can be treated as a plane wave and straight line geometry can be applied. One difficulty with the long baseline systems is the difficulty of identifying the same pulse feature in different antennas. Moreover, the number of impulsive events that excite the receiving systems at all the stations are limited. Some of these problems can be avoided by utilising short baseline systems. However, not withstanding these difficulties, the pioneering work of Proctor [1,3] demonstrated the feasibility of the technique as a tool for studying the physics and mechanism of the lightning flash. Proctor's system was tuned to a frequency of 355 MHz and the separations between stations were about 10–30 km. Today several systems that utilise this technique are in operation.

4.11.5 VHF radio interferometry

VHF radio interferrometry was first used for lightning studies by Hayenga and coworkers [242,243]. The technique was further developed and improved by ONERA in France [244], New Mexico Tech. in USA [4–6] and Osaka University, Japan [245].

The general principle of the VHF interferometry is the following. Assume that a plane sinusoidal wave is incident on two antennas separated by a distance d. The phase difference, ϕ, of the output signal of the two antennas will be related to the direction of arrival of the wave by:

$$\phi = 2\pi d \cos\theta/\lambda \tag{4.27}$$

where λ is the wavelength and θ is the angle between the direction of incidence of the wave and the line joining the two antennas. Thus by measuring the phase difference of the output signal the direction of the incoming wave can be obtained. If the system contains three antennas, by measuring the phase difference of the output of two independent pairs one can estimate the azimuth and the elevation of the incoming plane wave.

The above equation shows that for a given angle θ the rate of change of ϕ with respect to θ is proportional to d/λ. Thus the larger the value of d/λ the larger the sensitivity of the measurements. However, in order to obtain a phase measurement it is necessary that the distance between the two antennas or baseline, d, should satisfy the criterion $d/c \leq 1/B$ where c is the speed of light and B is the bandwidth of the antenna system. If $d = \lambda/2$ then as θ varies from 0 to π the phase angle also makes a complete circle and there is a one to one correlation between θ and ϕ. However,

if the baseline distance is larger than $\lambda/2$ then for a given measurement there are several solutions for the angle θ. This is called fringe ambiguity. On the other hand if the antennas are closely spaced then the resolution of the measurements is limited. Krehbiel and coworkers [4–6] overcame these problems by employing two pairs of antennas located perpendicular to each other one having a baseline of $\lambda/2$ and the other 4λ (later these distances were increased to λ and 4.5λ respectively). A set of antennas like this provides the azimuth and elevation of the sources that excite the antenna system. Utilising two similar spatially separated antenna sets it is possible

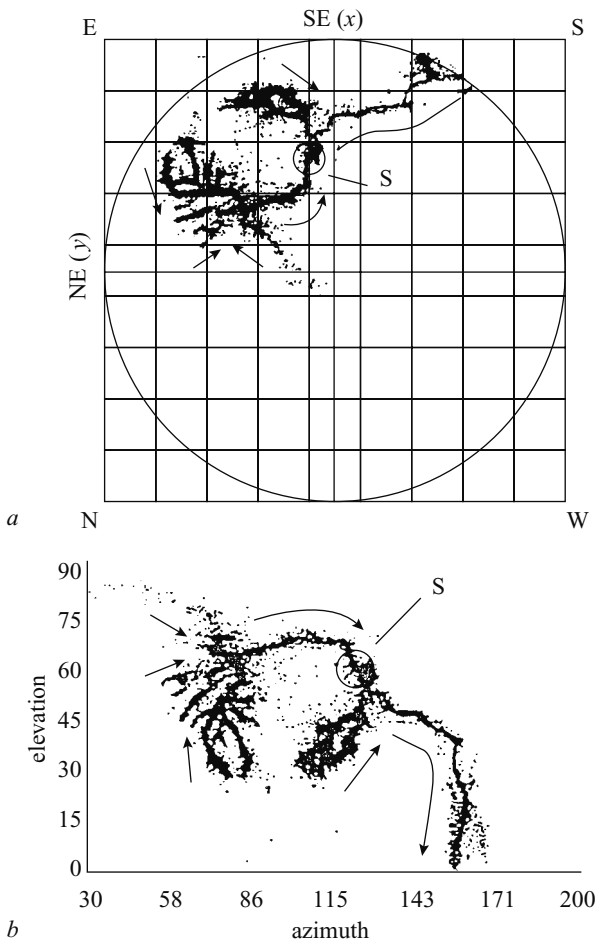

Figure 4.48 *The location of the radiation sources of a ground flash in both (a) projection plane and (b) azimuth-elevation format as located by the VHF interferometer technique. The discharge started in the region marked by a circle* (from [4])

to get the location of the sources in the cloud. The development of a cloud to ground flash as observed by this technique is shown in Figure 4.48.

The central frequency of the antenna system used by the New Mexico group is 274 MHz with a bandwidth of 6 MHz. The system that is in operation in France has a central frequency of 114 MHz with a bandwidth of 1 MHz. The Osaka group utilises a broadband system having a bandwidth of 10–200 MHz.

4.12 References

1 PROCTOR, D.E.: 'A radio study of lightning'. Ph.D. thesis, University of Witwarersrand, Johannesburg, South Africa, 1976
2 PROCTOR, D.E.: 'Lightning and precipitation in a small multicellular thunderstorm', *J. Geophys. Res.*, 1983, **88**, pp.5421–5440
3 PROCTOR, D.E.: 'VHF pictures of cloud flashes', *J. Geophys. Res.*, 1981, **86**, pp. 4041–4071
4 SHAO, X.M.: 'The development and structure of lightning discharges observed by VHF radio interferometer'. Ph.D. thesis, New Mexico Inst. Mining and Technolog., Socorro, 1993
5 SHAO, X.M. and KREHBIEL, P.R.: 'The spatial and temporal development of intracloud lightning', *J. Geophys. Res.*, 1996, **101**(26), pp.641–26,668
6 SHAO, X.M., KREHBIEL, P.R., THOMAS, R.J., and RISON, W.: 'Radio interferometric observations of cloud-to-ground lightning phenomena in Florida', *J. Geophys. Res.*, 1995, **100**, pp.2749–2783
7 LES RENARDIERES GROUP: 'Positive discharges in long air gaps at Les Renardieres – 1975. Results and conclusions', *Electra*, 1975, **53**
8 BEASLEY, W.H., UMAN, M.A., and RUSTAN, P.L.: 'Electric fields preceding cloud to ground lightning flashes', *J. Geophys. Res.*, 1982, **87**, pp.4883–4902
9 CLARENCE, N.D. and MALAN, D.J.: 'Preliminary discharge processes in lightning flashes to ground', *Q. J. R. Meteorol. Soc.*, 1957, **83**, pp.161–172
10 SCHONLAND, B.F.J.: 'The lightning discharge', *Handbuch der Physik*, 1956, **22**, pp.576–628
11 THOMSON, E.M.: 'Characteristics of Port Moresby ground flashes', *J. Geophys. Res.*, 1980, **85**, pp.1027–1036
12 GOMES, C., COORAY, V., and JAYARATNE, C.: 'Comparison of preliminary breakdown pulses observed in Sweden and in Sri Lanka', *J. Atmos. Terr. Phys.*, 1998, **60**, pp.975–979
13 COORAY, V. and JAYARATNE, R.: 'What directs a lightning flash towards the ground?', *Sri Lankan J. of Physics*, 2000, **1**, pp.1–10
14 CHAUZY, S. and SOULA, S.: 'Contribution of the ground corona ions to the convective charging mechanism', *Atmos. Res.*, 1999, **51**, pp.279–300
15 KREHBIEL, P.R., BROOK, M., and McCRORY, R.: 'An analysis of the charge structure of lightning discharges to the ground, *J. Geophys. Res.*, 1979, **84**, pp.2432–2456

16 RUSTAN, P.L., UMAN, M.A., CHILDERS, D.G., BEASELY, W.H., and LENNON, C.L.: 'Lightning source locations from VHF radiation data for a flash at Kennedy Space Center', *J. Geophys. Res.*, 1980, **85**, pp.4893–4903
17 OGAWA, T.: 'Initiation of lightning in clouds', *J. Atmos. Elec.*, 1993, **13**, pp.121–132
18 SAUNDERS, C.P.R.: 'Thunderstorm electrification laboratory experiments and charging mechanisms', *J. Geophys. Res.*, 1994, **99**, pp.10773–10779
19 WILLIEMS, E.R.: 'Large scale charge separation in thunderclouds', *J. Geophys. Res.*, 1985, pp.6013–6025
20 TAKAHASHI, T.: 'Electrification of growing ice crystals', *J. Atmos. Sci.*, 1973, **35**, pp.1220–1224
21 JAYARATNE, E.R., SAUNDERS, C.P.R., and HALLETT, J.: 'Laboratory studies of the charging of soft hail during ice crystal interactions', *Q. J. R. Meteorol. Soc.*, 1985, **109**, pp.609–630
22 MURPHY, M.J. and KRIDER E.P.: 'Lightning charge analyses in small convection and precipitation electrification (CaPE) experiment storms', *J. Geophys. Res.*, 1996, **101**, (D23), pp.29615–29626
23 CHEN, M., TAKAGI, N., WATANABE, T., WANG, D., KAWASAKI, Z.-I., and LIU, X.: 'Spatial and temporal properties of optical radiation produced by stepped leaders', *J. Geophys. Res.*, 1999, **104**, pp.27573–27584
24 BERGER, K.: 'Novel observations on lightning discharges: results of reaserch on mount San Salvatore', *J. Franklin Inst.*, 1967, **283**, pp.478–525
25 BEASLEY, W.H., UMAN, M.A., JORDAN, D.M., and GANESH, C.: 'Simultaneous pulses in light and electric field from stepped leaders near ground level', *J. Geophys. Res.*, 1983, **88**, pp.8617–8619
26 ORVILLE, R.E. and IDONE, V.P.: 'Lightning leader characteristics in the thunderstorm research international program (TRIP)', *J. Geophys. Res.*, 1982, **87**, pp.11172–11192
27 SCHONLAND, B.F.J.: 'Progressive lightning, 4, The discharge mechanism', *Proc. R. Soc., London, Ser. A*, 1938, **164**, pp.132–150
28 THOMSON, E.M., UMAN, M.A., and BEASLEY, W.H.: 'Speed and current for lightning stepped leaders near ground as determined from electric field records', *J. Geophys. Res.*, 1985, **90**, pp.8136–8142
29 ORVILLE, R.E.: 'Spectrum of the stepped leader', *J. Geophys. Res.*, 1968, **73**, pp.6999–7008
30 KRIDER, E.P. and RADDA G.J.: 'Radiation field waveforms produced by lightning stepped leaders', *J. Geophys. Res.*, 1975, **80**, pp.2653–2657
31 KITAGAWA, N.: 'On the electric field changes due to the leader processes and some of their discharge mechanism', *Pap. Meteorol. Geophys. (Tokyo)*, 1957, **7**, pp.400–414
32 COORAY, V. and LUNDQUIST, S.: 'Characteristics of the radiation fields from lightning in Sri Lanka in the tropics', *J. Geophys. Res.*, 1985, **90**, pp.6099–6109
33 KRIDER, E.P., WEIDMAN, C.D., and NOGGLE, R.C.: 'The electric fields produced by lightning stepped leaders', *J. Geophys. Res.*, 1977, **82**, pp.951–960

34 SCHONLAND, B.F.J.: 'The pilot streamer in the lightning and the long spark', *Proc. R. Soc. London Ser. A*, 1953, **220**, pp.25–38
35 BROOK, M., KITAGAWA, N., and WORKMAN, E.J.: 'Quantitative study of strokes and continuing currents lightning discharges to ground', *J. Geophys. Res.*, 1962, **67**, pp.649–659
36 BRUCE, C.E.R. and GOLDE, R.H.: 'The lightning discharge', *J. Inst. Electr. Eng. (London)*, 1941, **88**, pp.487–520
37 LARSSON, A. and COORAY, V.: 'Charge distribution in the lightning leader channel'. Proceedings of 23rd international conference on *Lightning protection*, Italy, 1996, pp.56–60
38 WILLIAMS, D.P. and BROOK, M.: 'Magnetic measurement of thunderstorm currents, I. Continuing currents in lightning', *J. Geophys. Res.*, 1963, **68**, pp.3243–3247
39 KREHBIEL, P.R.: 'An analysis of the electric field change produced by lightning'. Ph.D. thesis, UMIST, Manchester, England, 1981
40 SCHONLAND, B.F.J.: 'Lightning and the long electric spark', *Adv. Sci.*, 1962, **19**, pp.306–313
41 UMAN, M.A. and MCLAIN, D.K.: 'Radiation field and the current of the lightning stepped leader', *J. Geophys. Res.*, 1970, **75**, pp.1058–1066
42 SOPOR, S.: 'Review of the relaxation theory of the stepped leader', *Acta Geophys. Pol.*, 1970, **18**, pp.73–77
43 KASEMIR, H.W.: 'A contribution to the electrostatic theory of a lightning discharge', *J. Geophys. Res.*, 1960, **65**, pp.1873–1878
44 KASEMIR, H.W.: 'Static discharge and triggered lightning'. Proceedings of the 8th international conference on *Aerospace and ground lightning and static electricity*, Fort Worth, Texas, USA, June, 1983, pp.21–23
45 MAZUR, V.: 'Triggered lightning strikes to aircraft and natural intracloud discharges', *J. Geophys. Res.*, 1989, **94**, pp.3311–3325
46 MAZUR, V.: 'Physical model of lightning initiation in aircrafts in thunderstorms', *J. Geophys. Res.*, 1989, **94**, pp.3326–3340
47 MAZUR, V. and RUHNKE, L.H.: 'Common physical processes in natural and artificially triggered lightning', *J. Geophys. Res.*, 1993, **98**, pp.12913–12930
48 KAWASAKI, Z.-I. and MAZUR, V.: 'Common physical processes in natural and triggered lightning in winter storms in Japan', *J. Geophys. Res.*, 1992, **97**, pp.12935–12945
49 HECKMAN, S.J. and WILLIAMS, E.R.: 'Corona envelopes and lightning currents', *J. Geophys. Res.*, 1989, **94**, pp.13287–13294
50 LAROCHE, P., IDONE, V., EYBERT-BERARD, A., and BARRET, L.: 'Observations of bidirectional leader development in triggered lightning flashes'. Proceedings of the 1991 international conference on *Aerospace and ground lightning and static electricity*, Cocoa Beach, Florida, April, 1991 pp.57.1–57.10
51 BONDIOU-CLERGERIE, A., BACCHIEGA, G.L., CASTELLANI, A., LALANDE, P., LAROCHE, P., and GALLIMBERTI, I.: 'Experimental and theoretical study of bi-directional leader process Part I: Experimental Investigation'.

Proceedings of 10th international conference on *Atmospheric electricity*, Osaka, Japan, 1996
52 COORAY, V.: 'Energy dissipation in lightning flashes', *J. Geophys. Res.*, 1997, **102**, pp.21401–21410
53 WANG, D., KAWASAKI, Z.-I., YAMAMOTO, K., MATSUURA, K., CHANG J., and JANISCHEWSKYJ, W.: 'Luminous propagation of lightning attachment to CN tower', *J. Geophys. Res.*, 1995, **100**, pp.11661–11667
54 IDONE, V.P. and ORVILLE, R.: 'Lightning return stroke velocities in the thunderstorm research program', *J. Geophys. Res.*, 1982, **87**, pp.4903–4916
55 MACH, D.M. and RUST, W.D.: 'Photoelectric return stroke velocity and peak current estimates in natural and triggered lightning', 1989, **94**, pp.13237–13247
56 COORAY, V.: 'A model for negative first return strokes in lightning flashes', *Phys. Scr.*, 1997, **55**, pp.119–128
57 COORAY, V. and GALVAN, A.: 'A negative return stroke model for engineering applications'. Proceedings of the 25th international conference on *Lightning protection (ICLP)*, Rhodes, Greece, 2000
58 JORDAN, D.M. and UMAN, M.A.: 'Variation in light intensity with height and time from subsequent lightning return strokes', *J. Geophys. Res.*, 1983, **88**, pp.6555–6562
59 JORDAN, D.M., RAKOV, V.A., BEASLEY, W.H., and UMAN, M.A.: 'Luminosity characteristics of dart leaders and return strokes in natural lightning', *J. Geophys. Res.*, 1997, **102**, pp.22025–22032
60 MACH, D.M. and RUST, W.D.: 'Two-dimensional velocity, optical rise-time, and peak current estimates for natural positive lightning return strokes', *J. Geophys. Res.*, 1993, **98**, pp.2635–2638
61 IDONE, V.P. and ORVILLE, R.E.: 'Correlated peak relative light intensity and peak current in triggered lightning subsequent strokes', 1985, **90**, pp.6159–6164
62 KRIDER, E.P., DAWSON, G.A., and UMAN, M.A.: 'Peak power and energy dissipation in a single lightning flash', *J. Geophys. Res.*, 1968, **73**, pp.3335–3339
63 GUO, C. and KRIDER, E.P.: 'The optical radiation field signatures produced by lightning return strokes', *J. Geophys. Res.*, 1982, **87**, pp.8913–8922
64 GUO, C. and KRIDER, E.P.: 'The optical power radiated by lightning return strokes', *J. Geophys. Res.*, 1983, **88**, pp.8621–8622
65 MACCKERRAS, D.: 'Photoelectric observations of the light emitted by lightning flashes', *J. Atmos. Terr. Phys.*, 1973, **35**, pp.521–535
66 TURMAN, B.N.: 'Analysis of lightning data from the DMSP satellite', *J. Geophys. Res.*, 1978, **83**, pp.5019–5024
67 ORVILLE, R.E. and HENDERSON, R.W.: 'Absolute spectral irradiance measurements of lightning from 375 to 880 nm', *J. Atmos. Sci.*, 1984, **41**, pp.3180–3187
68 ORVILLE, R.E.: 'A high speed time resolved spectroscopic study of the lightning return stroke, Parts 1, 2, 3', *J. Atmos. Sci.*, 1968, **25**, pp.827–856

69 TAKAGI, N., WANG, D., WATANABE, T., ARIMA, I., TAKEUCHI, T., SIMIZU, M., KATURAGI, Y., YOKOYA, M., and KAWASHIMA, Y.: 'Expansion of the luminous region of the return stroke channel', *J. Geophys. Res.*, 1998, **103**, pp.14131–14134
70 COORAY, V. 'A model for subsequent return strokes', *J. Electrost.*, 1993, **30**, pp.343–354
71 SCHONLAND, B.F.J.: 'The diameter of the lightning channel', *Philos. Mag.*, 1937, **37**, pp.503–508
72 EVANS, W.H. and WALKER, R.L.: 'High-speed photographs of lightning at close range', *J. Geophys. Res.*, 1963, **68**, pp.4455–4461
73 ORVILLE, R.E.: 'Quantitative analysis of a lightning return stroke for diameter and luminosity changes as a function of space and time', *J. Geophys. Res.*, 1974, **79**, pp.4059–4067
74 SCHONLAND, B.F.J.: 'The flight of thunderbolts' (Oxford University Press, New York, 1950) p.63
75 HILL, R.D.: 'Determination of charges conducted in lightning strokes', *J. Geophys. Res.*, 1963, **68**, pp.1365–1375
76 JONES, R.D.: 'Return stroke core diameter', *J. Geophys. Res.*, 1968, **73**, pp.809–814
77 UMAN, M.A.: 'The diameter of lightning', *J. Geophys. Res.*, 1964, **69**, pp.583–585
78 TAYLOR, A.R.: 'Diameter of lightning as indicated by tree scars', *J. Geophys. Res.*, 1965, **70**, pp.5693–5695
79 GARBANATI, E. and LO PIPARO, G.B.: 'Parameter von Blitzströmen', *Elektrotech. Z. ETZ-A*, 1982, **103**, pp.61–65
80 NEWMAN, M.M.: 'In problems of atmospheric and space electricity' (New York, Elsevier, 1965) pp.482–490
81 FIEUX, R., GARY, C., and HUBERT, P.: 'Artificially triggered lightning above land', *Nature* 1975, **257**, 212–214
82 LIU, X.-S., WANG, C., ZHANG, Y., XIAO, Q., WANG, D., ZHOU, Z., and GUO, C.: *J. Geophys. Res.*, 1994, **99:10**, pp.727–731
83 HORII, K. and NAKANO, M.: *in* VOLLAND, H. (Ed.): 'Handbook of atmospheric electrodynamics, vol. 1' (CRC Press, Florida, USA) pp.151–166
84 FISHER, R.J., SCHNETZER, G.H., THOTTAPPILLIL, R., RAKOV, V.A., UMAN, M.A., and GOLDBERG, J.D.: *J. Geophys. Res.*, 1993, **98:22**, pp.887–902
85 LEITENTURIER, C., HAMELIN, J.H., and EYBERT-BERARD, A.: *IEEE Trans. Electromagn. Compat.*, 1991, **33**, pp.351–7
86 RAKOV, V.: 'Lightning discharges triggered using rocket- and wire techniques', *Recent Res. Devel. Geophysics*, 1999, **2**, pp.141–171
87 ANDERSON, R.B. and ERIKSSON, A.J.: 'Lightning parameters for engineering application', *Electra*, 1979, **170**, pp.65–102

88 BERGER, K.: 'Methoden und Resultate der Blitzforschung auf dem Monte San Salvador bei Lugano in den Jahren 1963–1971', *Bull. Schweiz. Elektrotech. Ver.*, 1972, **63**, pp.1403–1422
89 PETTERSSON, P.: 'A unified probabilistic theory of the incidence of direct and indirect lightning strikes', *IEEE Trans. on Power Delivery*, 1991, **6**, pp.1301–1310
90 ERIKSSON, A.J.: 'The ground flash–an engineering study'. ELEK 189, National Electrical Engineering Research Institute, Pretoria, South Africa, 1979
91 GUERRIERI, S., NUCCI, C.A., RACHIDI, F., and RUBINSTEIN, M.: 'On the influence of elevated strike objects on directly measured and indirectly estimated lightning current', *IEEE Trans. Power Deliv.*, 1998, **33**, pp.1543–1551
92 LIN, Y.T., UMAN, M.A., TILLER, J.A., BRANTLEY, R.D., BEASLEY, W.H., KRIDER, E.P., and WEIDMAN, C.D.: 'Characterization of lightning return stroke electric and magnetic fields from simultaneous two-station measurments', *J. Geophys. Res.*, 1979, **84**, pp.6307–6314
93 COORAY, V.: 'The modelling of positive return strokes in lightning flashes', *J. Atmos. Terr. Phys.*, 2000, **62**, pp.169–187
94 WEIDMAN, C.D. and KRIDER, E.P.: 'The fine structure of lightning return stroke wave forms', *J. Geophys. Res. Lett.*, 1980, **7**, pp.955–958; correction, *J. Geophys. Res.*, 1982, **87**, 7351
95 COORAY, V. and LUNDQUIST, S.: 'On the characteristics of some radiation fields from lightning and their possible origin in positive ground flashes', *J. Geophys. Res.*, 1982, **87:11**, pp.203–11. 214
96 COORAY, V.: 'Further Characteristics of Postive Radiation Fields from Lightning in Sweden', *J. Geophys. Res.*, 1984, **84:11**, pp.807–11, 815
97 COORAY, V., FERNANDO, M., GOMES, C., and SORENSSEN, T.: 'The fine structure of positive lightning return stroke radiation fields' accepted to be published in IEEE *Trans. (EMC).* 2003
98 ISHII, M. and HOJO, J.: 'Statistics of fine structure of cloud-to-ground lightning field waveforms', *J. Geophys Res.*, 1989, **94**, pp.13272–13274
99 KRIDER, E.P., LETENTURIER, C., and WILLETT, J.C.: 'Submicrosecond field radiated during the onset of first return strokes in cloud-to-ground lightning', *J. Geophys. Res.*, 1996, **101**, (D1), pp.1589–1597
100 WILLETT, J.C and KRIDER, P.E.: 'Rise times of impulsive high-current processes in cloud-to-ground lightning', *IEEE Trans. Antennas Propag.*, 2000, **48**, September
101 GOMES, C. and COORAY, V.: 'Long impulse currents associated with positive return strokes', *J. Atmos. Terr. Phys.*, 1998, **60**, pp.693–699
102 MASTER, M.J., UMAN, M.A., BEASLEY, W.H., and DARVENIZA, M.: 'Lightning induced voltages on power lines: experiment'. *IEEE Trans. PAS*, 1984, **PAS-103**, pp.2519–2529

103 WILLETT, J.C., KRIDER, E.P., and LETEINTURIER, C.: 'Submicrosecond field variations during the onset of first return strokes in cloud-to-ground lightning', *J. Geophys. Res.*, 1998, **103**, pp.9027–9034
104 RAKOV, V. and UMAN, M.: 'Long continuing current in negative lightning ground flashes', *J. Geophys. Res.*, 1990, **95**, pp.5455–5470
105 WEIDMAN, C. and KRIDER, E.P.: 'Submicrosecond risetimes in lightning return stroke fields', *J. Geophys. Res. Lett.*, 1980, **7**, pp.955–958
106 TAKAGI, M.: 'VHF radiation from ground discharges', *Proc. Res. Inst. Atmos. Nagoya Univ.*, 1969, pp.163–168
107 BROOK, M. and KITAGAWA, N.: 'Radiation from lightning discharges in the frequency range 400–1000 Mc/s', *J. Geophys. Res.*, 1964, **69**, pp.2431–2434
108 LEVINE, D.M. and KRIDER, E.P.: 'The temporal structure of HF and VHF radiations during Florida lightning return strokes', *Geophys. Res. Lett.*, 1977, **4**
109 COORAY, V. and PÉREZ, H.: 'HF radiation at 3 MHz associated with positive and negative return strokes, *J. Geophys. Res.*, 1994, **99**, pp.10633–10640
110 KAWASAKI, Z. and MAZUR, V.: 'Common physical processes in natural and triggered lightning in winter storms in Japan', *J. Geophys, Res.*, 1992, **97**, 12935–12945
111 COORAY, V.: 'Temporal behaviour of lightning HF radiation at 3 MHz near the time of first return strokes', *J. Atmos. Terr. Phys.*, **48**, pp.73–78
112 LEVINE, D.M., GESELL, L., and KAO, M.: 'Radiation from lightning return strokes over finitely conducting earth', *J. Geophys. Res.*, 1986, **91**, pp.11897–11908
113 JAYARATNE, K.P.S.C. and COORAY, V.: 'The lightning HF radiation at 3 MHz during leader and return stroke processes', *J. Atmos. Terr. Phys.*, **56**, pp.493–501
114 LEVINE, D.M.: 'Review of measurements of the RF spectrum of radiation from lightning', *Meteorol. Atmos. Phys.*, 1987, **37**, pp.195–204
115 TAYLOR, C.D.: 'External interaction of the nuclear EMP with aircraft and missiles', *IEEE Trans, Electromagn. Compat.*, 1978, **EMC-20**, pp.64–76
116 SERHAN, G.I., UMAN, M.A., CHILDERS, D.G., and LIN, Y.T.: 'The RF spectra of first and subsequent lightning return strokes in the 1–200 km range', *Radio Sci.*, 1980, **15**, pp.1089–1094
117 WEIMAN, C.D. and KRIDER, E.P.: 'The amplitude spectra of lightning radiation fields in the interval from 1 to 20 MHz', *Radio Sci.*, 1986, **21**, pp.964–970
118 WEIDMAN, C.D., KRIDER, E.P., and UMAN, M.A.: 'Lightning amplitude spectra in the interval from 100 kHz to 20 MHz', *Geophys. Res. Lett.*, 1981, **8**, pp.931–934
119 YE, M. and COORAY, V.: 'Propagation effects caused by a rough ocean surface on the electromagnetic fields generated by lightning return strokes', *Radio Sci.*, 1994, **29**, pp.73–85
120 COORAY, V.: 'Interaction of electromagnetic fields produced by lightning flashes with electrical networks: the influence of propagation effects'.

Proceedings of the international conference on *Lightning protection*, Birmingham, England, 1998
121 COORAY, V.: 'Variation of return stroke velocity over the first few hundred meters and its relationship to the slow front in return stroke radiation fields', *Inst. Phys. Conf. Ser.*, 1995, (143), pp.235–240
122 COORAY, V. and ORVILLE, R.E.: 'The effects of variation of current amplitude, current risetime and return stroke velocity along the return stroke channel on the electromagnetic fields generated by return strokes', *J. Geophys. Res.*, 1990, **95**, (D11)
123 BOCCIPPIO, D.J., WILLIAMS, E.R., HECKMAN, S.T., LYONS, W.A., BAKER, I.T., and BOLDI, R.: 'Sprites, Q-bursts and positive ground flashes', *Science* 1995, **269**, pp.1078–1091
124 BROOK, M. and OGAWA, T.: 'The cloud discharge', in GOLDE, R.H. (Ed.): 'Lightning, vol. 1, physics of lightning' (Academic, San Diego, Calif., 1977)
125 PIERCE, E.T.: 'Atmospherics and radio noise', *in* GOLDE, R.H. (Ed.): 'Lightning, vol. 1, Physics of Lightning' (Academic, San Diego, Calif., USA 1977)
126 LEVINE, D.M. and MENEGHINI, R.: 'Simulation of radiation from lightning return strokes: the effects of tortuosity', *Radio Sci.*, 1978, **13**, pp.801–809
127 OGAWA, T. and BROOK, M.: 'Charge distribution in thunder clouds', Q.J1 R. Met. Soc., 1969, **95**, pp.513–525
128 MALAN, D.J. and COLLENS, H.: 'Progressive lightning, III, the fine stucture of return lightning strokes', *Proc. R. Soc. London Ser. A*, 1937, **162**, pp.175–203
129 THOTTAPPILLIL, R., GOLDBERG, J.D., RAKOV, V.A., UMAN, M.A, FISHER, R.J., and SCHNETZER, G.H.: 'Properties of M components from currents measured at triggered lightning channel base', *J. Geophys. Res.*, 1995, **100**, pp.25711–25720
130 JORDAN, D.M., IDONE, V.P., ORVILLE, R.E., RAKOV, V.A., and UMAN, M.A.: 'Luminosity characteristics of lightning M components', *J. Geophys. Res.*, 1995 **100**, pp.25695–25700
131 RAKOV, V.A., THOTTAPPILLIL, R., UMAN, M.A., and BARKER, P.: 'Mechanism of the lightning M component', *J. Geophys. Res.*, 1995, **100**, pp.25701–25710
132 KITAGAWA, N. and BROOK, M.: 'A comparison of intracloud and cloud-to-ground lightning discharges', *J. Geophys. Res.*, 1960, **65**, pp.1189–1201
133 MALAN, D.J. and SCHONLAND, B.F.J.: 'The electrical processes in the intervals between the strokes of a lightning discharge', *Proc. R. Soc., London, A*, 1951, **206**, pp.145–163
134 RAKOV. V.A., THOTTAPPILLIL, R., and UMAN, M.A.: 'Electric field pulses in K and M changes of lightning ground flashes', *J. Geophys. Res.*, 1992, **97**, pp.9935–9950
135 THOTTAPPILLIL, R., RAKOV, V.A., and UMAN, M.A.: 'K and M changes in close lightning ground flashes in Florida', *J. Geophys. Res.*, 1990, **95**, pp.18631–18640

136 THOMSON, E.M.: 'The dependence of lightning return stroke characteristics on latitude', *J. Geophys. Res.*, 1980, **85**, pp.1050–1056
137 COORAY, V. and PÉREZ, H.: 'Some features of lightning flashes observed in Sweden', *J. Geophys. Res.*, 1994, **99**, pp.10683–10688
138 COORAY, V. and JAYARATNE, K.P.S.C.: 'Characteristics of lightning flashes observed in Sri Lanka in the tropics', *J. Geophys. Res.*, 1994, **99**, pp.21051–21056
139 THOTTAPPILLIL, R., RAKOV, V.A., UMAN, M.A., BEASLEY, W.H., MASTER, M.J., and SHELUKHIN, D.V.: 'Lightning subsequent-stroke electric field peak greater than the first stroke peak and multiple ground terminations', *J. Geophys. Res.*, 1992, **97**, pp.7503–7509
140 ORVILLE, R.E.: 'Spectrum of the lightning dart leader', *J. Atmos. Sci.*, 1975, **32**, pp.1829–1837
141 MACH, D.M. and RUST, W.D.: 'Two-dimensional speed and optical risetime estimates for natural and triggered dart leaders', *J. Geophys. Res.*, 1997, **102**, (D12), pp.13673–13684
142 COORAY, V., IDONE, P., and ORVILLE, R.E.: 'Velocity of a self-propagating discharge as a function of current parameters with special attention to return strokes and dart leaders'. Presented at the international conference on *Lightning and static electricity*, University of Bath, England, September 26–28, 1989, pp.14.3.1–14.3.9
143 KITAGAWA, N. and KOBAYASHI, M.: 'Field changes and variation of luminosity due to lightning flashes, Recent advances in Atmospheric Electricity' (L.G. Smith Ed., Pergamon Press, 1958)
144 BROOK, M., KITAGAWA, N., and WORKMAN, E.J.: 'Quantitative study of strokes and continuing currents in lightning discharges to ground', *J. Geophys. Res.*, 1962, **67**, pp.649–659
145 RUBINSTEIN, M., RACHIDI, F., UMAN, M.A., THOTTAPPILLIL, R., RAKOV, V.A., and NUCCI, C.A.: 'Characterization of vertical electric fields 500 m and 30 m from triggered lightning: *J. Geophys. Res.*, 1995, **100**, pp.8863–72
146 COORAY, V.: 'Predicting the spatial and temporal variation of the electromagnetic fields, currents, and speeds of subsequent return strokes', *IEEE Trans. Electromagn. Compat.*, 1998, **40**, pp.427–435
147 D. WANG., RAKOV, V.A., UMAN, M.A., TAKAGI, N., WATANABE, T., CRAWFORD, D.E., RAMBO, K.J., SCHNETZER, G.H., FISHER, R.J., and KAWASAKI, Z.I.: 'Attachment process in rocket-triggered lightning strokes', *J. Geophys. Res.*, 1999, **104**, (January 27)
148 WEIDMAN, C.D.: 'The submicrosecond structure of lightning radiation fields'. Ph.D. dissertation, University of Arizona, 1982
149 BAILEY, J.C. and WILLETT, J.C.: 'Catalog of absolutely calibrated range normalized wideband electric field waveforms from located lightning flashes in Florida: July 24 and August 14, 1985 data'. NRL memorandum report 6497, 1989

150 GOMES, C., COORAY, V., FERNANDO, M., and JAYARATNE, C.: 'Chaotic pulse trains associated with negative subsequent stokes'. Proceedings of the international conference on *Lightning protection*, Birmingham, England, 1998
151 COORAY, V.: 'A model for dart leaders in lightning flashes', *J. Atmos. Elec.*, 1996, **16**, pp.145–159
152 JORDAN, D.M., IDONE, V.P., RAKOV, V.A., UMAN, M.A., BEASLEY, W.H., and JURENKA, H.: 'Observed dart leader speed in natural and triggered lightning', *J. Geophys. Res.*, 1992, **97**, pp.9951–9957
153 SCHONLAND, B.F.J., MALAN, D.J., and COLLENS, H.: 'Progressive Lightning, pt.2', *Proc. R. Soc. London Ser. A*, 1935, **152**, pp.595–625
154 OGAWA, T. and BROOK, M.: 'The Mechanism of the intracloud lightning discharge', J. Geophys. Res., 1964, **69**, pp.5141–5150
155 BILS, J.R., THOMPSON, E.M., UMAN, M.A., and MACKERAS, D.: 'Electric field pulses in close lightning cloud flashes', *J. Geophys. Res.*, 1988, **93**, pp.15933–15940
156 VILLANUEVA, Y., RAKOV, V.A., UMAN, M.A., and BROOK, M.: 'Microsecond-scale electric field pulses in cloud lightning discharges', *J. Geophys. Res.*, 1994, **99**, pp.14353–14360
157 WEIDMAN, C.D. and KRIDER, E.P.: 'The radiation field wave forms produced by intracloud lightning discharge processes', *J. Geophys. Res.*, 1979, **84**
158 WILLETT, J.C., BAILEY, J.C., LETENTURIER, C., and KRIDER, E.P., 'Lightning electromagnetic radiation field spectra in the interval from 0.2 to 20 MHz, *J. Geophys. Res.*, 1990, **95**, pp.20367–20387
159 WEIDMAN, C. and KRIDER, E.P.: 'Variations á l'échelle submicroseconde des champs électro-magnétiques rayonnés par la foudre', *Ann. Telecommun.*, 1984, **39**, pp.165–174
160 KRIDER, E.P., RADDA, G.J., and NOGGLE, R.C.: 'Regular radiation field pulses produced by intracloud lightning discharges', *J. Geophys. Res.*, 1975, **80**, pp.3801–3804
161 RAKOV, V.A., UMAN, M.A., HOFFMAN, G.R., MASTERS, M.W., and BROOK, M.: 'Bursts of pulses in lightning electromagnetic radiation: observations and implications for lightning test standards', *IEEE Trans. Electromagn. Compat.*, 1996, **38**, (2)
162 LE VINE, D.M.: 'Sources of the strongest RF radiation from lightning', *J. Geophys. Res.*, 1980, **85**, pp.4091–4095
163 WILLETT, J.C., BAILEY, J.C., and KRIDER, E.P.: 'A class of unusual lightning electric field waveforms with very strong high-frequency radiation', *J. Geophys. Res.*, 1989, **94**, pp.16255–16267
164 FERNANDO, M. and COORAY, V.: 'Sub-microsecond structure of electric field pulses generated by cloud flashes'. Proceedings of the international conference on *Lightning protection*, Birmingham, England, 1998
165 BENDJAMIN, J.: 'Characteristics of electrostatic discharges (ESD) based on current, optical and magnetic radiation fields'. Doctoral thesis, University of Uppsala, 2000

166 WILSON, C.T.R.: 'Investigations on lightning discharges and on the electric field of thunderstorms', *Philos. Trans. R. Soc. Lond. A*, 1920, **221**, pp.73–115
167 MALAN, D.J.: 'Physics of lightning' (English Univ. Press, London, 1963)
168 KRIDER, E.P., DAWSON, G.A., and UMAN, M.A.: 'Peak power and energy dissipation in a single stroke lightning flash', *J. Geophys. Res.*, 1968, **73**, pp.3335–3339
169 UMAN, M.A.: 'Lightning' (McGraw-Hill, New York, 1969)
170 CONNER, T.R.: 'The 1967 APRA-AEC joint lightning study at Los Alamos, vol. 1'. LA-3754, Los Alamos Sci. Lab., Los Alamos, N.M., 1967
171 BERGER, K.: 'The earth flash', *in* GOLDE, R.H. (Ed.): 'Lightning' (Academic, San Diego, California) pp.119–190
172 BARASCH, G.E.: 'Spectral intensities emitted by lightning discharges', *J. Geophys. Res.*, 1970, **75**, pp.1049–1057
173 ZHIVLYUK, Y.N. and MANDEL'SHTAM, S.L.: 'On the temperature of lightning and force of thunder', *Sov. Phys. JEPT*, 1961, **13**, pp.338–340
174 FEW, A.A.: 'Power spectrum of thunder', *J. Geophys. Res.*, 1969, **74**, pp.6926–6934
175 PLOOSTER, M.N.: 'Numerical model of the return stroke of the lightning channel', *Phys. Fluids*, 1971, **14**, pp.2124–2133
176 HILL, R.D.: 'Channel heating in return stroke lightning', *J. Geophys. Res.*, 1971, **76**, pp.637–645
177 PAXTON, A.H., GARDNER, R.L., and BAKER, L.: 'Lightning return stroke: A numerical calculation of the optical radiation', *Phys. Fluids*, 1986, **29**, pp.2736–2742
178 ORVILLE, R.E.: 'Global distribution of midnight lightning September to November 1977', *Mon. Weather Rev.* 1981, **109**, pp.391–395
179 TURMAN, B.N. and EDGAR, B.C.: 'Global lightning distributions at dawn and dusk', *J. Geophys. Res.*, **87**, pp.1191–1206
180 PRENTICE, S.A.: 'Frequencies of lightning discharges', *in* GOLDE, R.H. (Ed.): 'Physics of Lightning' (Academic Press, New York, 1977) pp.465–496
181 KRIDER, E.P., NOGGLE, R.C., PIFER, A.E., and VANCE, D.L.: 'Lightning direction-finding system for forest fire detection', *Bull. Am. Meteorol. Soc.*, 1980, **61**, (9), pp.980–986
182 KOTAKI, M., KURIKI, I., KATOH, C., and SUGIUCHIJ, H.: 'Global distribution of thunderstorm activity', *J. Radio Res. Lab.*, 1981, **66**
183 SCHUMANN, W.O.: 'Über die strahlungslosen Eigenschwingungen einer leitenden Kügel, die von einer Luftschicht und einer Ionosphärenhulle umgeben ist', *Z. Naturforsch*, 1952, **72**, 149–154
184 WILLIAMS, E.R.: 'Schumann resonance: a global tropical thermometer', *Science*, 1992, **256**, pp.1184–1187
185 ORVILLE, R.E.: 'Cloud-to-ground lightning in the blizzard of '93', *Geophys. Res. Lett.*, 1993, **20**, (13), pp.1367–1370
186 PRENTICE, S.A. and MACKERRAS, D.: 'The ratio of cloud to cloud ground lightning flashes in thunderstorms, *J. Appl. Meterol.*, 1977, **16**, pp.545–549

187 RAKOV, V.A., UMAN, M.A., and THOTTAPPILLIL, R.: 'Review of lightning properties from electric field and TV observations', *J. Geophys. Res.*, 1994, **99**, pp.10745–10750
188 MACKERRAS, D. and DARVENIZA, M.: 'Latitudinal variation of lightning occurrence characteristics', *J. Geophys. Res.*, 1994, **99**, (D5), pp.10813–10821
189 COORAY and GALVAN, A.: 'The stepped leader as a source interference in electrical installations'. Proceedings of the 25th international conference on *Lightning protection* (ICLP), Rhodos, Greece, 2000
190 HILL, R.D.: 'A survey of lightning energy estimates', Reviews of Geophys. and Space Phy., 1979, **17**, pp.155–164
191 BALADONI, S. and GALLIMBERTI, I.: 'Basic data for air discharges'. Padua University report, UPee 72/05, Italy, 1972
192 AKYUZ, M. and COORAY, V.: 'The Franklin lightning conductor: conditions necessary for the initiation of a connecting leader', *J. Electrost*., **51**–**52**, pp.319–325
193 LALANDE, P.: 'Study of the lightning strike conditions on a grounded structure'. Ph.D. thesis, Publication of Office National D'études et de Recherches Aérospatiales (ONERA), France, 1996
194 KRIDER, P.E., MURPHY, M.J., and MAIER, L.M.: 'Electrical structure of Florida thunderclouds'. Proceedings of *Lightning and mountains 97*, Chamonix, France, 1997
195 HILL, E.L. and ROBB, J.D.: 'Pressure pulse from a lightning stroke', *J. Geophys. Res.*, 1968, **73**, pp.1883–1888
196 SCHONLAND, B.F.J. and COLLENS, H.: 'Progressive lightning I', *Proc. R. Soc., London Ser., A*, 1934, **143**, pp.654–674
197 McEACHRON, K.B.: 'Lightning to the Empire State Building', *J. Franklin Inst.*, 1939, **227**, pp.149–217
198 WANG, D., RAKOV, V.A., UMNA, M.A., TAKAGI, N., WATANABE, T., CRAWFORD, D.E., RAMBO, K.J., SCHNETZER, G.H., FISHER, R.J., and KAWASAKI, Z.-I.: 'Attachment process in rocket triggered lightning', *J. Geophys. Res.*, 1999, **104**, pp.2143–2150
199 WANG, D., TAKAGI, N., WATANABE, T., RAKOV, V.A., and UMAN, M.A.: 'Observed leader and return stroke propagation characteristics in the bottom 400 m of a rocket triggered lightning channel', *J. Geophys. Res.*, 1999, **104**, pp.14369–14376
200 PIERCE, E.T.: 'Electrostatic field changes due to lightning discharges', *Q. J. R. Meteorol. Soc.*, 1955, **81**, pp.211–228
201 BRAGINSKIII, S.I.: 'Theory of the development of spark channel', *Sov. Phys. – JETP*, 1958, **34**, pp.1068–1074
202 OETZEL, G.N.: 'Computation of the diameter of a lightning return stroke', *J. Geophys. Res.*, 1968, **73**, pp.1889–1375.
203 BERGER, K., ANDERSON, R.B., and KRÖNINGER, H.: 'Parameters of lightning flashes', *Electra*, 1975, **40**, pp.101–119
204 WINN, W.P.: 'A laboratory analog to the dart leader and return stroke of lightning', *J. Geophys. Res.*, 1965, **70**, pp.3265–3270

205 HUBERT, P. and MOUGET, G.: 'Return stroke velocity measurements in two triggered lightning flashes', *J. Geophys. Res.*, 1981, **86**, pp.5253–5261
206 IDONE, V.P., ORVUILLE, R.E., HUBERT, P., BARRET, L., and EYBERT-BERARD, A.: 'Correlated observations of three triggered lightning flashes', *J. Geophys. Res.*, 1984, **89**, pp.1385–1394
207 CRAWFORD, D.E., RAKOV, V.A., UMAN, M.A., SCHNETZER, G.H., RAMBO K.J., STAPLETON, M.V. and FISHER, R.J.: *J. Geophys. Res.*, 2001, **106**, pp.14909–14917
208 LEVINE, D.M.: 'The temporal structure of RF radiation from lightning'. NASA tech. memo, TM-78113, 1978
209 GUNN, R.: 'Electric field intensity inside of natural cloud', *J. Appl. Phys.*, 1948, **19**, pp.481–484
210 WINN, W.P., SCHWEDE, G.W., and MOORE, C.B.: 'Measurements of electric fields in thunderclouds', *J. Geophys. Res.*, 1974, **79**, pp.1761–1767
211 WINN, W.P., MOORE, C.B., and HOLMES, C.R.: 'Electric field structure in an active part of a small, isolated thundercloud', *J. Geophys. Res.*, 1981, **86**, pp.1187–1193
212 MARSHALL, T.C. and RUST, W.D.: 'Electric field soundings through thunderstroms', *J. Geophys. Res.*, 1991, **96**, pp.22297–22306
213 MARSHALL, T.C., McCARTHY, M.P., and RUST, W.D.: 'Electric field magnitudes and lightning initiation in thunderstorms', 3rd international workshop on *Physics of lightning*, France, 1997
214 COORAY, V., BERG, M., AKYUZ, M., LARSSON, A., ZITNIK, M., and SCUKA, V.: 'Initiation of ground flashes: some microscopic electrical processes associated with precipitation particles'. 24th international conference on *Lightning protection*, Birmingham, United Kingdom, 1998
215 TAYLOR, G.I.: 'Disintegration of water drops in an electric field', *Proc. R. Soc.*, 1964, **A 280**, pp.383–397
216 CRABB, J.A. and LATHAM, J.: 'Corona from colliding drops as a possible mechanism for the triggering of lightning', *Q. J. R. Meteorol. Soc.*, 1974, **100**, pp.191–202
217 NGUYEN M.D. and MICHNOWSKI, S.: 'On the initiation of lightning discharge in a cloud 2. The lightning initiation on precipitation particles', *J. Geophys. Res.*, 1996, **101**, pp.26675–26680
218 LATHAM, J. and DYE, J.E.: 'Calculations on the electrical development of a small thunderstorm', *J. Geophys. Res.*, 1989, **94**, pp.13141–13144
219 MASON, B.J.: 'The physics of clouds' (Clarendon Press, Oxford, 1971)
220 ROUSSEL-DUPRÉ, R.A., GUREVICH, A.V., JUNNEL, T., and MILIKH, G.M.: 'Kinetic theory of runaway breakdown', *Phys. Rev.*, 1994, **49**, pp.2257
221 MARSHALL, T.C., McCARTHY, M.P., and RUST, W.D.: 'Electric field magnitudes and lightning initiation in thunderstorms', *J. Geophys. Res.*, 1995, **100**, pp.7097–7103
222 DEPASSE, P.: 'Statistics on artificially triggered lightning', *J. Geophys. Res.*, 1994, **99**, pp.18515–18522

223 MALAN, D.J. and SCHONLAND, B.F.J.: 'An electrostatic fluxmeter of short response time for use in studies of transient field changes', *Proc. Phys. Soc. London Ser. B*, 1950, **63**, pp.402–408
224 FISHER, R.J. and UMAN, M.A.: 'Measured electric field risetimes for first and subsequent lightning strokes', *J. Geophys. Res.*, 1972, **77**, pp.399–406
225 NORINDER, H. and DAHLE, O.: 'Measurements by frame areals of current variations in lightning discharges', *Arkiv Mat. Astron. Fysik*, 1945, **32A**, pp.1–70
226 KRIDER, E.P. and NOGGLE, R.C.: 'Broadband antenna system for lightning magnetic fields', *J. Appl. Meterolog.*, 1975, **14**, pp.252–256
227 HORNER, F.: 'The design and use of instruments for counting local lightning flashes', *Proc. Inst. Electr. Eng.*, 1960, **107B**, pp.321–330
228 PIERCE, E.T.: 'The influence of individual variations in field change due to lightning discharges upon design and performance of lightning flash counters', 'Archiv Met. Geophys. Bioklim', Series A: *Met. Geophys.*, 1956, **A9**, pp.78–86
229 ANDERSON, R.B., VAN NIEKERK, H.R., PRENTICE, S.A., and MACKERRAS, D.: 'Improved lightning flash counters', *Electra*, 1979, **66**, pp.85–98
230 COORAY, V.: 'Response of CIGRE and CCIR lightning flash counters to the electric field changes from lightning: a theoretical study', *J. Geophys. Res.*, 1986, **91**, pp.2835–2842
231 MACKERRAS, D.: 'Automatic short range measurement of the cloud flash to ground flash ratio in thunderstorms', *J. Geophys. Res.*, 1985, **90**, pp.6195–6201
232 WATSON-WATT, R.A. and HERD, J.F.: 'An instantaneous direct-reading radiogoniometer', *J. Inst. Electr. Eng.*, 1926, **64**, pp.611–622
233 HORNER, F.: 'Very low frequency propagation and direction finding', *Proc. IEEE*, 1957, **101B**, pp.73–80
234 KRIDER, E.P., NOGGLE, R.C., and UMAN, M.A.: 'A gated wide band direction finder for lightning return strokes, *J. Applied. Meteorol.*, 1976, **15**, pp.301–306
235 LEWIS, E.A., HARVEY, R.B., and RASMUSSEN, J.E.: 'Hyperbolic direction finding with sferics of transatlantic origin', *J. Geophys. Res.*, 1960, **65**, pp.1879–1905
236 OETZEL, G.N. and PIERCE, E.T.: 'VHF technique for locating lightning', *Radio Sci.*, 1969, **4**, pp.199–201
237 LENNON, C.L.: 'LDAR–a new lightning detection and ranging system (abstract)', *EOS Trans. Am. Geophys. Union*, 1975, **56**, (12), p.991
238 RUSTAN, P.L.: 'Properties of lightning derived from time series analysis of VHF radiation data'. Ph.D. thesis, Univ. of Florida, Gainsville, USA, 1979
239 CIANOS, N., OETZEL, G.N., and PIERCE, E.T.: 'A technique for accurately locating lightning at close range', *J. Appl. Meteorol.*, 1972, **11**, pp.1120–1127
240 MURTY, R.C. and MACCLEMENT, W.D.: 'VHF direction finder for lightning location', *J. Appl. Metteorol.*, 1973, **12**, pp.1401–1405

241 TAYLOR, W.L.: 'A VHF technique for space time mapping of lightning discharge processes', *J. Geophys. Res.*, 1978, **83**, pp.3575–3583
242 HAYENGA, C.O.: 'Positions and movement of VHF lightning sources determined with microsecond resolution by interferometry'. Ph.D. thesis, Univ. of Colorado, Boulder, USA, 1979
243 HAYENGA, C.O. and WARWIK, J.W.: 'Two dimensional interferometric positions of VHF lightning sources', *J. Geophys. Res.*, 1981, **86**, pp.7451–7462
244 RICHARD, P. and AUFFRAY, G.: 'VHF-UHF interferometric measurements, application to lightning discharge mapping', *Radio Sci.*, 1985, **20**, pp.171–192
245 USHIO, T., KAWASAKI, Z., OHTA Y., and MATSUURA, K.: 'Broadband interferometric measurement of rocket triggered lightning in Japan, *Geophys. Res. Lett.*, 1997, **24**, pp.2769–2772
246 KRIDER, E.P., MAIER, L.M., MURPHY, M.J., and SCHIBER, D.J.: 'The onset of electrification in Florida thunderstorms'. 1998 fall meeting, AGU, San Francisco, CA, USA, 6–10 December 1998
247 GOMES, C. and COORAY, V.: 'Correlation between the optical signatures and current waveforms of long sparks: application in lightning research', *J. Electrost.*, 1998, **43**, 267–274
248 COORAY, V., RAKOV, V., and THEETHAYI, N.: 'On the relationship between the peak return stroke current and the charge on the leader channel-Berger's data revisited.' 27th International Conference on Lightning Protection (ICLP), France, 2004

Chapter 5

Computation of electromagnetic fields from lightning discharge

Rajeev Thottappillil

Electromagnetic fields from lightning can couple to electrical systems and produce transient overvoltages, which can cause power and telecommunication outages and destruction of electronics. Therefore calculation of the electric and magnetic fields from different lightning processes has practical applications. In this Chapter expressions for electric and magnetic fields are derived for some simplified charge and current configurations applicable to lightning. In general, lightning currents and charges vary with time. First, simple expressions for nontime-varying cases are presented, then electric and magnetic field expressions from time-varying lightning sources are given.

5.1 Electrostatics and magnetostatics

5.1.1 Electrostatic field from a dipole

Measurements indicate that thunderclouds have a bipolar structure with a lower negative charge region and an upper positive charge region. Therefore as far as the slowly varying fields at ground level are concerned, the thundercloud can be approximately modelled as a dipole. The charge structure of thunderclouds has been dealt with in Chapter 1. For simplicity we can assume a spherically symmetric distribution of charges for negatively and positively charged regions of the thundercloud, even though the charge distribution is more extended horizontally than vertically. The charge centres are separated by a distance Δh. The earth is assumed to be flat and a perfect conductor. We will now see how the static electric field at ground level will look as a function of distance from the thundercloud. The geometry of the problem is shown in Figure 5.1. The influence of ground on the fields is taken into account by the image charges.

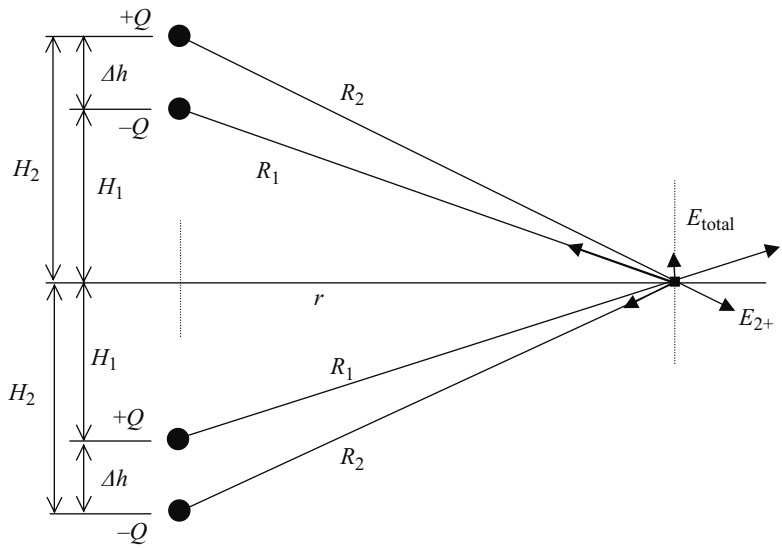

Figure 5.1 Diagram for the calculation of electrostatic fields from a dipole above ground

The electric field at ground from charge $+Q$ at height H_2 is given by:

$$E_{2+} = \frac{Q}{4\pi\varepsilon_0 R_2^2} \text{V/m} \tag{5.1}$$

where $R_2 = \sqrt{H_2^2 + r^2}$. The direction of E_{2+} is as shown in Figure 5.1, and the direction of fields from other point charges are also shown. From the geometry of the problem it is clear that there is no net horizontal component for the electric field at ground level. We define a net vertical component E_{Total} as shown in Figure 5.1. The contribution of E_{2+} in the direction of E_{Total} is given by multiplying eqn. 5.1 by $-H_2/R_2$, the cosine of the angle between the vectors E_{Total} and E_{2+}. Adding up the contribution to E_{Total} from the two point charges and their images we get an expression for the total field as:

$$E_{Total} = \frac{2Q}{4\pi\varepsilon_0}\left[\frac{H_1}{R_1^3} - \frac{H_2}{R_2^3}\right] \tag{5.2}$$

where $R_1 = \sqrt{H_1^2 + r^2}$.

The distance between the point charges is Δh and $H_2 = H_1 + \Delta h$. As the value of the horizontal distance r is increased, E_{Total} changes its polarity from a positive value (the same direction shown in Figure 5.1) when $r \ll H_1$ to a negative value when $r \gg H_1$. In between these extremes there is a certain distance r at which the net field E_{Total} becomes zero, which can be found by setting eqn. 5.2 equal to zero. It has been noticed that the field at ground created by a thunderstorm reverses its sign as the thunderstorm approaches the observing station from far away.

As mentioned in an earlier chapter, the fine weather electric field vector is directed downward towards the earth and by convention, in atmospheric electricity studies, this field is considered to be the positive field. The sign convention adopted in this Chapter is opposite to this convention.

5.1.2 Magnetostatic field from a line current

During cloud-to-ground lightning, the leader and the return stroke channels are predominantly vertical and carry a current. For most of its existence this current varies rapidly with time. However, for simplicity, let us first consider a line current above the ground whose current is directed upward and is steady or only slowly varying with time. The effect of the ground on the magnetic field is taken into account by considering an image channel carrying an equal current and also in the upward direction (Figure 5.2).

The magnetic flux density at any distance R from a current element Idz' is given by

$$d\bar{B} = \frac{\mu_0 I dz'}{4\pi R^2}(\hat{z} \times \hat{R}) \tag{5.3}$$

where $\hat{z}$ is a unit vector in the direction of current and $\hat{R}$ is a unit vector directed towards the field point from the current element dz'. Now:

$$\hat{z} \times \hat{R} = \sin\theta\hat{\phi} = \frac{r}{R}\hat{\phi} \tag{5.4}$$

where $R = \sqrt{z'^2 + r^2}$ and $\hat{\phi}$ is the unit vector in the direction of the magnetic field flux density.

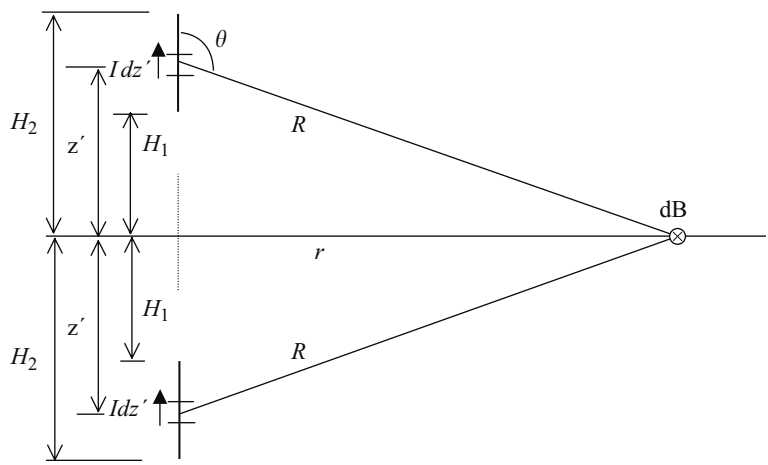

Figure 5.2 Diagram for the calculation of magnetostatic fields from a line current above ground

Total magnetic flux density is obtained by integrating eqn. 5.3 over the length of the channel. The image channel also creates an equal magnetic flux density at a horizontal distance r on the ground and in the same direction. Therefore the contribution from the image channel is included by multiplying eqn. 5.3 by 2. The total magnetic field is given by:

$$\bar{B} = \frac{\mu_0 I}{2\pi} \int_{H_1}^{H_2} \frac{r}{(z'^2 + r^2)^{3/2}} \, dz' \hat{\phi}$$

$$= \frac{\mu_0 I}{2\pi r} \left[\frac{H_2}{\sqrt{H_2^2 + r^2}} - \frac{H_1}{\sqrt{H_1^2 + r^2}} \right] \hat{\phi} \tag{5.5}$$

If a steady current flows between the ground ($H_1 = 0$) and the charge centre at height H ($H_2 = H$), then eqn. 5.5 becomes:

$$\bar{B} = \frac{\mu_0 I}{2\pi r} \left[\frac{H}{\sqrt{H^2 + r^2}} \right] \hat{\phi} \tag{5.6}$$

Very close to the channel (r $\ll$ H) the magnetic flux density becomes:

$$\bar{B} = \frac{\mu_0 I}{2\pi r} \hat{\phi} \tag{5.7}$$

and very far away from the channel (r $\gg$ H) the magnetic flux density becomes:

$$\bar{B} = \frac{\mu_0 I H}{2\pi r^2} \hat{\phi} \tag{5.8}$$

5.2 Time-varying fields from lightning

5.2.1 Introduction

Lightning discharge is a thin channel when compared with its overall length. Usually we are interested in the electromagnetic fields created by lightning several tens of metres or kilometres away. Therefore to calculate electric and magnetic fields from lightning, it is modelled as a linear antenna which has some current distribution or which has a certain line charge density distribution that changes with time. Besides, lightning discharge is self propagating and its length extends at great speeds, sometimes at a significant fraction of the speed of light. Therefore, field calculation requires careful consideration of the retardation phenomenon due to the finite travel time of the signals at the speed of light. In this Chapter the analytical expressions for calculating the electric and magnetic fields from lightning are presented. These are general expressions applicable to any line source distribution that varies with time.

5.2.1.1 Three approaches for calculating the electric fields

Expressions for electric and magnetic fields from an electric dipole in the frequency domain can be found in most books on electromagnetics. However, time-domain expressions are the most suitable for lightning discharge since it is a transient event that changes its current and charge distribution in space and time in a nonperiodic manner. Besides, the lightning discharge propagates and hence the linear dimensions of the discharge increase with time, often at speeds one third to one half the speed of light.

The problem of calculating the electric and magnetic fields from a known source distribution is discussed extensively in the literature. Usually the fields are calculated by using scalar and vector potentials. These potentials are directly related to the source distribution.

There are three equivalent approaches to calculating the electric fields produced by a specified source. Two of these equivalent approaches are discussed in [1,2,24], and the third equivalent approach in [4]. The first approach, the so-called dipole technique or Lorentz condition technique, involves:

(i) the specification of current density $\bar{J}$
(ii) the use of $\bar{J}$ to find the vector potential $\bar{A}$
(iii) the use of $\bar{A}$ and the Lorentz condition to find the scalar potential ϕ
(iv) the computation of electric field $\bar{E}$ using $\bar{A}$ and ϕ
(v) the computation of magnetic field $\bar{B}$ using $\bar{A}$.

In this technique, the source is described only in terms of current density, and the field equations are expressed only in terms of current. The use of the Lorentz condition eliminates the need for the specification of the line charge density along with the current density and assures that the current continuity equation, which is not explicitly used in this technique, is satisfied.

The second approach, the so-called monopole technique or the continuity equation technique, involves:

(i) the specification of current density $\bar{J}$ (or line charge density ρ)
(ii) the use of $\bar{J}$ (or ρ) and the continuity equation to find ρ (or $\bar{J}$)
(iii) the use of $\bar{J}$ to find $\bar{A}$ and ρ to find ϕ
(iv) the computation of electric field $\bar{E}$ using $\bar{A}$ and ϕ
(v) the computation of magnetic field $\bar{B}$ using $\bar{A}$.

In this technique, the source is described in terms of both current density and line charge density, and the field equations are expressed in terms of both charge density and current. The current continuity equation is needed to relate the current density and charge density. There is no need for the explicit use of the Lorentz condition in this technique, although properly specified scalar and vector potentials do satisfy the Lorentz condition.

In the third approach, the electric fields are expressed in terms of the apparent charge density, that is, the charge density that would be seen on the lightning channel by an observer at the field point. The difference between this apparent charge density and the charge density in the second approach above will be explained later in this

Chapter. Field equations obtained in either of the first two approaches can be converted into this third form.

In the first approach electric fields are completely expressed in terms of the current, in the second approach in terms of both current and charge and in the third approach completely in terms of apparent charge. Magnetic fields are expressed completely in terms of current in the first two approaches and completely in terms of apparent charge in the third approach.

5.3 Treatment of retardation effects

A lightning return stroke wavefront extends typically at speeds one third to one half the speed of light. The return stroke current above the extending wavefront is considered to be zero and the current below the extending wavefront is rapidly changing with time. The finite travel time from the source at the return stroke to the point where the field is measured cannot be ignored. At any given time the observer at the field point sees the current on the return stroke channel from an earlier time. Similarly, the observer does not see the true length of the channel, that is, only some portion of the actual lightning channel contributes to the field at a given time. Therefore retarded sources and retarded channel lengths are to be used in the calculation of return stroke fields. An extensive treatment of retardation effects in calculating the electromagnetic fields from the lightning discharge is given in [5]. The apparent length $L'(t)$ of the return stroke channel, to be used in the expressions for the fields in later sections of this Chapter, are derived in this section.

Consider a return stroke channel with one end fixed at A as shown in Figure 5.3. It takes a time r/c for the information from A to reach the observer at P and hence

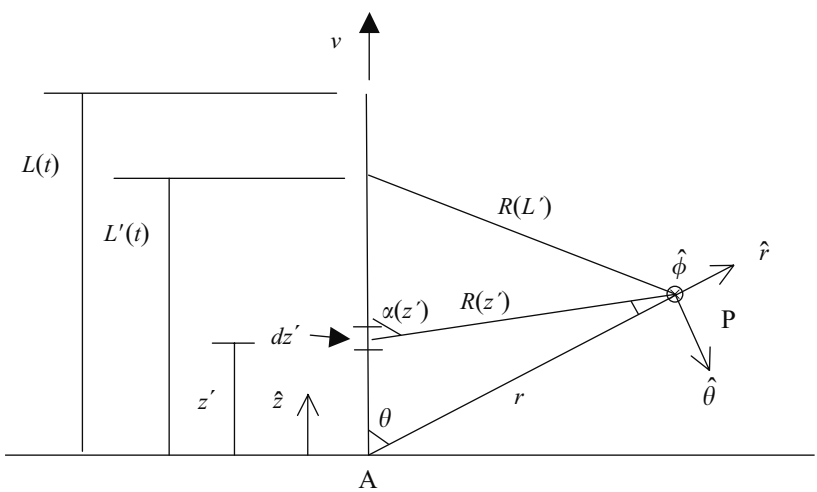

Figure 5.3 Geometry of the problem in the treatment of retardation effects

the observer sees the channel emerging from A at time r/c. The actual length $L(t)$ of the channel at a time t is given by $L(t) = vt$, where v is the speed of the return stroke wavefront. The apparent length of the channel at time t seen by the observer at P is different from $L(t)$. This length, $L'(t)$, can also be called the retarded length.

If we define the time t such that it is the sum of the time required for the return stroke wavefront to reach a height $L'(t)$ to the observer at P, t can be written as:

$$t = \frac{L'(t)}{v} + \frac{R(L')}{c} \tag{5.9}$$

where

$$R(L') = \sqrt{r^2 + L'^2(t) - 2L'(t)r\cos\theta} \tag{5.10}$$

The retarded length $L'(t)$ can be obtained by solving eqns 5.9 and 5.10, and is given by:

$$L'(t) = \frac{r}{1-(v^2/c^2)}\left(-\frac{v^2}{c^2}\cos\theta + \frac{vt}{r} - \frac{v}{c}\sqrt{\left(1-\frac{v^2}{c^2}\right) + \frac{v^2t^2}{r^2} + \frac{v^2}{c^2}\cos^2\theta - \frac{2vt}{r}\cos\theta}\right) \tag{5.11}$$

If the ground is treated as being perfectly conducting, eqn. 5.11 can also be used, with θ replaced by $(180° - \theta)$ to find the apparent length $L''(t)$ of the channel image seen by the observer.

If all the channel sections were equidistant from the observer, that is, if the discharge were to extend in a circular arc of radius r with the observer at the centre, the length of the discharge seen by the observer would be $L'(t) = v \cdot (t - r/c)$. For $\theta = 0$, that is, for the observer straight ahead of the propagating discharge, the apparent channel length is obtained from eqn. 5.11 as:

$$L'(t) = \frac{v}{1 - v/c} \cdot (t - r/c) \tag{5.12}$$

and the image channel length is obtained from eqn. 5.11 by replacing θ by 180° as:

$$L''(t) = \frac{v}{1 + v/c} \cdot (t - r/c) \tag{5.13}$$

If the channel is very small compared with the distance to the observer, that is, if $L'(t) \ll r$, then $R(L')$ can be approximated as $R(L') = r - L'(t)\cos\theta$, substitution of which in eqn. 5.9 gives:

$$L'(t) = \frac{v}{1 - (v/c)\cos\theta} \cdot (t - r/c) \tag{5.14}$$

5.4 Fields in terms of current (the Lorentz condition approach)

The lightning return stroke channel can be modelled as a straight line fixed at one end A, with the other end extending with speed v. The geometry of the problem is shown in Figure 5.4. The current on the lightning channel is represented by $i(z', t)$, where z' indicates the position along the z axis with origin at the base of the channel and t indicates the time. At time $t = 0$ the return stroke starts to propagate from the origin A. The observer at the fixed field point P sees the return stroke starting to propagate from the origin at time $t = r/c$, where c is the speed of light. The retarded current at any elemental channel section dz' is given by $i(z', t - R(z')/c)$, where z' is less than or equal to $L'(t)$, the length of the return stroke channel seen by the observer at P at time t. Note that the assumption of constant return stroke speed is not required in the derivations presented here.

In fact, the lightning channel can be considered to be composed of many electric dipoles of length dz'. An electric dipole is a linear current element whose length is vanishingly small compared with the distance at which the fields are to be calculated. Also, the current is assumed to be a constant over the length of the dipole. Field expressions in the time domain, with specific application to lightning, were popularised by the paper [3] in 1975, and later developed by others [2,4–7]. The treatment presented here closely follows that of [2].

The vector potential at P due to the entire extending channel is given by (eqn. 9 of [5]):

$$\bar{A}(r, \theta, \tau) = \frac{1}{4\pi\varepsilon_0 c^2} \int_0^{L'(\tau)} \frac{i(z', \tau - R(z'/c)}{R(z')} \hat{z}\, dz' \tag{5.15}$$

where τ is a time less than or equal to time t. At time τ, the return stroke wavefront is seen at a height $L'(\tau)$ by the observer at P and $L'(\tau)$ is less than or equal to $L'(t)$. Note that in eqn. 5.15 we have not considered the presence of ground, usually assumed to be perfectly conducting and replaced by the channel image.

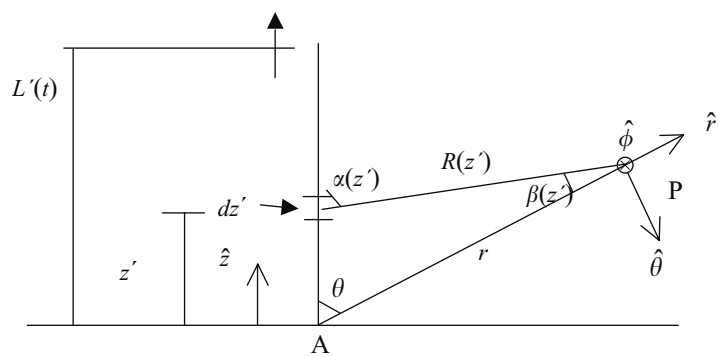

Figure 5.4 Geometry of the problem

The total electric field can be calculated using the relation:

$$\bar{E} = -\nabla\phi - \frac{\partial \bar{A}}{\partial t} \tag{5.16}$$

where ϕ can be obtained from the Lorentz condition

$$\nabla \bullet \bar{A} + \frac{1}{c^2}\frac{\partial \phi}{\partial t} = 0$$

as

$$\phi(r,\theta,t) = -c^2 \int_{r/c}^{t} \nabla \bullet \bar{A}\, d\tau \tag{5.17}$$

Taking the divergence of eqn. 5.15 it can be shown that:

$$\begin{aligned}\nabla \bullet \bar{A}(r,\theta,\tau) = +\frac{1}{4\pi\varepsilon_0 c^2}\int_0^{L'(\tau)} \Bigg[&\frac{z' - r\cos\theta}{R^3(z')} i(z', \tau - R(z')/c) \\ &+ \frac{z' - r\cos\theta}{cR^2(z')}\frac{\partial i(z', \tau - R(z')/c)}{\partial \tau}\Bigg] dz' \\ &+ \frac{1}{4\pi\varepsilon_0 c^2}\frac{L'(\tau) - r\cos\theta}{cR^2(L')} i(L', \tau - R(L')/c)\frac{dL'(\tau)}{d\tau}\end{aligned} \tag{5.18}$$

Substituting eqn. 5.18 into eqn. 5.17 and interchanging the order of integration, an expression for the scalar potential completely in terms of current can be obtained. As time increases from r/c to t, the channel length $L'(\tau)$ increases monotonically from 0 to $L'(t)$. Therefore the order of integration can be changed as follows according to the standard rule:

$$\int_{r/c}^{t}\int_0^{L'(\tau)} \Rightarrow \int_0^{L'(t)}\int_{\tau}^{t} \tag{5.19}$$

where the lower limit $\tau = t_b$ is the time at which the observer at the field point sees the return stroke front at height z' for the first time. For a constant return stroke speed v:

$$\tau = \frac{L'(\tau)}{v} + \frac{R(L'(\tau))}{c} = \frac{z'}{v} + \frac{R(z')}{c}$$

Performing the operations explained above and after some reductions, we get an expression for scalar potential as:

$$\begin{aligned}\phi(r,\theta,t) = -\frac{1}{4\pi\varepsilon_0}\int_0^{L'(t)} \Bigg[&\frac{z' - r\cos\theta}{R^3(z')}\int_{z'/v + R(z')/c}^{t} i(z', t - R(z')/c)\, d\tau \\ &+ \frac{z' - r\cos\theta}{cR^2(z')} i(z', t - R(z')/c)\Bigg] dz'\end{aligned} \tag{5.20}$$

Taking the gradient of eqn. 5.20, $\nabla\phi$, and the time derivative of eqn. 5.15, $\partial\bar{A}/\partial t$, we get an expression for the electric field according to eqn. 5.16 as given below:

$$
\begin{aligned}
\bar{E}(r,\theta,t) = &-\frac{1}{4\pi\varepsilon_0}\hat{r}\int_0^{L'(t)}\frac{\cos\theta - 3\cos\alpha(z')\cos\beta(z')}{R^3(z')} \\
&\times\int_{t_b}^{t} i\left(z',\tau-\frac{R(z')}{c}\right)d\tau\,dz' && a \\
&-\frac{1}{4\pi\varepsilon_0}\hat{r}\int_0^{L'(t)}\frac{\cos\theta - 3\cos\alpha(z')\cos\beta(z')}{cR^2(z')} i\left(z',t-\frac{R(z')}{c}\right)dz' && b \\
&-\frac{1}{4\pi\varepsilon_0}\hat{r}\int_0^{L'(t)}\frac{\cos\theta - \cos\alpha(z')\cos\beta(z')}{c^2R(z')}\frac{\partial i(z',t-R(z')/c)}{\partial t}dz' && c \\
&+\frac{1}{4\pi\varepsilon_0}\hat{\theta}\int_0^{L'(t)}\frac{\sin\theta + 3\cos\alpha(z')\sin\beta(z')}{R^3(z')} \\
&\times\int_{t_b}^{t} i\left(z',\tau-\frac{R(z')}{c}\right)d\tau\,dz' && d \\
&+\frac{1}{4\pi\varepsilon_0}\hat{\theta}\int_0^{L'(t)}\frac{\sin\theta + 3\cos\alpha(z')\sin\beta(z')}{cR^2(z')} i\left(z',t-\frac{R(z')}{c}\right)dz' && e \\
&+\frac{1}{4\pi\varepsilon_0}\hat{\theta}\int_0^{L'(t)}\frac{\sin\theta + \cos\alpha(z')\sin\beta(z')}{c^2R(z')}\frac{\partial i(z',t-R(z')/c)}{\partial t}dz' && f \\
&-\frac{1}{4\pi\varepsilon_0}\hat{r}\frac{\cos\theta - \cos\alpha(L')\cos\beta(L')}{c^2R(L')} i\left(L',t-\frac{R(L')}{c}\right)\frac{dL'}{dt} && g \\
&+\frac{1}{4\pi\varepsilon_0}\hat{\theta}\frac{\sin\theta + \cos\alpha(L')\sin\beta(L')}{c^2R(L')} i\left(L',t-\frac{R(L')}{c}\right)\frac{dL'}{dt} && h
\end{aligned}
\tag{5.21}
$$

In eqn. 5.21, dL'/dt is the speed of the current wavefront as seen by the observer at P, which is different from the real speed v. Also, from Figure 5.4 we get $\cos\alpha(z') = -(z' - r\cos\theta)/R(z')$, $\cos\beta(z') = (r - z'\cos\theta)/R(z')$, and $\sin\beta(z') = z'\sin\theta/R(z')$. In the electric field expression (5.21) terms containing the factors R^{-3}, $c^{-1}R^{-2}$, and $c^{-2}R^{-1}$ are called the static component, the induction component and the radiation component, respectively. The last two terms of eqn. 5.21 containing dL'/dt will have nonzero values only if there is a current discontinuity (nonzero current) at the wavefront.

A common problem in lightning is to find the electric and magnetic fields at ground level from a lightning return stroke, which is considered as straight and vertical above

ground. Under this case $\theta = 90^\circ$ and $\hat{\theta} = -\hat{z}$. The ground is assumed to be infinitly conducting. The effect of the ground plane can be included by considering an image channel carrying an image current. The magnitude and direction of this image current is identical to the current in the channel at any given position and time, for an observer at ground level. The field expressions corresponding to the image channel have their $\hat{r}$-directed components the same in magnitude, but opposite in sign to the $\hat{r}$-directed components in eqn. 5.21. However, the field expressions corresponding to the image channel have their $\hat{\theta}$-directed components the same both in magnitude and sign to that in eqn. 5.21. Therefore, adding the contribution of the image channel to eqn. 5.21, we get the complete field expression as:

$$\begin{aligned} E_V(r,t) = {} & \frac{1}{2\pi\varepsilon_0}\int_0^{L'(t)} \frac{2-3\sin^2\alpha(z')}{R^3(z')}\int_{t_b}^{t} i(z',\tau - R(z')/c)\,d\tau\,dz' \\ & \frac{1}{2\pi\varepsilon_0}\int_0^{L'(t)} \frac{2-3\sin^2\alpha(z')}{cR^2(z')} i(z',t-R(z')/c)\,dz' \\ & \frac{-1}{2\pi\varepsilon_0}\int_0^{L'(t)} \frac{\sin^2\alpha(z')}{c^2R(z')}\frac{\partial i(z',t-R(z')/c)}{\partial t}\,dz' \\ & \frac{-1}{2\pi\varepsilon_0}\frac{\sin^2\alpha(L')}{c^2R(L')} i(L',t-R(L')/c)\frac{dL'}{dt} \end{aligned} \tag{5.22}$$

The magnetic field is given by $\bar{B} = \nabla \times \bar{A}$. For a vertical channel the magnetic field has only a horizontal component and at ground level it is given by (taking the curl of eqn. 5.15 and adding the contribution of the image channel):

$$\begin{aligned} B_\phi(r,t) = {} & \frac{1}{2\pi\varepsilon_0 c^2}\int_0^{L'(t)} \left(\frac{\sin\alpha(z')}{R^2(z')} i(z',t-R(z')/c) \right. \\ & \left. + \frac{\sin\alpha(z')}{cR(z')}\frac{\partial i(z',t-R(z')/c)}{\partial t} \right) dz' \\ & + \frac{1}{2\pi\varepsilon_0 c^2}\frac{\sin\alpha(L')}{cR(L')} i(L',t-R(L')/c)\frac{dL'}{dt} \end{aligned} \tag{5.23}$$

In eqns 5.22 and 5.23, E_V is the vertical (z direction) electric field at ground level and B_ϕ is the horizontal (ϕ direction) magnetic field at ground level, and $L'(t)$ is the height of the return stroke wavefront as seen from the observation point. The lower limit of the time integral of the first term in eqn. 5.22, t_b, is the time at which the return stroke wavefront has reached the height z' for the first time, as seen from the observation point. Equations 5.22 and 5.23 are valid for any return stroke model. Individual terms on the right-hand side of eqn. 5.22 are labelled the electrostatic, induction and radiation components and on the right-hand side of eqn. 5.23 magnetostatic (or induction) and radiation components. It is customary to identify the electrostatic component by its R^{-3} distance dependence, induction components by their R^{-2} dependence and radiation components by R^{-1} dependence. The last term in eqn. 5.22

and the last term in eqn. 5.23 become zero if there is no current discontinuity at the propagating wavefront, i.e. if $i(L', t - R(L')/c) = 0$.

5.5 Fields in terms of current and charge (the continuity equation approach)

The purpose here is to find an expression for electric field using both scalar potential and vector potential related by the continuity equation that defines the relationship between the charge density and current locally. The continuity equation that relates the charge density and current locally, but at retarded time is given by [7,8]:

$$\frac{\partial \rho^*(z', t - R(z')/c)}{\partial t} = -\frac{\partial i(z', t - R(z')/c)}{\partial z'}\bigg|_{t-R(z')/c=const.} \tag{5.24}$$

In eqn. 5.24, the partial differentiation of retarded current with respect to the source coordinate z' is carried out keeping the retarded time constant. That is, the dependence of $R(z')$ on z' is ignored while taking the partial derivative. Note that as viewed by an observer at a remote point P, the relationship between the charge density and current could be different from that given in eqn. 5.24. We will come to this point later in section 5.7.

The return stroke starts from the ground level ($z' = 0$). To satisfy the continuity eqn. 5.24 at $z' = 0$, a point charge $Q(t - r/c)$ is required at $z' = 0$ as the source for the current emerging from $z' = 0$. This stationary point charge is given by:

$$Q(t - r/c) = -\int_{r/c}^{t} i(0, \tau - r/c)\, d\tau \tag{5.25}$$

The scalar potential from the whole lightning channel is given by:

$$\phi(r, t) = \frac{1}{4\pi\varepsilon_0}\frac{Q(t - r/c)}{r} + \frac{1}{4\pi\varepsilon_0}\int_0^{L'(t)} \frac{1}{R(z')}\rho^*(z', t - R(z')/c)\, dz' \tag{5.26}$$

The electric field can be obtained from eqn. 5.16. Using the spherical coordinate system centred at the starting point of the return stroke at ground (Figure 5.4) and ignoring the presence of ground for the moment, the negative gradient of the scalar potential $-\nabla\phi$ and the negative time derivative of the vector potential $-\partial A/\partial t$ can be found as described below. For $-\nabla\phi$ we have:

$$\begin{aligned} -4\pi\varepsilon_0\nabla\phi = &-\hat{r}\frac{\partial}{\partial r}\frac{Q(t - r/c)}{r} - \hat{r}\frac{\partial}{\partial r}\int_0^{L'(t)} \frac{\rho^*(z', t - R(z')/c)}{R(z')}\, dz' \\ &- \hat{\theta}\frac{1}{r}\frac{\partial}{\partial \theta}\int_0^{L'(t)} \frac{\rho^*(z', t - R(z')/c)}{R(z')}\, dz' \end{aligned} \tag{5.27}$$

Note that the first term of eqn. 5.27 is independent of the spatial coordinate θ. The maximum length of the channel $L'(t)$, as seen from the field point, is a function of r, θ and t. The distance to the field point from the differential channel segment $R(z')$ is a function of both r and θ, as given by eqns (5.28).

$$\begin{aligned} R(z') &= \sqrt{r^2 + z'^2 - 2rz'\cos\theta} \\ \frac{dR(z')}{dr} &= \frac{r - z'\cos\theta}{R(z')} \\ \frac{dR(z')}{d\theta} &= \frac{rz'\sin\theta}{R(z')} \end{aligned} \tag{5.28}$$

Carrying out the differentiation of the second and third terms in eqn. 5.27 and using eqns 5.28, we obtain the following expression:

$$\begin{aligned} -4\pi\varepsilon_0\nabla\phi = +\hat{r}\int_0^{L'(t)} &\left[\frac{r - z'\cos\theta}{R^3(z')}\rho^*(z', t - R(z')/c)\right. \\ &\left. + \frac{r - z'\cos\theta}{cR^2(z')}\frac{\partial\rho^*(z', t - R(z')/c)}{\partial t}\right] dz' \\ + \hat{\theta}\int_0^{L'(t)} &\left[\frac{z'\sin\theta}{R^3(z')}\rho^*(z', t - R(z')/c)\right. \\ &\left. + \frac{z'\sin\theta}{cR^2(z')}\frac{\partial\rho^*(z', t - R(z')/c)}{\partial t}\right] dz' \\ - \hat{r}\frac{\rho^*(L', t - R(L')/c)}{R(L')}\frac{\partial L'}{\partial r} &- \hat{\theta}\frac{\rho^*(L', t - R(L')/c)}{rR(L')}\frac{\partial L'}{\partial\theta} \\ - \hat{r}\frac{\partial}{\partial r}\frac{Q(t - r/c)}{r} & \end{aligned} \tag{5.29}$$

The time derivative of the vector potential (eqn. 5.15) is given by:

$$\begin{aligned} -4\pi\varepsilon_0\frac{\partial\bar{A}}{\partial t} = &-\hat{z}\int_0^{L'(t)}\frac{1}{c^2R(z')}\frac{\partial i(z', t - R(z')/c)}{\partial t}dz' \\ &-\hat{z}\frac{i(L', t - R(L')/c)}{c^2R(L')}\frac{dL'}{dt} \end{aligned} \tag{5.30}$$

where $\hat{z} = \hat{r}\cos\theta - \hat{\theta}\sin\theta$. (5.31)

The general expression for the electric field at a field point can be found by combining eqns 5.29, 5.30 and 5.31, and is given below:

$$
\begin{aligned}
\bar{E}(r,\theta,t) = &+\frac{1}{4\pi\varepsilon_0}\hat{r}\int_0^{L'(t)}\frac{\cos\beta(z')}{R^2(z')}\rho^*(z',t-R(z')/c)\,dz' \\
&+\frac{1}{4\pi\varepsilon_0}\hat{r}\int_0^{L'(t)}\frac{\cos\beta(z')}{cR(z')}\frac{\partial\rho^*(z',t-R(z')/c)}{\partial t}\,dz' \\
&-\frac{1}{4\pi\varepsilon_0}\hat{r}\int_0^{L'(t)}\frac{\cos\theta}{c^2R(z')}\frac{\partial i(z',t-R(z')/c)}{\partial t}\,dz' \\
&+\frac{1}{4\pi\varepsilon_0}\hat{\theta}\int_0^{L'(t)}\frac{\sin\beta(z')}{R^2(z')}\rho^*(z',t-R(z')/c)\,dz' \\
&+\frac{1}{4\pi\varepsilon_0}\hat{\theta}\int_0^{L'(t)}\frac{\sin\beta(z')}{cR(z')}\frac{\partial\rho^*(z',t-R(z')/c)}{\partial t}\,dz' \\
&+\frac{1}{4\pi\varepsilon_0}\hat{\theta}\int_0^{L'(t)}\frac{\sin\theta}{c^2R(z')}\frac{\partial i(z',t-R(z')/c)}{\partial t}\,dz' \\
&+\frac{1}{4\pi\varepsilon_0}\hat{r}\frac{\cos\beta(L')}{cR(L')}\rho^*(L',t-R(L')/c)\frac{dL'(t)}{dt} \\
&-\frac{1}{4\pi\varepsilon_0}\hat{r}\frac{\cos\theta}{c^2R(L')}i(L',t-R(L')/c)\frac{dL'(t)}{dt} \\
&+\frac{1}{4\pi\varepsilon_0}\hat{\theta}\frac{\sin\beta(L')}{cR(L')}\rho^*(L',t-R(L')/c)\frac{dL'(t)}{dt} \\
&+\frac{1}{4\pi\varepsilon_0}\hat{\theta}\frac{\sin\theta}{c^2R(L')}i(L',t-R(L')/c)\frac{dL'(t)}{dt} \\
&+\frac{1}{4\pi\varepsilon_0}\hat{r}\left[\frac{1}{r^2}Q(t-r/c)+\frac{1}{rc}\frac{dQ(t-r/c)}{dt}\right]
\end{aligned}
\tag{5.32}
$$

where $\cos\beta(z') = (r - z'\cos\theta)/R(z')$, $\sin\beta(z') = z'\sin\theta/R(z')$, and Q is given by eqn. 5.25.

We are interested in the return stroke field at ground level. For this case, $\theta = 90°$, and therefore $\cos\theta = 0, \sin\theta = 1$, and $\hat{\theta} = -\hat{z}$. The unit vector $\hat{r}$ is now horizontal, pointing away from the channel. A perfectly conducting plane at $z' = 0$ is introduced to simulate the effect of the earth. Using the image theory, we can replace this plane by an image channel carrying current in the same direction as the actual channel. Writing out the equations for image channel and adding them to eqn. 5.32 for the case $\theta = 90°$, we get the expression for the E-field,

as below:

$$
\begin{aligned}
E_V(r,t) = {} & \frac{-1}{2\pi\varepsilon_0}\int_0^{L'(t)} \frac{z'}{R^3(z')}\rho^*(z', t - R(z')/c)\,dz' \\
& \frac{-1}{2\pi\varepsilon_0}\int_0^{L'(t)} \frac{z'}{cR^2(z')}\frac{\partial\rho^*(z', t - R(z')/c)}{\partial t}\,dz' \\
& \frac{-1}{2\pi\varepsilon_0}\int_0^{L'(t)} \frac{1}{c^2R(z')}\frac{\partial i(z', t - R(z')/c)}{\partial t}\,dz' \\
& \frac{-1}{2\pi\varepsilon_0}\frac{L'(t)}{cR^2(L')}\rho^*(L', t - R(L')/c)\frac{dL'}{dt} \\
& \frac{-1}{2\pi\varepsilon_0}\frac{1}{c^2R(L')}i(L', t - R(L')/c)\frac{dL'}{dt}
\end{aligned}
\tag{5.33}
$$

The magnetic field expression using this approach is identical to eqn. 5.23 since it is completely determined by the vector potential. Note that, by definition, the current and charge density in eqn. 5.33 are related by the local continuity equation 5.24. Equation 5.33 contains both current and charge density, while eqn. 5.22 contains only current. The first three terms of eqn. 5.33 are similar to the corresponding terms of the expression for the E-field derived in the book of Jefimenko [9] for a volume charge and current distribution whose boundary is fixed in space. By analogy with eqn. 5.22, the first term of eqn. 5.33 can be considered as representing the electrostatic field (R^{-3} dependence), the sum of the second and fourth terms as representing the induction field ($c^{-1}R^{-2}$ dependence), and the sum of the third and last terms as representing the radiation field ($c^{-2}R^{-1}$ dependence). It appears that the electrostatic, induction and radiation terms (except for the last two terms associated with the wavefront) in eqn. 5.33 can also be identified as containing z' times the line charge density (charge), z' times the time derivative of the line charge density (time derivative of charge) or current, and the derivative of the current, respectively. If there is no current or charge discontinuity at the wavefront, the last two terms become zero.

5.6 Nonuniqueness of electrostatic, induction and radiation field components

Fields calculated using the Lorentz condition approach and the continuity equation approach, given by eqns 5.22 and 5.33, respectively, should be identical since both are derived by rigorous application of electromagnetic principles and use the same basic assumptions. However, in appearance the expressions are different. Therefore it would be interesting to compare the fields from eqns 5.22 and 5.33 due to a known current distribution. It will be shown that although the total fields given by the equations are identical, the individual field components (electrostatic, induction and radiation terms identified by their dependence on R) in these two equations are different. Take

the following numerical example. Imagine the return stroke as a current wave that starts from the ground, and travels up with a constant speed v. In that case the current at any height z' at time t is equal to the current at ground at an earlier time $t - z'/v$, where z'/v is the travel time between ground and the height z'. This is the so-called transmission line (TL) model and the current at any height is related to the current at ground by the relation:

$$i(z', t) = i(0, t - z'/v) \tag{5.34}$$

Since there is no discontinuity at the wavefront for the TL model, the last term of eqn. 5.22 and the last two terms of eqn. 5.33 drop out of the equations. The charge density in eqn. 5.33 is calculated using the local continuity equation 5.24, which for the transmission line model can be rewritten as [4]:

$$\rho^*(z', t - R(z')/c) = \frac{i(0, t - z'/v - R(z')/c)}{v} \tag{5.35}$$

where v is the return stroke speed.

Computed electric fields at distances 50 m, 1 km, and 100 km are shown in Figures 5.5, 5.6 and 5.7, respectively. In the curve labels in these figures, LC indicates the terms in eqn. 5.22, and CE indicates the terms in eqn. 5.33. The labels EQ, EI, and ER indicate the electrostatic (R^{-3} dependence), induction ($c^{-1}R^{-2}$ dependence) and radiation ($c^{-2}R^{-1}$ dependence) field components. The current waveform and return stroke speed used in the calculations are given in [2]. The following can be observed from Figures 5.5 to 5.7 and from eqns 5.22 and 5.33.

1 The total fields given by eqns 5.22 and 5.33 are identical (for up to several decimal places when numbers are compared).

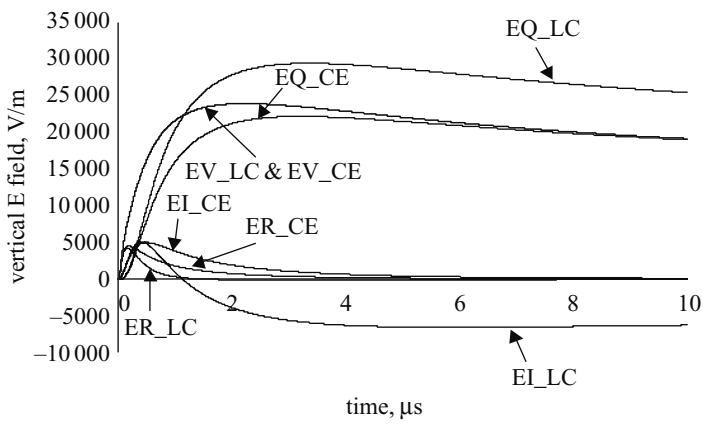

Figure 5.5 Comparison of the total electric field and its components at a distance of 50 m predicted by the TL model and field eqns 5.22 and 5.33. LC (Lorentz condition) at the end of the label corresponds to eqn. 5.22, and CE (continuity equation) to eqn. 5.33

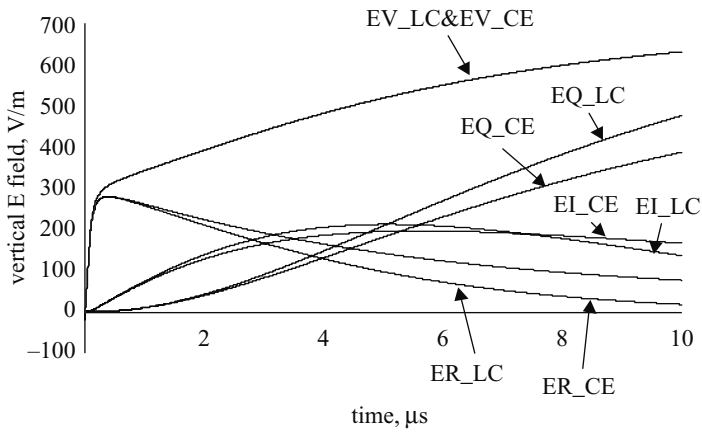

Figure 5.6 *Comparison of the total electric field and its components at a distance of 1 km predicted by the TL model and field eqns 5.22 and 5.33. LC (Lorentz condition) at the end of the label corresponds to eqn. 5.22, and CE (continuity equation) to eqn. 5.33*

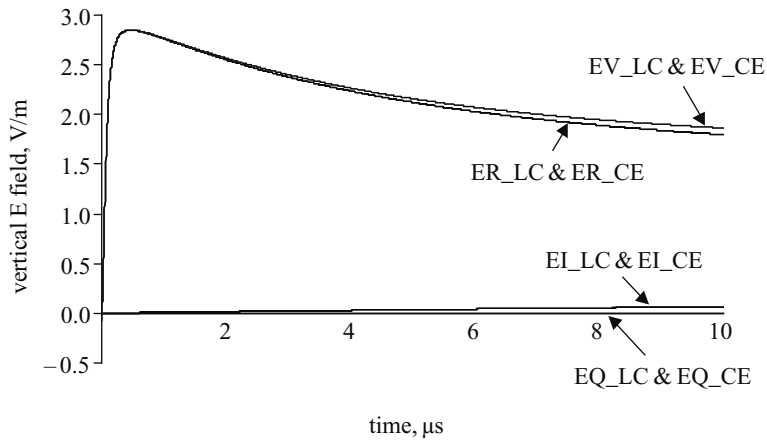

Figure 5.7 *Comparison of the total electric field and its components at a distance of 100 km predicted by the TL model and field eqns 5.22 and 5.33. LC (Lorentz condition) at the end of the label corresponds to eqn. 5.22, and CE (continuity equation) to eqn. 5.33*

2 In eqn. 5.33, the electrostatic and induction terms are given completely by the gradient of the scalar potential, and the radiation term is completely given by the time derivative of the vector potential. In contrast, in eqn. 5.22, both the gradient of the scalar potential and the time derivative of the vector potential contribute to the radiation field term.

3 The electrostatic (R^{-3} dependence), induction ($c^{-1}R^{-2}$ dependence) and radiation ($c^{-2}R^{-1}$ dependence) terms in eqn. 5.22 are different from the corresponding terms in eqn. 5.33. The difference is considerable at 50 m (very close to the channel) and almost negligible at 100 km (far away from the channel).
4 At 50 m (very close to the channel), the electrostatic term (R^{-3} dependence) in eqn. 5.22 is larger than its counterpart in eqn. 5.33 (compare curves EQ_LC and EQ_CE in Figure 5.5).

The above analysis clearly shows that, even though the total electric field from a current or charge distribution is unique, the division of total electric field in the time domain into so-called electrostatic (R^{-3} dependence), induction ($c^{-1}R^{-2}$ dependence) and radiation ($c^{-2}R^{-1}$ dependence) components is not unique. This was further verified by calculating the individual field components and the total fields using six different return stroke models (BG, TCS, MTLE, MTLL and DU models described by [10]). Of these models, the BG and TCS models have current discontinuity at the wavefront whereas other models do not have wavefront current discontinuity.

Note that in the Lorentz condition technique all field components are expressed in terms of current, and in the continuity equation technique both current and charge density are involved. In the Lorentz condition technique the gradient of the scalar potential contributes to all the three field components, whereas in the continuity equation technique it contributes only to the electrostatic and induction field components. In either case, the expression for the magnetic field at ground level is the same, eqn. 5.23, since it depends only on the vector potential. We get the same Poynting vector whether we calculate it from equation pairs 5.22 and 5.23 or 5.33 and 5.23, since the total electric fields given by eqns 5.22 and 5.33 are the same. In fact eqn. 5.22 can be analytically derived from eqn. 5.33, as shown in [2].

5.7 The continuity equation

The continuity equation expresses the principle of charge conservation and is a fundamental law. Let us inspect this with an example of a linear element having only one spatial dimension.

Consider a current-carrying channel segment of length $\Delta z'$ whose centre (midpoint) M is at a height z' (Figure 5.8). Let $q^*(z', t^*)$ be the charge contained in the segment at time t^*. Associated with $q^*(z', t^*)$ is a line charge density which is defined as $\rho^*(z', t^*) = \lim_{\Delta z' \to 0} (q^*(z', t^*))/(\Delta z')$. Charge conservation principles require that a positive rate of change of charge in segment $\Delta z'$ is equal to a negative net outflow of current from the segment. That is:

$$\frac{\partial q^*(z', t^*)}{\partial t^*} = -(i(z' + \Delta z'/2, t^*) - i(z' - \Delta z'/2, t^*))$$

Note that currents at the top and bottom boundaries (T and B) of the segment are specified at the same local time t^*. Dividing through by $\Delta z'$ and letting $\Delta z' \to 0$ we

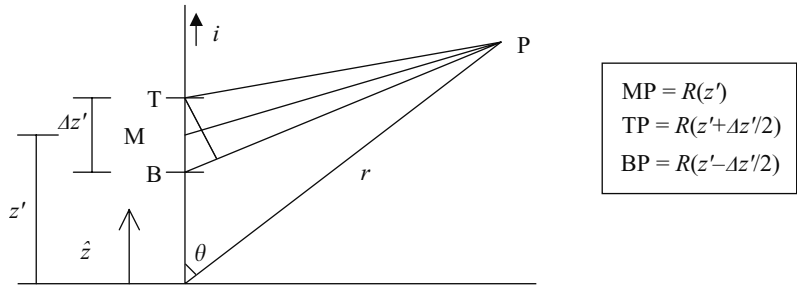

Figure 5.8 Geometry for explaining the physical meaning of two formulations of the continuity equation, which differ in how retardation effects are accounted for

can obtain the continuity equation:

$$\frac{\partial \rho^*(z', t^*)}{\partial t^*} = -\frac{\partial i(z', t^*)}{\partial z'}$$

with t^* kept constant while carrying out the partial differentiation with respect to z'. The local time t^* could as well be $t - R(z')/c$, where t is the time measured at a remote observation point P at a distance $R(z')$ from the midpoint of the segment, as shown in Figure 5.8. Then we can write the continuity equation as:

$$\frac{\partial \rho^*(z', t - R(z')/c)}{\partial t} = -\frac{\partial i(z', t - R(z')/c)}{\partial z'}\bigg|_{t-R(z')/c=const.} \tag{5.36}$$

Note that keeping the time $t - R(z')/c$ a constant in eqn. 5.36 implies that the current crossing the boundary of the element $\Delta z'$ is measured simultaneously at time $t - R(z')/c$. If the currents crossing the ends T and B send a signal to the observer at a certain time then these signals arrive at a remote point simultaneously only if the remote point is equidistant from the ends T and B. An observer on a line passing through the midpoint M of the segment and perpendicular to the segment can receive the signals from the end points simultaneously. Any observer away from this line, such as P in Figure 5.8 cannot receive the signal simultaneously from the end points because of different travel times for the signals. Now let us see the relationship between the charge and current in segment $\Delta z'$ as viewed from point P.

An observer at P does not see the currents at the top (T) and bottom (B) of the segment at the same time. The current at T that the observer sees at a given time t is from an earlier time $t - R(z' + \Delta z'/2)/c$ and the current at B is from a different earlier time $t - R(z' - \Delta z'/2)$. If the difference in the current from the endpoints is interpreted as the rate of change of charge in the segment, then the rate of change of

charge in the channel segment as seen by the observer at P is:

$$\frac{\partial q(z', t - R(z')/c)}{\partial t} = -\big(i(z' + \Delta z'/2, t - R(z' + \Delta z'/2)) - i(z' - \Delta z'/2, t - R(z' - \Delta z'/2))\big)$$

Dividing through by $\Delta z'$ and letting $\Delta z' \to 0$, we can get equation:

$$\frac{\partial \rho(z', t - R(z')/c)}{\partial t} = -\frac{\partial i(z', t - R(z')/c)}{\partial z'} \tag{5.37}$$

that relates charge density and current in the channel as seen by observer at P.

The line charge densities in eqn. 5.36 (ρ^*) and in eqn. 5.37 (ρ) are different. In eqn. 5.35, the partial differentiation of retarded current with respect to the source coordinate z' is carried out without keeping the retarded time constant; that is, the total partial derivative of the retarded current is taken. Equation 5.36 gives the local charge density or real charge density at retarded time, and eqn. 5.37 gives the apparent charge density or charge density as seen by the remote observer. Both charge densities can be used in calculating electric fields. In section 5.5 we saw how the local charge density ρ^* can be used in finding an expression for electric field (eqn. 5.33) and we found that in this expression both current and charge appears explicitly. Besides, in section 5.6 we found that the division of terms into electrostatic, induction and radiation field is different in eqn. 5.33 when compared with the electric field expression 5.22 completely in terms of current. It is possible to derive an electric field expression completely in terms of apparent charge density or charge density as seen by the remote observer. This derivation is done in section 5.8.

We can now find a relationship between the two charge densities ρ^* and ρ, corresponding to eqns 5.36 and 5.37, respectively. The total partial derivative of retarded current with respect to z' can be written as:

$$\frac{\partial i(z', t - R(z')/c)}{\partial z'} = \left.\frac{\partial i(z', t - R(z')/c)}{\partial z'}\right|_{t - R/c = const.} + \frac{\partial i(z', t - R(z')/c)}{\partial (t - R(z')/c)} \frac{\partial (t - R(z')/c)}{\partial z'} \tag{5.38}$$

From (5.28):

$$\frac{\partial (t - R(z')/c)}{\partial z'} = -\frac{z' - r\cos\theta}{cR(z')} \tag{5.39}$$

and

$$\frac{\partial i(z', t - R(z')/c)}{\partial (t - R(z')/c)} = \frac{\partial i(z', t - R(z')/c)}{\partial t} \tag{5.40}$$

Substituting eqns 5.40 and 5.39 in eqn. 5.38 and rearranging the terms we obtain:

$$\left.\frac{\partial i(z', t - R(z')/c)}{\partial z'}\right|_{t-R/c=const.} = \frac{\partial i(z', t - R(z')/c)}{\partial z'} + \frac{z' - r\cos\theta}{cR(z')}\frac{\partial i(z', t - R(z')/c)}{\partial t} \quad (5.41)$$

Applying eqns 5.36 and 5.37 in eqn. 5.41, we get the relationship between the two charge densities as:

$$\frac{\partial \rho(z', t - R(z')/c)}{\partial t} = \frac{\partial \rho^*(z', t - R(z')/c)}{\partial t} + \frac{z' - r\cos\theta}{cR(z')}\frac{\partial i(z', t - R(z')/c)}{\partial t} \quad (5.42)$$

where the second term on the right-hand side can be viewed as an adjustment term for the time rate of change of local charge density. Integration of both sides of eqn. 5.42 over time yields:

$$\rho(z', t - R(z')/c) = \rho^*(z', t - R(z')/c) + \frac{z' - r\cos\theta}{cR(z')} i(z', t - R(z')/c) \quad (5.43)$$

The factor $(z' - r\cos\theta)/(cR(z')) = -(\partial(R/c))/(\partial z')$ is the negative rate of change of time retardation with respect to z'.

In short, eqns 5.36 and 5.37 are two forms of the continuity equation, the former can be viewed as the local continuity equation in retarded time relating real charges and current on the channel and the latter can be viewed as the retarded form of the continuity equation in retarded time relating apparent charges (or charges as seen by the observer) and the current.

The scalar potential in terms of current is given by eqn. 5.20 and in terms of charge by eqn. 5.26. It is possible to show that eqns 5.20 and 5.26 are analytically equivalent [2]. A third equivalent expression for the scalar potential in terms of apparent charge density can be derived from eqn. 5.26 using eqn. 5.43.

5.8 Fields in terms of apparent charge distribution

In this section, exact time-domain expressions for remote electric and magnetic fields as a function of the spatial and temporal distribution of the charge density on the lightning channel are derived for the return stroke process and leader process. In section 5.5 we saw how the local charge density ρ^* can be used in finding an expression for the electric field (eqn. 5.33) and we found that in this expression both current and charge density appears explicitly. Besides, in section 5.6 we found that the division of terms into electrostatic, induction and radiation field is different in eqn. 5.33 when compared with the electric field expression 5.22 completely in terms of current. However, it is possible to derive an electric field

expression completely in terms of apparent charge density or charge density as seen by the remote observer. This derivation is done in this section. The relationship between apparent charge density and the local charge density in retarded time are established earlier in section 5.7. To illustrate the method, at first the field expressions are derived for the special case of an observer at ground, following [4]. Then a general expression for the electric field at any arbitrary point is presented.

5.8.1 Theory

5.8.1.1 General

The remote differential electric field dE_z and magnetic field dB_ϕ at ground due to a small, vertical, current carrying element dz' above a perfectly conducting earth is given by (e.g. [11]):

$$dE_z(r,t) = \frac{dz}{2\pi\varepsilon_0}\left[\frac{2z'^2 - r^2}{R^5(z')}\int_{t_b(z')}^{t} i(z',\tau^*)d\tau + \frac{2z'^2 - r^2}{cR^4(z')}i(z',t^*) - \frac{r^2}{c^2R^3(z')}\frac{\partial i(z',t^*)}{\partial t}\right] \tag{5.44}$$

$$dB_\phi(r,t) = \frac{d'z}{2\pi\varepsilon_0 c^2}\left[\frac{r}{R^3(z')}i(z',t^*) + \frac{r}{cR^2(z')}\frac{\partial i(z',t^*)}{\partial t}\right] \tag{5.45}$$

where $t^* = t - R(z')/c$ is the retarded time, $t_b(z')$ is the time at which the current is seen to begin in the channel section at z' by the observer at P, c is the speed of light in vacuum, $R(z') = (z'^2 + r^2)^{1/2}$ as shown in Figure 5.9. The right-hand sides of eqns 5.44 and 5.45 are the same as the integrands of eqns 5.22 and 5.23, respectively. Using the continuity equation relating the current and apparent

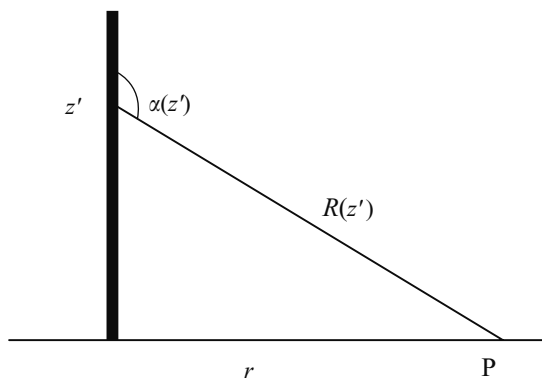

Figure 5.9 Geometry used in deriving the expressions for electric and magnetic fields at a point P on earth a horizontal distance r from the vertical lightning return stroke channel extending upward

charge, presented in eqn. 5.37, the electric and magnetic fields given by eqns 5.44 and 5.45 in terms of the channel current distribution can be rewritten in terms of the apparent channel charge density $\rho(z', t^*)$ distribution, as shown in the following sections.

5.8.1.2 Relation between apparent charge density and retarded current

Consider a section of the current carrying channel at an arbitrary height z' (Figure 5.9). The travel time of the electromagnetic signal from the channel segment at z' to an observer at ground, at P, is $R(z')/c$. The continuity equation relating the retarded charge density as seen by the observer (apparent charge density) and retarded current at an arbitrary time t is given by eqn. 5.37 and reproduced below:

$$\frac{\partial \rho(z', t^*)}{\partial t} = -\frac{\partial i(z', t^*)}{\partial z'} \tag{5.46}$$

where t^* is the retarded time as given earlier. The physical meaning of eqn. 5.46 is discussed earlier in section 5.6. The return stroke front is assumed to start from ground level ($z' = 0$) and to propagate upward with a constant speed v, reaching a height z' in a time z'/v. Taking the time integral from $z'/v + R(z')/c$ to t on both sides of eqn. 5.46, noting that z' and t are independent variables, we obtain an expression for the apparent charge density:

$$\rho(z', t^*) = \frac{i(z', z'/v)}{v_a(z')} - \int_{z'/v+R(z')/c}^{t} \frac{\partial i(z', \tau^*)}{\partial z'} d\tau \tag{5.47}$$

where $v_a(z')$ is the apparent speed of the front at z' as seen by a stationary observer at a distance r from the base of the channel and is given by:

$$\begin{aligned} \frac{1}{v_a(z')} &= -\frac{\partial}{\partial z'}\left(t - \frac{\sqrt{z'^2 + r^2}}{c} - \frac{z'}{v}\right) \\ &= \frac{1}{v}.\left(1 - \frac{v}{c}\cos\alpha(z')\right) \end{aligned} \tag{5.48}$$

The angle $\alpha(z')$ is defined in Figure 5.9. Note that the first term of eqn. 5.47 represents the apparent charge density at the wavefront when it has reached z' and is due to the extension of the front. Equation 5.47 defines the charge density distribution along the channel at any given time t as seen by a stationary observer at P at a distance r from the base of the channel (see Figure 5.9). Equation 5.47 can be rewritten as:

$$\rho(z', t^*) = -\frac{d}{dz'} \int_{z'/v+R(z')/c}^{t} i(z', \tau^*)\, d\tau \tag{5.49}$$

From eqn. 5.49, we find:

$$\rho(z', t^*)\, dz' = -d\left[\int_{z'/v+R(z')/c}^{t} i(z', \tau^*)\, d\tau\right] \tag{5.50}$$

Further, multiplying both sides of eqn. 5.46 by dz', we find:

$$\frac{\partial \rho(z', t^*)}{\partial t} dz' = -\frac{\partial i(z', t^*)}{\partial z'} d'z$$
$$= -di(z', t^*) \tag{5.51}$$

Finally, taking the partial derivative with respect to time of eqn. 5.51, we obtain:

$$\frac{\partial^2 \rho(z', t^*)}{\partial t^2} dz' = -d\left(\frac{\partial i(z', t^*)}{\partial t}\right) \tag{5.52}$$

Note that for a leader beginning from a height H_m at time $t = 0$ and travelling downward at a speed v the lower limit of the integral in eqns 5.49 and 5.50 will be the travel time to z' and from z' to the observer, that is, $(H_m - z')/v + R(z')/c$. In general, the lower limit of the integral in eqns 5.49 and 5.50 is the time, $t_b(z')$, at which the current is seen to begin in the channel at z' by the observer and with this modification eqn. 5.50, along with eqns 5.51 and 5.52 are valid for any lightning process. It is not necessary for the return stroke speed to be constant if the lower limit of eqn. 5.50 is written as $t_b(z')$.

5.8.1.3 General expressions for differential electric and magnetic fields

The remote differential electric field at ground due to a vertical, current carrying element dz′ above a perfectly conducting earth is given by eqn. 5.44. In the following eqn. 5.44 will be written in terms of charge density using eqns 5.50 to 5.52. Each term of eqn. 5.44 can be represented, omitting $1/(2\pi\varepsilon_0)$, by:

$$df_1(z') f_2(z', t) = d[f_1(z') f_2(z', t)] - f_1(z') df_2(z', t) \tag{5.53}$$

where $f_2(z', t)$ is the current integral, current or the current derivative and the total differential $df_1(z')$ is $(2z'^2 - r^2)/R^5(z')\,dz'$, $(2z'^2 - r^2)/cR^4(z')\,dz'$, or $-r^2/c^2R(z')\,dz'$. Using eqn. 5.53 the first (electrostatic) term of eqn. 5.44 can be expanded as follows:

$$2\pi\varepsilon_0 dE_s(r, t) = d\left(\frac{-z'}{R^3(z')} \int_{t_b(z')}^{t} i(z', \tau^*) d\tau\right) - \frac{-z'}{R^3(z')} d\left(\int_{t_b(z')}^{t} i(z', \tau^*) d\tau\right) \tag{5.54}$$

Similarly, the second (induction) term of eqn. 5.44 can be written as:

$$2\pi\varepsilon_0 dE_i(r, t) = d\left(\left[-\frac{3}{2}\frac{z'}{cR^2(z')} + \frac{1}{2}\frac{\tan^{-1}(z'/r)}{cr}\right] i(z', t^*)\right)$$
$$- \left[-\frac{3}{2}\frac{z'}{cR^2(z')} + \frac{1}{2}\frac{\tan^{-1}(z'/r)}{cr}\right] di(z', t^*) \tag{5.55}$$

Also, the third (radiation) term of eqn. 5.44 can be written as:

$$2\pi\varepsilon_0 dE_r(r,t) = d\left(\frac{-z'}{c^2R(z')}\frac{\partial i(z',t^*)}{\partial t}\right) - \frac{-z'}{c^2R(z')}d\left(\frac{\partial i(z',\tau^*)}{\partial t}\right) \tag{5.56}$$

Applying eqns 5.50, 5.51, and 5.52 to the second term of eqns 5.54, 5.55, and 5.56, respectively, and adding the resulting equations we get the expression 5.57 for the differential electric field, equivalent to eqn. 5.44:

$$\begin{aligned}
dE_z(r,t) = &-\frac{1}{2\pi\varepsilon_0}\frac{z'}{R^3(z')}\rho(z',t^*)\,dz' \\
&-\frac{1}{2\pi\varepsilon_0}\left[\frac{3}{2}\frac{z'}{cR^2(z')} - \frac{1}{2}\frac{\tan^{-1}(z'/r)}{cr}\right]\cdot\frac{\partial\rho(z',t^*)}{\partial t}\,dz' \\
&-\frac{1}{2\pi\varepsilon_0}\frac{z'}{c^2R(z')}\frac{\partial^2\rho(z',t^*)}{\partial t^2}\,dz' \\
&+\frac{1}{2\pi\varepsilon_0}d\left[\frac{-z'}{R^3(z')}\int_{t_b(z')}^{t} i(z',\tau^*)\,d\tau\right] \\
&+\frac{1}{2\pi\varepsilon_0}d\left[\left[-\frac{3}{2}\frac{z'}{cR^2(z')} + \frac{1}{2}\frac{\tan^{-1}(z'/r)}{cr}\right]i(z',t^*)\right] \\
&+\frac{1}{2\pi\varepsilon_0}d\left[\frac{-z'}{c^2R(z')}\frac{\partial i(z',t^*)}{\partial t}\right]
\end{aligned} \tag{5.57}$$

In a similar manner the differential magnetic field given by eqn. 5.45 can be rewritten as:

$$\begin{aligned}
dB_\phi(r,t) = &\frac{1}{2\pi\varepsilon_0c^2}\frac{1}{r}\frac{z'}{R(z')}\frac{\partial\rho(z',t^*)}{\partial t}\,dz' \\
&+\frac{1}{2\pi\varepsilon_0c^2}\frac{1}{c}\tan^{-1}\left(\frac{z'}{r}\right)\frac{\partial^2\rho(z',t^*)}{\partial t^2}\,dz' \\
&+\frac{1}{2\pi\varepsilon_0c^2}d\left(\frac{1}{r}\frac{z'}{R(z')}i(z',t^*)\right) \\
&+\frac{1}{2\pi\varepsilon_0c^2}d\left(\frac{1}{c}\tan^{-1}\left(\frac{z'}{r}\right)\frac{\partial i(z',t^*)}{\partial t}\right)
\end{aligned} \tag{5.58}$$

Note that eqns 5.57 and 5.58 are general and applicable to any lightning process in a vertical channel above a perfectly conducting ground. In the following

eqns 5.57 and 5.58 will be integrated for return strokes with the result being expressed in terms of charge density only.

5.8.2 Return stroke electric and magnetic fields

5.8.2.1 Exact expressions

As mentioned earlier, the return stroke is assumed to be an extending discharge with a discharge front speed v, assumed to be a constant and the observer at P sees the discharge front passing a height z' at time $t_b(z') = z'/v + R(z')/c$. The height of the channel $L'(t)$ seen at time t by the observer is given by the solution of the following equation:

$$t = \frac{L'(t)}{v} + \frac{(L'^2(t) + r^2)^{1/2}}{c} \tag{5.59}$$

If $L'(t)$ is the height of the discharge front seen by the observer, then the total electric field at P at time t is given by integrating eqn. 5.57 from 0 to $L'(t)$. Also, from eqn. 5.47 the current at the wavefront, as seen by the observer at P is given by:

$$i\left(L'(t), \frac{L'(t)}{v}\right) = \rho\left(L'(t), \frac{L'(t)}{v}\right)^{\cdot} v_a(L'(t)) \tag{5.60}$$

where

$$v_a(L') = \frac{dL'(t)}{dt} = v^{\cdot}\left[1 - \frac{v}{c}\cos\alpha(L')\right]^{-1} \tag{5.61}$$

is the apparent speed of the return stroke wavefront; that is, the front speed seen by the observer at P (see Figure 5.9). Differentiating both sides of eqn. 5.60 with respect to time we get:

$$\frac{\partial}{\partial t} i\left(L(t), \frac{L'(t)}{v}\right) = \frac{\partial}{\partial t}\left[\rho\left(L'(t), \frac{L'(t)}{v}\right)^{\cdot} v_a(L')\right] \tag{5.62}$$

Performing the integration of eqn. 5.57 from height 0 to $L'(t)$, using eqns 5.59, 5.60 and 5.62, we can obtain the relation expressing the total electric field from a return stroke channel in terms of the charge distribution on the channel. To this the radiation field term due to current discontinuity at the wavefront, that is a term equivalent to the last term of eqn. 5.22, has to be added to get the complete field expression at ground

level. The expression is given below:

$$
\begin{aligned}
E_z(r,t) = &-\frac{1}{2\pi\varepsilon_0}\int_0^{L'(t)} \frac{z'}{R^3(z')}\rho(z',t^*)\,d'z \\
&-\frac{1}{2\pi\varepsilon_0}\int_0^{L'(t)} \left(\frac{3}{2}\frac{z'}{cR^2(z')} - \frac{1}{2}\frac{\tan^{-1}(z'/r)}{cr}\right)\frac{\partial\rho(z',t^*)}{\partial t}\,dz' \\
&-\frac{1}{2\pi\varepsilon_0}\int_0^{L'(t)} \frac{z'}{c^2R(z')}\frac{\partial^2\rho(z',t^*)}{\partial t^2}\,dz' \\
&-\frac{1}{2\pi\varepsilon_0}\left(\frac{3}{2}\frac{L'(t)}{cR^2(L')} - \frac{1}{2}\frac{\tan^{-1}(L'(t)/r)}{cr}\right)\rho\left(L', \frac{L'(t)}{v}\right)\frac{dL'(t)}{dt} \\
&-\frac{1}{2\pi\varepsilon_0}\frac{L'(t)}{c^2R(L')}\frac{\partial}{\partial t}\left[\rho\left(L'(t), \frac{L'(t)}{v}\right)\frac{dL'(t)}{dt}\right] \\
&-\frac{1}{2\pi\varepsilon_0}\frac{r^2}{c^2R^3(L')}\rho\left(L', \frac{L'(t)}{v}\right)\left(\frac{dL'}{dt}\right)^2
\end{aligned}
\tag{5.63}
$$

To get the last term of eqn. 5.63, we have used the relationship of eqn. 5.60. Adopting a procedure similar to that used for obtaining eqn. 5.63, we can show that the horizontal component of the magnetic field at ground is given by:

$$
\begin{aligned}
B_\phi(r,t) = &\frac{1}{2\pi\varepsilon_0c^2}\int_0^{L'(t)} \frac{1}{r}\frac{z'}{R(z')}\frac{\partial\rho(z',t^*)}{\partial t}\,dz' \\
&+\frac{1}{2\pi\varepsilon_0c^2}\int_0^{L'(t)} \frac{1}{c}\tan^{-1}\left(\frac{z'}{r}\right)\frac{\partial^2\rho(z',t^*)}{\partial t^2}\,dz' \\
&+\frac{1}{2\pi\varepsilon_0c^2}\frac{1}{r}\frac{L'(t)}{R(L')}\rho\left(L'(t), \frac{L'(t)}{v}\right)\frac{dL'(t)}{dt} \\
&+\frac{1}{2\pi\varepsilon_0c^2}\frac{1}{c}\tan^{-1}\left(\frac{L'(t)}{r}\right)\cdot\frac{\partial}{\partial t}\left[\rho\left(L'(t), \frac{L'(t)}{v}\right)\frac{dL'(t)}{dt}\right] \\
&+\frac{1}{2\pi\varepsilon_0c^2}\frac{r}{cR^2(L')}\rho\left(L', \frac{L'(t)}{v}\right)\left(\frac{dL'(t)}{dt}\right)^2
\end{aligned}
\tag{5.64}
$$

The requirement that speed v be a constant can be relaxed to allow any arbitrary function of height if v is replaced by an average speed V_{av}:

$$
V_{av}(z') = \frac{z'}{\int_0^{z'} dz''/v(z'')} \tag{5.65}
$$

as defined by [12].

5.8.2.2 Numerical illustration

It is possible to show the analytical equivalence between the three different expressions for electric field at ground level due to a propagating lightning return stroke, that is between eqns 5.22, 5.33 and 5.63 and was done in [2]. The numerical equivalence between eqns 5.22 and 5.33 for the case of the transmission line model for the return stroke is shown in Figures 5.4–5.6. For the TL model the current and charge density in eqn. 5.33 is related by the continuity equation 5.24, giving a charge density given by eqn. 5.36. However, the apparent charge density to be used in eqns 5.63 and 5.64 is given by eqn. 5.37, giving a charge density as follows [2]:

$$\rho(z', t - R(z')/c) = \frac{i(0, t - z'/v - R(z')/c)}{vF_{TL}} \tag{5.66}$$

where

$$F_{TL} = \frac{1}{1 + vz'/(cR(z'))}$$

Calculation of electric fields at ground for the TL model using eqns 5.63 and 5.66 yielded exactly the same curves as that for EQ_LC, EI_LC, ER_LC, and EV_LC in Figures 5.4–5.6 as shown in [2].

5.8.2.3 Expression for electric field at an elevation

Often, it is necessary to calculate electric fields at an elevation above ground. Equation 5.63 gives the electric field only at ground level. It is possible to derive a general expression for the electric field at an elevation in terms of the apparent charge density. The general expression 5.21 in terms of current can be taken as a starting point. The procedure is the same as that outlined earlier in this section. In addition to eqns 5.50, 5.51 and 5.52, we use the following relations to convert each term of eqn. 5.21 into terms expressed in apparent charge density:

$$\frac{d}{dz'}\left(\frac{r - z'\cos\theta}{R^3(z')}\right) = -\left(\frac{\cos\theta - 3\cos\alpha(z')\cos\beta(z')}{R^3(z')}\right) \tag{5.67}$$

$$\frac{d}{dz'}\left(\frac{3}{2}\frac{r - z'\cos\theta}{cR^2(z')} + \frac{1}{2}\frac{\cot\theta}{cr}\tan^{-1}\frac{z' - r\cos\theta}{r\sin\theta}\right)$$
$$= -\left(\frac{\cos\theta - 3\cos\alpha(z')\cos\beta(z')}{cR^2(z')}\right) \tag{5.68}$$

$$\frac{d}{dz'}\left(\frac{r - z'\cos\theta}{c^2R(z')}\right) = -\left(\frac{\cos\theta - \cos\alpha(z')\cos\beta(z')}{c^2R(z')}\right) \tag{5.69}$$

$$\frac{d}{dz'}\left(\frac{z'\sin\theta}{R^3(z')}\right) = \frac{\sin\theta + 3\cos\alpha(z')\sin\beta(z')}{R^3(z')} \tag{5.70}$$

$$\frac{d}{dz'}\left(\frac{3}{2}\frac{z'\sin\theta}{cR^2(z')} - \frac{1}{2}\frac{1}{cr}\tan^{-1}\frac{z' - r\cos\theta}{r\sin\theta}\right) = \frac{\sin\theta + 3\cos\alpha(z')\sin\beta(z')}{cR^2(z')} \tag{5.71}$$

$$\frac{d}{dz'}\left(\frac{z'\sin\theta}{c^2R(z')}\right) = \frac{\sin\theta + \cos\alpha(z')\sin\beta(z')}{c^2R(z')} \tag{5.72}$$

The general expression for the electric field at an elevation in terms of apparent charge is given by:

$$\begin{aligned}
\bar{E}(r,\theta,t) = {} & +\frac{1}{4\pi\varepsilon_0}\hat{r}\int_0^{L'(t)}\frac{\cos\beta(z')}{R^2(z')}\rho(z', t - R(z')/c)\,dz' && a\\
& + \frac{1}{4\pi\varepsilon_0}\hat{r}\int_0^{L'(t)}\left[\frac{3}{2}\frac{\cos\beta(z')}{cR(z')} + \frac{1}{2}\frac{\cot\theta}{cr}\tan^{-1}(-\cot\alpha(z'))\right] \\
& \times \frac{\partial\rho(z', t - R(z')/c)}{\partial t}\,dz' && b\\
& + \frac{1}{4\pi\varepsilon_0}\hat{r}\int_0^{L'(t)}\frac{\cos\beta(z')}{c^2}\frac{\partial^2\rho(z', t - R(z')/c)}{\partial t^2}\,dz' && c\\
& + \frac{1}{4\pi\varepsilon_0}\hat{r}\frac{1}{r^2}Q(t - r/c) && d\\
& + \frac{1}{4\pi\varepsilon_0}\hat{r}\left[\frac{3}{2}\frac{1}{cr} + \frac{1}{2}\cot\theta\frac{\tan^{-1}(-\cot\theta)}{cr}\right]\frac{\partial Q(t - r/c)}{\partial t} && e\\
& + \frac{1}{4\pi\varepsilon_0}\hat{r}\frac{1}{c^2}\frac{\partial^2 Q(t - r/c)}{\partial t^2} && f\\
& + \frac{1}{4\pi\varepsilon_0}\hat{r}\left[\frac{3}{2}\frac{\cos\beta(L')}{cR(L')} + \frac{1}{2}\frac{\cot\theta}{cr}\tan^{-1}(-\cot\alpha(L'))\right] \\
& \times \rho(L', t - R(L')/c)\frac{dL'(t)}{dt} && g\\
& + \frac{1}{4\pi\varepsilon_0}\hat{r}\frac{\cos\beta(L')}{c^2}\frac{\partial}{\partial t}\left[\rho(L', t - R(L')/c)\frac{dL'(t)}{dt}\right] && h\\
& + \frac{1}{4\pi\varepsilon_0}\hat{\theta}\int_0^{L'(t)}\frac{\sin\beta(z')}{R^2(z')}\rho(z', t - R(z')/c)\,dz' && i
\end{aligned}$$

$$
\begin{aligned}
&+\frac{1}{4\pi\varepsilon_0}\hat{\theta}\int_0^{L'(t)}\left[\frac{3}{2}\frac{\sin\beta(z')}{cR(z')}-\frac{1}{2}\frac{1}{cr}\tan^{-1}(-\cot\alpha(z'))\right]\\
&\times\frac{\partial\rho(z',t-R(z')/c)}{\partial t}\,dz' && j\\
&+\frac{1}{4\pi\varepsilon_0}\hat{\theta}\int_0^{L'(t)}\frac{\sin\beta(z')}{c^2}\frac{\partial^2\rho(z',t-R(z')/c)}{\partial t^2}\,dz' && k\\
&-\frac{1}{4\pi\varepsilon_0}\hat{\theta}\frac{1}{2}\frac{\tan^{-1}(-\cot\theta)}{cr}\frac{\partial Q(t-r/c)}{\partial t} && l\\
&+\frac{1}{4\pi\varepsilon_0}\hat{\theta}\left[\frac{3}{2}\frac{\sin\beta(L')}{cR(L')}-\frac{1}{2}\frac{1}{cr}\tan^{-1}(-\cot\alpha(L'))\right]\\
&\times\rho(L',t-R(L')/c)\frac{dL'(t)}{dt} && m\\
&+\frac{1}{4\pi\varepsilon_0}\hat{\theta}\frac{\sin\beta(L')}{c^2}\frac{\partial}{\partial t}\left[\rho(L',t-R(L')/c)\frac{dL'(t)}{dt}\right] && n\\
&-\frac{1}{4\pi\varepsilon_0}\hat{r}\frac{\cos\theta-\cos\alpha(L')\cos\beta(L')}{c^2R(L')}\rho\left(L',t-\frac{R(L')}{c}\right)\left(\frac{dL'}{dt}\right)^2 && o\\
&+\frac{1}{4\pi\varepsilon_0}\hat{\theta}\frac{\sin\theta+\cos\alpha(L')\sin\beta(L')}{c^2R(L')}\rho\left(L',t-\frac{R(L')}{c}\right)\left(\frac{dL'}{dt}\right)^2 && p
\end{aligned}
\tag{5.73}
$$

where $\cos\alpha(z') = -(z'-r\cos\theta)/R(z')$, $\sin\alpha(z') = r\sin\theta/R(z')$, $\cos\beta(z') = (r-z'\cos\theta)/R(z')$, $\sin\beta(z') = z'\sin\theta/R(z')$, and $Q = -\int_{r/c}^{t} i(0,\tau-r/c)\,d\tau$. Note also that, $\tan^{-1}(-\cot(\alpha(z')) = \pi/2+\alpha(z')$. Expression 5.73 does not include the effect of the perfectly conducting ground plane. Inclusion of ground plane is discussed in section 5.9.

It is possible to derive a general expression for the magnetic field in terms of the apparent charge, even though it is not done here.

5.8.2.4 The moment approximation

Far from the channel, that is, for $L'(t) \ll r$, the integral terms of eqns 5.63 and 5.64 readily reduce to the familiar charge moment approximation (e.g., [13]) given by:

$$
E_z(r,t) = \frac{-1}{4\pi\varepsilon_0}\left[\frac{M(t)}{r^3}+\frac{1}{cr^2}\frac{dM(t)}{dt}+\frac{1}{c^2r}\frac{d^2M(t)}{dt^2}\right] \tag{5.74}
$$

$$B_\phi(r,t) = \frac{1}{4\pi\varepsilon_0 c^2}\left[\frac{1}{r}\frac{dM(t)}{dt} + \frac{1}{cr}\frac{d^2M(t)}{dt^2}\right] \tag{5.75}$$

where

$$M(t) = 2\int_0^H z'\rho_L\left(z', t - \frac{r}{c}\right)dz' \tag{5.76}$$

Note that in eqns 5.63 and 5.64 for $z' \ll r$, $\tan^{-1}(z'/r) \approx z'/r$ (in radians) and this result is used to arrive at eqns 5.74 and 5.75 from those equations, respectively.

5.8.3 Leader electric fields

5.8.3.1 Exact expressions

The electric field at ground level due to a descending leader can also be obtained from eqn. 5.57. The leader is assumed to be an extending discharge propagating down from a charge centre at height H_m (Figure 5.10). The observer sees the lower end of the leader at a height $h(t)$ given by the solution of:

$$t = \frac{H_m - h(t)}{v} + \frac{\sqrt{h^2(t) + r^2}}{c} \tag{5.77}$$

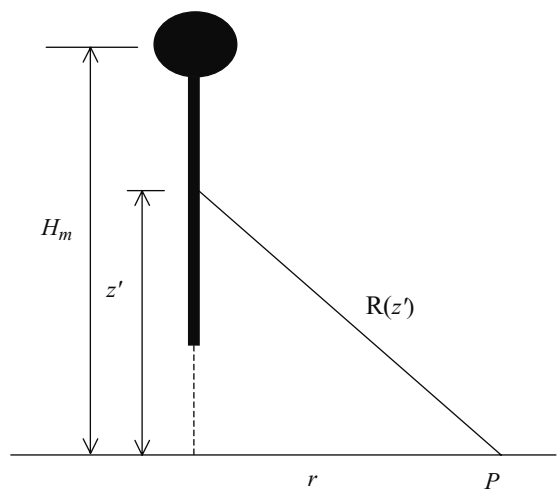

Figure 5.10 Geometry used in deriving the expressions for electric fields at a point P on earth a horizontal distance r from the vertical lightning leader channel extending downward

The total leader electric field is given by integrating eqn. 5.57 along the channel from $h(t)$ to H_m and is given by

$$\begin{aligned}
E_z(r,t) = &+\frac{1}{2\pi\varepsilon_0}\int_{h(t)}^{H_m}\frac{z'}{R^3(z')}\rho(z',t^*)\,dz' \\
&+\frac{1}{2\pi\varepsilon_0}\int_{h(t)}^{H_m}\left(\frac{3}{2}\frac{z'}{cR^2(z')}-\frac{1}{2}\frac{\tan^{-1}(z'/r)}{cr}\right)\frac{\partial\rho(z',t^*)}{\partial t}\,dz' \\
&+\frac{1}{2\pi\varepsilon_0}\int_{h(t)}^{H_m}\frac{z'}{c^2R(z')}\frac{\partial^2\rho(z',t^*)}{\partial t^2}\,dz' \\
&-\frac{1}{2\pi\varepsilon_0}\frac{H_m}{R^3(H_m)}\int_{h(t)}^{H_m}\rho(z',t^*)\,dz' \\
&-\frac{1}{2\pi\varepsilon_0}\left(\frac{3}{2}\frac{H_m}{cR^2(H_m)}-\frac{1}{2}\frac{\tan^{-1}(H_m/r)}{cr}\right)\cdot\frac{d}{dt}\int_{h(t)}^{H_m}\rho(z',t^*)\,dz' \\
&-\frac{1}{2\pi\varepsilon_0}\left(\frac{3}{2}\frac{h(t)}{cR^2(h)}-\frac{1}{2}\frac{\tan^{-1}(h(t)/r)}{cr}\right)\rho\left(h(t),\frac{h(t)}{v}\right)\frac{dh(t)}{dt} \\
&-\frac{1}{2\pi\varepsilon_0}\frac{H_m}{c^2R(H_m)}\frac{d^2}{dt^2}\int_{h(t)}^{H_m}\rho(z',t^*)\,dz' \\
&-\frac{1}{2\pi\varepsilon_0}\frac{h(t)}{c^2R(h)}\frac{\partial}{\partial t}\left[\rho\left(h(t),\frac{h(t)}{v}\right)\frac{dh(t)}{dt}\right] \qquad (5.78)
\end{aligned}$$

where $t^* = t - R(z')/c$.

5.8.3.2 Electrostatic approximation

As an example of the application of the leader field expression in terms of charge density, consider the electrostatic approximation for the leader electric field, expected to be applicable to close lightning. The first and fourth term of eqn. 5.78 represent the static terms, the first term represents the field change at ground due to the apparent charge on the leader channel, and the fourth term represents the field change due to the depletion of the charge at the charge source as it is drained by the extending leader. The total charge on the leader channel at any time is equal to the total charge drained from the charge source in the cloud up to that time. The time retardation effects can be neglected if the difference in travel times between sources on the channel and the remote observer is much less than the time required for significant variation in the sources. In that case the charge and the apparent charge, defined by eqns 5.36 and 5.37, become identical. Neglecting retardation effects we can combine the first and fourth terms of eqn. 5.78 as:

$$E_z(r,t) = \frac{-1}{2\pi\varepsilon_0}\int_{H_m}^{Z_t}\left[\frac{z'}{R^3(z')}-\frac{H_m}{R^3(H_m)}\right]\rho(z',t)\,dz' \qquad (5.79)$$

where $z_t = H - vt$ is the height of the leader tip at time t and v is the leader speed assumed to be a constant.

5.9 Calculation of fields from lightning return stroke

Different models of lightning return stroke are presented in Chapter 6. The commonly used engineering models of the return stroke give the spatial and temporal variation of the current along the return stroke channel. Once the source distribution is specified, the remote electric fields can be calculated from any one of the three different, but equivalent and exact, methods presented in this Chapter. The electric field is expressed in terms of the current in eqn. 5.21, in terms of both the current and local charge density in eqn. 5.32, and in terms of apparent charge density in eqn. 5.73. Expressions 5.21, 5.32, and 5.73 do not take into account the presence of the conducting ground. The effect of the ground plane, assumed to be perfectly conducting, on the fields can modelled by replacing the ground plane by an image channel. The total scalar potential from the real channel and the image channel and the total tangential component of the electric field should be zero at ground level ($z' = 0$). These boundary conditions can be met if the current in the image channel has the same magnitude and direction as in the real channel, or if the charge density in the image channel has the same magnitude, but opposite sign to that of the real channel. It can be shown that the expression for the field from the image channel can be readily written from eqn. 5.21 by replacing the height z' by its negative $-z'$, from eqn. 5.32 by changing the polarity of ρ^* and Q and its derivatives and by replacing z' by $-z'$, from eqn. 5.73 by changing the polarity of ρ and Q and by replacing z' by $-z'$. The upper limit of integration for the image channel is $L''(t)$, the effective length of the image channel seen by the observer at the field point at time t. $L''(t)$ is given by the solution of:

$$t = \frac{L''}{v} + \frac{\sqrt{L''^2 + r^2 - 2L''r\cos(\pi - \theta)}}{c}$$

and is less than the height of the real channel $L'(t)$ given by eqn. 5.11, if the observation point is above ground. $L''(t)$ can be obtained directly from eqn. 5.11 by replacing θ by $(\pi - \theta)$.

A number of measurements of the return stroke current waveform $i(0, t)$ at the base of the channel and the speed v of the return stroke wavefront are available. Therefore in calculating the electromagnetic fields from the return stroke the channel base current and speed are used as inputs. The current, local charge, and the apparent charge along the channel for different return stroke models, for use in eqns 5.21, 5.32 and 5.73, are summarised below. In addition to the known channel base current and return stroke speed, parameters such as discharge time constant τ, current attenuation constant λ and cloud charge centre height H are required for some of the models.

5.9.1 *Bruce–Golde model (BG)*

$$i(z', t - R(z')/c) = i(0, t - R(z')/c) \tag{5.80}$$

$$\rho^*(z', t - R(z')/c) = \frac{i(0, z'/v)}{v} \tag{5.81}$$

$$\rho(z', t - R(z')/c) = i(0, z'/v) \cdot \left[\frac{1}{vF(z')} + \frac{1}{cF_{BG}(z')}\right] - \frac{i(0, t - R(z')/c)}{cF_{BG}(z')} \tag{5.82}$$

where

$$F(z') = \frac{1}{1 - (v/c)\cos\alpha(z')} \quad \text{and} \quad F_{BG}(z') = \frac{1}{\cos\alpha(z')} \tag{5.83}$$

5.9.2 *Travelling current source model (TCS)*

$$i(z', t - R(z')/c) = i(0, t + z'/c - R(z')/c) \tag{5.84}$$

$$\rho^*(z', t - R(z')/c) = \frac{i(0, z'/v^*)}{v^*} - \frac{i(0, t + z'/c - R(z')/c)}{c} \tag{5.85}$$

$$\rho(z', t - R(z')/c) = i(0, z'/v^*)\left[\frac{1}{vF(z')} + \frac{1}{cF_{TCS}(z')}\right] - \frac{i(0, t + z'/c - R(z')/c)}{cF_{TCS}(z')} \tag{5.86}$$

where

$$v^* = \frac{v}{1 + v/c} \tag{5.87}$$

$$F_{TCS}(z') = \frac{1}{1 + \cos\alpha(z')} \tag{5.88}$$

and $F(z')$ is given by eqn. 5.83.

5.9.3 *Diendorfer–Uman model (DU)*

$$i(z', t - R(z')/c) = i(0, t + z'/c - R(z')/c) - i(0, z'/v^*) \cdot e^{-(t-(z'/v)-(R(z')/c))/\tau_D} \tag{5.89}$$

$$\rho^*(z', t - R(z')/c) = \frac{i(0, z'/v^*)}{v^*} + \frac{\tau_D}{v^*}\frac{di(0, z'/v^*)}{dt} - \frac{i(0, t + z'/c - R(z')/c)}{c} - e^{-(t-(z'/v)-(R(z')/c))/\tau_D} \times \left[\frac{\tau_D}{v^*}\frac{di(0, z'/v^*)}{dt} + \frac{i(0, z'/v^*)}{v}\right] \tag{5.90}$$

$$\rho(z', t - R(z')/c) = i(0, z'/v^*) \cdot \left[\frac{1}{vF(z')} + \frac{1}{cF_{TCS}(z')}\right] + \frac{\tau_D}{v^*}\frac{di(0, z'/v^*)}{dt} - \frac{i(0, t + z'/c - R(z')/c)}{cF_{TCS}(z')} - e^{-(t-(z'/v)-(R(z')/c))/\tau_D} \cdot \left[\frac{\tau_D}{v^*}\frac{di(0, z'/v^*)}{dt} + \frac{i(0, z'/v^*)}{vF(z')}\right] \tag{5.91}$$

where v^*, $F_{TCS}(z')$ and $F(z')$ are given by eqns 5.87, 5.88 and 5.83, respectively.

5.9.4 Transmission line model (TL)

$$i(z', t - R(z')/c) = i(0, t - z'/v - R(z')/c) \tag{5.92}$$

$$\rho^*(z', t - R(z')/c) = \frac{i(0, t - z'/v - R(z')/c)}{v} \tag{5.93}$$

$$\rho(z', t - R(z')/c) = \frac{i(0, t - z'/v - R(z')/c)}{vF(z')} \tag{5.94}$$

where $F(z')$ is given by eqn. 5.83.

5.9.5 Modified transmission line model, linear (MTLL)

$$i(z', t - R(z')/c) = i(0, t - z'/v - R(z')/c) \cdot (1 - z'/H) \tag{5.95}$$

$$\rho^*(z', t - R(z')/c) = (1 - z'/H) \cdot \frac{i(0, t - z'/v - R(z')/c)}{v} + \frac{Q(z', t - R(z')/c)}{H} \tag{5.96}$$

$$\rho(z', t - R(z')/c) = (1 - z'/H) \cdot \frac{i(0, t - z'/v - R(z')/c)}{vF(z')} + \frac{Q(z', t - R(z')/c)}{H} \tag{5.97}$$

where $Q(z', t - R(z')/c) = \int_{z'/v+R(z')/c}^{t} i(0, \tau - z'/v - R(z')/c)d\tau$

5.9.6 Modified transmission line model, exponential (MTLE)

$$i(z', t - R(z')/c) = i(0, t - z'/v - R(z')/c) \cdot e^{-z'/\lambda} \tag{5.98}$$

$$\rho^*(z', t - R(z')/c) = e^{-z'/\lambda} \cdot \frac{i(0, t - z'/v - R(z')/c)}{v} + e^{-z'/\lambda} \cdot \frac{Q(z', t - R(z')/c)}{\lambda} \tag{5.99}$$

$$\rho(z', t - R(z')/c) = e^{-z'/\lambda} \cdot \frac{i(0, t - z'/v - R(z')/c)}{vF(z')} + e^{-z'/\lambda} \cdot \frac{Q(z', t - R(z')/c)}{\lambda} \tag{5.100}$$

5.10 Transmission line model of the return stroke

The transmission line model (TL) of the lightning return stroke [14], has been widely used to calculate return stroke currents and current derivatives from measured electric fields and electric field derivatives (e.g., [15,16]). This model is interesting because many kilometres from the return stroke where the radiation field term of eqns 5.22 and 5.33 are dominant, the measured fields and field derivatives were directly proportional to the current and current derivative, respectively, of the return stroke current at the base of the channel. The TL model is characterised by a nonattenuating travelling current on the channel described by eqn. 5.92. The approximate relationship between remote fields at ground ($\theta = \pi/2$ in Figure 5.4) and currents are given by:

$$i(0, t) \approx -\frac{2\pi\varepsilon_0 c^2 r}{v} E_{far}(r, t + r/c) \tag{5.101}$$

and

$$\frac{\partial i(0, t)}{\partial t} \approx -\frac{2\pi\varepsilon_0 c^2 r}{v} \frac{\partial E_{far}(r, t + r/c)}{\partial t} \tag{5.102}$$

Equations 5.101 and 5.102 are good approximations in the far field and at ground where the static and induction terms of the total field are negligible and if eqns 5.101 and 5.102 are only used up to the peak value of the field/current waveform. These equations are the basis of the estimation of peak lightning return stroke currents by remote detection of electric and magnetic field by the lightning location system. The validity of eqns 5.101 and 5.102 has been tested by several authors (e.g., [17–19]). However, there are several drawbacks for the above simple equations. First, the return stroke speed v is generally not known for a given return stroke. Secondly, the attenuation due to finite conductivity of the earth (see Chapter 7) is not taken into account. Thirdly, these equations are not considered to be valid near to the lightning channel where the static and induction terms cannot be neglected.

Measurements of close field and field derivatives at distances from triggered lightning of 10–50 m simultaneously with the channel base current [20,21] showed that the electric field derivative and the current derivatives are similar for a time of the order of 100 ns. Since close to the channel calculation of fields by eqn. 5.22 does not give similar waveshapes for the current and the fields, the similarity of waveshapes in measured currents and fields appeared to be surprising. Later it was proven analytically [22] that with a return stroke speed equal the speed of light c, the waveshapes of the electric field the magnetic field and the current are identical at any distance, whereas this is not the case for speeds less than c (e.g., [3]). For any point in space the field and its derivatives are given by:

$$B_\phi(r,t) = \frac{1}{2\pi\varepsilon_0 c^2 r \sin\theta} i(0, t - r/c), \quad \theta \neq 0 \tag{5.103}$$

$$\frac{\partial B_\phi(r,t)}{\partial t} = \frac{1}{2\pi\varepsilon_0 c^2 r \sin\theta} \frac{\partial i(0, t - r/c)}{\partial t}, \quad \theta \neq 0 \tag{5.104}$$

$$\bar{E}(r,\theta,t) = \frac{1}{2\pi\varepsilon_0 c r \sin\theta} i(0, t - r/c)\hat{\theta}, \quad \theta \neq 0 \tag{5.105}$$

$$\frac{\partial \bar{E}}{\partial t} = \frac{1}{2\pi\varepsilon_0 c r \sin\theta} \frac{\partial i(0, t - r/c)}{\partial t}\hat{\theta}, \quad \theta \neq 0 \tag{5.106}$$

Thus for a return stroke speed equal to the speed of light, the electric and magnetic fields (field derivatives) and the current (current derivative) are shown, by direct calculation starting with the assumed current as a source function, to have identical and invariant waveshapes at all distances and directions.

The ideal and exact solution for a vertical wire antenna of infinite length and vanishing radius above a ground plane excited at the bottom, all conductors being perfect, is spherical TEM. The spherical TEM solution of the wave equation between two concentric conical surfaces of infinite conductivity and length with common cone apexes has been suggested in [23]. The case of a vertical antenna above a ground plane can be viewed as the limiting case in which the polar angle of one of the cones goes to zero (the vertical wire) and the polar angle of the other cone goes to 90 degrees (the ground plane) [22]. Currents along such an antenna do not suffer from attenuation and dispersion. Equations 5.103–5.106 can also be derived assuming a spherical TEM solution. All the energy lost due to radiation from such an antenna comes from the source at the bottom. In reality, the lightning return stroke is different from this ideal case and therefore eqns 5.103–5.106 are only applicable in some special cases.

5.11 References

1 RUBINSTEIN, M., and UMAN, M.A.: 'Methods for calculating the electromagnetic fields from a known source distribution: application to lightning', *IEEE Trans. Electromagn. Compat.*, 1989, **31**, pp.183–189

2 THOTTAPPILLIL, R., and RAKOV, V.A.: 'On different approaches to calculating lightning electric fields', *J. Geophys. Res.*, 2001, **106**, pp.14191–14205
3 UMAN, M.A., MCLAIN, D.K., and KRIDER, E.P.: 'The electromagnetic radiation from a finite antenna', *Am. J. Phys.*, 1975, **43**, pp.33–38
4 THOTTAPPILLIL, R., RAKOV, V.A., and UMAN, M.A.: 'Distribution of charge along the lightning channel: relation to remote electric and magnetic fields and to return-stroke models', *J. Geophys. Res.*, 1997, **102**, pp.6987–7006
5 THOTTAPPILLIL, R., UMAN, M.A., and RAKOV, V.A.: 'Treatment of retardation effects in calculating the radiated electromagnetic fields from the lightning discharge', *J. Geophys. Res.*, 1998, **103**, pp.9003–9013
6 RUBINSTEIN, M., and UMAN, M.A.: 'On the radiation field turn-on term associated with travelling current discontinuities in lightning', *J. Geophys. Res.*, 1990, **95**, pp.3711–3713
7 THOMSON, E.M.: 'Exact expressions for electric and magnetic fields from a propagating lightning channel with arbitrary orientation', *J. Geophys. Res.*, 1999, **104**, pp.22293–22300
8 STRATTON, J.A.: 'Electromagnetic theory' (McGraw-Hill, Inc., 1941)
9 JEFIMENKO, O.D.: 'Electricity and magnetism' (Electret Scientific Company, Star City, USA, 1989, 2nd edn)
10 RAKOV, V.A., and UMAN, M.A.: 'Review and evaluation of lightning return stroke models including some aspects of their application', *IEEE Trans. Electromagn. Compat.*, 1998, **40**, pp.403–426
11 UMAN, M.A.: 'The lightning discharge' (Academic Press, San Diego, Calif., 1987)
12 THOTTAPPILLIL, R., MCLAIN, D.K., UMAN, M.A., and DIENDORFER, G.: 'Extension of Diendorfer–Uman lightning return stroke model to the case of a variable upward return stroke speed and a variable downward discharge current speed', *J. Geophys. Res.*, 1991, **96**, pp.17143–17150
13 MCLAIN, D.K., and UMAN, M.A.: 'Exact expression and moment approximation for the electric field intensity of the lightning return stroke', *J. Geophys. Res.*, 1971, **76**, pp.2101–2105
14 UMAN, M.A., and MCLAIN, D.K.: 'The magnetic field of the lightning return stroke', *J. Geophys. Res.*, 1969, **74**, pp.6899–6910
15 WEIDMAN, C.D., and KRIDER, E.P.: 'Submicrosecond risetimes in lightning return-stroke fields', *Geophys. Res. Lett.*, 1980, **7**, pp.955–958
16 WILLET, J.C., KRIDER, E.P., and LETEINTURIER, C.: 'Submicrosecond field variations during the onset of first return strokes in cloud-to-ground lightning', *J. Geophys. Res.*, 1998, **103**, pp.9027–9034
17 WILLETT, J.C., BAILEY, J.C., IDONE, V.P., EYBERT-BERARD, A., and BARRET, L.: 'Submicrosecond intercomparison of radiation fields and currents in triggered lightning return strokes based on the transmission line model', *J. Geophys. Res.*, 1989, **94**, pp.13275–13286
18 WILLETT, J.C., IDONE, V.P., ORVILLE, R.E., LETEINTURIER, C., EYBERT-BERARD, A., BARRET, L., and KRIDER, E.P.: 'An experimental test of the

"transmission line model" of electromagnetic radiation from triggered lightning return strokes', *J. Geophys. Res.*, 1988, **93**, pp.3867–3878

19 THOTTAPPILLIL, R., and UMAN, M.A.: 'Comparison of lightning return stroke models', *J. Geophys. Res.*, 1993, **98**, pp.22903–22914

20 LETEINTURIER, C., WEIDMAN, C., and HAMELIN, J.: 'Current and electric field derivatives in triggered lightning return strokes', *J. Geophys. Res.*, 1990, **95**, pp.811–828

21 UMAN, M.A., RAKOV, V.A., SCHNETZER, G.H., RAMBO, K.J., CRAWFORD, D.E., and FISHER, R.J.: 'Time derivative of the electric field 10, 14, and 30 m from triggered lightning strokes', *J. Geophys. Res.*, 2000, **105**, pp.15577–15595

22 THOTTAPPILLIL, R., SCHOENE, J., and UMAN, M.A.: 'Return stroke transmission line model for stroke speed near and equal that of light', *Geophys. Res. Lett.*, 2001, **28**, pp.3593–3596

23 SCHELKUNOFF, S.A.: 'Antennas, theory and practice' (John Wiley and Sons, New York, 1952) p.104

24 THOTTAPPILLIL, R., and RAKOV, V.A.: 'On the computation of electric fields from a lightning discharge in time domain', 2001 IEEE EMC International Symposium, Montreal, Canada, Aug. 13–17, 2001.

Chapter 6

Mathematical modelling of return strokes

Vernon Cooray

6.1 Introduction

A lightning flash is initiated by electrical breakdown of the air in a cloud. This process, commonly known as the preliminary breakdown, signifies the initiation of a stepped leader. Such a stepped leader propagates towards the earth, in a succession of nearly discontinuous surges or steps. The stepped leader leaves a charged, conducting channel in its wake. When the leader reaches the ground, the current flowing in the channel increases abruptly, marking the beginning of the return stroke. After the first return stroke, several subsequent return strokes may occur, each of which is preceded by a fast, continuously moving leader – the dart leader – which propagates from cloud to earth down the channel made by the stepped leader. This Chapter is concerned with the mathematical modelling of return strokes.

From the point of view of an electrical engineer, the return stroke is the most important event in a lightning flash; it is the return stroke that causes most of the destruction and disturbance in electrical and telecommunication networks. In their attempts to provide protection, engineers seek the aid of return stroke models for three reasons. First, they would like to characterise and quantify the electromagnetic fields produced by return strokes at various distances to provide them with the input for mathematical routines that analyse the transient voltages and currents induced in electrical networks by these fields. This calls for return stroke models that are capable of generating electromagnetic fields similar to those created by natural return strokes. Secondly, their profession demands detailed knowledge of the effects of the direct injection of lightning current into electrical installations, electronic equipment and structures. In a real situation this direct injection of lightning current will be superimposed on currents and voltages induced by electromagnetic fields, in various electrical networks. This necessitates the use of return stroke models that are capable of generating channel base currents similar to those in nature. Finally, in order to

evaluate the level of threat posed by lightning, engineers require statistical distributions of peak currents and peak current derivatives in lightning flashes. Even though the characteristics of return stroke currents can be obtained through measurements at towers equipped with current measuring devices, gathering statistically significant data samples in different regions and under different weather conditions is an exceptionally difficult enterprise. Accurate return stroke models can simplify this task to a large extent by providing the connection between the electromagnetic fields and the currents so that the latter can be extracted from the measured fields. Having outlined the importance of return stroke models in the engineering profession, let us consider the attributes of a model in general and a return stroke model in particular.

A model, by definition, is a mathematical construct which, with the addition of certain verbal interpretations, describes observed phenomena. The justification for such a mathematical construct is solely and precisely that it is expected to be representative of a given situation. If the mechanism behind all the fundamental processes leading to an observed phenomenon is known, it is not necessary to construct a model to describe it. A model is needed when all or some of the basic principles governing the observed phenomenon are not completely understood. Thus, a model may contain hypotheses that have yet to be proved and variables whose values are selected *a priori* to fit the experimental observations. However, irrespective of the way it was constructed, a model should be able to explain at least some of the experimental observations concerning the physical process under consideration and should be able to make predictions so that its validity can be tested through further experimental investigations.

In the case of return strokes, a model is a mathematical formulate that is capable of predicting the temporal and spatial variation of the return stroke current, the variation of return stroke speed, the temporal spatial characteristics of optical radiation, the features of electromagnetic fields at different distances and the signature of thunder. From the point of view of an engineer, the lightning parameters of particular interest are the return stroke current and its electromagnetic fields, whence most of the return stroke models available today are constructed to predict either one or both of these features. On the other hand, the physicist is mostly concerned with the lightning-generated optical radiation and the shock waves. This is the case because they provide the physicist with information concerning the thermal, electrical and thermodynamic behaviour of air heated very rapidly by the discharge. Unfortunately, no single model available at present is capable of predicting all the facets of the return stroke that are of interest to both engineers and physicists. The reason for this is not only the complexity of the return stroke itself, but also that it encompasses various processes the understanding of which requires expertise in several branches of physics, such as electromagnetic field theory, discharge physics, thermodynamics and hydrodynamics. As a consequence, those modelling the return stroke may be compelled to keep within the subject matter of their own field of expertise. However, with the proper combination of different solutions available in the literature, it may be possible to construct an all inclusive return stroke model.

Unfortunately, researchers encounter problems not only in the construction stage of models, but also in making a comparison of model predictions with experimental

data. For example, one may not be able to provide an unequivocal answer to simple questions such as 'What is the speed of propagation of return strokes?' or 'What is the signature of the current generated at the base of the return stroke channel?'. The reason is that the lightning return stroke, as with any other discharge process for that matter, can only be described in statistical terms. The characteristics of return strokes may differ from one example to another and it may not be an easy task to find a typical return stroke. This fact makes it difficult to compare model predictions with the available experimental observations. For instance, the predictions of a model that is capable of generating a typical channel base current and typical electromagnetic fields may fall wide of the mark when the observations are confined to a single return stroke. Indeed, an appropriate comparison of model predictions with experimental observations requires simultaneous measurements of current at the channel base and at different heights, remote electromagnetic fields, and the optical and thunder signature of a single return stroke. Even though we still do not have proper techniques to quantify how the current signature varies as a function of height, all the other features mentioned above can be measured from a single stroke if both the time and the point of strike can be predetermined. This indeed is the case with triggered lightning flashes (the reader is referred to Chapter 4 for a discussion on triggered lightning). Simultaneous experimental data on various return stroke features gathered from such lightning flashes can provide enough information to validate return stroke models, but not beyond reasonable doubt. The triggering technique itself can introduce physical constraints and initial conditions that are very different to the natural conditions. Thus, even if a good agreement is observed between the experiment and theory, there will always be unknown parameters which may tip the balance between a good model and a bad one. Keeping these facts and warnings in mind, let us consider the principles behind various return stroke models.

The first mathematical model to describe return strokes was presented in 1939 by Norinder [1]. Since then a rapid and continuous development of return stroke models has taken place thanks to the diligent work of experimentalists whose work has kept the return stroke model builders on the right track. On the basis of the concepts and aims of these models, they can be separated into three main groups, namely:

(i) the electrothermodynamic models
(ii) the transmission line or LCR models
(iii) the semiphysical and engineering models

each of which will be discussed in this Chapter.

6.2 Electrothermodynamic models

Electrothermodynamic models were originally motivated by the need to understand the shock waves from line disturbances, some examples being long explosive charges, exploding wires, supersonic projectiles, sparks and lightning. Models of this kind describe the relationship between the observable parameters of the discharge, such as current–voltage characteristics, acoustic and radiative effects, plasma temperature,

plasma composition and the plasma column dimensions. Most of these models make the following three simplifying assumptions:

(i) The discharge column is straight and cylindrically symmetric so all the events are functions of a radial coordinate r and time t only. This assumption requires that the current in the channel be uniform along the length of the column so that there is no dependence on the z coordinate.
(ii) The conducting portion of the plasma is electrically neutral.
(iii) Local thermodynamic equilibrium exists at all times so that the state of the medium at a given point can be computed from a knowledge of the temperature and pressure.

The driving force of these models is the resistive heating of the plasma channel by a prescribed flow of electric current coupled with the computation of the electrical conductivity of the plasma. The model then describes the properties of the plasma column and its surroundings through numerical integration of three conservation equations (the conservation of mass, momentum and energy) and two state equations (the thermal equation of state and caloric equation of state). According to Hill [2], the conservation equations can be written as:

$$\frac{1}{\rho} = \frac{1}{2}\frac{\partial r^2}{\partial m} \quad \text{(conservation of mass)} \tag{6.1}$$

$$\frac{\partial u}{\partial t} = -r^2 \frac{\partial}{\partial m}(P + Q) \quad \text{(conservation of momentum)} \tag{6.2}$$

$$\frac{\partial E}{\partial t} + P\frac{\partial V}{\partial t} + Q\frac{\partial V}{\partial t} + \frac{\partial L}{\partial m} + D = 0 \quad \text{(conservation of energy)} \tag{6.3}$$

In these equations m which equals $\int \rho r\, dr$ is the particle mass (the mass per radian per unit length of channel), ρ is the density of air, V is the specific volume, r is radial distance, u is particle velocity, t is time, P is pressure, Q is artificial viscosity pressure, E is the specific internal energy, D is the specific energy source rate and L is luminosity (i.e., the radiant flux per radian per unit length of channel). The two state equations are given by:

$$P = \rho RT \quad \text{(thermal equation of state)} \tag{6.4}$$

$$E = \frac{RT}{(\gamma - 1)} \quad \text{(caloric equation of state)} \tag{6.5}$$

where R is the gas constant per unit mass, T is temperature and γ is the constant specific heat ratio. The evaluation of the equations of state requires information concerning the state of ionisation of air at a given temperature and pressure. This information is usually obtained through Saha's [3] equation by assuming local thermodynamic equilibrium. The initial boundary conditions imposed on the model are the temperature, pressure and the radius of the conducting channel formed by the processes subsequent to the initiation of the return stroke current. The outputs of

the model are the radial variation of pressure, electron density, temperature, optical radiation and parameters of the shock wave.

One of the first models of this kind applicable to spark discharges was introduced by Drabkina [4]. However, the theory she advanced is not complete. The electrical conductivity and the temperature in the channel are not computed in her theory, it only relates the hydrodynamic conditions to the energy released in the channel, which must be determined experimentally. Braginskii [5] extended this theory by removing the simplifying assumption. He considered the conductivity σ and temperature T to be uniform within the plasma channel and, outside this, the temperature is taken to be ambient temperature. He also made the simplifying assumption that the conductivity of the plasma channel takes a constant value (i.e. it is independent of time t). For a spark current increasing linearly with time, he then gives the following expression for the spark channel radius a:

$$a = 0.93 \times 10^{-3} \rho_0^{-1/6} I^{1/3} t^{1/2} \tag{6.6}$$

where a is in metres, $\rho_0 (= 1.29 \times 10^{-3}\,\mathrm{g/cm^3})$ is the density of the air at atmospheric pressure, I in kiloamperes, and t in microseconds. Even though Braginskii's treatment allows calculation of the energy input from the current waveform, both his and Drabkina's theory use the strong shock approximation – which assumes that the channel pressure is much greater than the ambient pressure – and therefore applicable to the initial stages of the spark. Plooster [6–8] extended the work of Brode [9], which is valid for spherical sources, to describe spark and lightning discharges. The work of Hill [2] is also an extension of Brode's work to cylindrical symmetries. Indeed, there is a qualitative agreement between the calculations of Hill and Plooster. More recently, Paxton *et al*. [10] improved the calculations made by Plooster by introducing a better radiative transfer algorithm.

These models have to overcome several problems in obtaining the correct initial conditions. Lightning discharges exhibit a great variation in observed parameters so that it is difficult to have a unique set of initial conditions that is valid for the majority of the return strokes. The models do not account for the processes occurring before the onset of high current and, therefore, the mechanism that leads to the generation of the return stroke current is not taken into account. As a consequence, the temporal variation of the return stroke current is used as an input parameter. But, there is no general consensus as to the temporal profile of the current waveform that should be used in the calculations. Moreover, in addition to it being a function of altitude, the current waveform at a given height may differ significantly from one stroke to another. The situation is made even more complicated by the fact that the initial conditions of the breakdown channel may differ from one point on the channel to another. In general, the initial conditions can be split up into two categories – those in which the gas density in the channel equals that in the surrounding atmosphere, and those in which the pressures are equal. The constant density condition corresponds to that portion of the return stroke channel close to the surface of the earth. Here, the time elapsed between the passage of the leader and the onset of the return stroke is usually short and the gas heated by the leader will not have sufficient time for the pressure to equilibrate with the

surrounding atmosphere. The initial density of the channel under these circumstances will be that of the surrounding atmosphere. The constant pressure condition applies in channel sections which are well above the earth. Here, a considerable time may elapse between the passage of the leader and the onset of the return stroke and there is enough time for the channel to achieve pressure equilibrium with the surrounding atmosphere. Not withstanding, throughout most of the channel length the initial conditions may fall in between these two extremes. In addition, the initial plasma temperature and the channel radius may also change from one location on the channel to another. However, the calculations of Plooster [7] show that the initial conditions only affect the channel properties at times immediately after the current onset.

The existence of a local thermodynamic equilibrium (LTE), which is one of the presumptions of these models, may be justified a few microseconds after the onset of the return stroke phase, but whether LTE prevails during the rising portion of the current waveform where the electric field driving the current is sufficiently high is doubtful. If this assumption is not valid immediately after the onset, any relationship between the peak return stroke current and the optical output over the first few microseconds as derived by these models may be in error. Besides, these models do not take into account the consequences associated with the neutralisation of the corona sheath surrounding the central core of the leader channel during the return stroke. Available evidence suggests that this neutralisation is accompanied by streamer-like discharges progressing into the corona sheath [11,12]. Even though the streamers are cold discharges, their stems may acquire conditions favourable for thermalisation – a rapid increase in temperature caused by thermal ionisation. In principle, this can be considered to be an expansion of the hot central core; a process not taken into account by the present electrothermodynamic models.

Due to these various assumptions and simplifying approximations, the results obtained from the electrothermodynamic models may be quantitatively in error, but they do show qualitatively the importance and effects of various processes in lightning discharges. Plooster [7] compared the results of his computations with those obtained from laboratory sparks by Orville *et al*. [13]. The model simulated temporal growth of channel temperature, and channel pressure and electron density are in reasonable agreement with the measurements. Plooster [8] also extended his theory to describe the return strokes. His results show a reasonable agreement with the experimental data gathered by Orville [14–16]. Recently, a rigorous and one-to-one comparison of the optical radiation predicted by the electrothermodynamic model of Paxton *et al*. [10] with measured lightning data was made by Baker *et al*. [17]. In the experiment, simultaneously with the channel base current, the light output of a small length of a triggered lightning channel was measured. The theory was used to make numerical predictions of the optical output for the measured current. The calculated and the measured waveforms are qualitatively similar, but there are differences in the details. Authors claim that these discrepancies are probably caused by the initial conditions selected for the simulations.

As indicated earlier, electrothermodynamic models are capable of qualitatively describing the thermodynamic and electrical properties of air in a lightning channel heated by the return stroke current. The main disadvantage of these models is their

inability to predict the temporal and spatial variation of the lightning current. Due to this deficiency, these models cannot be manipulated to predict the electromagnetic fields and channel base current, the parameters which are of prime interest to engineers. Nevertheless, the potential of these models can be enhanced by combining them with LCR or semiphysical models, which have the ability to predict the spatio–temporal characteristics of the return stroke current.

6.3 Transmission line or LCR models

The most simple model of a lightning return stroke is a lumped circuit model. This can be represented by a capacitor connected across a switch to an inductor in series with a resistor. The inductor and resistor represent the return stroke, and the capacitor the charge stored in the cloud. This model inherently assumes that the current in the return stroke channel at any given time is the same at any point on the channel. It also neglects the finite speed of propagation of the information along the channel. Such a simple model was used by Oetzel [18] to calculate the diameter of the lightning channel. First, he assumed that the current in the return stroke channel is given by a double exponential function, enabling him to determine the value of the resistor that is consistent with this current waveform. Once the resistance is known, assuming that the channel is cylindrical and filled with a finitely conducting plasma, he obtained the diameter of the channel. Even though the lumped circuit description of the lightning channel is an oversimplification, it provided reasonable values for the diameter of the channel. But, a transmission line is a better analogy to the physical reality (Figure 6.1).

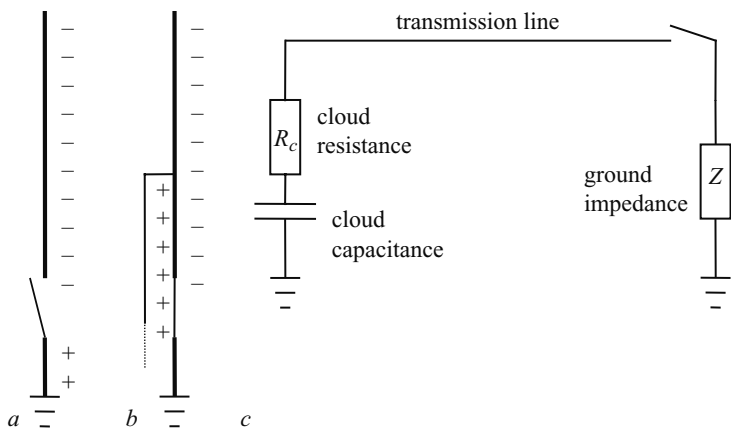

Figure 6.1 Schematic representation of the similarity between a return stroke and a transmission line model

a leader channel formation
b return stroke
c transmission line model

The initial charge on the transmission line is analogous to the charge stored on the channel of the leader. The velocity of waves on the line can be adjusted to fit the observed speed of propagation of the return stroke front. This representation also makes it possible to evaluate the current at different points along the channel, a prerequisite for the calculation of the electromagnetic fields. This procedure also provides a satisfactory approach to the extrapolation of the current measurements made at the bottom of the channel to other points along the channel. Oetzel [18] also considered a finite, lossy, uniform transmission line as a model for return strokes. He found that the double exponential form for the current at the base of the channel – used frequently in the existing literature – can be generated by a reasonably nonuniform initial charge distribution. As pointed out by Price and Pierce [19], however, such a charge distribution on a uniform transmission line implies a complex dynamic state just before the initiation of the return stroke. But, since the stepped leader speed is of the order of 10^6 m/s, there is ample time for the channel to reach equilibrium conditions.

Price and Pierce [19] considered an infinite, lossy, uniform transmission line with a given initial charge distribution to represent the return stroke. The line was characterised by its series resistance R, shunt capacitance C and series inductance L per unit length. At $t = 0$, the line was linked to ground through a resistance equal to the characteristic impedance. The main purpose of this study was to obtain a general picture of the current signature as a function of height along the channel. Thus, no attempt was made to evaluate values of L, C or R suitable for a lightning channel. Using this representation and assuming that the charge distribution at $t = 0$ is uniform along the line, they calculated the temporal and spatial variation of the current along the channel. The results produced a current at ground level which rose to its peak value instantaneously (i.e., a step-like rise), but the subsequent decay was more realistic than that of an exponential function. They employed the model to evaluate the signatures of remote electric and magnetic fields at 1, 10 and 100 km. The agreement with the measured fields was only qualitative. (The reader is referred to Chapters 4 and 7 for a review of the lightning-generated electromagnetic fields.)

A more general LCR representation of the return stroke was introduced by Little [20]. He assumed both the inductance per unit length L and capacitance per unit length C to vary with height. The value of C as a function of height was obtained by first calculating the charge distribution on the leader channel supposing it to be a good conductor extending down either from a spherical or a plane charge centre, and then converting the estimated charge per unit length ρ into C through the equation $\rho = VC$, where V is the line potential. The magnitude of L was calculated by means of the following concept. When the current flows from any channel segment to ground, the displacement current flows in the space between that segment and the ground, and along the electric field lines. These electric field lines were obtained from the calculated charge distribution along the transmission line and the inductance associated with the line segment was found from the area under the electric field lines. Little [20] was also aware of the fact that the value of R is a complex function of time and height. Notwithstanding this, he assumed a constant resistance that is capable of generating a unidirectional current pulse without oscillations. These considerations led him to

decide upon a resistance of 1 ohm/m which he used throughout the calculations. The ground end of the line was terminated by a resistance equivalent to a hemispherical earth conductor buried in soil of specific conductivity σ. In the simulations, the potential of the cloud and the channel were both set at 100 MV and the cloud was represented by a 1 μF capacitor. The simulations show that the current pulse amplitude decreases with height while its rise time increases. The speed of the return stroke front v, based on the time of travel of the current peak, was 1.5×10^8 m/s over the first 1000 m. Little [20] did not make any attempt to evaluate the remote electromagnetic fields.

A nonuniform transmission line model in which both the inductance and capacitance per unit length vary exponentially as a function of height was introduced by Amoruso and Lattarulo [21]. The return stroke was simulated by an injection of current of a given waveshape into this transmission line. The inductance and capacitance per unit length of the line were given by:

$$L = L_0 e^{kh}, \quad C = C_0 e^{-kh} \tag{6.7}$$

where C_0 and L_0 are unspecified quantities, h is the height and k is a suitable constant. The basis for the preference for an exponentially decreasing C is the following. The modellers assumed that the charge per unit length ρ on the leader channel decreases exponentially with height. If the potential of the leader channel is uniform throughout and equal to V, the capacitance C per unit length will also decrease exponentially with height (note that $C = \rho / V$). The impedance of the line Z and the propagation speed v of the waves travelling along this line were given by:

$$v = \sqrt{(L_0 C_0)^{-1}}, \quad Z = \sqrt{(L_0 C_0)} e^{kh} \tag{6.8}$$

Thus the impedance of the line increases with increasing height while the speed of propagation remains constant. As the current pulse propagates along this transmission line, an overall change in the current waveshape takes place. The higher frequency components, and hence the initial part of the current waveform, decrease almost exponentially along the channel with a decay height constant of $(k)^{-1}$. The lower harmonic components, and hence the tail of the current waveform, are reduced much more. In the simulations the authors assumed $v = c/3$, where c is the speed of light in free space. The authors used the model to calculate the remote electromagnetic fields and the results obtained are in reasonable agreement with the measured fields.

The LCR models discussed so far treated the line parameters as being time independent. As mentioned earlier, the channel may expand in diameter by over an order of magnitude during the initial 100 μs [8] so that time-independent values of line parameters cannot adequately represent the entire phase of the return stroke. But, however, the variation of L and C with time is weak due to the logarithmic nature of the expressions for these parameters. The variation of R with time, however, may significantly alter the model predictions. The temporal variation of R, of the lightning

channel, is governed by the discharge and plasma physics – disciplines which are not within the realm of transmission line theory. Fortunately, the electrothermodynamic models can correct for this deficiency in the LCR models. Even though they are neither complete nor completely self consistent, the electrothermodynamic models offer the possibility of incorporating discharge physics into the transmission line models. Moreover, the benefits of combining LCR and electrothermodynamic models are not only limited to the LCR models. Such a combination can also contribute to the further development of electrothermodynamic models. For example, in these models the current is assumed to be independent of the properties of the plasma channel. In reality, however, there is a complex interaction between the channel properties and the return stroke current making it difficult to consider the latter as a parameter that is independent of the state of the channel. This complex interaction, manifested mainly through the channel resistance, can be understood by combining the electrothermodynamic models with LCR models. A model with such a blend was first proposed by Strawe [22].

In the model of Strawe [22], the lightning channel was represented by an LCR network (unfortunately he neither gave the values of L and C used in the simulation nor a discussion of how they were evaluated) in which the resistance of the channel was simulated with the help of Braginski's [5] model. Strawe also took into account the presence of a connecting leader by simulating it with a short section of transmission line which was terminated by a 50 ohm resistance at ground level. The discharge was supposed to start when the downward leader got attached to the connecting leader. This attachment was represented by a switch placed between the short and long sections of the transmission line. At each time step in the simulation, a model subroutine calculated the channel resistance for each section of the transmission line from the past current history and fed it into the next time step. Consequently, the model-simulated return stroke current is influenced by the variation of the channel resistance and *vice versa*. Strawe mainly confined his simulations to the extraction of the current signature as a function of height and did not evaluate the remote electromagnetic fields. The most significant result obtained from the simulations is the rapid decline of the rate at which the current rises with elevation.

A model similar to Strawe's in which the resistance of the channel was simulated by means of an electrothermodynamic model was presented recently by André *et al*. [23], who also incorporated a time-dependent resistance, that Braginskii [5] anticipated should exist in spark channels, into LCR models. The conductivity of the channel was obtained from the Spitzer and Härm [24] conductivity formula assuming the electron temperature to be 30 000 K. Moreover, the capacitance and inductive elements of the channel were obtained in a manner identical to that of Little [20]. The cloud was represented by a resistance in series with a capacitor and the earth termination was represented by a linear resistance. The cloud resistor represents the resistance of the path from the outer boundary to the middle of the charge centre. This was estimated by first calculating the radius of the charge centre by accepting that the electric field at the outer boundary of the charge centre is about 10^6 V/m and assuming the resistance per unit length of the path to be about three ohms. The results obtained by André *et al*. are qualitatively similar to those obtained by Strawe.

The LCR models examined so far have taken no account of the physical structure of the leader channel. The leader channel consists of a central hot core surrounded by a corona sheath. In fact, most of the leader charge which is neutralised by the return stroke resides on the corona sheath. Baum and Baker [25] presented an LCR model which acknowledged the presence of the corona sheath. In this model, the return stroke was represented as a wave propagating along a conical transmission line. The modellers visualised the leader tip as a circular cone at the centre of which there is a conducting core carrying most of the current. The leader charge was assumed to reside primarily on the conical surface. As pointed out by Baum [26], although it seems overly simplified, this approximation has its physical merits. As the leader propagates through the air, the corona near the leader tip has only a short time in which to disperse outwards, but further down the tip the corona has more time to propagate outwards. Accordingly, the radius of the corona sheath increases as one moves down the leader tip – hence the approximation of a conical shape for the corona sheath. Note, however, that this approximation is only valid adjacent to the tip of the leader and therefore the conical model is only appropriate for times close to the initiation of the return stroke. By the time the return stroke has propagated a few tens of metres, it will encounter a fully developed corona sheath and hence the conical model has to be replaced by a cylindrical one. In the model Baum and Baker [25] neglected the dissipative effects and that made it possible for them to solve the model equations analytically.

One significant prediction of the conical model is that the speed of propagation of the return stroke front is initially close to the speed of light but after the front has propagated a few tens of metres it decreases to about one third the speed of light. The reason for this is the increase in capacitance per unit length of the channel with increasing height. Subsequently, Baker [27] expanded the model by introducing dissipative effects through a channel resistance which was allowed to vary as a function of time. The resistance at a given time was computed by using an electrothermodynamic model similar to that developed by Paxton *et al*. [10]. The model differs from that of Strawe [22] which had the simplifying approximation that the shock wave does not separate from the edge of the hot channel. Moreover, it incorporated improved treatments of the equation of state, radiative losses and shock wave propagation. The equivalent circuit (per unit length) of Baker's model is shown in Figure 6.2. In the simulations, however, Baker chose to neglect the conductance, G, per unit length. To calculate the capacitance and the inductance per unit length of the model it is necessary to have a value for the return current radius, which was assumed to be a fixed parameter. With this assumption, the per-unit parameters were calculated from the equations:

$$L = \frac{\mu_0}{2\pi} \ln\left[\frac{r_{return}}{r_{channel}}\right], \quad C_c = \frac{2\pi\varepsilon_0}{\ln\left[r_{corona}/r_{channel}\right]}, \quad C = \frac{2\pi\varepsilon_0}{\ln\left[r_{return}/r_{corona}\right]} \tag{6.9}$$

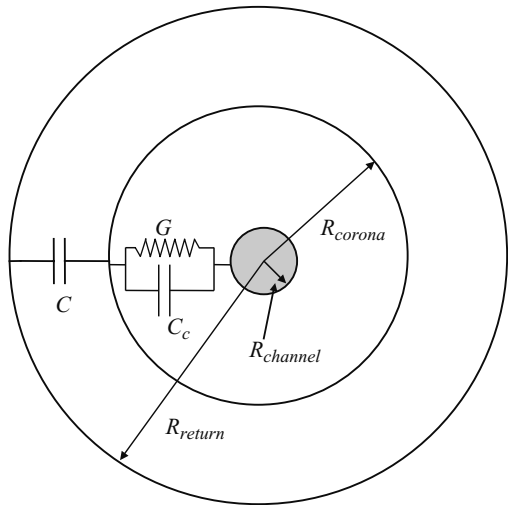

Figure 6.2 *Sketch of the assumed transmission line geometry of Baker's model (Baker, 1990). $R_{channel}$ is the radius of the central core of the return stroke, which carries essentially all the current. R_{corona} is the outer radius of the corona sheath. R_{return} is the radius of the conductor along which the return stroke current returns to ground. In the analysis, the leakage capacitance C_c was neglected, i.e., the resistor was assumed to be of negligible resistance or large conductance G, so that the time constant C_c/G is small compared to times of interest* (from [25] and [27])

where $r_{channel}$ is the radius of the return stroke core through which the return stroke current flows, r_{corona} is the radius of the corona sheath which is a function of height, and r_{return} is the return current radius – the radius of a hypothetical conductor along which the current returns to ground. The radius of the corona sheath is calculated by assuming that the electric field at the outer boundary of the channel is equal to 3 MV/m. The boundary conditions are the fixed impedances at the cloud and ground terminations. The starting parameters for the calculations are zero current flow everywhere and the voltage of the line. The latter is set to an initial value along the line as far down to as an initiation point above the ground, below which it decreases linearly to zero. Baker utilised the model first to understand how the return stroke current alters as a function of height and then to evaluate the remote electromagnetic fields. The simulations revealed that the front of the current waveform spreads out as it advances along the channel and its amplitude decreases. In this respect, the model predictions are qualitatively similar to those of Strawe [22] and André *et al.* [23]. The model-simulated vertical electric field at 50 km decayed rather rapidly after about five microseconds. This was probably due to the fixing of the channel length at 1.5 km. The initial ascent of the field does resemble the measured one whereas the decaying part of the electric field does not.

Utilisation of the transmission line as a vehicle to probe the return stroke has improved our knowledge about the possible behaviour of the lightning return stroke current along the channel. All the models that incorporated dissipative effects show a spreading out of the return stroke front as it propagates along the channel. This model prediction is in agreement with the results inferred from optical radiation (the reader is referred to Chapter 4 for a description of the measurements). The remote fields (these are only calculated in some studies) do not agree quantitatively with the measured ones, but there is a qualitative resemblance. On the other hand, using transmission line concepts to describe return strokes is not without its share of difficulties. The first problem is the static nature of inductance L and capacitance C per unit length assumed. The lightning channel is actually a monopole rather than a transmission line, and therefore L and C should vary as a function of time. This may give rise to current dispersion which is not accounted for by the present models. A second problem is the following: the transmission line models constrain the speed of propagation of the return stroke front to $\sqrt{(LC)^{-1}}$. This, of course, is correct in a conventional transmission line but in the case of the return stroke the speed of the front is probably governed to a large extent by the plasma properties and discharge physics and, to a lesser degree, by the apparent capacitance and inductance. It may be more correct to represent the return stroke as a transmission line extending upwards from ground level in the background electric field created by the stepped leader. The speed of extension of the transmission line is equal to the return stroke speed. A third problem is associated with the line terminations. In a transmission line the current signature at different locations is significantly altered by the conditions at the line terminations. In many LCR models it is imagined that the ground end is terminated with the characteristic impedance. Unfortunately researchers have not yet fathomed the nature of ground terminations of return strokes. In addition to soil ionisation – which creates a time-dependent impedance – the surface flashover may confuse the situation still further. A fourth problem is that the transmission line theory requires TEM propagation of waves. But, in the vicinity of the return stroke front where the longitudinal electric fields are strong, significant deviations from the TEM mode can be anticipated. A fifth problem is that all the transmission line models assume instantaneous charge depletion from the charged capacitor on the line. In reality, leader charge resides on the corona sheath so that the dimension and conductivity of the corona sheath could impose limitations on how rapidly the charge can be drained from it, limiting the current rise and fall times. In fact some of the semiphysical and engineering models to be described later do attempt to take this fact into consideration. Finally, the return current radius, the value of which determines the inductance, and hence the wave speed, is an *ad hoc* parameter. The models do not provide any indication as to how one should choose this radius. In reality, a current pulse on a lightning channel is not accompanied by a return current pulse; hence there is actually no return current conductor for a lightning channel. A better representation of the return stroke is to designate it as a TM wave propagating along a single conductor. Such an analysis was presented by Borovsky [28].

Borovsky's is not a transmission line model so there is little or no justification for discussing his model here in a section allocated to the description of transmission

line models. Yet, in principle, waves guided along both transmission lines and single conductors are characterised through Maxwell's equations; hence the reason for discussing this model here. Borovsky [28] made a detailed examination of the guided wave propagation along a single conductor with finite electrical conductivity. The input parameters required to obtain a solution are the radius of the channel and its electrical conductivity, which were both assumed to be uniform in space and constant in time. Since the constituent of the lightning channel is a plasma, the channel temperature determines the electrical conductivity. The conductivity corresponding to a certain temperature was obtained from empirical expressions, derived from experimental data. The model simulations show that the nature of the waves guided along the conductor depends on the relative size of the channel radius r_{ch} and the electromagnetic skin depth δ. If $r_{ch} \geq \delta$, the speed of the wavemode is approximately equal to the speed of light and there is little dispersion. If $\delta \gg r_{ch}$, the speed is less than that of light and the mode is strongly dissipative. Defining $dt = 1/\omega$ where ω is the frequency of the wavemode, Borovsky's calculations disclosed that the group velocity of the wavemode is increased if the channel radius is increased, the channel temperature is increased or the rise time, dt, of the wavemode is decreased. Additionally, the damping of the wave is decreased if the channel radius is increased, the channel temperature is increased or the rise time dt of the wavemode is increased. For $dt = 500$ ns (a number which lies in the range of values measured for current rise times) and for $T = 15\,000$ K, the calculated group velocities are in the range of 10^7–10^8 m/s, the correct range of observed return stroke speeds. The speed was found to decrease with declining channel temperature (i.e., with decreasing conductivity) or with growing wavemode rise times. Borovsky [28] pointed out that the observed drop in the return stroke speed with height is probably caused by the decrease in channel conductivity or the increase in the rise time of the current. Borovsky applied the model to take out information regarding the power dissipation and came up with values of the order of 10^9 W/m. Another interesting parameter extracted through this labour is the electric field at the front of the wavemode corresponding to rise times and temperatures close to return strokes. The estimated peak field was 3.0×10^5 V/m.

Even though the model of Borovsky is a step forward in the endeavour to understand return strokes, it does have several weaknesses. First, the simulations are valid for a single conductor in free space which may not be a suitable approximation at times close to the initiation of the return stroke due to the close proximity to ground. Secondly, the conductivity of the return stroke channel may change as a function of time in general, and close to the return stroke front in particular. As a consequence, the assumption of constant conductivity may fail in the vicinity of the return stroke front. Finally, as mentioned before, most of the charge on the leader resides on the corona sheath and the model does not take this fact into consideration.

There is no doubt that the results gained through the manipulation of LCR models have contributed a great deal to our understanding of the return stroke. However, the present author believes that one of the main contributions was the provision of a framework and vision on which the semiphysical and engineering models – the most successful in terms of their predictions from an engineering point of view – were built.

6.4 Engineering and semiphysical models

In engineering models, a spatial and temporal variation is assumed for return stroke current and then used to calculate the remote electromagnetic fields – the sole prediction of these models that can be compared with the measurements. Semiphysical models go one step further by invoking physical processes as the cause of the temporal and spatial variation of the return stroke current and speed. These models are capable of predicting at least two or more of the following return stroke features: the channel base current, the temporal and spatial variation of current along the channel, the variation of the return stroke speed with height and the remote electromagnetic fields. Regardless of whether they are engineering or semiphysical, all the models have utilised or adapted concepts from transmission line models. A reexamination of the LCR type models will disclose that they can be subdivided into two groups. In the first group the return stroke is considered as a transmission line driven by a source at ground level. For ease of identification the models that have their foundations within this group of LCR models are called 'current propagation models'. These models do not account for the generation of the return stroke current. Most of the engineering models belong to this category. In the second group of LCR models, the return stroke is viewed as the discharging of a charged transmission line. The models that have borrowed their main features from this group of LCR models are called 'current generation models'. Most of the semiphysical models belong to this category.

6.4.1 Current propagation models (CP models)

The measurements of the return stroke channel luminosity as a function of space and time have provided basic guidance in the development of current propogation models. These measurements have disclosed that, in an optical sense, the return stroke is a luminous front that propagates from the ground to the cloud along the leader channel. The channel is dark ahead of the luminous front but behind it it is bright all the way to the ground. Since the increase in luminosity of the channel is probably caused by an increase in the current, the visual picture provides a strong analogy to a current pulse propagating along a transmission line driven by a current source at one end – the channel base. Indeed, this is the main postulate of the current propagation models.

In the discussion to be followed, electromagnetic fields produced by some of the models are presented. Unless indicated otherwise, in the calculation of the electromagnetic fields the following current waveform is used at the channel base:

$$I(t) = \left(\frac{I_1}{\eta}\right)\left(\frac{t}{\tau_1}\right)^2 \frac{\exp(-t/\tau_2)}{1+(t/\tau_1)^2} + I_2[\exp(-t/\tau_3) - \exp(-t/\tau_4)] \qquad (6.10)$$

where t is the time, $I_1 = 9900$ A, $I_2 = 7500$ A, $\tau_1 = 7.2 \times 10^{-8}$ s, $\tau_2 = 5.0 \times 10^{-6}$ s, $\tau_3 = 60 \times 10^{-6}$ s, $\tau_4 = 6.0 \times 10^{-6}$ s and $\eta = 0.845$. This current waveform is shown in Figure 6.3; it has a peak of 12 kA, a peak current derivative of 105 kA/μs and it decays to its half peak value in 20 μs. These values are based on the average features of the triggered subsequent return stroke currents (see Chapter 4). This analytical form was used previously by Nucci *et al*. [29] to represent return stroke currents.

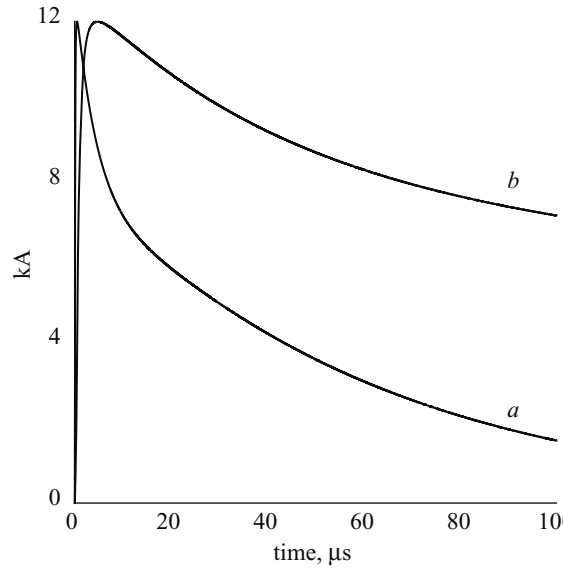

Figure 6.3 *a* the current waveform at the channel base used in many of the calculations presented in this chapter
b front portion of the current waveform shown in a ten times faster time scale

6.4.1.1 Norinder

Norinder's model [1] was the first return stroke model ever to be published in the open literature. It was introduced not as a description of the return stroke, but more as a tool with which to extract current features from the measured magnetic fields. Norinder assumed that the current in the whole channel, i.e., from the ground to the cloud, starts to flow instantaneously at the initiation of the return stroke. This current varies as a function of time, but at a given instant of time the current has the same amplitude along the whole channel. The model tacitly assumes, therefore, that the speed of propagation of the return stroke front and the speed of information transfer along the channel is infinite.

The magnetic induction field B_i at a distance D from this hypothetical return stroke is given by:

$$B_i = \frac{\mu_0 i(t)}{2\pi D} \frac{H}{\sqrt{(H^2 + D^2)}} \tag{6.11}$$

where H is the channel height and $i(t)$ is the current at the channel base. Norinder employed the above equation to extract $i(t)$ from the measured magnetic field. This equation may provide the correct current signature if the measurements are confined to distances within about 20 m of the lightning flashes. Consequently, it can be employed

to evaluate the approximate strength of magnetic fields inside small structures during direct lightning strikes, provided that the path of propagation of the current is confined to the down conductor of the lightning protection system. At greater distances, the above equation may introduce significant errors in the estimated current due to the presence of an important contribution from the radiation field term. Indeed, Bruce and Golde [30] heavily criticised Norinder's results because he exercised his model beyond its limits by employing it to extract return stroke currents from magnetic fields measured many kilometres away.

6.4.1.2 Bruce and Golde

Bruce and Golde's model [30] is the first return stroke model that strived to integrate the then available experimental observations into a mathematical foundation so that the remote electromagnetic fields from return strokes can be calculated. This model is based on two assumptions:

(i) the return stroke front surges upward with a finite speed which is less than the speed of light
(ii) at a given instant in time, the magnitude of the current flowing below the return stroke front is the same along the whole channel and is equal to the strength of the current at the channel base.

Mathematically, the current at any point on the channel $I(z, t)$ can be expressed as:

$$\begin{aligned} I(z,t) &= I(0,t) \qquad t \geq \zeta \\ I(z,t) &= 0 \qquad\quad\ t < \zeta \end{aligned} \tag{6.12}$$

where z is the coordinate directed along the channel, t is the time, ζ is the time taken by the return stroke front to reach the height z and $I(0, t)$ is the current at the channel base. Bruce and Golde assume that the temporal variation of the current at the channel base and the return stroke speed, v, are given by:

$$I(0,t) = I_0(e^{-\alpha t} - e^{-\beta t}) \quad v(z) = v_0 e^{-\gamma t} \tag{6.13}$$

where $I_0 = 3.0 \times 10^4$, $\alpha = 4.4 \times 10^4\ \mathrm{s}^{-1}$, $\beta = 4.6 \times 10^5\ \mathrm{s}^{-1}$, $v_0 = 0.8 \times 10^8\ \mathrm{m/s}$ and $\gamma = 3 \times 10^4\ \mathrm{s}^{-1}$. A graphical representation of the spatio–temporal variation of the Bruce and Golde model current is given in Figure 6.4. Since the current at any instant is the same all the way from the bottom of the channel to the return stroke front, there is a current discontinuity at the front, i.e., the current increases instantaneously to a finite value there. This implies an instantaneous neutralisation of the charge located on the leader channel at the return stroke front. Another limitation of the model is the assumption that the current at all points along the channel adjusts itself instantaneously to the magnitude of the current at the channel base at that instant. This would require information transfer along the channel with a speed greater than that of light; a physical impossibility.

Input parameters: the input parameters of the model are the channel base current and the return stroke speed.

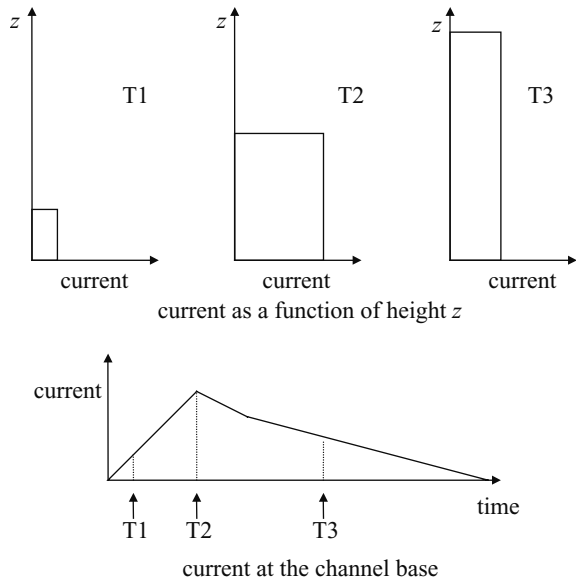

Figure 6.4 A schematic representation of the current distribution for Bruce and Golde's model [30]

Predictions of the model: the characteristics of the remote electromagnetic fields are the sole output of the model. The predicted results are in general agreement with the measured fields [29].

6.4.1.3 Dennis and Pierce

The simplicity of the Bruce and Golde model persuaded nearly twenty decades of lightning researchers to overlook its overwhelming limitations. Dennis and Pierce [31] were the first to contest the use of this model when they provided an alternative in 1964. These authors visualised the return stroke as follows. At the initiation of the return stroke a return stroke front starts propagating upward with a speed v which may be a function of height. This front can be considered as a plasma phenomenon which converts the leader channel into a state suitable for the propagation of the return stroke current. Simultaneously with the launching of the return stroke front the ground commences the injection of a current pulse into the leader channel. The current pulse propagates along the channel with a speed u, which can also be a function of height, but with the restriction that it remains equal to or larger than v, the speed of propagation of the front. Mathematically, the Dennis and Pierce current at height z and at time t is given by:

$$\begin{aligned} I(z,t) &= I\left(0, t - \frac{z}{u}\right) \quad t \geq z/v \\ I(z,t) &= 0 \qquad\qquad\qquad\quad t < z/v \end{aligned} \tag{6.14}$$

Note that in the above equation z/v and z/u are the times taken by the return stroke front and the current pulse, respectively, to reach the height z. If these speeds were a function of z they would have to be changed accordingly.

A pictorial representation of the variation of the Dennis and Pierce current as a function of height and time for the cases $u > v$ and $u = v$ is shown in Figures 6.5 and 6.6, respectively. The case $u > v$ (i.e., when the current pulse travels faster than the return stroke front) tends to form a shock at the front. The situation is then qualitatively as in a shock wave in a gas, for which the shock front is subsonic with respect to the flow behind it. As a consequence, the current will be chopped at the front. In this situation more charge will reach the front than can be accommodated through the movement of the front. This excess charge reaching the front is assumed to neutralise the charge on the leader channel instantaneously. For example, consider the instant when the front is at height z. Since, the amplitude of the current at the front when the front is at height z is $I(0, z/v - z/u)$, the charge deposited by the return stroke (or neutralised) per unit length ρ at height z is given by:

$$\rho = I\left(0, \frac{z}{v} - \frac{z}{u}\right)\left(\frac{1}{v} - \frac{1}{u}\right) \tag{6.15}$$

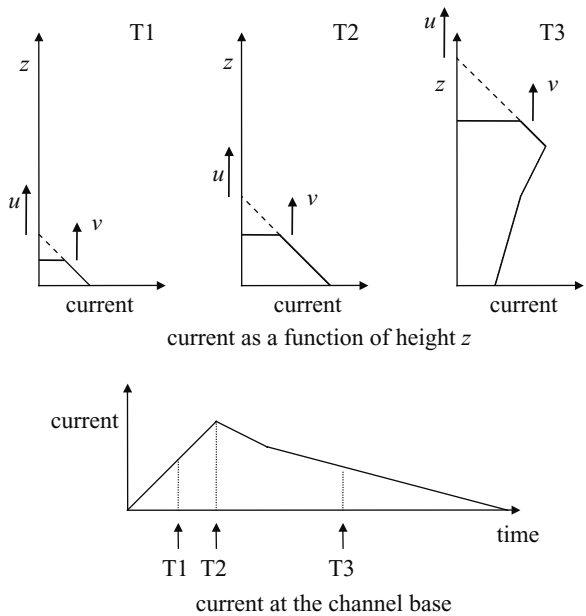

Figure 6.5 A schematic representation of the current distribution using Dennis and Pierce's [31] model for the case u > v, where u is the speed of propagation of the current pulse and v is the speed of propagation of the return stroke front

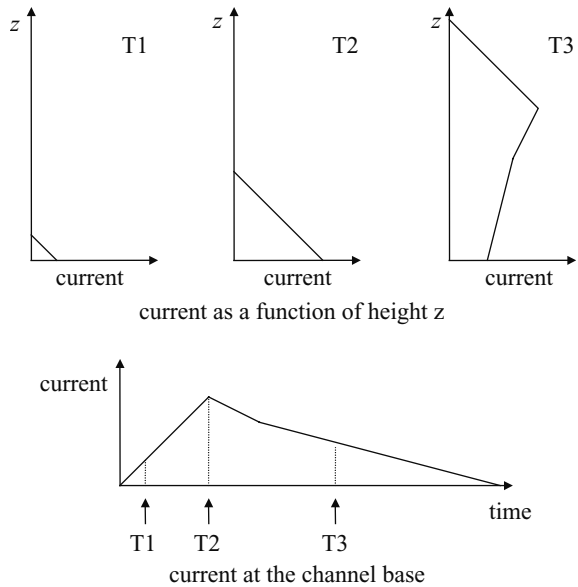

Figure 6.6 A schematic representation of the current distribution obtained with Dennis and Pierce's [31] model for the case $u = v$, where u is the speed of propagation of the current pulse and v is the speed of propagation of the return stroke front

The case $v = u$ is identical to a current pulse propagating along a uniform transmission line (Figure 6.6). The current pulse retains its shape and amplitude as it travels along the channel. Note, however, that under these circumstances, the charge deposited by the return stroke on the leader channel is zero – there is no neutralisation of the leader charge by the return stroke. When $u = \infty$, the current below the return stroke front at any instant remains constant and the Dennis and Pierce model mimics that of Bruce and Golde.

Input parameters: the input parameters of the model are the channel base current, the speed of the return stroke front and the speed of the current pulse.

Predictions of the model: as in the Bruce and Golde model, the sole predictions of the model are the remote electromagnetic fields. The predicted results are in general agreement with the measured fields.

6.4.1.4 Uman and McLain – the transmission line model (TLM)

Uman and McLain [32] assumed that the return stroke can be simulated by a current pulse propagating along a uniform transmission line driven at the grounded end – hence the name transmission line model. In this model, the return stroke current propagates along the leader channel with constant speed v and without any distortion. Actually, the model is identical to the special case of Dennis and Pierce model in

which $u = v$. In the light of this, the current at any height z along the return stroke channel is given by:

$$\begin{aligned} I(z,t) &= I\left(0, t - \frac{z}{v}\right) \qquad t \geq z/v \\ I(z,t) &= 0 \qquad\qquad\qquad\quad t < z/v \end{aligned} \tag{6.16}$$

The first difficulty associated with this model is that its basic hypothesis does not tally with the available experimental observations. For example, the results inferred from optical observations show that the current amplitude and current waveshape do change with height. Moreover, return stroke speed measurements demonstrate that the return stroke speed decreases with increasing height, the change being significant even within the first few hundred metres. The second problem associated with this model is the fact that it does not account for the neutralisation of the leader charge. It is difficult to understand how positive charge rushes towards the cloud without noticing the negative charge residing on the leader channel. Notwithstanding this, as will be shown in a moment, some of the predictions are in good agreement with the corresponding measured values.

Input parameters: the input parameters of the model are the channel base current and the return stroke speed.

Predictions of the model: the model predicts that the distant radiation field $E_r(t)$ is coupled to the return stroke current through the equations:

$$E_r(t, D) = \frac{\mu_0 v}{2\pi D} I\left(0, t - \frac{D}{c}\right) \quad t \leq \frac{H}{v} + \frac{D}{c} \tag{6.17a}$$

$$E_r(t, D) = \frac{\mu_0 v}{2\pi D}\left[I\left(0, t - \frac{D}{c}\right) - I\left(0, t - \frac{H}{c} - \frac{D}{c}\right)\right] \quad t \geq \frac{H}{v} + \frac{D}{c} \tag{6.17b}$$

where D is the distance to the point of observation and H is the channel length. From these equations one can see that the model predicts:

$$E_p = \frac{\mu_0 v}{2\pi D} I_p \tag{6.17c}$$

$$\left(\frac{dE}{dt}\right)_p = \frac{\mu_0 v}{2\pi D}\left(\frac{dI}{dt}\right)_p \tag{6.17d}$$

where E_p, I_p, $(dE/dt)_p$ and $(dI/dt)_p$ are the peak values of the electric field, channel base current, time derivative of the electric field and the time derivative of the current, respectively.

Some of these predictions have been confirmed and others not, by experimental observations. For example:

a The experimental data confirms the relationship given by eqn. 6.17*c* to an accuracy of about 20 per cent [33, 34].

b Equation 6.17*a* predicts that the shape of the radiation field is identical to that of the current waveform. The experimental data shows, however, that the radiation field decays faster than the current after the initial peak. On the other hand the electric field measurements conducted within about 50 m of the triggered lightning flashes show that the electric field derivative and the current derivative have similar shapes [35].

c Note that for a given return stroke speed and distance the constant of proportionality between the variables in eqns 6.17*c* and 6.17*d* is the same. However, observations indicate that the two equations are satisfied by two different constants. For example, for a given distance D, the value of v that satisfies eqns 6.17*c* and 6.17*d* are 1.5–1.7 $\times$ 10^8 m/s and 2.0–3.0 $\times$ 10^8 m/s, respectively [33,35].

d Equation 6.17*b* indicates that the initial radiation waveshape will be repeated in a negative form (a so-called mirror image) starting at $t = H/v + D/c$; the time, as measured by the observer, at which the return stroke front reaches the channel top. This is called a mirror image. This is seldom observed in lightning radiation fields from subsequent return strokes.

The electromagnetic fields at different distances as predicted by the model are shown in Figure 6.7. In the calculation the return stroke speed is assumed to be constant and equal to 1.5 $\times$ 10^8 m/s and the channel length was assumed to be longer than 15 km to avoid sudden termination of the channel during the first 100 μs. Therefore, in the electric fields given in this Figure the mirror image does not appear because the return stroke front takes more than 100 μs to reach the top of the channel. Observe the peculiar behaviour of the electric field at 50 m. It rises to a peak in about a few microseconds and then decays to zero with time. This is in disagreement with measurements which indicate that the field rises to its peak value within a few microseconds and then maintains that field at a more or less constant value with increasing time (see Chapter 4).

6.4.1.5 Nucci *et al.* [36] and Rakov and Dulzon [37] – modified transmission line models (MTL)

These authors modified the transmission line model by allowing the current amplitude to decrease with height while maintaining its original shape; hence the name modified transmission line models (MTLs). The model current at a given height z can be mathematically expressed as:

$$\begin{aligned} I(z,t) &= A(z)I\left(0, t - \frac{z}{v}\right) \qquad t > \frac{z}{v} \\ I(z,t) &= 0 \qquad\qquad\qquad\qquad\quad t < \frac{z}{v} \end{aligned} \tag{6.18}$$

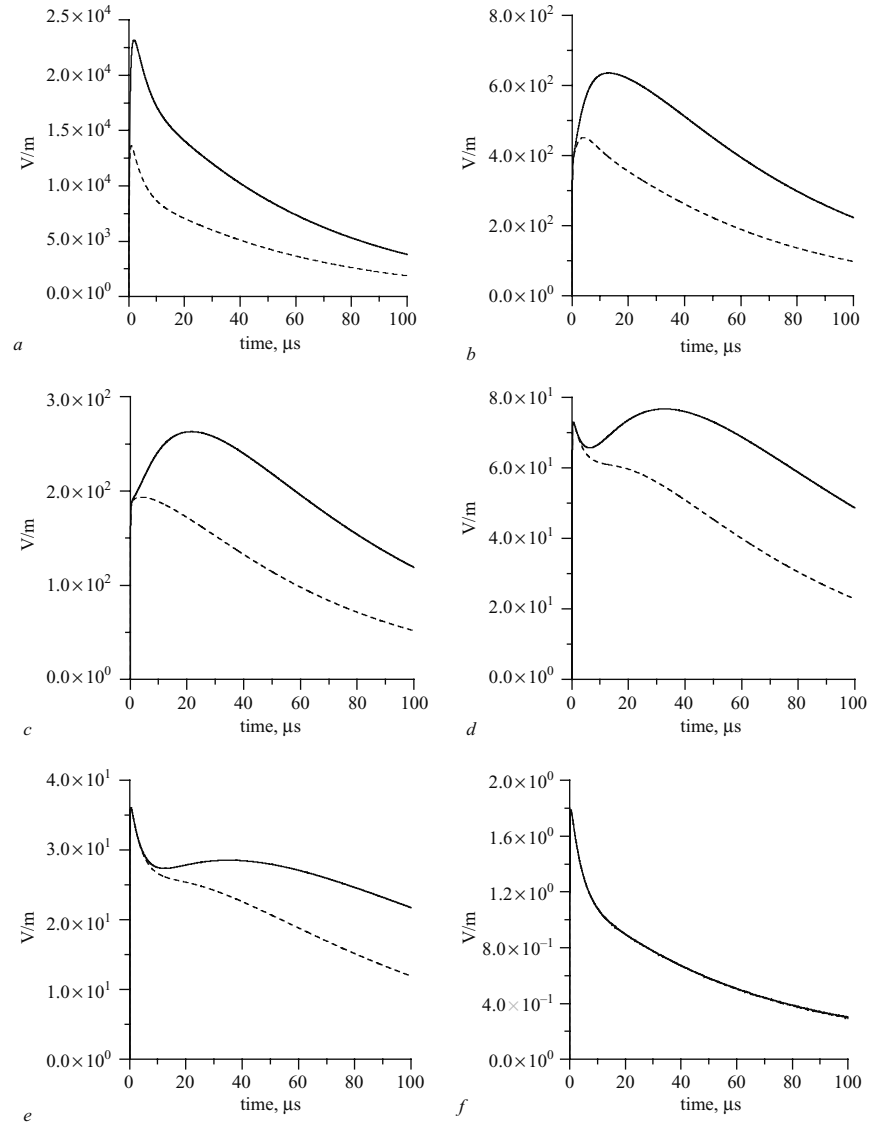

Figure 6.7 *The electromagnetic fields (electric field: solid line, magnetic field × c: dashed line) at different distances as predicted by the transmission line model. The current at the channel base is identical to that in Figure 6.3 and the return stroke speed is equal to 1.5 × 10^8 m/s. Note that c is the speed of light in free space*

a 50 m
b 1 km
c 2 km
d 5 km
e 10 km
f 200 km

where $A(z)$ accounts for the decrease in the current amplitude. The models of Nucci *et al*. [36] and Rakov and Dulzon [37] differ in the assumed form of the attenuation function as follows:

$$\text{Nucci } et\ al.\text{: } A(z) = \exp\left(-\frac{z}{\lambda_c}\right) \qquad \text{where } \lambda_c = 2000\,\text{m} \tag{6.19}$$

$$\text{Rakov and Dulzon: } A(z) = \left(1 - \frac{H}{z}\right) \qquad \text{where } H \text{ is the channel length} \tag{6.20}$$

In the literature the MTL model with exponential current decay is referred to as the MTLE model and the one with linear current decay is referred to as the MTLL model.

These models removed the problem of charge neutralisation from the TLM. The attenuation of the current leads to a deposition of positive charge along the channel (hence charge neutralisation). The charge deposited per unit length ρ as a function of z is given by:

$$\rho(z) = \frac{dA(z)}{dz} \int_0^\infty I(0, t)\, dt \tag{6.21}$$

Input parameters: the input parameters of the models are the channel base current, the return stroke speed, and the function $A(z)$ which describes the way that the current amplitude decreases with height.

Predictions of the model: the first few microseconds of the radiation fields produced by the MTLs are essentially the same as those due to the TLM if the same channel base current and speed are used as the inputs. The reason for this is that the initial portion of the radiation field including the peak is radiated during the first few microseconds of the return stroke when the current pulse is close to ground and therefore cannot have changed much in amplitude. Consequently, the relationships given by eqns 6.17*c* and 6.17*d* are also valid for the modified models and the points *a* and *c*, discussed under the TLM model, are applicable also to these models. (Note that how fast the current amplitude decreases with height depends on the assumed form of $A(z)$. Therefore, the above statements are only correct if $A(z)$ is a slowly varying function of z.)

As mentioned previously, the mirror image effect predicted by the TLM is seldom observed in the measured fields and modified models can account for this fact. When the current is allowed to decay with height so that it has a negligible value when it reaches the end of the channel, the mirror image will no longer be manifested in the calculated fields. Moreover, unlike the TLM fields, the electric radiation fields predicted by the MTL models decay faster than the current after the initial peak.

The electromagnetic fields produced at different distances by these two models are shown in Figures 6.8 and 6.9. In the calculation the return stroke speed is assumed to be constant and equal to 1.5×10^8 m/s. The predicted electromagnetic fields of modified models are in better agreement with the measurements than those of the TLM. Note, however, that the field at 50 m predicted by the MTLE model does not show the saturation which is observed in the close fields measured from triggered

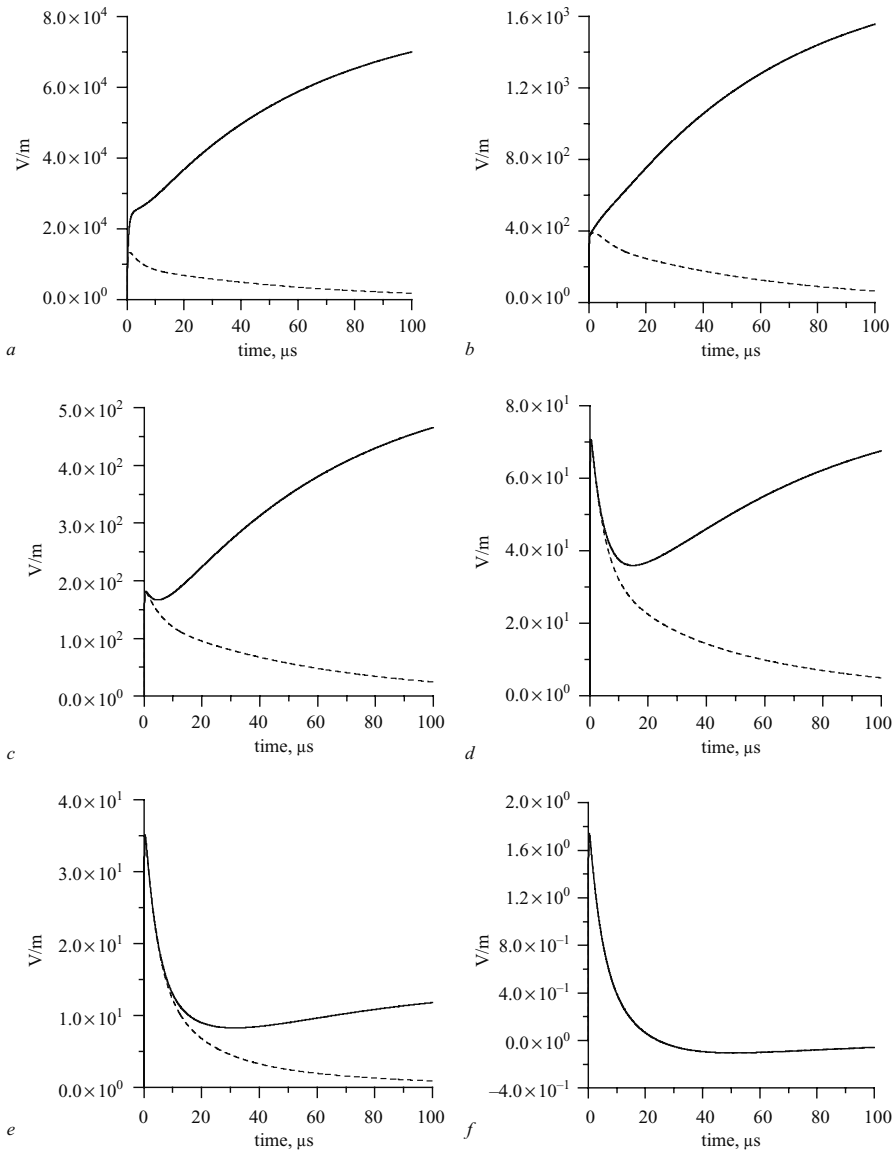

Figure 6.8 *The electromagnetic fields (electric field: solid line, magnetic field × c: dashed line) at different distances as predicted by the MTLE model. The current at the channel base is identical to that in Figure 6.3 and the return stroke speed is equal to 1.5 × 10^8 m/s. Note that c is the speed of light in free space. In the calculation λ = 2 km.*

a 50 m
b 1 km
c 2 km
d 5 km
e 10 km
f 200 km

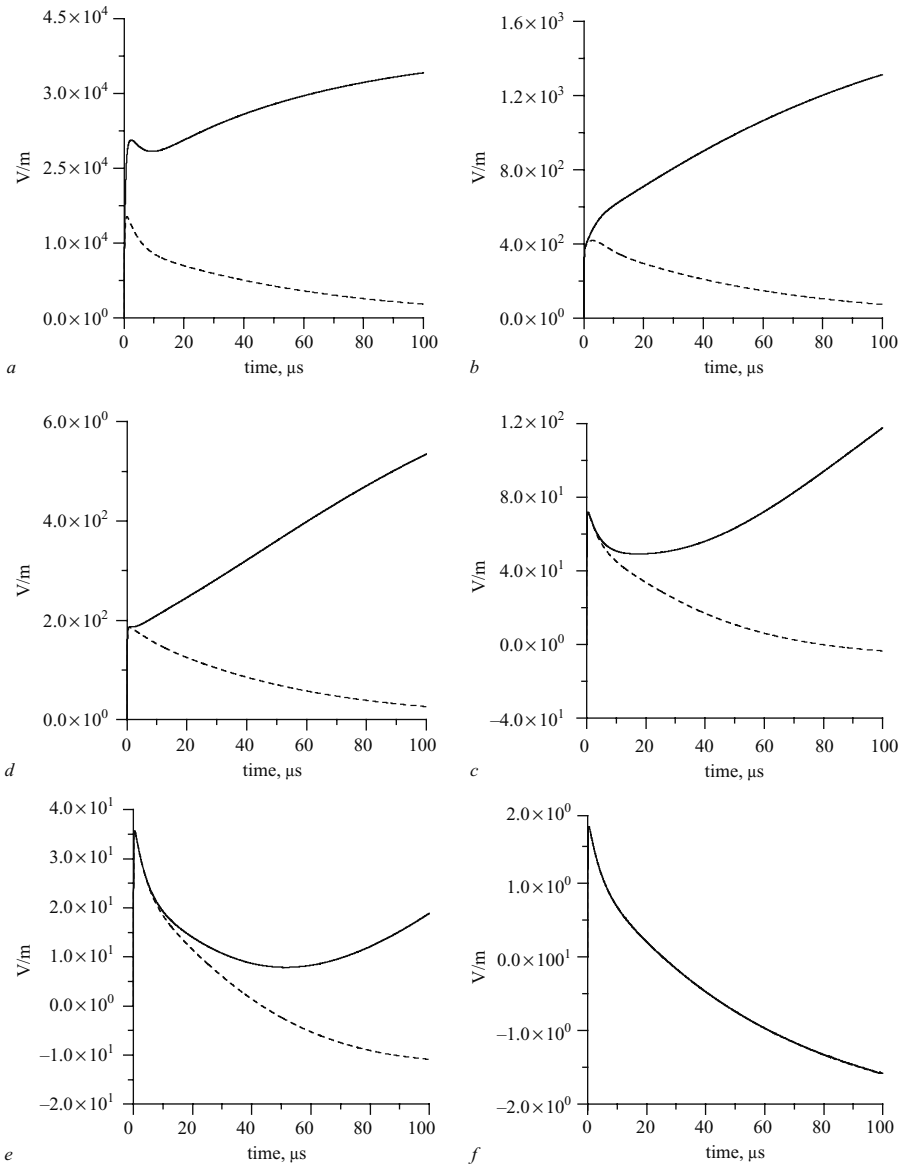

Figure 6.9 *The electromagnetic fields (electric field: solid line, magnetic field × c: dashed line) at different distances as predicted by the MTLL model. The current at the channel base is identical to that in Figure 6.3 and the return stroke speed is equal to 1.5 × 10^8 m/s. Note that c is the speed of light in free space. In the calculations H = 5 km.*

a 50 m
b 1 km
c 2 km
d 5 km
e 10 km
f 200 km

subsequent return strokes (see Chapter 4). In this respect, the MTLL model generates field signatures at 50 m which are better matched to the measured fields than are those from the exponential decay. Authors calculations indicate, however, that the shape of the close field predicted by the MTLMs is sensitive to the duration of the current.

6.4.2 Current generation models (CG models)

6.4.2.1 The relationship between the transmission lines and current generation models

The models described in the previous section envisage the return stroke as a transmission line driven by a current source at one end – the channel base. Such a model is not necessarily the most appropriate one for describing the flow of charge deposited on the leader channel to ground. For example, it is not clear how the base current can be assumed to provide just the right total amount of charge to the channel. This suggests that an important ingredient is lacking in these models, namely the propagation down the channel of currents driven by the initial charge distribution along the channel. On the contrary, in LCR models which treat the return stroke as a discharge of a transmission line, the current is determined completely by the charge stored on the leader channel. The central postulate of the current generation models, which actually account for the downward propagating neutralising currents, is acquired from these LCR models. To illustrate this subject further, consider the principle of operation of a cable generator which is used in high-voltage engineering practice. Consider a transmission line (a cable) of characteristic impedance Z charged to a voltage V_0. At $t = 0$ the line is allowed to discharge through a resistance R which is equal to its characteristic impedance. The conventional explanation of the events taking place after $t = 0$ is the following. When the switch is closed, the line behaves as a generator of e.m.f. V_0 and internal resistance R. This causes a voltage drop across the resistance equal to $V_0/2$, creating a voltage step of magnitude $-V_0/2$ that propagates along the line. At the end of the line (an open end) this wave will be reflected and, after a time $t = 2L/c$, where L is the length of the line and c is the speed of light, the reflected wave reaches the resistor bringing the voltage across it to zero. Accordingly, the voltage measured across the resistor is a step with a peak $V_0/2$ and duration $2L/c$.

The events happening after the closure of the switch can also be portrayed in a different way. At the instant the connection is made between the charged transmission line and the ground, a wavefront propagates along the line releasing the charge bound on it. When this front reaches a given point z on the line, the charge bound at that point is released instantaneously and the resulting current, a Dirac delta function, propagates down the line at the speed of light. Now, let us proceed to describe these events mathematically. Consider an elementary section dz of the line located at height z. The current $dI(t)$ reaching the base of the line due to this element is:

$$dI(t) = I_0 \delta\left(t - \frac{2z}{c}\right) dz \tag{6.22}$$

where I_0 is a constant to be estimated and $\delta(t)$ represents the Dirac delta function. Note that the time $2z/c$ is equal to the time taken by the wavefront to reach the height

z added to the time taken by the current pulse to reach the bottom of the line. The total current $I(t)$ reaching the bottom of the line can be obtained by integrating the above result from $z = 0$ to $z = L$. The outcome of this exercise is:

$$I(t) = I_0 \left[H(t) - H\left(t - \frac{2L}{c}\right) \right] \frac{c}{2} \tag{6.23}$$

where $H(t)$ represents the Heaviside's step function. Since the cable is terminated with its characteristic impedance, this current is absorbed without reflections by the resistor leading to a voltage $V(t)$ across it. This is given by:

$$V(t) = I_0 \left[H(t) - H\left(t - \frac{2L}{c}\right) \right] \frac{cR}{2} \tag{6.24}$$

where R is the characteristic impedance. The charge per unit length ρ originally stored on the line is V_0C, where C is the capacitance per unit length of the line. Thus, I_0 can be calculated from the equation:

$$\rho = \int_0^\infty I_0 \delta(t)\, dt = I_0 \tag{6.25}$$

This shows that $I_0 = V_0C$. Substituting this in eqn. 6.24 and noting that $RC = 1/c$, the voltage across the resistor is given by:

$$V(t) = \frac{V_0}{2} \left[H(t) - H\left(t - \frac{2L}{c}\right) \right] \tag{6.26}$$

which is identical to that deduced from the conventional method. The current generation models use this scenario to describe the development of the return stroke current resulting from the discharge of the corona sheath.

6.4.2.2 Mathematical derivation of return stroke current using the principles of current generation models

Current generation models postulate that as the return stroke front propagates upwards at speed v, the charge stored on the leader channel collapses into the highly conducting return stroke channel. Accordingly, each point on the leader channel can be treated as a current source which is turned on by the arrival of the return stroke front at that point. The corona current injected by these sources into the highly conducting return stroke channel travels to ground at speed u (in the discussion given below it is assumed that $u = c$ the speed of light). One main difference between the various models belonging to the category of current generation models is in the assumed temporal and spatial variation of the corona current.

Consider a leader channel that is assumed to be straight and vertical and is located above a ground plane. The z coordinate is directed along the leader channel and the origin is at ground level. The return stroke front is initiated from ground level at time $t = 0$ and propagates along this channel with a speed that is a function of z, $v(z)$.

The corona current source at a given height is turned on when the return stroke front reaches that height. Once turned on, the corona current source injects a current pulse into the return stroke channel. This current pulse will travel along the return stroke channel to ground with the speed of light. Consider the situation at time t when the return stroke front is at a height Z from ground level. The quantities Z and t are related through the equation:

$$t = \int_0^Z \frac{dz}{v(z)} \tag{6.27}$$

The geometry pertinent to this situation is shown in Figure 6.10. Consider a point along the channel whose coordinate is z where $z < Z$. The problem is to calculate the total current at height z at time t when the return stroke front is at a distance Z from ground level. Consider a channel element $d\lambda$ at a distance λ from ground level where $\lambda > z$. The corona source associated with this channel element is turned on at time $t = t_{on}$ where:

$$t_{on} = \int_0^\lambda \frac{dz}{v(z)} \tag{6.28}$$

Assume that the corona current per unit length generated by this channel element is given by $I_c(\lambda, t)$. This corona current will take a time of $(\lambda - z)/c$ to reach the height z, where again c is the speed of light in a vacuum. Therefore, the current $dI(z, t)$

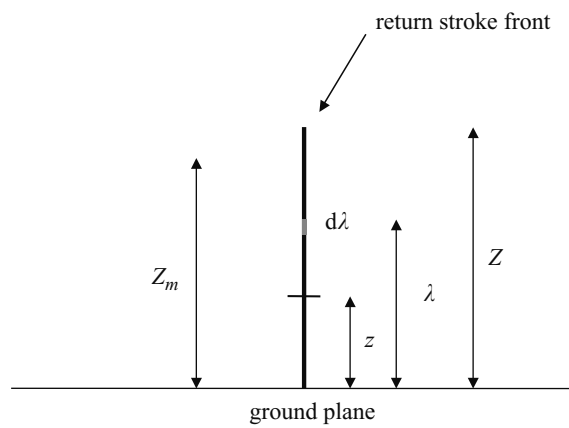

Figure 6.10 Drawing defining the pertinent geometrical factors used in deriving an expression for the return stroke current in current propagation models. Z is the height of the return stroke channel, λ is the height of the elementary channel section $d\lambda$, Z_m is the highest point in the channel that will contribute to the current at height z when the return stroke front is at height Z

at height z and at time t caused by the neutralisation of the channel element $d\lambda$ is given by:

$$dI(z,t) = I_c\left(\lambda, t - t_{on} - \frac{\lambda - z}{c}\right) d\lambda \tag{6.29}$$

Let Z_m be the highest point on the channel that will contribute to the current at height z when the return stroke front is at a distance Z from ground level. One can then write:

$$t = \int_0^{Z_m} \frac{d\varsigma}{v(\varsigma)} + \frac{Z_m - z}{c} \tag{6.30}$$

Consequently, the total current at height z at time t is given by:

$$I(z,t) = \int_z^{Z_m} dI(z,t) = \int_z^{Z_m} I_c\left(\lambda, t - t_{on}\frac{\lambda - z}{c}\right) d\lambda \tag{6.31}$$

Let us solve these equations for the following case. Suppose that the corona current per unit length $I_c(z,t)$ injected into the return stroke channel can be represented mathematically by:

$$I_c(z,t) = I_0(z)[e^{-(t-\xi)/\tau_d} - e^{-(t-\xi)/\tau_r}] \quad t \geq \xi \tag{6.32}$$

where ξ is the time taken by the return stroke front to reach the height z, τ_r is the rise time constant which determines the rise time of the corona current pulse, and τ_d is the discharge time constant which is related to the time taken by the return stroke to neutralise the corona sheath at the given height. In general, both τ_r and τ_d are functions of z. If the corona current at a given height completely removes the charge stored on the leader channel at that height, one may write:

$$\rho(z) = I_0(z)[\tau_d - \tau_r] \tag{6.33}$$

where $\rho(z)$ is the charge per unit length on the leader channel. These equations can be used to evaluate the total current at the channel base (i.e. $z = 0$) with the result:

$$I(0,t) = \int_0^{h_e} \left(\frac{\rho(z)}{\tau_d - \tau_r}\right)\left\{e^{-(t-(z/v_a(z))-(z/c))/\tau_d} - e^{-(t-(z/v_a(z))-(z/c))/\tau_r}\right\} dz \tag{6.34}$$

In this equation $v_a(z)$ is the average return stroke speed over the channel section from ground level to z and h_e is the highest point on the channel that will contribute to the channel base current at time t. These parameters are given by:

$$v_a(z) = \frac{z}{\int_0^z d\varsigma/v(\varsigma)}, \quad t = \int_0^{h_e} \frac{d\varsigma}{v(\varsigma)} + \frac{h_e}{c} \tag{6.35}$$

If the return stroke speed is known, assumed or derived by some other means, the model currents can be completely defined by specifying any two of the following parameters: the channel base current, the mathematical form of the corona current (all models available today consider the nature of this to be either a single or double exponential) and the discharge time constants and the charge distribution along the leader channel.

Having outlined the basic principles of the current propagation models and the mathematical manipulations necessary to evaluate the return stroke current at any point along the channel, let us study the main features of the different models belonging to this category.

6.4.2.3 Wagner

Even though this model is seldom mentioned in the literature, it earns some credit for being the first of its kind. In constructing the model Wagner [38] made three assumptions. First, that the distribution of charge per unit length along the leader channel is given by:

$$\rho(z) = \rho_0 e^{-z/\lambda} \tag{6.36}$$

where λ is a constant. Second, that the temporal variation of the corona current per unit length $I_c(z, t)$ is given by:

$$I_c(z, t) = I_0(z) e^{-t/\tau} \tag{6.37}$$

where τ is a constant. Finally, he assumed that the return stroke speed v is a constant and the speed of propagation of the corona current down the return stroke channel is infinite. With these assumptions and recalling that $I_0(z)\tau = \rho(z)$, the total current at any height z as a function of time can be written as:

$$\begin{aligned} I(z, t) = {} & \frac{\rho_0}{\tau} \frac{1}{\{(1/v\tau) - (1/\lambda)\}} \\ & \times \quad e^{-z/\lambda} \left\{ e^{-v(t-z/v)/\lambda} - e^{-(t-z/v)\tau} \right\} \quad \text{for } t > z/v \end{aligned} \tag{6.38}$$

Note that the current has the form of a double exponential function with the rise time being determined by the duration of the corona current and the decay time by the return stroke speed and how quickly, as a function of z, the charge decreases along the leader channel. A closer examination of the above equation shows that it describes a current pulse propagating along the leader channel with constant speed and with an exponentially decreasing amplitude. In this respect it is similar to the modified transmission line model (see sections 6.4.1.5 and 6.6).

Input parameters: the input parameters are the temporal variation of the corona current, the charge distributed along the leader channel and the return stroke speed.

Predictions of the model: the model predicts the temporal variation of the return stroke current (including the channel base current) as a function of height and the remote electromagnetic fields. It can account for the decrease in current amplitude with height, but it predicts a current rise time that does not vary along the channel. Wagner [38] did not try to use his model to generate remote electromagnetic fields, but simulations carried out by the present author show that their features are not far from the measured ones.

6.4.2.4 Lin *et al.*

The model by Lin *et al.* [39] is a union between current propagation and current generation models. It breaks up the return stroke current into three components:

a A short duration upward propagating current pulse associated with the electrical breakdown at the return stroke front. This travels up the channel with the speed of the front of the return stroke and is treated by the TLM – a current propagation model.
b A uniform current, assumed to be the continuation of the leader current, fed from a cloud charge source at a fixed height.
c A current component generated by the neutralisation of the corona sheath and treated in a manner identical to those in current generation models.

The corona current sources located along the channel are switched on sequentially as the peak of the breakdown current pulse reaches them. The temporal variation of the corona current, $I_c(z, t)$ was assumed to be a double exponential in form and its amplitude was taken to decrease exponentially with height. Master *et al.* [40] modified this model by introducing an attenuation factor to the breakdown current component while keeping all the other features the same.

Input parameters: the input parameters of the model are the return stroke speed and the temporal variation of the corona current. The shape and amplitude of the breakdown current pulse, the magnitude of the uniform current, the duration of the corona current and information concerning its attenuation with height were obtained by comparing the simulations with electromagnetic fields measured at different distances.

Predictions of the model: the main prediction of the model is the temporal and spatial variation of the return stroke current. Although the predicted current at the channel base is in general agreement with the measured currents the model does have a deficiency – it does not predict a change in current rise time with height.

6.4.2.5 Heidler – travelling current source model

In 1985 Heidler [41] proposed a model in which he assumed an instantaneous drain of charge from the corona sheath as the return stroke front surges along the leader channel. Consequently, the corona current $I_c(z, t)$ per unit length at height z was

represented by a Dirac delta function. Thus:

$$I_c(z,t) = I_0(z)\delta\left(t - \frac{z}{v}\right) \quad t > z/v \tag{6.39}$$

where v is the speed, assumed to be independent of z, of the return stroke. Thus, the form of the corona current is identical to that used previously to describe the action of the cable generator. The speed of propagation of the corona currents down the return stroke channel was set equal to c, the speed of light. The total current generated by this model, $I(z,t)$, is given after several mathematical manipulations by:

$$I(z,t) = \frac{I_0((t+z/c)/\{1/v+1/c\})}{(1/v+1/c)} \quad t > z/v \tag{6.40}$$

The current at the channel base (i.e. $z = 0$) is:

$$I(0,t) = \frac{I_0(t/\{1/v+1/c\})}{(1/v+1/c)} \quad t > 0 \tag{6.41}$$

Note also that there is a current discontinuity at the return stroke front (i.e., $I(z,t) \neq 0$ when $t = z/v$) except at $z = 0$. Heidler called his model the travelling current source model (TCS model) although the model does not actually incorporate a current source that travels along the channel.

Input parameters: the input parameters for the model are the channel base current, the return stroke speed, and the temporal variation of the corona current, the form of which was represented by a Dirac delta function. Note that the function $I_0(z)$ in eqn. 6.39 can be obtained easily from eqn. 6.41 if the channel base current is given.

Predictions of the model: the model predicts the signature of remote electromagnetic fields and, for a given channel base current, the temporal and spatial variation of the current as a function of height and the distribution of the charge deposited by the return stroke as a function of height. Let us consider these predictions one by one. In the calculations to be followed the return stroke speed is assumed to be 1.5×10^8 m/s.

The electromagnetic fields produced by the model at different distances are shown in Figure 6.11. The general features of the electromagnetic fields do agree with the measurements. The model-predicted current waveform at different heights is shown in Figure 6.12. Note that there is a current discontinuity at the front except at ground level. It is doubtful whether such current discontinuities exist in natural processes.

The model-predicted distribution of the charge per unit length deposited by the return stroke as a function of height is given by (the time integral of the corona current):

$$\rho(z) = I_0(z) \tag{6.42}$$

Comparison of this equation with eqn. 6.41 shows that the temporal variation of the channel base current has the same mathematical form as that of the spatial variation of the charge density along the channel.

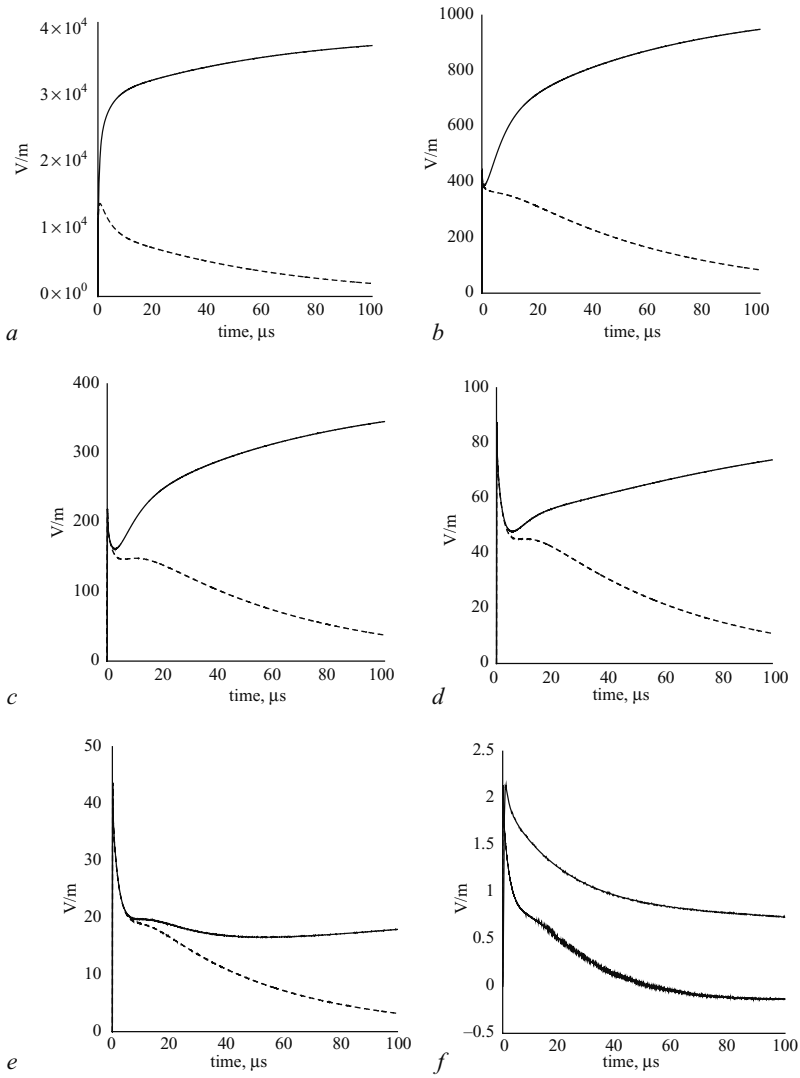

Figure 6.11 *The electromagnetic fields (electric field: solid line, magnetic field × c: dashed line) at different distances as predicted by the TCS model. The current at the channel base is identical to that in Figure 6.3 and the return stroke speed is equal to 1.5 × 10^8 m/s. Note that c is the speed of light in free space. The electric field at 200 km is also shown in a ten times faster time scale*

a 50 m
b 1 km
c 2 km
d 5 km
e 10 km
f 200 km

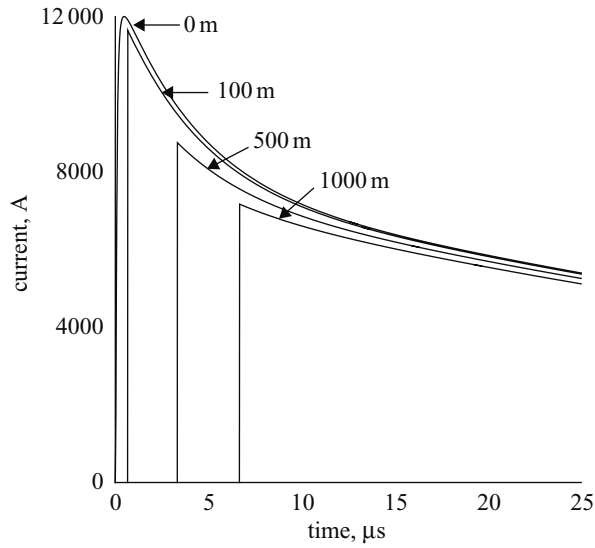

Figure 6.12 *The current waveform as predicted by the TCS model. Note that the current at the channel base (i.e. at ground level) is an input parameter of the model*

a ground level
b 100 m
c 500 m
d 1000 m along the return stroke channel

Thottappillil *et al*. [34] have shown that once the channel base current and the return stroke speed is given this model can predict the peak electric field to a reasonable accuracy.

6.4.2.6 Cooray and collaborators

Cooray introduced the basic concept of a return stroke model in 1989 [42] and subsequently improved upon these ideas to construct models for subsequent return strokes [43]. In these studies he attempted to give a physical meaning to the discharge type models.

He divided the dart leader channel into two coaxial sections, one with a high conductivity and the other with a relatively low one. The highly conducting region is called the hot corona sheath and that with a low conductivity, the cold corona sheath. As the return stroke front reaches a certain height, the charge located on the hot corona sheath is rapidly neutralised giving rise to a fast component to the corona current. The charge on the cold corona sheath is neutralised slowly through the action of positive streamers originating at the hot core of the return stroke channel leading to a slow corona current component. The two corona current components were represented by double exponential functions.

In constructing the model he introduced a novel method to evaluate the return stroke velocity as a function of height along the channel. The method is based on the assumption that the return stroke speed is controlled by the electric field at the tip of the return stroke front (see section 6.5).

In a review article, Rakov and Uman [44] directed several criticisms against this model. Gomes and Cooray [45] pointed out that the criticisms raised by Rakov and Uman were groundless.

Following these initial studies Cooray and collaborators introduced models to represent both first and subsequent return strokes [46–49]. Three models described below are based on these studies. However, some parts of the models may differ from the information given in original publications and they are based on the studies conducted later by the author.

6.4.2.6.1 Subsequent return stroke models # 1

Input parameters of the model

a the channel base current
b the charge per unit length at the ground end of the dart leader which is a function of the peak channel base current
c the potential gradient of the dart leader channel.

Basic concepts and assumptions

Charge distribution along the leader return stroke channel. The charge brought to ground by the return stroke is distributed uniformly along the leader return stroke channel. Thus, the charge brought to ground from a unit channel length at height z by the return stroke, $\rho(z)$, can be described mathematically as:

$$\rho(z) = \rho_0 \tag{6.43a}$$

where ρ_0 is a function of the peak return stroke current at the channel base. Recent research work carried out with triggered lightning flashes shows that the charge per unit length at the ground end of a leader channel which is neutralised by the return stroke increases almost linearly with the peak return stroke current [50]. When interpreted using a uniformly charged leader channel, these results indicate that the value of ρ_0 lies in the range of 7–12 μC/m for each kA of the return stroke peak current at the channel base. In the simulations it is assumed that ρ_0 is 10 μC/m for each kA of the peak current. That is:

$$\rho_0 = 1.0 \times 10^{-5} * I_p \tag{6.43b}$$

where I_p is the peak return stroke current in kA.

Temporal variation of the corona current. The corona current injected into the return stroke channel at each point on the leader channel, $I_c(z, t)$, is represented by:

$$I_c(z, t) = I_0(z)[e^{-t/\tau(z)} - e^{-t/\tau_r}] \tag{6.44}$$

where τ_r is the time constant that determines the rise time of the corona current pulse, and $\tau(z)$, which is a function of height, is the discharge time constant and hence the duration of the corona current. Owing to charge conservation, $\rho(z)$ and $I_c(z,t)$ are related to each other through the equation:

$$\rho(z) = \int_0^\infty I_c(z,t)\,dt \tag{6.45}$$

Performing the integration one finds $I_0(z) = \rho_0/[\tau(z) - \tau_r]$. By substituting this expression into eqn. 6.44, it can be seen that the corona current may be written as:

$$I_c(z,t) = \frac{\rho_0}{[\tau(z) - \tau_r]}[e^{-t/\tau(z)} - e^{-t/\tau_r}] \tag{6.46}$$

Since the neutralisation process is assumed to be caused by the penetration of streamer discharges into the corona sheath, the value of τ_r is fixed at 10^{-8} s, a value approximately equal to the rise time of the streamer discharges (see Chapter 3). The next problem is to find the function $\tau(z)$. Assume that the return stroke speed is a function of height and is given by $v(z)$. Then the average speed $v_a(z)$ of the return stroke over the channel section from ground level to z is given by:

$$v_a(z) = \frac{z}{\int_0^z dz/v(z)} \tag{6.47}$$

The current at ground level, $I_b(t)$, is given by (from eqn. 6.34):

$$I_b(t) = \int_0^{h_e} \left(\frac{\rho_0}{\tau(z) - \tau_r}\right)\left[\exp\left[-\left(t - \frac{z}{v_a(z)} - \frac{z}{c}\right)\right]\Big/\tau(z) - \exp\left[-\left(t - \frac{z}{v_a(z)} - \frac{z}{c}\right)\right]\Big/\tau_r\right]dz \tag{6.48}$$

where h_e can be extracted by the solution of the equation:

$$t - \frac{h_e}{v_a(h_e)} - \frac{h_e}{c} = 0 \tag{6.49}$$

If one divides the channel into a large number of segments of equal length dz, the above integral can be written as a summation as follows:

$$I_b(t_m) = \sum_{n=1}^{m} \frac{\rho_0}{\tau_n - \tau_r} \exp\left[-\left(t_m - \frac{(n-1)dz}{v_{an}} - \frac{(n-1)dz}{c}\right)\right]\Big/\tau_n - \sum_{n=1}^{m} \frac{\rho_0}{\tau_n - \tau_r} \exp\left[-\left(t_m - \frac{(n-1)dz}{v_{an}} - \frac{(n-1)dz}{c}\right)\right]\Big/\tau_r \tag{6.50}$$

where τ_n is the discharge time constant of the corona current for the nth section and v_{an} is the average return stroke speed over the channel section connecting the ground

and the nth element. In this equation t_m is the time taken for the corona current released from the mth segment to reach the ground. This is given by the equation

$$t_m = \left[\frac{m - 1/2}{v_{am}} + \frac{m - 1/2}{c}\right] dz \tag{6.51}$$

If the return stroke speed and the current at the channel base is known, then a progressive estimation can be made of the discharge time constant at different heights by starting at $n = 1$ and making successive integer steps. For example when $n = 1$ the only unknown is the τ_1. Once this has been found the value of τ_2 can be obtained by considering the situation for $n = 2$. In this way the values of discharge time constants up to the mth element can be obtained sequentially.

Return stroke speed. A procedure to evaluate the return stroke speed as a function of the return stroke current parameters is described in section 6.5. In the procedure outlined there it is assumed that the field at the tip of the return stroke is equal to the potential gradient of the leader channel. This provided an additional equation through which the variation of the return stroke speed could be obtained as a function of height. In the model under consideration the channel base current and the charge distribution along the leader return stroke channel are known but since $v(z)$ is unknown, $\tau(z)$ is undetermined. Fortunately, $\tau(z)$ and $v(z)$ are not independent parameters. Once the channel base current and the charge distribution have been specified, for a given $v(z)$ there is a unique $\tau(z)$ that gives the appropriate channel base current. In the model, the magnitude of the electric field at the front introduces an additional constraint which can be satisfied by one set of speed and discharge time constant profiles. This unique set can be extracted through an iterative procedure as follows. First an arbitrary speed profile is assumed along the channel (usually a constant speed) and this is used to estimate the discharge time constants using eqn. 6.50. The resultant discharge time constants are used to estimate the return stroke speed assuming that the field at the front of the return stroke is equal to the leader potential gradient. The mathematical details of how to estimate the speed are given in section 6.5. The new speed profile is then used to estimate the discharge time constants whereupon the procedure is repeated until a speed and a profile for the discharge time constant are found that are mutually consistent. Once the speed and the discharge time constants are known as a function of height, the temporal variation of the current along the channel and hence the electromagnetic fields generated by the return stroke can be evaluated.

In order to estimate the return stroke speed it is necessary to know the potential gradient of the dart leader channel. In the calculations it is assumed that the dart leader can be represented by an transient arc and its potential gradient lies in the range of 2–10 kV/m.

Predictions of the model

The model predicts the variation of the return stroke speed as a function of height, the temporal variation of the current as a function of height, the remote electromagnetic fields and, since the return stroke speed is not an assumed parameter, it also predicts that there is a linear correlation between the peak electric radiation field and the

peak current and between the peak radiation field derivative and the peak current derivative. Now, let us take these predictions one by one and compare them with the available experimental data. In any such comparison it is necessary to remember that the experimental data is based on the average values obtained from a large number of return strokes. Thus, before the model predictions can be compared with the experimental data it is necessary to perform a Monte Carlo simulation and obtain the distributions of the predicted parameters. The procedure for making the Monte Carlo simulation is as follows:

(i) The peak return stroke current is assumed to follow a log normal distribution with the mean and logarithmic standard deviation being 12.3 kA and 0.484, respectively [51].
(ii) For a given peak current, I_p (in kA), the peak current derivative, $(di/dt)_p$ (in kA/μs), is given by $(di/dt)_p = A + 4.6I_p$ where the value of A varies between 81.8 and 24.2 kA/μs with a mean value of 48 kA/μs. This result is based on the data published by Lateinturier *et al.* [52].
(iii) For a given peak current, I_p (in kA), the charge per unit length on the lower tip of the dart leader (in C/m), is assumed to be $\rho_0 = B * I_p$ where $B = 10^{-5}$ C/m.
(iv) The potential gradient of the dart leader channel is assumed to vary uniformly between 2 and 10 kV/m.
(v) On the basis of the measurements of Fisher *et al.* [53], the half peak width of the current is assumed to be independent of the maximum current and to have a mean value of 20 μs with upper and lower limits at 40 μs and 5 μs, respectively.

In the Monte Carlo simulation the peak current was selected from the observed distribution and the other parameters have been chosen by assuming that their values varied uniformly between the lower and upper limits. The mathematical form of the current waveform used in the calculation is identical to that given by eqn. 6.10.

Whenever model simulations are presented for a given return stroke peak current the average model parameters are used. These are, $(di/dt)_p = 48.0 + 4.6I_p$ (in kA/μs), $\rho_0 = 10^{-5} * I_p$ (in C/m), current half peak width of 20 μs and 6 kV/m for the potential gradient of the dart leader channel.

Variation of return stroke speed along the channel. Figure 6.13 illustrates how the return stroke speed profile varies from one peak current to another. Note that in general the return stroke speed rises to a value of about 2.0–2.5 $\times$ 10^8 m/s within a few tens of metres then it starts to decay and in fact there is a significant decrease in the speed of the return stroke over the first few hundred metres. The simulations also show that for a given peak current the return stroke speed decreases with an increasing rise time of the current and with an increasing potential gradient of the dart leader channel. Since the potential gradient decreases with increasing conductivity, the results show that the return stroke speed will increase as the leader channel conductivity increases. Experimental data is not available at present to test these model predictions. (An empirical expression that can be used to get the velocity profile along the channel as predicted by this model is given in section 6.9.)

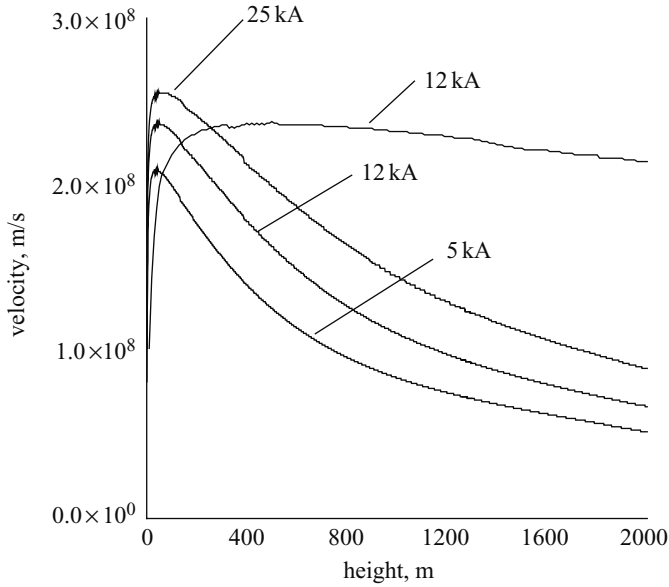

Figure 6.13 Return stroke speed as a function of height for 5 kA, 12 kA and 25 kA channel base currents as predicted by the subsequent return stroke model # 1 of Cooray. The profile corresponding to 12 kA is also shown on a 10 times smaller height scale

In order to obtain the model-predicted distributions of the return stroke speed over different channel lengths, a Monte Carlo simulation based on about 1000 return strokes was conducted. Figure 6.14 shows the results of this simulation. The average speed over the first 300 metres simulated by the model was 2.1×10^8 m/s with a standard deviation of 1.0×10^8 m/s. The maximum and the minimum velocities were 2.6×10^8 m/s and 1.5×10^8 m/s. In the measured distribution the average was 1.9×10^8 m/s, the standard deviation was 7.0×10^7 m/s and the maximum and minimum values were 3.0×10^8 m/s and 1.0×10^8 m/s, respectively [54]. The average speed simulated over the first 1000 metres is 1.5×10^8 m/s with a standard deviation of 0.3×10^8 m/s. The maximum and the minimum velocities were 2.4×10^8 m/s and 0.4×10^8 m/s. In the measured distribution the average was 1.3×10^8 m/s, the standard deviation was 0.5×10^8 m/s and the maximum and minimum values were 2.6×10^8 m/s and 0.3×10^8 m/s, respectively [54]. Thus, there is a reasonable agreement between the model predictions and the experimental observations.

Duration of the corona current and the current signature at different heights. The duration of the corona current is determined by the discharge time constant τ_d; the larger the discharge time constant, the longer the duration of the corona current. The discharge time constant $\tau_{(z)}$ is shown as a function of height for three different peak currents in Figure 6.15.

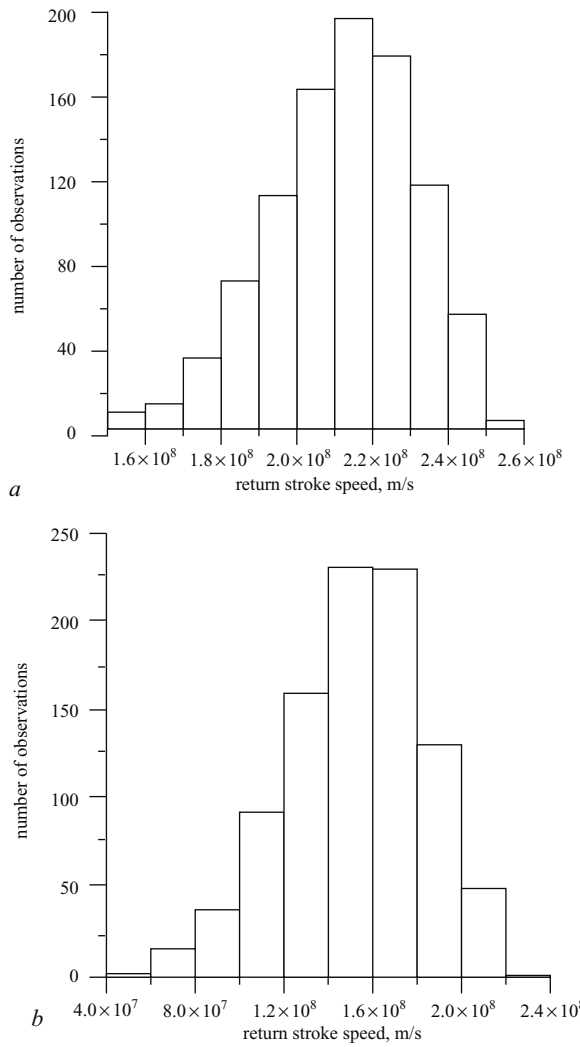

Figure 6.14 *The distribution of the return stroke speed as predicted by the subsequent return stroke #1 model of Cooray. The results obtained from a Monte Carlo simulation based on 952 return strokes. The mean and the standard deviation is also given for each histogram*

a over first 300 m; mean $= 2.1 \times 10^8$ m/s; sd $= 1.0 \times 10^7$ m/s
b over first 1000 m; mean $= 1.5 \times 10^8$ m/s; sd $= 3.1 \times 10^7$ m/s

At points located close to the ground end of the channel the discharge time constant is much faster and, therefore, the corona current is of short duration. This in turn indicates a rapid neutralisation of the charge located at the ground end of the leader

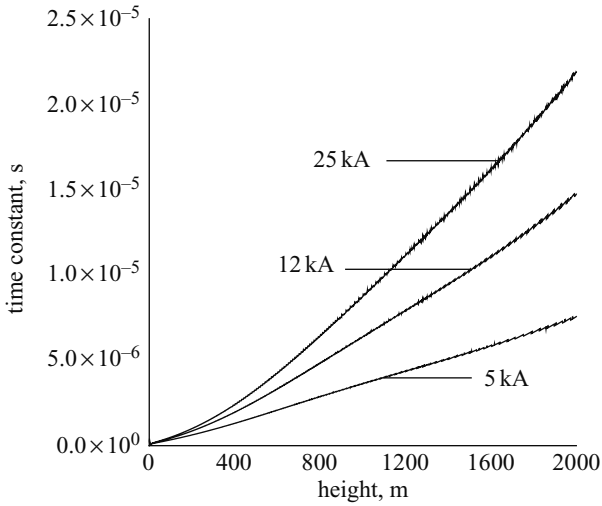

Figure 6.15 The discharge time constant, $\tau_{(z)}$, of the subsequent return stroke model # 1 of Cooray as a function height. Results are given for three channel base peak currents

channel. The model predicts an increase in the discharge time constant with height. This increase can be associated with the ageing of the corona sheath. Note that the discharge time constant at a given height decreases with decreasing current amplitude. This is also physically reasonable because a current waveform with a smaller amplitude is associated with a lower charge per unit length along the leader return stroke channel. The radius of the corona sheath decreases with decreasing charge making the neutralisation process quicker. Indeed, this result is unique to the model presented here. For example, if one assumes the return stroke speed to be the same for different peak currents, the discharge time constants would not change from one peak current to another. Unfortunately, no experimental data exists as yet against which to check this prediction.

Figure 6.16 depicts the return stroke current at four different heights along the channel. Note that with increasing height the peak of the current decreases and its rise time increases.

Electromagnetic fields generated by the return strokes. When comparing the model-generated electromagnetic fields with the values obtained from experiments, there are several points that one should take into account. First, one has to consider the general features of the electromagnetic fields close to and far from the lightning strike and check whether they correspond to those of the measurements. This is often the only test of the suitability of a model. However another test is to see whether the model-generated distributions of the electromagnetic fields agree with the measured distributions. A third control is to check whether the model can predict any relationship between the current and electromagnetic fields and then to compare the relationships derived with the measured ones.

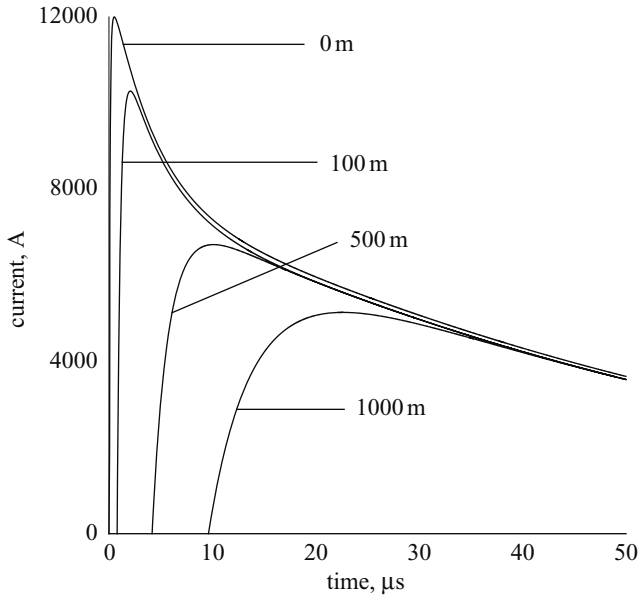

Figure 6.16 *Return stroke current at different heights along the channel as predicted by the subsequent return stroke model # 1 of Cooray. Note that the channel base current (i.e. $z = 0$) is an input parameter of the model*

The model-simulated electric and magnetic fields are shown in Figure 6.17 for distances of 50 m, 1, 2, 5, 10 and 200 km. In the simulation the peak channel base current was 12 kA.

The simulated signatures are similar to those measured from triggered and natural subsequent strokes ([50,53,55,56] see also Chapter 4). For example, note that at 50 m the electric field rises almost to its peak value in just a few microseconds. This is a common feature observed in the electric fields within about 50 m of the triggered subsequent return strokes. At these distances the signature of the magnetic field bears a resemblance to the channel base current. At around 1 km the peak of the radiation field separates out from the rest of the electric field and there is a pronounced hump in the magnetic field. At 200 km both the magnetic and electric fields are pure radiation and they rise to their initial peak in about 0.3–0.5 μs. After this peak the field decays monotonically reaching the zero line in about 40 μs, which is also a common feature in the fields measured from natural subsequent return strokes.

Let us consider the distributions of the peak electric field, the peak electric field derivative and the FWHM of the electric field derivative as predicted by the model and compare them with the experimental observations. These distributions are shown in Figure 6.18 for a point 100 km away from a lightning strike after travelling over perfectly conducting ground. The mean value of the peak in the electric field was 4.3 V/m and the maximum and minimum values are 1 and 14 V/m. These values are in agreement with the measured distributions. For example, the mean and the maximum

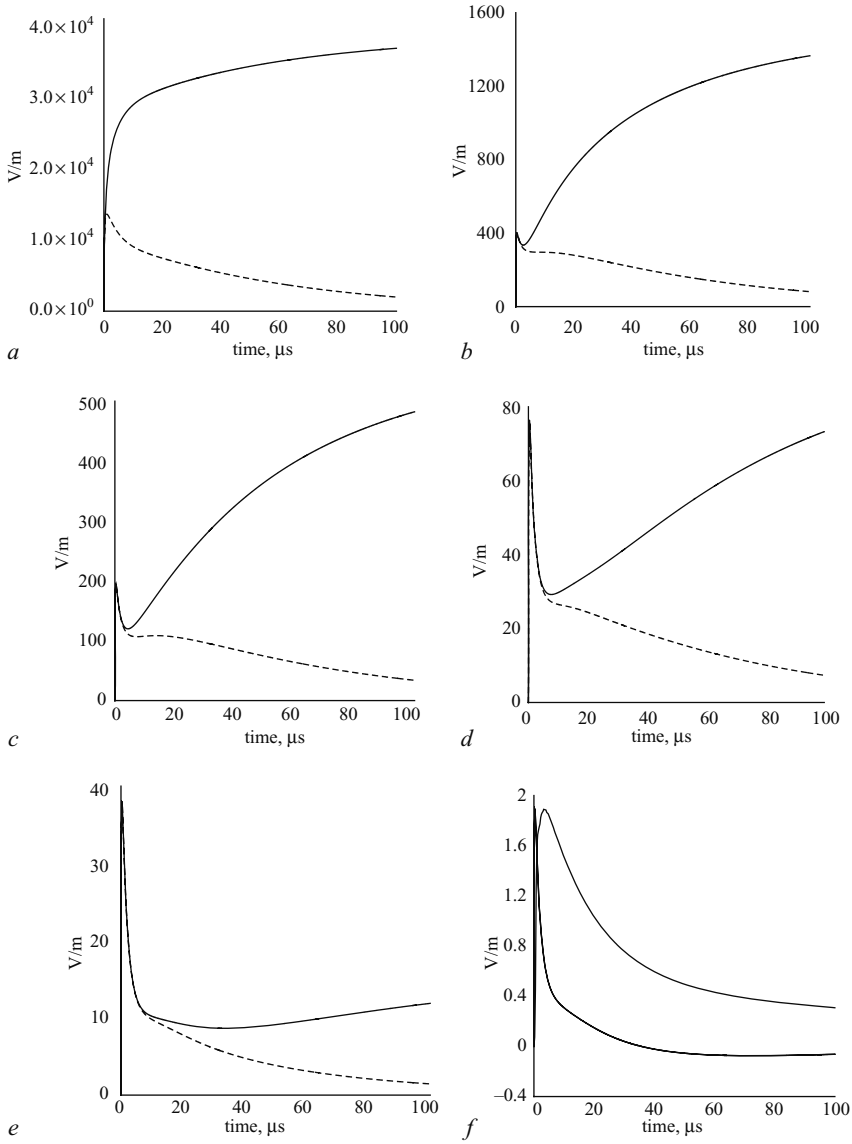

Figure 6.17 *The electromagnetic fields (electric field: solid line, magnetic field × c: dashed line) at different distances as predicted by the subsequent stroke model # 1 of Cooray. The current at the channel base is identical to that in Figure 6.3. Note that c is the speed of light in free space; the electric field at 200 km is also shown in a ten times faster time scale*

a 50 m
b 1 km
c 2 km
d 5 km
e 10 km
f 200 km

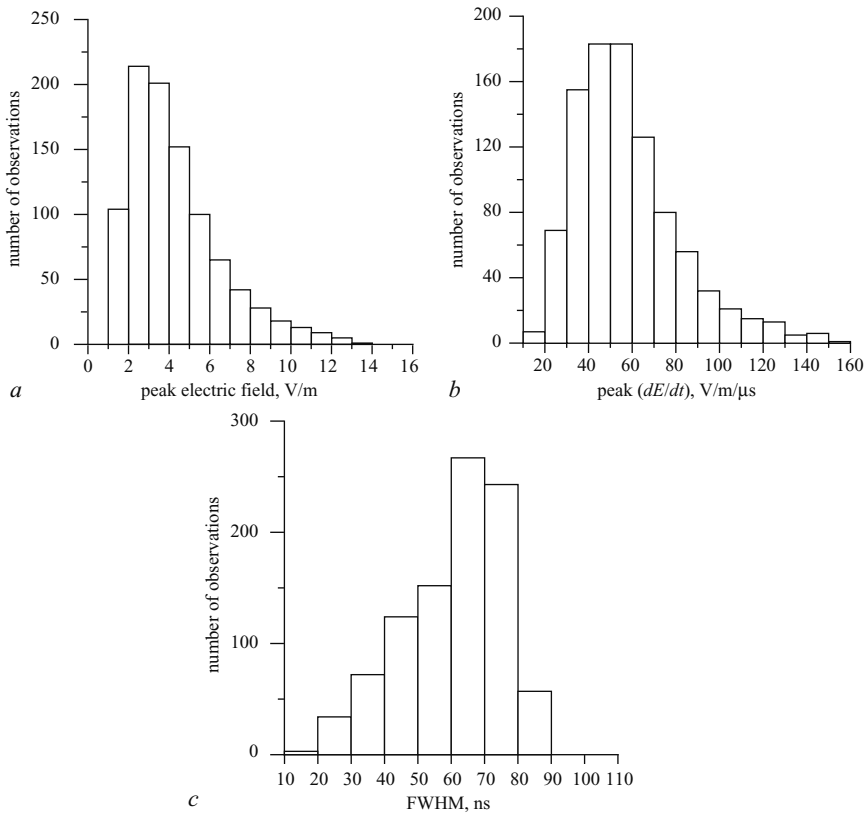

Figure 6.18 *Distribution as predicted by the subsequent return stroke model # 1 of Cooray. The results are obtained from a Monte Carlo simulation based on 952 return strokes*

- *a* peak electric field at 100 km; mean = 4.3 V/m, sd = 2.2 V/m
- *b* peak electric field derivative at 100 km; mean = 57 V/m/μs, sd = 24 V/m/μs
- *c* FWHM of the electric field derivative; mean 56 ns, sd = 15 ns

value of the electric field distribution published by Rakov and Uman [57] are 4.2 and 14 V/m, respectively. Consider the distributions of the model-simulated peak electric field derivative. The mean, minimum and the maximum values of the distribution are 57, 10 and 150 V/m/μs. The corresponding parameters for the distribution of the FWHM are 56, 10 and 90 ns. It is important to point out that the experimental data shows that the signatures of electric field derivatives are similar in both first and subsequent strokes. Thus the distribution of the parameters of the derivative of the electric field could also be used in the comparison. The experimental data on these distributions was obtained and published by Willett and Krider [58] and Willett *et al.* [59]. It is important to point out, however, that in the measurements the electric fields have propagated 20 km over a rough ocean surface followed by about 50 m over land.

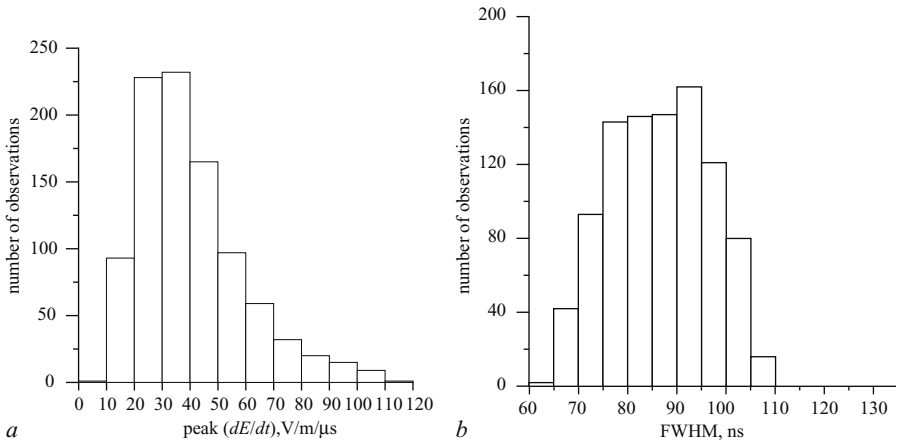

Figure 6.19 *Distributions as predicted by the subsequent return stroke model # 1 of Cooray. The results are obtained after propagating undistorted electric fields 20 km over a rough sea surface (wind speed 20 m/s, conductivity 4 S/m) followed by a 50 m strip of land of conductivity 0.01 S/m. The results are obtained from a Monte Carlo simulation based on 952 return strokes*

a peak electric field derivative at 100 km; mean = 40.3 V/m/μs; sd = 18.9 V/m/μs

b FWHM of the electric field derivative; mean = 84 ns; sd = 10 ns

Thus, it is necessary to subject the model-generated fields to such a path before one can make a fair comparison. The distributions obtained after this exercise are shown in Figure 6.19. The mean values of the peak electric field derivative and the FWHM are 40 V/m/μs and 84 ns, respectively. These values agree fairly well the measured values of 37.5 V/m/μs (for 194 strokes) and 85 ns (for 192 strokes). In Chapter 7 the results obtained from the actual field derivatives and the model simulated ones are compared and it is also shown that the model-simulated waveforms agree with the measurements to such an extent that the model is evidently suitable for obtaining distributions of different parameters over finitely conducting ground.

Finally, let us consider the predictions the model makes about the relationship between various parameters. The model-predicted relationship between the peak electric field and the peak current is shown in Figure 6.20. The relationship between the two parameters can be represented by:

$$E_p = V_{tlm1} \frac{\mu_0 I_p}{2\pi D} \tag{6.52}$$

where I_p is the peak return stroke current and E_p is the peak electric field at distance D. The value of V_{tlm1} is 1.6×10^8 m/s. This prediction made by the model agrees with the experimental observations of Willett *et al.* [33]. The relationship between the

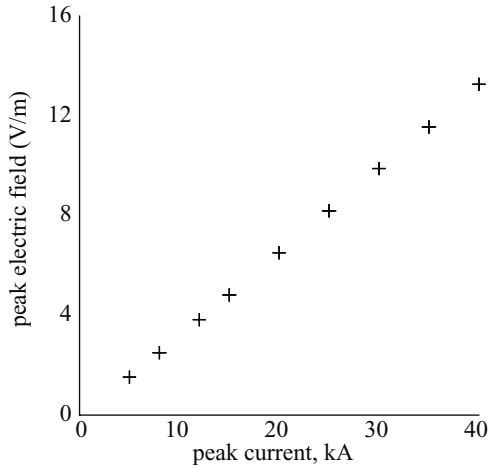

Figure 6.20 The relationship between the peak electric field (normalised to 100 km) and the peak return stroke current as predicted by the subsequent return stroke model # 1 of Cooray. The equivalent TLM speed corresponding to the shown relationship is 1.6 × 10^8 m/s

peak current derivative and the peak electric field derivative is shown in Figure 6.21. It can be described mathematically as:

$$\frac{dE_p}{dt} = V_{tlm2}\frac{\mu_0}{2\pi D}\frac{dI_p}{dt} \tag{6.53}$$

where dI_p/dt is the peak current derivative, and dE_p/dt is the peak electric field derivative at distance D. The value of $V_{tlm2} = 2.8 \times 10^8$ m/s. In the experimental data Willet *et al*. [33] found a similar relationship but the value of V_{tlm2} required to fit the data was 2.0×10^8 m/s. This difference is probably attributable to propagation effects. In the experiment the path of the propagation was mostly (about 1.3–1.4 km) over brackish water with the exception of the last 100–200 m section which was over land. In order to see whether the propagation could explain the discrepancy the model-simulated waveforms were propagated over a path similar to that of the experiment by assuming the conductivity of the land section to be 0.01 S/m. The results obtained are shown in Figure 6.22. Note that, as indicated in the Figure caption, as the length of the strip of land increases the value of V_{tlm2} decreases until at 200 m it agrees with the experimental value.

Figure 6.23 illustrates the relationship between the peaks of the derivatives of electric field and the current at 100, 30 and 15 m. The values of V_{tlm2} corresponding to these three distances are 2.9×10^8, 3.05×10^8 and 3.1×10^8 m/s, respectively. These predictions agree with the results published by Uman *et al*. [35,60]. Note that if the electric field derivative is pure radiation and varies inversely with distance, then the value of V_{tlm2} should be independent of distance. The reasons for the observed

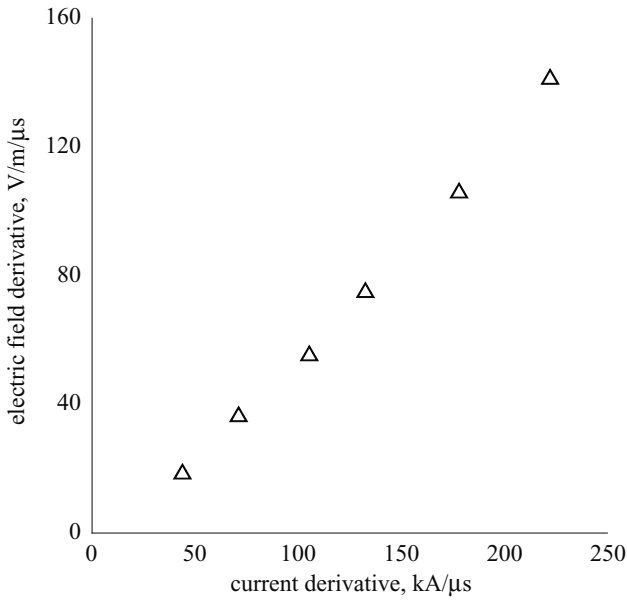

Figure 6.21 *The relationship between the peak electric field derivative (normalised to 100 km) and the peak return stroke current derivative as predicted by the subsequent return stroke model # 1 of Cooray. The equivalent TLM speed corresponding to the shown relationship is* $2.8 \times 10^8\ m/s$

variation in V_{tlm2} with distance are the following. The first reason is that the peak of the electric field derivative is not pure radiation at these small distances. The second reason is that the peak radiation field does not vary with $1/D$ very close to the channel. For example, the way in which the various contributions to the peak of the radiation field derivative vary with distance for a 12 kA current are shown in Figure 6.24. Note that at 100 m nearly 100 per cent of the peak electric field derivative is attributable to radiation whereas at 30 and 15 m this fraction reduces to 80 and 65 per cent, respectively. Observe also that the radiation field does not increase by a factor of two when moving from 30 to 15 m. This is the reason why the value of V_{tlm2} (also shown as a function of distance in the Figure) does not increase very much when moving from 100 to 15 m even though the contribution of the radiation field to the peak electric field derivative decreases from 100 to about 65 per cent. Indeed, the static and induction field contributions counterbalance the departure of the radiation field from an inverse dependence with distance, making the total peak vary roughly like $1/D$.

The model simulations also show that the signature of the electric field derivative within a few tens of metres from the lightning channel is similar to that of the return stroke current derivative. This point is illustrated in Figure 6.25 in which both the current derivative and the electric field derivative at 100 and 15 m are shown in an

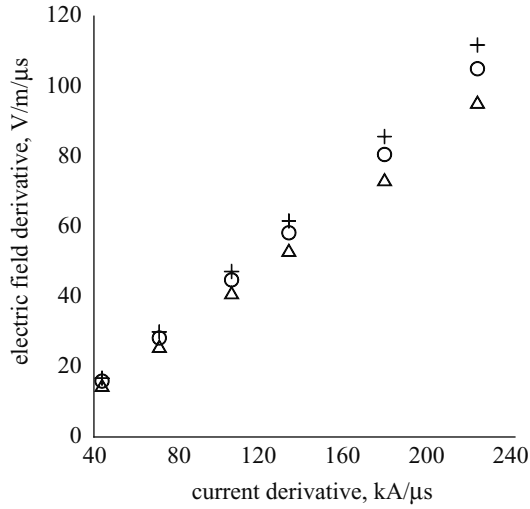

Figure 6.22 The relationship between the peak electric field derivative (normalised to 100 km) and the peak return stroke current derivative as predicted by the subsequent return stroke model # 1 of Cooray. The results are obtained after propagating undistorted electric fields 5.1 km over brackish water (conductivity 4 S/m) followed by a strip of land of conductivity 0.01 S/m. Length of the strip of land: crosses – 50 m, circles – 100 m, triangles – 200 m. The equivalent TLM speeds corresponding to the relationships are: crosses – 2.4×10^8 m/s, circles – 2.25×10^8 m/s, triangles – 2.05×10^8 m/s

amplitude scale normalised to unity. The similarity of these two quantities within a few tens of metres from triggered subsequent return strokes were demonstrated by Uman *et al*. [35].

6.4.2.6.2 Subsequent return stroke model # 2 [76]

This model, which is a CG model, can be treated as a modification of the TLM. This statement one can understand when one reads through the section dealing with the CG and CP models (section 6.6). The model generates results identical to those of the TL model at short times but does not have the disadvantages inherent in the TL model at longer times. Moreover, unlike the TLM model, the present model takes into account the neutralisation of the leader channel.

Input parameters of the model

a channel base current
b return stroke velocity.

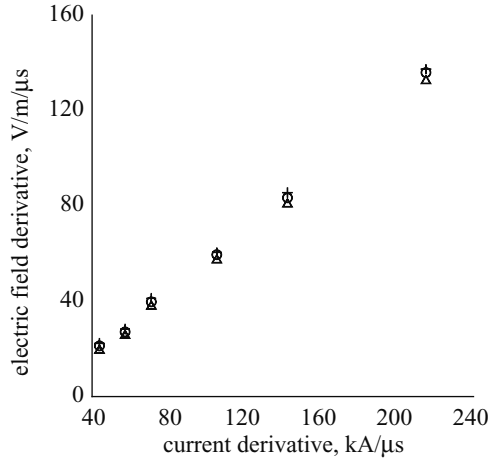

Figure 6.23 *The peak electric field derivative, normalised to 100 km assuming inverse distance dependence, at 100 m (triangles), 30 m (circles) and at 15 m (crosses) as predicted by the subsequent return stroke model #1 of Cooray. The equivalent TLM speed corresponding to the data points at different distances are: 2.9 × 10^8 m/s at 100 m; 3.05 × 10^8 m/s at 30 m; 3.1 × 10^8 m/s at 15 m*

Assumptions of the model

The corona current per unit length at height z, $I_c(z, t)$, is given by:

$$I_c(z,t) = k(z)\left(\frac{1}{v(z)} + \frac{1}{c}\right)\frac{\partial I(0, t - z/v_{av}(z))}{\partial t} \quad \text{for } 0 \le t - z/v_{av}(z) \le t_{ris} \tag{6.54}$$

$$I_c(z,t) = 0 \quad \text{for } t - z/v_{av}(z) > t_{ris} \tag{6.55}$$

where z is directed along the channel with the origin at ground level, $v(z)$ is the return stroke velocity, $v_{av}(z) = z/\int_0^z [1/v(\varsigma)]\, d\varsigma$, $I(0, t)$ is the current at the channel base, c is the speed of light in free space, t_{ris} is the rise time (0–100%) of the current and $k(z)$ is a function to be evaluated.

Evaluation of the function $k(z)$: One can make use of the fact that the channel base current, $I(0, t)$ is composed of the sum of corona currents generated by the elementary channel segments distributed uniformly along the channel to evaluate the function $k(z)$. Consider the infinitesimal time interval from 0 to t_0. The value of the channel base current at time t_0 is given by:

$$I(0, t_0) = k(z_1)F(z_1, t_0)\Delta z_1 \tag{6.56}$$

where $F(z, t) = I_c(z, t)/k(z)$, $\Delta z_1 = t_0/[1/v(0)+1/c]$ and $z_1 = t_0/[1/v(0)+1/c]$. Note that z_1 is the maximum channel height that contributes to the total current at the

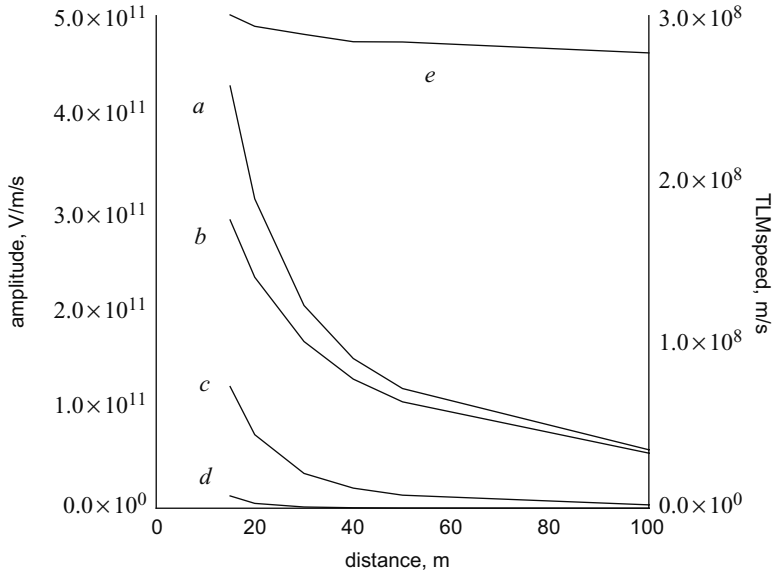

Figure 6.24 *The way in which the contribution of the radiation field (curve b), induction field (curve c) and static field (curve d) to the peak of the electric field derivative (curve a) vary with distance for a 12 kA current. The equivalent TLM speed (based on the ratio of the peak field derivative to the peak current derivative) as a function of distance is also shown in the diagram (curve e)*

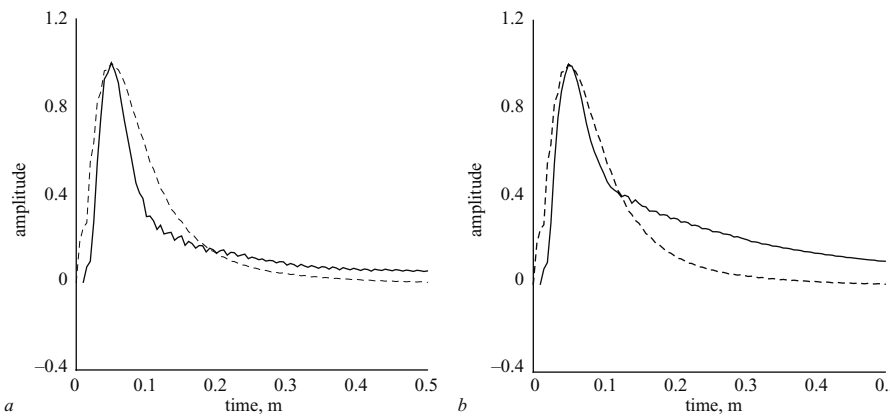

Figure 6.25 *Comparison of the signature of the electric field derivative (solid line) and the current derivative (dashed line) at (a) 100 m and (b) 15 m from the lightning channel carrying 12 kA current as predicted by the subsequent return stroke model # 1 of Cooray. The curves are normalised to unit amplitude and shifted in such a way so that the peaks coincide*

channel base at time t_0. From this equation one obtains:

$$k(z_1) = I(0, t_0)/F(z_1, t_0)\Delta z_1 \tag{6.57}$$

Similarly at time $2t_0$ the value of the channel base current is given by:

$$I(0, 2t_0) = k(z_1)F(z_1, 2t_0)\Delta z_1 + k(z_2)F(z_2, t_0)\Delta z_2 \tag{6.58}$$

where $\Delta z_2 = t_0/[1/v(z_1) + 1/c]$ and $z_2 = z_1 + \Delta z_2$. Note again that z_2 is the maximum channel height that contributes to the total current at the channel base at time $2t_0$. This equation gives:

$$k(z_2) = [I(0, 2t_0) - k(z_1)F(z_1, 2t_0)\Delta z_1]/F(z_2, t_0)\Delta z_2 \tag{6.59}$$

Continuing in this manner, one can write:

$$k(z_n) = \left\{ I(0, nt_0) - \sum_{m=1}^{n-1} k(z_m)F(z_m, (n-m+1)t_0)\Delta z_m \right\} \Big/ F(z_n, t_0)\Delta z_n \quad n > 1 \tag{6.60}$$

This equation can be used to obtain the function $k(z)$ to any accuracy by selecting the appropriate value for the time interval t_0. Once the function $k(z)$ has been determined, the corona current at any height is known and the return stroke current at any level can be obtained by the standard procedure.

The close fields and the corona current: The electric field calculated at 50 m shows that, even though the fields reach about 80 per cent of their peak value in just a few microseconds, the peak value is only attained after about 100 μs. In the case of the measured fields the field rises almost to its peak value in a few microseconds. After searching for the reason for this discrepancy, it was realised that it is caused by the induction field component and this deficiency can be rectified if the corona current is bipolar and is given by:

$$I_c(z, t) = k(z)\left(\frac{1}{v(z)} + \frac{1}{c}\right)\frac{\partial I(0, t - z/v_{av}(z))}{\partial t} \quad \text{for } 0 \le t - z/v_{av}(z) \le t_{ris} \tag{6.61}$$

$$I_c(z, t) = k(z)\left(\frac{1}{c}\right)\frac{\partial I(0, t - z/v_{av}(z))}{\partial t} \quad \text{for } t - z/v_{av}(z) > t_{ris} \tag{6.62}$$

Note that the corona current becomes negative when $t - z/v_{av}(z) > t_{ris}$. Observe however, that the integral of the corona current at a given point is positive. Therefore a net positive charge is deposited by the return stroke on the leader channel. The same procedure as before can be used to evaluate the function $k(z)$. One question that one may ask here is whether a bipolar corona current is physically reasonable. More research work is needed before this can be answered.

Predictions of the model

Return stroke current and charge. Assume that the velocity is constant. Then:

$$k(z) = 1 \quad \text{for } z < t_{ris}/[1/v + 1/c] \tag{6.63}$$

Thus the total charge per unit length deposited by the return stroke along the channel, which is given by the integral of the corona current (equation 6.61 and 6.62), is given by:

$$\rho(z) = I_p/v \quad \text{for } z < t_{ris}/[1/v + 1/c] \tag{6.64}$$

where I_p is the peak return stroke current.

The return stroke current as a function of height is shown in Figure 6.26. Note that the peak current decreases with height but the current rise time does not because the waveshape of the corona current has been assumed to be independent of height. However, if the model is modified to include a corona current that disperses with height, the rise time of the return stroke current will increase with height.

Electromagnetic fields generated by the model. The model-predicted electric and magnetic fields are depicted in Figure 6.27. In these figures the electric fields that would be present if the corona current was assumed to be monopolar (eqns 6.54 and 6.55) are also depicted. In this calculation the return stroke speed, v, was assumed to be 1.5×10^8 m/s. The general features of the electromagnetic fields do agree with

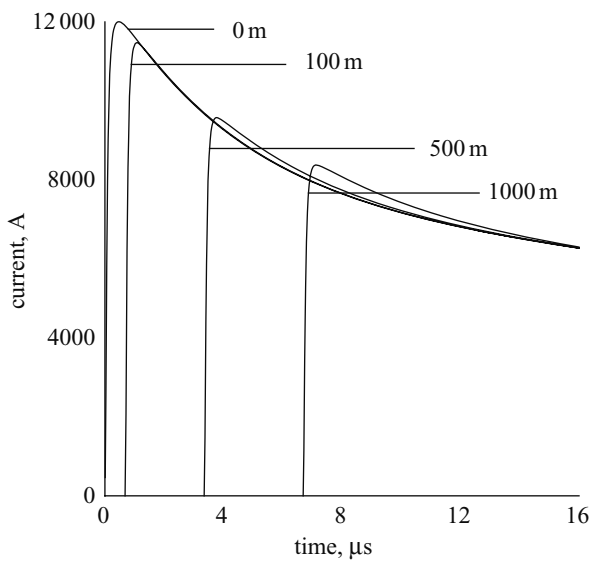

Figure 6.26 *The return stroke current along the channel as predicted by the subsequent return stroke model # 2 of Cooray. Note that the channel base current is an input parameter of the model*

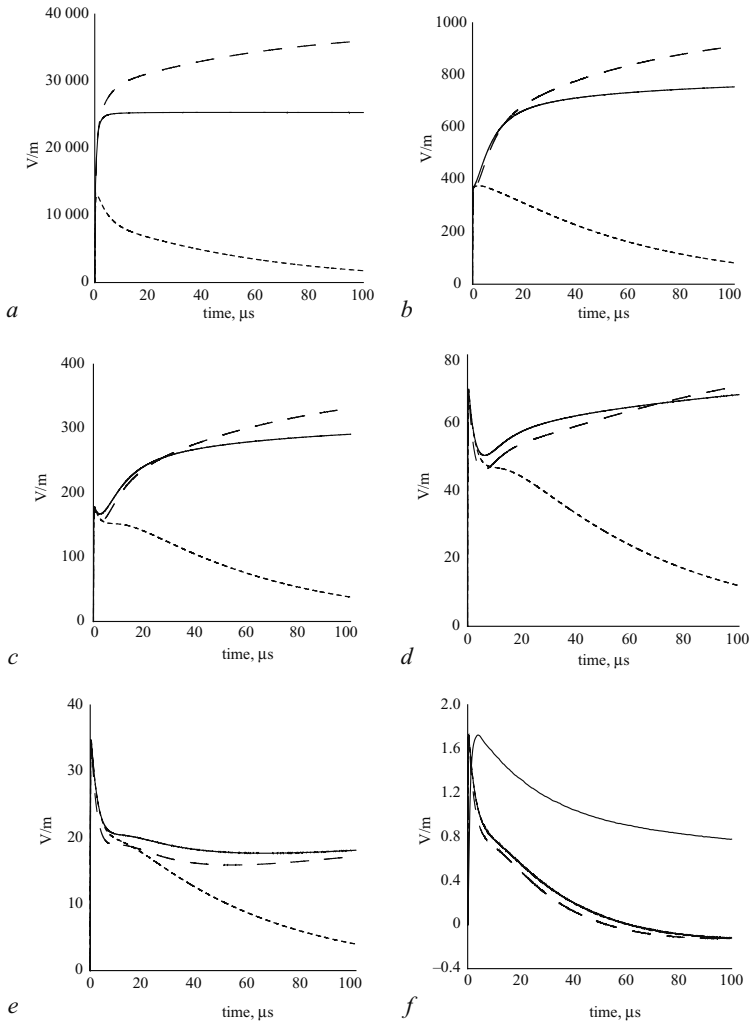

Figure 6.27 *The electromagnetic fields (electric field: solid line, magnetic field × c: short-dashed line) at different distances as predicted by the subsequent return stroke model # 2 of Cooray. The current at the channel base is identical to that in Figure 6.3 and the return stroke speed is equal to 1.5 × 10^8 m/s. Note that c is the speed of light in free space. The long dashed line depicts the electric fields when the corona current is monopolar (i.e. equations 6.54 and 6.55). Note that the electric field at 200 km is also shown in a ten times faster time scale*

a 50 m
b 1 km
c 2 km
d 5 km
e 10 km
f 200 km

those of the measurements. Note that, like the experimental observations, the near field flattens out within a few microseconds. Moreover, as in the TL model, the rising part of the electric radiation field is identical to that of the current waveform and the peak current and the peak current derivative conform to the equations:

$$E_p = \frac{\mu_0 v}{2\pi D} I_p \tag{6.65}$$

$$\left(\frac{dE}{dt}\right)_p = \frac{\mu_0 v}{2\pi D}\left(\frac{dI}{dt}\right)_p \tag{6.66}$$

where D, E_p, $(dE/dt)_p$, I_p, $(dI/dt)_p$ are the distance, the peak electric radiation field, the peak electric radiation field derivative, the peak current and the peak current derivative, respectively.

Comparison of the two subsequent return stroke models

The reader might wonder why the author has introduced two models of a completely different nature to describe subsequent return strokes. In model # 1 the author attempted to create a model that is physically meaningful, with a minimum number of model parameters. As the reader has seen, the model predictions agree well with the available experimental observations. On the other hand the TLM model is frequently used in engineering applications. In model # 2 the author has kept all the advantages of the TLM intact while eliminating all its disadvantages. This model can be used without much computation in many engineering applications.

6.4.2.6.3 First return stroke model for both negative and positive polarities

The main difference between the first return stroke and the subsequent return strokes is the nature of the leader that initiates the discharge. The stepped leader propagates in an unionised media whereas the dart leader propagates along a medium at elevated temperature. The leading edge of the leader channel consists of three parts: a streamer region, a cold leader and a hot leader (i.e. an arc region) [61,63]. It is doubtful whether such features exist in dart leaders. Moreover, the first return strokes contain connecting leaders whereas in subsequent strokes these are either absent or very short. In any model that attempts to simulate first return strokes these points should be considered. Cooray [47] and Cooray and Galvan [48] have constructed a first return stroke model in such a way that the input parameters are the leader charge density and the corona current with the channel base current being predicted. The general features of the model are depicted in Figure 6.28. The leader channel surges forward through the action of the negative streamers originating from the highly conducting or the arc portion of the leader channel. When the tip of the negative streamer region makes contact with the ground (Figure 6.28*a*), the neutralisation process proceeds upwards along the path taken by the streamers. This neutralisation process, which occurs before the beginning of the return stroke proper,

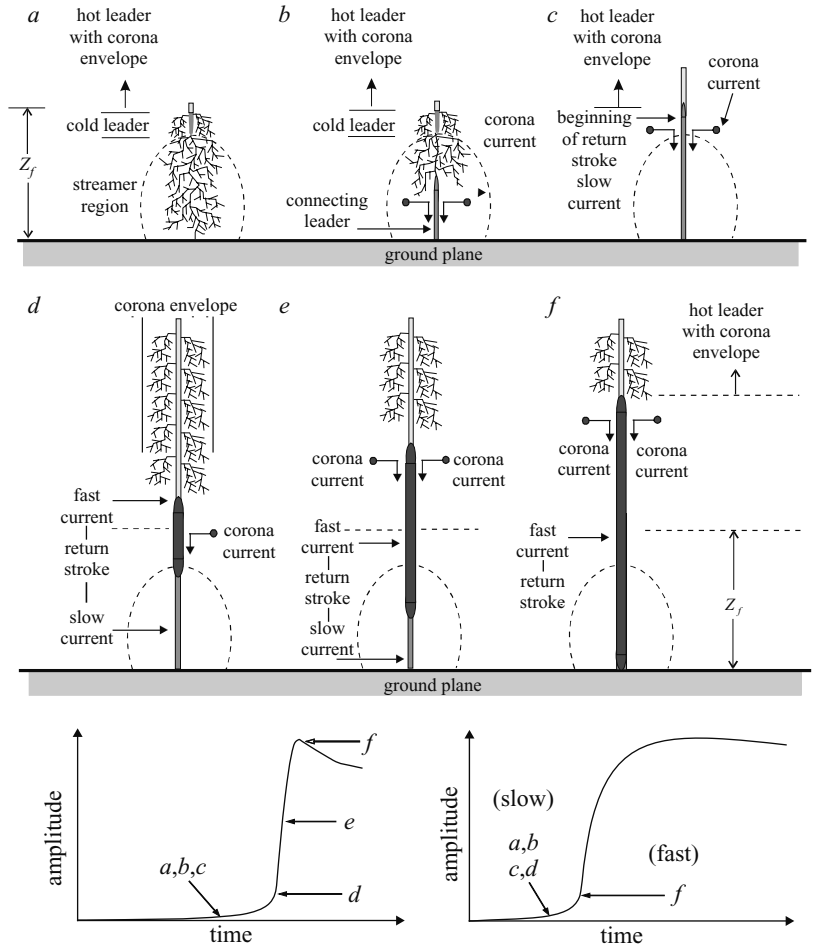

Figure 6.28 *A schematic representation of the mechanism of the first return stroke and the possible events in the first return stroke that lead to the various features observed in the channel base current and the distant radiation field. The temporal growth of the channel base current and the radiation field at various stages of the development of the first return stroke are also shown in the figure*

- *a* the streamer region of the leader reaches the ground
- *b* the return stroke grows within the streamer region; the stroke velocity increases with height and the current at ground level and the distant radiation generate a slow front
- *c* the return stroke grows within the cold leader and it is just about to reach the hot part of the leader; the stroke velocity still increases with height; the current at ground level continues to generate the slow front; the distant radiation field is just about to generate the fast front

can be interpreted as a connecting discharge moving towards the highly conducting region of the stepped leader. This scenario agrees with that of Golde [62], who assumed that the connecting leader from the ground is initiated when the streamers from the stepped leader channel reach the ground. The return stroke proper is initiated when this connecting leader makes contact with the arc portion of the stepped leader channel (Figure 6.28*c*). The model calculations show that the meeting of the connecting leader with the hot stepped leader generates two fast current waveforms that travel in opposite directions, one towards the cloud and the other towards the ground (Figure 6.25*d*). The model also predicts that the return stroke is initiated at a speed equal to the speed of light. The results of this study show that the slow front in the first return stroke current waveforms is generated by the connecting leader rising up to meet the down-coming stepped leader. Even though this model is physically reasonable and can predict many of the observed features of first return strokes it has one drawback when it comes to engineering applications, namely, the extensive computations required to obtain the velocity profile of the return stroke. However, one can use the basic concepts of this model to construct a first return stroke model with a channel base current as an input which could be used in engineering applications. Following is a description of such a model [79].

Input parameters of the model

a channel base current
b charge per unit length at the ground end of the stepped leader channel
c return stroke velocity.

Assumptions of the model

a The charge density per unit length, ρ_0, deposited by the return stroke along the channel is independent of the height (the model can accommodate any other charge profile too without difficulty).
b The leading edge of the stepped leader supports a streamer system and a connecting leader is initiated from the ground at the instant these streamers touch the ground.
c The slow front of the current waveform is produced by the connecting leader as it moves through the streamer region of the stepped leader.

---

d the return stroke front reaches the hot leader channel and the current in the return stroke channel increases rapidly; at this time the return stroke velocity almost reaches the speed of light; the fast current waveform travels towards ground while the return stroke front moves upwards; the rapidly rising portion of the radiation field is generated during this time
e the fast current component reaches the ground, the slow front of the current waveform ends here, and the channel base current shows a rapid increase

d The connecting leader moves upwards with an exponentially increasing speed and it merges into the return stroke proper when it encounters the hot region of the stepped leader channel.

e The corona current injected into the channel at a given point decays exponentially with time.

Mathematical representation

Based on the above assumptions one can develop the necessary equations as follows. The speed of the connecting leader, $v_c(z)$, is given by:

$$v_c(z) = v_0 \exp(z/\lambda_c) \tag{6.67}$$

where v_0 and λ_c are constants to be determined. Since the connecting leader merges into the return stroke proper at a height l_c:

$$v_c(l_c) = v_0 \exp(l_c/\lambda_c) = v_i \tag{6.68}$$

where v_i is the initial speed of the return stroke proper (note that the return stroke is initiated at height l_c) and $l_c$is the length of the connecting leader. Note that l_c is the same as the length of the streamer region in the final jump and hence is equal to the striking distance of the return stroke over flat ground [62]. Since the model belongs to the CG class of models, the duration of the slow front in the channel base current waveform, t_s, and the length of the connecting leader, l_c, are related through the equation:

$$t_s = [\lambda_c(1 - \exp(-l_c/\lambda_c))/v_0] + l_c/c \tag{6.69}$$

where c is the speed of light in free space. Since the current waveform and the return stroke velocity profile are given, both t_s and v_c are known quantities. Thus eqns 6.67, 6.68 and 6.69 can be solved to obtain v_0 and λ_c provided $l_c$is known. Fortunately, the value of l_c can be calculated for any leader charge distribution by assuming that at the final jump the average potential gradient between the leader tip and the ground is about (5–6) $\times 10^5$ V/m. For linear charge distribution along the leader channel, this exercise resulted in the following approximate relationship between the length of the streamer region l_c and the charge density per unit length ρ_0:

$$l_c = (6 - 8) \times 10^4 \rho_0 \tag{6.70}$$

This calculation requires the radius of the stepped leader channel, R_l. It was assumed that it is given by:

$$R_l = \frac{\rho_0}{2\pi\varepsilon_0 E_b} \tag{6.71}$$

where $E_b = 3.0 \times 10^6$ V/m. In eqn. 6.70 l_c is given in metres and ρ_0 is in C/m. The results would not change significantly even if the charge density of the leader channel decreased linearly with height.

Since the velocity of the return stroke, v_r, is assumed to decrease exponentially with height, one can write:

$$v_r = v_i \exp(-(z - l_c)/\lambda_r) \tag{6.72}$$

where λ_r is the decay height constant. The corona current injected into the channel at a given point can be represented by:

$$I_c(z, t) = I_0(z)\lfloor e^{-t/\tau(z)} \rfloor \tag{6.73}$$

where $\tau(z)$, which is a function of height, is the discharge time constant and hence the duration of the corona current. Owing to charge conservation, ρ_0 and $I_c(z, t)$ are related to each other through the equation:

$$\rho_0 = \int_0^\infty I_c(z, t)\, dt \tag{6.74}$$

This gives a value for I_0 of:

$$I_0(z) = \rho_0/[\tau(z)] \tag{6.75}$$

By substituting this expression into the above equation, it can be seen that the corona current may be written as:

$$I_c(z, t) = \frac{\rho_0}{[\tau(z)]}[e^{-t/\tau(z)}] \tag{6.76}$$

Since the velocity of the upward moving discharge (both the connecting leader and the return stroke) and the channel base current are given, the function $\tau(z)$ can be estimated without difficulty using eqns 6.50 and 6.51 with $\tau_r = 0$.

Channel base current

An analytical expression for a waveform that can represent the first return strokes was presented by the working group 01 (lightning) of the CIGRE study committee 33 [51]. This current waveform is used to represent the channel base current in the present application. This current waveform is given by:

$$I(t) = At + Bt^n \qquad \text{for} \quad t \le t_n \tag{6.77}$$

$$I(t) = I_1 e^{-(t-t_n)/t_1} + I_2 e^{-(t-t_n)/t_2} \qquad \text{for} \quad t \ge t_n \tag{6.78}$$

with

$$n = 1 + 2(S_n - 1)\left(2 + \frac{1}{S_n}\right) \tag{6.79}$$

$$t_n = 0.6t_f \frac{3S_n^2}{(1 + S_n^2)} \tag{6.80}$$

$$S_n = S_m t_f / I_p \tag{6.81}$$

$$t_1 = (t_h - t_n)/\ln(2) \tag{6.82}$$

$$t_2 = 0.1 I_p / S_m \tag{6.83}$$

$$I_1 = \frac{t_1 t_2}{t_1 - t_2}\left(S_m + 0.9\frac{I_p}{t_2}\right), \quad A = \frac{1}{n-1}\left(0.9\frac{I_p}{t_n}n - S_m\right), \tag{6.84}$$

$$I_2 = \frac{t_1 t_2}{t_1 - t_2}\left(S_m + 0.9\frac{I_p}{t_1}\right), \quad B = \frac{1}{t_n^n(n-1)}(S_m t_n - 0.9 I_p) \tag{6.85}$$

In these equations I_p is the peak current, S_m is the peak current derivative, t_f is the 30–90 per cent front time and t_h is the time to half value. For an average return stroke current the recommended values are $I_p = 30\,\text{kA}$, $S_m = 26\,\text{kA}/\mu\text{s}$, $t_f = 3\mu\text{s}$ and $t_h = 75\,\mu\text{s}$. This current waveform has a slow front of 5 μs (time from the beginning of the waveform to the point at which the peak is reached) and the impulse charge associated with this current waveform is 3 C. The charge associated with this current waveform over the first 100 μs is 1.8 C (see Chapter 4, Figure 4.14). In the calculations presented here the value of S_m was increased to 37 kA/ μs, which is slightly higher than the recommended value for negative first strokes. With this value the model is capable of generating peak dE/dt values that agree with measurements. This current waveform is shown in Figure 6.29.

Values of model parameters

In the calculation it is assumed that $\rho_0 = .001$ C/m.

The available experimental observations indicate that the first return stroke speeds averaged over channel lengths of about 300 and 1000 m are about 1.7×10^8 m/s and 1.4×10^8 m/s, respectively [54]. Both these observations could be satisfied by assuming $v_i = 2.0 \times 10^8$ m/s and $\lambda_r = 1500$ m.

Substituting $\rho_0 = 0.001$ C/m and $t_s = 5 \times 10^{-6}$ s into eqn. 6.70 and using the resulting value of l_c in solving eqns 6.67–6.69 one finds that $v_0 = 3.5 \times 10^6$ m/s. This value is higher than measured speeds of upward connecting leaders of the order of 10^5 m/s [64]. However, these measured speeds are for a 200 m high object, for which an upward connecting leader is expected to be initiated long before the streamer zone of the descending leader touches the object top. Let us consider some of the results obtained from this model.

Predictions of the model

Return stroke current. The temporal variation of the return stroke current as a function of height is depicted in Figure 6.30. The way in which the peak and the rise time (0 to peak) of the current vary with height is depicted in Figures 6.31 and 6.32,

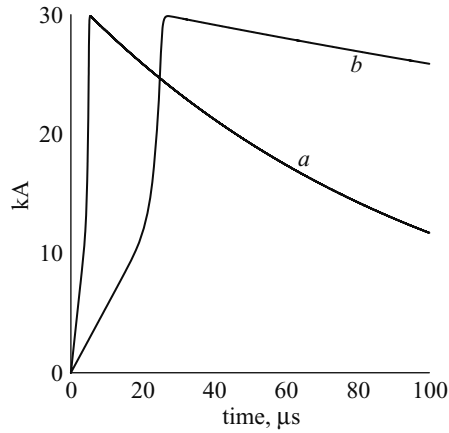

Figure 6.29 *a* current waveform recommended by CIGRE study committee 33 (overvoltages and insulation coordination) to represent the channel base current of negative first return strokes
b same current waveform shown in a five times faster time scale

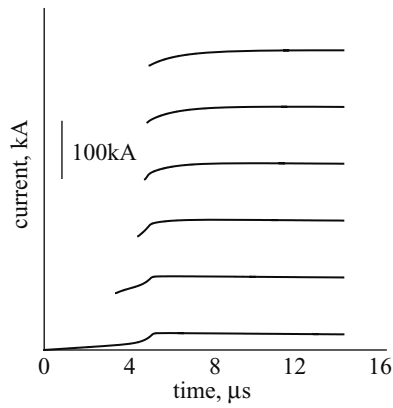

Figure 6.30 *Temporal variation of the first return stroke current as a function of height (From bottom trace to top trace; 0, 20, 40, 60, 80 and 100 m) along the return stroke as predicted by the negative first return stroke model. Note how the slow front disappears gradually as the height increases*

respectively. First note how the slow front decreases with height and finally disappears around 70 m, the height at which the connecting leader met the stepped leader. Second observe that the peak current decreases and the current rise time increases with height. This is an important prediction of the model and it agrees with the indirect inferences made from the optical observations. Figure 6.33 shows how the peak current derivative varies with height. Note that the current derivative increases initially, reaches a peak around 70 m and decreases rapidly with further increase in height.

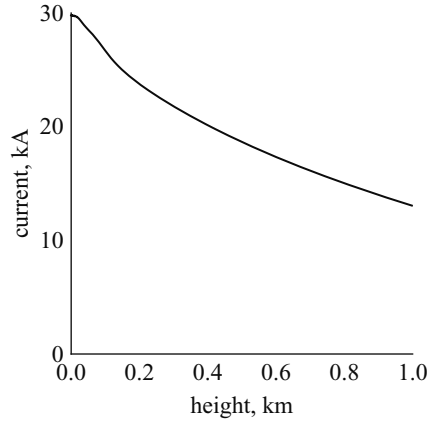

Figure 6.31 *Variation of the first return stroke peak current as a function of height along the channel*

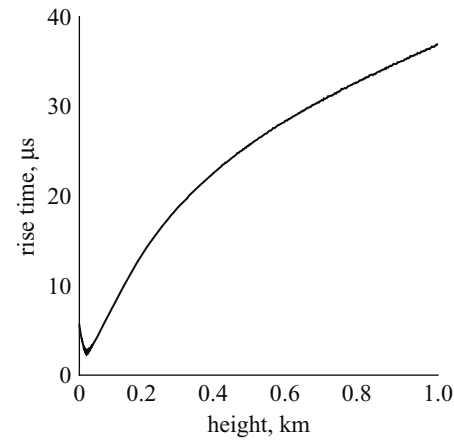

Figure 6.32 *Variation of the rise time (0 to peak) of the first return stroke current as a function of height along the channel*

Figure 6.34 shows the time at which the peak current derivative occurs as a function of height. Note that the maximum derivative first occurs not at ground level but at the meeting point of the connecting leader and the stepped leader. The current derivative reaches a peak at later times at points located below and above this critical point. This shows that the encounter between the connecting leader and the stepped leader gives rise to two fast current waveforms, one travelling towards the cloud and the other travelling towards the ground. This is one of the important predictions of the model.

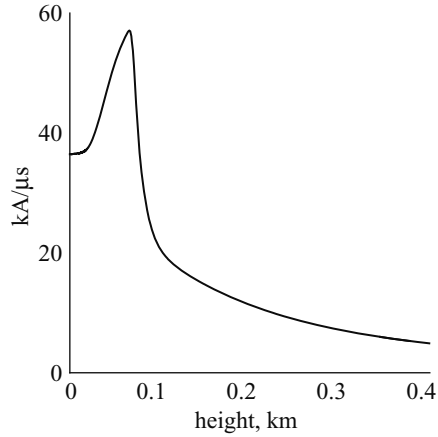

Figure 6.33 Variation of the return stroke peak current derivative as a function of height along the channel

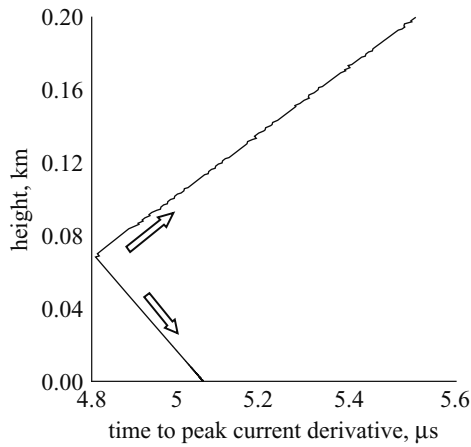

Figure 6.34 The time (measured from the beginning of the return stroke) at which the peak of the return stroke current derivative occurs as a function of height along the channel. Note that this represents two fast current waveforms originating at height 70 m (the point of contact of the connecting leader and the stepped leader) and travelling in opposite directions

Electromagnetic fields. The model-simulated electric and magnetic fields at distances of 50 m, 1, 2, 5, 10 and 200 km are shown in Figures 6.35 for a 30 kA current at the channel base. At 100 km, the fields are pure radiation and they show a slow front followed by a fast transition. This is a common feature in the first return stroke fields. After attaining a peak value, the field crosses the zero line around 60 μs. The electric field within about 2–10 km exhibits a ramp-like increase and

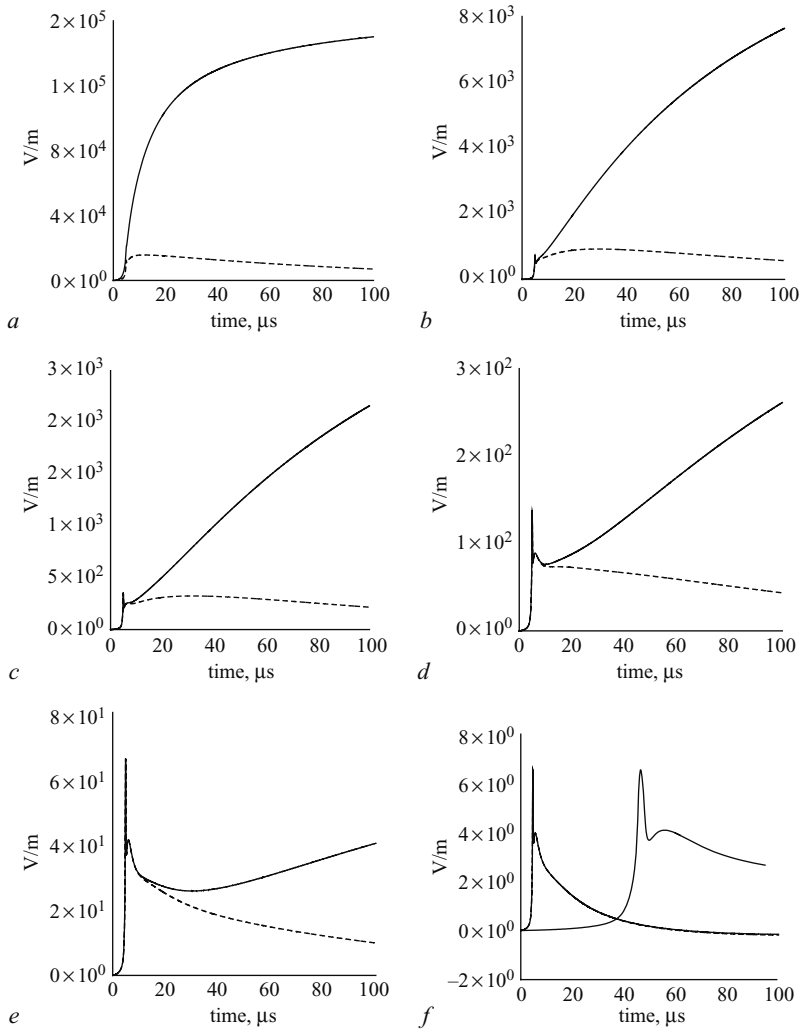

Figure 6.35 *The electromagnetic fields (electric field: solid line, magnetic field × c: dashed line) at different distances as predicted by the first return stroke model. Note that c is the speed of light in free space. The electric field at 100 km is also given in a 10 times faster time scale*

a 50 m
b 1 km
c 2 km
d 5 km
e 10 km
f 100 km

the magnetic field has a hump. The electric field within 50 m of the strike shows a rapid saturation within a few tens of microseconds. Both of these features are observed in the subsequent strokes of triggered lightning flashes. However, data is not available yet to find out whether this is a feature common to first return stroke fields.

Connection between the field and current parameters. It is common practice today to extract the peak return stroke currents from the measured fields by using the equations from the transmission line model. However, there is no general consensus on the value of the effective speed that should be used in such studies. Let us consider the predictions of the present model on this subject. The peak radiation field corresponding to the 30 kA current is about 6.5 V/m. When these two numbers are used in the transmission line equation (i.e. eqn. 6.52) one obtains 10^8 m/s as the effective transmission line speed. Observe that this value is less than the assumed initial speed, 2.0×10^8 m/s, in the model simulations. Since the return stroke speed used in the model is based on the average return stroke speeds obtained from experiments, the model results show that an effective return stroke speed of 10^8 m/s may be used in converting the measured peak values of the first return strokes to peak currents using the transmission line equation.

Let us consider the relationship between the peak current derivative and the peak electric field derivative. According to the model, a current derivative of 37 kA/μs generates a peak electric field derivative of about 30 V/m/μs at 100 km. When these two numbers are used in eqn. 6.53 the effective transmission line speed will become 4×10^8 m/s, which is indeed larger than the speed of light. This value is similar to that obtained previously by Cooray [47]. The reason for this high value for the effective transmission line speed is the two current waveforms propagating in opposite directions at the initiation of the return stroke. These two current waveforms boost the amplitude of the radiation field peak derivatives making the effective speed needed in the transmission line model to obtain the correct current derivatives larger than the speed of light. The calculated effective transmission line speed may depend to some extent on the shape of the current waveform and the initial speed of the return stroke used in the calculations. Based on the results obtained from this model, one can recommend an effective transmission line speed of 4–5 $\times$ 10^8 m/s in converting the measured first return stroke peak electric field derivatives to peak current derivatives using the transmission line equation. In other words, using an effective transmission line speed of about 1–1.5 $\times$ 10^8 m/s in converting the peak electric field derivatives to peak current derivatives, which indeed is the common practice today, may overestimate the peak current derivatives of first return strokes by a factor of about three to four.

Connecting leader and the slow front. The new concept incorporated in the model presented here is the identification of the slow front in the channel base current waveform as the current signature generated by the connecting leader. This idea is mathematically incorporated into the model as a modification of the velocity profile of the discharge.

It is not new for attempts to be made to connect the slow front in electromagnetic fields and currents in first return strokes to the connecting leader. One such attempt was made by Weidman and Krider [56] when they studied this problem and came to the conclusion that the measured currents in connecting leaders are not large enough to give rise to the slow front in electromagnetic fields. Recall, however, that the current measurements from connecting leaders that are available in the literature are from those initiated at the top of high towers and which did not succeed in making a connection to a stepped leader. The scenario presented here is that the slow front is generated by the connecting leader when it enters into the streamer zone of the stepped leader (see Figure 6.28). That is, at the final jump stage (to borrow jargon from laboratory work on sparks, see Chapter 3). At this stage the return stroke is inevitable and the growth of the connecting leader within the streamer zone can be treated as the initiation phase of the return stroke. The slow front in the current waveform is indeed a manifestation of the return stroke.

Extension of the model to include positive return strokes

Experimental observations based on both electric field and direct current measurements indicate that the main difference between the positive and negative return stroke currents is the presence of a long current tail in the former. The electric field measurements indicate that the first few tens of microseconds of the positive return stroke current is qualitatively similar to that of the negative first strokes. After this initial stage the negative current continues to decay, whereas the positive current starts to increase again, reach a second peak within about 100–300 μs and decay within a few milliseconds (see Chapter 4).

The current waveform shown in Figure 6.36 has these features and can be used to represent a typical positive first return stroke current. This current waveform can be represented analytically by the equation:

$$
\begin{aligned}
I(t) &= At + Bt^n \quad \text{for } t \le t_n \\
I(t) &= I_1 e^{-(t-t_n)/t_1} + I_2 e^{-(t-t_n)/t_2} \\
&\quad + \left\{ I_3 \frac{[(t-t_n)/\tau_4]^5}{1+[(t-t_n)/\tau_4]^5} \exp[-(t-t_n)/\tau_5] \right\} \quad \text{for } t \ge t_n
\end{aligned}
\tag{6.86}
$$

$I_3 = 69 \times 10^3$ A, $\tau_4 = 150 \times 10^{-6}$ s and $\tau_5 = 480 \times 10^{-6}$ s. The values of $A, B, n, I_1, I_2, t_n, t_1$, and t_2 are estimated from eqns 6.79–6.85 using $I_p = 60$ kA, $S_m = 30$ kA/μs, $t_f = 12$ μs and $t_h = 75$ μs.

The slow front duration, t_s, of this current waveform is 21 μs and the rise time of this current waveform is 22 μs. This rise time is close to the corresponding median values of positive return stroke currents [65]. The peak value of the current waveform is 60 kA. This is larger than the median positive current of 35 kA. This choice is based on the experimentally observed fact that, on average, the peak radiation fields of positives are two times larger than those of negative first strokes. Since the positive return stroke speeds do not differ significantly from those of negatives, the only plausible explanation for this experimental observation is the two times higher median

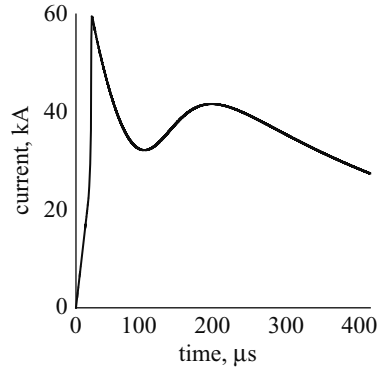

Figure 6.36 The channel base current of a typical positive return stroke used in the simulation. The waveform is based on the inferences made from the measured currents and the electromagnetic fields of positive return strokes ([66], see also Chapter 4)

current in positives than in the negatives. The derivative of the current waveform is 30 kA/μs. This is also higher than the median value measured in positives but it will lead to electric field derivatives similar to those measured. The impulse charge associated with it is 28 C which is close to the experimentally measured value for a 60 kA positive current.

The velocity profile used in calculating electromagnetic fields is similar to that used earlier for negative, return strokes. Since the peak current is twice that of the negative, the value ρ_0 is assumed to be 0.002 C/m. This leads to a connecting leader of length about 130 m which is longer than the corresponding length obtained for a typical negative first stroke.

Electromagnetic fields of positive return strokes. The electromagnetic fields generated by the model at several distances are given in Figures 6.37 and 6.38. Note the long slow front and the slow tail of the radiation field. These signatures are similar to those observed in measured fields [66] (see also Chapter 4). The peak radiation field and the peak radiation field derivative at 100 km are about 14 V/m and 26 V/m/μs, respectively. These values also agree with the typical values observed for positive strokes [67].

Use of the model in Monte Carlo type simulations

It is a known fact that the properties of return strokes vary from one stroke to another. Thus a given set of model parameters cannot be expected to reproduce the variability that is observed in the actual return stroke parameters. This in turn suggests that the model variables, i.e. the channel base current and the velocity profile, vary from one return stroke to another. The following procedure can be used to incorporate this variability into the negative first return stroke model:

(i) The peak return stroke current can be assumed to follow a log normal distribution with a certain mean and a standard deviation.

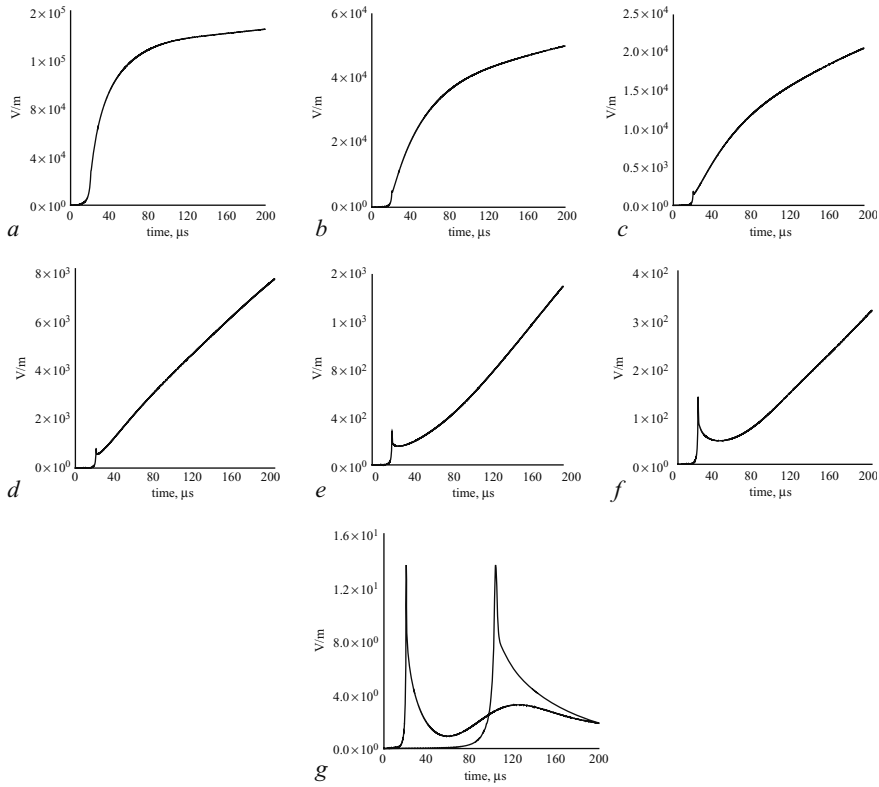

Figure 6.37 *The electric field at different distances as predicted by the positive first return stroke model. The electric field at 100 km is also given in a 5 times faster time scale. Note that the polarity of the field is inverted with respect to the electric fields of negative first return stroke shown in Figure 6.29 for clarity*

a 200 m
b 500 m
c 1 km
d 2 km
e 5 km
f 10 km
g 100 km

(ii) The charge per unit length on the leader channel can be assumed to vary linearly with the return stroke peak current. This assumption is supported by the strong linear correlation found between the peak first return stroke current and the charge brought to ground during the first 100 μs of the return stroke (see Chapter 4).

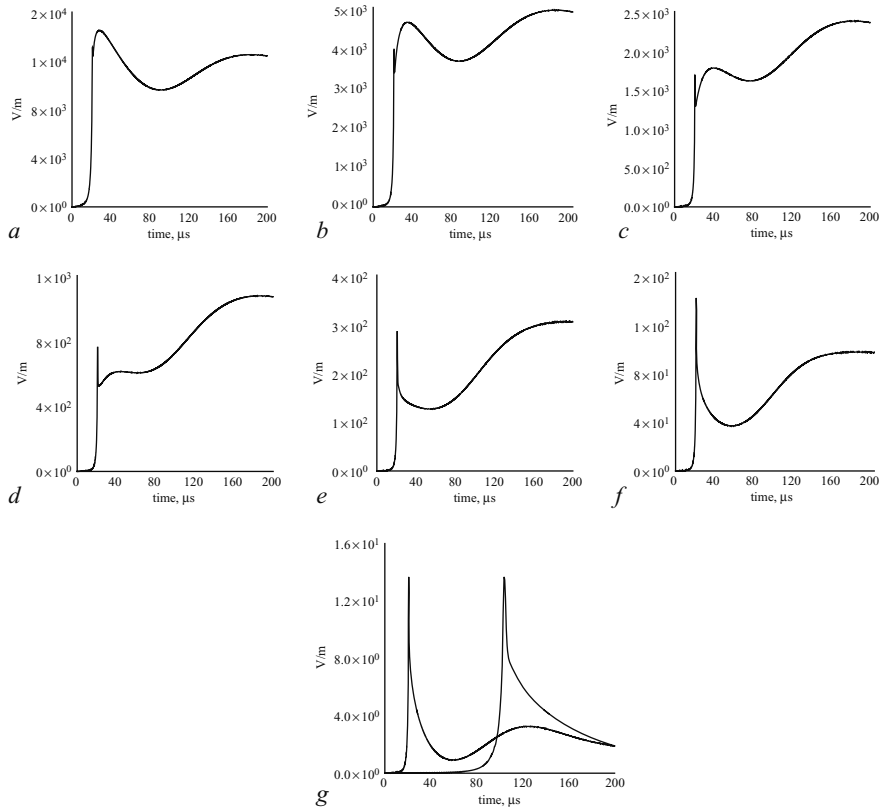

Figure 6.38 *The magnetic field ($\times c$) at different distances as predicted by the positive first return stroke model. The magnetic field at 100 km is also shown in a 5 times faster time scale. Note that c is the speed of light in free space*

- *a* 200 m
- *b* 500 m
- *c* 1 km
- *d* 2 km
- *e* 5 km
- *f* 10 km
- *g* 100 km

(iii) For a given peak current, the front parameters of the current, i.e. S_m and t_f can be estimated from the derived correlations between the front parameters and the peak current of the current as given in the reference [51].

(iv) The duration of the current waveform for a given peak current can be obtained by appealing to the different correlations found between the peak current and

the total charge, peak current and the charge brought to ground within the first 100 μs or the peak current and the action integral (68, see also Chapter 4).

(v) The distribution of the average return stroke velocity over the first 300 m and 1000 m as published by Mach and Rust [54] could be used in obtaining the velocity profile of first return strokes.

6.4.2.7 Diendorfer and Uman

Diendorfer and Uman [69] independently proposed a model somewhat similar to the subsequent return stroke model of Cooray [42,43]. The assumptions of the model are the following:

a the channel base current is known
b the speed of propagation of the return stroke, v, is constant
c the speed of propagation of the corona current down the channel, c, is equal to the speed of propagation of light in free space
d the corona current is divided into two parts: one fast and the other slow.

The corona current $I_c(z, t)$ at any height z is given by:

$$I_c(z,t) = I_{bo}(z)e^{-(t-z/v)/v/\tau_f} \text{ (fast component)} + I_{co}(z)e^{-((t-(z/v)/v)/\tau_s)} \text{ (slow component)} \tag{6.87}$$

where τ_f and τ_s are the discharge time constants. It was assumed that the discharge time constants do not vary as a function of height. In order to evaluate the corona current parameters, the channel base current was arbitrarily divided into two sections: one was assumed to be generated by the fast corona current and the other by the slow one. Representing these two parts of the channel base current by $I_{fast}(t)$ and $I_{slow}(t)$ one can show that:

$$I_{bo}(z,t) = \left\{ \left[\frac{dI_{fast}(t)}{v^* dt} \right]_{t=z/v^*} + \frac{I_{fast}(z/v^*)}{v^* \tau_d} \right\} \tag{6.88}$$

$$I_{co}(z,t) = \left\{ \left[\frac{dI_{slow}(t)}{v^* dt} \right]_{t=z/v^*} + \frac{I_{slow}(z/v^*)}{v^* \tau_d} \right\} \tag{6.89}$$

with $1/v* = 1/c + 1/v$. These assumptions provide all the information necessary to determine the spatial and temporal variation of the return stroke current. Thottappillil *et al*. [70] modified this model to accommodate a height dependent v (the return stroke speed) and u (the speed of propagation of the corona current down the return stroke channel).

Input parameters: the input parameters for the model are the channel base current, the return stroke speed and the discharge time constants for the two corona current components.

Predictions of the model: the model predicts the remote electromagnetic fields and, for a given channel base current, it describes how the return stroke current changes as a function of height and the spatial distribution of the charge deposited by the return stroke along the channel.

The electromagnetic fields generated by this model at different distances are shown in Figure 6.39. The slow and fast components of the channel base current (i.e. $I_{slow}(t)$ and $I_{fast}(t)$) used in the calculation are identical to those given by Diendorfer and Uman. The total current (i.e. the sum of two components) has a peak value of 14 kA and a peak current derivative of 75 kA/ μs. The discharge time constants used in the calculations are $\tau_f = 0.1\,\mu s$ and $\tau_s = 5\,\mu s$. The return stroke speed used in the calculation is 1.5×10^8 m/s. The fields generated by the model are in reasonable agreement with the measurements.

The current waveform as a function of height along the channel is shown in Figure 6.40. The model predicts an increase in rise time and a decrease in the peak current with height. These predictions also agree with the information inferred from the variation of the optical radiation generated by the return strokes.

The model-predicted distribution of the charge deposited by the return stroke along the leader channel is depicted in Figure 6.41. Note that the charge per unit length increases initially, reaches a peak value and then decays continuously with increasing height. It is important to remember that the magnitude of the charge per unit length depends on the assumed return stroke velocity and the peak amplitude and the form of the assumed channel base current.

The model also predicts that the effective TLM velocity corresponding to the peak current peak electric field relationship is less than that of the peak current derivative peak electric field derivative relationship. For example, for an assumed return stroke velocity of 1.5×10^8 m/s the effective TLM values corresponding to the above relationships are 1.35×10^8 m/s and 2.3×10^8 m/s, respectively.

Thottappillil *et al*. [34] have shown that once the channel base current and the return stroke speed is given this model can predict the peak electric field to a reasonable accuracy.

6.5 Return stroke speed

The return stroke speed is one of the main parameters in the modelling of return strokes. The available experimental observations show that the return stroke speed decreases with height, both in the first and the subsequent return strokes. Most of the return stroke models described here had the return stroke speed as an input parameter. Some of them assumed it to be a constant with height, and the others assumed it to vary along the channel. However, a few models have deviated from this general trend and attempted to predict the return stroke speed within the assumptions of the model. These are the Lundholm [71] model, the Wagner [72] model, the Rai [73] model and the Cooray models [43, 46]. The basic assumptions these authors have used to calculate the return stroke speed are discussed below.

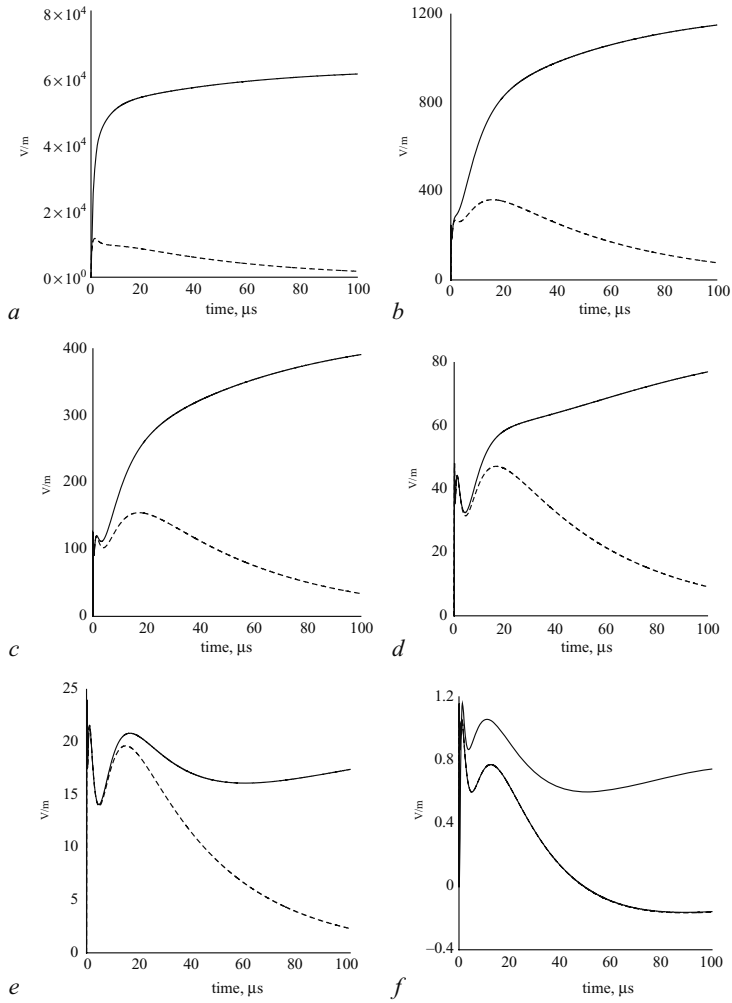

Figure 6.39 *The electromagnetic fields (electric field: solid line, magnetic field × c: dashed line) at different distances as predicted by the Diendorfer and Uman model. The current at the channel base is identical to that specified in the reference [69]. The peak current is 14 kA and the peak current derivative 75 kA/μs. The return stroke speed is equal to 1.5 × 10^8 m/s. Note that c is the speed of light in free space. The discharge time constants used in the calculation are $\tau_f = 0.1\ \mu s$ and $\tau_s = 5\ \mu s$. The electric field at 200 km is also shown in a ten times faster time scale*

a 50 m
b 1 km
c 2 km
d 5 km
e 10 km
f 200 km

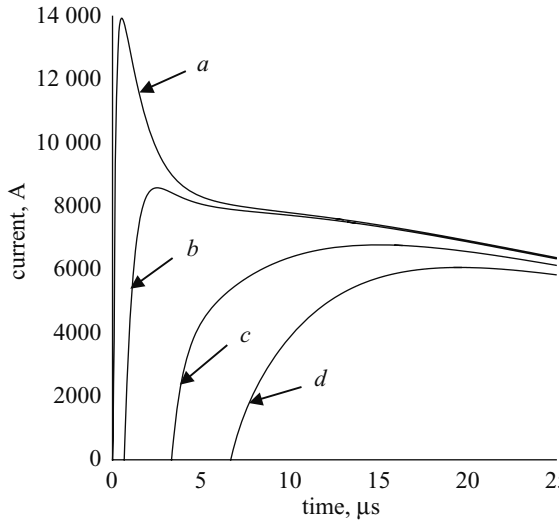

Figure 6.40 *Current waveform at different heights as predicted by the DU model. The current at ground level is an input of the model*

a ground level
b 100 m
c 500 m
d 1000 m

6.5.1 Lundholm and Wagner

Both Lundholm [71] and Wagner [72] visualised the return stroke as a step current pulse propagating along the leader channel with a constant speed v. This model, which of course is a gross simplification of the return stroke, was launched in an attempt to discover the relationship between the return stroke current and its speed. The treatment of Lundholm was as follows. The upward moving current pulse generates an electric field at the surface of the current carrying conductor. The component of this field parallel to the surface of the conductor and at a point just below the return stroke front is given approximately by:

$$E_z = \frac{I_p}{4\pi\varepsilon_0 c}\left[\frac{c^2 - v^2}{cv^2(t - z/v)}\right] = I_p R \quad t > z/v \tag{6.90}$$

where I_p is the peak current and R is the resistance per unit length of the return stroke channel. Assume the validity of Toepler's law [74], which describes the resistance of a spark channel by the equation:

$$R(z) = \frac{k}{Q(z)} \tag{6.91}$$

where $R(z)$ is the resistance per unit length of the spark channel at z, $Q(z)$ is the charge that has passed through the point z and k is the Toepler's spark constant

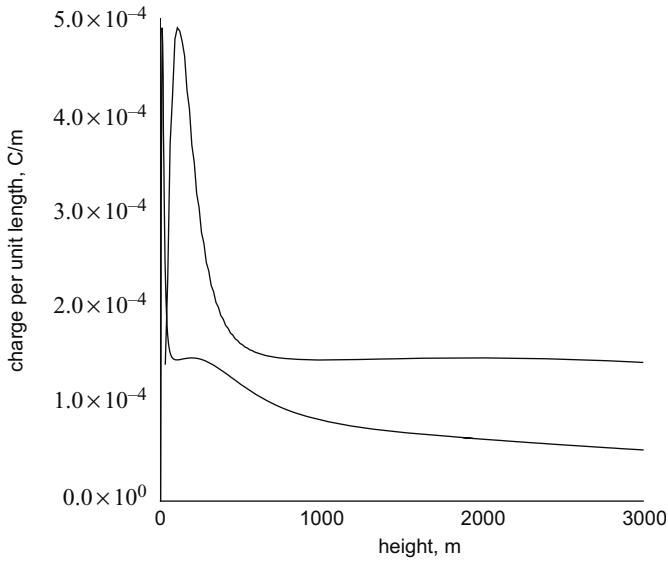

Figure 6.41 The spatial distribution of the charge per unit length deposited (or neutralised) by the return stroke as predicted by the DU model. The curve is also shown in a 10 times longer height scale. The data corresponds to a return stroke speed of 1.5 × 10^8 m/s and for the channel base current as specified in [69]

(see Chapter 3). Since $Q = I_p \times (t - z/v)$ for the situation under consideration, the combination of eqns 6.90 and 6.91 provides a relationship between I_p and v, namely:

$$v = \frac{c}{\sqrt{1 + \left(4\pi\varepsilon_0 c^2 k / I_p\right)}} \tag{6.92}$$

The basics of the Wagner [72] treatment can be described in the following manner. Consider the return stroke as a transmission line with inner and outer conductor radii a and b. A charge per unit length ρ is deposited on this transmission line during the leader stage. The energy of the system is electrostatic. As the return stroke surges up through the transmission line releasing the bound charge, the energy of the system changes from electrostatic to magnetic energy. Consequently, the energy E_u released per unit length of the return stroke channel is:

$$E_u = \frac{\rho^2}{2C} - \frac{L I_p^2}{2} \tag{6.93}$$

where $L$and C are the inductance and capacitance per unit length, respectively. Observe that if the speed of propagation v of the return stroke is equal to the speed of light c, then $E_u = 0$. This is the case since $c = \sqrt{(LC)^{-1}}$ and $I_p = \rho v$. When

$v \neq c$, the above equation gives the power that must be absorbed by the front of the return stroke. From experiments conducted in the laboratory, it was observed that an energy of 0.2 J/m A is required to raise a spark to a conducting state. Then the energy E_u per unit length that must be absorbed by the front of the wave to bring the channel to a conductivity which will support a current of I_p Amperes is equal to 0.2 I_p. Substituting this into eqn. 6.93 and after some mathematical manipulations one arrives at the equation:

$$v = \frac{c}{\sqrt{1 + \left(0.4/L\, I_p\right)}} \tag{6.94}$$

The value of the inductance per unit length was calculated by assuming a (the radius of the inner core) $= 0.03$ m and b (the radius of the current return conductor) $=$ 180 m. No discussion or justification was given for the value assumed for the latter parameter.

The derivations of Lundholm and of Wagner could be criticised on several points. Both assumed the current to be a step function, which is an oversimplification. Furthermore, due to the assumption of an instantaneous rise in the current at the front, any relationship between the rise time of the return stroke current and the speed is lost. The validity of Lundholm's derivation is based on the assumed validity of the Toepler law. This law characterises the temporal variation of the channel resistance in the early stages of a discharge and may not be applicable to return strokes since they propagate along highly conducting channels already thermalised by leaders. Wagner's simulations depend on the radius of the return current conductor which does not exist in practice. These simplifications cast doubt on the quantitative validity of both Lundholms and Wagners results. Nonetheless, the expressions derived may still provide a qualitative description of the relationship between the return stroke current and the speed.

6.5.2 Rai

Rai [73] incorporated discharge physics into Bruce and Golde's model [30] in an attempt to couple the return stroke current to its speed. He envisaged the return stroke front as an upward moving equipotential surface which separates a highly ionised gas region below and a neutral gas region with low temperature (virgin air) above. Albright and Tidman [75] derived the following expression to connect the speed v and the electric field E at the wavefront of such an ionising potential wave:

$$E = \frac{vm\chi}{e\{1 + (T_0/\eta)\}} \tag{6.95}$$

where m and e are the electronic mass and charge, χ is the elastic scattering frequency of electrons, T_0 is the electron temperature of the channel and η is the ionisation potential of the constituent gas. In addition to the assumption that the above equation can describe the processes at the return stroke front, Rai also supposed that the conductivity in the vicinity of the return stroke tip can be described by an equation of

the form:

$$\sigma(t) = \sigma_0 e^{-pt} \tag{6.96}$$

where σ_0 and p are constants. A combination of eqns 6.95 and 6.96 through the identity $J = E\sigma$, where J is the current density at the return stroke front, led to the relationship:

$$v(t) = \frac{e\{1 + T_0/\eta\} J(t)}{m\chi\sigma(t)} \tag{6.97}$$

According to Bruce and Golde [30], the current at the return stroke front at any instant of time is equal to the current at the channel base at the same instant. Thus, it was possible to replace $J(t)$ in the above expression with the double exponential expression used by Bruce and Golde to describe the channel base current (i.e. eqn. 6.13). The resulting mathematical identity:

$$v(t) = \frac{eI_0\{1 + T_0/\eta\}\{e^{-(\alpha-p)t} - e^{-(\beta-p)t}\}}{m\chi\sigma_0 A} \tag{6.98}$$

expresses how the return stroke speed varies as a function of time and current. Note that in the above equation, A is the cross sectional area of the return stroke channel. This relationship shows that the return stroke speed has the same mathematical form as that of the return stroke current at the channel base; provided of course the assumptions used in the derivation are justified. Unfortunately the actual situation may differ from the ideal circumstances assumed in the derivation in several ways. First, eqn. 6.98 is valid as long as the medium ahead of the front is virgin air. In reality, the return stroke propagates through the core of the leader channel which is highly conducting due to its elevated temperature. Second, the theory is only applicable if there is a current discontinuity at the return stroke front; such a discontinuity is not physically possible. Third, the validity of the final result depends on the assumptions of Bruce and Golde which, as discussed previously, violate the basic laws of physics.

6.5.3 Cooray

The procedure used by Cooray [43, 46] to calculate the return stroke speed is based on the following facts. Return strokes propagate along the channels of either the stepped or the dart leaders. With the exception of the very tip, these leader channels can be treated as arc channels in air with an axial potential gradient of the order of 2–10 kV/m. Thus, to induce a significant change in the current in the leader channel, the minimum field required is of the same order of magnitude as this axial field. During the return stroke phase the current in the leader channel starts to increase, and the first significant change in the current takes place at the tip of the return stroke. Thus, the return stroke should maintain a field at the tip which is of the order of the axial field along the leader channels. When this condition is satisfied, electrons

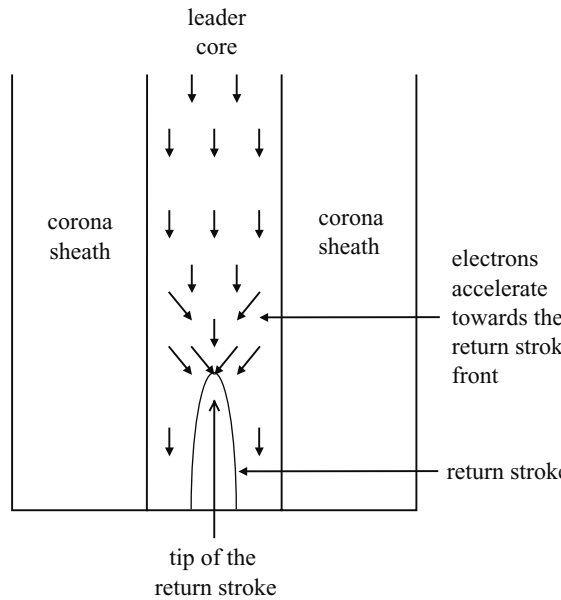

Figure 6.42 *In the model it is assumed that the field at the tip of the return stroke is of the order of the external field that exists along the core of the leader channel. When this condition is satisfied electrons will be accelerated towards the return stroke front, enhancing ionisation and leading to an increase in the current*

will be accelerated towards the tip of the return stroke, causing an increase in the current (see Figure 6.42). On the basis of this reasoning Cooray [43] assumed that the field at the tip of the return stroke is equal to the potential gradient of the leader channel. Let us consider how this assumption can be used to evaluate the return stroke speed as a function of height. First let us derive an expression for the field at the front of the return stroke and then use it to obtain the velocity profile of the return stroke.

Consider the situation at time t when the discharge front is at a distance Z from ground. If $v(z)$ is the velocity of the return stroke (which is a function of z), then Z and t are connected by the equation:

$$t = \int_0^Z \frac{dz}{v(z)} \tag{6.99}$$

Assume that the current in the return stroke is uniformly distributed along its cross section and the current density is given by $j(z, t)$. The radius of the return stroke is taken to be R. The geometry of the situation is shown in Figure 6.43. The problem is to find the field at $z = Z$ at time t, which is the field at the front of the return stroke.

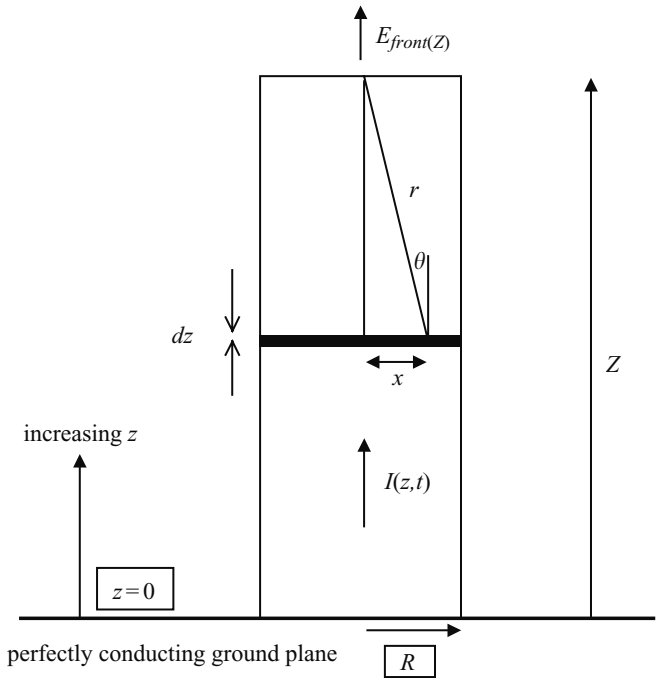

Figure 6.43 The geometry relevant to the calculation of the electric field at the front of the return stroke

The result is given by:

$$
\begin{aligned}
&E_{real}(Z) \\
&\quad = -\frac{1}{2\varepsilon}\int_0^Z dz \int_0^R \left\{ \cos^2\theta \left[\frac{2}{r^3}\int_\zeta^{t-r/c} j(z,\tau-\zeta)\,d\tau + \frac{2}{cr^2} j(z,t-\zeta-r/c) \right] \right. \\
&\qquad + \sin^2\theta \left[\frac{1}{r^3}\int_\zeta^{t-r/c} j(z,\tau-\zeta)\,d\tau + \frac{1}{cr^2} j(z,t-\zeta-r/c) \right. \\
&\qquad\qquad \left. \left. + \frac{1}{cr^2}\frac{d}{dt} j(z,t-\zeta-r/c) \right] \right\} x\,dx
\end{aligned}
\tag{6.100}
$$

where ζ is the time, measured from the beginning of the discharge, at which the current in the element at z is turned on. We assume that it is turned on when the front reaches the height z. With that assumption:

$$
\zeta = \int_0^z \frac{dz}{v(z)} \tag{6.101}
$$

So far we have calculated the field at the front owing to the actual channel section being considered. Now it is necessary to include the image contribution for an assumed

perfectly conducting ground plane. This can easily be obtained by changing the limits of the integration of variable z in eqn. 6.100 from (0, Z) to (Z, $2Z$). Performing this change in eqn. 6.100, the image field at the front is given by:

$$\begin{aligned} E_{image}(Z) &= -\frac{1}{2\varepsilon}\int_{Z}^{2Z} dz \int_{0}^{R} \left\{ \cos^2\theta \left[\frac{2}{r^3}\int_{\zeta}^{t-r/c} j(z,\tau-\zeta)\,d\tau + \frac{2}{cr^2} j(z,t-\zeta-r/c) \right] \right. \\ &\quad + \sin^2\theta \left[\frac{1}{r^3}\int_{\zeta}^{t-r/c} j(z,\tau-\zeta)\,d\tau + \frac{1}{cr^2} j(z,t-\zeta-r/c) \right. \\ &\quad \left. \left. + \frac{1}{cr^2}\frac{d}{dt} j(z,t-\zeta-r/c) \right] \right\} x\,dx \end{aligned} \tag{6.102}$$

Although exact, these equations may require rather extensive mathematical manipulation before they can be solved. They can be simplified considerably as follows. First the radiation field term can be neglected because its contribution is very small. Again consider an element dz. The static electric field produced by this element at the front of the return stroke has two contributions. One from the positive charge deposited in this element and the other from the negative charge which is momentarily located in this element as it flows to ground. Fortunately, this latter contribution is cancelled by the induction term, leaving just the contribution from the deposited charge. Let the charge deposited in this element when the front is at height Z be $q_c(z,t)$. Then the electric field at the front can be written as:

$$E_{real}(Z) = \int_{0}^{Z-R} q_c[t-\zeta-(Z-z)/c]\,dz/4\pi\varepsilon_0(Z-z)^2 \tag{6.103}$$

where

$$q_c(t,z) = \int_{0}^{t} I_c(z,\tau-\zeta)\,d\tau \tag{6.104}$$

Similarly:

$$E_{image}(Z) = \int_{0}^{Z-R} q_c[t-\zeta-(Z+z)/c]\,dz/4\pi\varepsilon_0(Z+z)^2 \tag{6.105}$$

The total field at the front, $E_{front}(Z)$, is given by:

$$E_{front}(Z) = E_{image}(Z) + E_{real}(Z) \tag{6.106}$$

The velocity of the return stroke at any height is obtained by equating the field at the front, as given by the above equation, to the potential gradient of the stepped leader channel. That is:

$$E_{front}(Z) = E_c(Z) \tag{6.107}$$

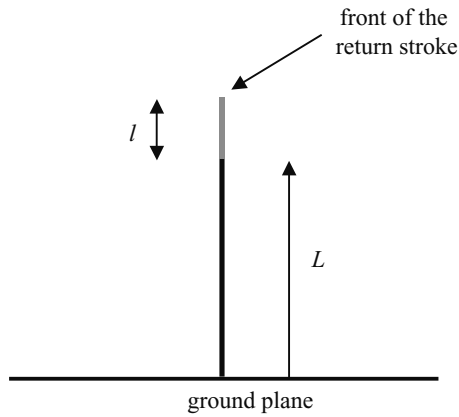

Figure 6.44 *Intermediate stage in the calculation of the return stroke velocity. The return stroke velocity over the section labelled L is known and the task is to obtain the return stroke velocity over the section l. The length of the section l is selected in such a way that the return stroke speed over that section can be considered constant*

where $E_c(Z)$ is the potential gradient of the leader channel at Z. All the parameters in this equation are specified through eqns 6.103 and 6.106. The only unknown parameter in this equation is $v(z)$, the speed of the return stroke at height z. This can be determined by numerically solving this equation. The numerical procedure adopted in this calculation is the following. Let us refer to the diagram displayed in Figure 6.44. This shows an intermediate step in the calculation in which the velocity of the return stroke over the section labelled L is known, and one would like to know the velocity of the return stroke over the section labelled l. One can make the section l as small as possible so that the assumption the return stroke speed is constant along this section of the channel, can be made. An iterative solution of equation 6.107 can be made to obtain this unknown speed. Once this has been obtained, the channel is extended again, and the same procedure is applied to obtain the speed over the new channel section.

It is important to note that even though the return stroke channel radius appears in the calculations its value does not affect significantly the electric field at the front. The reason for this is that the electric field at the front is determined by the charge on the section of the channel below the front and for values of Z larger than the radius of the channel (which is only a few centimetres) the charge on the channel can be assumed to be concentrated at the centre of the return stroke channel. Thus, irrespective of whether the value of R is 0.001 or 0.1 m, the field at the front would be more or less the same. In the calculations, however, a value had to be decided upon and $R = 0.01$ m was taken.

On the basis of this procedure, the main conclusion is that the return stroke speed is determined primarily by three parameters: the rise time of the return stroke current, its peak value and the potential gradient of the leader channel. The return stroke

speed decreases with increasing rise time and with decreasing peak of the current. Moreover, the return stroke velocity increases as the potential gradient of the leader channel decreases.

It is important to note that the procedure outlined above can also be used to estimate the dart leader speed and the speed of M components.

6.6 Current propagation versus current generation models

From an engineering point of view both current propagation models (CPM) and current generation models (CGM) are equally successful in mimicking the behaviour of electromagnetic fields generated by lightning return strokes. There are some differences, however, particularly in the fine structure of the fields, which bring the predictions of the CGM a little closer to the measured values than those of CPM. These differences may play only a minor role in most of the engineering applications of interest. In this section it is shown that any CP model can be described mathematically as a CG model [76]. The two descriptions give rise to identical spatial and temporal variations in the return stroke current.

6.6.1 The corona current

Consider a channel element of length dz at height z and let $I(z, t)$ represent the temporal variation of the total return stroke current at that height. In the case of CG models, this current is generated by the action of corona current sources located above this height. Assume for the moment that the channel element does not generate any corona current. In this case the channel element will behave as a passive element that will just transport the current that is being fed from the top, and one can write:

$$I(z + dz, t) = I(z, t + dz/c) \tag{6.108}$$

That is, the current injected at the top of the element will appear without any change at the bottom of the channel element after a time dz/c which is the time taken by the current to travel from the top of the channel element to the bottom. Here we have assumed that the speed of propagation of the current down the channel is equal to the speed of light. Now let us consider the real situation in which the channel element dz will also generate a corona current. As the current injected at the top passes through the channel element the corona sources will add their contribution resulting in a larger current appearing at the bottom than was injected at the top. The difference in these two quantities will give the corona current injected by the channel element. Thus the average corona current generated by the element dz is given by:

$$\frac{dI_{dz}(z + dz, t) + dI_{dz}(z, t + dz/c)}{2} = I(z, t + dz/c) - I(z + dz, t) \tag{6.109}$$

In deriving the above identity it was assumed that, once injected into the return stroke channel, the corona current propagates downwards with speed c. Using Taylor's

expansion, the above equation can be rewritten as:

$$\frac{dI_{dz}(z+dz,t)+dI_{dz}(z,t+dz/c)}{2} = I(z,t) - I(z+dz,t) + \frac{dz}{c}\frac{\partial I(z,t)}{\partial t} \tag{6.110}$$

Dividing both sides by dz and taking the limit $dz \to 0$, the corona current per unit length, $I_c(z,t)$, injected into the return stroke channel at height z, is given by:

$$I_c(z,t) = -\frac{\partial I(z,t)}{\partial z} + \frac{1}{c}\frac{\partial I(z,t)}{\partial t} \tag{6.111}$$

Indeed one can show that eqn. 6.111 is identical to the continuity equation as applied for CG models. Let us rewrite eqn. 6.111 as:

$$I_c(z,t) - \frac{1}{c}\frac{\partial I(z,t)}{\partial t} = -\frac{\partial I(z,t)}{\partial z} \tag{6.112}$$

The first term in the above equation, which is the corona current, can be written as the time derivative of the deposited charge per unit length, $\rho_d(z,t)$, on the channel element. The quantity $I(t,z)/c$ is nothing but the negative charge per unit length released from the upper channel sections, but momentarily located in the channel element. Let us denote this by $\rho_t(z,t)$. Again, the assumption is made that the corona currents travel down the channel with the speed of light. Thus one can rewrite the above equation as:

$$\frac{\partial(\rho_d - \rho_t)}{\partial t} = -\frac{\partial I(z,t)}{\partial z} \tag{6.113}$$

This is the continuity equation since $(\rho_d - \rho_t)$ is the total charge per unit length located at height z at time t.

Using eqn. 6.111 the corona current corresponding to a CG representation of any CP model can be obtained. With the resulting corona current as one of the inputs, the CG representation produces a temporal and spatial variation of the return stroke current identical to that obtained with the CP model. The equivalent corona currents of three commonly used CP models are derived in the next section.

6.6.2 Mathematical expressions for the equivalent corona currents for CG representation of three commonly applied CP models

6.6.2.1 Transmission line model

In the transmission line model the temporal and spatial variation of the return stroke current, $I(z,t)$ is given by:

$$I(z,t) = I(0, t - z/v) \quad t \geq z/v \tag{6.114}$$

where $I(0, t)$ is the current at the ground level and v is the constant return stroke speed. Using eqn. 6.111 one can obtain the equivalent corona current, $I_{c,TLM}(z, t)$ as:

$$I_{c,TLM}(z, t) = \left(\frac{1}{v} + \frac{1}{c}\right) \frac{\partial I(0, t - z/v)}{\partial t}, \quad t - z/v \geq 0 \tag{6.115}$$

6.6.2.2 MTLE model

In the MTLE model, the spatial and temporal variation of the return stroke current is given by:

$$I(z, t) = I(0, t - z/v) \exp(-z/\lambda), \quad t > z/v \tag{6.116}$$

where λ is the constant describing the current decay with height. Substituting this into eqn. 6.111, the equivalent corona current, $I_{c,MTLE}(z, t)$, is found to be:

$$\begin{aligned} I_{c,MTLE}(z, t) = &\left(\frac{1}{v} + \frac{1}{c}\right) \frac{\partial I(0, t - z/v)}{\partial t} \exp\left(-\frac{z}{\lambda}\right) \\ &+ \frac{I(0, t - z/v)}{\lambda} \exp\left(-\frac{z}{\lambda}\right), \quad t - z/v \geq 0 \end{aligned} \tag{6.117}$$

6.6.2.3 MTLL model

According to the MTLL model the return stroke current at any level along the channel is given by:

$$I(z, t) = I(0, t - z/v) \left(1 - \frac{z}{H}\right), \quad t > z/v \tag{6.118}$$

where H is the height of the return stroke channel. Substituting this into eqn. 6.111, the equivalent corona current for this model, $I_{c,MTLL}(z, t)$, is given by:

$$\begin{aligned} I_{c,MTLL}(z, t) = &\left(\frac{1}{v} + \frac{1}{c}\right) \frac{\partial I(0, t - z/v)}{\partial t} \left(1 - \frac{z}{H}\right) \\ &+ \frac{I(0, t - z/v)}{H}, \quad t - z/v \geq 0 \end{aligned} \tag{6.119}$$

Using these equivalent corona currents one can convert the common CP models into CG models.

6.7 Remote sensing and return stroke models

In general, neither the channel base current nor the return stroke speed is known and the only available parameter could be the electromagnetic field measured at several distances from the lightning flash. One important goal of lightning research is to find a procedure to extract the return stroke current parameters from the measured fields. In this context, it is important to remember that no two return strokes have

electromagnetic fields which are identical to each other. This natural variation inherent in the return strokes, even when they have the same peak current, makes it impossible to use a fixed set of model parameters in remote sensing studies. What one can do is to optimise the model parameters to reproduce the given set of electromagnetic fields and to use optimised set of parameters to obtain the return stroke current and other related parameters. The feasibility of this procedure was demonstrated by Cooray and Gomes [77] and Papov *et al*. [78].

6.8 The future of return stroke models

Although not very successful in generating electromagnetic fields with correct features, LCR models have contributed significantly to the development of engineering and semiphysical models. The engineering models played down the physics and performed a game of trial and error to extract the correct electromagnetic fields. The achievements made through these numerical studies have led to the development of semiphysical models, which is a step forward in our endeavour to understand the physical principles behind the return stroke process. These models promise to be as revolutionary as Bruce and Golde [30] were nearly half a century ago. The new understanding gained through these models shows how the leader and the earth interact to create spectacular return strokes and the computer simulations adopted within these models have proved very successful in reproducing the features of return strokes. It is clear, however, that there is ample room for both theoretical and experimental studies on several aspects:

1 The current generation models, although much closer to physical reality than the current propagation models, are not yet self consistent. What is needed is a theory for the neutralisation process of the leader corona and more experimental data on the radial discharge processes that may take place during the return stroke stage. In this respect, experiments of the kind performed by Takagi *et al*. [12] should be mentioned. More stringent tests of return stroke models may emerge from such observations.
2 Many return stroke models make predictions as to the way in which the peak and the rise time of the return stroke current vary as a function of height. Within this subject there is an urgent need to develop remote sensing techniques to feel the signature of return stroke currents at different altitudes. One possible course of action is to find the correlation between the optical radiation and the current waveforms and then use this information to infer the way in which the return stroke current varies with height.
3 Theories should be developed concerning the speed of the return stroke front. On the experimental side, simultaneous measurements of the leader temperature, the return stroke speed and the temporal variation of the optical radiation may provide valuable clues to guide the efforts of the theorists.
4 A few return stroke models predict the spatial variation of the return stroke speed close to the point of initiation. This calls for experimental studies of the luminous features associated with the development of the return stroke within about 100 m

of the point of initiation. In addition to providing a rigorous test of the existing models, the data will serve as the foundation on which the next stage of return stroke models will be built.

Even though our knowledge about the mechanism of the return stroke is still far from complete, the modellers have built up theories and syntheses to fill in the gaps. Ultimately, it may be found that the final consensus will depend to a large extent on the diligent work of experimentalists, which will eventually weed out the bad theories from the good ones.

6.9 Appendix: analytical expression for the velocity profile as predicted by the subsequent return stroke model 1 (section 6.4.2.6.1)

The velocity profile of the subsequent return stroke can be represented by the following equations:

$$v = v_1 + (v_2/2)[2 - \exp(-(z-1)/\lambda_1) - \exp(-(z-1)/\lambda_2)], \quad 1.0 \leq z \leq 50 \tag{6.120}$$

$$v = v_3 \exp(-z/\lambda_3) + v_4 \exp(-z/\lambda_4) \quad \text{for } 50 \leq z \tag{6.121}$$

The unknown variables in the above equations for a number of peak currents in the range of 3–30 kA are given in Table 6.1. The values of these variables for other peak currents in this range can be obtained through linear extrapolation. For a given peak current the above equations give the velocity profile. This velocity profile can be used in eqn. 6.50 to evaluate the discharge time constants. Once these are evaluated the spatial and temporal variation of the current and the electromagnetic fields can be calculated using the standard procedure.

Table 6.1 Parameters of the velocity profile of subsequent return strokes

I_p (kA)	v_1	v_2	v_3	v_4	λ_1	λ_2	λ_3	λ_4
3	7.2×10^7	1.18×10^8	1.9×10^7	1.71×10^8	1.8	6.2	400	900
4	7.8×10^7	1.23×10^8	2.01×10^7	1.81×10^8	1.6	6.6	120	1200
6	8.6×10^7	1.29×10^8	8.6×10^7	1.29×10^8	1.6	6.8	370	2200
9	9.5×10^7	1.34×10^8	6.87×10^7	1.60×10^8	1.4	7.4	320	2000
12	1.02×10^8	1.35×10^8	7.11×10^7	1.66×10^8	1.4	7.4	400	2100
15	1.07×10^8	1.37×10^8	4.88×10^7	1.95×10^8	1.2	8.0	330	2000
18	1.12×10^8	1.36×10^8	4.96×10^7	1.98×10^8	1.2	7.8	400	2100
21	1.16×10^8	1.36×10^8	5.04×10^7	2.02×10^8	1.2	8.0	400	2200
24	1.2×10^8	1.34×10^8	2.54×10^7	1.29×10^8	1.2	7.6	340	2100
27	1.23×10^8	1.34×10^8	2.57×10^7	1.31×10^8	1.2	7.8	400	2100
30	1.26×10^8	1.33×10^8	2.59×10^7	1.33×10^8	1.2	7.8	400	2200

6.10 References

1 NORINDER, H.: CIGRE, paper 303, 1939
2 HILL, H.L.: *J. Geophys. Res.*, 1971, **76**, p.637
3 SAHA, M.H.: *Phil. Mag.*, 1920, **40**, p.472
4 DRABKINA, S.I.: *J. Exp. Theor. Phys. (USSR)*, 1951, **21**, p.473
5 BRAGINSKI, S.I.: *J. Exp. Theor. Phys. (USSR)*, 1958, **34**, p.1548
6 PLOOSTER, M.N.: *Phy. Fluids*, 1970, **13**, p.2665
7 PLOOSTER, M.N.: *Phys. Fluids*, 1971, **14**, p.2111
8 PLOOSTER, M.N.: *Phys. Fluids*, 1971, **14**, p.2124
9 BRODE, H.L.: *Phys. Fluids*, 1959, **2**, p.217
10 PAXTON, A.H., GARDINE, R.L., and BAKER, L.: *Phys. Fluids*, 1986, **29**, p.2736
11 CABRERA, V., and COORAY, V.: *J. Electrost.*, 1992, **28**, p.187
12 TAKAGI, N., WANG, D., WATANABE, T., ARIMA, I., TAKEUCHI, T., SIMIZU, M., KATURAGI, Y., YOKOYA, M., and KAWASHIMA, Y.: *J. Geophys. Res.*, 1988, **103**, pp.14131–14134
13 ORVILLE, R.E., UMAN, M.A., and SLETTEN, A.M.: *J. Appl. Phys.*, 1967, **39**, p.895
14 ORVILLE, R.E.: *J. Atmos. Sci.*, 1968, **25**, p.839
15 ORVILLE, R.E.: *J. Atmos. Sci.*, 1968, **25**, p.852
16 ORVILLE, R.E.: *J. Atmos. Sci.*, 1968, **25**, p.827
17 BAKER, L., GARDNER, L., PAXTON, A.H., BAUM, C.E., RISON, W. in GARDNER, R.L. (Ed.): 'Lightning electromagnetics' (Hemisphere Publishing Co., New York, 1990) pp.365–374
18 OETZEL, G.N.: *J. Geophys. Res.*, 1968, **73**, p.1889
19 PRICE, G.H., and PIERCE, E.T.: *Radio Sci.*, 1977, **12**, p.381
20 LITTLE, P.F.: *J. Phys. D, Appl Phys.*, 1978, **11**, p.1893
21 AMORUSO, V., and LATTARULO, F.: *IEEE Trans. Electromagn. Compat.*, 1993, **35**, p.3317
22 STRAWE, D.F.: Proceedings of Fed. Aviation Admin./Florida Inst. Rep. FAA-RD-79-6,9, 1979
23 ANDRÉ, M., MATTOS, M.A.F., and CHRISTOPOULOS, C.: *IEEE, Trans. Electromagn. Compat.*, 1988, **30**, p.401
24 SPITZER, L., and HÄRM, R.: *Phys. Rev.*, 1953, **89**, p.977
25 BAUM, C., and BAKER, L. in GARDNER, R.L. (Ed.): 'Lightning electromagnetics', (Hemisphere Publishing Co., New York, 1990) pp.17–40
26 BAUM, C.E. in GARDNER, R.L. (Ed.): 'Lightning electromagnetics', (Hemisphere Publishing Co., New York, 1990) pp.101–114
27 BAKER, L. in GARDNER, R.L. (Ed.): 'Lightning electromagnetics', (Hemisphere Publishing Co., New York, 1990) pp.63–74
28 BOROVSKY, J.E.: *J. Geophys. Res.*, 1995, **100**, p.2697
29 NUCCI, C.A., DIENDORFER, G., UMAN, M.A., RACHIDI, F., IANOZ, M., and MAZZETTI, C.: *J. Geophys. Res.*, 1990, **95**, p.20395
30 BRUCE, C.E.R., and GOLDE, R.H.: *J. IEE*, 1941, **88**, p.487

31 DENNIS, A.S., and PIERCE, E.T.: *Radio Sci.*, 1964, **779**
32 UMAN, M.A., and McLAIN, D.K.: *J. Geophys. Res.*, 1969, **74**, p.6899
33 WILLETT, J.C., BAILEY, J.C., IDONE, V.P., EYEBERT-BERARD A., and BARRET, L.: *J. Geophys. Res.*, 1989, **94**, p.13275
34 THOTTAPPILLIL, R., and UMAN, M.A.: 'Comparison of lightning return stroke models', *J. Geophys. Res.*, 1993, **98**, p.22903–22914
35 UMAN, M.A., RAKOV, V.A., SCHNETZER, G.H., RAMBO, K.J., CRAWFORD, D.E., and FISHER, R.J.: *J. Geophys. Res.*, 2000, **105**, pp.15577–15595
36 NUCCI, C.A., MAZZETTI, C., RACHIDI, F., IANOZ, M.: Proceedings of the international conference on *Lightning protection*, Graz, 1988.
37 RAKOV, V.A., and DULZON, A.A.: 9th international symposium on *EMC*, Zurich, Switzerland, 44H1, 229, 1991
38 WAGNER, C.F.: *Trans. Am. Inst. Elect. Engrs.*, 1956, **1232**, p.1985
39 LIN, Y.T., UMAN M.A., and STANDLER, R.B.: *J. Geophys. Res.*, 1980, **85**, p.1571
40 MASTER, M.J., UMAN, M.A., LIN, Y.T., and STANDLER, R.B.: *J. Geophys. Res.*, 1982, **86**, p.12127
41 HEIDLER, F.: 'Travelling current source model for LEMP calculation', Proceedings of 6th international symposium on *EMC*, Zurich, Switzerland, 29F2, 157–162, 1985
42 COORAY, V.: Proceedings of the international conference on *Lightning and Static Electricity*, UK, 6B.4.1, 1989
43 COORAY, V.: *J. Electrostat.*, 1993, **30**, 343
44 RAKOV, V., and UMAN, M.A.: *IEEE Trans. Electromagn. Compat.*, 1998, **40**, pp.403–426
45 GOMES, C., and COORAY, V.: *IEEE Trans. Electromagn. Compat.*, 2000, **42**, pp.82–96
46 COORAY, V.: *IEEE Trans. Electromagn. Compat.*, 1998, **40**, pp.427–435
47 COORAY, V.: *Physica Scripta*, 1997, **55**, p.119–128
48 COORAY, V., and GALVAN, A.: Proceedings of the 25th international conference on *Lightning protection* (ICLP), Rhodos, Greece, 2000
49 COORAY, V., ZITNIK, M., STRANDBERG, G., RAHMAN, M., MONTANO, R., and SCUKA, V.: Proceedings of the 26th international conference on *Lightning protection* (ICLP), Krakow, Poland, 2002, pp. 50–55
50 RAKOV, V.: *Recent. Res. Devel. Geophysics*, 1999, **2**, pp.141–171
51 CIGRE, paper 63, report of the working group 01 (lightning) of study committee 33, 1991
52 LETEINTURIER, C., HAMLIN, J.H., and EYBERT-BERARD, A.: *IEEE Trans. Electromagn. Compat.*, 1999, **41**, pp.265–271
53 FISHER, R.J., SCHNETZER, G.H., THOTTAPPILLIL, R., RAKOV, V.A., UMAN, M.A., and GOLDBERG, J.D.: *J. Geophys. Res.*, 1993, **98**, p.22887–22902
54 MACH, D.M., and RUST, W.D.: *J. Geophys. Res.*, 1989, **94**, p.13237

55 LIN, Y.T., UMAN, M.A., TILLER, J.A., BRANTLEY, R.D., BEASLEY, W.H.: *J. Geophys. Res.*, 1979, **84**, pp.6307–6314
56 WEIDMAN, C.D., and KRIDER, E.P.: *J. Geophys. Res.*, 1978, **83**, pp.6239–6247: correction, *J. Geophys. Res.*, 1978, **87**, p.7351
57 RAKOV, V., and UMAN, M.A.: *J. Geophys. Res.*, 1990, **95**, pp.5455–5470
58 WILLETT, J.C., and KRIDER, E.P.: *IEEE Trans. Antennas Propag.*, 2000, **48**, pp.1452–1451
59 WILLETT, J.C., KRIDER, E.P., and LETENTURIER, C.: *J. Geophys. Res.*, 1998, **103**, pp.9027–9034
60 UMAN, M.A., RAKOV, V.A., SCHNETZER, G.H., RAMBO, K.J., and SCHOENE, J.: *J. Geophys. Res.*, 2002, **107**, pp. ACL 1–1 to ACL 1–11
61 GALLIMBERTI, I.: *J. Phys.*, 1979, **40**, pp.C7–C193
62 GOLDE, R.H. in GOLDE, R.H. (Ed.): 'Lightning, Vol. II' (Academic Press, New York, 1977) pp.546–576
63 BONDIOU-CLERGERIE, A., and GALLIMBERTI, I.: *J. Phys. D, Appl. Phys.*, 1994, **27**
64 YOKOYAMA, S.: Presented at CIGRE SC 33 (WG 01) meeting, Milano, 1995
65 BERGER, K., ANDERSON, R.B., and KRÖNINGER, H.: *Electra*, 1975, **40**, pp.101–119
66 COORAY, V.: *J. Geophys. Res.*, 1984, **84**(11), pp.807–811, 815
67 COORAY, V., FERNANDO, M., SORENSSEN, T., GÖTSCHL, T., and PEDERSEN, A.: *Journal of Atmospheric and Solar-Terrestrial Physics*, 2000, **62**, pp.583–600
68 GARBAGNATI, E., and LO PIPARO, G.B.: *Elektrotech. Z. ETZ A*, 1982, **103**, pp.61–65
69 DIENDORFER, G., and UMAN, M.A.: *J. Geophys. Res.*, 1990, **95**, pp.13621–13644
70 THOTTAPPILLIL, R., McLAIN, D.K., UMAN M.A., DIENDORFER, G.: *J. Geophys. Res.*, 1991, **96**, p.17143–17150
71 LUNDHOLM, R.: Ph.D. thesis, KTH, Stockholm, Sweden, 1957
72 WAGNER, C.F.: *Trans. Am. Inst. Elect. Engrs.*, 1963, **82**, pp.609–617
73 RAI, J.: *J. Atmos. Terr. Phys.*, 1978, **40**, pp.1275–1280
74 TOEPLER, M.: *ETZ*, 1932, **A53**, p.1219
75 ALBRIGHT, N.W., and TIDMAN, D.A.: *Phys. Fluid*, 1972, **15**, p.86
76 COORAY, V.: *IEEE Trans. Electromagn. Compat.*, 2003, **45**, pp.101–108
77 COORAY, V., and GOMES, C.: *J. Electrostat.*, 1998, **43**, pp.163–172
78 PAPOV, M., HE, S., and THOTTAPPILLIL, R.: *J. Geophys. Res.*, 2000, **105**, pp.24469–24481
79 COORAY, V., MONTANO, R., and RAKOV, V.: 'A channel base current model to represent both negative and positive first return strokes with connecting leaders' to be published in the *Journal of Electrostatics*, 2003

Chapter 7

The effects of propagation on electric radiation fields

Vernon Cooray

7.1 Introduction

The protection of structures and electrical systems from lightning requires knowledge of the characteristics of electromagnetic fields generated by lightning and of the statistical distribution of lightning current parameters. The statistical distributions of lightning current parameters can be obtained by recording the currents in lightning flashes striking high towers [1]. However, the presence of the tower itself may distort these distributions to some extent and there is always the unresolved question of whether these distributions are valid for lightning flashes striking flat regions. On the other hand, all the information necessary to obtain the characteristics of currents in lightning return strokes is embedded in the lightning-generated electromagnetic fields. However, in propagating from source to measuring station, the electromagnetic fields will change in a number of ways depending on the geometry and the electrical characteristics of the propagation path. For example, in propagating over finitely conducting ground, the electromagnetic fields will lose their higher frequency components. As a result, the amplitude of the electromagnetic field decreases, and the rise time of the electromagnetic field increases with increasing propagation distance over land [2–6]. When the ground is stratified the propagation effects may enhance or attenuate high frequencies, depending on the conductivity and the depth of the conducting layers.

To avoid these propagation effects many researchers have measured the electromagnetic fields in ways which minimise them. For example, by measuring electromagnetic fields from lightning flashes striking the sea so that the propagation path of the electromagnetic fields was over sea water [6–10]. Sea water is a good conductor with a conductivity of about $4\,\mathrm{S/m}$ and, in propagating over salt water, electromagnetic fields are subjected to much less severe propagation effects than when they propagate over land. However, sea water is not a perfect conductor,

and in the presence of wind the sea surface cannot be considered as a smooth surface. The finite conductivity and roughness of the ocean surface leads to the attenuation and scattering of high frequencies in the lightning-generated electromagnetic fields. Furthermore, during some of the experimental observations mentioned above, the electromagnetic field recording station was situated in such a way that the propagation path was entirely over sea water except for the last few hundred metres, which was over land. The presence of this strip of land over which the electromagnetic fields have propagated can enhance the propagation effects. Moreover, in general the ground is not homogeneous. In many cases a more realistic model is to represent the ground as several layers with different conductivities stratified horizontally. In this Chapter, the impact that the different ground conditions and the propagation paths have on the lightning-generated electromagnetic fields is presented.

The theoretical side of the propagation effects on lightning-generated electromagnetic fields was not devoted much attention until recent years perhaps because the calculations were too time consuming to be feasible and no good return stroke models that can mimic the return stroke fields accurately were available. The author has been trying to rectify this situation over the last decade and, although the author has not been alone in this task, he has published a large number of papers on the subject. Thus, although the author apologises for the extensive number of references to work that he has conducted he hopes that the readers will be inspired by the progress made and will join the author in his research.

The discussion given in this Chapter will be confined to propagation distances of less than about 300 km. Therefore, the curvature of the earth and the ionospheric effects have been neglected in the analyses. Readers interested in analysing the propagation effects caused by long distance propagation are directed to a review article published by Wait [11]. In addition to new simulations carried out by the author, the material presented has been adapted from the published work conducted by the author with his collaborators [4,6,12–17].

7.2 Theory

7.2.1 Basic equations

Let us assume that the lightning channel is straight and vertical. The lower end of the channel can be either at ground level (for return strokes) or located inside the cloud (for cloud flashes). The relevant geometry for the problem under consideration is given in Figure 7.1. The point of observation is located at P on ground level. The horizontal distance between the point of observation and the vertical channel is D. The variation of the current in this channel as a function of height and time is denoted by $I(z, t)$. The radiation field generated by the discharge (return stroke or cloud flash), $E_z(t, D)$, at the point of observation when the ground is perfectly conducting is given by:

$$E_z(t, D) = \frac{1}{2\pi\varepsilon_0} \int_{Z_i}^{Z_f} \frac{\sin^2\theta}{c^2 R} \frac{dI(t - R/c, z)}{dt} dz \tag{7.1}$$

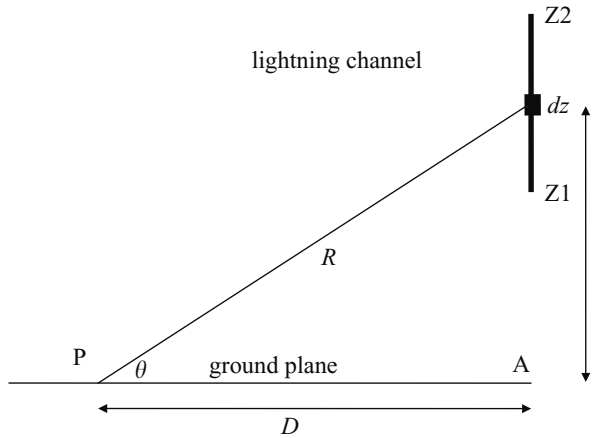

Figure 7.1 *The channel geometry relevant to the calculation of the effects of propagation over a homogeneous ground. The origin of the discharge is at* $Z1$. *In the case of return strokes* $Z1 = 0$

where c is the speed of light in free space, ε_0 is the electric permittivity of free space. The geometrical parameters are defined in Figure 7.1. To find the radiation field when the ground is finitely conducting, let us write eqn. 7.1 in the frequency domain:

$$e_z(j\omega, D) = \frac{1}{2\pi\varepsilon_0}\int_{Z_i}^{Z_f} \frac{\sin^2\theta}{c^2 R} i(j\omega, z)\, j\omega e^{-j\omega R/c}\, dz \tag{7.2}$$

where $i(j\omega, z)$ and $e_z(j\omega, D)$ are related to the time domain quantities $I(t, z)$ and $E_z(t, D)$ through the Fourier transform:

$$i(j\omega, z) = \int_0^\infty I(t, z) e^{-j\omega t}\, dt \tag{7.3}$$

$$e_z(j\omega, D) = \int_0^\infty E_z(t, D) e^{-j\omega t}\, dt \tag{7.4}$$

The radiation field in the frequency domain $e_{z,\sigma}\ (j\omega, D)$ when the ground is finitely conducting is given by:

$$e_{z,\sigma}(j\omega, D) = \frac{1}{2\pi\varepsilon_0}\int_{Z_i}^{Z_f} \frac{\sin^2\theta}{c^2 R} S(z, D, j\omega)\, i(j\omega, z)\, j\omega e^{-j\omega R/c}\, dz \tag{7.5}$$

where $S(z, D, j\omega)$ is the attenuation function that describes the effect of the finitely conducting earth.

7.2.2 Homogeneous ground

The attenuation function corresponding to the homogeneous ground, $S(z, D, j\omega) = S_f(z, D, j\omega)$, is given by the equation:

$$S_f(z, D, j\omega) = \{[(1 + R_v)] + [(1 - R_v)F(w, z)]\}/2.0 \tag{7.6}$$

where

$$R_v = \frac{\cos\theta - \Delta_0}{\cos\theta + \Delta_0} \tag{7.7}$$

$$\Delta_0 = \frac{k_0}{k}\left[1 - \frac{k_0^2}{k^2}\sin^2\theta\right]^{1/2} \tag{7.8}$$

$$k = k_0[\varepsilon_r - j60\sigma\lambda_0]^{1/2} \tag{7.9}$$

$$k_0 = \frac{2\pi}{\lambda_0} = \omega(\mu_0\varepsilon_0)^{1/2} \tag{7.10}$$

$$w = -\frac{jk_0R}{2\sin^2\theta}[\cos\theta + \Delta_0]^2 \tag{7.11}$$

$$F(w) = 1 - j(\pi w)^{1/2}e^{-w}\text{erfc}(jw^{1/2}) \tag{7.12}$$

In these equations, erfc stands for the complementary error function, μ_0 is the magnetic permeability of free space, ε_r is the relative dielectric constant and σ the conductivity of the soil; $j = \sqrt{-1}$.

7.2.2.1 A simplified equation to calculate propagation effects

The propagation effects can be evaluated by numerically solving eqn. 7.5 by substituting in the expression for the attenuation function given in eqn. 7.6. However, Cooray [6] simplified this expression by using the following arguments. Since one is interested in propagation effects, the section of the waveform which is of interest is that occurring within the first few microseconds. This is the case because the rapidly varying part of the waveform occurs within the first few microseconds. If the speed of propagation of the discharge front is about 10^8 m/s, the length of the channel that contributes to the radiation field during this time would not be larger than a few hundred metres. Thus, in eqn. 7.5, the attenuation function $S(z, D, j\omega)$ can be replaced by $S(Z_i, D, j\omega)$ which is the attenuation function corresponding to a dipole located at the lower end of the channel. With this approximation, eqn. 7.5 can be transformed into the time domain to find an expression for $E_{z,\sigma}(t, D)$ which is the vertical electric field over finitely conducting ground. The result is:

$$E_{z,\sigma}(t, D) = \int_0^t E_z(t - \tau, D)S_f(Z_i, D, \tau)\,d\tau \tag{7.13}$$

where $S_f(Z_i, D, t)$ is the inverse Fourier transformation of $S_f(Z_i, D, j\omega)$ and $E_z(t, D)$ is the radiation field over perfectly conducting ground and is given by

eqn. 7.1. One can obtain $S_f(Z_i, D, t)$ through a direct Fourier transformation of $S_f(Z_i, D, j\omega)$. In the case of return strokes, $Z_i = 0$ and hence $S_f(Z_i, D, t) = S_f(0, D, t)$. Wait [18,19] derived a time domain expression for $S_f(0, D, t)$:

$$S_f(0, D, t) = \frac{d}{dt}\left\{1 - \exp\left(-\frac{t^2}{4\zeta^2}\right) + 2\beta(\varepsilon_r + 1)\frac{J(x)}{t}\right\} \tag{7.14}$$

where $J(x) = x^2(1 - x^2)\exp(-x^2)$, $x = t/2\zeta$ $\beta = 1/\mu_0\sigma c^2$ and $\zeta^2 = D/2\mu_0\sigma c^3$. Comparison of this expression with that obtained through a direct Fourier transformation of $S_f(0, D, j\omega)$ shows that it provides a good approximation for the time domain attenuation function if the propagation distance is larger than about one kilometre (unpublished results of the author). For smaller distances it may be necessary to obtain the function $S_f(0, D, t)$ from $S_f(0, D, j\omega)$ by performing a direct Fourier transformation. Thus, if the lightning-generated radiation fields before they are distorted by propagation effects are available, eqns 7.13 and 7.14 can be used to derive the fields over finitely conducting ground. It is important to point out that in eqn. 7.14, the third term inside the bracket takes into account the effects of the displacement current in the ground. Calculations presented in [6] and unpublished results of the author show that, as far as the rise times and the attenuation of the peak of the waveforms are concerned, the contribution from this term can be neglected if the propagation distance is larger than about 1 km. Consequently, the propagation effects over homogeneous ground are mainly governed by the parameter D/σ and the results can be normalised against this parameter.

7.2.2.2 Experimental validation of the simplified equation

The theoretical calculations of Cooray and Ming [12] and unpublished results of the author, show that eqn. 7.13 is valid for distances as small as 100 m from the lightning return stroke channel. In order to test the validity of this equation experimentally, Cooray *et al.* [15] conducted an experiment in Denmark. In the experiment, the electric fields from lightning return strokes striking the sea were measured simultaneously at two stations, one located on the coast and the other situated 250 km inland. The antenna system used in the measurements could record electromagnetic fields to a resolution of better than 5 ns and the total decay time constant of the antenna system was 20 ms; which is much longer than the duration of the electromagnetic fields of interest. The signals coming out from the antenna system were recorded with a resolution of 10 ns in a transient recorder working in pretrigger record mode. The propagation path of the electromagnetic fields from the strike point to the coastal station was over salt water, with the exception of the last 10–50 metres. Thus, the electric fields measured at this station can be assumed to represent the undistorted electric fields generated by return strokes (i.e., $E_z(t, D)$ of eqn. 7.13).

Of course, return stroke radiation fields can be distorted to some extent even when propagating over an ocean surface, and the measured fields may not be a faithful representation of the fields that would be present if the ground were a perfect

conductor. Moreover, the propagation effects are enhanced by a rough ocean surface. Furthermore, the strip of land (a sandy beach) between the edge of the sea and the measuring station could also enhance the propagation effects. However, the effects on the electromagnetic fields as they propagate 250 km over finitely conducting ground are much larger than those introduced by an ocean surface and the narrow strip of land (see sections 7.3.5 and 7.3.6). Thus, as far as the propagation effects caused by a path over land are concerned, the radiation fields that have propagated over the ocean surface can be assumed to represent the undistorted fields.

During the experiment more than 25 waveforms were measured simultaneously at the two stations. For each waveform measured at the coastal station, the electric field that would be anticipated at the inland station was calculated for several conductivities using eqn. 7.13 with $D = 250$ km. The shapes of the calculated and the measured waveforms at the inland station were compared by normalising their amplitudes to unity. The comparison was done with more than 20 waveforms and in each case a good agreement was found between the calculation and the measurement for values of conductivities in the vicinity of 0.01 S/m. The available data obtained from measurements of the resistance of buried vertical conductors does indicate that the conductivity at some points of the propagation path of lies close to this value. Several examples of this comparison are shown in Figure 7.2. To check whether this agreement is unique to the above mentioned conductivity, calculations were also made for several other conductivities. As shown in Figure 7.3, when values other than 0.01 S/m are tried the agreement between the measurements and the theory deteriorates. The reason why Cooray *et al*. [15] have not compared the exact amplitudes of the measured and calculated waveforms at the distant station is the following. The calibration of the inland antenna did not have an accuracy suitable for a direct comparison of amplitudes to be made. However, both the decrease in amplitude and the change in shape are determined by the attenuation of the high frequencies in the electric field. Thus the change in the shape of the radiation fields owing to the propagation will also uniquely determine the change in the amplitude of the waveform. Because of this, a comparison of the shapes alone suffices to test the validity of propagation eqn. 7.13 and the results show that this equation can be used to predict the propagation effects to a high degree of accuracy.

7.2.3 Stratified ground

The geometry relevant to the question under consideration is shown in Figure 7.4. Let us represent the ground as a stratum of thickness h, conductivity σ_1 and relative dielectric constant ε_1 below which the medium is semiinfinite with conductivity σ_2 and dielectric constant ε_2. The lightning channel is located at a distance D from the point of observation. As before, the vertical electric field at distance D is then given by the equation:

$$E_{z,\sigma}(t, D) = \int_0^t E_z(t - \tau, D) S_{str}(0, D, \tau)\, d\tau \tag{7.15}$$

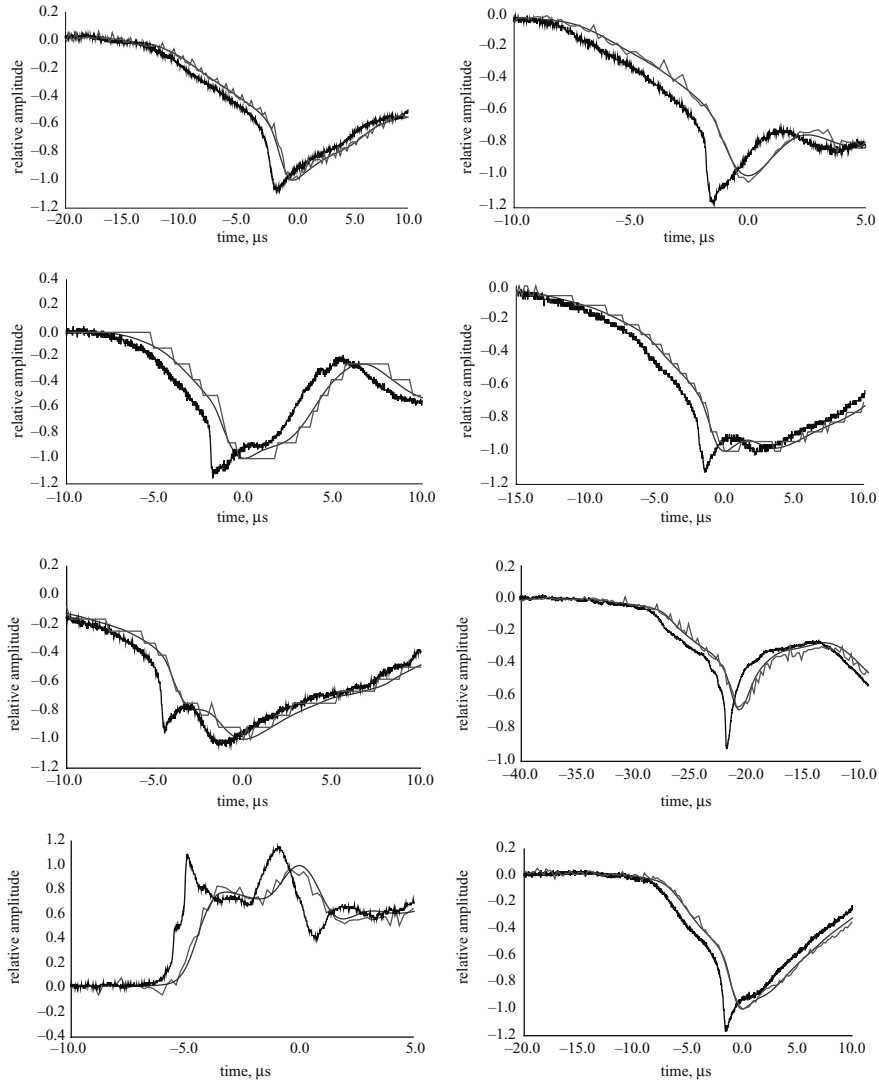

Figure 7.2 *Comparison between theory and experiment. The thick line denotes the radiation field measured at the coastal station, the rugged line denotes the radiation field measured at the inland station and the smooth line represents the calculated radiation field at the inland station using eqn. 7.13.* (adapted from [15])

where $S_{str}(0, D, t)$ is the attenuation function corresponding to the stratified ground. An expression for $S_{str}(0, j\omega)$ is given by Wait [20] and is as follows:

$$S_{str}(0, D, jw) = 1 - j(\pi w)^{1/2} e^{-w} \text{erfc}(jw^{1/2}) \tag{7.16}$$

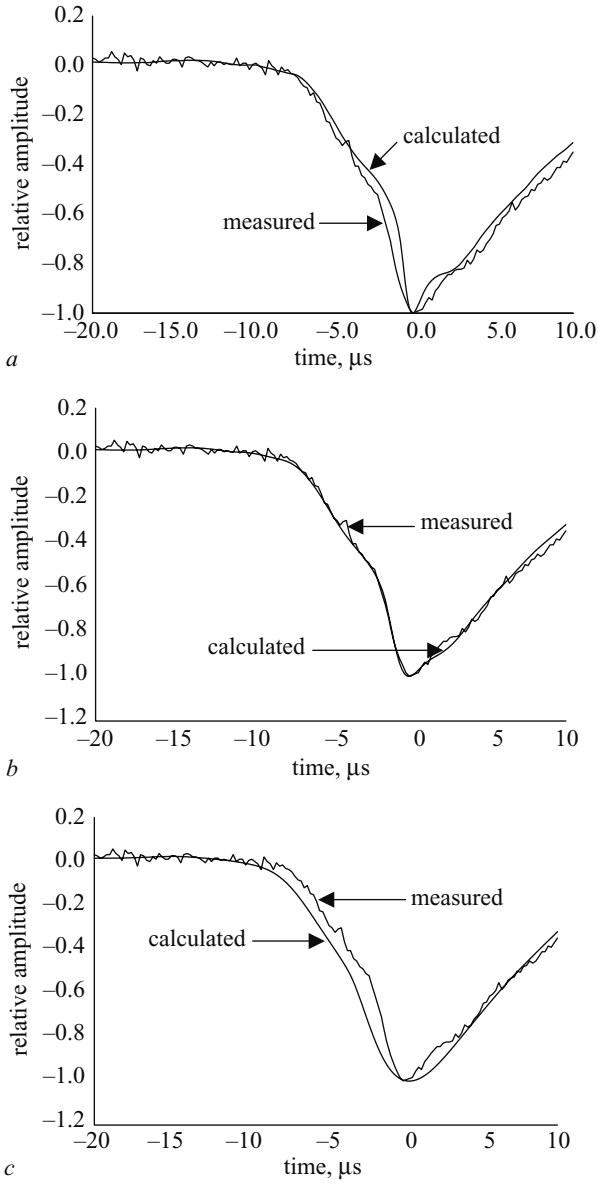

Figure 7.3 *Comparison of the calculated and measured waveforms at the inland station when the conductivity used in the calculations differ from that of the actual path*

a the conductivity used in the calculation was 0.05 S/m
b the conductivity used in the calculation was 0.01 S/m which is the actual conductivity of the path of propagation
c the same calculation was repeated for 0.002 S/m

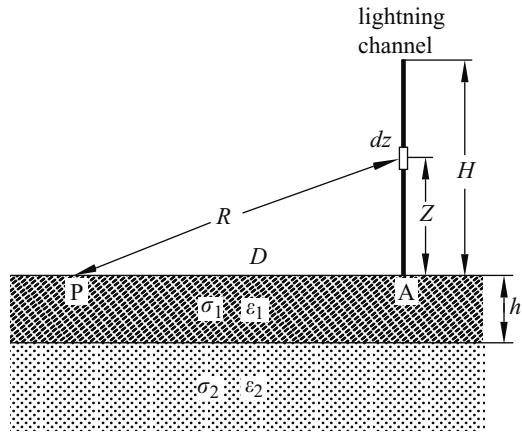

Figure 7.4 Geometry relevant to the calculation of propagation effects over stratified ground

where w is given by:

$$w = -\frac{jk_0 D}{2}\Delta_{eff}^2 \tag{7.17}$$

In this equation Δ_{eff} is the effective normalised surface impedance of the stratified ground; it is defined as:

$$\Delta_{eff} = \Delta_1 Q \tag{7.18}$$

where

$$\Delta_1 = \frac{k_0}{k_1}\left[1 - \frac{k_0^2}{k_1^2}\right]^{1/2} \tag{7.19}$$

$$Q = \frac{k_1 + k_2 \tan h(k_1 h)}{k_2 + k_1 \tan h(k_1 h)} \tag{7.20}$$

with

$$k_1 = k_0[\varepsilon_1 - j60\sigma_1\lambda_0]^{1/2} \tag{7.21}$$

$$k_2 = k_0[\varepsilon_2 - j60\sigma_2\lambda_0]^{1/2} \tag{7.22}$$

Note that when $\sigma_1 = \sigma_2$ and $\varepsilon_1 = \varepsilon_2$ the equations can be reduced to those corresponding to homogeneous ground. In the above equation λ_0 is the free space wavelength. The function $S_{str}(0, D, t)$ can be obtained through a direct Fourier transformation of the function $S_{str}(0, D, j\omega)$.

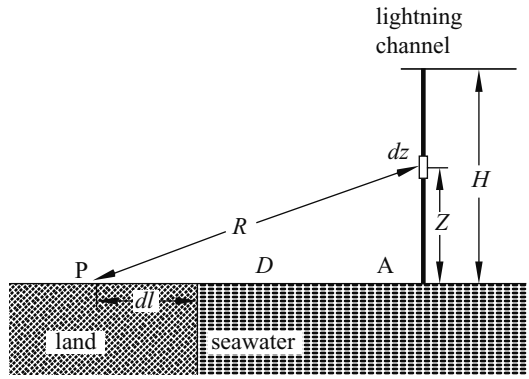

Figure 7.5 Geometry relevant to the calculation of propagation effects caused by a sea–land boundary

7.2.4 Propagation along a mixed path of two sections

The geometry of the situation under consideration is shown in Figure 7.5. The lightning channel is situated over medium 1 at a distance $D - d\ell$ from the boundary. The point of observation is situated over medium 2 at a distance $d\ell$ from the boundary. The boundary line is assumed to be straight, and the direction in which the electromagnetic fields propagate is assumed to be perpendicular to the boundary line. Under these circumstances the vertical electric field at the point of observation is given by:

$$E_{z,\sigma}(t, D) = \int_0^t E_z(t - \tau, D)\, S_{sl}(0, D, \tau)\, d\tau \tag{7.23}$$

where $S_{sl}(0, D, t)$ is the attenuation function corresponding to the two sections of path. An expression for $S_{sl}(0, D, j\omega)$ as given by Wait [21, 22] is:

$$S_{sl}(0, D, j\omega) = S_1(0, D, j\omega) - \frac{1}{2}\left[\frac{jD}{\lambda_0}\right]^{1/2} \Delta_2 - \Delta_1 \int_0^{d\ell} \frac{S_1(0, D - x, j\omega) S_2(0, x, j\omega)}{(x\{D - x\})^{1/2}}\, dx \tag{7.24}$$

where Δ_1 and Δ_2 are the surface impedances of mediums 1 and 2 respectively, and S_1 and S_2 are the respective attenuation functions for these mediums. The above expression for the attenuation function has been experimentally tested in a small scale model in the laboratory by King *et al.* [23, 24] using microwaves. The results showed that this expression is capable of accurately predicting the propagation effects on electromagnetic fields as they cross a boundary between two finite conductors.

As mentioned previously, in the case of finitely conducting and homogeneous ground, the propagation effects for distances of more than about 1 km are mainly determined by the parameter (D/σ). Cooray and Perez [17] investigated the possibility of replacing the two-section path with homogeneous land with an effective

conductivity. They showed that when the source and the point of observation are located at a distance larger than about 10 km from the boundary, the two-section path of lengths d_1 and d_2 with respective conductivities σ_1 and σ_2 can be replaced by homogeneous land with an effective conductivity, σ_e, given by:

$$\sigma_e = \frac{\sigma_1 \sigma_2 D}{\sigma_1 d_2 + \sigma_2 d_1} \tag{7.25}$$

with $D = d_1 + d_2$. Using this formula the results obtained for homogeneous ground can be used to estimate the propagation effects of a two-section path.

7.2.5 Propagation across a finitely conducting rough ocean surface

Let us consider the situation in which the lightning channel is situated over a finitely conducting rough ocean surface. As before, the vertical electric field at distance D is given by the equation:

$$E_{z,\sigma}(t, D) = \int_0^t E_z(t - \tau, D) S_{ro}(0, D, \tau)\, d\tau \tag{7.26}$$

where $S_{ro}(0, D, t)$ is the attenuation function corresponding to the rough ocean surface. To take into account the effect of the roughness of the ocean surface on the attenuation function it is first necessary to describe mathematically the geometry of the rough ocean surface. If $z = 0$ is the flat ocean surface, then a rough ocean surface can be represented by the parameter $\zeta(x, y)$ which is the surface height above the $z = 0$ plane. When the surface height is a nonperiodic random variable it can be represented by its Fourier spectrum $V(\gamma, \eta)$ where γ (this should not be confused with the same symbol used to characterise the propagation effects) and η are the radial wave numbers (or spatial frequencies) in the x and y directions, respectively. There are several models available in the literature for the wave height spectrum of a rough ocean surface. Ming and Cooray [14] considered a Newmann–Pierson spectrum as proposed by Kinsman [25]. The form of this spectrum is:

$$V(\gamma, \eta) = \frac{C(\gamma \cos\alpha + \eta \sin\alpha)^2}{g^{5/2}(\gamma^2 + \eta^2)^{13/4}} \exp\left[-\frac{2g}{U^2(\gamma^2 + \eta^2)^{1/2}}\right] \tag{7.27}$$

where α is the angle between the direction of the wind and the x axis, U the wind speed, g is the acceleration due to gravity and C is a constant empirically estimated to be $3.05\,\mathrm{m}^2/\mathrm{s}^5$. The mean square height of the ocean waves, σ^2, corresponding to this spectrum is given by:

$$\sigma^2 = \frac{3C}{2}(\pi/2)^{3/2}(U/2g)^5 \tag{7.28}$$

Barrick [26,27] showed that the roughness of the ocean surface can be expressed as an increase in the normalised surface impedance. For example, in the case of a rough ocean surface, the effective impedance Δ_{eff} is given by:

$$\Delta_{eff} = \Delta_0 + \delta \tag{7.29}$$

where

$$\Delta_0 = \frac{k_0}{k}\left[1 - \frac{k_0^2}{k^2}\right]^{1/2} \tag{7.30}$$

is the normalised surface impedance of the smooth ocean surface with a conductivity σ and a relative dielectric constant ε_r, and δ is the increase in the surface impedance due to the rough ocean surface. According to Barrick [26,27]:

$$\delta = \frac{1}{4}\int_{-\infty}^{\infty}\int_{-\infty}^{\infty} G(\gamma, \eta)V(\gamma, \eta)\, d\gamma\, d\eta \tag{7.31}$$

where

$$G(\gamma, \eta) = \frac{\gamma^2 + b\Delta_0\left(\gamma^2 + \eta^2 - (\omega/c)\gamma\right)}{b + \Delta_0(b^2 + 1)} + \Delta_0\left(\frac{\gamma^2 - \eta^2}{2} + \frac{\omega}{c}\gamma\right) \tag{7.32}$$

with

$$b = \frac{c}{\omega}\left[(\omega/c)^2 - \left(\gamma^2 + \frac{\omega}{c}\right)^2 - \gamma^2\right]^{1/2} \tag{7.33}$$

Note that in this derivation Ming and Cooray [14] neglected the curvature of the ocean surface having shown that this approximation is valid for distances of less than about a few hundred kilometres.

7.3 Results

7.3.1 Mathematical procedure

One can investigate the propagation effects by measuring the lightning-generated electromagnetic field at two stations, one close to the lightning channel and one far away. In this manner, however, it is difficult to obtain data pertinent to different distances and ground conductivities. It is much easier to make a mathematical evaluation of the propagation effects under different conditions and then use the experimental data to test the validity of the calculations under the conditions in which the experiment is performed. The first step in analysing the propagation effects mathematically is to gather a sample of electric radiation fields from return strokes recorded in such a way that the propagation effects are minimal. One can also use a return stroke model to generate the electromagnetic fields over perfectly conducting ground provided that the model-generated fields have signatures similar to the electromagnetic fields generated by return strokes. Once the undistorted radiation fields are available, they can be used in eqn. 7.13 to calculate the signature of the fields at different distances over finitely conducting ground. The results of the propagation effects on the initial peaks of the negative, positive and triggered return stroke radiation fields presented here

were calculated by Cooray *et al*. [15] using real waveforms. The results of the propagation effects on the electric field derivatives were derived by the author using model simulated signatures. The sets of negative return stroke fields used by Cooray *et al*. [15] were recorded by Bailey and Willett [28] and Izumi and Willett [29] with a time resolution of 0.1 μs. The sets of positive return stroke fields used in the analysis were obtained by Cooray *et al*. [30] with a time resolution of 10 ns. In these experiments the recording stations were located within a few to a few tens of metres from the coast line and the recorded electric radiation fields are from lightning flashes striking the sea at a known distance.

As mentioned in section 7.2.2.1, propagation effects are mainly determined by the ratio σ/D where σ is the conductivity and D is the distance of propagation. Thus, one can normalise the results as a function of σ/D, which is denoted here by γ.

7.3.2 Homogeneous ground

7.3.2.1 Propagation effects on radiation fields of the first return strokes of negative and positive lightning flashes

In order to make the presentation easier, one can define the coefficient of attenuation, A, as $A = E_\sigma/E_\infty$ where E_σ is the peak of the radiation field at a given distance corresponding to a certain γ and E_∞ is the radiation field at that distance over perfectly conducting ground. With this definition of A, the quantity $(1 - A)$ gives the amount of attenuation of the radiation field peak due to propagation over finitely conducting ground. The mean value (based on a large number of return stroke waveforms) of the attenuation coefficient as a function of γ can be represented by the equations:

$$A = 0.24 \exp\left[\frac{-\gamma}{10^7}\right] + 0.24 \exp\left[\frac{-\gamma}{50 \times 10^7}\right] + 0.525 \quad \text{(for negative return strokes)} \tag{7.34}$$

$$A = 0.134 \exp\left[\frac{-\gamma}{1.5 \times 10^7}\right] + 0.312 \exp\left[\frac{-\gamma}{55 \times 10^7}\right] + 0.555 \quad \text{(for positive return strokes)} \tag{7.35}$$

It is important to note that these equations are valid for $10^6\,\mathrm{m^2/S} < \gamma < 2 \times 10^9\,\mathrm{m^2/S}$, and $1\,\mathrm{km} < D < 300\,\mathrm{km}$. The reason why D should not be allowed to exceed 300 km is that the equations used to estimate the propagation effects were derived by neglecting the curvature of the earth, which could lead to significant errors for distances larger than about 300 km. Comparison of the data obtained for positive return strokes with that obtained for negative ones shows that the propagation effects are more pronounced for negative return strokes and the differences are more important for small values of γ. The reason for the latter could be the much narrower initial peaks of negative return stroke fields than positive return stroke fields.

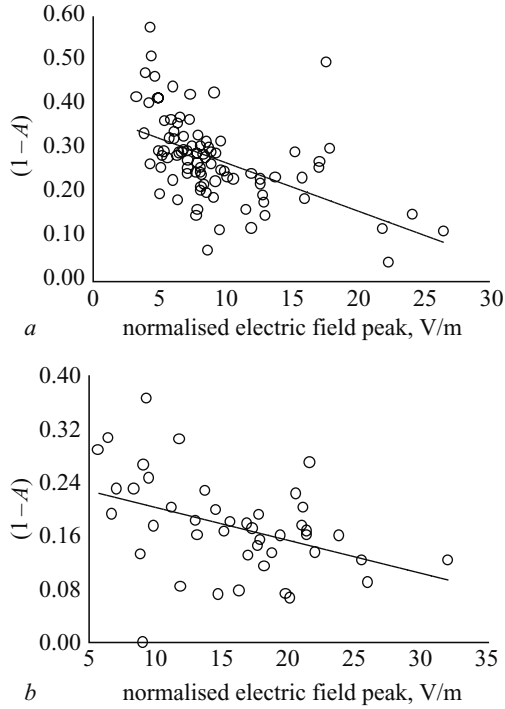

Figure 7.6 *Distribution of $1 - A$ for $\gamma = 10^8\ m^2/S$ as a function of the undistorted peak E_∞. Note that the electric field peak was normalised to 100 km by using the inverse distance dependence. The best linear fit that represents the variation is also shown in each diagram. $A = E_\sigma / E_\infty$ where E_σ is the peak electric radiation field over finitely conducting ground and E_∞ is the peak electric radiation field that would be present if the ground was perfectly conducting. $\gamma = D/\sigma$ where D is the distance of propagation (in metres) and σ is the conductivity in S/m (adapted from [15])*

a negative return strokes
b positive return strokes

The data in Figures 7.6*a* and 7.6*b* shows the distribution of $(1 - A)$ for $\gamma = 10^8\ m^2/s$ as a function of the undistorted peak E_∞ of negative and positive return strokes. Note that the initial peaks were normalised to 100 km by using the inverse distance dependence. In the results, one can observe a slight tendency for the attenuation of the initial peak to decrease with an increase in the initial peak of both the negative and positive return strokes, and the linear correlation coefficients between the two variables for different values of γ lie in the range of -0.58 to -0.6. This decreasing attenuation indicates that the width of the initial peak of both the negative and positive first return stroke radiation fields increases as the peak increases.

Since A is a function of E_∞ one can evaluate how E_σ varies as a function of E_∞. To achieve this goal, Cooray *et al*. [15] have calculated how these two parameters are

Table 7.1 Parameters a and b as a function of γ of the best straight line fit of the form $E_\infty = aE_\sigma + b$ that describes the variation of E_∞ as a function of E_σ of negative return stroke fields

γ	a	b
10^6	1.01	0.32
2×10^6	1.02	0.46
5×10^6	1.03	0.70
10^7	1.04	0.91
2×10^7	1.05	1.15
5×10^7	1.07	1.53
10^8	1.09	1.73
2×10^8	1.12	1.90
5×10^8	1.18	2.22
10^9	1.22	2.37
2×10^9	1.28	2.53

related to each other by fitting a straight line of the form $E_\infty = aE_\sigma + b$ for data obtained for different values of γ. The values of a and b that provided the best fit for different values of γ are given in Table 7.1. All these values can be combined into the following general equation:

$$E_\infty = F_1(\gamma)E_\sigma + F_2(\gamma) \tag{7.36}$$

where

$$F_1(\gamma) = a_0 + a_1 x + a_2 x^2 + a_3 x^3 \tag{7.37}$$

$$F_2(\gamma) = b_0 + b_1 x + b_2 x^2 + b_3 x^3 \tag{7.38}$$

with $x = \log(\gamma/10^7)$. The coefficients of the above equations are tabulated in Table 7.2. Note that the values for the peak radiation field are normalised to 100 km and that the equation is valid for $10^6 < \gamma < 2 \times 10^9$ m^2/S. This equation can be used to correct for the propagation effects once the peak field over finitely conducting ground is known. For example, assume that the peak radiation field measured at a distance of D_x over finitely conducting ground of conductivity σ_x is E_x. Then γ equals D_x/σ_x. Let us denote this by γ_x. The value of E_{nx}, the measured electric field normalised to 100 km, is given by $E_{nx} = D_x \times E_x/10^5$. Substitution of γ_x and E_{nx} for γ and E_σ, respectively, in the above equations will give the value of E_∞, the undistorted field normalised to 100 km. The absolute value of the undistorted field can then be obtained by performing the transformation $E_\infty \times 10^5/D_x$.

Table 7.2 Values of coefficients of eqns 7.37 and 7.38

	Negative return strokes	Positive return strokes
a_0	1.02	1.01
a_1	1.38×10^{-2}	7.62×10^{-3}
a_2	1.91×10^{-3}	4.89×10^{-3}
a_3	8.06×10^{-4}	1.95×10^{-3}
b_0	9.28×10^{-1}	7.91×10^{-1}
b_1	3.26×10^{-1}	2.85×10^{-1}
b_2	1.62×10^{-2}	1.55×10^{-2}
b_3	-3.95×10^{-3}	-3.44×10^{-3}

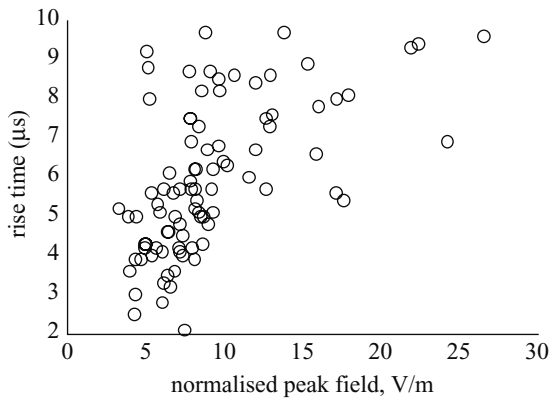

Figure 7.7 The variation of zero to peak rise time of the undistorted radiation fields of negative return strokes as a function of initial field peak (adapted from [15])

Another parameter of physical interest, especially in the case of lightning localisation by time of arrival, is the increase in the rise time of the waveforms when they propagate over finitely conducting ground. Figure 7.7 shows the variation of the zero to peak rise time of the undistorted negative return stroke waveforms as a function of the initial field peak. Figure 7.8 depicts the variation of the mean value of the rise time and Figure 7.9 the variation of the mean value of the increase in rise time as a function of γ. The data presented in Figure 7.8 shows that the rise time of the radiation fields increases by about 1 μs in propagating 100 km over finitely conducting ground of conductivity 0.01 S/m. Such information is of interest in evaluating the errors associated with lightning localisation by the time of arrival method.

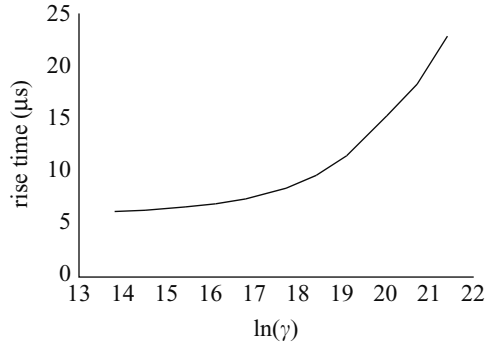

Figure 7.8 *Variation of the mean value of the rise time of the negative return stroke radiation fields as a function of* γ (adapted from [15])

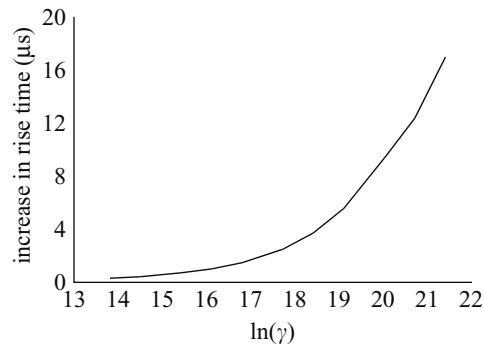

Figure 7.9 *Variation of the mean value of the increase in rise time of the negative return stroke radiation fields as a function of* γ (adapted from [15])

7.3.2.2 The effect of propagation on the time derivative of the radiation fields of negative return strokes

The time derivative of the radiation fields is more sensitive to the propagation effects than the radiation field itself (as far as the peak values are concerned). This is so since the electric field derivative contains more high frequencies than the electric field itself and the high frequencies are selectively attenuated by the propagation effects. This makes it difficult, if not impossible, to obtain a set of electromagnetic fields from measurements of lightning whose derivatives are not distorted by propagation effects. One can, of course, utilise electromagnetic fields simulated by return stroke models provided that the model can generate electromagnetic fields similar to those of undistorted lightning-generated electromagnetic fields. Unfortunately, this takes us round in circles because undistorted fields are not available to make such a comparison. One can overcome this problem as follows. As mentioned previously, the best set of electromagnetic fields available for the study (i.e., data presented in [28,29]

were measured in such a way that they have propagated about 20 km over finitely conducting rough ocean with just the last few tens of metres over finitely conducting land. Thus, before one can utilise a return stroke model for propagation studies, one has to show that the features of the model-predicted electric field derivatives (especially the peak values and the full width at half maximum (FWHM)) do agree with the measured features once the latter has propagated over a path identical to that of the measurements. In Chapter 6 it is shown that this is the case with a model introduced by Cooray [31]. Of course, there might be other models that satisfy this strict requirement. The results presented below are based on the simulations conducted with the above model. Note that, since the signature of the magnetic radiation field is identical to that of the electric radiation field, the results obtained for the electric field derivative are also valid for the magnetic field derivatives. Thus the results presented here also show how the magnetic field derivative is modified by propagation effects.

The way in which the signature of the electric field derivative changes as it propagates along finitely conducting ground is depicted in Figure 7.10. In many engineering studies it is important to know how the distribution of the peak and the FWHM of the electric field derivative change as a function of time. This information is obtained here by using the return stroke model mentioned earlier in a Monte Carlo simulation. The details of this Monte Carlo simulation are given in Chapter 6, but in a nut shell the procedure is the following. The input parameters of the model are the channel base current and the charge per unit length at the lower end of the leader channel. In the Monte Carlo simulation, the peak current, the peak current derivative and the decay time of the channel base current are forced to follow the measured distributions. The charge per unit length at the lower end of the leader channel is connected to the peak channel base current through the experimentally obtained relationship between the peak return stroke current and the peak electric field of the leader at distances less than about 100 m. The whole procedure is validated by generating the distribution of peaks and of the FWHM of electric field derivatives after they have propagated along a two-section path composed of 20 km over a rough ocean surface with the last 50 m over finitely conducting ground (identical to the path of propagation in the studies reported in references [32,33]) and comparing it with the corresponding distributions obtained by Krider *et al*. [32] and Willett and Krider [33]. The results show that the model can predict the distributions of the peak and FWHM of the return stroke field derivatives reasonably well.

Figures 7.11 and 7.12 depicts the distributions of the peaks and FWHM of electric field derivatives at 200 m for $\rho = 0.01$ S/m and $\rho = 0.001$ S/m. For comparison purposes the corresponding distributions over perfectly conducting ground are also shown in the Figures. Note that in propagating 200 m the peak value of the electric field derivative can decrease by about twenty per cent and fifty per cent for $\rho = 0.01$ S/m and $\rho = 0.001$ S/m, respectively. Furthermore, the FWHM can also increase significantly in propagating over the same distance. The mean, median, standard deviation, maximum and minimum values of the distributions of the peaks and the FWHM of electric field derivatives for several distances and conductivities are tabulated in Tables 7.3 and 7.4. The results can be summarised using the following two equations

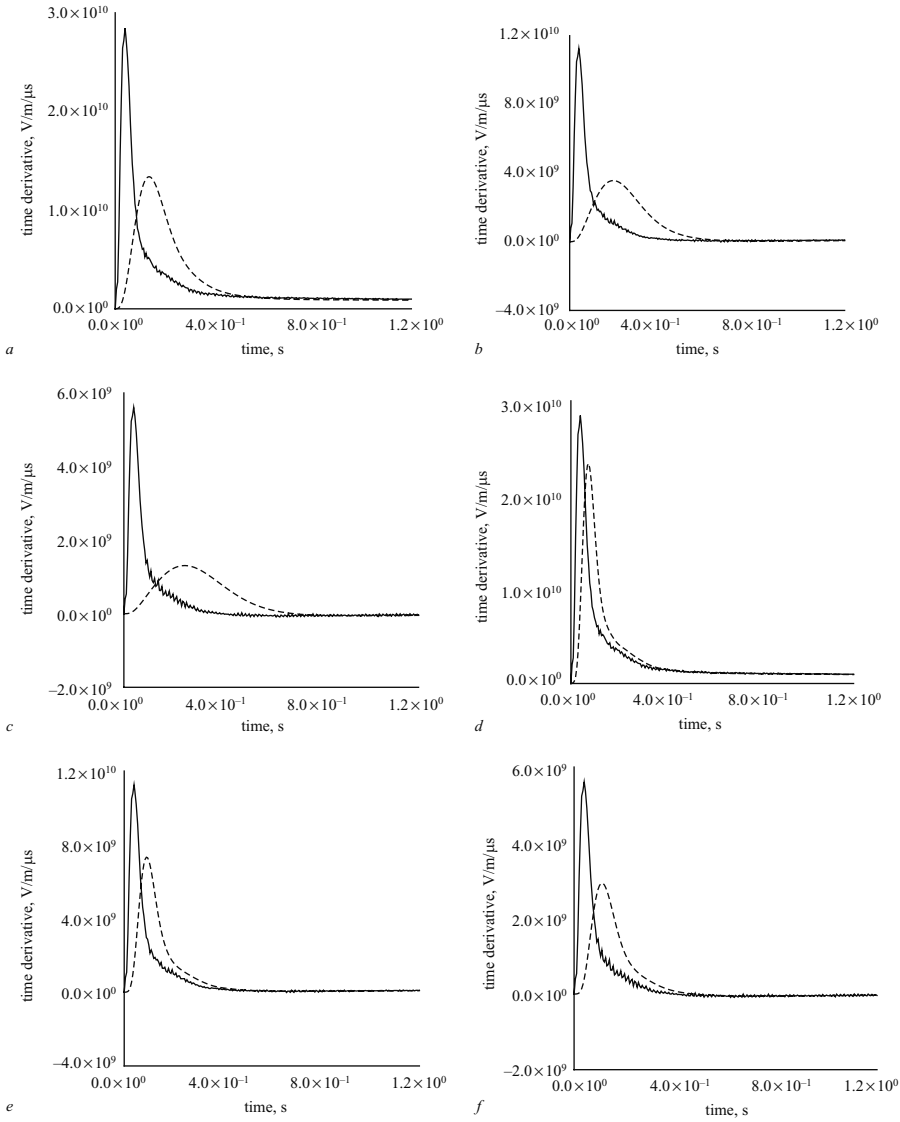

Figure 7.10 *Electric field derivative (dashed line) generated by a 12 kA return stroke at different distances over finitely conducting ground. The solid line depicts the electric field derivative at the same distance that would be present over a perfectly conducting ground. The fields were generated by a return stroke model introduced by Cooray [31]*

a $D = 200\,\text{m}, \sigma = 0.001\,\text{S/m}$
b $D = 500\,\text{m}, \sigma = 0.001\,\text{S/m}$
c $D = 1000\,\text{m}, \sigma = 0.001\,\text{S/m}$
d $D = 200\,\text{m}, \sigma = 0.01\,\text{S/m}$
e $D = 500\,\text{m}, \sigma = 0.01\,\text{S/m}$
f $D = 1000\,\text{m}, \sigma = 0.01\,\text{S/m}$

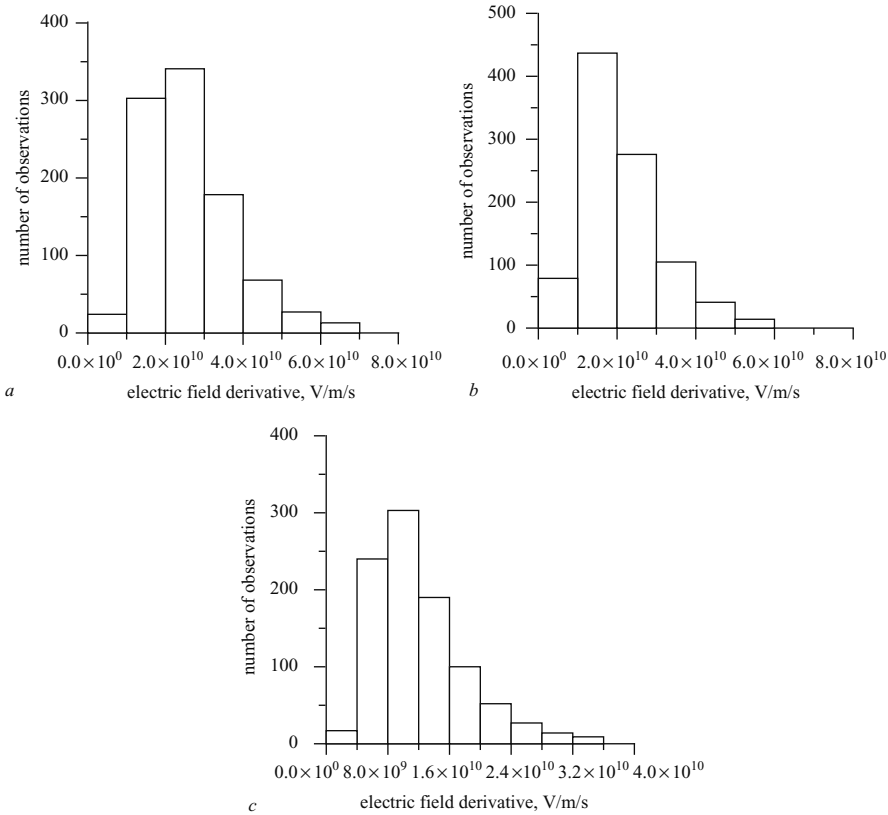

Figure 7.11 Distributions of the peak electric field derivative at a distance of 200 m from the lightning flashes. The distributions are obtained through a Monte Carlo simulation utilising a channel base current model introduced by Cooray [31]

a $\sigma = \infty$; mean $= 2.6 \times 10^{10}$ V/m/s
b $\sigma = 0.01$ S/m; mean $= 2.1 \times 10^{10}$ V/m/s
c $\sigma = 0.001$ S/m; mean $= 1.2 \times 10^{10}$ V/m/s

which show how the mean values of the peak and the FWHM of the electric field derivative vary as a function of γ:

$$E_f = a\gamma^b \tag{7.39}$$

$$W_f = c\gamma^d \tag{7.40}$$

where E_f (in V/m/s) is the mean (normalised to 100 km) of the peak field derivative over finitely conducting ground, W_f (in ns) is the mean FWHM over finitely conducting ground, $a = 21.64, b = -0.39, c = 0.84$ and $d = 0.36$. These equations are valid when $2 \times 10^4 < \gamma < 2 \times 10^7$ m^2/S and 200 m $<$ D $<$ 20 000 m.

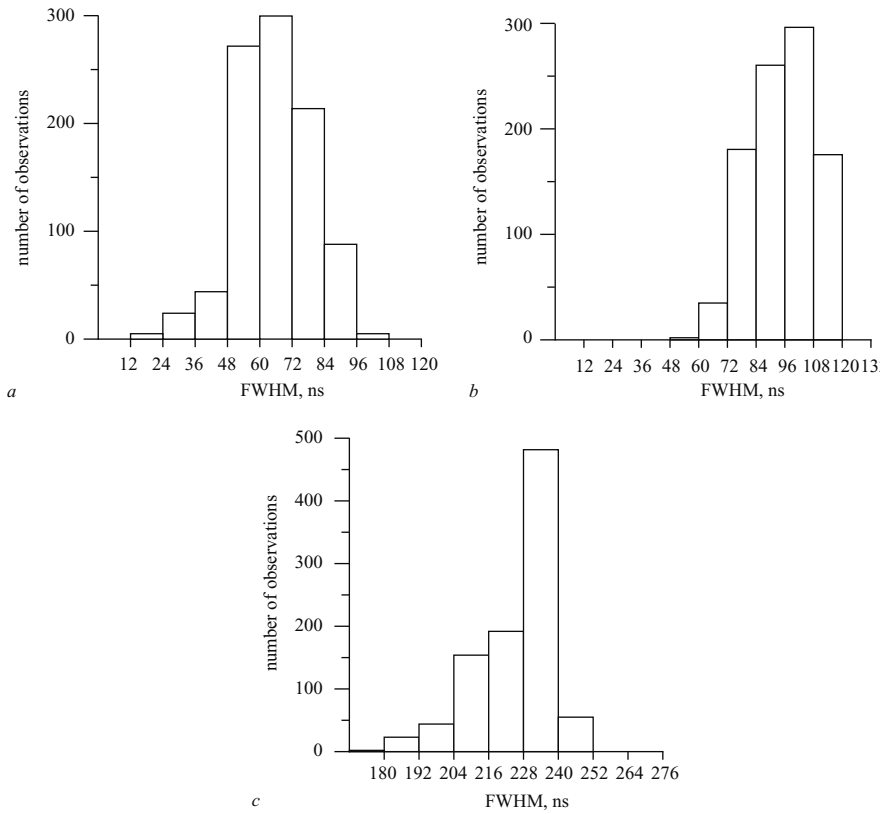

Figure 7.12 *Distributions of the FWHM of the electric field derivative at a distance of 200 m from lightning flashes. The distributions are obtained through a Monte Carlo simulation utilising a channel base current model introduced by Cooray [31]*

a $\sigma = \infty$; mean = 68 ns
b $\sigma = 0.01$ S/m; mean = 95 ns
c $\sigma = 0.001$ S/m; mean = 226 ns

Recently, Fernando and Cooray [16] analysed the propagation effects on electric field derivatives utilising the electromagnetic fields recorded by Bailey and Willett [28] and Izumi and Willett [29]. As mentioned previously, the propagation path of these waveforms was 20 km over the sea with the exception of the last fifty metres, which was over land. Since the electric field derivative can be attenuated to some extent when propagating along such a path, the results of Fernando and Cooray cannot be directly compared with the data presented above. In order to make a comparison, the model-generated waveforms were first propagated over such a path, then the resulting waveforms were used to calculate the propagation effects on derivatives as was done by Fernando and Cooray. In the calculation,

Table 7.3 Parameters of the distributions of peak electric field derivatives at different distances from lightning flashes over finitely conducting ground of conductivity σ. The results are obtained from a Monte Carlo simulation conducted using the return stroke model of Cooray [31]. Note that for $\sigma = \infty$ data are given only for $D = 200$ m. The mean and the median of the distributions at other distances over perfectly conducting ground can be obtained from these results by assuming inverse distance dependence

D (metres)	σ (S/m)	Mean (V/m/s)	Median (V/m/s)	Standard deviation	Max. value (V/m/s)	Min. value (V/m/s)
200	∞	2.59×10^{10}	2.38×10^{10}	1.12×10^{10}	6.63×10^{10}	6.13×10^{9}
200	0.010	2.11×10^{10}	1.9×10^{10}	9.9×10^{9}	5.92×10^{10}	5.15×10^{9}
200	0.001	1.21×10^{10}	1.08×10^{10}	5.98×10^{9}	3.56×10^{10}	2.98×10^{9}
500	0.010	6.94×10^{9}	6.18×10^{9}	3.36×10^{9}	2.0×10^{10}	1.69×10^{9}
500	0.001	3.29×10^{9}	2.93×10^{9}	1.64×10^{9}	9.76×10^{9}	8.09×10^{8}
1000	0.010	2.9×10^{9}	2.59×10^{9}	1.43×10^{9}	8.5×10^{9}	7.07×10^{8}
1000	0.001	1.24×10^{9}	1.11×10^{9}	6.21×10^{8}	3.67×10^{9}	3.01×10^{8}
2000	0.010	1.18×10^{9}	1.05×10^{9}	5.84×10^{8}	3.48×10^{9}	2.87×10^{8}
2000	0.001	4.64×10^{8}	4.16×10^{8}	2.37×10^{8}	1.39×10^{9}	1.1×10^{8}
5000	0.010	3.44×10^{8}	3.06×10^{8}	1.72×10^{8}	1.02×10^{9}	8.37×10^{7}
5000	0.001	1.23×10^{8}	1.11×10^{8}	6.45×10^{7}	3.76×10^{8}	2.82×10^{7}
10 000	0.010	1.32×10^{8}	1.18×10^{8}	6.66×10^{7}	3.93×10^{8}	3.17×10^{7}
10 000	0.001	4.37×10^{7}	3.94×10^{7}	2.33×10^{7}	1.36×10^{8}	9.84×10^{6}
20 000	0.010	4.956×10^{7}	4.44×10^{7}	2.536×10^{7}	1.49×10^{8}	1.16×10^{7}
20 000	0.001	1.51×10^{7}	1.36×10^{7}	8.19×10^{6}	4.7×10^{7}	3.36×10^{6}

the wind speed was assumed to be 10 m/s (typical of thunderstorm conditions), the length of the land path was taken to be 50 m of soil with a conductivity of 0.01 S/m. The results are depicted in Figure 7.13. Note that the results obtained from the model-generated fields agree with those obtained from the measured waveforms, justifying the utilisation of the model-generated data in the propagation studies.

7.3.3 The effect of propagation on triggered return strokes

There are a vast number of lightning direction finders deployed at different geographical locations to measure the initial peak of the magnetic field. For distances of more than about a kilometre the magnetic field consists mainly of radiation. The initial peak of the magnetic field is measured in uncalibrated units sometimes referred to as LLP units. One of the important problems in lightning directing finding is to determine the connection between these LLP units and the return stroke peak current. Thus,

Table 7.4 Parameters of the distributions of FWHM of electric field derivatives at different distances from lightning flashes over finitely conducting ground of conductivity σ. The results are obtained from a Monte Carlo simulation conducted using the return stroke model of Cooray [31]. Note that when $\sigma = \infty$ the parameters of the distributions of FWHM do not vary with distance

D (metres)	σ (S/m)	Mean (ns)	Median (ns)	Standard deviation	Max. value (ns)	Min. value (ns)
200	∞	68	70	14.7	100	20
200	0.010	95	90	11.92	120	60
200	0.001	226	230	14	250	170
500	0.010	113	110	9.43	130	90
500	0.001	291	290	14.36	320	250
1000	0.010	137	140	8.16	160	110
1000	0.001	362	360	14.9	390	320
2000	0.010	172	169	7	190	150
2000	0.001	456	460	14.7	490	420
5000	0.010	239	240	9.4	250	210
5000	0.001	630	630	12.95	660	600
10 000	0.010	310	310	11.43	330	280
10 000	0.001	819	820	11.54	850	800
20 000	0.010	430	405	12.4	430	379
20 000	0.001	1074	1069	12.3	1110	1040

the calibration of the direction finders was attempted using the data from triggered lightning flashes (Orville [34]). As in the case of natural return strokes, the triggered lightning waveforms also attenuate as they propagate over finitely conducting ground and one cannot assume *a priori* that the attenuation of the initial peak caused by propagation effects is the same for both natural and triggered lightning flashes. Thus, in any calibration procedure of the sort mentioned above, it is necessary to know how the fields from triggered lightning flashes are attenuated as they propagate over finitely conducting ground. In order to gain some knowledge on this topic Cooray *et al*. [15] have evaluated the effects of propagation on electric radiation fields from triggered lightning using a sample of 28 waveforms measured by Willett *et al*. [8] in a study conducted in Florida. The location of the measuring system used by these authors was such that the propagation path of the fields was over brackish water with the exception of the last few hundred metres. Thus Cooray *et al*. assumed these waveforms to represent the undistorted waveforms generated by triggered lightning flashes. Employing eqn. 7.13 as before, they studied the effect of propagation on these waveforms. Figure 7.14 depicts the variation of $1 - A$ as a function of the undistorted normalised initial peak of the radiation fields. Note that the attenuation coefficient, A, again increases with increasing peak value demonstrating that even in the case

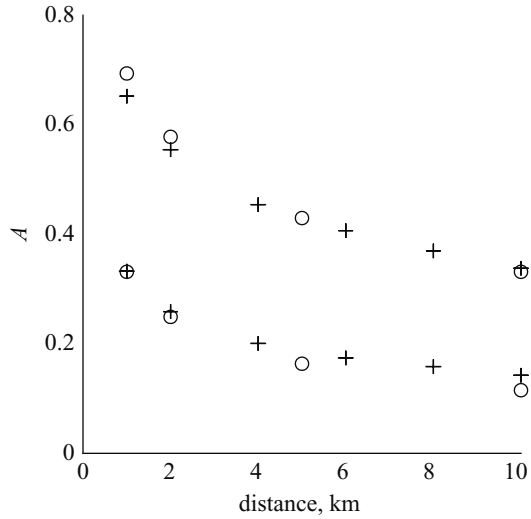

Figure 7.13 *Comparison of the results obtained by Fernando and Cooray [16] (crosses) using the measured radiation fields from return strokes with the results obtained through Monte Carlo simulations (982 waveforms) using the channel base current model of Cooray [31] (circles). The points shown are the average values. The upper curve corresponds to* $\sigma = 0.01\,S/m$ *and the lower one corresponds to* $\sigma = 0.001\,S/m$. $A = E_\sigma / E_\infty$ *where* E_σ *is the peak electric radiation field over finitely conducting ground and* E_∞ *is the peak electric radiation field that would be present if the ground was perfectly conducting*

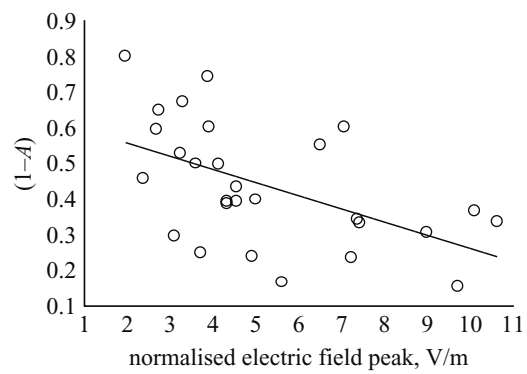

Figure 7.14 *Distribution of* $1 - A$ *for* $\gamma = 10^8\,m^2/S$ *as a function of the undistorted peak* E_∞ *of triggered subsequent return strokes. Note that the latter was normalised to 100 km by using the inverse distance dependence. The best linear fit that represents the variation is also shown in each diagram* (adapted from [15])

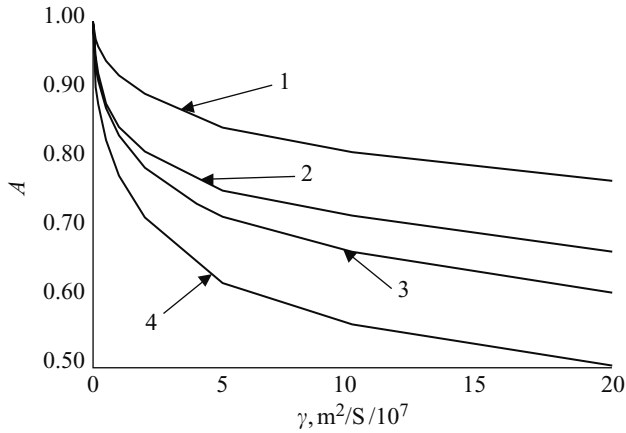

Figure 7.15 *The mean value of the attenuation coefficient, as defined by eqn. 7.15, as a function of* γ (adapted from [15])

1 positive return strokes
2 negative return strokes
3 natural subsequent return strokes
4 triggered subsequent return strokes

of triggered lightning return stroke fields the width of the initial peak increases with increasing peak value.

For comparison purposes, the variation of the average value of A as a function of γ for triggered lightning return strokes is shown together with the negative and positive values in Figure 7.15. Note that the attenuation of triggered lightning fields is much stronger than that of negative and positive first return strokes.

With the specific aim of checking whether the attenuation of the triggered subsequent strokes is different from that of natural subsequent strokes, Cooray *et al.* [15] used 17 natural subsequent return strokes recorded by Bailey and Willett [28] and Izumi and Willett [29] to obtain the value of A as a function of γ. The results are also shown in Figure 7.15. It can be seen that they indicate that the average attenuation of natural subsequent return strokes lies somewhere between the natural first return stroke and the triggered subsequent strokes. The results also show that the attenuation coefficients obtained from subsequent return strokes, whether from natural or triggered lightning flashes, should be applied with caution in correcting the propagation effects of first return strokes.

Let us now find out the reason why the attenuation is different for different types of return stroke. The attenuation of the initial peak mainly depends on the width of the initial peak of the radiation fields. In Figure 7.16 the average waveforms of first negative return strokes, first positive return strokes, triggered subsequent strokes and natural subsequent strokes are depicted. The average waveforms were generated by normalising each individual waveform to a common amplitude (i.e., setting the value of the peak to unity) and then aligning the peaks and averaging.

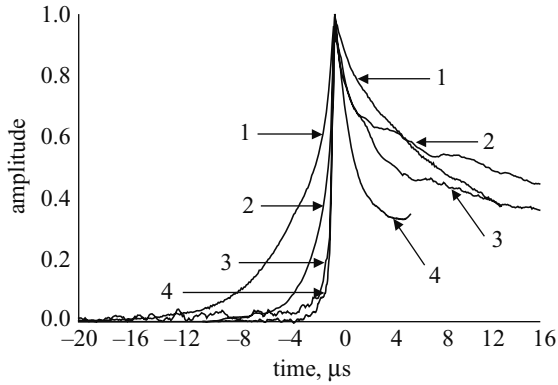

Figure 7.16 *The average radiation fields* (adapted from [15])

1 positive first return strokes
2 negative first return strokes
3 natural negative subsequent return strokes
4 triggered negative subsequent strokes

Note that the average width of the positive return strokes is larger than that of the negative first return strokes and the average width of the natural subsequent return strokes lies between those of negative return strokes and triggered subsequent return strokes. The attenuation of the waveforms owing to propagation depends mainly on the width of the initial peak and the amount of attenuation decreases with increasing width. This fact explains the relative position of the curves given in Figure 7.15.

7.3.4 The effect of propagation on electromagnetic fields generated by cloud flashes

From the point of view of power engineers, the lightning events which are of most interest are the return strokes. Until recent times, the same was true for the lightning protection engineers. The rapid development of low-voltage electronic devices and their incorporation in modern day decision making apparatus, however, made it necessary for the engineer to consider the threats imposed by lightning events other than return strokes – cloud flashes, for example. This is because modern day electronics are sensitive to overvoltages of a few volts, and such voltage magnitudes can easily be generated by the interaction of electrical networks with electromagnetic fields generated by cloud flashes. A strong need exists today to categorise and quantify the electromagnetic fields generated by cloud flashes and to understand the way in which they can interact with the low-voltage power installations. This, in turn, requires that one can explain the effects of propagation of radiation field pulses generated by cloud flashes as they propagate over finitely conducting ground. In this section the effects

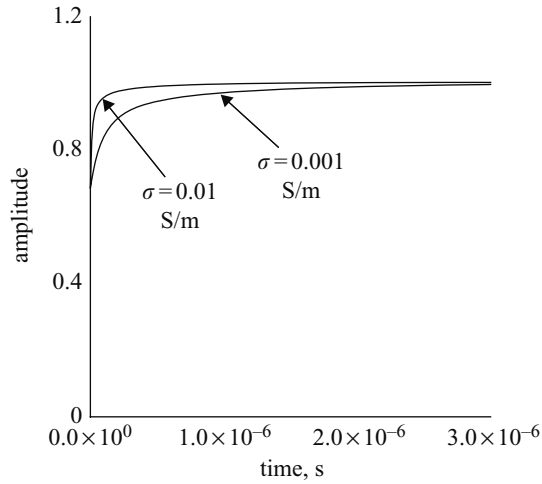

Figure 7.17 *The variation of $E_{z,\sigma}(t, D)$ of eqn. 7.13 when $E_z(t, D)$ is a step function. In the calculation $D = 1000\,m$ and $Z1 = 5000\,m$. Note the step which is produced by the sky wave at $t = 0$*

of propagation on the pulses generated by cloud flashes are described. Some of the results presented are adapted from the work published by Cooray [35].[1]

The geometry of the situation under consideration is shown in Figure 7.1, and the vertical electric field at the point of observation is given by eqn. 7.13. So, if the undistorted radiation fields generated by cloud flashes are available, they can be used in the above equation to evaluate the propagation effects. However, before one proceeds to more complicated waveforms, it is illuminating to calculate the effects of propagation when the undistorted radiation field is a step function. Such calculations are shown for $D = 1\,\text{km}$, $Z1 = 5\,\text{km}$ and $\sigma = 0.01\,\text{S/m}$ and $0.001\,\text{S/m}$ in Figure 7.17. For comparison purposes, the step responses for the same parameters but with $Z1 = 0$ (i.e., corresponding to a return stroke) are depicted in Figure 7.18. Note that in the case of cloud flashes the field over finitely conducting ground consists of two sections. Initially, the field rises like a step until it reaches an amplitude that is smaller than the amplitude of the undistorted waveform. Then it rises slowly until it reaches the amplitude of the undistorted waveform. The reason for this behaviour is as follows. The radiation field from the discharge reaching the point of observation can be divided into a space wave (the terms in the first square bracket of eqn. 7.6) and a ground wave (the terms in the second square bracket of eqn. 7.6). The space wave is not attenuated by the finitely conducting ground, whereas the ground wave is strongly affected by it. The rapidly rising part of the waveform which occurs at $t = 0$ in Figure 7.17 is generated by the space wave and the subsequent slow increase is caused

[1] In a revised version of this paper, to be published in the Proc. IEEE (EMC), 2003, it is shown that results given in here are also valid for horizontal channels in the cloud.

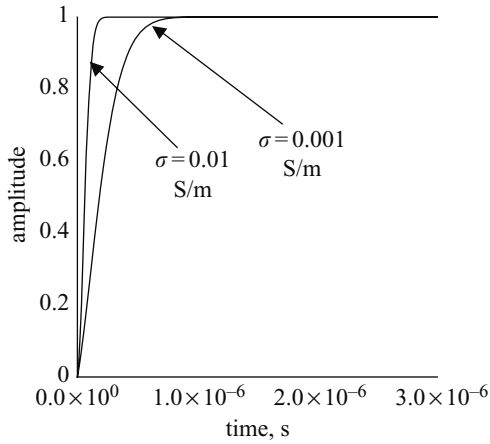

Figure 7.18 The variation of $E_{z,\sigma}(t, D)$ of eqn. 7.13 when $E_z(t, D)$ is a step function. In the calculation $D = 1000\,m$ and $Z_i = 0\,m$

by the ground wave. The amplitude of the space wave is zero for a channel section located at ground level. In the case of return strokes of ground flashes, the section of the channel which radiates during the first few microseconds of the radiation field is located close to ground. Thus the initial portion of the radiation field from a return stroke consists mainly of the surface wave. Since the high-frequency components of the surface wave are strongly attenuated by the finitely conducting ground, the radiation fields from return strokes in ground flashes experience strong propagation effects. As the height of the radiating end of the channel increases, the contribution to the total field from the space wave increases. The sources of a cloud flash are located at altitudes of 3–8 km and a significant portion of the total radiation field is contributed by the space wave. Thus, for the reasons mentioned earlier, the attenuation of the radiation fields of cloud flashes is not as strong as that experienced by return strokes in ground flashes. These facts make the effect of propagation on the radiation fields from cloud flashes differ from that on the radiation fields from return strokes.

The experimental data indicates that the peak and the FWHM of the electric field derivatives of cloud pulses are comparable to those of return strokes [36,37]. Thus the differences in the effects of propagation on the radiation fields of cloud and ground flashes can be illustrated better by simulating the cloud pulses and the return stroke fields by the same model, with the exception that the point of initiation is different in the two cases. With this idea in mind, a Monte Carlo simulation identical to that described in section 7.3.2.2 was performed with the origin of the flash at a height of 5 km. The parameters of the resulting distributions for the peak and the FWHM of the electric field derivatives at different distances for different soil conductivities are tabulated in Tables 7.5 and 7.6. One can compare these results with those obtained for return strokes given in Tables 7.3 and 7.4. In order to make this comparison easier, the means of the peak electric field derivative for cloud and ground flashes are depicted as a

Table 7.5 Parameters of the distributions of peak electric field derivatives of cloud pulses at different distances over ground of conductivity σ. In the simulation the origin of the discharge was taken to be at a height of 5 km from ground level. In the simulation it was assumed that in the absence of propagation effects the peak derivatives of cloud pulses are similar in magnitude and distribution to that of return strokes

D (metres)	σ (S/m)	Mean (V/m/s)	Median (V/m/s)	Standard deviation	Max. value (V/m/s)	Min. value (V/m/s)
1000	∞	2.1×10^7	1.976×10^7	7.85×10^6	4.84×10^7	6.76×10^6
1000	0.010	1.8×10^7	1.63×10^7	7.02×10^6	4.1×10^7	5.17×10^6
1000	0.001	1.48×10^7	1.4×10^7	5.63×10^6	3.45×10^7	4.62×10^6
2000	∞	7.77×10^7	7.3×10^7	2.97×10^7	1.8×10^8	2.4×10^7
2000	0.010	6.6×10^7	6.14×10^7	2.7×10^7	1.6×10^8	1.9×10^7
2000	0.001	55.7×10^7	5.17×10^7	2.2×10^7	1.31×10^8	1.63×10^7
5000	∞	2.4×10^8	2.21×10^8	9.3×10^7	5.8×10^8	7×10^7
5000	0.010	1.97×10^8	1.8×10^8	8.3×10^7	5.05×10^8	5.32×10^7
5000	0.001	1.6×10^8	1.5×10^8	6.5×10^7	4.1×10^8	4.4×10^8
10 000	∞	2.74×10^8	2.6×10^8	1.13×10^8	6.98×10^8	7.5×10^7
10 000	0.010	2.1×10^8	1.9×10^8	9.1×10^7	5.51×10^8	5.12×10^7
10 000	0.001	1.5×10^8	1.4×10^8	6.6×10^7	4.03×10^8	4×10^7
20 000	∞	1.96×10^8	1.8×10^8	8.4×10^7	5.16×10^8	4.98×10^7
20 000	0.010	1.25×10^8	1.14×10^8	5.6×10^7	3.4×10^8	2.93×10^7
20 000	0.001	8.1×10^7	7.3×10^7	3.6×10^7	2.16×10^8	1.96×10^7

function of distance for several conductivities in Figures 7.19 and 7.20. First, consider the values over perfectly conducting ground. In the case of return strokes, the peak amplitude of the derivatives decreases inversely with the distance. For example, the average field peak at 10 km is twice the average value at 20 km. However, in the case of the cloud flash, the variation of the peak field derivative is much more complex. As the distance decreases the peak derivative increases and reaches a maximum value around 10 km. After that it decreases with decreasing distance. The reason for this is the presence of the $\sin^2\theta$ term in eqn. 7.1. As the distance decreases, this term also decreases thereby counterbalancing the increase in the peak amplitude caused by the decrease in distance. In the case of ground flashes, this term remains close to one (as far as small times are concerned) and as a result the field changes inversely with distance. The distribution of the electric field derivatives over different conductivities shows that the peak derivative of cloud flashes can overwhelm the return stroke values for distances in the range 5–20 km (compare the data in Table 7.5 with the data in Table 7.3). In this range cloud flashes may induce higher voltages in low-voltage power installations than the ground flashes. Neglecting this fact may lead to the wrong conclusions concerning the relative importance of cloud and ground flashes as the

Table 7.6 Parameters of the distributions of FWHM of electric field derivatives of cloud pulses at different distances over ground of conductivity σ. In the simulation the origin of the discharge was taken to be at a height of 5 km from ground level. In the simulation it was assumed that in the absence of propagation effects the FWHM of electric field derivatives of cloud pulses are similar in magnitude and distribution to that of return strokes

D (metres)	σ (S/m)	Mean (ns)	Median (ns)	Standard deviation	Max. value (ns)	Min. value (ns)
1000	∞	60.91	60	18.2	100	10
1000	0.010	67	70	14.95	90	20
1000	0.001	64.2	70	17.64	100	10
2000	∞	68.25	70	19.33	110	10
2000	0.010	75.45	80	17.2	110	20
2000	0.001	76.02	80	20.66	120	20
5000	∞	69.2	70	18.1	100	10
5000	0.010	78.19	80	16.5	110	20
5000	0.001	80.1	80	21.03	120	20
10 000	∞	67.38	70	16.02	100	10
10 000	0.010	81.1	80	15.54	110	30
10 000	0.001	83.3	90	20.7	130	20
20 000	∞	66.17	70	15.52	100	20
20 000	0.010	90.46	90	16.13	130	30
20 000	0.001	93.01	90	24.4	150	20

source of disturbances in low-voltage power installations. However, with decreasing distance, the ground flash will take over simply because the $\sin^2\theta$ term approaches zero with decreasing distance for cloud flashes.

7.3.5 The effect of a sea–land boundary on propagation

The effect of a mixed sea–land path on propagation is of interest in many practical situations. For example, in the measurements of Willett *et al*. [8,10] and Cooray [6] the measuring station was situated on land, at a distance of several tens to several hundreds of metres from the sea–land boundary. In these experiments the propagation path of the electromagnetic fields was entirely over sea water except for the last few tens or few hundreds of metres. It would therefore be interesting to investigate the effect this strip of land, which lies in the path of propagation, has on the propagation. In order to evaluate the propagation effects introduced by a sea–land path, a Monte Carlo simulation was performed for 982 lightning flashes by placing the lightning flashes over the sea at a distance of 20 km from the coast line. The point of observation was located on the land of conductivity σ at a distance *dl* from the coastline. Calculations have been performed for different values of σ and *dl*. The results obtained from this

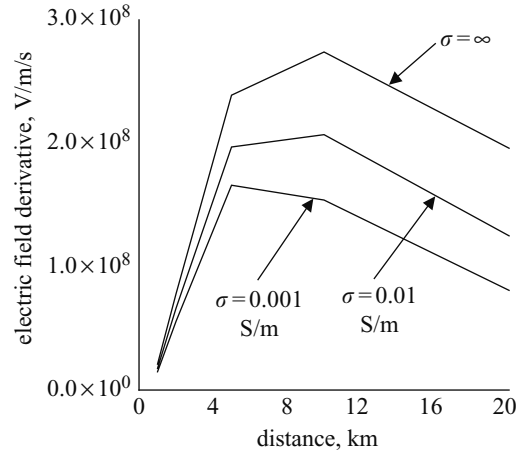

Figure 7.19 *The mean values of the peak electric field derivatives at different distances obtained through a Monte Carlo simulation assuming the origin of the discharge to be located at a height of 5000 m*

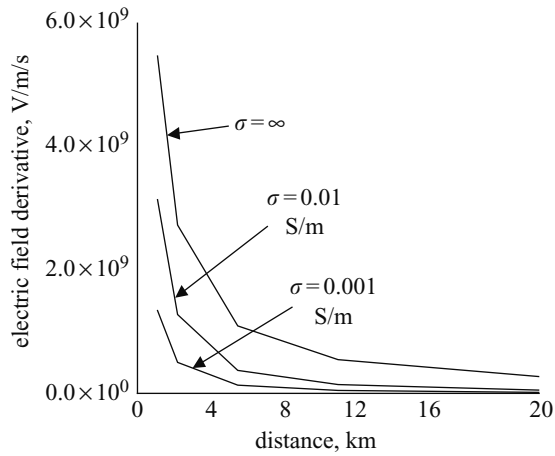

Figure 7.20 *The mean values of the peak electric field derivatives at different distances obtained through a Monte Carlo simulation assuming the origin of the discharge to be located at ground level*

study are summarised in Tables 7.7 and 7.8. The distributions of the peak and the FWHM of the electric field derivatives are shown for $dl = 50\,\text{m}$ and $\sigma = 0.01\,\text{S/m}$ and $0.001\,\text{S/m}$ in Figures 7.21 and 7.22. For comparison purposes, the corresponding distributions for the same location but over perfectly conducting ground (i.e., both

Table 7.7 Parameters of the distributions of the peak electric field derivative at a distance of 50 m from a coast line. The lightning flashes are located at a distance of 20 km over a sea surface of conductivity 4 S/m. The distributions are obtained through a Monte Carlo simulation utilising the channel base current model of Cooray [31]. Note that the peak values are normalised to 100 km using inverse distance dependence

Length of land-section, *dl* (metres)	σ (S/m)	Mean (V/m/s)	Median (V/m/s)	Standard deviation	Max. value (V/m/s)	Min. value (V/m/s)
50	0.010	4.534×10^7	4.125×10^7	2.052×10^7	1.21×10^8	1.089×10^7
100	0.010	4.334×10^7	3.919×10^7	1.987×10^7	1.045×10^8	1.045×10^7
200	0.010	4.041×10^7	3.638×10^7	1.883×10^7	1.12×10^8	9.8×10^6
50	0.001	3.415×10^7	3.075×10^7	1.6×10^7	9.489×10^7	8.24×10^6
100	0.001	2.976×10^7	2.682×10^7	1.41×10^7	8.393×10^7	7.23×10^6
200	0.001	2.49×10^7	2.23×10^7	1.203×10^7	7.163×10^7	6.04×10^6

Table 7.8 Parameters of the distributions of the FWHM of electric field derivative at a distance of 50 m from a coast line. The lightning flashes are located at a distance of 20 km over a sea surface of conductivity 4 S/m. The distributions are obtained through a Monte Carlo simulation utilising the channel base current model of Cooray [31]

Length of land section, *dl* (metres)	σ (S/m)	Mean (ns)	Median (ns)	Standard deviation	Max. value (ns)	Min. value (ns)
50	0.010	72	75	12	95	40
100	0.010	77	75	11	100	50
200	0.010	85	85	11	105	60
150	0.001	102	105	14	130	65
100	0.001	123	125	14	150	80
200	0.001	153	155	13	180	105

the surface of the sea and the strip of land perfectly conducting) are also shown in the same Figures. Note that in performing these calculations the conductivity of the sea water was taken to be 4 S/m and the peak field derivatives are normalised to 100 km, assuming an inverse dependence on distance.

Calculations have also been performed to estimate the effects of propagation on the peak electric fields. For the range of parameters specified above the maximum

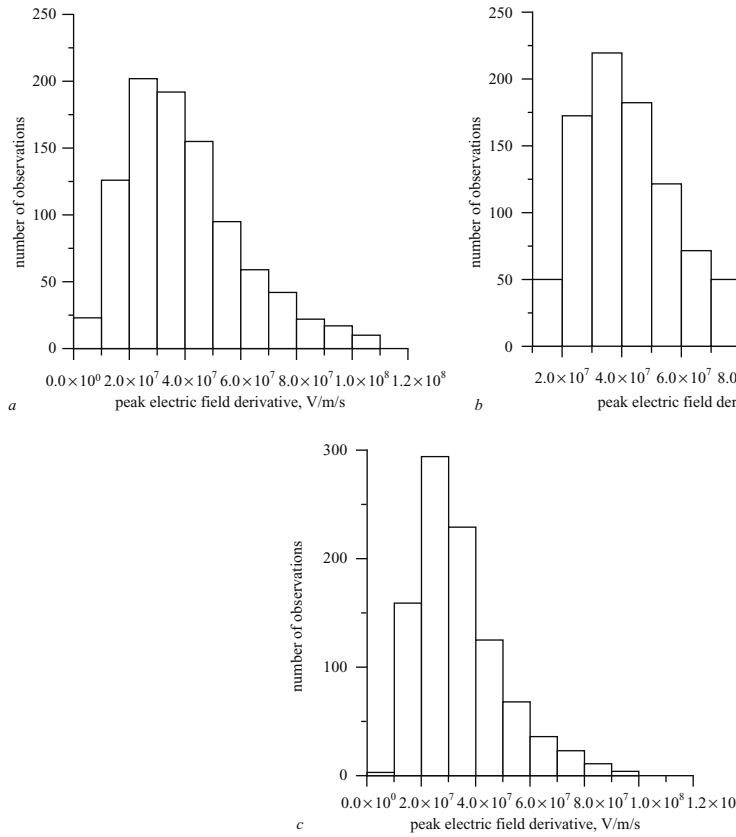

Figure 7.21 *Distributions of the peak electric field derivative at a distance of 50 m from a coast line. The lightning flashes are located at a distance of 20 km over a sea surface of conductivity 4 S/m. The distributions are obtained through a Monte Carlo simulation utilising a channel base current model of Cooray [31]. The peak values are normalised to 100 km*

a mean $= 51.0 \times 10^6$ V/m/s; soil conductivity $= \infty$
b mean $= 45.0 \times 10^6$ V/m/s; soil conductivity $= 0.01$ S/m
c mean $= 34.0 \times 10^6$ V/m/s; soil conductivity $= 0.001$ S/m

attenuation ($dl = 200, \sigma = 0.001$ S/m) was about two per cent. Thus, the effects of propagation on the electric field are not very significant for values of dl in the range of 50–200 m. However, the peak amplitude and the FWHM of the electric field derivative may change significantly in propagating across the strip of land. It is important to note that in this calculation we have assumed the sea surface to be smooth. The effects of propagation resulting from propagation across a smooth sea surface of 20 km are shown in Figures 7.23 and 7.24. These results show that in propagating 20 km along a smooth sea surface the average peak electric field derivative may decrease from 51×10^6 to 47×10^6 V/m/s. Comparison of this result with the data

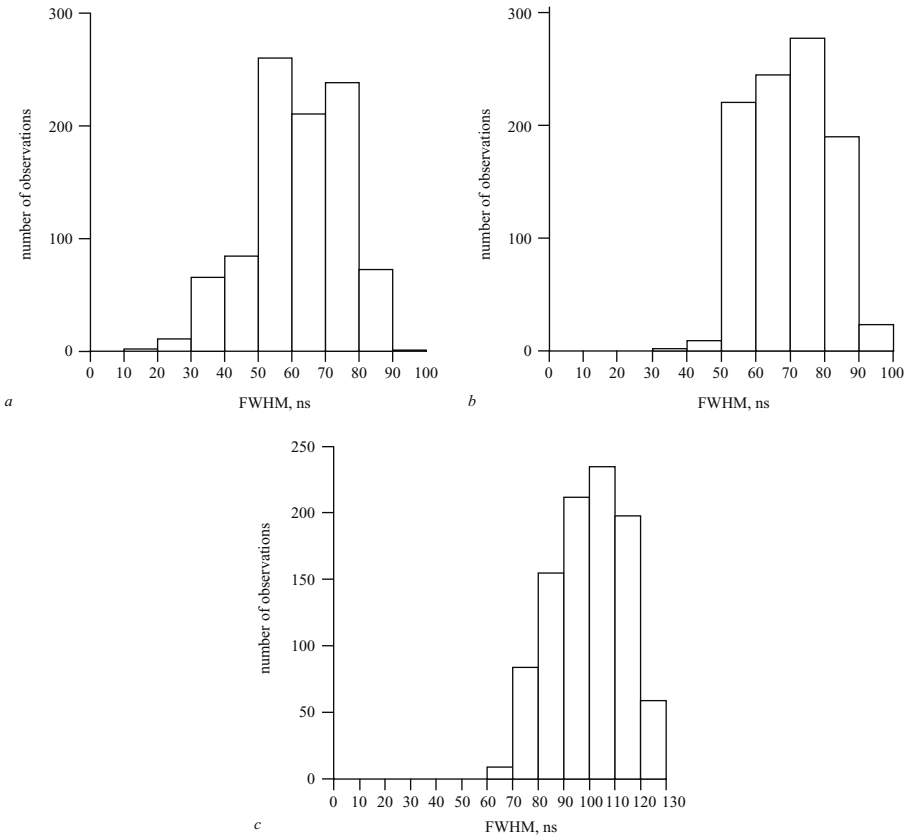

Figure 7.22 *Distributions of the FWHM of the electric field derivative at a distance of 50 m from a coast line. The lightning flashes are located at a distance of 20 km over a sea surface of conductivity 4 S/m. The distributions are obtained through a Monte Carlo simulation utilising a channel base current model of Cooray [31]*

a mean = 64 ns; soil conductivity = ∞
b mean = 72 ns; soil conductivity = 0.01 S/m
c mean = 102 ns; soil conductivity = 0.001 S/m

given in Table 7.7 shows that the propagation effects are mainly determined by the strip of land, especially when $\sigma = 0.001$ S/m.

7.3.6 The effect of a rough ocean on propagation

Since propagation over finitely conducting ground surface can attenuate the higher frequency content of the lightning-generated electromagnetic fields, as mentioned previously, many researchers have measured the high-frequency content of the electromagnetic fields by using fields that have propagated entirely over sea water. However,

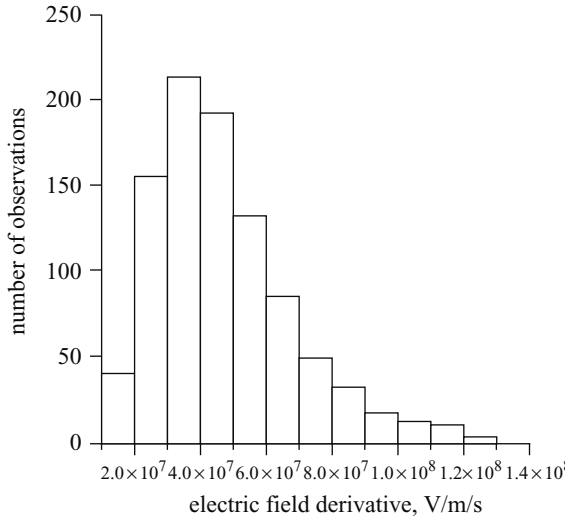

Figure 7.23 *Distributions of the peak electric field derivative after propagating 20 km over a smooth sea surface of conductivity 4 S/m (mean = 47.0×10^6 V/m/s). The distribution is obtained through a Monte Carlo simulation utilising a channel base current model of Cooray [31]*

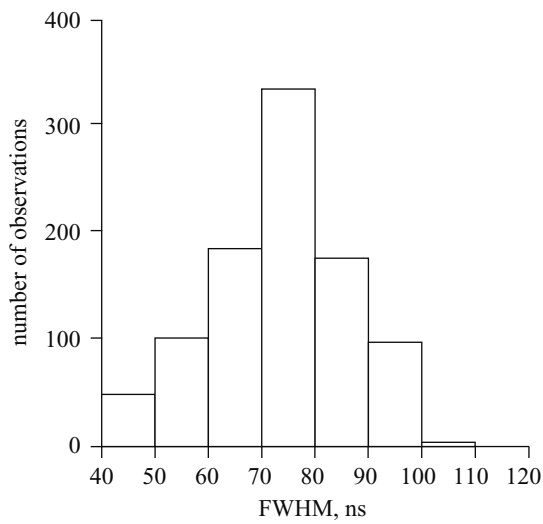

Figure 7.24 *Distributions of the FWHM of the electric field derivative after propagating 20 km over a smooth sea surface of conductivity 4 S/m (mean = 69 ns). The distribution is obtained through a Monte Carlo simulation utilising a channel base current model of Cooray [31]*

Table 7.9 Parameters of the distributions of the peak electric field derivative at 10 km, 20 km and 50 km after propagation over a rough ocean surface characterised by wind speeds of 10 m/s and 15 m/s. In the calculation $\alpha = 0^\circ$ where α is the angle between the direction of the wind and the direction of propagation of the electromagnetic field. The distributions are obtained through a Monte Carlo simulation utilising a channel base current model of Cooray [31]. The peak values are normalised to 100 km

D (metres)	Wind speed (m/s)	Mean (V/m/s)	Median (V/m/s)	Standard deviation	Max. value (V/m/s)	Min. value (V/m/s)
10 000	10	4.65×10^7	4.24×10^7	2.1×10^7	1.23×10^8	1.11×10^7
10 000	15	4.24×10^7	3.82×10^7	1.96×10^7	1.16×10^8	1.03×10^7
20 000	10	4.38×10^7	3.97×10^7	2.01×10^7	1.19×10^8	1.06×10^7
20 000	15	3.8×10^7	3.43×10^7	1.8×10^7	1.07×10^8	9.25×10^6
50 000	10	3.85×10^7	3.5×10^7	1.82×10^7	1.08×10^8	9.35×10^6
50 000	15	3.12×10^7	2.8×10^7	1.52×10^7	8.99×10^7	7.62×10^6

sea water has a finite conductivity, which is of the order of 4 S/m, thus leading to the attenuation of the high frequencies of the electromagnetic fields. Furthermore, under certain situations the waves on the ocean surface can lead to further attenuation and scattering of the electromagnetic fields. The calculations of Ming and Cooray [14] show that propagation over a rough ocean surface does not significantly attenuate the initial peak field of the radiation field, but there could be significant changes in the time derivative of the electric field. In order to investigate these effects more thoroughly a Monte Carlo simulation was conducted as described previously to study how the peak amplitude of the electric field, peak amplitude of the electric field derivative and the FWHM of the electric field derivative are influenced by the propagation of electromagnetic fields over a rough ocean surface. In the simulation, calculations are performed for different distances of propagation and for different surface roughness. The results of the simulation are summarised in Tables 7.9 and 7.10. The distributions of the peak and the FWHM of the electric field derivatives for 10 and 20 km propagation over a rough sea surface characterised by a wind speed of 10 m/s and $\alpha = 0^\circ$, where α is the angle between the direction of the wind and the direction of propagation of the electromagnetic field, are depicted in Figures 7.25 and 7.26. For comparison purposes, the distributions over perfectly conducting ground are also depicted in these Figures. Note that all the peak values of the electric field derivatives are normalised to 100 km assuming an inverse distance relationship. Note also that winds of 10 m/s are not uncommon during thunderstorms. The results show that the effects of a rough sea surface on propagation are significant and should not be neglected. Calculations have also been performed to estimate the effects of propagation on the peak electric fields. For the range of parameters specified above, the maximum attenuation (50 km; wind speed:15 m/s) was less than one per cent.

Table 7.10 Parameters of the distributions of the FWHM of electric field derivative at 10 km, 20 km and 50 km after propagation over a rough ocean surface characterised by wind speeds of 10 m/s and 15 m/s. In the calculation $\alpha = 0°$ where α is the angle between the direction of the wind and the direction of propagation of the electromagnetic field. The distributions are obtained through a Monte Carlo simulation utilising a channel base current model of Cooray [31]. The peak values are normalised to 100 km

D (metres)	Wind speed (m/s)	Mean (ns)	Median (ns)	Standard deviation	Max. value (ns)	Min. value (ns)
10 000	10	69.32	70.0	12.13	90	40
10 000	15	78.87	80	10.86	100	50
20 000	10	75.15	75	10.99	95	45
20 000	15	91.49	90	9.11	110	70
50 000	10	89.78	90	8.94	110	70
50 000	15	119.43	120	7.0	135	100

Ming and Cooray [14] performed calculations to estimate the effects of propagation over a rough ocean surface on the spectrum of the electric fields. They concluded that the rapid attenuation of the spectral amplitudes above 10 MHz in the measured spectra obtained by Weidman *et al.* [37] could be due to propagation effects. The results obtained by them are depicted in Figure 7.27.

7.3.7 Propagation over stratified ground

In many practical situations the surface of the earth can be represented by a stratum of thickness h, conductivity σ_1 and relative dielectric constant ε_1 below which the medium is semiinfinite with conductivity σ_2 and dielectric constant ε_2. Ming and Cooray [13] used eqn 7.15 together with the return stroke model of Cooray [38] to estimate the effect of propagation on the return stroke fields in similar situations. In the case of stratified ground, propagation effects depend on the electrical parameters of the two layers and on the thickness of the upper layer. For example, in the case where $\sigma_1 < \sigma_2$, depending on the thickness of the upper layer, certain frequencies will be enhanced in propagating over certain distances. This can be seen, for example, in Figure 7.28 the amplitude of $S_{tr}(0, D, j\omega)$ as a function of frequency is shown for different values of h and D. Note the enhancement of frequencies (i.e., $|S_{tr}| > 1$) in the vicinity of 1 MHz and above. However, in the opposite case, i.e., $\sigma_1 > \sigma_2$, such an enhancement does not take place, and the attenuation function decreases monotonically with increasing frequency. The electric radiation field over stratified ground is shown for different parameters in Figure 7.29. In these calculations the length of the propagation path was also kept constant at 10 km. Note that in the case where $\sigma_1 < \sigma_2$ the peak of the radiation field can exceed the peak of the

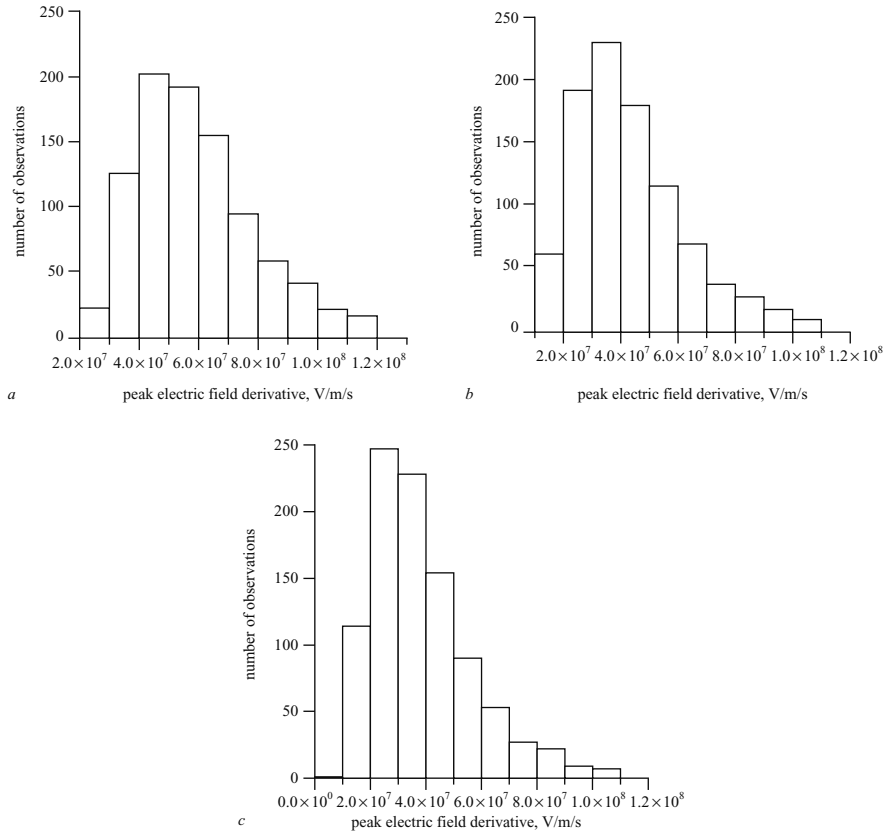

Figure 7.25 *Distributions of the peak electric field derivative at 20 and 50 km after propagation over a rough ocean surface characterised by a wind speed of 10 m/s. The distributions are obtained through a Monte Carlo simulation utilising a channel base current model of Cooray [31]. The peak values are normalised to 100 km. For comparison purposes the distribution over perfectly conducting ground is also given. Note that $\alpha = 0°$ where α is the angle between the direction of the wind and the direction of propagation of the electromagnetic field*

a mean $= 51.0 \times 10^6$ V/m/s; conductivity $= \infty$
b mean $= 44.0 \times 10^6$ V/m/s; distance $= 20$ km
c mean $= 39.0 \times 10^6$ V/m/s; distance $= 50$ km

radiation field over perfectly conducting ground. This result is in direct contrast to that observed in the case of homogeneous ground where propagation always leads to a decrease in the peak of the electric field. In the case where $\sigma_1 > \sigma_2$ the peak of the electric field decreases monotonically with decreasing thickness of the upper layer. Figure 7.30 depicts the derivative of the electric fields corresponding to the

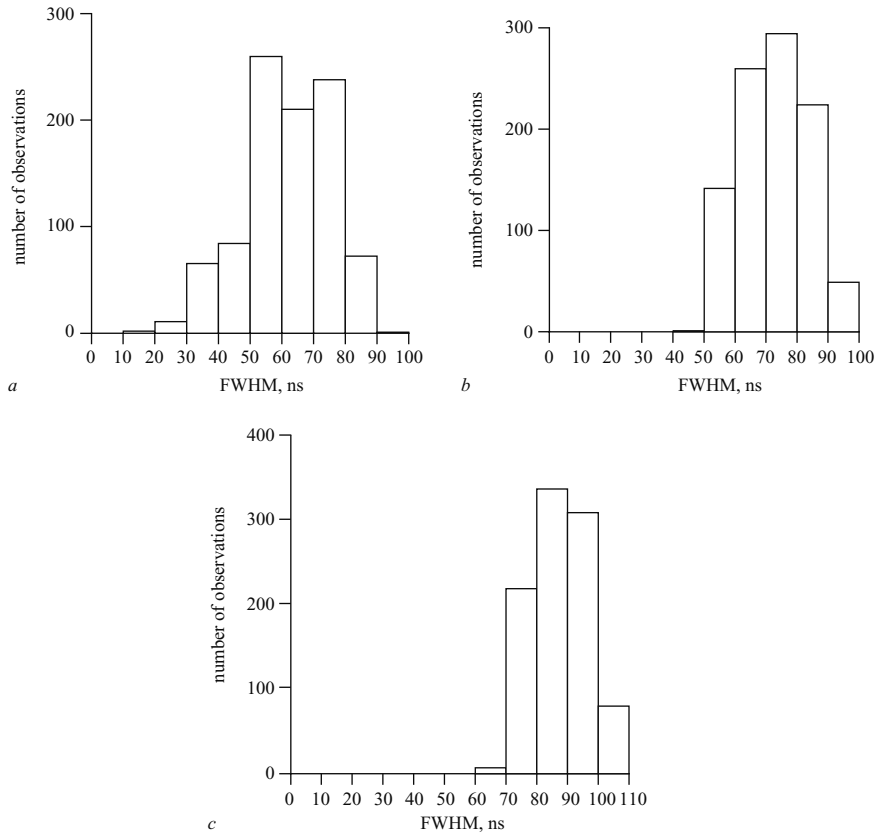

Figure 7.26 Distributions of the FWHM of electric field derivative at 20 km and 50 km after propagation over a rough ocean surface characterised by a wind speed of 10 m/s. The distributions are obtained through a Monte Carlo simulation utilising a channel base current model of Cooray [31]. For comparison purposes the distribution over perfectly conducting ground is also given. Note that $\alpha = 0°$ where α is the angle between the direction of the wind and the direction of propagation of the electromagnetic field

a mean = 64 ns; conductivity = ∞
b mean = 75 ns; distance = 20 km
c mean = 90 ns; distance = 50 km

situations considered in Figure 7.29. Note that, unlike the peak electric field, propagation results in a decrease in the derivative of the peak electric field both where $\sigma_1 > \sigma_2$ and $\sigma_1 < \sigma_2$. When $\sigma_1 < \sigma_2$ it may be possible, however, that for certain ranges of conductivities and for certain thicknesses of the upper layer, even the electric field derivative increases in comparison with that over perfectly conducting ground.

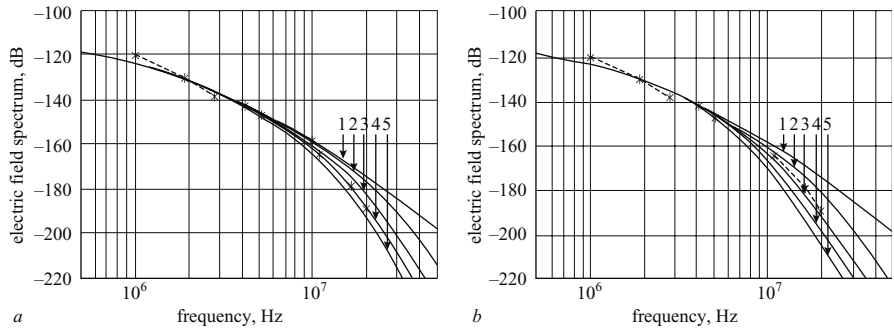

Figure 7.27 *Effects of propagating different distances over a finitely conducting ($\sigma = 4\,S/m$), rough surface on the spectrum of the electric fields generated by lightning return strokes. The results are normalised to 100 km by assuming inverse distance dependence and 0 dB corresponds to 1 $V\,m^{-1}\,Hz^{-1}$. Curve 1: spectrum of the undistorted radiation field; curve 2: $D = 10\,km$; curve 3: $D = 30\,km$; curve 4: $D = 50\,km$; curve 5: $D = 70\,km$. The measurements of Widman et al. [37] are shown by a dashed line*

a wind speed = 5.1 m/s, $\alpha = 0°$
b wind speed = 10.3 m/s, $\alpha = 0°$

7.4 Obtaining the lightning-generated electromagnetic fields required for the evaluation of induced voltages in power distribution systems

In analysing the interaction of electromagnetic fields of lightning flashes with power lines or any other electrical or telecommunication installations, it is necessary to know the temporal and spatial variation of the electric field parallel to the conductors (i.e., the horizontal component of the electric field) and the temporal variation of the vertical electric field at the terminations ([39] see also Chapter 8). If part of the system is located underground, one should also evaluate the electric field at different depths below the ground. In this section the way to obtain these field components is illustrated step by step.

The vertical electric field at the line terminations located over finitely conducting ground can be obtained by making use of eqn. 7.13 to correct for the effect of propagation on the radiation term. Since the induction term is affected only slightly and the static term is not affected at all by the propagation, the total vertical electric field at the point of observation can be written as:

$$E_v(t, D) = E_{s,\infty}(t, D) + E_{i,\infty}(t, d) + \int_0^t E_{r,\infty}(t - \tau, D)\, S_f(Z_i, D, \tau)\, d\tau \tag{7.41}$$

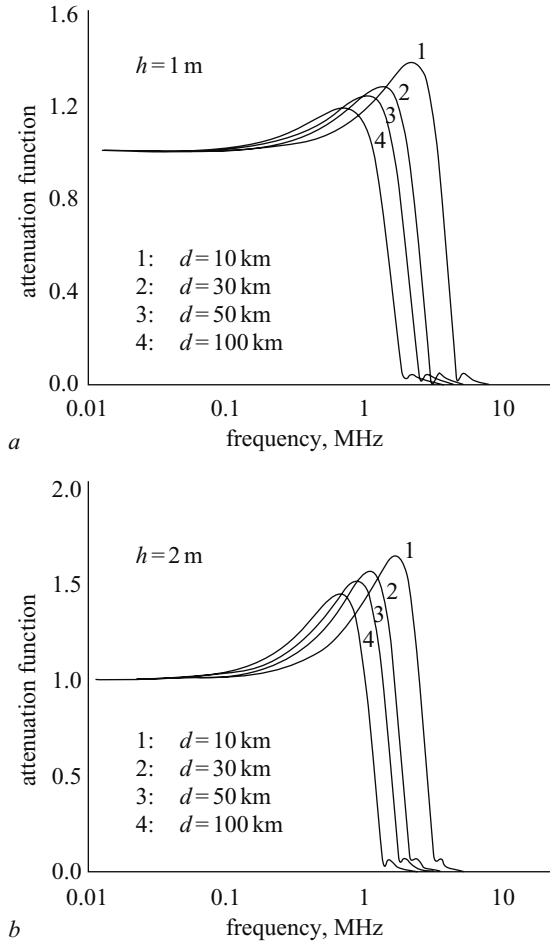

Figure 7.28 *Attenuation function of a stratified ground as a function of frequency for different distances of propagation and ground constants*
a $\sigma_1 = 0.002\,\mathrm{S/m}, \varepsilon_1 = 5, \sigma_2 = 0.1\,\mathrm{S/m}, \varepsilon_2 = 81, h = 1m$
b $\sigma_1 = 0.002\,\mathrm{S/m}, \varepsilon_1 = 5, \sigma_2 = 0.1\,\mathrm{S/m}, \varepsilon_2 = 81, h = 2m$

where $E_v(t, D)$ is the total vertical electric field at the point of observation, $E_{s,\infty}(t, D)$, $E_{i,\infty}(t, D)$ and $E_{r,\infty}(t, D)$ are the electrostatic field, the induction field and the radiation field, respectively, at the point of observation calculated assuming the ground to be perfectly conducting. The azimuthal magnetic field at the point of observation can be written as:

$$B_\phi(t, D) = B_{i,\infty}(t, D) + \int_0^t B_{r,\infty}(t - \tau, D)\, S_f(Z_i, D, \tau)\, d\tau \tag{7.42}$$

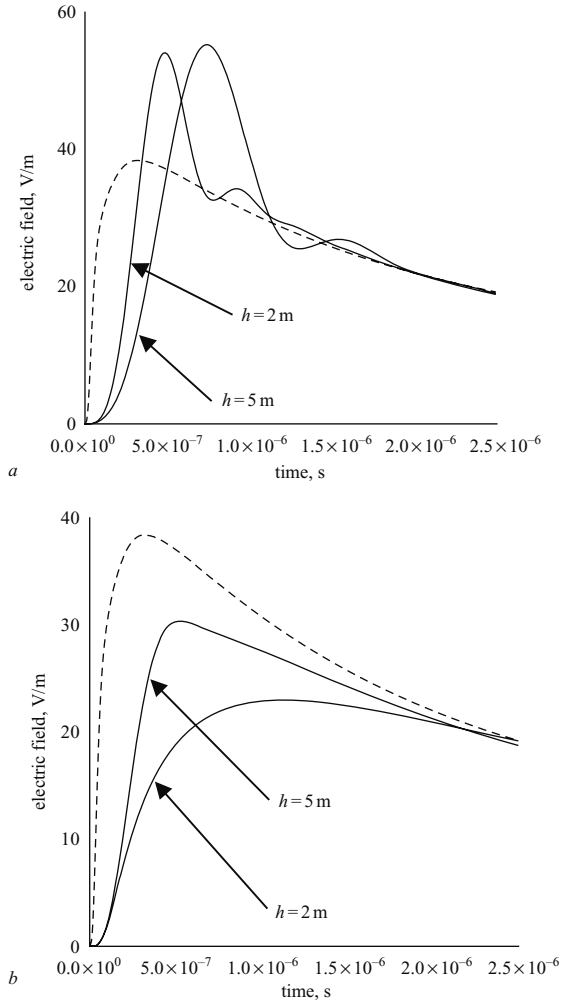

Figure 7.29 *The electric radiation field generated by a lightning return stroke at a distance of 10 km over a stratified ground with two layers. In each example the electric radiation field generated by lightning return stroke over a perfect conducting ground is shown by the dashed line*

a $\sigma_1 = 0.002\,\mathrm{S/m}$, $\sigma_2 = 0.1\,\mathrm{S/m}$, $\varepsilon_1 = 5$, $\varepsilon_2 = 81$
b $\sigma_1 = 0.01\,\mathrm{S/m}$, $\sigma_2 = 0.0001\,\mathrm{S/m}$, $\varepsilon_1 = 5$, $\varepsilon_2 = 5$

$B_\phi(t, D)$ is the total azimuthal magnetic field at the point of observation, $B_{i,\infty}(t, D)$ and $B_{r,\infty}(t, D)$ are the induction field and the radiation field, respectively, at the point of observation, calculated assuming the ground to be perfectly conducting. Figures 7.31 and 7.32 depict the vertical electric field and the azimuthal magnetic field, respectively, over finitely conducting ground of conductivity 0.001 S/m at a distance

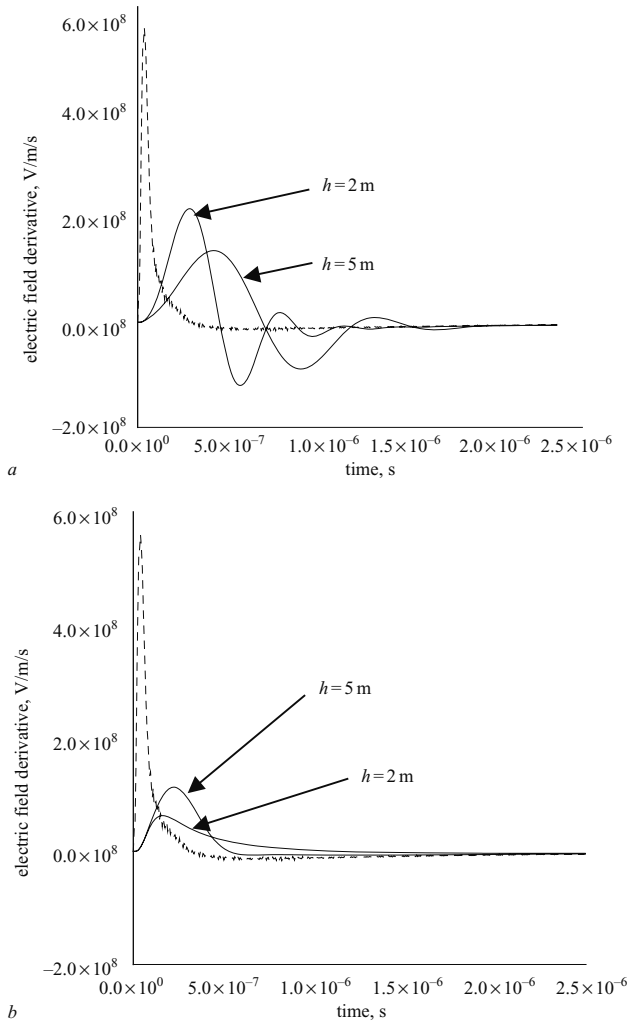

Figure 7.30 *The electric radiation field derivative generated by a lightning return stroke at a distance of 10 km over a stratified ground with two layers. In each example the electric radiation field generated by lightning return stroke over a perfect conducting ground is shown by the dashed line*

a $\sigma_1 = 0.002\,\text{S/m}, \sigma_2 = 0.1\,\text{S/m}, \varepsilon_1 = 5, \varepsilon_2 = 81$
b $\sigma_1 = 0.01\,\text{S/m}, \sigma_2 = 0.0001\,\text{S/m}, \varepsilon_1 = 5, \varepsilon_2 = 5$

of 200 m from the lightning strike together with the field components that would arise at the same location if the ground were to be perfectly conducting. The next task is to obtain the horizontal electric field at the height where the conductors are located. However, let us consider first how to obtain the horizontal electric field

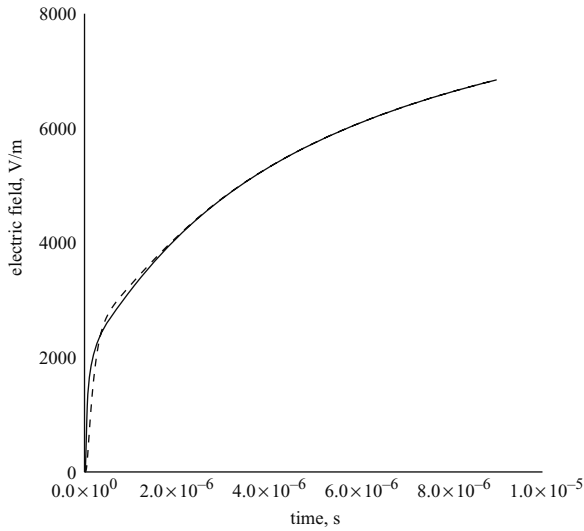

Figure 7.31 *The vertical electric field at 200 m generated by a 12 kA return stroke over perfectly conducting ground (solid line) and over finitely conducting ground of conductivity 0.001 S/m and effective dielectric constant of 5 (dotted line). The electric field was obtained from a channel base current model of Cooray [31]*

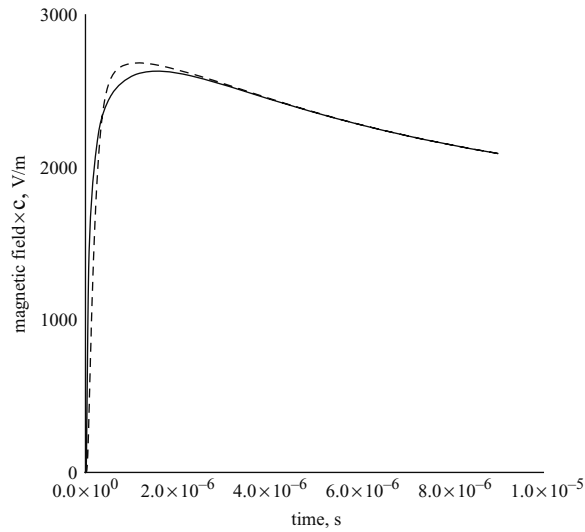

Figure 7.32 *The azimuthal magnetic field at 200 m generated by a 12 kA return stroke over perfectly conducting ground (solid line) and over finitely conducting ground of conductivity 0.001 S/m and effective dielectric constant of 5 (dotted line). The magnetic field was obtained from a channel base current model of Cooray [31]*

at ground level at the point of interest. The horizontal electric field over finitely conducting ground can be obtained by either solving the Sommerfeld equations [46] or by using the formulations given by Norton [42] and Bannister [47]. However, these methods of calculation are not practical because of the limitations on computational time. Instead, many researchers have used approximate solutions of the Sommerfeld integral to calculate the horizontal fields generated by return strokes. One of the approximations used frequently in the literature to calculate the horizontal fields generated by lightning is the method of wave tilt. When a plane electromagnetic field propagates over the finitely conducting ground, the electric field at the surface is tilted towards the ground. That is, at the surface of the ground, the electric field component parallel to the surface is nonzero. The magnitude of this tilt – and hence the amplitude of the horizontal field – depends on the conductivity and the dielectric constant of the soil. According to the wave tilt expression, the ratio between the electric field component perpendicular to the ground E_z and the electric field component parallel to the ground E_h in frequency domain is given by:

$$E_h(D, 0, j\omega) = -E_z(D, 0, j\omega)\frac{k_0}{k}\sqrt{1 - \frac{k_0^2}{k^2}} \tag{7.43}$$

where $k_0 = \omega\sqrt{\mu_0\varepsilon_0}$, $k = k_0\sqrt{\varepsilon_r - j\varepsilon_0\sigma\lambda_0}$, D is the distance to the point of observation, ε_r is the relative dielectric constant, σ is the conductivity, ε_0 is the permittivity of free space and ω is the angular frequency. This equation is valid provided that the field is incident at a grazing angle and that it is a radiation field. One can show that the term inside the square root does not make a significant contribution [40], and hence the horizontal field can be written as:

$$E_h(D, 0, j\omega) = -E_z(D, 0, j\omega)\frac{k_0}{k} \tag{7.44}$$

This equation, which is known as the wave tilt expression, has been used frequently to calculate the horizontal electric field from either the measured or calculated vertical electric field. Unfortunately, very close to the lightning return stroke both of the assumptions made in deriving this equation could be violated so the horizontal field that was calculated from the wave tilt expression could be in error.

The horizontal field at ground level can also be calculated by making use of the surface impedance relationship [41]. According to this relationship, the horizontal electric field at ground level in the frequency domain, $E_h(j\omega)$, is given by:

$$E_h(D, 0, j\omega) = -cB_\phi(D, 0, j\omega)\frac{k_0}{k}\sqrt{1 - \frac{k_0^2}{k^2}} \tag{7.45}$$

where $B_\phi(j\omega)$ is the horizontal magnetic field in the frequency domain at ground level, ε the relative dielectric constant of the ground, σ the conductivity of the ground, ω the angular frequency and ε_0 the permittivity of free space. Neglecting the square

root term, the horizontal electric field, $E_h(t)$, in the time domain at ground level can be written as:

$$E_h(t) = \int_0^t b_\phi(\tau) z_s(t-\tau)\, d\tau \tag{7.46}$$

with

$$z_s(t) = \sqrt{\frac{1}{\varepsilon_r}} e^{-\varphi t}[J_0(\varphi t) + J_1(\varphi t)] \tag{7.47}$$

where $b_p(t)$ is the horizontal magnetic field in the time domain, $\varphi = \sigma/2\varepsilon_0\varepsilon$, $J_0(\varphi t)$ and $J_1(\varphi t)$ are modified Bessel functions of zero and first order. Cooray [40,41] showed that this relationship is capable of generating horizontal fields more accurately than the wave tilt approximation can. He compared the fields calculated by using both surface impedance and the wave tilt expression with the horizontal field obtained directly from Norton's [42] equations; he showed that the expression for the surface impedance is capable of accurately predicting the horizontal field for distances down to about 200 m from the return stroke channel. Figure 7.33 depicts the horizontal electric field calculated in this manner at the point of observation. Now let us consider the horizontal electric field that exists at the height where the conductors of the power line are located.

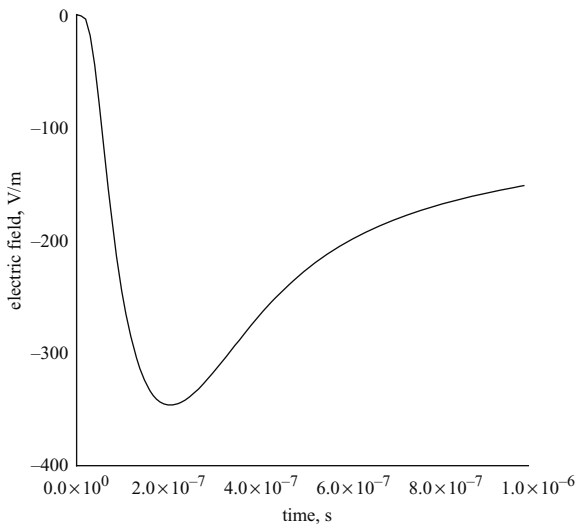

Figure 7.33 The horizontal electric field at 200 m generated by a 12 kA return stroke over finitely conducting ground of conductivity 0.001 S/m and effective dielectric constant of 5

7.4.1 The Cooray–Rubinstein approximation

Several researchers have calculated the horizontal field at overhead cables by adding the horizontal field calculated at line height over perfectly conducting ground to the horizontal field calculated at ground level over finitely conducting ground. In the literature this is known as the Cooray–Rubinstein approximation [41,43,44]. According to this approximation, the horizontal field at a distance D and at a height z is given by:

$$E_h(D, z, t) = E_h(D, 0, t) + E_\infty(D, z, t) \tag{7.48}$$

where $E_\infty(D, z, t)$ is the horizontal electric field at height z when the ground is perfectly conducting, and $E_h(D, 0, t)$ is the horizontal electric field at the surface of the finitely conducting ground. The validity of this expression was investigated by Cooray [40]. His results show that the approximation is generally valid except on a few occasions when the deviation can be larger than about 25 per cent. The reason for this is the following. The horizontal field at height z contains a radiation term, an induction term and a static term. The last two terms are independent of the ground conductivity (actually, the induction term depends only slightly on the ground conductivity) and, therefore, are the same over perfectly and finitely conducting ground. The horizontal field at ground level is mainly radiation and this does not vary significantly with increasing height if the heights are confined to a few tens of metres. Thus the term $E_h(D, 0, t)$ in eqn. 7.48 can partly account for the radiation term at line height. The term $E_\infty(D, z, t)$ exactly accounts for the induction and static terms at height z, but this term also contains a radiation field term which has already been partly compensated for by the term $E_h(D, 0, t)$. Therefore, the radiation field term in $E_\infty(D, z, t)$ makes the calculated field deviate from the exact signature, especially when the radiation terms are important. This can easily be corrected by writing eqn. 7.48 as follows:

$$\begin{aligned} E_h(D, z, j\omega) = {} & E_h(D, 0, t) + E_{\infty,s}(D, z, t) \\ & + E_{\infty,i}(D, z, t) + 0.4E_{\infty,r}(D, z, t) \end{aligned} \tag{7.49}$$

where $E_{\infty,s}(D, z, t)$, $E_{\infty,i}(D, z, t)$ and $E_{\infty,r}(D, z, t)$ are the static, induction and radiation horizontal fields at line height over perfectly conducting ground. Cooray [40] showed that this equation can predict the horizontal field at line height to a better accuracy than the original Cooray–Rubinstein approximation. Note, however, that the original formulation is exact when the ground is perfectly conducting, whereas eqn. 7.49 accounts for 40 per cent of the radiation field term when the ground is perfectly conducting (note that the horizontal field at the surface is zero under these conditions). However, the Cooray–Rubinstein formulation is derived to calculate the horizontal fields over finitely conducting ground and in this case the modified version can be used to generate more accurate results. The horizontal electric field at height z calculated using this equation is shown in Figure 7.34. For comparison purposes the

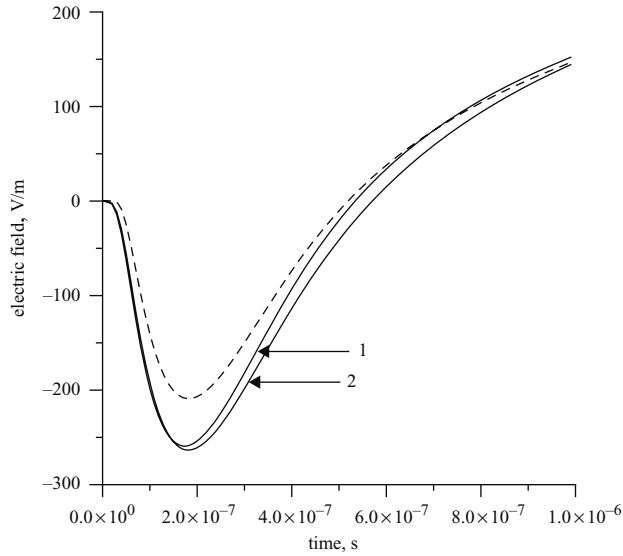

Figure 7.34 Comparison of the horizontal electric field at line height (marked 1) with that calculated by the original Cooray–Rubinstein approximation (dotted line) and the modified Cooray–Rubinstein approximation (marked 2). In the calculation $D = 200m$, $Z = 10m$ *and* $\sigma = 0.01s/m$

exact horizontal field at line height together with the horizontal field calculated using the original Cooray–Rubinstein approximation are also shown in the same Figure.

7.4.2 Electromagnetic fields underground

There are many situations, however, in which the low voltage power installation or the telecommunication lines are laid underground and, although it is the general consensus that underground installations are more immune to induction effects from electromagnetic fields than are overhead ones, the sensitivity and the low threshold energies needed to destroy modern day electronics call for a thorough investigation of the effects of induction in these installations. To facilitate such investigations, a detailed description is required of the electromagnetic field, attributable to lightning, at different depths below the earth's surface. Cooray [45] derived time domain expressions for the lightning-generated electromagnetic fields at different depths below the ground. According to this study, the horizontal electric field at a depth s is given by:

$$E_{h,\sigma}(t, D, s) = \int_0^t E_{h,\sigma}(t - \tau, D, 0)\mathrm{Y}(\tau)\, d\tau \tag{7.50}$$

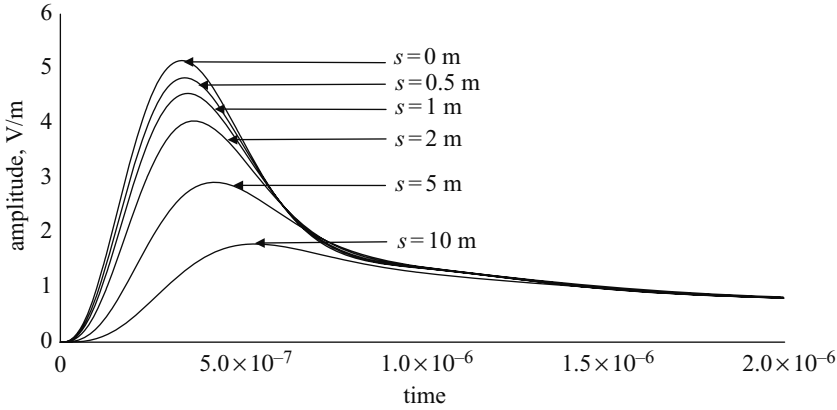

Figure 7.35 *The horizontal electric field at different depths below the earth's surface. The results presented are for the depths of 0 m, 0.5 m, 1 m, 2 m, 5 m and 10 m. The distance to the point of observation is 5 km from a return stroke carrying a 13 kA of peak current. The conductivity of the ground is 0.005 S/m*

with

$$\Upsilon(t) = \frac{e^{-at/2}a\mu}{2\sqrt{t^2-\mu^2}} I_1\left(\frac{a\sqrt{t^2-\mu^2}}{2}\right) u(t-\mu) + e^{-at/2}\delta(t-\mu) \tag{7.51}$$

$$a = \frac{\sigma}{\varepsilon_0 \varepsilon} \tag{7.52}$$

$$\mu = s\sqrt{\mu_0 \varepsilon_0 \varepsilon_r} \tag{7.53}$$

where I_1 is the modified Bessel function of order one, $E_{h,\sigma}(t, D, 0)$ is the horizontal electric field at a distance D over a surface of finitely conducting earth of conductivity σ and $E_{h,\sigma}(t, D, s)$ is the horizontal electric field at a distance D and at a depth s below the surface. In these equations $\delta(t)$ is the delta function and $u(t)$ is Heaviside's unit step function. Figure 7.35 shows the horizontal electric field at several depths below the ground; the ground has a conductivity of 0.005 S/m. Note that the rise time of the underground field increases and the peak amplitude decreases as the field penetrates into the ground. The reason for this is that higher frequencies are selectively attenuated as the field penetrates the ground. Mathematically, the azimuthal magnetic field penetrates in exactly the same way as the horizontal field. Thus the magnetic field under ground is related to the magnetic field at the surface through the equation:

$$B_{\phi,\sigma}(t, D, s) = \int_0^t B_{\phi,\sigma}(t-\tau, D, 0)\Upsilon(\tau)\, d\tau \tag{7.54}$$

where $B_{\phi,\sigma}(t, D, s)$ is the azimuthal magnetic field at a distance D and at a depth s below the surface of finitely conducting earth of conductivity σ and $B_{\phi,\sigma}(t, D, 0)$ is

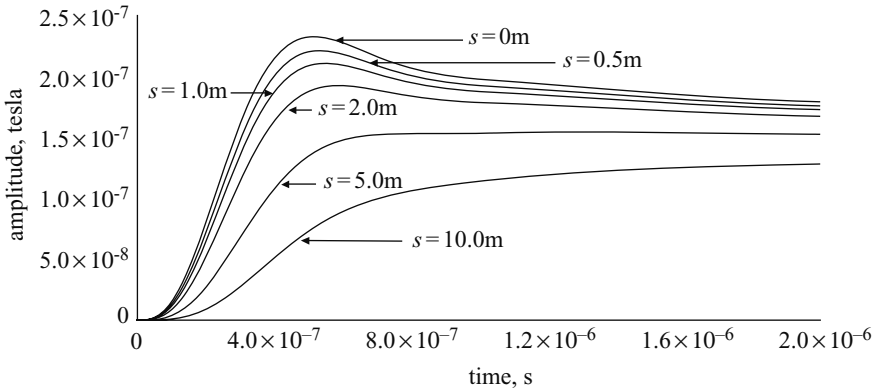

Figure 7.36 *The azimuthal magnetic field at different depths below the earth's surface. The results presented are for the depths 0 m, 0.5 m, 1 m, 2 m, 5 m and 10 m. The distance to the point of observation is 5 km from a return stroke carrying a 13 kA of peak current. The conductivity of the ground is 0.005 S/m*

the azimuthal magnetic field at a distance D over the surface of finitely conducting earth of conductivity σ. Figure 7.36 shows the magnetic field at several depths. Note that the decrease in the peak amplitude as the magnetic field penetrates the ground is not identical to that of the horizontal field. Actually, the attenuation of the peak of the magnetic field with depth is not as strong as that of the horizontal field. The reason for this is that, at a given distance, the frequency content of the magnetic field is different to that of the horizontal field (or they have different temporal signatures). Finally, the vertical electric field at depth s is related to the vertical electric field at the surface through the equation:

$$E_{z,\sigma}(t, D, s) = \int_0^t E_{z,\sigma}(t - \tau, D, 0)\Psi(\tau)\, d\tau \tag{7.55}$$

where

$$\Psi(t) = \int_0^t \Psi_1(t - \tau)Y(\tau)\, d\tau \tag{7.56}$$

$$\Psi_1(t) = \frac{1}{\varepsilon} e^{-at} \tag{7.57}$$

where $a = \sigma/(\varepsilon_0\varepsilon)$, $E_{z,\sigma}(t, D, 0)$ is the vertical electric field at a distance D over the surface of finitely conducting earth of conductivity σ and $E_{z,\sigma}(t, D, s)$ is the vertical electric field at a distance D and at a depth s. The surface fields together with the underground field at 1 m depth are depicted for several conductivities in Figures 7.37 and 7.38. The vertical field attenuates significantly in crossing the boundary; in fact it is discontinuous across the boundary and the field just below the ground is less than

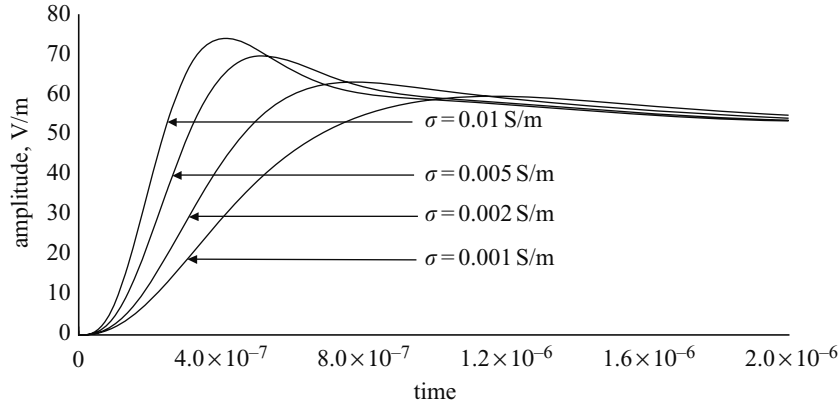

Figure 7.37 *The vertical electric fields at the surface of the earth ($s = 0$) for different conductivities. The results shown are for $\sigma = 0.01\ S/m$, $\sigma = 0.005\ S/m$, $\sigma = 0.002\ S/m$ and $\sigma = 0.001\ S/m$. The distance to the point of observation is 5 km from a return stroke carrying a 13 kA peak current*

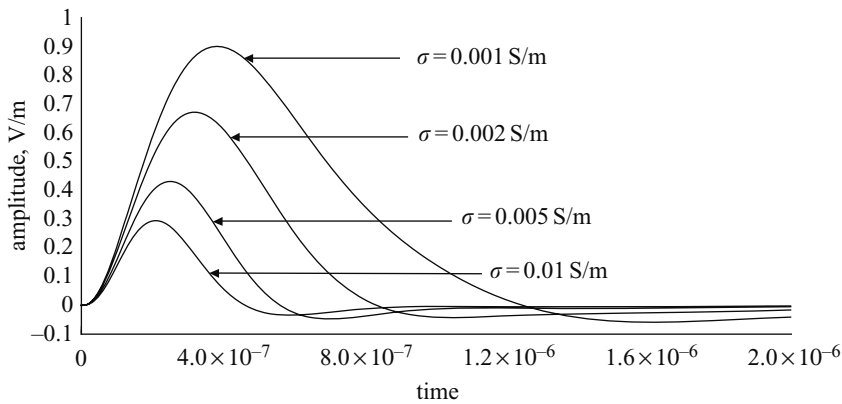

Figure 7.38 *The vertical electric fields at a depth of 1 m below the surface of the earth for different conductivities. The results shown are for $\sigma = 0.01\ S/m$, $\sigma = 0.005\ S/m$, $\sigma = 0.002\ S/m$ and $\sigma = 0.001\ S/m$. The distance to the point of observation is 5 km from a return stroke carrying 13 kA of peak current*

that above the surface. Moreover, note that the half width of the underground field is smaller than that of the surface field. How fast the electric field at a given depth decays with time depends on the relaxation time of the soil under consideration. The decay becomes more marked with increasing conductivity.

7.5 Future research work

The large scale deployment of lightning localisation systems based on time of arrival and the demand on the accuracy of these systems, which to a large extend depends on the propagation effects, calls for more detailed experimental and theoretical studies of propagation effects. In this respect, not much research work has been conducted on the effects of propagation along irregular terrain especially propagation across mountains. In addition to advancing our knowledge of the effects of propagation, such studies would lead to more accurate lightning localisation systems.

7.6 References

1 BERGER, K.: 'Novel observations on lightning discharges: results of research on Mount San Salvatore', *J. Franklin Inst.*, 1967, **238**, pp.478–525

2 UMAN, M.A., SWANBERG, C.E., TILLER, J.A., LIN, Y.T., and KRIDER, E.P.: 'Effects of 200 km propagation on lightning return stroke electric fields', *Radio Sci.*, 1976, **11**, pp.985–990

3 GARDNER, R.L.: 'Effects of propagation on lightning induced transient fields', *Radio Sci.*, 1981, **16**, pp.337–384

4 COORAY, V. and LUNDQUIST, S.: 'Effects of propagation on the risetime and the initial peaks of radiation fields from return strokes', *Radio Sci.*, 1983, **18**, pp.409–415

5 LE VINE, D.M., GESELL, L., and KAO, M.: 'Radiation from lightning return strokes over a finitely conducting earth', *J. Geophys. Res.*, 1986, **91**, pp.11897–11908

6 COORAY, V.: 'Effects of propagation on the return stroke radiation fields', *Radio Sci.*, 1987, **22**, pp.757–768

7 WEIDMAN, C.D. and KRIDER, E.P.: 'Submicrosecond structure of the return stroke waveforms', *Geophys. Res. Lett.*, 1980, **7**, pp.955–958

8 WILLETT, J.C., IDONE, V.P., ORVILLE, R.E., LETEINTURIER, C., EYBERT-BERARD, A., and KRIDER, E.P.: 'An experimental test of the "transmission line model" of electromagnetic radiation from triggered lightning return strokes', *J. Geophys. Res.*, 1988, **93**, pp.3867–3878

9 LE VINE, D.M., WILLETT, J.C., and BAILEY, J.C.: 'Comparison of fast electric field changes from subsequent return strokes of natural and triggered lightning', *J. Geophys. Res.*, 1989, **94**, (D11), pp.13259–13265

10 WILLETT, J.C., BAILEY, J.C., LETEINTURIER, C., and KRIDER, E.P.: 'Lightning electromagnetic radiation field spectra in the interval from 0.2 to 20 MHz', *J. Geophys. Res.*, 1990, **95**, pp.20367–20387

11 WAIT, J.R.: 'Propagation effects for electromagnetic pulse transmission', *Proc. IEEE*, 1986, **74**, pp.1173–1181

12 COORAY, V., and MING, Y.: 'Propagation effects on the lightning generated electromagnetic fields for homogeneous and mixed sea land paths', *J. Geophys. Res.*, 1994, **99**, pp.10641–10652

13 MING, Y., and COORAY, V.: 'Electromagnetic radiation fields generated by lightning return strokes over stratified ground'. 22nd international conference on *Lightning protection*, Budapest, 1994, paper R1c-05
14 MING, Y., and COORAY, V.: 'Propagation effects caused by a rough ocean surface on the electromagnetic fields generated by lightning return strokes', *Radio Sci.*, 1994, **29**, pp.73–85
15 COORAY, V., FERNANDO, M., SÖRENSEN, T., GÖTSCHL, T., and PEDERSEN, Aa.: 'Propagation of lightning generated transient electromagnetic fields over finitely conducting ground', *J. Atmos. Terr. Phys.*, 2000, **62**, pp.583–600
16 FERNANDO, M., and COORAY, V.: 'The peak, risetime and the half-width of lightning generated electric field derivatives over finitely conducting ground'. Proceedings of the 10th international conference on *Electromagnetic compatibility*, University of Warwick, UK, 1997
17 COORAY, G.V., and PEREZ, H.: 'Propagation effects on the first return stroke radiation fields: homogeneous paths and mixed two section paths, Propagation effects on return stroke fields'. 22nd international conference on *Lightning protection*, Budapest, 1994, paper R1a-06
18 WAIT, J.R.: 'Transient fields of a vertical dipole over homogeneous curved ground', *Can. J. Phys.*, 1956, **36**, pp.9–17
19 WAIT, J.R.: 'Propagation of a pulse across a coast line', *Proc. IRE*, 1957, **45** (11), pp.1550–1551
20 WAIT, J.R.: 'Electromagnetic waves in stratified media' (Pergamon Press, Oxford, England, 1962)
21 WAIT, J.R.: 'Mixed path ground wave propagation: 1, short distances', *J. Res. National Bureau of Standards*, 1956, **57**,(4), pp.1–15
22 WAIT, J.R.: 'The propagation of electromagnetic waves along the earth's surface', *in* LANGER, R.E. (Ed.): 'Electromagnetic waves' (Univ. Wisconsin Press, 1962) pp.243–290
23 KING, R.J., CHO, S.H., JAGGARD, D.J., and SOKOLOV, V.: 'Height–gain experimental data for groundwave propagation, 1, homogeneous paths', *Radio Sci.*, 1973, **8**, pp.7–15
24 KING, R.J., CHO, S.H., and JAGGARD, D.J.: 'Height–gain experimental data for groundwave propagation, 2, heterogeneous paths', *Radio Sci.*, 1973, **8**, pp.17–22
25 KINSMAN, B.: 'Wind waves' (Prentice Hall, Englewood Cliffs, New Jersey, 1965) pp.386–403
26 BARRICK, D.E.: 'Theory of HF and VHF propagation across the rough sea, 1, the effective surface impedance for a slightly rough highly conducting medium at grazing incidence', *Radio Sci.*, 1971, **6**, (56), pp.527–533
27 BARRICK, D.E.: 'Theory of HF and VHF propagation across the rough sea, 2, application to HF and VHF propagation above the sea', *Radio Sci.*, 1971, **6**, (56), pp.517–526
28 BAILEY, J.C., and WILLETT, J.C.: 'Catalog of absolutely calibrated, range normalised, wideband, electric field waveforms from located lightning flashes

in Florida'. NRL memorandum report 6497, Naval Research Laboratory, Washington, DC, USA, 1989
29 IZUMI, Y., and WILLETT, J.C.: 'Catalog of absolutely calibrated, range normalised, wideband, electric field waveforms from located lightning flashes in Florida'. Environmental Research Papers, no. 1082, Philips Laboratory, Directorate of Geophysics, Hanscom Air Force Base, Masachussets, USA, 1991
30 COORAY, V., FERNANDO, M., GOMES, C., and SORENSSEN, T.: 'The fine structure of positive return stroke radiation fields' – *IEEE Trans. Electromagn. Compat.*, in press 2003.
31 COORAY, V.: 'Predicting the spatial and temporal variation of the electromagnetic fields, currents and speeds of subsequent return strokes', *IEEE Trans. Electromagn. Compat.*, 1998, **40**, pp.427–435
32 KRIDER, E.P., LETEINTURIER, C., and WILLETT, J.C.: 'Submicrosecond fields radiated during the onset of first return strokes in cloud-to-ground lightning', *J. Geophys. Res.*, 1996, **101**, pp.1589–1597
33 WILLETT, J.C., and KRIDER, E.P.: 'Rise times of impulsive high current processes in cloud to ground lightning', *IEEE Trans. Antennas and Propagation*, 2000, **48**, pp.1442–1451
34 ORVILLE, R.E.: 'Calibration of a magnetic direction finding network using measured triggered lightning return stroke peak currents', *J. Geophys. Res.*, 1991, **96**, pp.17135–17142
35 COORAY, V.: 'Interaction of electromagnetic fields produced by lightning flashes with electrical networks: the influence of propagation effects'. Proceedings of the international conference on *Lightning protection*, Birmingham, England, 1998
36 WILLETT, J.C., and KRIDER, E.P.: 'Rise times of impulsive high-current processes in cloud-to-ground lightning', *IEEE Trans. Antennas Propag.*, 2000, **48**, pp.1442–1451
37 WEIDMAN, C.D., KRIDER, E.P., and UMAN, M.A.: 'Lightning amplitude spectra in the interval from 100 kHz to 20 MHz', *Geophys. Res. Lett.*, 1981, **8**, pp.931–934
38 COORAY, V.: 'A model for the subsequent return strokes', *J. Electrostat.*, 1993, **30**, pp.343–354
39 AGRAWAL, A.K., PRICE, H.J., and GURBAXANI, S.H.: 'Transient response of multiconductor transmission lines excited by a nonuniform electromagnetic field', *IEEE Trans. Electromagn. Compat.*, 1980, **EMC-22**, pp.119–129
40 COORAY, V.: 'Some considerations on the Cooray–Rubinstein approximation used in deriving the horizontal electric field over finitely conducting ground', *IEEE Trans. Electromagn. Compat.*, 2001, **44**, pp.560–566
41 COORAY, V.: 'Horizontal fields generated by return strokes', *Radio Sci.*, 1992, **27**, pp.529–537
42 NORTON, K.A.: 'Propagation of radio waves over the surface of earth and in the upper atmosphere, II', *Proc. IEEE*, 1937, **25**, pp.1203–1236
43 RUBINSTEIN, M.: 'An approximate formula for the calculation of the horizontal electric field from lightning at close, intermediate and long ranges', *IEEE Trans. Electromagn. Compat.*, 1996, **38**, pp.531–535

44 RACHIDI, F., NUCCI, C.A., IANOZ, M., and MAZZETTI, C.: 'Influence of a lossy ground on lightning-induced voltages on overhead lines', *IEEE Trans. Electromagn. Compat.*, 1996, **38**, pp.250–264
45 COORAY, V.: 'Underground electromagnetic fields generated by the return strokes of lightning flashes', *IEEE Trans. Electromagn. Compat.*, 2001, **33**, pp.75–84
46 SOMMERFELD, A.: 'On the propagation of waves in wireless telegraphy', *Ann. Phys.*, 1926, **81**, pp.1135–1153
47 BANNISTER, P.R.: 'New formulas that extend Norton's far field elementary dipole equations to the quasi-near field range', Technical Report 6883, Naval Underwater Systems Center, Newport Laboratory, Newport, Rhode Island, USA, 1984

Chapter 8

Interaction of electromagnetic fields generated by lightning with overhead electrical networks

Carlo Alberto Nucci and Farhad Rachidi

8.1 Introduction

Overvoltages induced by indirect lightning on overhead lines can cause damage to power systems, communication networks and electronic control and management systems. Moreover, due to its more frequent occurrence, indirect lightning constitutes a more important cause of short interruptions and voltage sags than direct strikes, especially for distribution networks. Estimation of indirect lightning is therefore crucial for the correct protection and insulation coordination of overhead lines and, as a consequence, has been the subject of various studies during the past decades. The problem has been seriously reconsidered in recent years due to the increasing demand by customers for good quality in the power supply, and new models have consequently been developed to obtain a more accurate estimation of lightning-induced voltages.

Evaluation of lightning-induced voltages requires knowledge of the electromagnetic field change along the considered line. This electromagnetic field is generally determined assuming that the lightning return stroke channel is a straight vertical antenna above a conducting plane (see Chapter 5). The spatial and temporal distribution of the current along the channel is specified using a return stroke model (see Chapter 6).

In this Chapter, we will present the theory describing the interaction of lightning electromagnetic fields with overhead lines, with particular reference to power systems. In the first part of the Chapter, we will present the different approaches and formulations that can be used to describe the coupling between an external electromagnetic field and a transmission line. Then, we will extend the selected field-to-transmission line coupling model to include the effects of a lossy earth serving as a return conductor and to deal with the case of multiconductor lines. The time-domain representation of coupling equations, useful for analysing nonlinearities, will also be dealt with.

Experimental test and validation of coupling models using data from natural and artificially triggered lightning, EMP simulators, or reduced scale modelling will also be presented in the first part of the Chapter. Finally, in the second part of the Chapter, we will apply the mathematical models to compute lightning-induced overvoltages on overhead power distribution lines[1]. We will discuss, in particular, the influence on the amplitude and waveshape of lightning-induced voltages of:

- finite ground conductivity
- the presence of shielding wires
- the downward leader phase of the lightning discharge that precedes the return stroke phase
- the corona effect.

8.2 Field-to-transmission line coupling models

8.2.1 Use of the transmission line theory

To solve the problem of lightning electromagnetic field coupling to an overhead line, use could be made of the antenna theory, the general approach based on Maxwell's equations[2] [1]. However, due to the length of overhead lines, the use of such a theory for the calculation of lightning-induced voltages implies long computation time, especially when statistical studies are desired (e.g. [2]). On the other hand, the use of a quasistatic approximation [1], according to which propagation is neglected and coupling between incident electromagnetic fields and line conductors can be described by means of lumped elements, is not appropriate. In fact, such an approach requires that the overall dimensions of the circuit be smaller than about one tenth of the minimum significant wavelength of the electromagnetic field, an unacceptable assumption for the case of power lines illuminated by lightning electromagnetic pulse (LEMP)[3].

Assuming that the cross sectional dimensions of the line are electrically small, we can consider that propagation occurs only along the line axis. This is one of the basic assumptions of the transmission line (TL) theory. In this way, the line can be represented by a distributed-parameter structure along its axis. Another fundamental assumption in the TL theory is that the response of the line is quasitransverse electromagnetic (quasi-TEM). In other words, the electromagnetic field produced by the electric charges and currents along the line is confined in the transverse plane and perpendicular to the line axis. Finally, another assumption in the TL theory is that the sum of the line currents at any cross section of the line is zero. In other words, the

[1] Lightning-induced voltages are of concern essentially for distribution overhead lines. Transmission lines are characterised by basic insulation levels larger than typical magnitudes of lightning-induced voltages

[2] Different methods based on this approach generally assume that the wire's cross section is smaller than the minimum significant wavelength (thin wire approximation)

[3] The LEMP frequency spectrum extends up to significant frequencies of a few MHz and beyond, which corresponds to minimum wavelengths of about 100 m or less

ground – the reference conductor – is the return path for the currents in the n overhead conductors.

For uniform transmission lines with electrically small cross sectional dimensions (not exceeding about one tenth of the minimum significant wavelength of the exciting electromagnetic field), several theoretical and experimental studies have shown a fairly good agreement between results obtained using the TL approximation and results obtained either by means of antenna theory or experiments (see section 8.2.12). A detailed discussion of the validity of the basic assumptions of TL theory is beyond the scope of this Chapter. However, it is worth making the following remarks.

- It is in practice impossible that the response of a line be purely TEM. In fact, a pure TEM mode would occur only for the case of a lossless line above a perfectly conducting ground and when the exciting electromagnetic field has no electric field component tangential to the line conductors. Note, however, that for LEMP-illuminated power lines, the quasi-TEM line response can be considered as a reasonable approximation [1].
- By assuming that the sum of all the currents is equal to zero, we are considering only transmission line mode currents and neglecting the so-called antenna mode currents. If we desire to compute the load responses of the line, this assumption is adequate, because the antenna mode current response is small near the ends of the line. Along the line, however, and even for electrically small line cross section, the presence of antenna mode currents means that the sum of the currents at a cross section is not necessarily equal to zero [1,3]. However, the quasisymmetry due to the presence of the ground plane results in a very small contribution of antenna mode currents and, consequently, the predominant mode on the line will be transmission line [1].

8.2.2 Case of single wire line above a perfectly conducting ground

We will consider first the simple case of a lossless single wire line above a perfectly conducting ground. This simple case will be helpful for introducing various coupling models and discussing some basic concepts. Later in this Chapter (sections 8.2.8 and 8.2.10), we will cover the cases of lossy and multiconductor lines. The transmission line is defined by its geometrical parameters (wire radius a and height above ground h) and its terminations Z_A and Z_B (see Figure 8.1). The line is illuminated

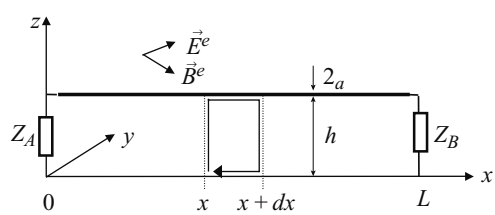

Figure 8.1 Geometry of the problem

by an external electromagnetic field. The problem of interest is the calculation of the induced voltages and currents along the line and at the terminations.

It is worth noting that the external exciting electric and magnetic fields $\vec{E}^e$, $\vec{B}^e$ are defined as the sum of the lightning channel incident fields $\vec{E}^i$, $\vec{B}^i$ and the ground-reflected fields $\vec{E}^r$, $\vec{B}^r$, determined in absence of the line conductor.

8.2.3 Agrawal, Price, and Gurbaxani model

By integrating Maxwell's equations along the integration path defined in Figure 8.1 and using the transmission line approximation, Agrawal, Price and Gurbaxani [4] have derived a set of coupling equations which, for the case of Figure 8.1, can be written in the frequency domain as [1]:

$$\frac{dV^s(x)}{dx} + j\omega L' I(x) = E_x^e(x, h) \tag{8.1}$$

$$\frac{dI(x)}{dx} + j\omega C' V^s(x) = 0 \tag{8.2}$$

in which L' and C' are the per unit length inductance and capacitance of the line, respectively[4], $I(x)$ is the induced current and $V^s(x)$ is the scattered voltage, related to the total voltage $V(x)$ by the following expression:

$$V^s(x) = V(x) - V^e(x) \tag{8.3}$$

where

$$V^e(x) = -\int_0^h E_z^e(x, z)\, dz$$

is the exciting voltage and $E_x^e(x, h)$ and $E_z^e(x, z)$ are the horizontal (along the conductor) and vertical components of the exciting electric field, respectively.

The terminal conditions in terms of the scattered voltage and the total current, as used in eqns 8.1 and 8.2, are given by:

$$V^s(0) = -Z_A I(0) + \int_0^h E_z^e(0, z)\, dz \tag{8.4}$$

$$V^s(L) = Z_B I(L) + \int_0^h E_z^e(L, z)\, dz \tag{8.5}$$

The equivalent circuit representation of eqns 8.1, 8.2, 8.4 and 8.5 is shown in Figure 8.2. For this model, the forcing function is the exciting electric field tangential to the line conductor represented by distributed voltage sources along the line. Note that, in accordance with terminal conditions 8.4 and 8.5, two lumped voltage sources (equal to the line integral of the exciting vertical electric field) are inserted at the line terminations.

[4] Expressions for the line inductance and capacitance will be given in section 8.2.8

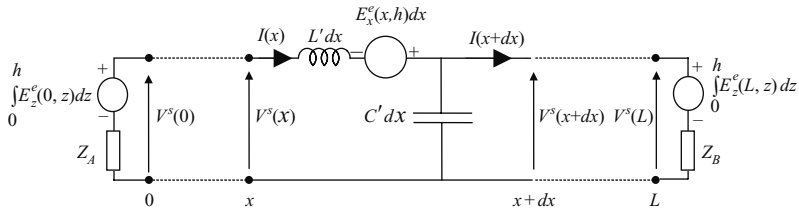

Figure 8.2 Equivalent circuit of a lossless, single-wire overhead line excited by an electromagnetic field. Agrawal et al. formulation

8.2.4 Taylor Satterwhite, and Harrison model

Although the Agrawal model is the most adopted in the power/lightning literature, it is worth observing that an equivalent formulation of field-to-transmission line coupling equations was proposed earlier by Taylor, Satterwhite and Harrison in 1965 [5]. In the Taylor *et al*. formulation, the coupling equations are expressed in terms of the total induced current and the total induced voltage. They are given by:

$$\frac{dV(x)}{dx} + j\omega L' I(x) = -j\omega \int_0^h B_y^e(x,z)\,dz \tag{8.6}$$

$$\frac{dI(x)}{dx} + j\omega C' V(x) = -j\omega C' \int_0^h E_z^e(x,z)\,dz \tag{8.7}$$

and the terminal conditions are expressed as:

$$V(0) = -Z_A I(0) \tag{8.8}$$

$$V(L) = Z_B I(L) \tag{8.9}$$

These equations contain two forcing functions that are expressed in terms of the exciting transverse magnetic induction (distributed series voltage source) and of the exciting vertical electric field (distributed parallel current source), respectively, as shown in the equivalent circuit in Figure 8.3.

The Taylor formulation has been widely used in the electromagnetic compatibility literature, with particular reference to the interaction between nuclear electromagnetic pulse (NEMP) and transmission lines (e.g. [6]).

8.2.5 Rachidi model

Another form of coupling equation, equivalent to the Agrawal *et al*. and the Taylor *et al*. models, has been derived by Rachidi [7]. In this formulation, only the exciting magnetic field components appear explicitly as forcing functions in

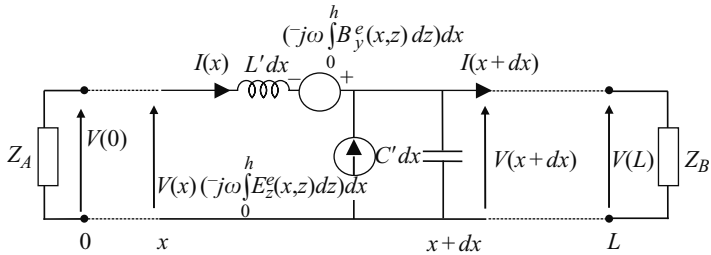

Figure 8.3 Equivalent circuit of a lossless single-wire overhead line excited by an electromagnetic field. Taylor et al. formulation

the equations:

$$\frac{dV(x)}{dx} + j\omega L' I^s(x) = 0 \tag{8.10}$$

$$\frac{dI^s(x)}{dx} + j\omega C' V(x) = \frac{1}{L'} \int_0^h \frac{\partial B_x^e(x,z)}{\partial y}\, dz \tag{8.11}$$

in which $I^s(x)$ is the so-called scattered current related to the total current by:

$$I(x) = I^s(x) + I^e(x) \tag{8.12}$$

where the excitation current $I^e(x)$ is defined as:

$$I^e(x) = -\frac{1}{L'} \int_0^h B_y^e(x,z)\, dz \tag{8.13}$$

The terminal conditions corresponding to this formulation are:

$$I^s(0) = -\frac{V(0)}{Z_A} + \frac{1}{L'} \int_0^h B_y^e(0,z)\, dz \tag{8.14}$$

$$I^s(L) = \frac{V(L)}{Z_B} + \frac{1}{L'} \int_0^h B_y^e(L,z)\, dz \tag{8.15}$$

The equivalent circuit corresponding to the above equivalent set of coupling equations is shown in Figure 8.4. Note that the equivalent circuit associated with the Rachidi model could be seen as the dual circuit – in the sense of electrical network theory – of the one corresponding to the Agrawal model (Figure 8.2).

8.2.6 *Contribution of the different components of the electromagnetic field in the coupling mechanism*

In this section, we show that it is misleading to speak about the contribution of a given electromagnetic field component to the total induced voltage and current, without first specifying which coupling model one is using [8].

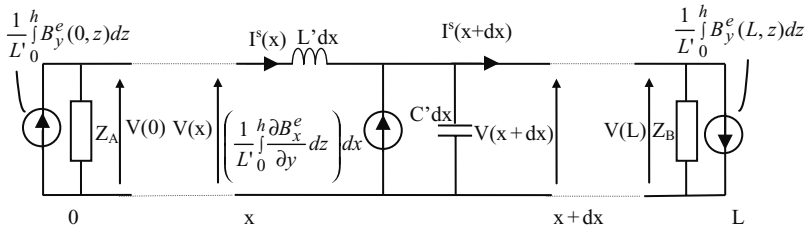

Figure 8.4 Equivalent circuit of a lossless single-wire overhead line excited by an electromagnetic field. Rachidi formulation

Consider a 1 km long, 10 m high single wire overhead line matched at both ends, above a perfectly conducting plane, illuminated by the electromagnetic field radiated by a nearby lightning return stroke. The components of the exciting electromagnetic field are calculated assuming a return stroke channel base current typical of subsequent return strokes (peak value of 12 kA and maximum time derivative of 40 kA/μs) and using the MTLE return stroke current model by Nucci *et al.* [9] (see Chapter 6). Nevertheless, the conclusions we will draw are independent of the nature of the transient electromagnetic source. The results predicted by the three coupling models are shown in Figure 8.5. These results have been obtained by solving numerically in the time domain the coupling equations associated with the three considered formulations using the point-cantered finite difference technique. In addition to the total induced voltage at the line extremities, the contributions of the electromagnetic field components pertinent to each formulation are also shown.

Figure 8.5 shows that, as predicted theoretically, the total induced voltage waveforms obtained using the three coupling formulations are identical. However, the contribution of a given component of the exciting electromagnetic field to the total induced voltage varies depending on the adopted coupling formulation. For instance, for the considered case, the contribution of the vertical electric field E_z, significant indeed in the formulation of Taylor *et al.* (Figure 8.5*a*), is practically negligible when using the equations of Agrawal *et al.* (Figure 8.5*b*). This result can be explained considering that the source terms due to the vertical electric field are not the same in the two formulations: in the formulation of Taylor *et al.*, the source term related to the vertical electric field acts along the whole line length, whereas in the formulation of Agrawal *et al.*, the source related to the vertical electric field is localised only at the line terminations. The same reasoning can be applied to the contribution of other components, such as the transverse magnetic field B_y in the Taylor *et al.* and in the Rachidi formulations, or the horizontal electric field E_x, which contributes significantly to the total voltage in the Agrawal *et al.* model, but does not explicitly appear in the two other formulations.

The above illustrates that the three coupling formulations, absolutely equivalent and thus predicting the same total voltages, take into account the electromagnetic coupling in different ways, the various components of the electromagnetic field being related through Maxwell's equations. In other words, the three coupling formulations

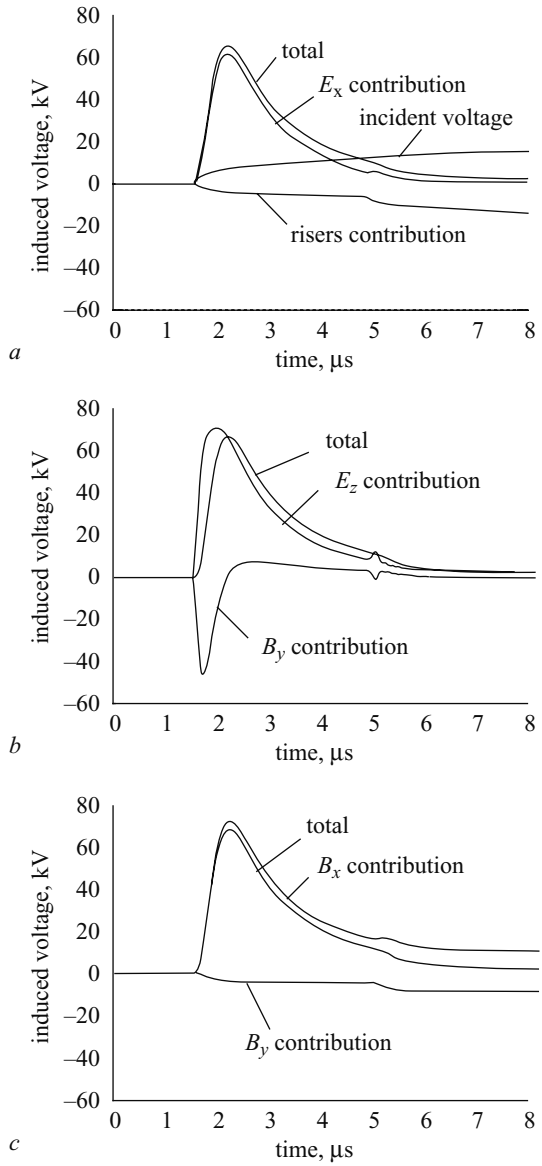

Figure 8.5 *Illustration of the contribution of the various field components in the coupling mechanism* (adapted from Nucci and Rachidi [8])

a Agrawal *et al*. formulation
b Taylor *et al*. formulation
c Rachidi formulation

are different expressions of the same equations, cast in terms of different combinations of the various electromagnetic field components.

In conclusion, we have shown that the contribution of a given electromagnetic field in the coupling mechanism appears to depend strongly on the model used. Thus, when speaking about the contribution of a given electromagnetic field component to the induced voltages, one has first to specify the coupling model one is using.

8.2.7 Other models

Two other models were also developed and are often used in the literature to compute lightning-induced voltages on overhead lines, namely the model by Rusck [10], and the model by Chowdhuri and Gross [11]. These two models are different from the Agrawal *et al*. model and its equivalent formulations, and the differences among these models have caused considerable discussion, disagreement and controversies between researchers and engineers dealing with lightning-induced voltage calculations (e.g. [12–19]). This is probably due to the fact that the models are expressed in terms of different quantities: the Rusck equations are written in terms of potentials, the Chowdhuri equations in terms of total voltage and the Agrawal model is expressed in terms of scattered voltage. In two papers presented, respectively, by Nucci *et al*. [16] and Cooray [17], the different coupling equations have been algebraically rearranged in terms of similar quantities and it has been demonstrated that the Agrawal model (or any of its equivalent formulations) is the only one that can be considered as rigorous within the limits of transmission line approximation, independently from the electromagnetic field source. In both the Rusck and Chowdhuri–Gross models, some source terms are omitted. However, it is important to note that for the case of an electromagnetic field originated by a straight vertical channel[5], the Rusck model becomes absolutely equivalent to the Agrawal model and can be therefore adopted to predict the voltages induced by such a vertical lightning channel.

Since it is still adopted by many engineers and researchers, it is worth reminding ourselves here of the simplified analytical Rusck formula [10], which applies to the case of an infinitely long single conductor line above a perfectly conducting ground. This formula gives the maximum value V_{max} of the induced overvoltages at the point of the line nearest the stroke location:

$$V_{max} = Z_0 \frac{Ih}{d} \left(1 + \frac{1}{\sqrt{2}} \cdot \beta \cdot \frac{1}{\sqrt{(1 - 0.5 \cdot v^2)}} \right) \tag{8.16}$$

where

$$Z_0 = \frac{1}{4\pi} \sqrt{\frac{\mu_0}{\varepsilon_0}} = 30\Omega \tag{8.17}$$

in which I is the amplitude of the lighting current assumed to have a step function waveshape, h is the height of the line, d is the distance to the stroke location and β is the ratio between the return stroke velocity and the velocity of the light.

[5] Namely, the geometry for which the Rusck model was originally developed

Note that this formula includes not only the coupling model between the electromagnetic field and the line, but also the return stroke model for the calculation of the electromagnetic field radiated by the lightning current. The Rusck simplified formula will be compared with the Agrawal *et al*. model in section 8.3.3.

Finally, it is worth mentioning that the Agrawal *et al*. coupling model and its equivalent formulations (namely the models by Taylor *et al*., by Rachidi, and – provided the lightning channel is straight and perpendicular to the ground plane – by Rusck) are the only ones that have been validated versus experimental results (see section 8.2.12).

8.2.8 Inclusion of losses

In the calculation of lightning-induced voltages, losses are, in principle, to be taken into account both in the wire and in the ground. Losses due to the finite ground conductivity are the most important ones, and affect both the electromagnetic field and the surge propagation along the line [20]. However, for relatively short lines (typically not exceeding 2 km), it is the influence of the ground losses on the electromagnetic field that is prominent [20].

Let us make reference to the same geometry of Figure 8.1, and now take into account losses both in the wire and in the ground plane. The wire conductivity and relative permittivity are σ_w and ε_{rw}, respectively, and the ground is characterised by its conductivity σ_g and its relative permittivity ε_{rg}. The Agrawal coupling equations extended to the present case of a wire above an imperfectly conducting ground can be written as (for a step by step derivation see [1]):

$$\frac{dV^s(x)}{dx} + Z'I(x) = E_x^e(x,h) \tag{8.18}$$

$$\frac{dI(x)}{dx} + Y'V^s(x) = 0 \tag{8.19}$$

where Z' and Y' are the longitudinal and transverse per-unit-length impedance and admittance, respectively, given by [1,20][6]:

$$Z' = j\omega L' + Z'_w + Z'_g \tag{8.20}$$

$$Y' = \frac{(G' + j\omega C')Y'_g}{G' + j\omega C' + Y'_g} \tag{8.21}$$

in which:

- L', C' and G' are the per-unit-length longitudinal inductance, transverse capacitance and transverse conductance, respectively, calculated for a lossless wire

[6] In [1] the per-unit-length transverse conductance has been disregarded

above a perfectly conducting ground:

$$L' = \frac{\mu_0}{2\pi}\cosh^{-1}\left(\frac{h}{a}\right)$$
$$\cong \frac{\mu_0}{2\pi}\ln\left(\frac{2h}{a}\right) \qquad \text{for } h \gg a \tag{8.22}$$
$$C' = \frac{2\pi\varepsilon_0}{\cosh^{-1}(h/a)}$$
$$\cong \frac{2\pi\varepsilon_0}{\ln(2h/a)} \qquad \text{for } h \gg a \tag{8.23}$$
$$G' = \frac{\sigma_{air}}{\varepsilon_0}C' \tag{8.24}$$

- Z'_w is the per-unit-length internal impedance of the wire; assuming a round wire and an axial symmetry for the current, the following expression for the wire internal impedance can be derived (e.g. [21]):

$$Z'_w = \frac{\gamma_w I_0(\gamma_w a)}{2\pi a\sigma_w I_1(\gamma_w a)} \tag{8.25}$$

where $\gamma_w = \sqrt{j\omega\mu_0(\sigma_w + j\omega\varepsilon_0\varepsilon_{rw})}$ is the propagation constant in the wire and I_0 and I_1 are the modified Bessel functions of zero and first order, respectively;

- Z'_g is the per-unit-length ground impedance, which is defined as [20,22]:

$$Z'_g = \frac{j\omega\int_{-\infty}^{h} B_y^s(x,z)\,dx}{I} - j\omega L' \tag{8.26}$$

where B_y^s is the y component of the scattered magnetic induction field.

Several expressions for the ground impedance have been proposed in the literature (e.g. [23–37]). Here, we will use the one proposed by Sunde [25] given by:

$$Z'_g = \frac{j\omega\mu_0}{\pi}\int_0^{\infty}\frac{\mathrm{e}^{-2hx}}{\sqrt{x^2+\gamma_g^2}+x}dx \tag{8.27}$$

where $\gamma_g = \sqrt{j\omega\mu_0(\sigma_g + j\omega\varepsilon_0\varepsilon_{rg})}$ is the propagation constant in the ground. The above expression is adopted essentially for two reasons:

(i) Equation (8.27) is directly connected to the general expressions obtained from the scattering theory. As a matter of fact, it is shown in [1] that the general expression for the ground impedance derived using scattering theory reduces to the Sunde approximation when considering the transmission line approximation.

(ii) The results obtained using eqn. 8.27 are shown to be accurate within the limit of the transmission line approximation [1, page 409].

The general eqn. 8.27 is not suitable for a numerical evaluation since it involves an integral over an infinitely long interval. Several approximations for the ground impedance of a single wire line have been proposed in the literature (see [20] for a survey). One of simplest and most accurate was proposed by Sunde himself and is given by the following logarithmic function:

$$Z'_g \cong \frac{j\omega\mu_0}{2\pi} \ln\left(\frac{1+\gamma_g h}{\gamma_g h}\right) \tag{8.28}$$

It has been shown [20] that the above logarithmic expression represents an excellent approximation to the general expression 8.27, over the whole frequency range of interest;

- Finally, Y'_g is the so-called ground admittance, given by [1,22]:

$$Y'_g \cong \frac{\gamma_g^2}{Z'_g} \tag{8.29}$$

8.2.9 *Discussion on the relative importance of different transmission line parameters when calculating lightning-induced voltages*

Figure 8.6 presents a comparison between ground and wire impedances for a 10 mm radius copper wire located 10 m above ground. The ground conductivity and relative permittivity are equal to 0.01 S/m and to 10, respectively. The results show that within the frequency range of interest, the wire impedance can be neglected as regard to the ground impedance. Note that for poorer conductivities, the ratio $|Z'_g/Z'_w|$ will become even higher. We have also plotted in Figure 8.7 the ratios $|Z'_g/j\omega L'|$ and $|Z'_w/j\omega L'|$.

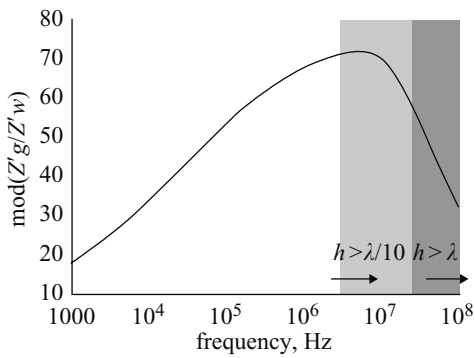

Figure 8.6 Ratio of the magnitude of the ground impedance to the wire impedance as a function of frequency. Copper wire of radius 10 mm located at 10 m above the ground ($\sigma_g = 0.01$ S/m, $\varepsilon_{rg} = 10$) (adapted from Rachidi *et al.* [20])

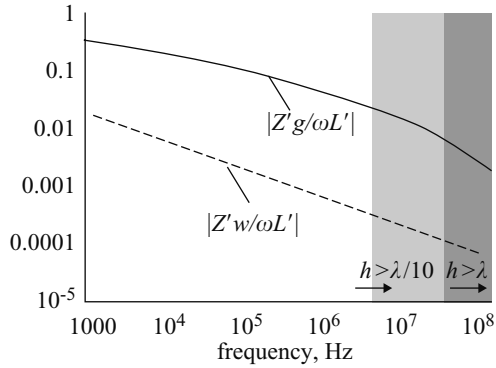

Figure 8.7 *Comparison between longitudinal impedance terms: ground impedance, wire impedance, and $j\omega L'$. Copper wire of radius 10 mm located at 10 m above the ground ($\sigma_g = 0.01$ S/m, $\varepsilon_{rg} = 10$)* (adapted from Rachidi *et al.* [20])

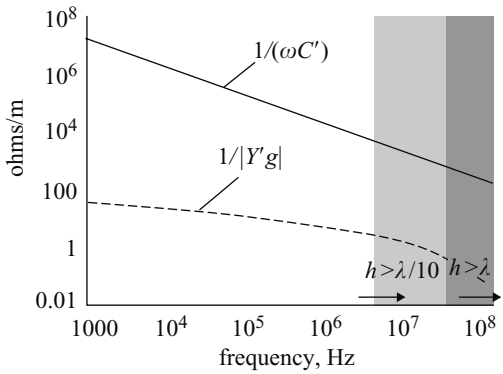

Figure 8.8 *Comparison between the inverse of the ground admittance and $1/j\omega C'$. Copper wire of radius 10 mm located at 10 m above the ground ($\sigma_g = 0.01$ S/m, $\varepsilon_{rg} = 10$)*

It can be seen that while $|Z'_g|$ represents a nonnegligible fraction of $\omega L'$ over a wide frequency range, again $|Z'_w|$ can be neglected.

In Figure 8.8, we have presented a comparison between $1/|Y'_g|$ and $1/\omega C'$ as a function of frequency. It can be seen that $1/|Y'_g|$ is about five orders of magnitude lower than $1/\omega C'$, and therefore it can be neglected in the computation of lightning-induced voltages on overhead power lines. Even though the computations in Figures 8.6 to 8.8 are performed up to 100 MHz, it is important to realise that for a line height $h = 10$ m, the transmission line (TL) approximation is valid up to a frequency of about 3 MHz corresponding to $\lambda = 10\,h$; for frequencies higher that about 30 MHz, corresponding in our case to $\lambda = h$, the validity of the TL approximation becomes

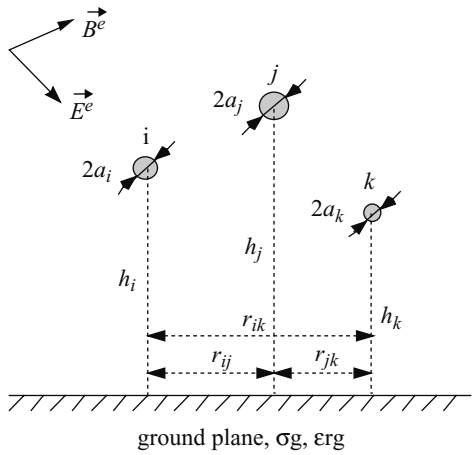

Figure 8.9 Cross sectional geometry of a multiconductor line in the presence of an external electromagnetic field

seriously questionable. For this reason, computed results for these frequencies are presented in shaded areas.[7]

8.2.10 Case of multiconductor lines

Making reference to the geometry of Figure 8.9, the generalised[8] telegrapher's equations for the case of a multiwire system along the x axis above an imperfectly conducting ground and in presence of an external electromagnetic excitation are given by [1,37]:

$$\frac{d}{dx}\left[V_i^s(x)\right] + j\omega\left[L'_{ij}\right][I_i(x)] + \left[Z'_{g_{ij}}\right][I_i(x)] = \left[E_x^e(x, h_i)\right] \tag{8.30}$$

$$\frac{d}{dx}[I_i(x)] + \left[G'_{ij}\right]\left[V_i^s(x)\right] + j\omega\left[C'_{ij}\right]\left[V_i^s(x)\right] = [0] \tag{8.31}$$

in which:

- $\left[V_i^s(x)\right]$ and $[I_i(x)]$ are frequency-domain vectors of the scattered voltage and the current along the line;

[7] It is worth mentioning that in Figures 8.6–8.8, we have neglected any variation of ground conductivity and relative permittivity as a function of frequency, even though there is experimental evidence that these two parameters are frequency dependent [38]. However, studies on the variation of ground parameters as a function of frequency [38,39] show that (a) the ground conductivity variation becomes very appreciable only for frequencies higher than about 10 MHz, and (b) significant variation of the ground relative permittivity as a function of frequency occurs up to a few MHz, for which the ground impedance is not appreciably affected by the value of the ground relative permittivity

[8] The word 'generalised' is here used to emphasise the presence of an external illumination of the line

- $\left[E_x^e(x,h_i)\right]$ is the vector of the exciting electric field tangential to the line conductors;
- [0] is the zero matrix (all elements are equal to zero);
- $\left[L'_{ij}\right]$ is the matrix of the per-unit-length line inductance. Assuming that the distances between conductors are much larger than their radii, the general expression for the mutual inductance between two conductors i and j is given by [1]:

$$L'_{ij} = \frac{\mu_0}{2\pi} \ln\left(\frac{d^*}{d}\right) = \frac{\mu_0}{4\pi} \ln\left(\frac{r_{ij}^2 + (h_i + h_j)^2}{r_{ij}^2 + (h_i - h_j)^2}\right) \tag{8.32}$$

The self inductance for the conductor i is given by:

$$L'_{ii} = \frac{\mu_0}{2\pi} \ln\left(\frac{2h_i}{r_{ii}}\right) \tag{8.33}$$

- $\left[C'_{ij}\right]$ is the matrix of the per-unit-length line capacitance. It can be evaluated directly from the inductance matrix using the following expression [1]:

$$\left[C'_{ij}\right] = \varepsilon_0\mu_0[L'_{ij}]^{-1} \tag{8.34}$$

- $\left[G'_{ij}\right]$ is the matrix of per-unit-length transverse conductance. The transverse conductance matrix elements can be evaluated starting either from the capacitance matrix or the inductance matrix using the following relations:

$$\left[G'_{ij}\right] = \frac{\sigma_{air}}{\varepsilon_0}[C'_{ij}] = \sigma_{air}\mu_0[L'_{ij}]^{-1} \tag{8.35}$$

However, for most practical cases, the transverse conductance matrix elements G'_{ij} are negligible in comparison with $j\omega C'_{ij}$ [3] and can therefore be neglected in the computation;

- And, finally, $[Z'_{g_{ij}}]$ is the matrix of the ground impedance. The general expression for mutual ground impedance between two conductors i and j derived by Sunde is given by [25]:

$$Z'_{g_{ij}} = \frac{j\omega\mu_0}{\pi} \int_0^\infty \frac{e^{-(h_i+h_j)x}}{\sqrt{x^2 + \gamma_g^2} + x} \cos(r_{ij}x)dx \tag{8.36}$$

In a similar way as for the case of a single wire line, an accurate logarithmic approximation is proposed by Rachidi *et al*. [37] which is given by:

$$Z'_{g_{ij}} \cong \frac{j\omega\mu_0}{4\pi} \ln\left[\frac{\left(1 + \gamma_g((h_i + h_j)/2)\right)^2 + \left(\gamma_g(r_{ij}/2)\right)^2}{\left(\gamma_g((h_i + h_j)/2)\right)^2 + \left(\gamma_g(r_{ij}/2)\right)^2}\right] \tag{8.37}$$

Note that in eqns 8.30 and 8.31, we have neglected the terms corresponding to the wire impedance and the so-called ground admittance. Indeed, and as we have seen in the previous section, for the typical overhead lines and for typical frequency range

of interest (below 10 MHz), these parameters can be disregarded with reasonable approximation.

The boundary conditions for the two-line terminations are given by:

$$[V_i^s(0)] = -[Z_A][I_i(0)] + \left[\int_0^{h_i} E_z^e(0, z)\, dz\right] \tag{8.38}$$

$$[V_i^s(L)] = [Z_B][I_i(L)] + \left[\int_0^{h_i} E_z^e(L, z)\, dz\right] \tag{8.39}$$

in which $[Z_A]$ and $[Z_B]$ are the impedance matrices at the two-line terminations.

8.2.11 Time-domain representation of coupling equations

A time-domain representation of field-to-transmission line coupling equations is sometimes preferable because it allows us to handle in a straightforward manner nonlinear phenomena such as corona, the presence of nonlinear protective devices at the line terminals (see sections 8.3.4 and 8.3.5) and also variation in the line topology (opening and reclosure of switches). On the other hand, frequency-dependent parameters, such as the ground impedance, need to be represented using convolution integrals, which require important computation time and memory storage.

The field-to-transmission line coupling eqns 8.30 and 8.31 can be converted into the time domain to obtain the following expressions:

$$\frac{\partial}{\partial x}\left[v_i^s(x,t)\right] + \left[L'_{ij}\right]\frac{\partial}{\partial t}[i_i(x,t)] + \left[\xi'_{g_{ij}}\right] \otimes \frac{\partial}{\partial t}[i_i(x,t)] = \left[E_x^e(x, h_i, t)\right] \tag{8.40}$$

$$\frac{\partial}{\partial x}[i_i(x,t)] + \left[G'_{ij}\right]\left[v_i^s(x,t)\right] + \left[C'_{ij}\right]\frac{\partial}{\partial t}\left[v_i^s(x,t)\right] = 0 \tag{8.41}$$

in which $\otimes$ denotes convolution product and the matrix $[\xi'_{g_{ij}}]$ is called the transient ground resistance matrix; its elements are defined as:

$$[\xi'_{g_{ij}}] \cong F^{-1}\left\{\frac{Z'_{g_{ij}}}{j\omega}\right\} \tag{8.42}$$

The inverse Fourier transforms of the boundary conditions written, for simplicity, for resistive terminal loads read:

$$[v_i(0,t)] = -[R_A][i_i(0,t)] + \left[\int_0^{h_i} E_z^e(0, z, t)\, dz\right] \tag{8.43}$$

$$[v_i(L)] = [R_B][i_i(0)] + \left[\int_0^{h_i} E_z^e(L, z, t)\, dz\right] \tag{8.44}$$

where $[R_A]$ and $[R_B]$ are the matrices of the resistive loads at the two-line terminals.

The general expression for the ground impedance matrix terms in the frequency domain eqn. 8.36 does not have an analytical inverse Fourier transform. Thus, the

elements of the transient ground resistance matrix in time domain are to be, in general, determined using a numerical inverse Fourier transform algorithm.[9]

8.2.12 *Experimental validation of the field-to-transmission line coupling models*

Rigorously, to test a coupling model it is necessary to know the incident electromagnetic field and the voltage (or current) induced by such a field on a given experimental line. This can be achieved by means of experimental installations and measurements; indeed, a number of experimental installations have been set up in different research centres in the world with such an aim. Then, using the exciting incident field as an input to the coupling model, one has to evaluate the voltage (or current) induced by such a field on the line as predicted by the model and to compare the calculated waveshape with the measured one.

The exciting field can be of different origin, such as the field radiated by natural or artificially-triggered lightning [42–50], by EMP simulators [51–54], or by vertical antennas simulating a reduced-scale lightning channel [55–57]. As a general comment, we can observe that the use of lightning is complicated by the intrinsic difficulty

[9] However, the following analytical expressions are shown to be reasonable approximations to the numerical values obtained using an inverse FFT [40]:

$$\xi'_{g_{ii}}(t) = \min\left\{\frac{1}{2\pi h_i}\sqrt{\frac{\mu_0}{\varepsilon_0\varepsilon_{rg}}},\ \frac{\mu_0}{\pi\tau_{g_{ii}}}\left[\frac{1}{2\sqrt{\pi}}\sqrt{\frac{\tau_{g_{ii}}}{t}} + \frac{1}{4}\exp(\tau_{g_{ii}}/t)\operatorname{erfc}\left(\sqrt{\frac{\tau_{g_{ii}}}{t}}\right) - \frac{1}{4}\right]\right\} \tag{8.45}$$

$$\begin{aligned}\xi'_{g_{ij}}(t) = \min\Bigg\{&\frac{1}{2\pi\hat{h}}\sqrt{\frac{\mu_0}{\varepsilon_0\varepsilon_{rg}}},\ \frac{\mu_0}{\pi T_{ij}}\Bigg[\frac{1}{2\sqrt{\pi}}\sqrt{\frac{T_{ij}}{t}}\cos(\theta_{ij}/2)\\ &+ \frac{1}{4}\mathrm{e}^{T_{ij}\cos(\theta_{ij})/t}\cos\left(\frac{T_{ij}}{t}\sin(\theta_{ij}) - \theta_{ij}\right)\\ &- \frac{1}{2\sqrt{\pi}}\sum_{n=0}^{\infty}a_n\left(\frac{T_{ij}}{t}\right)^{\frac{2n+1}{2}}\cos\left(\frac{2n-1}{2}\theta_{ij}\right) - \frac{\cos(\theta_{ij})}{4}\Bigg]\Bigg\}\end{aligned} \tag{8.46}$$

in which

$$\tau_{g_{ii}} = h_i^2\mu_0\sigma_g, \tag{8.47}$$

T_{ij} and θ_{ij} are defined as follows:

$$\hat{\tau}_{g_{ij}} = \hat{h}_{ij}^2\mu_0\sigma_g = \left(\frac{h_i + h_j}{2} + j\frac{r_{ij}}{2}\right)^2\mu_0\sigma_g = T_{ij}\mathrm{e}^{j\theta_{ij}} \tag{8.48}$$

and erfc is the complementary error function defined as:

$$\operatorname{erfc}(x) = \frac{2}{\sqrt{\pi}}\int_x^{\infty}\exp(-t^2)\,dt = 1 - \frac{2\exp(-x^2)}{\sqrt{\pi}}\sum_{n=0}^{\infty}a_n x^{2n+1} \tag{8.49}$$

where $a_n = 2^n/(1\cdot 3\cdots(2n+1))$.

Equations 8.45 and 8.46 extend the well known Timotin formula [41] to the early time region, within the limits of the transmission line approximation [40]

in performing a controlled experiment, although triggered lightning is clearly a better technique in this respect. More controlled conditions can be achieved using the above mentioned EMP simulators or reduced-scale models. In what follows we give a brief description of the results that have been obtained using these techniques with the aim of testing the coupling models.

8.2.12.1 Natural and triggered lightning experiments

Concerning the validation of coupling models, it is not crucial to distinguish between natural and triggered lightning, and for this reason we have grouped in the same paragraph the two types of experiment. We will limit ourselves here to discussing only some of the experimental results published in the literature, a complete survey of the existing publications being beyond the scope of this paragraph.

A large number of experimental recordings has been published by Yokoyama *et al*. [42–44] using an experimental three-conductor, 820 m long, unenergised overhead line. The overvoltages measured by Yokoyama *et al*. were induced by lightning strokes having known impact point, a 200 m high tower, 200 m distant from the closest point of the line. Both current and overvoltages were recorded, but the corresponding fields were not. Indeed Yokoyama *et al*. used their experimental data to test the model by Rusck, in the complete form, which uses as input the lightning current and gives as output the induced voltage. In this respect, the results by Yokoyama *et al*. cannot be used to test the coupling model as specified at the beginning of this section, but certainly provide an indication on the adequacy of the Rusck model.

The first simultaneous measurements of lightning electric and magnetic fields and the power line voltages induced by those fields were performed by Uman and coworkers in the Tampa Bay area of Florida during the summer of 1979 (Master *et al*. [12,45]). Voltage measurements were made at one end of a 500 m unenergised overhead distribution line. Comparison of voltages calculated according to the Agrawal coupling model and measured ones yielded reasonably good agreement in voltage waveshapes, but the magnitudes of the first were systematically about a factor of four smaller than the latter [12,45]. Then, a series of experiments was carried out in the following years by the University of Florida research group (Rubinstein *et al*. [46], Georgiadis *et al*. [47]) in which some corrections were made on the first experiment procedure and in which, overall, a better agreement between theory and experimental results concerning voltage waveshapes was reached, although the agreement between amplitudes was not always satisfactory. Possible causes for the disagreement can be: calibration errors, imperfect determination of the angle of incidence of the electromagnetic wave, uncertainties about the ground conductivity value, the presence of trees and other objects in the vicinity of the line which may cause a field distortion.

De la Rosa and coworkers [48] presented measurements of voltage at one end of 13 kV three-phase overhead line of standard construction type. The line was 2.8 km long, nearly 10 m high. The three line conductors were bound together to a common point at both line ends, used to take a connection down to the voltage divider and

matching resistor placed at ground level at both ends of the line. Amplitude, polarity and waveshape of the voltage at one end of the Mexican line were found to be a strong function of the position of lightning with respect to the line (in general quite distant from the line) and of ground conductivity. Their results were used by Cooray and De la Rosa [49], who found a good agreement between measured voltages and those calculated using the Agrawal *et al*. model.

Barker *et al*. [50] published the results of a study carried out at Camp Blanding in Florida to characterise lightning-induced voltages amplitude and waveshapes. They tested the Rusck simplified formula eqn. 8.16 (see section 8.2.7) and the Agrawal model, finding a reasonable agreement between theory and measurements. The comparison presented in [50] is, however, affected by the assumption of a perfectly conducting ground, which was not the case in the field experiment.

8.2.12.2 EMP simulators

Coupling models can also be tested by means of EMP simulators. An EMP simulator is a facility able to radiate within the so-called working volume an electromagnetic wave with very short rise time (of the order of some ns) and with some tens of kV/m electric field intensity. EMP stands, as a matter of fact, for electromagnetic pulse [51]. The main components of an EMP simulator are a pulse generator and an antenna (of guided wave type, conical etc.) excited by the first one. With an EMP simulator it is possible, in principle, to avoid contamination of the incident field due to the wire scattering, as might be the case when the field and the induced voltages are measured simultaneously (e.g. for lines illuminated by natural lightning fields). In this respect, the repeatability of the pulse generator is crucial, in that the electromagnetic field that is measured within the working volume in absence of the victim must be the same as that which excites the victim when put within the working volume.

An example of comparison between measured and calculated results obtained by Guerrieri *et al*. [53,54] using the SEMIRAMIS EMP simulator of the Swiss Federal Institute of Technology of Lausanne [52] is shown in Figure 8.10.

8.2.12.3 Reduced scale modelling

Another example of an experiment that can be carried out under controlled conditions is reduced scale modelling. Ishii *et al*. [55] published voltage and current measurements obtained from a simple geometrical line model on a finitely conducting ground and found very good agreement between theory and calculations. The Japanese experiment was of interest since it also allowed for the assessment of the Agrawal coupling model extended to the case of an overhead line above a lossy ground.

Piantini and Janiszewski [56] obtained experimental data from a reduced scale model of a distribution line at the University of Saõ Paulo in Brazil, which has been used by Nucci *et al*. [57] to test, successfully, the Agrawal model. In Figure 8.11 we show an example of comparison between measurement and calculations taken from [56]. Another example will be given in section 8.3.5.

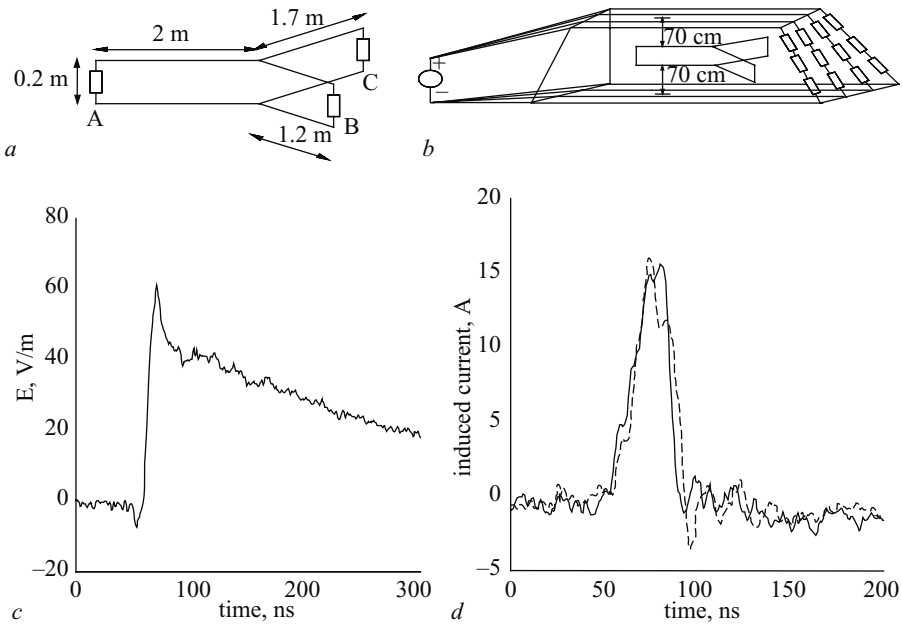

Figure 8.10 *Example of comparison performed using the EMP simulator of the Federal Institute of Technology of Lausanne [52] between calculated (using the Agrawal model) and induced currents on a Y-shaped test structure* (adapted from Guerrieri *et al*. [53,54])

- *a* test structure
- *b* arrangement of the Y-shaped structure within the working volume of the simulator
- *c* typical shape of the vertical electric field in the working volume of the simulator (measurement of the field is performed in absence of the Y-shaped structure)
- *d* measured (solid line) and calculated (dotted line) induced currents at point A of the structure

8.3 Lightning-induced voltages on overhead power lines

8.3.1 Return stroke current model, computation of the incident electromagnetic field, and coupling model

A computer program (LIOV, *l*ightning-*i*nduced *o*ver*v*oltage) was developed by the authors of this Chapter, which allows for the evaluation of lightning-induced voltages on a multiconductor overhead line above a lossy ground (see [58,20] for the theoretical background). LIOV has been developed in the framework of an international collaboration involving the University of Bologna (Department of Electrical Engineering), the Swiss Federal Institute of Technology (Power Systems Laboratory) and the University of Rome La Sapienza (Department of Electrical Engineering). The

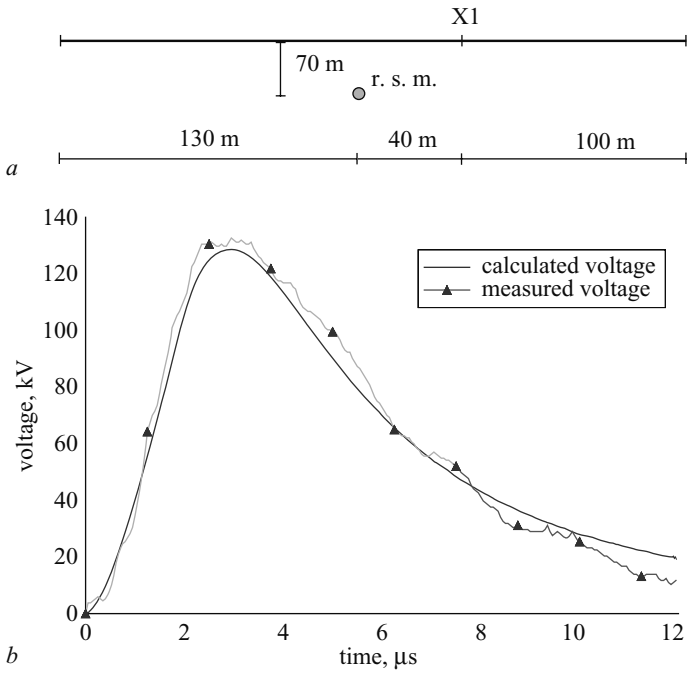

Figure 8.11 *Test of the Agrawal et al. coupling model using a reduced-scale line model* (adapted from Nucci *et al*. [57])

a a simple single-conductor overhead line (top view). R.s.m. denotes the return stroke location, the real dimensions of the reduced scale model are scaled by a factor 50

b comparison between measurements and experimental results

code is based on the field-to-transmission line coupling formulation of Agrawal *et al*., suitably adapted for the calculation of induced overvoltages when lightning strikes near a horizontal overhead transmission line. In the LIOV code, the electromagnetic field radiated by the lightning channel is calculated using the field equations in the form given by Uman *et al*. [59] with the extension to the case of lossy ground introduced by Cooray and Rubinstein [60,61] and assuming the modified transmission line (MTLE) return stroke current model for the description of the spatial–temporal distribution of the lightning current along the return stroke channel (Nucci *et al*. [16]; Rachidi and Nucci [62]). The amplitude decay constant of the MTL model, λ, is fixed at 2 km, as implied in [63] by means of simultaneously measured electromagnetic fields at two different distances.

The forcing functions in the Agrawal *et al*. coupling model are expressed, as seen in section 8.2.3, in terms of the vertical and horizontal electric field components. The vertical electric field radiated by the lightning channel is calculated assuming the ground as a perfectly conducting plane, since such a field component is not affected

significantly by the soil resistivity in the frequency and distance range of interest, using the equations of Chapter 5. For the calculation of the horizontal electric field component, we adopt the approximate formula proposed by Cooray and Rubinstein [60,61].[10]

The LIOV code allows for the calculation of lightning-induced voltages along an overhead line as a function of lightning current waveshape (amplitude, front steepness, duration), return stroke velocity, line geometry (height, length, number and position of conductors), stroke location with respect to the line, ground resistivity, ground relative permittivity and termination impedances. Induction effects of downward leader electric fields [64] and corona effect on the induced voltages [65] can be also dealt with. As a matter of fact, all calculation results presented in previous sections and those that will be presented in the next ones have been obtained using the LIOV code.[11]

8.3.2 Mechanism of voltage induction by a nearby lightning return stroke on an overhead line

Let us consider a 1 km long, 10 m high, single wire overhead line, matched at both ends, to avoid reflections that would render less simple the following discussion. The stroke location is at a distance $y = 50$ m from the line centre and equidistant to the line terminations. We now for simplicity assume the ground as a perfect conductor. The influence of ground losses will be dealt with in the following sections. The lightning return stroke field is calculated assuming the MTLE return stroke model, a channel base current typical of subsequent return strokes (12 kA peak amplitude, 40 kA/μs maximum-time derivative) and a return stroke velocity of 1.3×10^8 m/s. The overvoltages at three different positions along the line calculated according to the Agrawal model are shown in Figure 8.12 (*a*: $x = 0$; *b*: $x = 250$ m; *c*: $x = 500$ m). For illustrative purposes, the contributions to the total overvoltage of the incident voltage, of the voltage due to the horizontal electric field and of the voltage due to the vertical electric field coupling with the risers are shown in Figure 8.12; note that the first and the third terms represent the contribution of the vertical electric field to the total overvoltage according to this model. Although the total induced voltage has essentially the same waveshape independently of the observation point location, the various contributions to the total overvoltage differ as a function of the observation point. See, for instance, the voltage produced by the horizontal electric field coupling. Figure 8.13 gives a schematic explanation of the

[10] Note that Cooray [66] has proposed an improved version of such a formula, taking into account remarks by Wait [67]. We assume in what follows that, for the adopted values for ground conductivity, our results will not be significantly affected by the adoption of one expression instead of the other one. The improved Cooray–Rubinstein expression [66] has been recently implemented in an improved version of the LIOV code [68]

[11] It is worth adding that in the LIOV code, both the MTLE and the Agrawal models equations are dealt with in the time domain; the field-to-transmission line coupling equations of the Agrawal model are solved by means of the point-centred finite-difference method

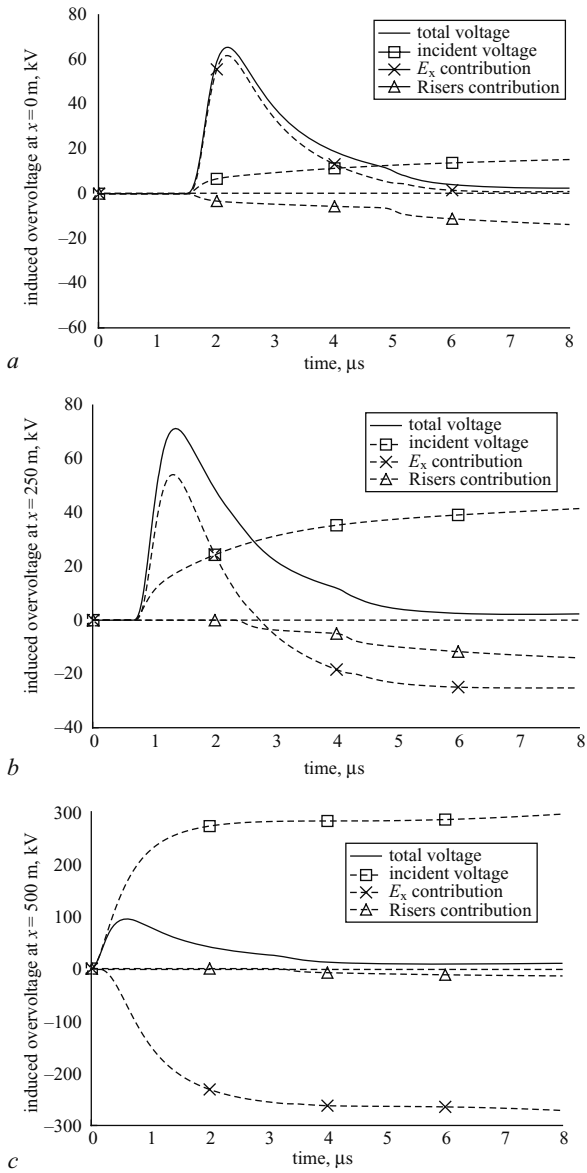

Figure 8.12 *Overvoltages calculated at three different positions along a 1 km long, matched overhead line, according to the Agrawal coupling model. Stroke location: 50 m from the line centre and equidistant from line terminations. Channel-base current: typical of subsequent return-stroke as shown in Figure 2 of [1]. Return stroke model: MTL model with* $\lambda = 2$ *km and* $v = 1.9 \times 10^8$ *m/s* (adapted from Nucci *et al.* [58])

a $x = 0$ m
b $x = 250$ m
c $x = 500$ m

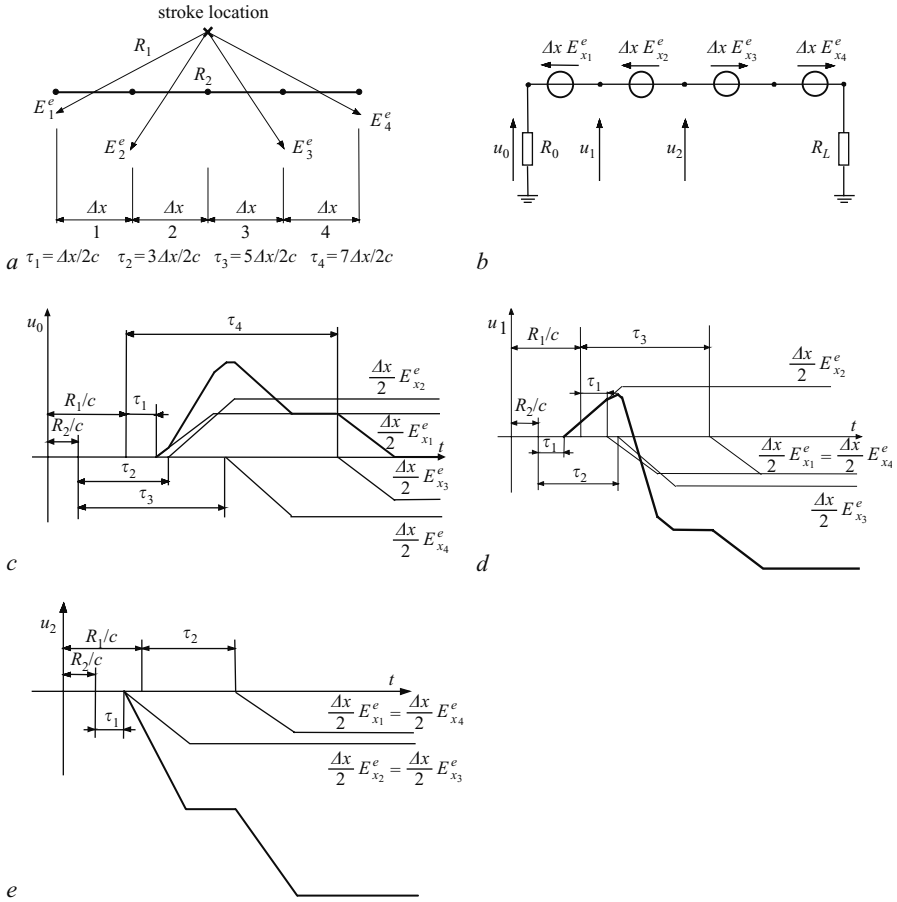

Figure 8.13 *Schematic explanation of the different wave shapes of the induced voltage due to the horizontal field at three different positions according to the Agrawal model* (adapted from Diendorfer [14] and Nucci [69])

a line segmentation
b equivalent sources
c $x = 0\,\mathrm{m}$
d $x = 250\,\mathrm{m}$
e $x = 500\,\mathrm{m}$

different waveshapes at different observation points along the line of such a voltage contribution and explains the mechanism of formation of lightning-induced voltages. Note that due to the symmetry of the considered case, for low-frequency lighting electromagnetic fields or for short line lengths, no voltage would be induced along the line.

8.3.3 Preliminary remarks on the influence of the ground resistivity on the induced voltages

Ground resistivity is one of the most important parameters affecting the induced voltage amplitude and waveshape [20,45,70–74], and this is the case even for stroke locations close to the line. In the next paragraphs we shall perform a systematic analysis, varying current waveshape, stroke location and observation point, aimed both at explaining the reasons for the different possible shapes and polarities of the induced voltages and at consolidating the knowledge on the subject. First it is useful, however, to make some preliminary remarks on the influence of the ground resistivity on the induced voltages.

Let us consider again a 1 km long, 10 m high, single conductor overhead line. In order to clearly illustrate the influence of ground conductivity, a low value, namely 0.001 S/m, has been chosen. The ground relative permittivity is assumed to be equal to ten. The line is terminated at both ends on resistances of about 500 Ω (a value corresponding to the characteristic impedance of the line when considered as lossless). The same lightning strike location (equidistant from the line terminations and at 50 m from the line centre), return stroke current (12 kA peak amplitude, 40 kA/μs maximum time derivative) and return stroke velocity (1.3×10^8 m/s) considered in section 8.3.2 are assumed.

The induced voltage calculated at the line terminations is presented in Figure 8.14*a*. In the same Figure, we have also presented the results obtained for the same configuration but considering the ground as a perfectly conducting plane. It can be seen that the ground conductivity affects significantly the induced voltages in magnitude, shape and polarity. It is important to remember, as earlier mentioned in section 8.2.8, that the ground conductivity affects the induced voltages *via* two mechanisms: (i) in the calculation of the exciting electromagnetic fields and (ii) in the calculation of line parameters, which means in the propagation of the induced surges along the line. Now, the contribution of each of these two effects of the ground resistivity is shown, for the same line of Figure 8.14*a*, in Figure 8.14*b*, where the induced voltages for the three following cases are reproduced [20]:

case 1: the ground conductivity is taken into account in both field calculation and surge propagation along the line (solid line in Figure 8.14*b*)
case 2: the effect of the finite ground conductivity is taken into account only in the surge propagation along the line (ideal field curve in Figure 8.14*b*); for this case, the exciting electric field has been calculated assuming a perfectly conducting ground
case 3: the effect of the finite ground conductivity is taken into account only in the calculation of the exciting electric field, neglecting the ground impedance (ideal line curve in Figure 8.14*b*).

It can clearly be seen that for the considered case, namely for a relatively short line, the surge propagation along the line is not appreciably affected by the finite ground conductivity. This conclusion has important implications both for the computational aspects of the problem and for the interpretation of the results.

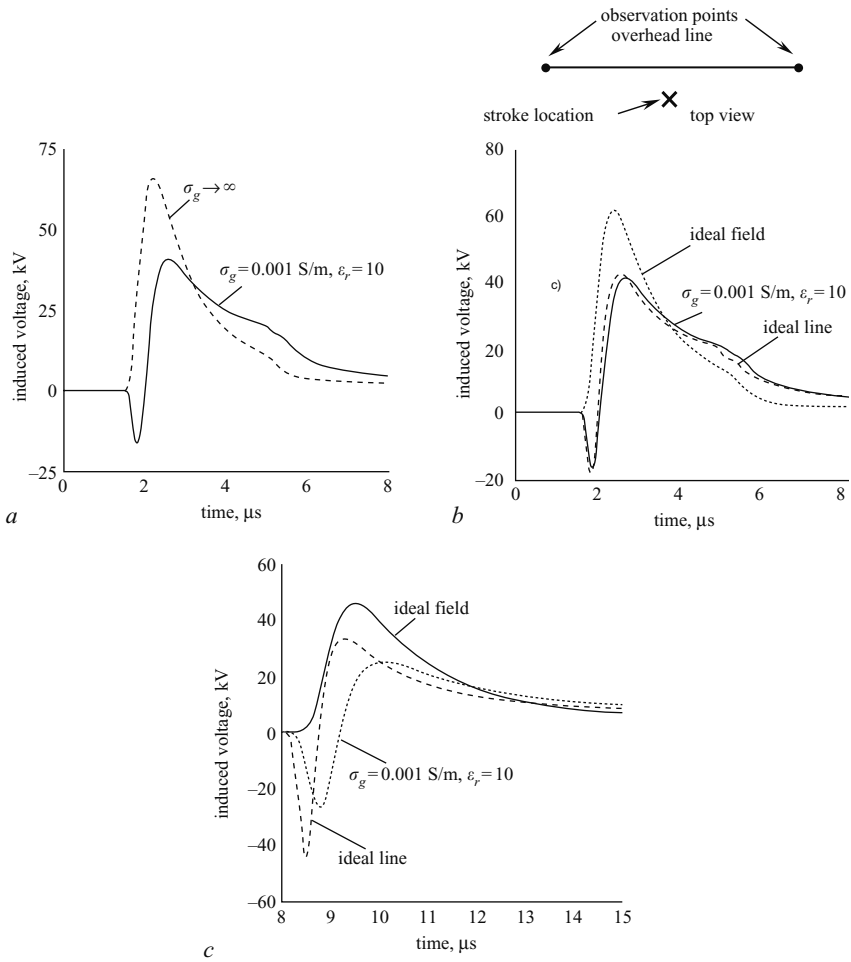

Figure 8.14 *Influence of ground resistivity on lightning-induced voltages for the case of a stroke location equidistant to the line terminations. Lightning current: typical of subsequent return strokes (12 kA peak amplitude, 40 kA/μs maximum time-derivative). Observation points: line terminations* (adapted from Rachidi *et al.* [20])

- *a* case of a 1 km overhead line, solid line: $\sigma_g = 0.001\ S/m$, $\varepsilon_r = 10$, dotted line: perfectly conducting ground
- *b* as in a, dashed line (ideal line): induced voltage calculated taking into account the ground finite conductivity only when calculating the exciting electric field, and not in the surge propagation (ground impedance); dotted line (ideal field): results obtained when the effect of ground finite conductivity is taken into account only in the surge propagation along the line
- *c* as in b but for a 5 km long line

Note, however, that the influence of the ground on the surge propagation depends obviously on the line length. This issue is discussed with more detail in [20,75]. We limit ourselves here to reporting that for line lengths in the range of two kilometres or so and for values of ground conductivity not lower than 0.001 S/m, for the evaluation of the early time response of the line it is sufficient to take into account the presence of a lossy ground only in the calculation of the incident electromagnetic field.[12] In Figure 8.14*c*, we show results similar to those presented in Figure 8.14*b*, but considering a 5 km long line. It is clear that the surge attenuation and distortion along the line are no longer negligible and that the induced voltages are appreciably affected by the ground losses through both radiated field and surge propagation along the line.

8.3.4 Sensitivity analysis and discussion

Although computer programs are nowadays popular and widely applied to solving a number of classical, yet complex, problems in electrical engineering (load flow, short circuits, stability), when dealing with the electromagnetic effects produced by lightning on distribution systems, often a simple equation, able to predict the amplitude of lightning-induced overvoltages without massive use of computer memory and/or numerical algorithms, is preferred. This somewhat obsolete concept of coping with the problem of interest can be due, on the one hand, to the random and unpredictable nature of the lightning discharge that apparently makes worthless any effort towards the achievement of accurate calculations – as, according to the above mentioned concern, what is really needed is just some order of magnitude of the amplitude that the induced voltages may reach – and, on the other hand, to the inherent complexity of the problem, which involves many aspects of several disciplines (physics, electromagnetics, power systems, numerical analysis, statistics). This partially explains the success of the simplified Rusck formula, which – as we shall see – in some simplified cases can still represent a valuable engineering tool. However, the results of the research activities on the subject carried out in the last decades in many countries have permitted the development of more realistic models and their implementation in relevant computer codes, as will be further discussed in the following section. These more recent models and computer programs can deal with more realistic cases than those considered by the previous models, where the overhead line was generally assumed to be of infinite length and above a perfectly conducting ground. They are applied in the following sections to perform a sensitivity analysis aimed at providing the magnitude and waveshape of lightning-induced surges as a function of the involved physical and geometrical parameters. Clearly, additional model improvements are still highly desirable, as even the most up-to-date ones do not still take into account some aspects of the problem (e.g. channel branches, lightning current attachment processes and relevant effects on the radiated electromagnetic field).

[12] If the line is not matched, one has to be aware that the multiple reflections of surges propagating along it would be attenuated by the line losses

8.3.4.1 Channel base current and return stroke speed

The sensitivity analysis is carried out first assuming five different channel base currents, whose main parameters (peak value and maximum front steepness) are reported in Table 8.1. Note that current A2 = D2, with a peak amplitude of 12 kA and a maximum time derivative of 40 kA/μs, corresponds to a typical subsequent return stroke, according to Berger *et al.* [76]. Waveshapes A1, A2 and A3 correspond to channel base currents with different maximum time derivatives, the peak value being kept constant and equal to 12 kA. Waveshapes D1, D2 and D3 correspond to currents having the same maximum time derivative (40 kA/μs), but with different peak values. The selected minimum and maximum values for maximum time derivative correspond to the 5 and 95 per cent of cumulative probability according to [76].

All the channel base currents A1, A2, A3 and D1, D2, D3 are reproduced by the sum of two Heidler functions [77], whose parameters are reported in Table 8.2.

For all calculations, if not otherwise indicated, we will assume the return stroke speed equal to 1.9×10^8 m/s, a typical value along the first 500 m portion of the channel [78]. The effect of the variation of such a parameter will be discussed later in this section.

Table 8.1 Subsequent return stroke current peak values and maximum time derivatives of the adopted currents

Parameter	Currents					
	A1	A2 = D2	A3	D1	D2 = A2	D3
I_{peak} [kA]	12	12	12	4.6	12	50
$(di/dt)_{max}$ [kA/μs]	12	40	120	40	40	40

Table 8.2 Parameters of the two Heidler functions reproducing the adopted currents

Parameter	Currents					
	A1	A2 = D2	A3	D1	A2 = D2	D3
I_{01} [kA]	10.7	10.7	7.4	4.3	10.7	47
τ_{11} [μs]	0.95	0.25	0.063	0.086	0.25	0.9
τ_{12} [μs]	4.7	2.5	0.5	3.3	2.5	66
I_{02} [kA]	6.5	6.5	9	2.5	6.5	0
τ_{21} [μs]	4.6	2.1	0.27	2.8	2.1	0
τ_{22} [μs]	900	230	66	270	230	0
n	2	2	2	2	2	2

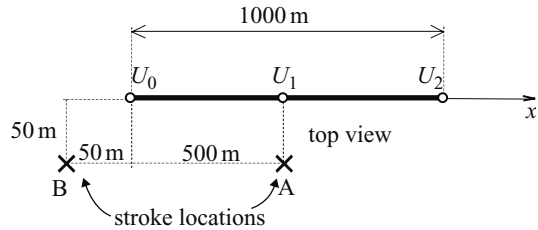

Figure 8.15 Geometry of the study. The line is matched at the two ends

8.3.4.2 Ground electrical parameters

The calculations are performed considering (i) a perfectly conducting ground ($\sigma_g \to \infty$), and (ii) a ground characterised by a conductivity $\sigma_g = 0.01\,\mathrm{S/m}$ and a relative permittivity $\varepsilon_{rg} = 10$.

8.3.4.3 Line configuration and stroke location

As a base case we consider a 1 km long, 8 m high, single conductor (diameter equal 1 cm) overhead line. We can reasonably assume that the length of 1 km is significant enough to assess the influence of the various parameters involved in the sensitivity analysis, although distribution lines are, in general, longer than 1 km. Such an assumption will be discussed later (see section 8.3.4.8).

Two different stroke locations are selected: stroke location A, equidistant to the line terminations, and stroke location B, close to one of the line terminations (see Figure 8.15). The first is representative of all the stroke locations far from the distribution line terminations; the second represents the stroke locations close to one of the two line terminations. As the purpose of this section is a sensitivity analysis, for both cases the line is assumed to be matched at both ends.

8.3.4.4 Influence of channel base current: stroke location A

In Figure 8.16 we show the induced voltages at the line terminations due to the channel base currents of Table 8.1, for stroke location A. Curves in solid line refer to the case of a perfectly conducting ground (letter P in figure legend), whereas the dotted curves refer to the imperfect ground (letter I).[13] It can be seen that, for the considered case (stroke location A and observation point at the line termination), the finite ground conductivity reduces both the peak value and the front steepness of the induced voltages by about 20–30 per cent. Further, the ground resistivity plays a more important role for fast rising currents and is responsible for an initial negative peak, which increases with the maximum time derivative of the lightning current. These results can be explained by observing that, as shown in Figure 8.12*a*, for the considered stroke location and observation point, the induced voltage is practically

[13] Letter P in the figure legend denotes a perfectly-conducting ground and letter I denotes an imperfectly conducting ground.

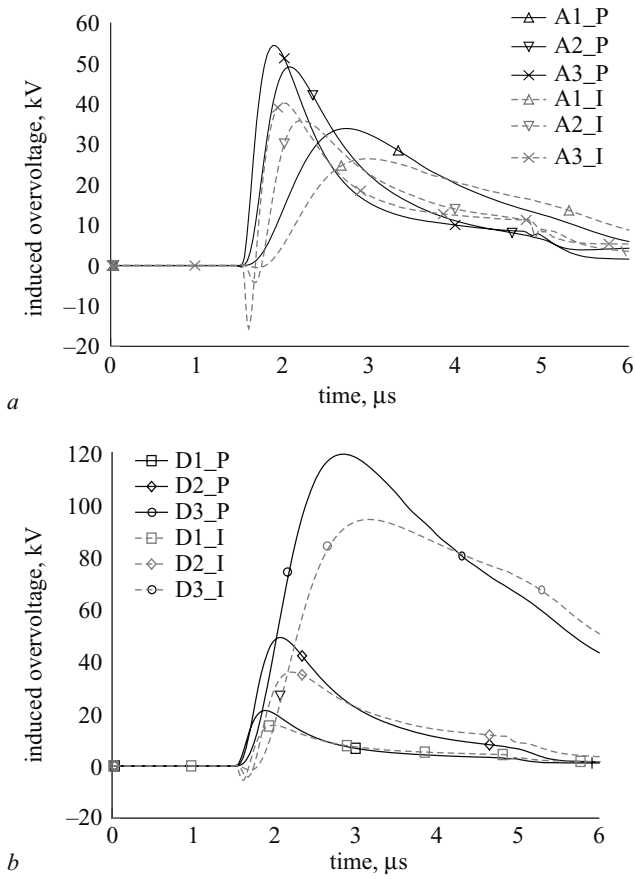

Figure 8.16 *Voltages induced at the line terminations for stroke location A* (adapted from Guerrieri *et al*. [71])

a using channel base currents with the same peak value but different time derivative (A1, A2 and A3 of Table 8.1)

b vice versa (current D1, D2 and D3 of Table 8.1)

given by the contribution of the horizontal electric field in the Agrawal *et al*. coupling model. As the ground conductivity decreases, the voltage due to the horizontal field contribution decreases as well, and results in an attenuation of the total induced voltage amplitude. (See [79,80] for additional details.)

However, the situation changes if, for the same stroke location, we consider a different observation point. For instance, concerning the voltage at the middle point of the line, the soil resistivity produces an increase in the induced voltage, as can be seen in Figure 8.17 where the peak value of the induced voltage is represented along the line, for the stroke location A. This can be explained considering that, for this observation point, as shown in Figure 8.12*c*, the contribution of the vertical electric

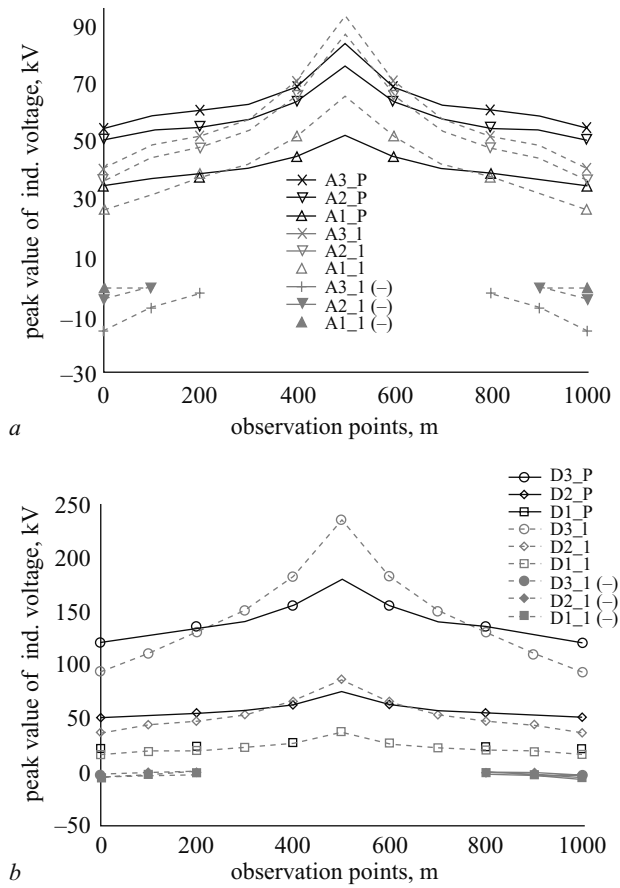

Figure 8.17 *Maximum amplitude of the induced overvoltage along the line. Stroke location A* (adapted from Guerrieri *et al*. [71])

a using channel base currents with the same peak value but different time derivative (A_1, A_2 and A_3 of Table 8.1)

b *vice versa* (currents D_1, D_2, D_3 of Table 8.1)

field to the induced voltage (incident voltage plus risers) is, overall, positive (and, contrary to the previous case, can no longer be disregarded); on the other hand, for the considered observation point, the voltage due to the horizontal electric field is of negative polarity and, as its magnitude decreases with the ground resistivity, the total induced voltage increases (see Figure 8.12*c* and Figure 8.13*e*).

Figure 8.17 presents also the negative initial peaks resulting from the finite ground conductivity (more pronounced for current A3 having the largest maximum steepness).

8.3.4.5 Influence of channel base current: stroke location B

For stroke location B, the results are presented in Figures 8.18 and 8.19. Figure 8.18*a* shows the induced voltages at the left line termination for currents A1, A2 and A3; Figure 8.18*b* presents the induced voltages at the same termination for currents D1, D2 and D3. Again, solid line curves refer to the perfectly conducting ground assumption, and dotted line curves to a finitely conducting ground. Similarly, Figure 8.19 shows the induced voltages at the right line termination.

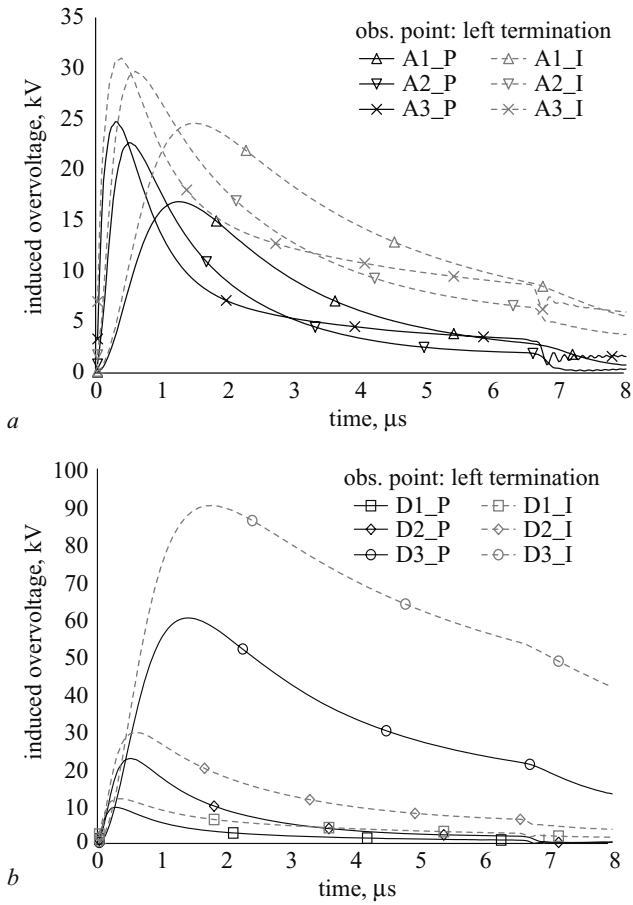

Figure 8.18 *Voltages induced at the left line termination for stroke location B.* (adapted from Guerrieri *et al*. [71])

a using channel base currents with the same peak value but different time derivative (A_1, A_2 and A_3 of Table 8.1)

b *vice versa* (currents D_1, D_2, D_3 of Table 8.1)

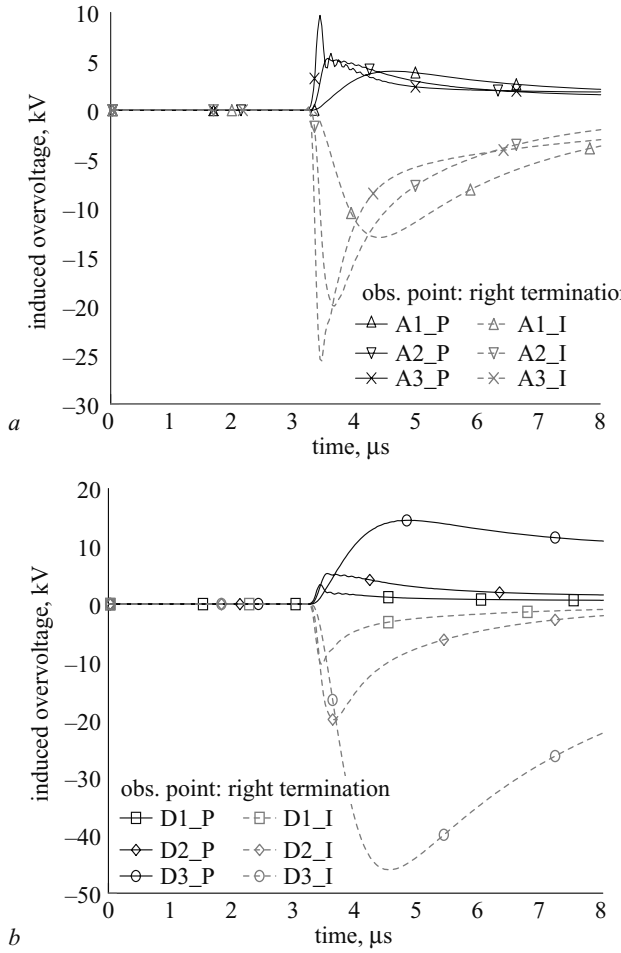

Figure 8.19 *Voltages induced at the right line termination for stroke location B* (adapted from Guerrieri *et al.* [71])

a using channel base currents with the same peak value but different time derivative (A_1, A_2 and A_3 of Table 8.1)

b *vice versa* (currents D_1, D_2, D_3 of Table 8.1)

It can be seen that for an imperfectly conducting ground, the induced voltage at the near line termination (with respect to the stroke location) reaches larger magnitudes than for the case of a perfectly conducting ground. Note further that, at the far line termination, the effect of the finite ground conductivity is even more evident, in that it produces an inversion of polarity in the induced voltages. For lossy soils, the induced voltage can indeed exhibit a bipolar waveshape. This can be explained, again, by considering the various contributions that form the total voltage (see [79,74] for additional details).

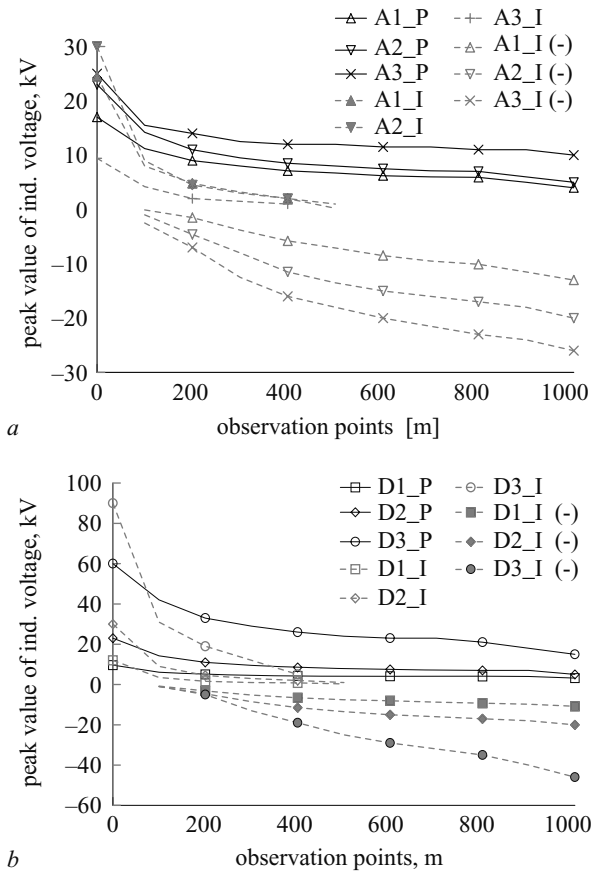

Figure 8.20 *Induced overvoltage peaks along the line. Stroke location B* (adapted from Guerrieri *et al.* [71])

a using channel base currents with the same peak value but different time derivative (A_1, A_2 and A_3 of Table 8.1)
b *vice versa* (currents D_1, D_2, D_3 of Table 8.1)

In Figure 8.20 we show the peak values of the induced voltages along the line for stroke location B. As for Figure 8.17, we have reported also the values of the negative peaks appearing when the ground is lossy.

It is interesting to note that while positive peaks decrease with distance from the near end, negative peaks increase, reaching their maximum value at the far end. For longer lines, the negative peak at the far termination of the line could even exceed the positive peak at the closest one. This is consistent with experimental results obtained by De la Rosa *et al.* [48], which revealed the occurrence of flashovers at the far end termination of an overhead line above a poor conducting soil in Mexico, and not at the close end termination. It is important to realise however, that beyond a

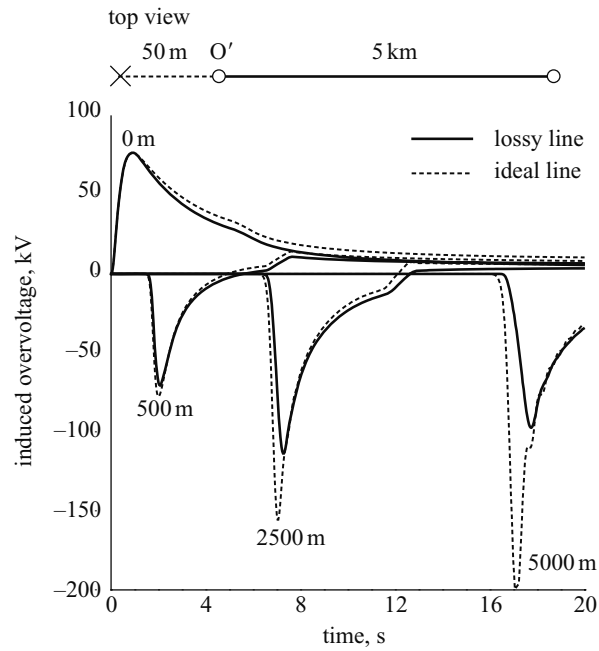

Figure 8.21 *Lightning-induced voltages at four observation points along a 5 km long line for a stroke location type B. Return stroke current A2. Ground conductivity is 0.001 S/m. In dashed lines we show the voltages calculated considering the ground resistivity only in the field calculation, but not in the surge propagation; in solid lines we show the voltages calculated considering the ground resistivity in both field calculation and surge propagation* (adapted from Borghetti and Nucci [81])

certain length, depending on the ground characteristics and field waveshape, such an enhancing effect will tend to be compensated for by the attenuation of the surges due to line (ground) losses, as shown in Figure 8.21.

8.3.4.6 Influence of line height

For a perfectly conducting ground, the induced voltage magnitude is nearly proportional to the line height [75,82]. Considering the finite ground conductivity, the induced voltage peak still experiences an increase with the line height, but the increase is not rigorously linear and varies as a function of the ground conductivity, the position of the stroke location and the observation point along the line. The values of induced voltage peak as a function of line height and ground conductivity for the base case are presented in Table 8.3.

8.3.4.7 Multiconductor lines

The induced voltage on one conductor of a multiconductor loaded line is affected by the presence of other conductors. For typical line constructions, the voltages

Table 8.3 Effect of line height on the induced voltage peak for the base case, current waveshape A2, and stroke location at 50 m to the line centre and symmetrical to the line ends (adapted from [75])

Observation point	Ground conductivity [S/m]	Line height [m]		
		7.5	9	10.5
V_P at line end [kV]	∞	49.5	59.5	69
	0.01	40.5	50	60
	0.001	26.5	35	44
V_P at the line centre [kV]	∞	67	81	95
	0.01	77.5	91.5	105.5
	0.001	101.5	115	128.5

induced on each of the line conductors are generally 15–25 per cent lower than those corresponding to a single conductor located at the same location [82]. The presence of ground wires helps in reducing the magnitude of induced voltages by a factor of about 20–40 per cent depending on the line configuration [82].

8.3.4.8 Influence of line length

It is useful to know up to which distance range the illumination of the line by the lightning electromagnetic field has to be considered in the evaluation of the induced overvoltages. As a matter of fact, when the LEMP response of a complex distribution network is to be evaluated, it might be useless to extend the coupling calculation beyond a certain distance.

Figure 8.22 shows the amplitude of the induced voltage calculated at two observation points along an overhead line, as a function of the line length, for the adopted current waveshapes and three values of ground conductivity. The stroke is located 50 m from the line centre and equidistant to the line terminations. Note that for line length exceeding about 2 km, for any of the examined current waveshapes, the coupling between the LEMP and the line conductors becomes negligible. Note, further, that when the line is lossless, the voltage peak amplitude reaches a maximum value (that clearly depends on the current waveshape), and then remains constant with the line length. On the other hand, for poor conducting ground ($\sigma_g = 0.001$ S/m), the voltage peak amplitude, after reaching a maximum value, exhibits first a pronounced decrease, followed by a slighter one. This is the result of the combined effect of the inversion of polarity of the excitation field that, beyond a certain distance range, acts in producing an inversion of polarity in the induced voltage [79], and of the surge propagation along the line. As the line length increases, the initial negative peak becomes predominant with respect to the positive one. For this reason, in Figure 8.20*c*, beyond a certain distance, we have plotted negative values.

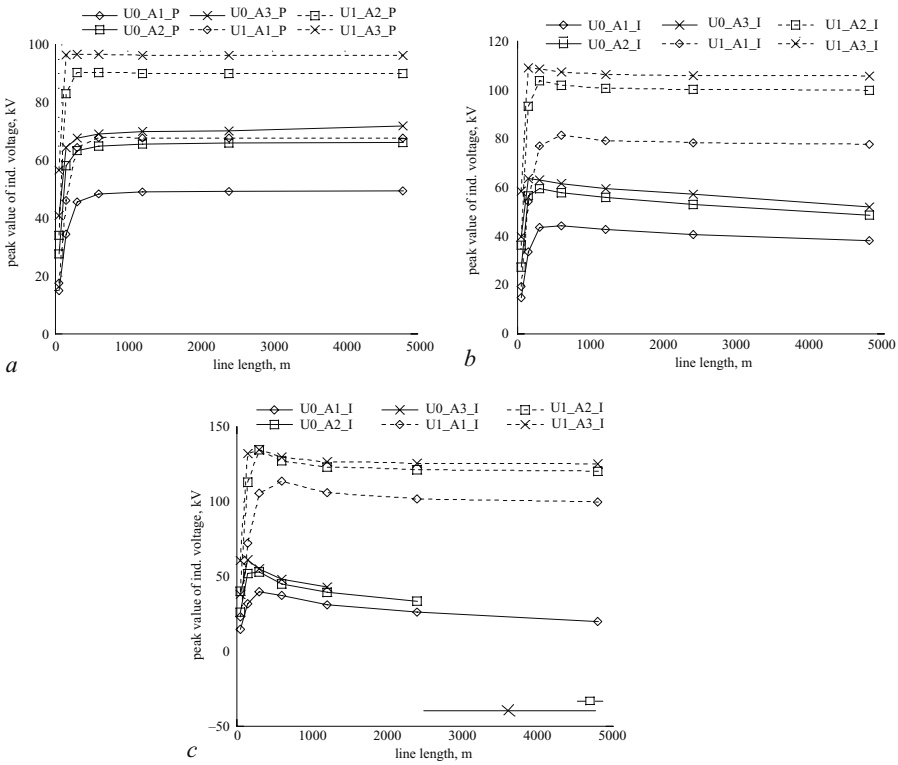

Figure 8.22 *Influence of line length on the amplitude of the lighting-induced voltages along an overhead line. Stroke location equidistant from line terminations at 50 m from the line centre. Observation points: U_0 line terminations; U_1 line centre. Ground conductivity: a infinite, b 0.01 S/m, c 0.001 S/m. A1, A2 and A3 denote the different lightning current waveshapes adopted in the calculations (see Table 8.1). Ux_Ay_Z: Induced voltage U at observation point x (1 or 2) (see Figure 8.15), channel base current Ay (A1, A2 or A3), Ground: perfectly (Z=P) or imperfectly (Z=I) conducting* (adapted from Borghetti *et al.* [75])

If one repeats the computation for strokes located in the vicinity of one of the line terminations, it can be found that the induced voltage peak at termination close to the stroke location remains unvaried for line lengths beyond about 2 km. It is important to realise, however, that for such a case, the maximum induced voltage might occur along the line, far away from the stroke location, as shown in Figure 8.21.

8.3.4.9 Influence of the position of the stroke location with respect to the line and observation point

For an overhead line above a perfectly conducting ground, in general, the maximum amplitude of the induced voltage is attained at the point of the line closest to the

stroke location. However, as earlier discussed, when the resistivity of the ground cannot be neglected, the maximum amplitude may not be reached at the point of the line closest to the stroke location; additionally, the induced voltage can exhibit a bipolar waveshape and a pronounced negative peak. Figure 8.23 shows the voltage induced at both ends of a 1 km long line as a function of relative position of the stroke location, and provides an illustrative summary of the effect of stroke location and value of ground conductivity with respect to the line and to the observation point.

8.3.4.10 Influence of return stroke speed

The induced voltage magnitude at distances not exceeding a few hundred meters is not appreciably affected by the return stroke speed [58,75]. For more distant stroke locations (beyond a few kilometres), the induced voltage peak becomes nearly proportional to the return stroke speed, although at these distances, the magnitude of induced voltages, in general, does not represent a threat.

8.3.4.11 Influence of distance of the stroke location to the line

To analyse the effect of the distance of the stroke location to the line, we consider a stroke location symmetrical to the line terminations. The variation of the induced voltage at the line centre as a function of the distance to the stroke location is presented in Figure 8.24. For the analysis, we have considered the three current shapes of Table 8.1, two different values for the return stroke velocity: 1.3×10^8 m/s (left column) and 1.9×10^8 m/s (right column), and the three adopted values for the ground conductivity. It can be seen that, for the considered stroke location, the voltage drops approximately inversely proportional to the distance. Also, for a given distance, the induced voltage is larger for poorer conductivities and/or higher current steepnesses.

In the same Figures, we have plotted the results calculated using the simplified analytical Rusck formula [10], for the two different values of return stroke velocity, namely 1.3×10^8 and 1.9×10^8 m/s, which we discuss next.

8.3.4.12 Comparison with the results obtained using the simplified Rusck formula

As earlier mentioned, the Rusck simplified analytical formula (see eqns 8.16 and 8.17 of section 8.2.7) gives the maximum value V_{max} of the induced overvoltages at the point of an infinitely long line nearest to the stroke location (for convenience, we report the Rusck formula below):

$$V_{max} = Z_0 \frac{Ih}{d} \left(1 + 1/\sqrt{2} \cdot \beta \cdot \frac{1}{\sqrt{(1 - 0.5 \cdot v^2)}} \right) \tag{8.16}$$

where

$$Z_0 = \frac{1}{4\pi} \sqrt{\frac{\mu_0}{\varepsilon_0}} = 30\,\Omega \tag{8.17}$$

where the various quantities have been already defined in section 8.2.7.

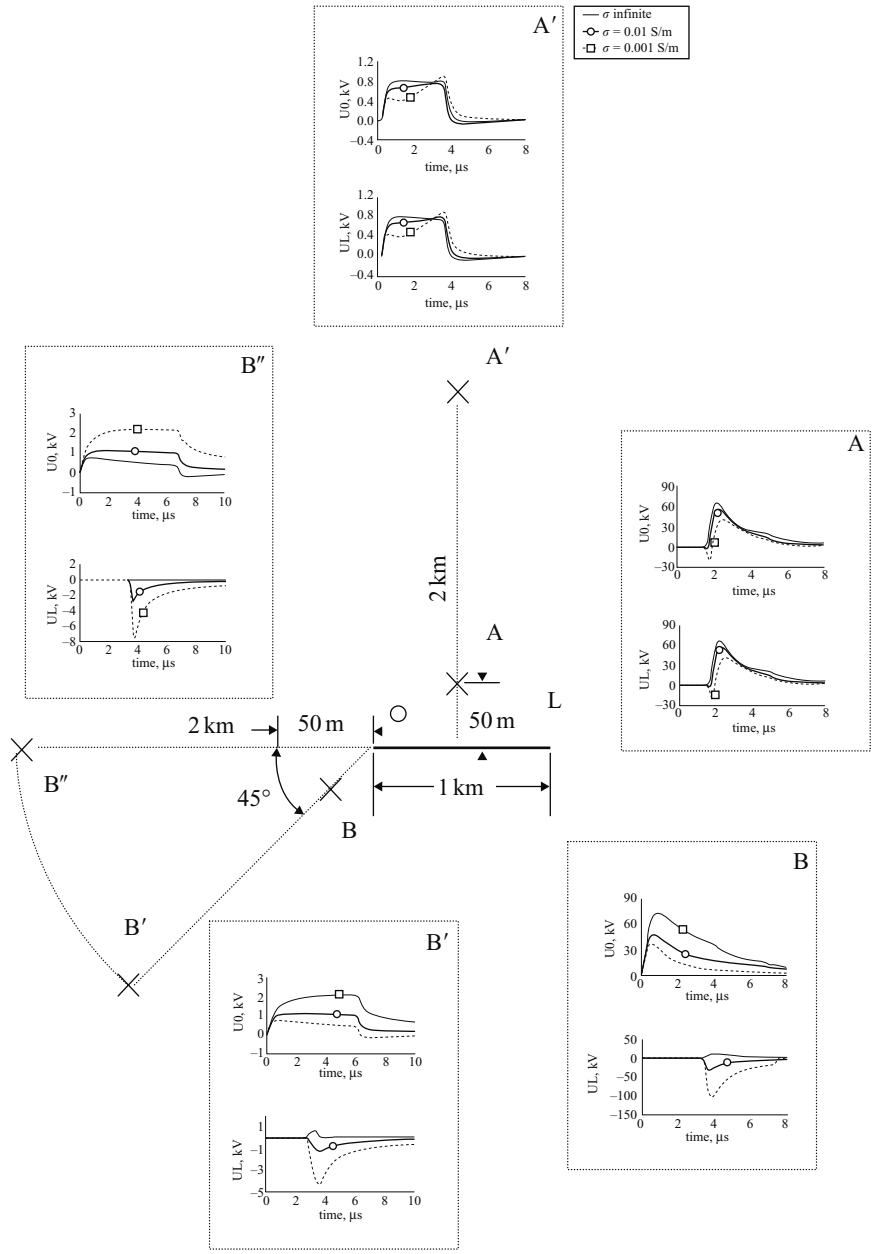

Figure 8.23 *Effects of stroke location with respect to the line, with return stroke current A2, for two different observation points and for three different values of ground conductivity* (adapted from Borghetti *et al.* [75])

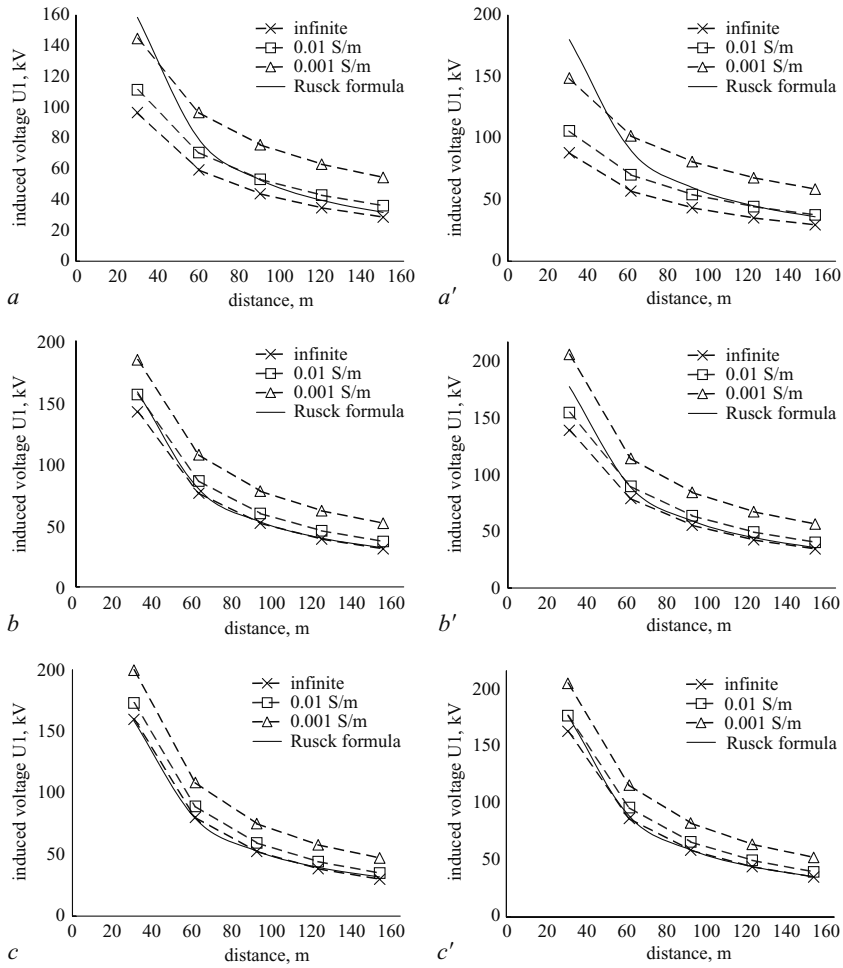

Figure 8.24 *Variation of the induced voltage magnitude at the line centre as a function of distance to the stroke location. Left column: return stroke velocity equal to* $1.3 \times 10^8\ m/s$*; right column: return stroke velocity equal to* $1.9 \times 10^8\ m/s$*. a and a′: current A; b and b′: current A2, c and c′: current A3. In solid line we have reported the results obtained from the Rusck simplified analytical expression* (adapted from Borghetti *et al*. [75])

If we examine Figures 8.24*a*, *b* and *c*, we can conclude that, in general, when the channel base currents exhibit a steep front (current A3), and when the ground is approximated as a perfectly conducting plane, the Rusck simplified analytical expression provides an estimation for the induced voltages close to the one predicted by the more general Agrawal model in which the forcing functions are calculated by means of the MTLE return stroke model. The disagreement between the voltage predicted

by the two approaches (Rusck formula and Agrawal-MTLE models) increases with the return stroke velocity, with the ground resistivity and with the front duration of the lightning current. As a result, in general, the Rusck simplified formula should not be applied to the case of overhead lines above a lossy ground.

8.3.5 Influence of additional factors (downward leader, corona, channel inclination and tortuosity)

8.3.5.1 Downward leader electromagnetic field change

Most studies on lightning-induced voltages use as the excitation source only the return stroke electric field change, neglecting any field changes prior to it. This assumption is based on theoretical considerations [83] and experimental observations made beyond a few hundred metres from the lightning channel, where the leader field change in a time scale of tens of microseconds is slow and small compared with the return stroke change [84]. More recent measurements, however, show that the leader electric field change due to triggered lightning at very close distance from the channel (e.g. 30 m) is comparable to that of the return stroke [85]. Although triggered lightning and natural lightning are dissimilar in that they are initiated by different physical processes, it is generally agreed that rocket-triggered lightning current and electromagnetic fields are very similar to those associated with natural subsequent return strokes. The implications of this observation to our understanding of lightning-induced voltages at close range have been studied in [64] and are summarised below.

In order to assess the inducing effect of the leader, the simple model originally proposed by Schonland [86] is adopted; it has been shown to produce satisfactory results at distances from the lightning channel not exceeding a few hundred metres [85]. According to this model [64,85], a uniformly charged leader channel emerges from the centre of a volume of charge Q located in the cloud centre at height H_T and propagates vertically downward at a constant speed v_L. The return stroke is assumed to start when the leader channel reaches the ground, propagating upward at a constant speed v_{RS} and discharging the leader channel.

To calculate the return stroke fields, we assume that the return stroke discharges the previously established leader channel as it progresses towards the cloud at a constant speed. The model described above has the advantage that the electromagnetic field expressions can be evaluated analytically for both leader and return stroke phase (see [64]).[14]

Figure 8.25 shows the results of some simulations performed for a 500 m long, 10 m high, lossless single wire overhead line matched at both ends. A relatively short line (500 m) is considered since, for such a case, the surge propagation over a finitely

[14] It is worth noting that several return stroke models specifying the spatial–temporal current distribution during the return stroke phase are proposed in the literature (see Chapter 6). If one assumes that, during the return stroke phase, all the charges deposited by the leader along the channel are removed, it follows that a specific leader charge distribution could be associated with a given return stroke model. It is therefore possible to consistently extend any return stroke model to take into account the leader phase and to calculate the electromagnetic field change

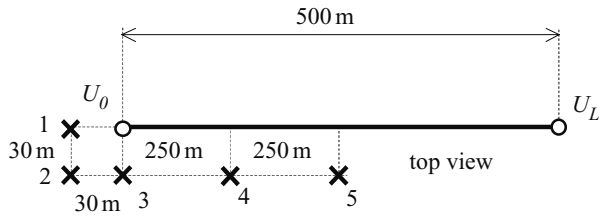

Figure 8.25 *Map of considered stroke locations. The line is matched at both ends and its height above ground is 10 m* (adapted from Rachidi *et al.* [64])

conducting ground could be neglected. Several stroke locations, shown in Figure 8.25, have been considered. For each case, the induced voltages U_0 and U_L at both ends were computed in [64]. Some results of the simulations are shown in Figure 8.27. In it, the induced voltages calculated disregarding the leader electric field change are presented too (dashed lines). Note that in Figure 8.27, time $t = 0$ corresponds to the transition from the leader to the return stroke phase, as seen from the point of the line closest to the lightning channel. The values adopted for all the calculations are $v_L = 10^7$ m/s [88], $v_{RS} = 1.9 \times 10^8$ m/s [78], $H_T = 5$ km. The linear charge density was assumed to be $\rho_L = 10^{-4}$ C/m (consistent with the total charge lowered by subsequent strokes which ranges approximately from 0.2 to 1 C [84]).

The computed results show that, for stroke locations approximately along the line prolongation (Figures 8.26*a* and 8.26*b*), the dart leader electric field change contributes appreciably to the amplitude and waveshape of the induced voltages. For different stroke locations (e.g. stroke location 3), the effect of the leader is, for the considered observation points, less pronounced (Figures 8.26*c* and 8.26*d*). Note, additionally, that although the initial excursion exhibited by the dart leader-induced voltages had the same polarity for all the cases studied, its overall shape could be either unipolar, e.g. Figure 8.26*a* (U_0) or bipolar, e.g. Figure 8.26*b* (U_L).

One of the main conclusions of [64] is that voltage protection devices could be triggered by the leader-induced voltage, before the return stroke initiates.[15]

8.3.5.2 Effect of corona

The influence of corona on the voltages induced on overhead lines by nearby lightning has been investigated in [65]. The first conclusion of that study is that only for particularly severe excitation conditions, e.g. lightning stroke locations very close to the line and/or large return stroke current amplitudes, need corona to be taken into account. The corona process was described macroscopically by a charge–voltage diagram and included in Agrawal field-to-transmission line coupling equations described by eqns 8.18 and 8.19. Additionally, the results show that the influence of corona on the induced voltages is in general as important as the effect of the ground finite

[15] Continuing currents, which could also be responsible of protection operation [87], were disregarged in [64]

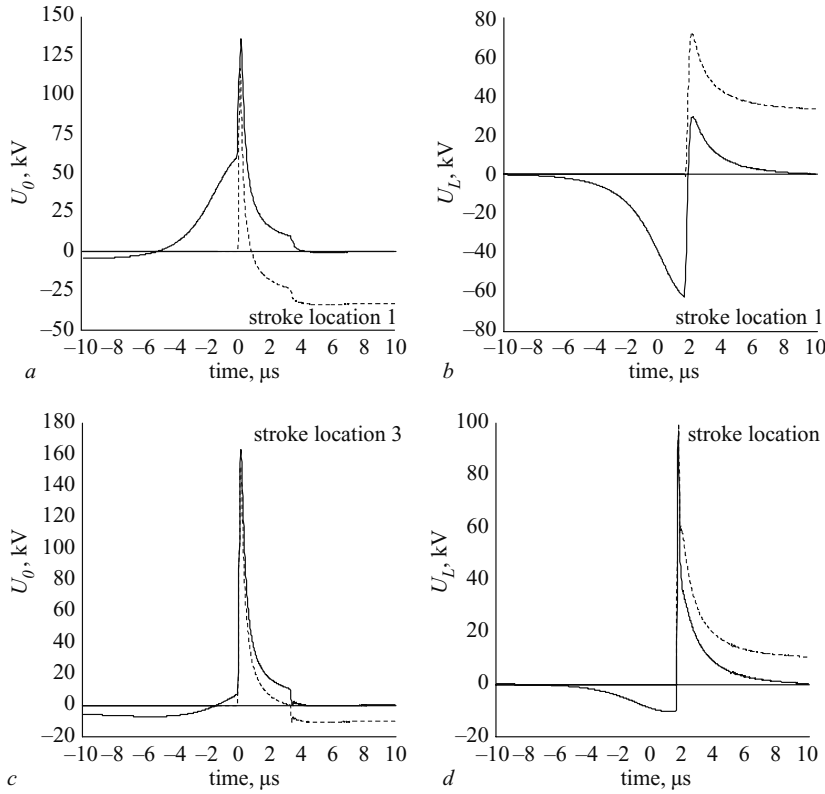

Figure 8.26 Lightning-induced voltages for stroke location 1 (a and b) and stroke location 3 (c and d) in Figure 8.25. Solid line: leader return stroke induced voltage; dotted line: return stroke induced voltage (adapted from Rachidi *et al.* [64])

conductivity. This differs from the direct strike behaviour, where corona, when present, affects the surge propagation more than the ground resistivity. Further, it has been shown that corona tends to increase the rise time and decrease the front steepness of the induced voltages, as for the case of direct strikes. The computation results also show a significant increase in the amplitude of the induced voltages in presence of corona, contrary to the case of direct strikes. Such a phenomenon can be explained, theoretically, by considering that the increase of the line capacitance produced by corona results in a decrease of the propagation velocity of the various surges induced by lightning.[16] This makes it possible for the total induced

[16] If we think of the line as excited by a number of sources relevant to the impinging electromagnetic field – see, for instance, Figure 8.13 – we can associate to each of these sources the corresponding surge propagating on the line

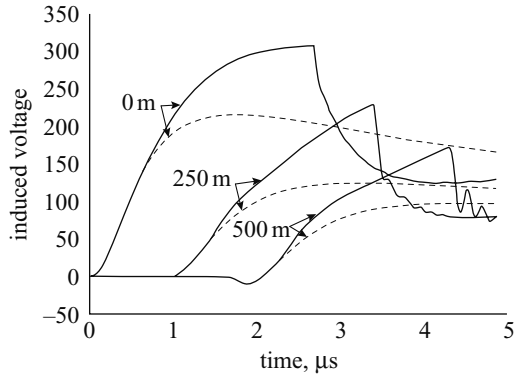

Figure 8.27 *Voltages induced by a nearby lightning at three observation points along a 1 km long, 10 m high, overhead line in presence of corona. Solid lines: taking into account corona; dotted lines: disregarding corona. Stroke location: 50 m from the line centre, equidistant from the line ends. Lightning current: peak value* $I_p = 35\,kA$*; maximum time derivative* $(di/dt)_{max} = 42\,kA/\mu s$ (adapted from Nucci *et al.* [65])

voltage – which results from the contributions of the various induced surges – to reach a larger value (see [65] for a more detailed explanation). An example showing the effect of corona on lightning-induced voltages, according to the model proposed in [89] is presented in Figure 8.27. The corona effect on multiconductor lines illuminated by LEMP has been studied in [89], where it has been found that taking into account the influence of corona on the mutual coupling between conductors can produce even higher increases of the voltage amplitudes in the most exposed conductors, while in the less exposed ones a reduction of the voltage amplitudes is obtained.

8.3.5.3 Channel inclination and tortuosity

The real geometry of a lightning channel differs from the one assumed in the analysis carried out so far, although, especially concerning subsequent return strokes, it may be a reasonable approximation.

Sakakibara [90] has first considered the effect of an inclined channel on the amplitude of the induced voltages, finding that such an effect, at least as far as the channel lies in a plane parallel to the line, is not extremely important. In a study by Kordi *et al*. [91], it is also shown that the channel inclination could affect very differently the field and induced voltage magnitudes. Indeed, depending on the channel orientation and its relative position to the observation point or to the line, the channel inclination could result either in an increase or in a decrease of the electromagnetic field and induced voltage magnitude.

8.3.6 Application to realistic cases: use of the LIOV–EMTP

In order to analyse the response of realistic configurations such as an electrical medium and low-voltage distribution network, to the excitation of a lightning electromagnetic field, the original LIOV code was interfaced with the electromagnetic transient program (EMTP) [902]. It is in fact unreasonable to expect from simplified formulas, such as the Rusck one, an accurate prediction of the amplitude and waveshape of the voltages induced by lightning on complex distribution systems (see Figure 8.28), as they were not developed to deal with those cases.

In principle, the LIOV code could serve for such a purpose, provided that the presence of the specific type of termination, as well as of the line discontinuities (e.g. surge arresters across the line insulators along the line) be properly taken into account. This procedure, however, requires that the boundary conditions for the transmission line coupling equations be properly rewritten case by case, which can be a quite complex issue. Note, additionally, that when the termination is a power system component for which a complex circuit model is required (e.g. [93,94]) the boundary conditions assume a complex expression [95,54,96]. To deal with the problem of lightning-induced voltages on complex systems, two interfacing methods between LIOV and EMTP were then developed, the first one in collaboration with CESI [96] and the second one with EdF [97].

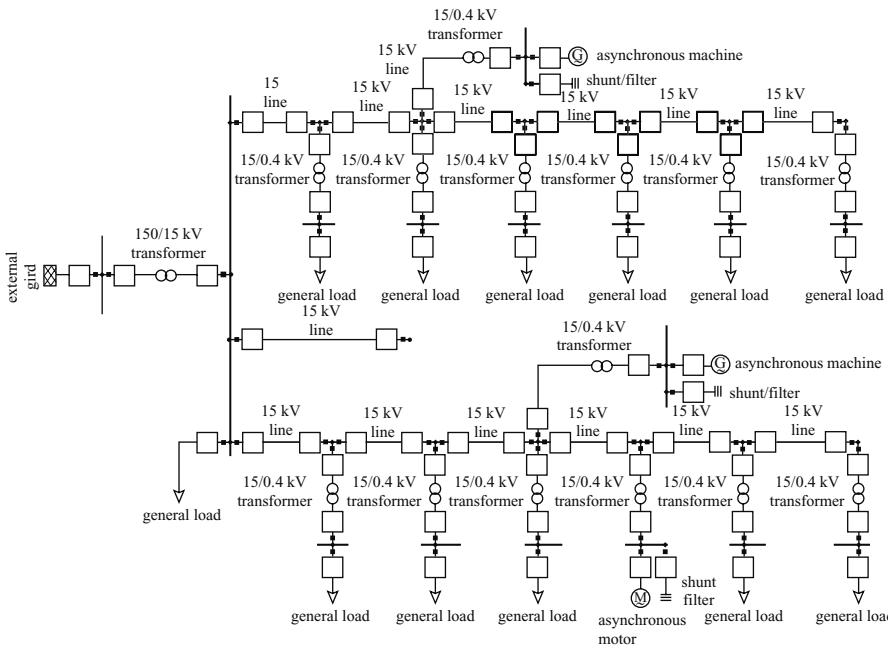

Figure 8.28 Power distribution network with complex topology (adapted from Borghetti *et al.* [102])

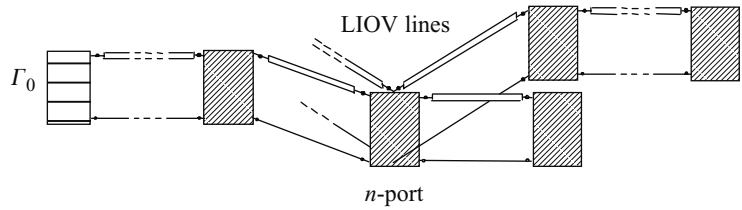

Figure 8.29 Electrical distribution system illuminated by LEMP

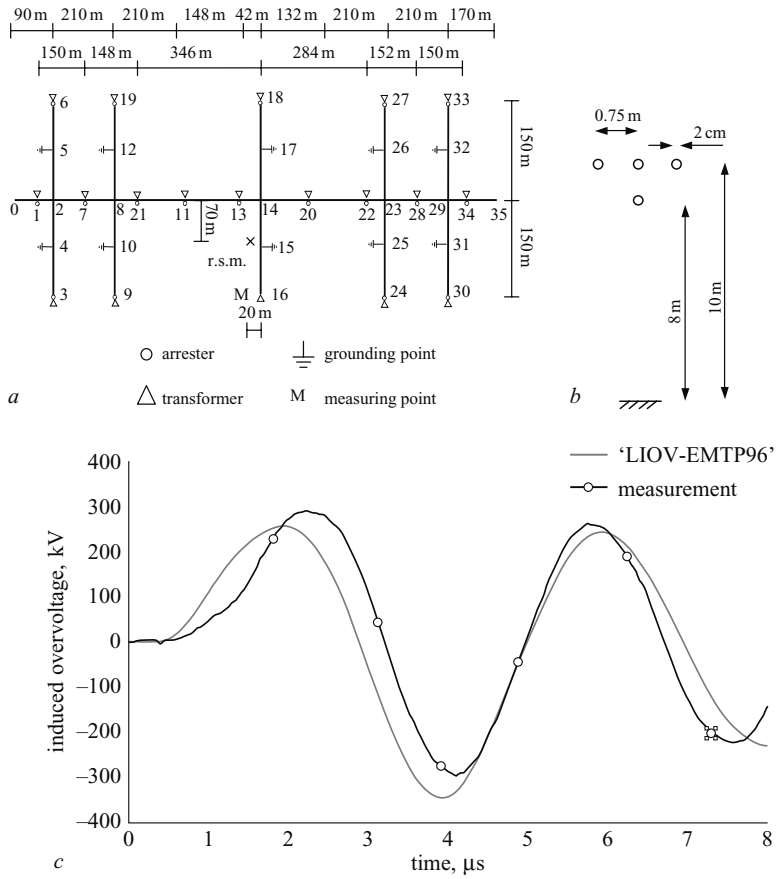

Figure 8.30 Computed and measured induced voltage on a reduced scale model of complex configuration. r.s.m. stands for stroke location (*see [56,98] for details.* Adapted from Paolone *et al.* [99])

a topology of the analysed system
b line transverse geometry
c measured and calculated induced voltage

The concept at the basis of the first interface [96] is the following. A distribution line can be viewed as a group of lines such as the one represented in Figure 8.1, electrically connected by means of equivalent n-port circuits, as shown in Figure 8.29. Each of these n-port circuits represents a power component located along the line (such as surge arresters, or distribution transformers), or the periodical grounding of neutral conductor for LV lines, of shielding wires for MV lines, etc. The LIOV code computes the voltages induced along the various lines that form the overall network (which we shall therefore call LIOV lines), and the EMTP solves the boundary conditions equations relevant to the various n-ports currents of the network.

The above concept has been applied to implement an improved LIOV–EMTP code [75,98,99], based on EMTP96 [100].[17] With the developed LIOV–EMTP it is possible to compute the response of realistic distribution lines to nearby lightning and, therefore, it can be used for insulation coordination of specific distribution lines, i.e. to determine the basic insulation level suitable for a given line, as well as to infer the optimal number and location of lightning surge arresters. An example of simulation using the LIOV–EMTP code is presented in Figure 8.30. The experimental results are obtained on the reduced scale model developed at the University of Sao Paulo, earlier mentioned in section 8.2.12.

8.4 References

1 TESCHE, F.M., IANOZ, M., and KARLSSON, T.: 'EMC analysis methods and computational models' (John Wiley and Sons, 1997)
2 BORGHETTI, A., GUERRIERI, S., NUCCI, C.A., PAOLONE, M., and RACHIDI, F.: 'Lightning performance of distribution lines', International symposium on *Electric power engineering at the beginning of the third millenium*, Capri, Italy, May 2000
3 PAUL, C.R.: 'Analysis of multiconductor transmission lines' (John Wiley and Sons, 1994)
4 AGRAWAL A.K., PRICE, H.J., and GURBAXANI, S.H.: 'Transient response of a multiconductor transmission line excited by a nonuniform electromagnetic field', *IEEE Trans. Electromagn. Compat.*, 1980, **22**, (2), pp.119–129
5 TAYLOR, C.D., SATTERWHITE, R.S., and HARRISON, C.W.: 'The response of a terminated two-wire transmission line excited by a nonuniform electromagnetic field', *IEEE Transaction on Antenna propagation*, 1965, **13**
6 IANOZ, M., NUCCI, C.A., and TESCHE, F.M.: 'Transmission line theory for field-to-transmission line coupling calculations', *Electromagnetics*, 1988, **8**, (2–4), pp.171–211

[17] The differences between this LIOV–EMTP96 program compared with others previously developed [96,97,101] are discussed in [68,102]. We limit ourselves here to noting that besides all the features of the LIOV code, the LIOV–EMTP96 code allows for the evaluation of the LEMP response of any complicated overhead power network with any power system component connected to it, provided it is included in the EMTP96 library, the only limit being the computer memory

7 RACHIDI, F.: 'Formulation of the field-to-transmission line coupling equations in terms of magnetic excitation fields', *IEEE Trans. Electromagn. Compat.*, 1993, **35**, (3)

8 NUCCI, C.A. and RACHIDI, F.: 'On the contribution of the electromagnetic field components in field-to-transmission lines interaction', *IEEE Trans. Electromagn. Compat.*, 1995, **37**, (4), pp.505–508

9 NUCCI, C.A., MAZZETTI, C., RACHIDI, F., and IANOZ, M.: 'On lightning return stroke models for LEMP calculations'. Proceedings of 19th International Conference on *Lightning protection*, Graz, 25–29 April 1988, pp.463–469

10 RUSCK, S.: 'Induced lightning overvoltages on power transmission lines with special reference to the overvoltage protection of low voltage networks', *K. Tek. Hoegsk. Handl. (Sweden)*, 1958, (120)

11 CHOWDHURI, P., and GROSS, E.T.B.: 'Voltage surges induced on overhead lines by lightning strokes', *Proc. IEE*, 1967, **114**,(12), pp.1899–1907

12 MASTER, M.J., and UMAN, M.A.: 'Lightning induced voltages on power lines: theory', *IEEE Trans. Power Appar. Syst.*, 1984, **103**, (9), pp.2502–2518

13 CHOWDHURI, P.: 'Analysis of lightning induced voltages on overhead lines', *IEEE Trans. Power Deliv.*, 1989, **6**, (1)

14 DIENDORFER, G.: 'Induced voltage on an overhead line to nearby lightning', *IEEE Trans. Electromagn. Compat.*, 1990, **32**, (4), pp.292–299

15 CHOWDHURI, P.: 'Response of overhead lines of finite length to nearby lightning strokes', *IEEE Trans. Power Deliv.*, 1991, **6**, (1)

16 NUCCI, C.A., RACHIDI, F., IANOZ, M., and MAZZETTI, C.: 'Comparison of two coupling models for lightning-induced overvoltage calculations', *IEEE Trans. Power Deliv.*, 1995, **10**, (1), pp.330–338

17 COORAY, V.: 'Calculating lightning-induced overvoltages in power lines: a comparison of two coupling models', *IEEE Trans. Electromagn. Compat.*, 1994, **36**, (3), pp.179–182

18 CHOWDHURI, P.: 'Electromagnetic transients in power systems' (Research Studies Press Ltd, England, 1996) Ch. 8

19 CHOWDHURI, P., LI, S., and YAN, P.: 'Review of research on lightning-induced voltages on an overhead line', *IEE Proc., Gener. Transm. Distrib.*, 2001, **148**, (1), pp.91–95

20 RACHIDI, F., NUCCI, C.A., IANOZ, M., and MAZZETTI, C.: 'Influence of a lossy ground on lightning-induced voltages on overhead lines', *IEEE Trans. Electromagn. Compat.*, 1996, **38**, (3), pp.250–264

21 RAMO, S., WHINNERY, J.R., and VAN DUZER, T.: 'Fields and waves in communication electronics' (John Wiley and Sons, 1994)

22 TESCHE, F.M.: 'Comparison of the transmission line and scattering models for computing the HEMP response of overhead cables', *IEEE Trans. Electromagn. Compat.*, 1992, **34**

23 CARSON, J.R.: 'Wave propagation in overhead wires with ground return', *Bell Syst. Tech. J.*, 1926, **5**, pp.539–554

24 POLLACZEK, F.: 'On the field produced by an infinitely long wire carrying alternating current', *Elekztrische Nachtrichten Technik*, 1926, **III**, (9), pp.339–359. French translation by POMEY, J.B.: *Rev. Gén. Electr.*, 1931, **29**, (2), pp.851–867
25 SUNDE, E.D.: 'Earth conduction effects in transmission systems' (Dover, New York, 1968)
26 WAIT, J.R.: 'Theory of wave propagation along a thin wire parallel to an interface', *Radio Sci.*, 1972, **7**, pp.675–679
27 KING, R.W.P., WU, T.T., and SHEN, L.C.: 'The horizontal wire antenna over a conducting or dielectric half space: current and admittance', *Radio Sci.*, 1974, **9**, pp.701–709
28 PERZ, M.C. and RAGHUVEER, M.R.: 'Generalized derivation of fields and impedance correction factors of lossy transmission lines. Part II: lossy conductors above lossy ground', *IEEE Trans.* Power Appar. Syst., 1974, **93**, pp.1832–1841
29 CHANG, D.C. and OLSEN, R.G.: 'Excitation of an infinite antenna above a dissipative earth', *Radio Sci.*, 1975, **10**, pp.823–831
30 GARY, C.: 'Approche complète de la propagation multifilaire en haute fréquence par l'utilisation des matrices complexe', *EDF Bulletin de la direction des études et recherches, Série B*, 1976, (3/4), pp.5–20
31 VANCE, E.F.: 'Coupling to shielded cables' (R.E. Krieger Publishing Company, Florida, 1987)
32 SEMLYEN, A.: 'Ground return parameters of transmission lines. An asymptotic analysis for very high frequencies', *IEEE Trans. Power Appar. Syst.*, **100**, (3), pp.1031–1038
33 OLSEN, R.G. and PANKASKIE, T.A.: 'On the exact, Carson and image theories for wires at or above the earth's interface', *IEEE Trans. Power Appar Syst.*, 1983, **102**, pp.760–778
34 CHEN, K.C.: 'Time harmonic solutions for a longhorizontal wire over the ground with grazing incidence', *IEEE Trans. Antennas Propag.*, 1985, **33**
35 D'AMORE, M. and SARTO, M.S.: 'A new formulation of lossy ground return parameters for transient analysis of multiconductor dissipative lines'. IEEE-PES Winter Meeting, Baltimore, 1996
36 BRIDGES G.J. and SHAFAI, L.: 'Plane wave coupling to multiple conductor transmission lines above a lossy earth', *IEEE Trans. Electromagn. Compat.*, 1989, **31**, (1)
37 RACHIDI, F., NUCCI, C.A., and IANOZ, M.: 'Transient analysis of multiconductor lines above a lossy ground', *IEEE Trans. Power Deliv.*, 1999, **14**, (1), pp.294–302
38 SCOTT, J.H.: 'Electrical and magnetic properties of rock and soil'. Note 18 in AFWL EMP 2-1, Electromagnetic Pulse Theoretical Notes, April 1971
39 LONGMIRE, C.L. and GILBERT, J.L.: 'Theory of EMP coupling in the source region'. DNA report, contract no. DNA 001-79-C-0186, 1980

40 RACHIDI, F., LOYKA, S.L., NUCCI, C.A., and IANOZ, M.: 'A new expression for the ground transient resistance matrix elements of multiconductor overhead transmission lines', *Electr. Power Syst. Res.*, 2003, **65**, pp.41–46
41 TIMOTIN, A.: 'Longitudinal transient parameters fo a unifilar line with ground return', *Rev. Roum. Sci. Tech. Sec. Electrotech. Energ.*, 1967, **12**, (4), pp.523–535
42 YOKOYAMA, S., MIYAKE, K., MITANI, H., and TAKANISHI, A.: 'Simultaneous measurement of lightning induced voltages with associated stroke currents', *IEEE Trans. Power Appar. Syst.*, 1983, **102**, (8), pp.2420–2429
43 YOKOYAMA, S., MIYAKE, K., MITANI, H., and YAMAZAKI, N.: 'Advanced observations of lightning induced voltage on power distribution lines', *IEEE Trans. Power Oel.*, 1986, **1**, (2), pp.129–139
44 YOKOYAMA, S., MIYAKE, K., and FUKUI, S.: 'Advanced observations of lighting induced voltages on power distribution lines (II)', *IEEE Trans. Power Deliv.*, 1989, **4**, (4), pp.2196–2203
45 MASTER, M.J., UMAN, M.A., BEASLEY, W.H., and DARVENIZA, M.: 'Lightning induced voltages on power lines: Experiment', *IEEE Trans. Power Appar. Syst.*, 1984, **103**, (9), pp.2519–2529
46 RUBINSTEIN, M., TZENG, A.Y., UMAN, M.A., MEDELIUS, P.J., and THOMSON, E.M.: 'An experimental test of a theory of lightning-induced voltages on an overhead wire', *IEEE Trans. Electromagn. Compat.*, 1989, **31**, (4), pp.376–383
47 GEORGIADIS, N., RUBINSTEIN, M., UMAN, M.A., MEDELIUS, P.J., and THOMSON, E.M., 'Lightning-induced voltages at both ends of a 488-m power distribution line', *IEEE Trans. Electromagn. Compat.*, 1992, **34**, (4), pp.451–460
48 DE LA ROSA, F., VALDIVIVA, R., PÉREZ, H., and LOZA, J.: 'Discussion about the inducing effects of lightning in an experimental power distribution line in Mexico', *IEEE Trans. Power Deliv.*, 1988, **3**, (3), pp.1080–1089
49 COORAY, V., and DE LA ROSA, F.: 'Shapes and amplitudes of the initial peaks of lightning-induced voltage in power lines over finitely conducting hearth: theory and comparison with experiment', *IEEE Trans. Antennas Propag.*, 1986, **34**, (1), pp.88–92
50 BARKER P.P., SHORT, T.A., EYBERT-BERARD, A., and BERLANDIS, J.B.: 'Induced voltage measurements on an experimental distribution line during nearby rocket triggered lightning flashes', *IEEE Trans. Power Deliv.*, 1996, **11**, pp.980–995
51 BAUM, C.E.: 'EMP simulators, for various types of nuclear EMP environment: and interim categorization', *IEEE Trans. Electromagn. Compat.*, 1978, **20**, (1), pp.35–53
52 ARREGHINI, F., IANOZ, M., ZWEIACKER, P., and GIRI, D.V.: 'SEMIRAMIS: an asymmetrical bounded wave EMP simulator with a good confinement inside the transmission line', Proceedings of 10th international Zurich symposium on *Electromagnetic compatibility*, March 1993

53 GUERRIERI, S., RACHIDI, F., IANOZ, M., ZWEIACKER, P., BORGHETTI, A., and NUCCI, C.A.: 'Effet d'une impulsion électromagnétique sur des réseaux électriques à plusieurs branches. Modélisation et validation expérimentale'. Proceedings. of the 7ème colloque internationale sur la *CEM*, Toulouse, March 1994, pp.475–480

54 GUERRIERI, S., RACHIDI, F., IANOZ, M., ZWEIACKER, P., and NUCCI, C.A.: 'A time-domain approach to evaluate induced voltages on tree-shaped electrical networks by external electromagnetic fields'. Proceedings of 11th international Zurich symposium on *Electromagnetic compatibilty*, March 1995

55 ISHII, M., MICHISHITA, K., HONGO, Y., and OGUME, S.: 'Lightning-induced voltage on an overhead wire dependent on ground conductivity', *IEEE Trans. Power Deliv.*, 1994, **9**, (1), pp.109–118

56 PIANTINI, A. and JANISZEWSKI, J.M.: 'An experimental study of lightning induced voltages by means of a scale model'. Proceedings of the 21st international conference on *Lightning protection*, Berlin, September 1992, paper 4.08, pp.195–199

57 NUCCI, C.A., BORGHETTI, A., PIANTINI, A., and JANISZEWSKI, J.M.: 'Lightning-induced voltages on distribution overhead lines: Comparison between experimental results from a reduced-scale model and most recent approaches', Proceedings of 24th international conference on *Lightning protection*, Birmingham, 14–18 Sept. 1998, pp.314–320

58 NUCCI, C.A., RACHIDI, F., IANOZ, M., and MAZZETTI, C.: 'Lightning-induced voltages on overhead power lines', *IEEE Trans. Electromagn. Compat.*, 1993, **35** (corrections 1993, **35** (4)), pp.75–86

59 UMAN, M.A., McLAIN, D.K., and KRIDER, E.P.: 'The electromagnetic radiation from a finite antenna', *Am. J. Phys.*, 1975, **43**, pp.33–38

60 COORAY, V.: 'Lightning-induced overvoltages in power lines: validity of various approximations made in overvoltage calculations'. Proceedings of 22nd international conference on *Lightning protection*, Budapest, Sept. 19–23, 1994

61 RUBINSTEIN, M.: 'An approximate formula for the calculation of the horizontal electric field from lightning at close, intermediate, and long range', *IEEE Trans. Electromagn. Compat.*, 1996, **38**, (3), pp.531–535

62 RACHIDI, F. and NUCCI, C.A.: 'On the Master, Lin, Uman, Standler and the modified transmission line lightning return stroke current models', *J. Geophys. Res.*, 1990, **95**, pp.20389–20394

63 NUCCI, C.A. and RACHIDI, F.: 'Experimental validation of a modification to the transmission line model for LEMP calculations'. 8th international symposium *Electromagnetic compatibility*, Zurich, 7–9 March 1989, pp.389–394

64 RACHIDI, F., RUBINSTEIN, M., GUERRIERI, S., and NUCCI, C.A.: 'Voltages induced on overhead lines by dart leaders and subsequent return-strokes in natural and rocket triggered lightning', *IEEE Trans. Electromagn. Compat.*, 1997, **39**, (2), pp.160–166

65 NUCCI, C.A., GUERRIERI, S., CORREIA DE BARROS, M.T., and RACHIDI, F., 'Influence of corona on the voltages induced by nearby lightning

on overhead distribution lines', *IEEE Trans. Power Deliv.*, 2000, **15**, 4, pp.1265–1273

66 COORAY, V.: 'Some considerations on the 'Cooray–Rubinstein' approximation used in deriving the horizontal electric field over finitely conducting ground'. Proceedings of the 24th international conference on *Lightning protection*, pp.282–286, Birmingham, Sept., 1998

67 WAIT, J.R.: 'Concerning horizontal electric field of lightning', *IEEE Trans. Electromagn. Compat*, 1997, **39**, (2), p.186

68 PAOLONE, M.: 'Modeling of lightning-induced voltages on distribution networks for the solution of power quality problems, and relevant implementation in a transient program'. PhD thesis, University of Bologna, 2001

69 NUCCI, C.A.: 'Lightning-induced voltages on overhead power lines. Part II: Coupling models for the evaluation of the induced voltages', *Electra*, 1995, (162), pp.121–145

70 HERMOSILLO, V.F. and COORAY, V.: 'Calculation of fault rates of overhead power distribution lines due to lightning induced voltages including the effect of ground conductivity', *IEEE Trans. Elecromagn. Compat*., 1995, **37**, (3), pp.392–399

71 GUERRIERI, S., IANOZ, M., MAZZETTI, C., NUCCI, C.A., and RACHIDI, F.: 'Lightning induced voltages on an overhead line above a lossy ground: a sensitivity analysis', Proceedings of 23rd *ICLP*, Florence, 23–27 Sept., 1996

72 MICHISHITA, K., ISHI, M., and IMAI, Y.: 'Lightning-induced voltages on multiconductor distribution line influenced by ground conductivity'. 23rd international conference on *Lightning protection*, Firenze, 23–27 September, 1996, **I**, pp.30–35,

73 HOIDALEN, H.K., SLETBAK, J., and HENRIKSEN, T.: 'Ground effects on induced voltages from nearby lightning', *IEEE Trans. Electromagn. Compat.*, 1997

74 COORAY, V. and SCHUKA V.: 'Lightning-induced overvoltages in power lines: validity of various approximations made in overvoltage calculations', *IEEE Trans. Electromagn. Compat*., 1998

75 BORGHETTI, A., NUCCI, C.A., PAOLONE, M., and RACHIDI, F.: 'Characterization of the Response of an Overhead Line to Lightning Electromagnetic Fields'. 25th international conference on *Lightning protection*, ICLP'2000, Rhodos, Greece, September 2000. Correction: Cigré WG 33.02 meeting, IWD n*, Bologna, Sept. 2000

76 BERGER, K., ANDERSON, R.B., and KRONINGER, H.: 'Parameters of lightning flashes', *Electra*, 1975, (1), pp.23–37

77 HEIDLER, F.: 'Analytische Blitzstromfunktion zur LEMP – Berechnung'. Proceedings 18th international conference on *Lightning protection*, Munich, September 16–20, 1985, paper 1.9, pp.63–66

78 MACH, D.M., and RUST, W.D.: 'Photoelectric return-stroke velocity and peak current estimates in natural and triggered lightning', *J. Geophys. Res.*, 1989, **94**, (D11), pp.13237–13247

79 GUERRIERI, S., NUCCI, C.A., and RACHIDI, F.: 'Influence of the ground resistivity on the polarity and intensity of lightning induced voltages'. Proceedings of 10th international symposium on *High voltage engineering*, Montreal, 24–30 Aug. 1997
80 NUCCI, C.A.: 'Lightning-induced effects on transmission lines' (Edited by EMC Zurich Symposium, ETH Zentrum - 1kT-CH-8092, Zurich). Invited Tutorial, Proceedings of 14th international Zurich Symposium on *Electromagnetic Compatibility*, Zurich, February 20–22, 2001.
81 BORGHETTI, A., and NUCCI, C.A.: 'Frequency distribution of lightning-induced voltages on an overhead line above a lossy ground'. Proceedings 5th international symposium on *Lightning protection*, Sao Paulo, 17–21 May 1999
82 RACHIDI, F., NUCCI, C.A., IANOZ, M., and MAZZETTI, C.: 'Response of multiconductor power lines to nearby lightning return stroke electromagnetic fields', *IEEE Trans. Power Deliv.*, 1997, **12**, pp.1404–1411
83 WAGNER, C.F., and McCANN, G.D.: 'Induced voltages on transmission lines', *Trans. AIEE*, 1942, **61**, pp.916–930
84 UMAN, M.A.: 'The lightning discharge' (Academic Press, 1987)
85 RUBINSTEIN, M., RACHIDI, F., UMAN, M.A., THOTTAPPILLIL, R., RAKOV, V.A., and NUCCI, C.A.: 'Characterization of vertical electric fields 500 m and 30 m from triggered lightning', *J. Geophys. Res.*, 1995, **100**, (D5), pp.8863–8872
86 SCHONLAND, B.F.: 'The lightning discharge', *Handbook Phys.*, 1956, **22**, pp.576–628
87 UMAN, M.A., private communication
88 JORDAN, D.M., IDONE, V.P., RAKOV, V.A., UMAN, M.A., BEASLEY, W.H., and JURENKA, H.: 'Observed dart leader speed in natural and triggered lightning', *J. Geophys. Res.*, 1992, **97**, pp.9951–9957
89 CORREIA DE BARROS, M.T., FESTAS, J., NUCCI, C.A., and RACHIDI, F.: 'Corona on multiconductor overhead lines illuminated by LEMP'. Proceedings of 4th international symposium on *Power system transients*, Budapest, June 1999
90 SAKAKIBARA, A.: 'Calculation of lightning-induced voltages on overhead lines caused by inclined lightning strokes', *IEEE Power Appar. Syst.*, 1989, **4**, (1), pp.683–693
91 KORDI, B., MOINI, R., and RACHIDI, F.: 'Modeling an inclined lightning return stroke channel using the antenna theory model'. Proceedings of 14th international Zurich symposium on *Electromagnetic compatibility*, February 2001, Zurich
92 Electromagnetic Transient Program (EMTP) Rule Book, Bonneville Power Administration, Portland, Oregon, 1984
93 VAESSEN, P.T.M.: 'Transformer model for high frequencies', *IEEE Trans. Power Deliv.*, 1992, **7**, (3), pp.1761–1768
94 MORCHED, A., MARTÍ, L., and OTTEVANGENRS, J.: 'A high-frequency transformer model for the EMTP', *IEEE Trans. Power Deliv.*, 1993, **8**, (3), pp.1615–1626

95 IORIO, R., NUCCI, C.A., PORRINO, A., and RACHIDI, F.: 'Lightning-induced overvoltages on distribution overhead lines in presence of distribution transformers or short cables'. Proceedings of CIGRE symposium on *Power system electromagnetic compatibility*, Paper 300–09, Lausanne, Switzerland, 18–20 Oct., 1993

96 NUCCI, C.A., BARDAZZI, V., IORIO, R., MANSOLDO, A., and PORRINO, A.: 'A code for the calculation of lightning-induced overvoltages and its interface with the electromagnetic transient program'. Proceedings of 22nd international conference on *Lightning protection*, Budapest, 19–23 Sept., 1994

97 ORZAN, D., BARATON, P., IANOZ, M., and RACHIDI, F.: 'Comparaison entre deux approches pour traiter le couplage entre un champ EM et des réseaux de lignes' (in French). Proceedings of 8^{éme} colloque international sur la *CEM*, Lille, Sept. 1996, pp.55–60

98 PAOLONE, M., NUCCI, C.A., and RACHIDI, F.: 'A new finite difference time domain scheme for the evaluation of lightning induced overvoltages on multiconductor overhead lines'. Proceedings of 5th international conference on *Power system transients*, Rio de Janeiro, June 2001

99 PAOLONE, M., NUCCI, C.A., BORGHETTI, A., PETRACHE, E., and RACHIDI, F.: 'A new interface for lightning induced overvoltages calculation between EMTP and LIOV code'. *IEEE summer meeting*, Vancouver, British Columbia, Canada, *July 15–19 2001* (EMTP user group meeting)

100 'EMTP96 rule book'. DCG, 1996

101 HØIDALEN, H.K.: 'Calculation of lightning-induced overvoltages using models', Proceedings of the international conference on *Power systems transients.*, Budapest, Hungary, 1999, pp.359–64

102 BORGHETTI, A., GUTIERREZ, A., NUCCI, C.A., PAOLONE, M., PETRACHE, E., and Rachidi, F.: 'Software tools for the calculation of lightning-induced voltages on complex distribution systems'. in Proceedings of the 26th international conference on *Lightning protection*, 2–6 Sept. 2002, Krakow Poland

Chapter 9

Lightning and EMC

Michel Ianoz

9.1 Introduction

The very impressive natural phenomenon of lightning has been considered from the oldest times of humanity as a sign of power and as an instrument of punishment in the hands of the gods. The ancient Greeks imagined Zeus the ruler of the gods in Olympus as being the master of lightning which he could use as a symbol of his supremacy. Similar stories can be found in the mythology of almost all cultures.

For many centuries lightning has been a danger during thunderstorms for people, buildings and storage places where, for instance, wheat was stored. It can be assumed by extrapolating modern statistics that fires due to lightning took place often and that natural features, like a high tree in the proximity of a construction, were not always efficient protection.

When he began to use electricity man had to build overhead lines to transport energy and information, lines which were exposed to lightning strokes causing disruption in the supply of energy or of the information. In the last case, direct danger for persons could occur due to the overvoltages which, when the insulation level is inadequate, arrive on telephonic handsets and potentially kill people. The probability of direct impacts is however much higher for power lines due to their height over the ground. This explains the fact that practically from the beginning of the twentieth century to the 1960s the attention of scientists was concentrated on protecting this kind of installation. The solution of installing a grounding wire at the top of towers used for the high-voltage lines proved to be quite efficient and after the 1960s, the interest in studying lightning was retained by only a small circle of scientists. It was no longer a necessity for engineers involved in practical applications such as power or even telecommunications.

In order to understand why lightning has again become a major item of concern for many applications of electricity a short look into the history of electromagnetic compatibility (EMC) is necessary.

9.2 Short overview of EMC history

Contrary to what is usually thought, EMC is not such a young discipline. Its birth is in fact related to the beginning of radiocommunications which were disturbed by natural noise or man-made interference. This problem was at the origin of the creation in 1935 of the Commission Internationale Spéciale pour les Perturbation Radioélectriques (CISPR) in charge of specifying limits of electric and magnetic fields to avoid disturbing radiocommunications. The main sources of disturbance for radio reception were thunderstorms which produced parasitic noise and corona in the proximity of high-voltage transmission lines. Direct lightning impacts could also represent a major threat for the antenna towers. Lightning rods with grounding wires connected to the earth were installed and in general this rather simple approach was sufficient to protect these towers. However, at that time the fight against electromagnetic noise did not yet use the term electromagnetic compatibility.

The increase of electromagnetic problems for various electric and electronic installation is related to the miniaturisation of the electronic components which began in the 1950s and 1960s. This miniaturisation, which was needed to reduce the weight of electronic devices, is of course connected to the development of various sciences and in particular to the use of satellites for military purposes. It increased the sensitivity of electronic components and therefore also the probability of interference. Figure 9.1 shows the decrease during the last 50 years of the energy needed to destroy different kinds of electric and electronic component. A constant decrease of the energy with a rather high slope can be noted around the 1960s and 1970s.

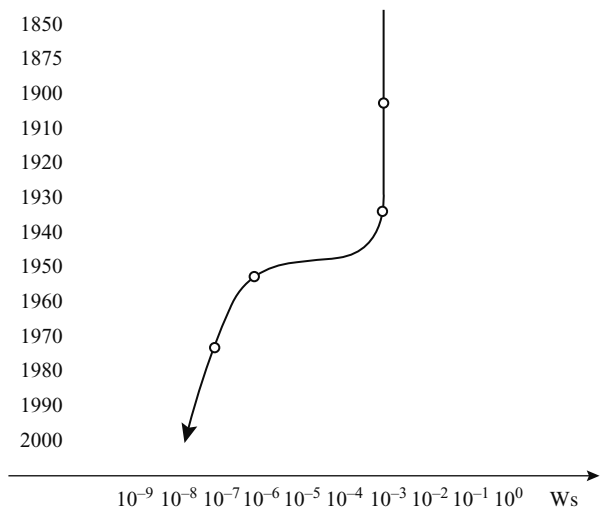

Figure 9.1 Change of the level of energy needed for the destruction of electric and electronic components

The fact that much less energy was needed made the indirect lightning effects, e.g. the electromagnetic fields due to the lightning discharge, one of the major threats for electronics today.

9.3 Lightning as a disturbance source

In order to determine the potential danger that lightning can represent as a source of disturbance, it is necessary to use the knowledge we have about the characteristic lightning parameters. The important parameters to characterise the potentiality of lightning to become a source of interference are:

- the lightning current value
- the derivative of the lightning current
- the energy contained in a lightning discharge.

Characteristic values of the lightning discharge have been obtained by systematic measurement of natural lightning. The most complete data on natural lightning is probably that obtained by Berger [1] during more than 20 years of systematic recordings on Monte San Salvatore in Switzerland. Lightning parameters are discussed in Chapter 3 of this book.

The Berger data and data obtained by other scientists have permitted us to construct the probability curves of positive and negative lightning amplitudes shown in Figure 9.2 [2].

The main problem with this data is that it has mostly been recorded in the 1960s and 1970s, with techniques which probably did not obtain the fastest of rise times due

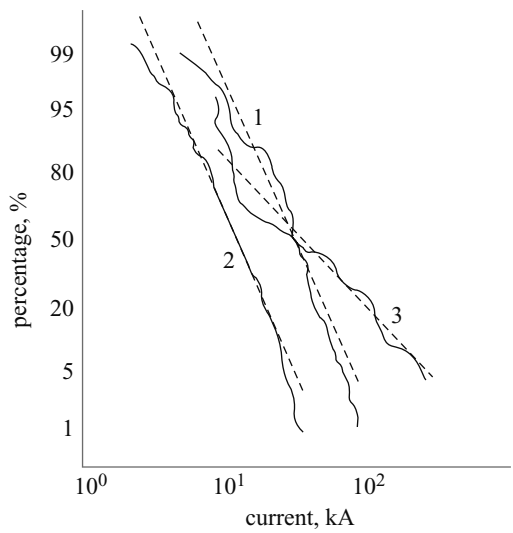

Figure 9.2 Probability curves of lightning amplitudes [2]

to frequency limitation in the bandwidth. Another problem which modern techniques have revealed is that in order to increase the chances of capturing lightning, towers as high as possible have been used; new data has shown that the lightning current is reflected by the ground and it is probable that the recordings of the 1960s and 1970s have been polluted by these kinds of reflection, which could not have been observed with the technical capability of the time [3].

When considering lightning as a source of disturbance, two aspects should be regarded:

(i) the direct lightning strike
(ii) the indirect effects due to the electromagnetic field created by the discharge.

In both cases, the two parameters mentioned previously stay at the basis of the assessment. For the estimation of the indirect effects, more data is however necessary, as discussed in other chapters. This is essentially the following:

- the soil conductivity, which is the most important parameter as it determines the value of the horizontal electric field component radiated by the lightning channel
- the geometry of the victim which will determine, as discussed in Chapter 7, the value of the currents or voltages induced in the victim circuits.

These parameters are discussed in other chapters. As also discussed in Chapter 7, field-to-transmission line coupling models today permit numerical estimation of the indirect effects of lightning.

Using the existing measured data and other such approaches, and in spite of the probable errors in the data and the approximations in the models, the existing knowledge has permitted us to assess the electromagnetic effects of lightning on circuits and installations and develop protection concepts and mitigation methods.

9.4 Types of coupling between lightning and circuits or installations

9.4.1 Coupling modes

In order to permit modelling, the coupling modes between a disturbance source and a victim have been classified in different ways and under different criteria. One kind of classification is shown in Figure 9.3 [4] and it is this approach which will be used in what follows in order to discuss effects due to lightning. In this Chapter, the following definition of direct and indirect lightning effects will be used. The term direct effect will be used only if a lightning strike hits an installation or a conductor galvanically connected to the installation. The term indirect effect will be used in two kinds of situation:

(i) when a nearby lightning stroke induces a current in an installation or a conductor galvanically connected to the installation
(ii) when a lightning current injected in a conductor or in a metallic structure induces a current in a nearby circuit or installation or gives a voltage drop at the input of an electronic circuit.

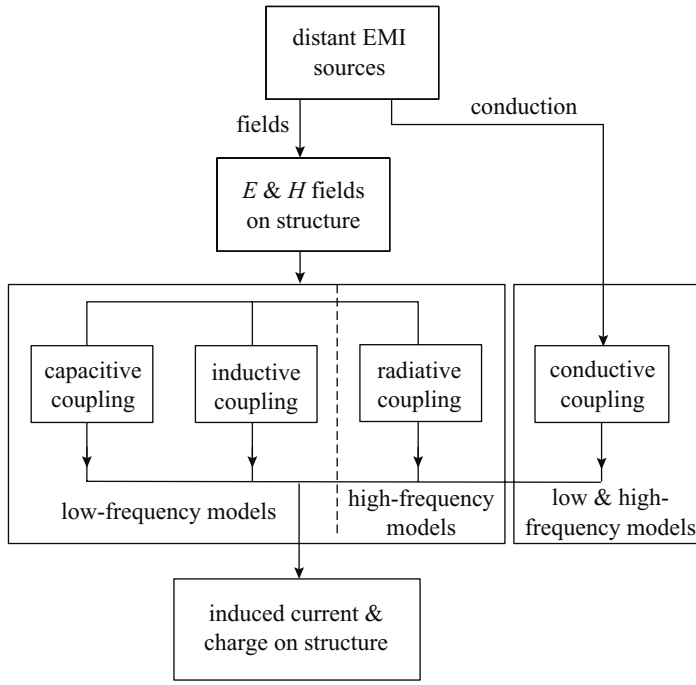

Figure 9.3 Classification of coupling modes [4]

This means that only conductive coupling will generate direct lightning effects on installations, and all kinds of coupling mode can be at the origin of indirect lightning effects.

9.4.2 Effects due to conductive coupling

As stated in the above paragraph, in the case of conductive coupling both direct or indirect lightning effects have to be considered. The conductive or galvanic coupling is defined as a direct penetration of a current into an installation. This current is initiated by a direct lightning strike. It will produce two types of effect:

(i) a direct effect if the strike takes place on a conductor connected to the installation
(ii) an indirect effect if the strike takes place on a metallic structure and, as stated previously, the potential difference created by this current will be transmitted at the input of an electronic circuit.

The probability of a direct strike on an overhead conductor connected to installation depends on the solution adopted in different countries for the construction of electric supply or telecommunication lines. This probability is very low in urban areas and in Europe where most of the distribution and telephone network is underground. In North and South America, for historical reasons, most of the low-power electric distribution

is aerial even in towns. The same situation prevails in Japan where, due to the frequent earthquakes, practically the whole energy and telephone network is constructed over the ground: the repair of an underground circuit is much more expensive than that of an aerial one. In general a rural network is also built using overhead lines. For aerial networks the probability of being hit by lightning is much higher. This probability can be calculated based on the keraunic level of the region.

9.4.3 Calculation of the average number of lightning strokes per year on a overhead line

The average density of lightning strokes per year on the ground (lightning strokes per km per year) can be calculated from the keraunic level of the region [5]:

$$N_s = N_k/7 \ 1/\text{km}^2 \text{ per year} \tag{9.1}$$

where N_k is the keraunic level or coefficient, i.e. the number of thunderstorm days per year. A thunderstorm day is defined as a day during which at least one lightning stroke has been observed at a given location. The world keraunic level map is shown in Figure 9.4 [6].

As an example, for most regions of western Europe, $N_k = 15$–50 (except the northern part which has a lower thunderstorm activity). This means that an average number of $N_k = 30$ can be taken which gives an average density of $N_s = 4.3$ lightning strokes/km^2 per year.

The average number of lightning strokes on an overhead line per year can be calculated with an empirical formula [6–8]:

$$N_l = N_s(b + 28H^{0.6})(1 - Sf) \cdot 10^{-1} \tag{9.2}$$

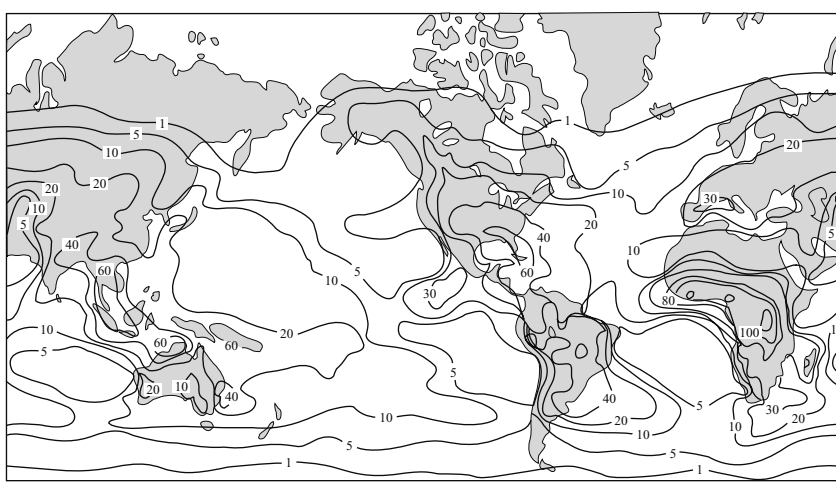

Figure 9.4 Map of the world keraunic levels

lightning strokes on 100 km of line, where N_s is the lightning stroke density on the ground previously defined, b (in metres) the horizontal distance between the lateral conductors of the three-phase line, H (in metres) is the line height and Sf the shielding factor due to the presence of other nearby objects. For heights of several metres over the ground, b is much smaller than $28H^{0.6}$ and can be neglected, eqn. (9.2) becomes:

$$N_l = 2.8N_s \cdot H^{0.6} \cdot (1 - Sf) \tag{9.3}$$

lightning strokes on 100 km of line. And for a line of length L:

$$N_l = 2.8LN_s \cdot H^{0.6} \cdot (1 - Sf)/10^5$$

For western Europe with an $N_s = 4.3$ and an average shielding factor of 0.5 this gives 24 strokes per year on a distribution power line 10 m high and a length of 100 km.

Lightning current from a stroke on the ground can also arrive in an underground structure such as a water or a gas pipe. The probability for such a structure to collect lightning current flowing in the ground due to a nearby discharge can be even higher than for the line due to the larger surface around the structure on which the stroke can occur.

These structures usually penetrate into buildings and are therefore connected to the grounding network of the construction. For security reasons all the electronic installations inside the building are of course also connected to this grounding network. The lightning current can in this way penetrate inside the installation. It should also be noted that as grounding should usually have a low impedance, penetration of the lightning current is facilitated in this way.

9.4.4 Effects due to electromagnetic field coupling

Two kinds of mechanism can be at the origin of electromagnetic field coupling:

(i) a direct stroke on a building built in reinforced concrete and in which different devices and circuits are installed
(ii) a lightning stroke near enough to the building in which sensitive devices are installed to create an electromagnetic field which can induce dangerous currents in the circuits of the installations.

9.4.4.1 Direct strokes on a building

If modern protection concepts are used, all the metallic parts of the building will be connected and the lightning current will be distributed in the rebars of the construction. This lightning current will create an electromagnetic field inside the building. Due to the high current value flowing in the rebars, the magnetic field will be predominant.

The technique of triggering lightning with small rockets carrying a wire which brings the lightning current to a choosen location has been used to strike the grounding rod of a real telecommunication tower. The measurements have shown that if the earthing of the tower is correctly achieved only 30 per cent of the lightning current flows into the metallic structure of the tower and the rest into the ground. However, if

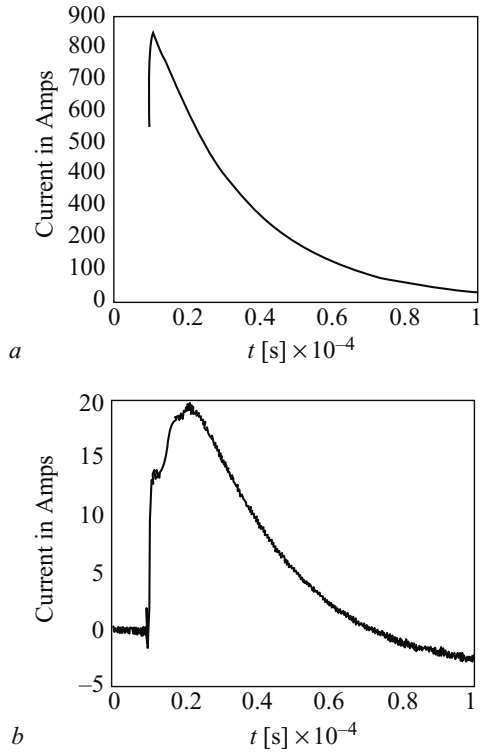

Figure 9.5 Laboratory simulation of magnetic field in a reinforced concrete building due to a lightning strike on it

a simulated lightning current
b measured horizontal magnetic field component

the lightning strike hits the top of a building and not its grounding rod the current will circulate in the whole metallic structure. Scale model measurements on a metallic cube of 2 × 2 × 2 m in high voltage laboratory [9] show that a lightning current of about 1 kA peak value creates a peak magnetic field of 20 A/m (Figure 9.5). In a loop of 1 m^2 a magnetic field variation of 20 A/m on 10 μs can create an induced voltage of 2.5 V.

Other laboratory simulations [10] on a 2 × 2 × 2 m rebar cage (Figure 9.6*a*), show that the current induced in a loop inside a metallic structure in which a lightning current is flowing can in some cases (depending on the position in the cage and the rebar density) be higher than the current in the same loop but without the presence of the cage (Figure 9.6*b*). This is due to the high lightning current flowing in a *rebar* near which the measurement loop was situated. This simulation shows that the solution of distributing the lightning current in the whole metallic structure of a

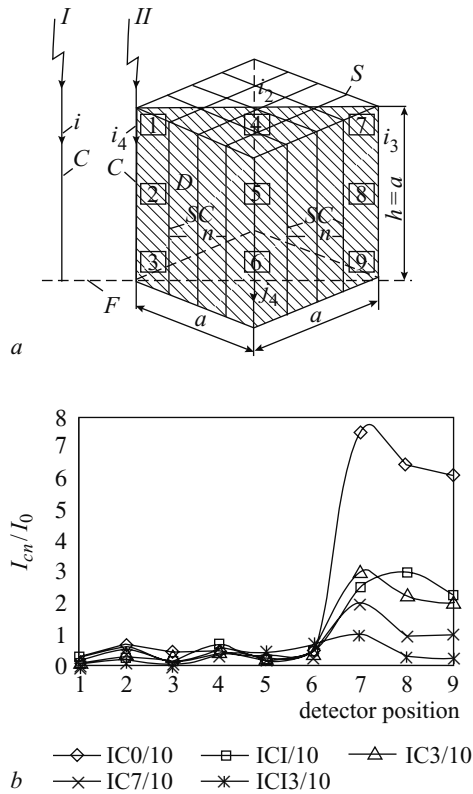

Figure 9.6 Laboratory simulation of the effect of rebars and position on current induced in a circuit due to a lightning strike on a building [10]

a experimental cage

b ratio I_{cn}/I_0 as a function of detector position in the cage, where I_{cn} is the current measured at different positions (from 1 to 9) when the cage has 1, 2, . . . , 13 rebars on each side and I_0 is the current measured at different positions (from 1 to 9) without the cage

reinforced concrete building can be, from the immunity point of view, worse for some installations than the solution of concentrating the discharge lightning current in a single descending conductor. These installations should be, in such a case, correctly protected.

9.4.4.2 Lightning stroke near a building

The expressions 'near' or 'near enough' are relative and depend on the amplitude and derivative of the lightning current and of its energy content. Measurements using triggered lightning permit us to predict that lightning strokes at distances of about 50–500 m, with average amplitudes of 30 kA and average di/dt values of 30–100 kA/μs,

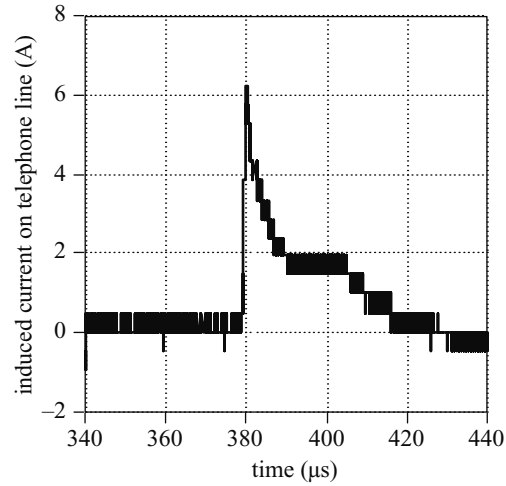

Figure 9.7 Lightning current measured on a 8 m long line situated at a distance of 70 m from a lightning stroke of about 6 kA

can induce currents of tens of amperes in circuits forming a loop with a perimeter of a few metres [11]. Figure 9.7 shows the current measured in a line 8 m long and 1.8 m high and installed at 70 m from the impact point of triggered lightning on the Camp Blanding site in Florida. The measured value of the lightning current was equal to about 6 kA. It can be seen that the induced current reached a peak value of 6 A. Assuming an attenuation of the electromagnetic field of about 6–10 dB inside a reinforced concrete building, the induced current amplitude in a circuit inside the building could be of about 2–3 A which would be a real threat for any electronics connected to this circuit.

9.5 Typical EMC problems due to lightning

In this section we shall try to present a very summarised overview of different but typical EMC problems which can be experienced in different kinds of electricity application. These examples are far from being exhaustive but should give a good idea of kinds of specific problem that can arise in the particular applications which will be reviewed. Specific protection methods for each example will be briefly mentioned in this section and then discussed in general in section 9.6.

9.5.1 Lightning effects in power networks

The best known effect of lightning in power transmission or distribution networks is the direct lightning stroke either on a phase conductor or on a tower (or ground conductor). The protection of HV overhead lines against direct strikes is achieved by grounding wires mounted on towers where the wire is grounded. Today, the danger of

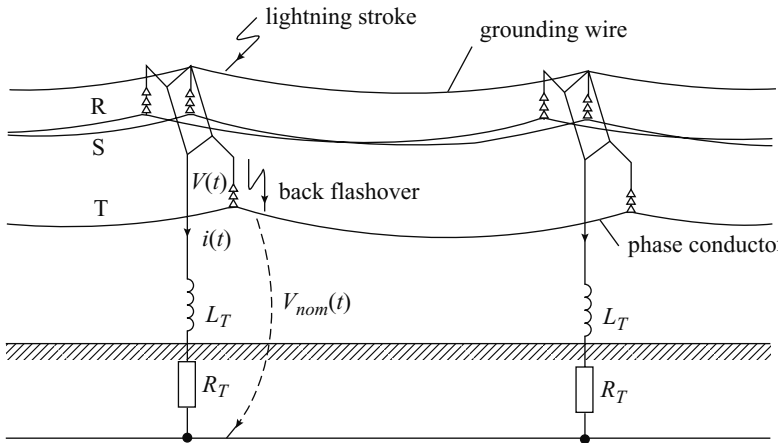

Figure 9.8 The backflash from a ground to a phase conductor

a direct strike on a phase conductor is minimised by the presence of ground conductors for transmission lines of 125 kV and higher. However, there is a certain probability that distribution lines of 60 kV and lower voltage could be hit by a direct lightning strike.

Another possible outage danger comes from the backflash or return arc which occurs if a lightning stroke hits the grounding wire and the potential rise of the tower top exceeds the insulation strength of the insulator chain. In this case an arc between the ground wire and a phase conductor takes place injecting at least a fraction of the total lightning current into the phase conductor (Figure 9.8).

Indirect lightning strokes, which can induce 50–60 kV or even higher overvoltages for the case of a nearby lightning stroke (50 m from the line) with a relatively low peak discharge current of 12 kA [12] should have little effect on power HV transmission lines but could easily exceed the insulation strength of the distribution network causing short circuits and disruption of the energy supply.

A recorded overvoltage on a 13 kV distribution line in Mexico due to a natural lightning stroke of unknown amplitude and distance to the line is shown in Figure 9.9 [13].

Tests for protection efficiency on a real scale have been performed [14]. Lightning currents triggered using the rocket launching technique have been injected at the Camp Blanding site in Florida in a 730 m long overhead line. Several Metal-Oxide Varistor arresters were installed on the line. The injected current, the MOV discharge current and the arrester voltage are shown in Figure 9.10 [14].

In the cases discussed above, a direct strike of the line produces a galvanic coupling of the interference, but with the indirect effect all three components (electrostatic, inductive and radiation) enter the structure of the incident electromagnetic field, their respective contribution depending on the distance between the strike location and the line [15].

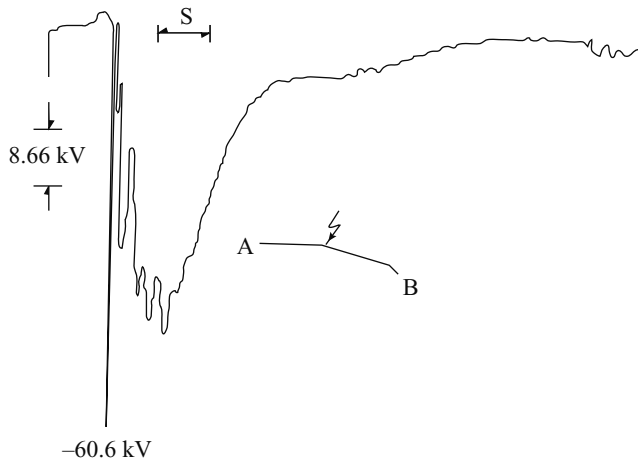

Figure 9.9 Overvoltage recorded on a 13 kV distribution line induced by a natural lightning stroke of unknown amplitude and distance to the line. Here A–B figures the line position; the arrow indicates the direction from which the electromagnetic field produced by the lightning stroke came

The increasing sensitivity of the different equipment used today in the power network has increased the threat represented by these induced voltages on medium or low-voltage distribution lines. Insulation coordination and definition of protection using lightning arresters, even at lower voltage levels, must take into account the danger due to indirect lightning.

9.5.2 Lightning effects on power network substation equipment

Here again direct and indirect lightning stroke effects can take place, related as above to galvanic or electromagnetic field coupling. However, the direct galvanic coupling acts on substation equipment through a chain of effects in a quite perverse way. Figure 9.11 shows a typical configuration for a circuit used for information transmission (data from equipment to the dispatching room, alarms, control). Two devices, T which is a translator used to convert information given for instance by a voltage or current transformer and A which is a receiver, are connected through a shielded coaxial cable. The shield is connected at the two extremities to the metallic box of the two devices which can be grounded or not. The substation ground is usually a metallic mesh buried at 30–50 cm under the earth's surface. Any lightning current hitting an overhead line entering the substation will be conducted to the ground by the arrester usually installed at the entrance of the substation. The large lightning current flowing in the grounding mesh will create a voltage drop, U. If the equipment A is not grounded, this voltage drop is found between A and the ground and this can be dangerous for the safety of the personnel. If A is grounded, the voltage drop appears

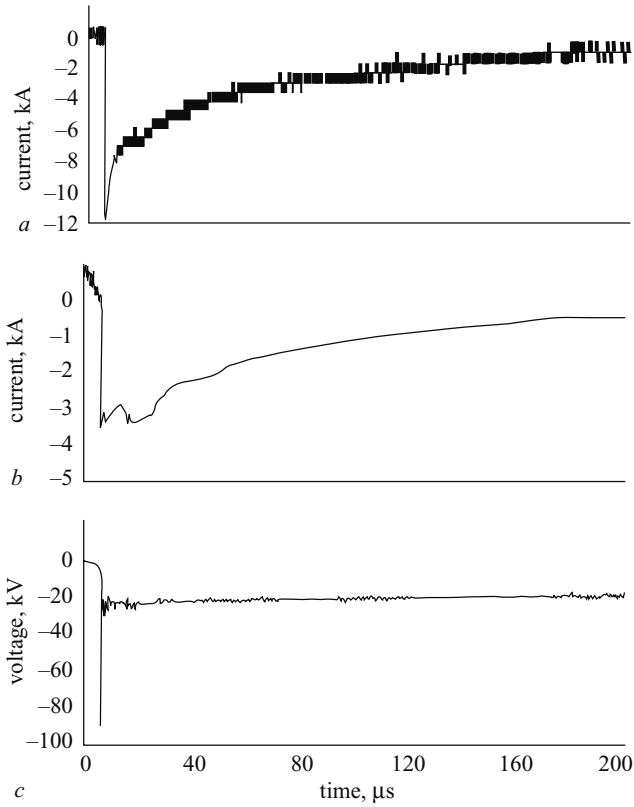

Figure 9.10 *Injected lightning current on the overhead line and responses of one MOV arrester*

a injected triggered lightning current
b arrester discharge current
c arrester voltage

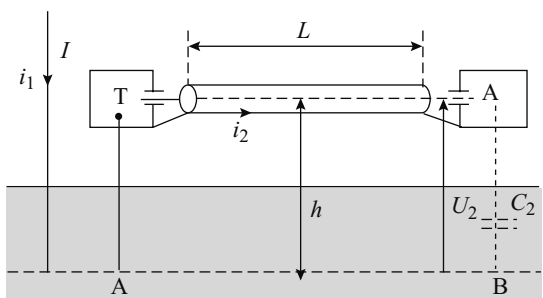

Figure 9.11 *Effect of a lightning current flowing in the ground plane of a power network substation*

between the internal conductor of the coaxial cable and the sheath, i.e. at the POE (point of entry) of the electronics of equipment A.

Currents induced in common or differential mode in the substation circuits due to indirect lightning effects also represent a large category of threats for sensitive electronic components. Usual EMC protection measures like proper grounding or bonding must be applied in order to avoid outages due to lightning in the power network.

9.5.3 Lightning effects on telecommunication networks

The effects of lightning on telecommunication networks are quite similar to those discussed for power networks, with the difference that telecommunication lines are lower than power lines and in many cases buried; this decreases the probability of direct strikes. However, the effects due to indirect lightning can be more dangerous as the telecommunication equipment is more sensitive than that conected in a power network. Figure 9.12 shows the results of a two-year lightning-induced overvoltage measurement campaign in the french telecommunication network which has been performed in five different sites in France: rural and urban, industrial and residential and in regions with different thunderstorm activity[16]. By counting the number of cases shown in Figure 9.12*b*, it can be seen that values 27 times higher than 2 kV have been measured in a network designed for a supply of 48 V or for transmitting signals at an even lower level.

Protection of the telecommunications equipment installed inside the switching entity is achieved by installing suppressors at the POE of the buildings or of the sensitive equipment (see primary and secondary protection discussed in section 9.6).

9.5.4 Lightning effects on low-voltage power networks

Less spectacular, the effects of a lightning stroke in the proximity of low voltage power networks supplying residential areas can be quite damaging in many cases. Examples are not very often recorded, because they are mainly known to the insurance companies and not to scientists or engineers and are not published. However a few cases can be refered to, like the destruction of all the TV sets in a residential building on the heights of the town of Montreux in 1996 and the destruction of TV sets through a current induced by a nearby lightning strike in the parabolic antenna of a big hotel in the town of Lausanne in 1997, both in Switzerland.

Figure 9.13 shows the statistics of overvoltages due mainly to lightning strokes in different environments in Switzerland [17]. For comparison a composite curve for a 120 V distribution network in the USA is also shown.

Simulations of lightning-induced effects in the low-voltage network of a residential house have been performed by current injection in Sweden [18]. And for aircraft lightning immunity tests, the current injection was used as an approximation to assess the immunity of the residential distribution system instead of field radiation testing because of its low cost and high repeatability. The current injection was

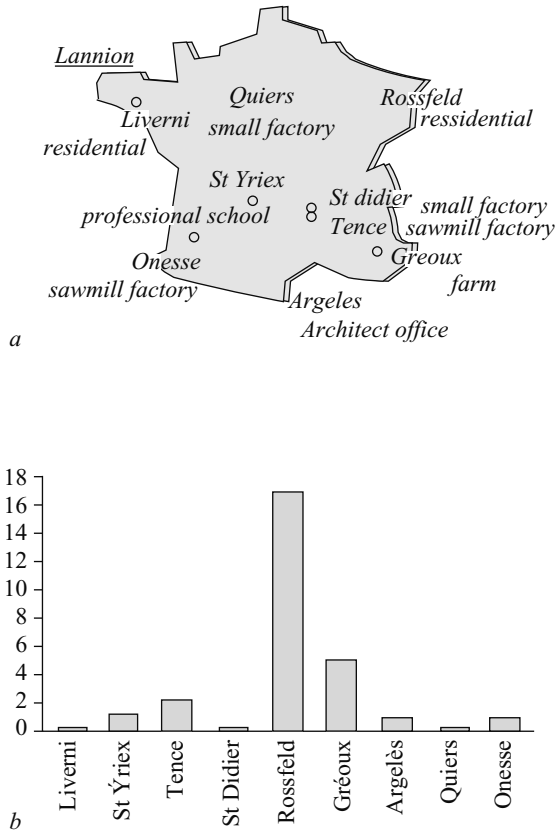

Figure 9.12 Results of a lightning-induced overvoltage measurement campaign in the French telecommunication network [15]

a measurement sites
b histogram of overvoltages higher than 2 kV

performed in:

- common mode between phase and ground
- differential mode between two phases of the three-phase domestic network.

Different transfer functions were tested and the example of Figure 9.14 shows the transfer voltage factor between the load response and the injected voltage at the house point of entry (POE).

9.5.5 Lightning effects on aircraft

Aeroplanes are often hit by lightning. Thunderstorm clouds cannot always be avoided by the aircraft and usually the plane forms a conducting bridge between two charged

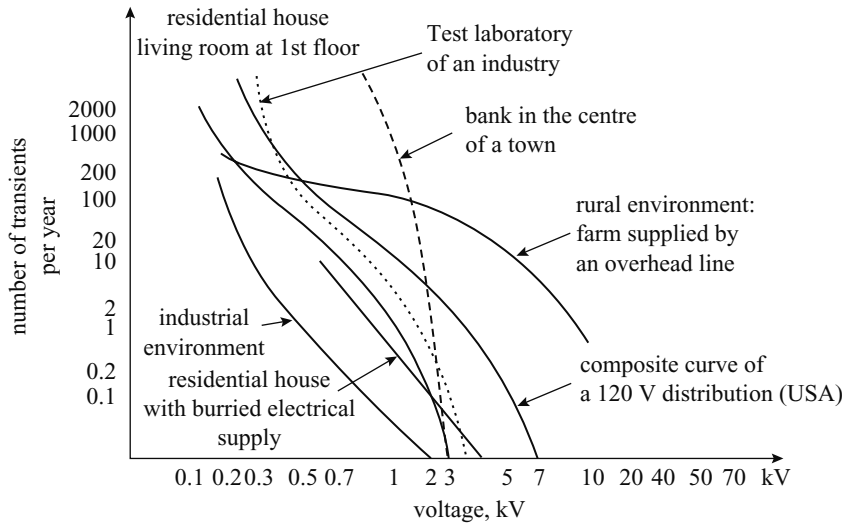

Figure 9.13 Statistics of the number of transients per year in different types of low voltage networks in Switzerland [17]

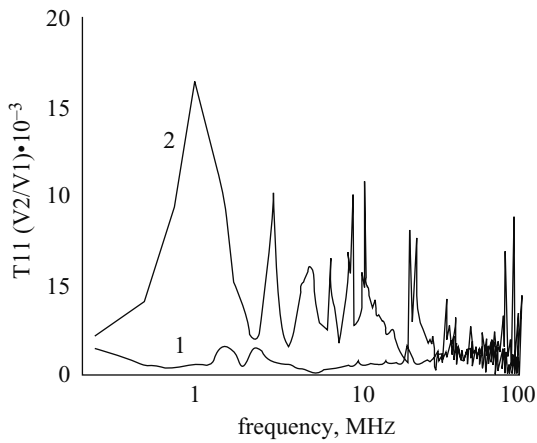

Figure 9.14 Transfer voltage function between a load and the house POE for a current injected test in a residential house (1. CM injection; 2. DM injection) [18]

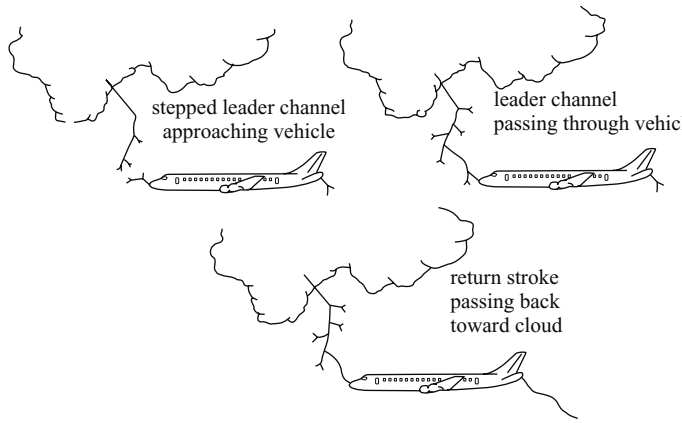

Figure 9.15 Lightning discharge through an aeroplane

thunderclouds triggering a lightning discharge which flows on the metallic surface of the plane fuselage (Figure 9.15).

Two trends in modern technology have increased the need to consider carefully the threat represented by lightning for an aircraft:

(i) the increase of sensitive electronics used in aircraft
(ii) the possible use of nonconductive or less conductive materials for the aeroplane body.

Both can be at the origin of EMC problems. In order to estimate the threat, experiments with an instrumented aircraft flying inside thunderstorms have been performed and currents induced by lightning discharges on the aeroplane have been recorded at real scale. Another way of estimating the threat and the protection level offered by the metallic envelope represented by the plane fuselage has been achieved by injecting pulses similar to lightning currents in an instrumented aircraft on ground [19]. These studies have permitted specific standards to be written which define the test methods (Figure 9.15), the shape of the injected current and the test levels (Figure 9.16) [19].

9.6 Specific EMC lightning protection parameters

9.6.1 General

Protection measures against the direct effects of lightning on buildings and relatively huge installations which are discussed in Chapter 8 must be combined and coordinated with protection against direct or induced lightning effects on all kinds of sensitive equipment. This means that specific EMC lightning protection concepts have been developed and should be achieved. Lightning parameters which are important for EMC are the general parameters which characterise the physical process of a lightning discharge. In what follows they will be viewed from an EMC point of view with

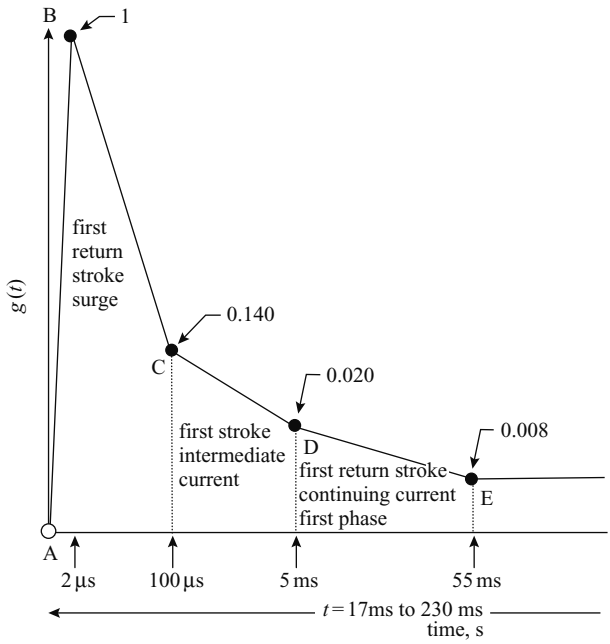

Figure 9.16 Shape of the impulse current injected in the aeroplane fuselage for the lightning test

Table 9.1 Lightning current waveforms which can be used for tests [20]

Event	Amplitude/waveform	Remarks
Lightning stroke:		
– direct stroke	30 kA/10 × 350 μs	– estimated average peak current values at the end of the line
– indirect stroke	5 kA/8 × 20 μs	– values may be 5–6 times higher

an emphasis on protection against effects which can create disturbances to sensitive circuits and equipment. The protection deals mainly with the primary lightning conducted environment due to direct strikes. However, more and more consideration is given to the secondary lightning conducted environment due to the indirect effect. As an example, Table 9.1 [20] shows test lightning parameters corresponding to average short circuit currents due to both the direct and indirect effects to be expected on an overhead telephone subscriberline of 1 km length. Note that the lightning currents which are given here as normed waveforms may be considerably different in practice.

As lines become shorter the probability of lightning surge occurence goes down, but direct strokes now have a higher probability of reaching the end of the line with all their energy.

It should be mentioned that currents and voltages due to very fast transients like those due to switches in GIS power networks, electrostatic discharges or other various sources of such kinds of interference always represent a certain probability for various installations together with the lightning threats. Combined protection measures against lightning and such very fast transients can be used. As EMC problems are usually viewed as being generated by HF phenomena (i.e. fast transients), in the following such combined protection measures are analysed by looking at basic surge parameters on long lines ($L > 1$ km) and by considering the consequences of the two threats. As the very fast transient effects are very similar to high altitude EMP (HEMP) effects, the data which will be used for the following comparison has been taken from the HEMP literature, regarded here as representative for all kind of fast transient.

9.6.2 Peak current

The peak current is only responsible for voltage drops on ohmic resistances, e.g. the grounding resistance. In a direct lightning stroke the local ground potential of a protected area may be raised by several hundred kV relative to a distant point. This may result in unpredictable dielectric breakdowns to ground in the protected area. The phenomena is clearly limited to lightning events and to installations with an imperfect shield or an unfavourable grounding system. In most cases the effect of di/dt on inductive voltage drops is much more important.

9.6.3 Peak current derivative

Inductive voltage drops and induced voltages are proportional to di/dt. In general, it is this parameter that gives rise to the most and severest problems in all protection concepts. For direct lightning strokes the di/dt value chosen for the protection concept may be as high as 100–200 kA/μs. For fast transients this parameter may attain values as high as 150 kA/μs. Although sometimes higher than for lightning, it is still of the same order of magnitude and can be addressed with the same conceptual methods.

9.6.4 Peak rate of change of voltage

Peak rate of change of voltage may only be applied to surge protectors with great precaution. Voltage rise times given in the literature are based on coupling calculations assuming certain field or current waveforms and linear line parameters. The theoretical peak voltage level may be as high as several 100 kV or even in the MV range for lightning. Typical values are in the range of 100 kV/μs–1 kV/ns for lightning and 1–10 kV/ns for fast transients. One does not usually consider nonlinear effects like insulation breakdown and firing actions of gas filled surge arresters which may occur in the subnanosecond range even in the course of a lightning event. One also

neglects ionisation effects and line losses in the 100 MHz frequency range. Assuming a low-pass characteristic for the line, the maximum du/dt will occur somewere near half. There is no doubt that du/dt at lower levels (most primary protection elements switch from the insulating into the conducting state well below 10 kV) is smaller than $(du/dt)_{max}$. This uncertainty is mostly due to unsufficient calculating models for frequencies above 100 MHz and a limited knowledge of nonlinear line parameters.

9.6.5 Total charge

Total charge can be obtained by integrating the measured current. Values vary from 50×10^{-6} A for fast transients to 70 A in a very powerful direct lightning stroke. As most voltage breakdown and voltage limiting devices exhibit a distinct voltage stabilising action (a very low impedance above a typical threshold voltage), their current carrying capability may approximatly be described in terms of the integral $i \times dt$. An 8×8 mm gas filled arrester is about equaly stressed by an indirect lightning stroke of 12 kA, 8/20 µs and by another type of fast transient.

9.6.6 The action integral: integral $i^2 \times dt$

The action integral is a parameter which is proportional to the energy. It has the units $A^2s = J/\bullet$; and it gives the energy that would be absorbed in a resistance of 1 Ω when the lightning current flows through it. As surge arresters have a low dynamic resistance in the mΩ range, they absorb only a comparatively small part of the potential energy. The capacity for energy absorbance of a surge arrester is therefore not relevant for its quality. The integral $i^2 \times dt$ is several thousand times higher in a lightning stroke than in different fast transients. It is relevant for thermal effects in ohmic resistances, e.g. current carrying capability of cable wires, and magneto-dynamic effects in current loops. Short powerful current surges (for example: 40 kA, 8/20 µs) may mechanically destroy an 8×8 mm gas filled protector before it is thermically destroyed.

9.6.7 Time to half value of the current

The time to half value of the current waveform is one of the most important determinants for protection circuits, i.e. combinations of primary and secondary protection elements. It varies from about 100 ns for fast transients to 350 µs in a direct lightning stroke.

9.6.8 Conclusions on LEMP and fast transients protection comparison

Except for du/dt lightning represents a more severe threat than any other kind of fast transient as far as conducted disturbance is concerned. However, we must also consider the possible degradation of the shield attenuation by installing protection devices against conducted disturbance. For economic reasons and because a radiation shield is missing in most cases, lightning protection elements are usually not designed as feedthrough elements. They will therefore degrade the shield attenuation of a

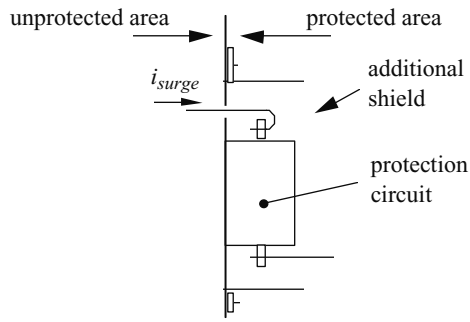

Figure 9.17 Solution to prevent the surge current for irradiating into the protected area

shielded protection concept unless special care is taken in their installation. The most important rule to observe is that the surge current should not radiate into the protected zone. This can be achieved by installing at least the primary protection element outside the shield or by adding a supplementary shield as shown in Figure 9.17.

Assuming that an installation is correctly done, then a well designed only lightning protection concept may be completed into a lightning + fast transient concept at almost no additional cost. An only fast transient concept should not be chosen unless the lightning threat can be completely excluded.

9.7 Specific EMC lightning protection concepts

9.7.1 General EMC protection concepts

As lightning is one of the most powerful sources of electromagnetic disturbance, general EMC protection concepts can and are used for the protection against lightning.

The general EMC protection concepts are:

(i) against conducted disturbances:
- suppressing of overvoltages or overcurrents

(ii) against radiated electromagnetic fields:
- increase the distance between a potential disturbance source and the victim
- shielding.

The concepts pertaining to conducted disturbances apply to direct lightning and those pertaining to radiated fields to indirect lightning effects. As the lightning discharge is an arbitrary phenomena regarding its parameters but also its striking point, an increase of distance between lightning and a potential victim is impossible to achieve. Therefore, only shielding will be considered as a possible protection against lightning electromagnetic fields.

9.7.2 Suppressors

Suppressors are protection elements which stop the penetration of conducted disturbances inside a protected volume. They can be:

- filters
- overvoltage suppressors
- separation transformers.

As lightning is a high energetic phenomena, filters and separation transformers are usually not used to stop the propagation and penetration of lightning currents inside protected areas. Therefore only overvoltage suppressors will be discussed here.

The overvoltage suppressors are components with a nonlinear voltage–current characteristic. They pass rather abruptly from a nonconduction (or very low conduction) to a conduction mode if a certain voltage threshold is attained. Examples of such components and the way in which they pass through a shielded wall are:

- gas tubes (Figure 9.18*a*)
- varistors (Figure 9.18*b*)
- Zener diodes.

In both cases shown in Figures 9.18*a* and 9.18*b*, the protection elements are combined with an inductance which will increase the rise time of the surge wave.

Note that in the case of lightning only very sensitive and essential installations are installed in shielded cages. This means that in fact what has been called above a shielded wall is in many cases just the reinforced concrete structure of a building.

The protection of sensitive devices installed inside buildings is often achieved in several steps. A primary protection is installed at the point of entry (POE) where a conductor enters into a building. This primary protection is intended to absorb the

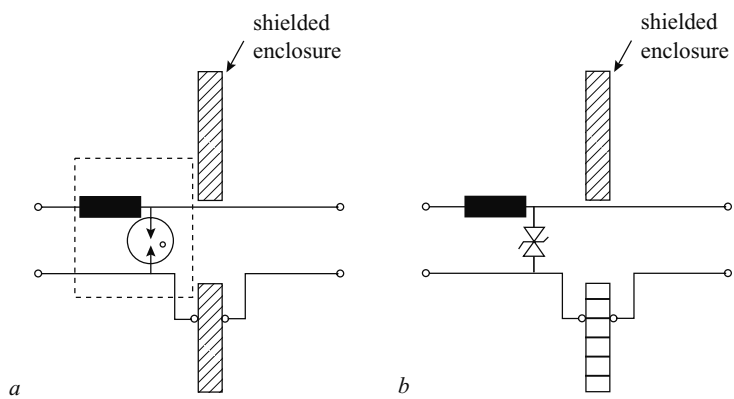

Figure 9.18 Protection elements at points of entry (POE) of buildings or shielded cages

a protection using a gas tube and an inductance
b protection using a varistor and an inductance

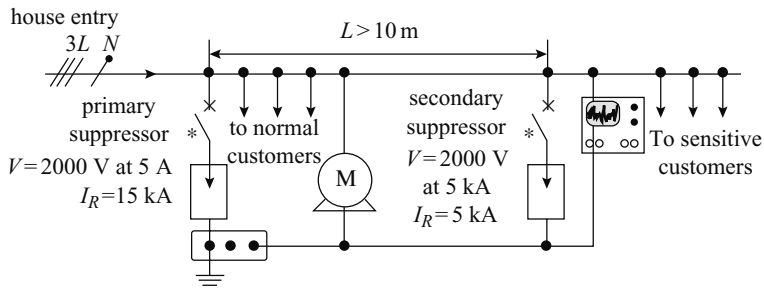

Figure 9.19 Protection cascade [17]

high energy of a direct lightning stroke on the conductor and gas tubes can respond to such a stress. In case of sensitive and important equipment, a secondary protection can be installed inside the building (Figure 9.19) [17]. The lightning current remaining after the primary protection will have a much smaller energy content and a varistor can be used for this secondary step.

This kind of protection design corresponds to the zoning concept.

9.7.3 Shielded cages

The shielded cage is a protection against electromagnetic fields. It can be used against lightning indirect effects if very sensitive equipment must be protected against possible lightning electromagnetic fields coming from nearby strikes.

In this case general EMC shielding concepts are applied, i.e. shielding continuity, penetration of conductors into the cage through filters, apertures closed by honeycombes.

However, protection by shielded cages against lightning is not really common. It can be combined for essential installations with protection against HEMP or high power microwaves (HPM).

9.8 References

1 BERGER, K., ANDERSON, R.B., and KRONINGER, H.: 'Parameters of lightning flashes', *Electra*, 1975, (41), pp.23–37
2 UMAN, M.A.: 'The lightning discharge' (Academic Press, New York, 1987)
3 BERMUDEZ, J.L., RUBINSTEIN, M., RACHIDI, F., and PAOLONE, M.: 'A method to find the reflection coefficients at the top and bottom of elevated strike objects from measured lightning currents'. Proceedings of 14th international symposium on EMC, Zurich, Feb. 20–22, 2001, paper 63J8
4 TESCHE, F.M., IANOZ, M., and KARLSSON, T.: 'EMC analysis methods and computational models' (J. Wiley & Sons, New York, 1996)
5 PRENTICE, S.A.: 'Lightning strike counter', *Electra*, CIGRE, 1972, (22), 1972, pp.149–159

6 IEEE PES Power Transmission Distribution Committee Lightning Performance of Distribution Lines Working Group, 'Calculating lightning performance of distribution lines', *IEEE Trans. Power Deliv.*, 1990, (July), **5**(3), pp.1408–1417
7 PARISH, D.E. and KVALTINE, D.J.: 'Lightning faults on distribution lines', *IEEE Trans. Power Deliv.*, 1989, **4**(4), pp.2179–2186
8 ERIKSSON, A.J.: 'The incidence of lightning strikes to power lines', *IEEE Trans. Power Deliv.*, 1987, **PWRD-2**, (3), pp.859–870
9 NICOARA, B. and IANOZ, M.: 'Etude sur les effets électromagnétiques dues à un coup de foudre sur un bâtiment ou à proximité d'un bâtiment'. Rapp. Int. LRE, EPFL, Oct. 1999
10 MAZZETTI, C. and FLISOWSKI, Z.: 'Spatial distribution of lightning interferences inside different LPS models'. Proceedings of 13th International Wroclaw symposium on *EMC*, June 25–28, 1996, pp.532–536
11 RACHIDI, F., RUBINSTEIN, M., ZWEIACKER, P., IANOZ, M., BRAENDLI, B., and KAELIN, A.: 'Indirect lightning effects on short overhead lines'. Proceedings of international symposium *EMC'98*, Roma, Sept. 14–18, 1998, paper I – 1
12 RACHIDI, F., NUCCI, C.A., IANOZ, M., and MAZZETTI, C.: 'Response of multiconductor power lines to nearby lightning return stroke electromagnetic fields'. IEEE /PES *Transmission and distribution conference*, Los Angeles, September 15–20, 1996
13 DE LA ROSA, F., VALDIVIVA, R., PEREZ, H., and LOSA, J.: 'Discussion about the induction effects of lightning in an experimental power distribution line in Mexico', *IEEE Trans. Power Deliv.*, 1988, **3**, (3), pp.1080–1089
14 FERNANDEZ, M.I., RAMBO, K.J., RAKOV, V.A., and UMAN, M.A.: 'Performance of MOV arresters during very close, direct lightning strikes to a power distribution system'. *IEEE Trans. Power Deliv.*, 1999, **14**, (2), pp.411–418
15 MAZZETTI, C., NUCCI, C.A., IANOZ, M., and RACHIDI, F.: 'Frequency analysis of lightning stroke electromagnetic fields'. Proceedings of 7th Zürich international Symposium on *EMC*, Zürich, March 3–5, 1987, paper 16D4
16 DJEBARI, B., GUÉRIN, L., and GLÉONEC, M.: 'Conducted EM disturbances on the telecommunication terminal equipment ports'. Proceedings of International Symposium on *EMC'94*, Roma, Sept. 13–16, 1994, paper B-5
17 SÉRAUDE, CH.: 'Surtensions et parafoudres en BT-Coordination de l'isolement en BT'. Cahier Technique Merlin Gérin no. 179, Sept. 1995
18 MING, Y., PEREZ, H., COORAY, G.V., and SCUKA, V.: 'Response characteristic of a low voltage power installation network to the EMP irradiation obtained by an impulse current injection method'. Proceedings of international symposium on *EMC'94*, Roma, Sept. 13–16, 1994, pp.543–548
19 FISHER, F.A, *et al.*: 'Lightning protection of aircraft'. Lightning Technologies, Inc., Pittsfield, MA, 1990
20 BUECHLER, W., FLISOWSKI, Z., IANOZ, M., and MAZZETTI, C.: 'Comparisons between protection concepts against HEMP and LEMP'. Proceedings of International symposium on *EMC'95*, St. Petersburg, 26–30 June, 1995, pp.369–374

Chapter 10

Principles of protection of structures against lightning

Carlo Mazzetti

Thunderstorms are natural weather phenomena and there are no devices and methods capable of preventing lightning discharges. Direct and nearby cloud-to-ground discharges can be hazardous to structures, persons, installations and other things in or on them, so that the application of lightning protection measures must be considered.

The decision for the need for protection and the selection of protection measures should be determined in terms of risk, which means that these measures should be adequate to reduce the risk to a tolerable level.

The modern approach is that of risk management which integrates the need for protection and the selection of adequate protection measures taking into account both the efficiency of the measures and the cost of their provision. In the risk management approach, the lightning threats that create risk are identified, the frequencies of all risk events are estimated, the consequences of the risk events are determined and, if these are above a tolerable level of risk, protection measures are applied to reduce the risk (R) to below the tolerable level (R_T).

It should be stressed that the selection of adequate protection measures aims to reduce not only the risk by direct flashes to the structure but even the risk for low-voltage and electronic systems against indirect flashes, which means the risk due to flashes to ground near the structure, flashes direct to the lines or flashes to ground near the lines entering the structure.

According to the new publications' plan recently approved by IEC TC81 [1], the criteria for design, installation and maintenance of lightning protection measures may be distiguished in three separate groups:

(i) protection measures to reduce physical damages (mechanical damages, fire and explosion danger) and life hazard due to direct lightning flashes to the structure
(ii) protection measures against the electromagnetic effects of lightning on electrical and electronic systems in a structure

(iii) protection measures to reduce the loss of services entering the structure, namely electrical and telecommunication lines.

10.1 Parameters of lightning current

Lightning parameters were investigated from the middle of the last century and a reliable synthesis of the collected data was published within CIGRE activities [2,3].

Lightning current parameters are usually obtained from measurements taken on high objects.The statistical distributions, log-normal type, of lightning current parameters given in section 10.11 are used for the aim of lightning protection.

Also in section 10.11 are reported the values of the parameters and the waveforms of lightning current used for protection purposes [4].

The most important parameters for the purpose of designing protection systems [5,6] are:

a *Peak value of the first stroke*: the lowest values of the statistical distribution of current amplitude of downward flashes are important for the choice of the number and position of the air termination system to prevent direct lightning flashes to the structure to be protected (see section 10.7); the highest values of the statistical distribution of current amplitude are important for sizing of protection measures (electrodynamic effects etc.).

b *Maximum rate of rise*: the highest values of the statistical distribution are important for dimensioning the protection measures in order to avoid inductive effects of lightning current (induced overvoltages) and dangerous sparking.

c *Flash duration and total charge in the flash*: the highest values of the statistical distribution are important for sizing the air termination system aimed at limiting the thermal effects at the impact point of the lightning flash.

d *Specific energy in a flash*: the highest values of the statistical distribution are important for the selection of a conductor for the protective system, aimed at preventing damage due to thermal effects and for setting up a suitable earthing system in order to prevent hazard to life.

For the protection of structures some additional information is necessary to assess more general models of lightning phenomenon, such a charge distribution in the channel and channel velocities [20].

Furthermore, in risk assessment it is crucial to know the average lightning flash density (N_g) of the region where the structure and the incoming lines are placed. N_g values (expressing the number of flashes per km^2 per year) can be assessed by different methods – thunderstorm day maps, lightning flash counters – and, more recently, by lightning location systems.

10.2 Classification of structures

For the purposes of lightning protection structures may be usefully classified according to consequential effects of lightning flash which can cause damage to the structure,

their contents or their surroundings [11]:

- common structures
- structures with risk of explosion, containing solid explosive materials or hazardous zones type 0 as determined in IEC 60079-10; for the purposes of lightning protection, structures with hazardous zones type 1 or type 2 are not considered to be at risk of explosion due to very low probability of contemporary presence of lightning and explosive gas atmospheres
- structures with electronic systems, in which a large amount of electronic equipment is installed, such as systems including telecommunication equipment, control systems, measuring systems
- structures dangerous to the environment, which may cause biological, chemical and radioactive emission as a consequence of lightning, such as chemical, petrochemical, nuclear plants etc.

Structures may be also classified according to the risk of fire:

(i) Structures with a high risk of fire:
  - structures made by combustible materials
  - structures with a roof made of highly combustible materials
  - structures with a specific fire load larger than 45 kg/m^2.

(ii) Structures with an ordinary risk of fire:
  - structures with a specific fire load between 20 and 45 kg/m^2.

(iii) Structures with a low risk of fire:
  - structures with a specific fire load of less than 20 kg/m^2
  - structures containing combustible materials only occasionally.

The specific fire load may be calculated as the ratio of the total amount of combustible material and the overall surface of the structure.

10.3 Damage due to lightning

Lightning striking a structure can result in damage to the structure itself and to its occupants and contents, including failure of equipment and especially of electrical and electronic systems. The damages and failures may also extend to the surroundings of the structure and may even involve the local environment. The scale of this extention depends on the characteristics of the structure and on the characteristics of lightning flash.

10.3.1 Effects of lightning

The main characteristics of structures of relevance to lightning effects include [4]:

- construction (wood, brick, concrete, reinforced concrete, steel frame)
- function (dwelling house, office, farm, theatre, hotel, school, hospital, museum, church, prison, department store, bank, factory, industry plant, sports area)
- occupants and contents (persons and animals, noninflammable materials, inflammable materials, nonexplosive mixtures, explosive mixtures, equipment immune to electromagnetic fields or sensitive to electromagnetic fields)

- entering installations (electricity mains, telecommunication and data lines, other services)
- measures to limit consequential effects of damages (e.g. protection to reduce mechanical damages, the consequences of fire, protection to limit the concentration of explosive mixtures, protection to limit the overvoltages, protection to limit step and touch voltages)
- scale of the extension of danger (structure with small local danger, structure with greater but confined danger, structure with danger to the surroundings, structure with danger to the environment).

10.3.2 Causes and types of damage

The lightning current is the source of damage. The following causes of damage are to be taken into account according to the position of the striken point in relation to the structure [4]:

- flashes direct to a structure
- flashes direct to the incoming lines (mains, telecommunication and data lines) or other services
- flashes to ground near the structure
- flashes to ground near the incoming lines and services.

Direct flashes to the structure can cause:

- immediate mechanical damage, fire and/or explosion due to the lightning channel itself, or its current (overheated conductors) and its charge (molten metal)
- fire and/or explosion initiated by sparks caused by overvoltages resulting from resistive and inductive coupling
- injuries to people by step and touch voltages resulting from resistive and inductive coupling
- failure of electrical and electronic systems due to passage of part of the lightning currents and to overvoltages resulting from resistive and inductive coupling
- failure of apparatus internal to the structure due to direct coupling of lightning electromagnetic impulsive field (LEMP).

Direct flashes to the incoming lines can cause:

- fire and/or explosion triggered by sparks due to overvoltages appearing on external power lines entering the structure
- injuries to people due to overcurrents and to overvoltages appearing on external lines entering the structure
- failures of electrical and electronic systems due to overvoltages appearing on external lines entering the structure.

Flashes to the ground surface near the structure can cause:

- failures or malfunction of electrical and electronic systems due to overvoltages resulting from inductive coupling with lightning current.

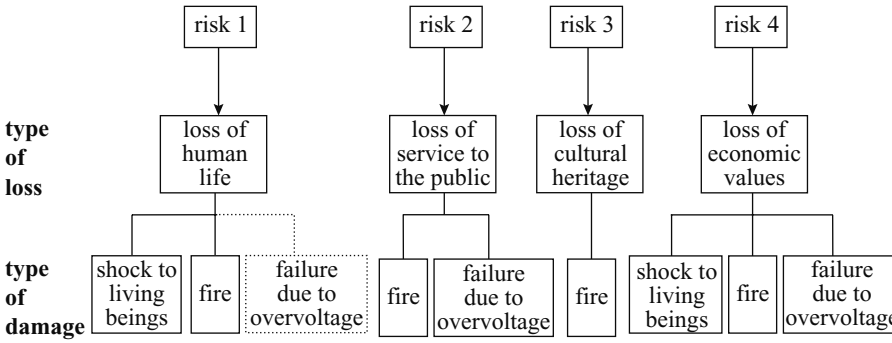

Figure 10.1 Types of loss resulting from different types of damage [10]

- failure of apparatus internal to the structure due to their direct coupling with LEMP.

Flashes to the ground surface near incoming lines can cause:

- failures or malfunction of electrical and electronic systems due to overvoltages induced in external lines entering the structure.

As result, the lightning can cause three basic types of damage:

(i) shock to living beings due to touch and step voltages
(ii) fire, explosion, mechanical destruction, chemical release (physical damages) due to mechanical and thermal effects by lightning current including sparking
(iii) failure of electrical and electronic systems due to overvoltages.

10.3.3 Types of loss

Each type of damage, alone or in combination with others, may produce different consequential loss in a structure. The type of loss that may appear depends on the characteristics of the structure.

According to [4] the following types of loss are to be considered:

- loss of human life
- loss of service to the public
- loss of cultural heritage
- loss of economic value (structure, content and loss of activity).

More than one loss may appear in a structure. Loss of economic value always appears. The first three losses belong to social value; the fourth loss belongs to private property.

The correspondance between causes of damage, types of damage and loss is reported in Figure 10.1.

10.4 Risk

The lightning hazard impending over a structure is a random process composed of a set of effects which are correlated with the parameters of lightning discharge, the

characteristics of the structure, its content, the installation internal to the structure, the lines and other services entering the structure [7].

If the time of observation is fixed (usually $t = 1$ year), it is possible to demonstrate [7–9] that the risk, defined as the probability of having an annual loss in a structure due to lightning, may be calculated by the following expression:

$$R = 1 - \exp(-NPL) \tag{10.1}$$

where N is the average yearly number of flashes influencing the structure and its content, P is the damage probability of the structure due to a single flash and L is the average amount of loss, with consequential effects, due to a specified type of damage.

The quantity NPL is the level of risk or the number (or frequency) of annual loss in a structure due to lightning.

It is evident that if $NPL \ll 1$ (in practice $NPL < 0.1$), the risk (as probability) and the level of risk are coincident.

The International Standard [4] defines the risk as the probable annual loss in a structure due to lightning, and suggests [10] evaluating it by the following general formula:

$$R = NPL \tag{10.2}$$

where L is expressed as relative to the total amount of persons or goods.

10.4.1 Number of flashes

It is generally accepted that the number of flashes N can be evaluated by the product of the lightning ground flash density N_g by an equivalent collection area A of the structure or the incoming line.

The lightning ground flash density, in number of lightning flashes per km^2 and per year, should be determined by measurements. Networks of flash counters or, more recently, of lightning location systems are installed in several countries to build maps of N_g.

If the map is not available, values of N_g may be estimated by different relationships [3,15,40] as a function of the number of thunderstorm days per year or keraunic level of the region T_d. The International Standard [10] suggests using the following approximate relation:

$$N_g \cong 0.1\, T_d \tag{10.3}$$

where T_d may be obtained from the isokeraunic maps.

The equivalent collection area of the structure (or the incoming service), i.e. the surface crossed by all the lightning flashes (upwards and downwards) which hit the structure (or the service), depends on several parameters. The most significant are:

- structure (or service) characteristics: in particular the height, the position with respect to the other structures, the type of incoming line (MV or LV, overhead or underground etc.)
- environment characteristics: orography, resistivity of soil

- lightning characteristics: electrical parameters and statistical distribution of the relevant values.

The methods for equivalent area calculation are based on different models (see section 10.12) used to evaluate the exposure of structures (or lines). A good summary of different models is reported in [20]; in [10] approximate formulas for equivalent collection area calculations are proposed for structures and incoming lines.

10.4.2 Probability of damage

Different difficulties are encountered when evaluating the probability of damage P. Reference [10] gives the guideline and table tools for evaluating the probabilities of different types of damage taking into account the effect of protection measures provided in reducing such probabilities.

It is important to note that in some cases the probability of a damage due to a single stroke is a result of the product of two probabilities of two events related in series sequence, but in some other cases the probability of damage has to be calculated as the parallel combination of two probabilities of two events in parallel sequence.

As an example, the first case is relevant to the probability of fire calculated as the product of the probability of spark (p_s) and the probabililty that a spark could trigger a fire (p_f):

$$P = p_s p_f \tag{10.4}$$

and the second case is related to the probability of a failure of a electronic system due to overvoltages by direct flash to a structure, calculated by the following relation:

$$P = [1 - (1 - p_r)(1 - p_i)] \tag{10.5}$$

where p_r is the probability of failure due to overvoltage by resistive coupling of the system with current flowing into the earth and p_i is the probability of failure due to overvoltage by inductive coupling of the internal loop installation with the lightning current flowing along the conductors.

10.4.3 Amount of loss

The values of consequent loss L depend on the use to which the structure is assigned, the attendance time of persons in the structure, the type of service provided to public, the value of goods affected by damage, measures provided to limit the amount of damage.

For more detailed information on the methods of calculation of N, P and L see Reference [10].

The following risks are to be taken into accont, corresponding to the types of loss:

- R_1: risk of loss of human life
- R_2: risk of loss of services to the public
- R_3: risk of loss of cultural heritage
- R_4: risk of loss of economic value.

10.4.4 Risk components

Each risk may be calculated as the sum of different risk components [10], each expressed by eqn. 10.2, depending on the cause of damage:

(i) lightning flashes direct to the structure may generate:
- R_A component related to shock of living beings due to touch and step voltages
- R_B component related to fire, explosion, mechanical and chemical effects inside the structure due to mechanical and thermal effect including dangerous sparking
- R_C component related to the failure of electrical and electronic systems due to overvoltages on internal installations and incoming services.

(ii) lightning flashes to ground near the structure may generate:
- R_M component related to the failure of electrical and electronic systems due to overvoltages on internal installations mainly caused by the magnetic field generated by the lightning current.

(iii) lightning flashes direct to the incoming line may generate:
- R_U component related to shock of living beings due to touch and step voltages
- R_V component related to fire, explosion, mechanical and chemical effects inside the structure due to mechanical and thermal effect including dangerous sparking between incoming lines and metal installations (generally at the entrance point of the line into the structure)
- R_W component related to the failure of electrical and electronic systems due to overcurrents and overvoltages, transmitted by external lines to the structure.

(iv) lightning flashes to ground near the incoming line may generate:
- R_Z component related to the failure of electrical and electronic systems due to induced overvoltages, trasmitted through the incoming lines.

For each type of loss, the value of risk R is then given by the sum of its components and may be calculated (see Figure 10.1) with reference to the point of strike with reference to the various types of damage.

With reference to the point of strike:

$$R = R_D + R_I \tag{10.6}$$

where $R_D = R_A + R_B + R_C$ is the risk due to direct flashes to the structure and $R_I = R_M + R_U + R_V + R_W + R_Z$ is the risk due to indirect flashes to the structure.

With reference to the various types of damage:

$$R = R_S + R_F + R_O \tag{10.7}$$

where $R_S = R_A + R_U$, the risk related to shock of living beings $R_F = R_B + R_V$, the risk related to physical damages and $R_O = R_C + R_M + R_W + R_Z$, the risk related to the failure of electrical and electronic systems due to overvoltages.

Table 10.1 Typical values of tolerable risk R_T [10]

Type of losses	R_T
Loss of human life	10^{-5}
Loss of service to the public	10^{-3}
Loss of cultural heritage	10^{-3}

10.4.5 Tolerable value of risk

The aim of protection against lightning is to reduce the risk R to a maximum level R_T which can be tolerated for the structure to be protected:

$$R \leq R_T \tag{10.8}$$

If more than one type of damage could appear in the structure, the condition $R \leq R_T$ shall be satisfied for each type of damage.

The values of tolerable risk R_T where lightning involves loss of social values should be under the responsibility of the national body concerned; representative values are reported in Table 10.1.

The values of tolerable risk R_T, where lightning strikes involve only private economic loss, could be fixed by the owner of the structure or by the designer of protection measures according to a criterion of purely economic convenience.

For further information see [10].

10.4.5.1 Procedure for selection of protection measures

For the structure to be protected, the lightning protection design engineer should decide if the protection is required and, if it is, suitable protection measures should be selected.

The main steps to be followed are:

a identify the structure to be protected and its characteristics
b identify the types of damage (and relevant risks) due to lightning in the structure
c for each type of damage:
- evaluate the risk R
- select the tolerable value of the risk R_T
- compare R with R_T
- if $R \leq R_T$ lightning protection is not necessary
- if $R > R_T$ protection measures shall be adopted in order to reduce $R \leq R_T$

d select all protection measures which reduce $R \leq R_T$ for all damages relevant to the structure
e select the most suitable protection according to the technical and economic aspects.

10.4.5.2 Protection measures

The lightning protection measures include:

(i) A lightning protection system (LPS) with adequate levels of protection in order to reduce the risk R_D by direct flashes to the structure. The LPS for the structure comprises an air termination system to intercept the lightning strike, a down conductor system to conduct the lightning current safely to earth and an earth termination system to dissipate the current into the earth. When an LPS is installed, equipotentialisation is a very important measure to reduce fire and explosion danger and life hazard. Equipotentialisation is achieved by means of bonding conductors or surge protective devices (SPD) where bonding conductors are not allowed.

(ii) Protection against lightning electromagnetic impulse (LEMP) caused by direct and nearby flashes. LEMP protection includes a number of measures to protect electronic systems including the use of a mesh of down conductors to minimise the internal magnetic field, the selection of LEMP protection zones (LPZ), equipotential bonding and earthing, cable and equipment magnetic shielding (MS) and the installation of an SPD system.

(iii) Protection against transient currents and voltages of electrical and communication services entering the structure. Includes the use of isolation devices, the shielding of cables and the installation and coordination of SPD adequately selected.

Additional measures, other than LPS/SPD/MS should be provided in order to limit:

- touch and step voltages (insulation of exposed conductors etc.)
- the development and propagation of the fire (extinguishers, hydrants, fire alarm installations, fire compartment proof, protected escape routes etc.)
- the overvoltages induced in internal installations (cable routing precautions etc.).

The selection of the most suitable protection measures shall be made by the designer according to the share of each risk component in the total risk, and according to the technical and economic aspects of the different protection measures.

10.5 Basic criteria of protection

10.5.1 Protection of structures against physical damages and life hazard

The main and most effective protection measure, intended for protection of structures against mechanical damage, fire and explosion danger and life hazard due to direct flashes, is the lightning protection system (LPS). It consists of both external and internal lightning protection systems [11].

The functions of the external LPS are:

(i) to intercept a direct lightning strike to the structure (with an air terminal system)

(ii) to conduct the lightning current safely towards earth (using a down conductor system)

(iii) to disperse it into the earth (using an earth termination system).

In addition, there is an internal LPS which prevents dangerous sparking within the structure using either equipotential bonding or a separation distance (and hence electrical insulation) between the LPS components and other electrically conducting elements internal to the structure.

Protection measures additional to external LPS may be required in order to avoid the hazard due to touch and step voltages for persons outside the structure in the vicinity of the down conductor system. Injuries to living beings due to touch and step voltages are mainly avoided by increasing the surface resistivity of the soil outside the structure, of the floor inside the structure and by insulation of the exposed conductive parts (see 10.7.4).

Four types of LPS (I, II, III and IV) are defined as a set of construction rules, based on the corresponding lightning protection level. Each set includes level-dependent (e.g. rolling sphere radius, mesh width etc.) and level-independent (e.g. cross sections, materials etc.) construction rules.

For each lightning protection level a set of maximum and minimum lightning current parameters values is fixed. The maximum values of lightning current parameters influence the sizing selection of protection measures.

Maximum values of lightning current parameters fixed by the International Standard [4] according to the lightning protection levels are reported in Table 10.3.

For protection level I the fixed maximum values (see also black points in Figure 10.15) shall not be exceeded with a probability of 99 per cent. According to the polarity ratio (ten per cent positive and 90 per cent negative flashes), values taken from positive flashes must have probabilities below ten per cent, those from negative flashes below one per cent. The maximum values of protection level I are reduced to 75 per cent for level II and to 50 per cent for levels III and IV (linear for I, Q and di/dt, but quadratic for W/R). The time parameters are unchanged.

The minimum values of lightning current amplitude have an influence on the positioning of the air termination system of an LPS in order to intercept the lightning flashes direct to the structure.

The minimum values of lightning current parameters fixed by International Standard [4] together with the related rolling sphere radius, according to the protection levels, are reported in Table 10.2. From the statistical distributions given in Figure 10.15, a weighted probability can be determined, that the lightning current parameters are smaller than the maximum values and respectively greater than the minimum values defined for each protection level (see Table 10.4).

The protection measures are effective against lightning whose current parameters are in the range defined by the LPL assumed for design. Therefore the efficiency of a protection measure is assumed equal to the probability with which lightning current parameters are inside such range.

10.5.2 Protection of electrical and electronic systems within the structure against lightning electromagnetic impulse (LEMP)

The protection of electrical and electronic systems within the structure against overvoltages due to LEMP is based on the principle of LEMP protection zones (LPZ). According to this principle [12] the structure to be protected shall be divided into

Table 10.2 Minimum values of lightning current and related rolling sphere radius corresponding to the lightning protection levels of LPS [11]

Protection level	Rolling sphere radius R, m	Minimum peak current I, kA
I	20	3
II	30	5
III	45	10
IV	60	16

Note – Flashes with peak values lower than the minimum peak current of the relevant rolling sphere radius may still strike the structure.

Table 10.3 Maximum values of lightning current parameters corresponding to lightning protection levels [4,12]

First short stroke			Protection level		
current parameters	symbol	unit	I	II	III–IV
Peak current	I	kA	200	150	100
Short stroke charge	Q_{short}	C	100	75	50
Specific energy	W/R	MJ/Ω	10	5.6	2.5
Time parameters	T_1/T_2	μ s/μ s		10/350	
Subsequent short stroke			**Protection level**		
current parameters	symbol	unit	I	II	III–IV
Peak current	I	kA	50	37.5	25
Average steepness	di/dt	kA/μ s	200	150	100
Time parameters	T_1/T_2	μ s/μ s		0.25/100	
Long stroke			**Protection level**		
Current parameters	Symbol	Unit	I	II	III–IV
Long stroke charge	Q_{long}	C	200	150	100
Time parameter	T_{long}	s		0.5	
Flash			**Protection level**		
Current parameters	Symbol	Unit	I	II	III–IV
Flash charge	Q_{flash}	C	300	225	150

Table 10.4 Probabilities for the limits of the lightning current parameters [11]

Probability	Lightning protection level			
probability that value is	I	II	III	IV
higher than minimum defined in Table 10.2	0.99	0.97	0.91	0.84
lower than maximum defined in Table 10.3	0.99	0.98	0.97	0.97

lightning protection zones defined as zones of different LEMP severities and locations for bonding points designated on the zone boundaries. Each individual zone will be characterised by significant changes in the electromagnetic conditions at their boundaries. In general, the higher the number of the zones, the lower the electromagnetic environment parameters.

At the boundary of the individual zones, bonding of all metal penetrations shall be provided and screening measures might be installed.

The general principle for the division of a structure to be protected into different lightning protection zones is shown in Figure 10.2.

The protection should be completed by adequate measures of protection:

- earthing in order to achieve the maximum of equipotentiality between the equipment connected to the same earthing system; a meshed earthing system is suitable to fullfill this requirement;
- shielding, that is the basic measure to reduce the electromagnetic interference; shielding may include apparatus and lines or may be extended to whole zone; suitable routing of cables is an additional measure to reduce the electromagnetic interferences
- bonding in order to reduce the potential differences between metal parts and electronic systems inside the structure to be protected; bonding shall be provided at the boundaries of LPZs for metal parts and systems crossing the boundaries and may be performed by means of bonding conductors or, when necessary, by surge protection devices (SPDs).

10.5.3 Protection of services entering the structure

Services entering the structures (e.g. telecommunication lines) and connected equipment must be protected against the direct and indirect influence of lightning by limiting the risk due to overvoltages and overcurrents, liable to occur in these services, to values which are lower than or equal to tolerable risk [13].

The main criteria of protection, which can also be combined, are:

a to avoid as far as possible the lightning flashes striking the service directly by selecting underground instead of aerial routing or by using adequately positioned ground wires, where effective according to the line characteristics, or

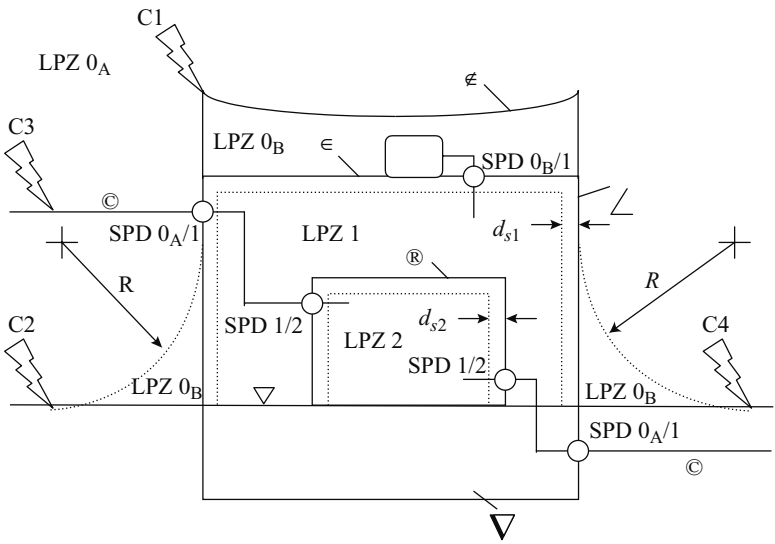

∈	structure (shield of LPZ 1)	C1	strike to structure
∉	air termination system	C2	strike near to structure
∠	down conductor system	C3	strike to incoming service
∇	earth termination system	C4	strike near to incoming service
®	room (shield of LPZ 2)	R	rolling sphere radius
©	incoming services	d_s	safety distance against too high magnetic field

O lightning equipotential bonding (SPD 0A/X class I, other SPD class II tested)

LPZ 0_A	direct strikes, full lightning current, full magnetic field
LPZ 0_B	no direct strikes, partial lightning or induced current, full magnetic field
LPZ 1	no direct strikes, partial lightning or induced current, damped magnetic field
LPZ 2	no direct strikes, induced currents, further damped magnetic field
	protected volumes inside LPZ 1 and LPZ 2 must respect safety distances d_s

Figure 10.2 Protection by LEMP protection zones (LPZ) according to IEC [12]

by increasing the pipe thickness to an adequate value and assuring the metallic continuity of pipes

b to reduce the level of the overvoltages induced by lightning by means of adequate shielded cables

c to divert overcurrent and to limit overvoltages by means of adequate SPD

d to increase the rated impulse withstand voltage of lines and connected equipments, where convenient.

10.6 Protection by means of SPD

SPDs are very effective protection measures for reducing the probability of occurrence of dangerous sparking or dangerous overvoltages due to direct and indirect

flashes to the structure. They are the most convenient devices for achieving lightning equipotential bonding for live conductors in the form of incoming lines and internal live conductors with induced voltages.

The effectiveness of an SPD in reducing the overvoltage level is not easy to evaluate but recent International Standards [12,21] help in the selection, coordination and installation of these protection measures.

SPDs should be located according to the LEMP protection zones (LPZs) concept (see Figure 10.2) at the boundary of each zone. In practice, SPDs are generally installed at the entrance point of incoming services and on the installation and equipment internal to the structure.

The protection of an SPD installed at the entry point of a line in a structure is effective, provided that SPDs:

- at the boundary LPZ $0/X$, are dimensioned according to class I test requirements (impulse current 10/350 μs)
- at the boundary LPZ X/Y ($X > 0$, $Y > 1$), are dimensioned according to class II test requirements (nominal current 8/20 μs)
- comply with standard requirements [12]
- are coordinated with internal installations to be protected (and where together) in accordance with the requirements of [11] and [12].

The principles of coordination of SPDs are reported in [21], but effective operation of SPDs depends not only on their adequate selection and coordination but also on their proper installation.

One of the installation problems is the proper selection of the so-called protection distance, which means the maximum distance from the equipment, measured along the circuit, at which the SPD still protects the equipment.

The evaluation of the protection distance depends on the:

- level of protection of SPD
- type of SPD (spark gap, varistor, diode etc.)
- impulse withstand voltage level (or the immunity level) of the equipment and its input surge impedance
- steepness of the lightning current
- characteristics of the conductors linking the SPD to the equipment (i.e. the mains supplying the equipment).

The evaluation of the protection distance of an SPD may be performed by means of the relations reported in [12] or, in a more accurate way, by computer simulation (e.g. PSICE or ATP programs) [22].

10.7 Main features of lightning protection system (LPS)

10.7.1 External lightning protection system

The external LPS is intended to intercept direct lightning strokes, including flashes to the side of structure, to conduct lightning current from the point of strike to ground and

to disperse it to earth without causing thermal, mechanical and electrical damages to the structure to be protected, including sparking and touch and step voltages dangerous for persons inside the structure. Protection measures additional to external LPS may be required in order to avoid the hazard due to touch and step voltages for persons outside the structure in the vicinity of the down conductor system.

In most cases, the external LPS may be attached to the structure to be protected.

An isolated external LPS should be also considered when the thermal and explosive effects at the point of strike or on the conductors carrying the lightning current may cause damage to the structure or to the content. Typical cases are:

- structures with combustible covering
- structures with combustible walls
- areas with danger of explosion and fire.

Dangerous sparking between an LPS and structures shall be avoided:

- in an isolated external LPS by insulation or separation
- in a nonisolated external LPS by bonding or by insulation or separation.

Natural components made of conductive materials that will always remain in the structure and will not be modified (e.g. interconnected reinforced steel, metal framework of the structure etc.) should preferably be used as part of the LPS. Other natural components should be used as additional to the LPS.

10.7.2 Positioning of the air termination system

The probability of the current of a lightning stroke penetrating the structure to be protected is considerably decreased by the presence of a properly designed air termination system.

10.7.2.1 Principles of positioning

The positioning of an air termination system would require knowledge of the physics of lightning discharge.

Basically, the lightning is characterised by downward leaders which progress to earth in successive steps following, approximatively, a direction defined by the maximum field stress. The point of strike is found within those earthed points from which upward leaders may develop; these points, characterised by highest electrical fields, are usually localised on parts which are placed on the top of structures. It is therefore highly probable that an upward leader is initiated at the top of a high structure or a structure placed on a hill.

The complexity of the phenomenon has forced scientists to introduce assumptions and simplifications in order to assess models which allow them to obtain results more and more in accordance with experimental results.

One of the best known models, widely used for practical applications, is the model referring to the concept of striking distance, which is the particular distance between the downward leader and earth at which the striken point is chosen. This parameter is usually related to the peak value of the lightning current (see Figure 10.4); reference

is made to the electrogeometrical model (Golde, Whitehead and others) based on the striking distance concept [14].

As an improvement to this model, the configuration of the electric field at earth is also considered [15] in order to take into account the conditions of the inception of an upward leader at an earthed point. In particular, an improved electrogeometrical model for transmission line shielding analysis was proposed in 1987 by Eriksson [16] and a generalised leader inception model has been developed in 1990 by Rizk [17] and improved by Petrov and Waters in 1995 [18]. These models together with the leader progression model [19], based on the physics of the upward leader inception as derived from laboratory experiments, have proved to be of great value for evaluating the exposure of the structures and for providing a rough assessment of interception probability.

By application of these models the exposure of different simple structures (slim structures, horizontal conductors and square buildings and facades) located in various orographic conditions has been determined. In particular, the probabilility of lateral strikes is evaluated together with the height of structures at which the phenomenon becomes significant [20].

A more detailed overview of different models proposed in different times is outlined in section 10.12.

10.7.2.2 Types of air termination system

The air termination systems can be composed of any combination of the following elements:

- rods
- catenary wires
- meshed conductors.

Radioactive air terminals are not allowed and the use of air terminations with intensificated ionisation are to be positioned only as conventional ones.

In determining the position of the air termination system, particular care must be given to the interception protection of corners and edge surfaces under consideration, especially those at its top level(s) and on the upper 20 per cent of its facades.

Three methods are suggested by the International Standard [11] for the positioning of the air termination system, namely the protection angle method, the rolling sphere method (which is an implementation of simple electrogeometrical model) and the mesh method, also known as the Faraday cage method.

The Standard was set up taking into account the technical data which was available on the basis of measurements of lightning parameters, practical experience and on theoretical approaches related to various models proposed to analyse the mechanism of the lightning impact.

The protection angle method is suitable for most simple shape buildings but it has the height limits indicated in Figure 10.3.

The rolling sphere method was first proposed by Lee [41] as an extention of the electrogeometric model to the design of air terminals for buildings and structures. It is suggested [11] in any cases with the radii given in Table 10.5.

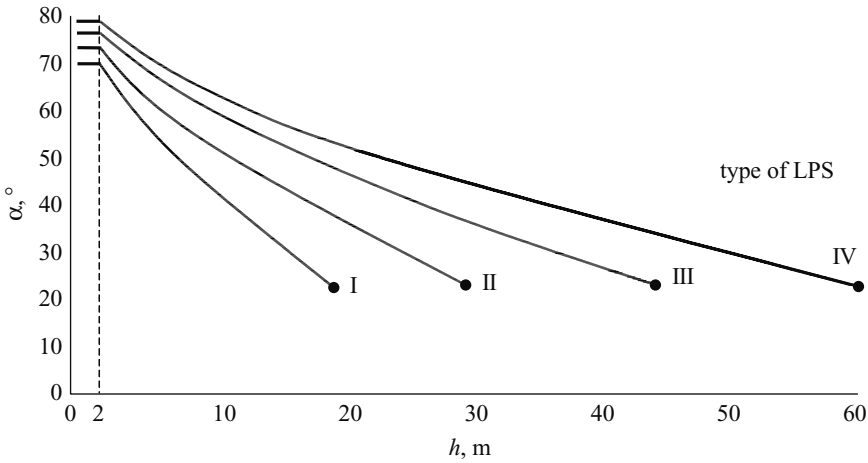

Figure 10.3 Height limits for protection angle method (not applicable beyond the values marked with •; only rolling sphere and mesh methods apply in these cases. h is the height of air termination above the area to be protected. The angle will not change for values of h below 2 m)

Table 10.5 Minimum values for rolling sphere radius, mesh size and protection angle corresponding to lightning protection levels [11]

Lightning protection level	Protection method		
	rolling sphere radius R, m	mesh size M, m	protection angle $\alpha°$
I	20	5 × 5	
II	30	10 × 10	See Figure
III	45	15 × 15	10.3
IV	60	20 × 20	

Applying this method, the positioning of the air termination system is adequate if no point of the volume to be protected comes into contact with a sphere with radius R depending on the lightning protection level (Table 10.5), rolling around and on top of the structure in all possible directions. Therefore, the sphere will have to touch only the air termination system.

On tall structures higher than the rolling sphere radius R, side flashes may occur. Each lateral point of the structure touched by the rolling sphere is a possible point of strike. But the probability for side flashes is generally negligible for structures lower than 60 m. For taller structures the major part of all flashes will hit the top, horizontal leading edges and corners of the structure. Only a few per cent of all flashes will be side flashes to the structure.

Moreover, the probability for side flashes decreases rapidly as the height of the point of strike on tall structures decreases, when measured from the ground [20]. Therefore, it seems sufficient that consideration should be given to installing a lateral air termination system on the upper part of tall structures, typically the top 20 per cent of the height of the structure (see paragraph 10.12 and Figure 10.19).

The mesh method is a suitable form of protection where plane surfaces are to be protected.

The values for protection angle, rolling sphere radius and mesh size suggested by International Standards [11] are given in Table 10.5 according to the minimum value of the lightning current to be intercepted by the air termination system and to the type of LPS selected. These values are assessed in order to have equivalent protected volumes by using either protection angle or rolling sphere methods. Detailed information on the positioning of the air termination system is given in [23].

10.7.3 Down conductor systems

In an LPS the down conductors have the task of carrying the current from the air termination to the earth termination system. In order to reduce the probability of damage due to lightning current flowing in the LPS, the following problems have to be considered:

- the conductor sizing depending on the lightning current flowing; in the case of tall structures, the upper parts of down conductors act also as air termination
- the conductor number and positioning in order to get a good sharing of the current in the various conductors and to minimise the electromagnetic field inside the structure
- the down conductor spacing from the conducting parts inside the structure, or equipotentialisation with them.

The down conductors are to be arranged in such way that from the point of strike to earth:

a several parallel current paths shall exist
b the length of the current paths is kept to a minimum
c equipotential bonding to conducting parts of the structure is performed everywhere it is necessary, connection of down conductors at the ground level and every 10/20 m of height is a good practice.

A great number of down conductors, as far as possible at equal spacing around the perimeter and interconnected by ring conductors, reduces the probability of dangerous sparking and facilitates the protection of the installations internal to the structure. This condition is fulfilled in metal framework structures and in reinforced concrete structures in which the interconnected steel is electrically continuous.

The down conductors shall be arranged so that they become, as far as possible, the direct continuation of the air termination conductors. They shall be installed straight and vertical such that they provide the shortest most direct path to earth. The formation of loops shall be avoided.

Down conductors of LPS not isolated from the structure to be protected may be installed as follows:

- if the wall is made of noncombustible material the down conductors may be positioned on the surface or in the wall
- if the wall is made of flammable material the down conductors can be positioned on the surface of the wall, provided that their temperature rise due to the passage of lightning current is not dangerous for the material of the wall
- if the wall is made of flammable material and the temperature rise of the down conductors is dangerous, the down conductors shall be placed in such a way that the distance between them and the wall is always greater than 0.1 m; mounting brackets may be in contact with the wall; with the dimensions given in the tables of the International Standard [11] the temperature rise is of the order of tens of degrees centigrade.

Metal installations of a structure, facade elements, profile rails and metallic subconstructions of facades, provided that the electrical continuity between the various parts is made durable and their dimensions are at least equal to that specified for standard down conductors, as well as the metal or reinforced concrete framework of the structure and the interconnected reinforcing steel of the structure should be considered as natural down conductors.

10.7.4 Protection measures against touch and step voltages

Outside the structure, in the surrounding of the down conductors, in particular conditions the touch and step voltages may be hazardous to life even if the LPS has been designed and constructed according to the above mentioned rules.

The risk for persons can be considered negligible [11] if one of the following conditions is fulfilled:

1 the probability of persons approaching or the time of their presence outside the structure and close to the down conductors is very low
2 insulation over the exposed conductor is provided giving a 100 kV, 1.2/50 μs impulse withstand voltage, e.g. at least 3 mm cross linked polyethylene
3 the resistivity of the surface layer of the soil, in the range distance of 3 m from the conductor, is not less than 5000 Ωm; in general a layer of insulating material, e.g. asphalt of 5 cm thickness (or a layer of gravel of 10 cm thickness) satisfies this requirement
4 the natural down conductor system consists of several columns of the extensive metal framework of the structure or of several pillars of the interconnected steel of the structure, electrically continuous
5 for the case of step voltage, equipotentialisation by means of a meshed earthing system.

If none of these conditions is fulfilled, the down conductors should be placed in order to minimise the probability of being touched or persons should not be allowed to approach the down conductors to within 3 m or a panel indicating a warning hoarding should be placed.

10.7.5 Earth termination system

10.7.5.1 Principles of design

The earth termination of an LPS must be able to disperse lightning current into the ground without causing any danger to people or damage to installations inside the protected structure.

When dealing with the dispersion of the lightning current into the ground while minimising any potentially dangerous overvoltages, the transient behaviour of earthed electrodes under impulse current with high peak value should be considered.

The purpose of many of the studies published up to now was to acquire a deeper knowledge of the behaviour in transient conditions of earthed electrodes of various shapes (horizontal conductors, driven rods, grid systems) both from a theoretical [6,24–27] and experimental [28–30] point of view, in frequency and in time domains. It is therefore possible to clarify some typical phenomena characterising the behaviour of earthed electrodes in transient conditions, namely:

(i) The lightning current, independently from the polarity, propagates into the soil according to the typical laws of conducting, taking into account the range of frequencies involved in the lightning current (from some hundreds of kHz up to 1 MHz) and for soil resistivity up to 5000 Ωm. It is therefore of basic importance, even for dimensioning the earth termination system under lightning current, to have knowledge of the soil resistivity and to pay attention to the inhomogeneity of the soil involved in the current discharge.

(ii) The transient behaviour of earthed electrodes is basically defined by inductive phenomena (see Figure 10.5). The rate of rise of the front of current impulses is therefore of major importance as it increases the importance of the inductive voltage drop in comparison with the resistive drop [6,31,32].

(iii) The high values of lightning currents associated with very short front durations can result in high current density in the layers of soil nearest the surface of ground electrodes so that the critical gradients may be exceeded and discharges into the soil can occur [33].

In order to analyse and compare the behaviour of different kinds of earth electrode it is convenient to define some typical parameters:

- transient, or surge, impedance, defined as the ratio between the instantaneous values of the earth termination voltage (potential difference between the earth termination system and the remote earth) and the earth termination current which, in general, do not occur simultaneously
- conventional earth resistance, defined as the ratio of the peak values of the earth termination voltage and the earth termination current, it is used conventionally to indicate the resistance of the earth termination system when subjected to lightning current
- the impulse factor, defined as the ratio between the conventional earth resistance and the low-frequency resistance of the earth electrode.

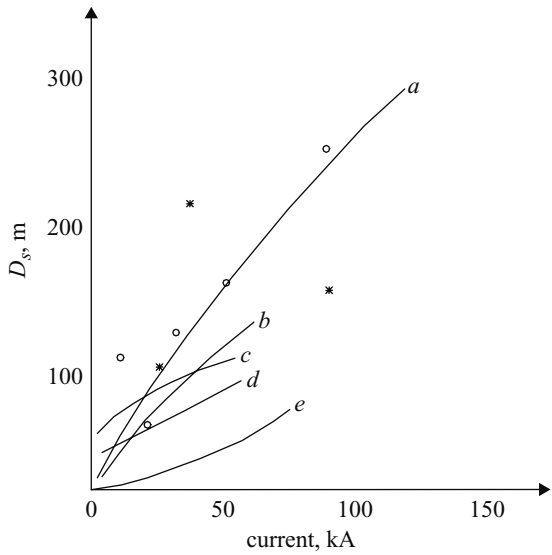

Figure 10.4 Striking distance as a function of peak value of the lightning current according to different authors; ○ estimates from two dimensional photos [35]; ∗ estimates from three dimensional photos [35]

a ref. [34]
b ref. [14]
c ref. [38]
d ref. [37]
e ref. [36]

The main conclusions today widely accepted, based on comparison between theoretical studies and experimental works, may be summarised as follows:

a the earth electrode length which actually contributes to the impulsive current dispersion depends to a large extent on soil resistivity (ρ), on time to crest (T_1) and on peak value of the current (I)

b the analytical expression used to evaluate the effective length of earth electrodes is:

$$l_e = K_o(\rho T_1)^{1/2} \qquad [m; \Omega m; \mu s] \tag{10.9}$$

where l_e is the effective length of the involved earth electrode from the current injection point to a distance at which the value of the conventional earth resistance does not undergo any significant reduction, K_o is a factor depending on the geometrical configuration of the earth electrode, ranging from 1.40 a single conductor energised at one end to 1.55 for a single conductor energised in the middle, to 1.65 for conductors arranged in star configuration energised in the centre

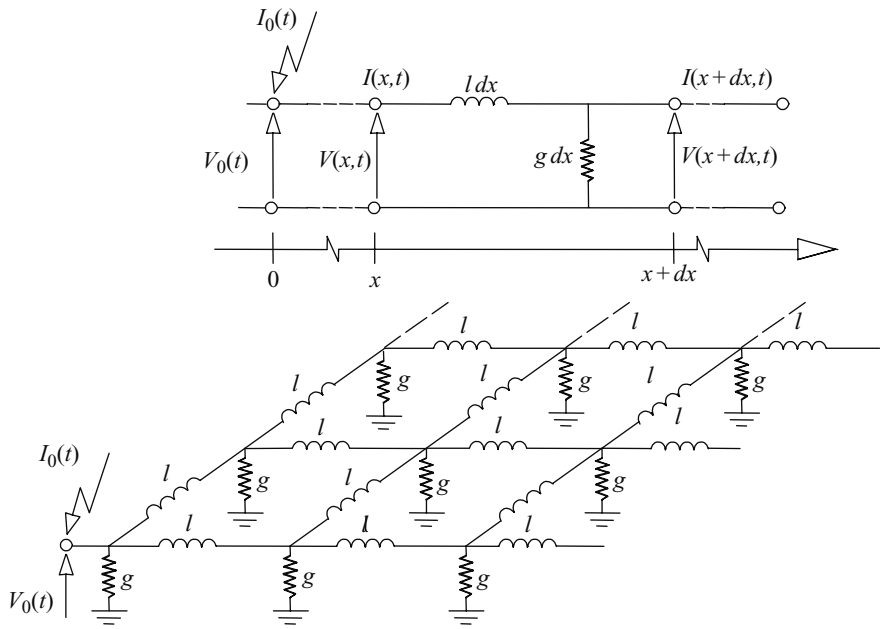

Figure 10.5 Equivalent electric circuit for a single horizontal wire and for a meshed system. l: wire inductance for unit of length; g: earth conductance for unit of length

c since amplitude and wave shape of the injected current, earth electrode dimensions and soil resistivity define the voltage distribution along the electrode (and consequently the contribution of different parts of the electrode to discharge current), these same parameters define the conventional earth resistance of the considered earth electrode; Figures 10.6–10.9 show the trends of the conventional earth resistance as a function of soil resistivity, current waveshape and earth conductor arrangement

d localised earth electrodes present conventional earth resistance lower than power frequency resistance if the value of the lightning impulse current is sufficiently high to cause soil ionisation.

In the designing of the earth termination system in order to disperse lightning current in the soil without danger to people, two items should be considered, namely, the maximum energy which can be tolerated by a human body in transient conditions typical of lightning, assumed equal to 20 Ws [6], and the risk, assumed as tolerable [10], that this maximum value of energy can be exceeded.

As a function of the tolerable risk, the values of the parameters of the lightning current have to be chosen from the relevant probabilistic distributions (see section 10.11); the earth termination system shall be designed so that the dispersion of the above fixed

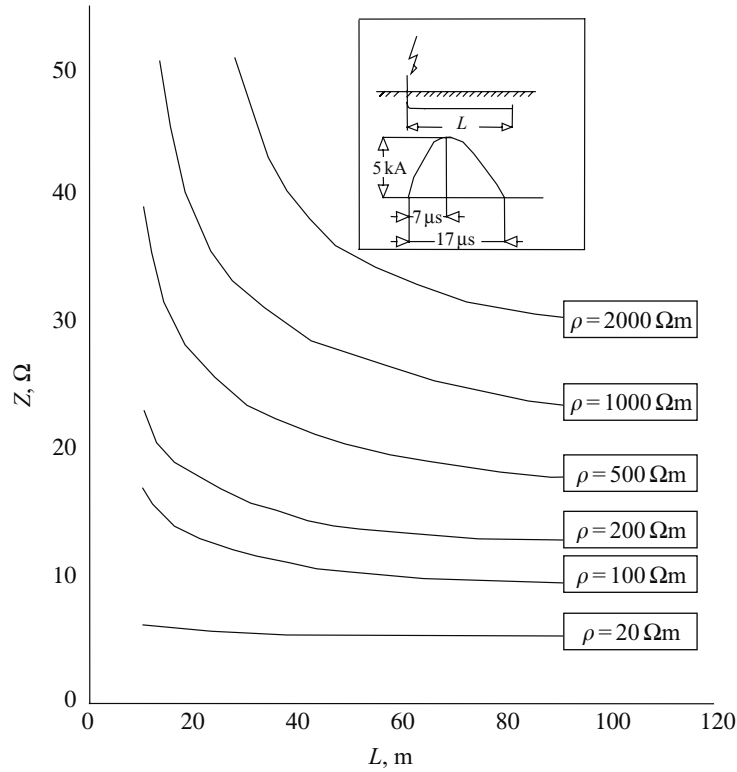

Figure 10.6 Conventional earth resistance of buried wires as a fuction of their length for different values of soil resistivity [6]

lightning current does not result in step voltages higher than necessary to dissipate the 20 W energy in the human body resistance of 500 Ω conventionally fixed.

For different values of fixed risk the maximum admissible values of the conventional earth resistance may be evaluated in different earth termination system configurations in order to keep the step voltage within the safety limits. The results of application of this procedure allow us to establish the minimum required dimension of an earth termination system, as accepted by the International Standard [11] and reported in the section 10.7.5.2.

10.7.5.2 Earthing arrangement in general conditions

From the viewpoint of lightning protection of buildings and structures, a single integrated structure earth termination system is preferable and is suitable for all purposes (i.e. lightning protection, power systems, telecommunication systems). Serious corrosion problems can occur when earthing systems made by different materials are connected to each other.

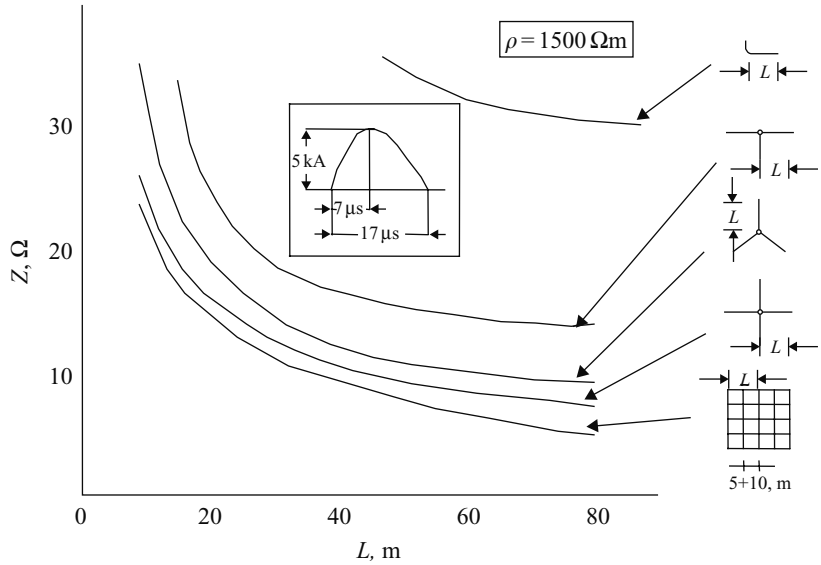

Figure 10.7 Conventional earth resistance of different arrangements of earth termination system [6]

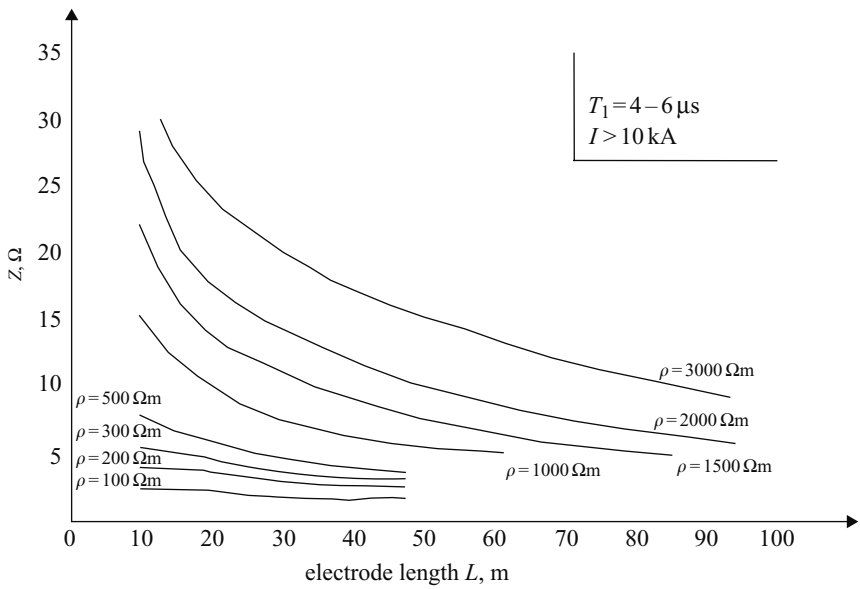

Figure 10.8 Conventional earth resistance of earth termination system (impulse current at the centre of a star arrangement) as a fuction of the length for different values of soil resistivity [6]

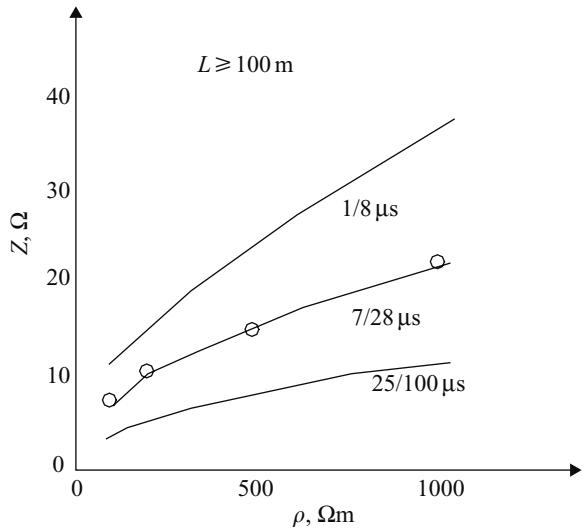

Figure 10.9 Conventional earth resistance as a function of soil resistivity; ○ experimental results [6]

According to the International Standard [11] for earth termination systems, two basic types of earth electrode arrangement apply:

(i) type A arrangement which comprises horizontal or vertical earth electrodes connected to each down conductor, in this case the minimum total number of earth electrodes shall be two
(ii) type B arrangement which comprises either a ring conductor external to the structure in contact with the soil for at least 80 per cent of its total length or a foundation earth electrode; these earth electrodes may be also meshed.

For the ring earth electrode (or foundation earth electrode), the mean radius r of the area enclosed by the ring earth electrode (or foundation earth electrode) shall be not less than the value l_1:

$$r > l_1 \tag{10.10}$$

l_1 being represented in Figure 10.10 according to the types I, II and III and IV of LPS and then according to the values of lightning current parameters selected for dimensioning.

When the required value of l_1 is larger than the convenient value of r, additional radial or vertical (or inclined) electrodes shall be added whose individual lengths l_r (horizontal) and l_v (vertical) are given by:

$$l_r = l_1 - r \tag{10.11}$$

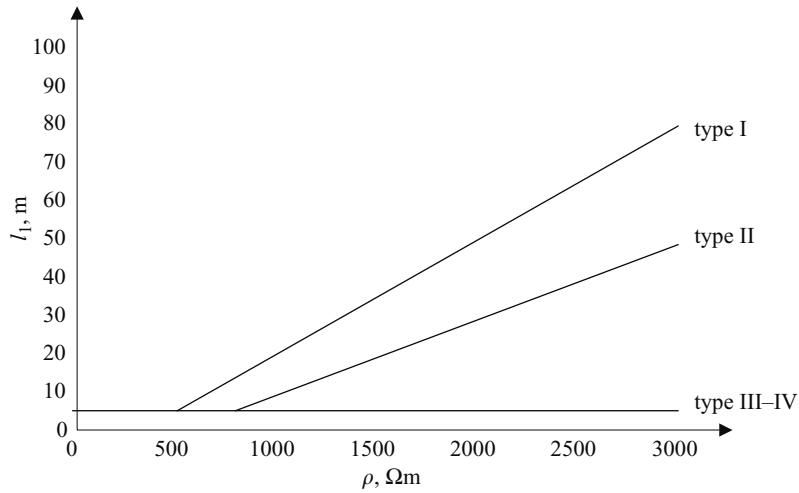

Figure 10.10 Minimum length l_1 of earthing arrangement according to the type of LPS [11]. Types III and IV LPS are independent of soil resistivity

and

$$l_v = (l_1 - r)/2 \tag{10.12}$$

The number of additional electrodes shall not be less than the number of down conductors with a minimum of two. The additional electrodes should be connected to the ring earth electrode in correspondence to the down conductors and, as far as possible, with equal spacing.

The embedded depth and the type of the earth electrodes shall be such to minimise the effects of corrosion, soil drying and freezing and thereby stabilise the conventional earth resistance.

The interconnected reinforcing steel of concrete foundations or other suitable underground metal structures should preferably be used as an earth electrode. When the metallic reinforcement of concrete is used as an earth electrode, special care shall be exercised at the interconnections to prevent mechanical splitting of the concrete.

In the case of prestressed concrete, consideration should be given to the consequences of the passage of lightning discharge currents which may produce unacceptable mechanical stresses.

10.7.6 Materials and dimensions

The materials used for the LPS shall have the following main characteristics:

- good conductivity, to allow the flowing of the current
- suitable mechanical strength, to withstand the electrodynamic stresses caused by the high peak values of the current
- good resistance against the corrosion due to atmospheric environment.

The materials usually adopted are iron, copper and aluminium. Configuration and minimum cross sectional areas of air termination conductors, air termination rods, down conductors and earth electrodes are given in different Tables of [11].

10.8 Internal lightning protection system

10.8.1 General

The internal LPS should avoid the occurrence of dangerous sparking within the structure to be protected due to lightning current flowing in the external LPS or in other conductive parts of the structure. Sparking occurring between the external LPS on the one hand and the metal installations, the electrical, signal and telecommunication installations, inside the structure to be protected, the external conductive parts and lines entering the structure on the other hand, should be considered dangerous. Dangerous sparking between different parts may be avoided with the aid of:

- lightning equipotential bonding
- adequate electrical insulation between the parts.

Damage to vulnerable instrumentation and control equipment due to their inductive coupling with partial lightning currents flowing through the external lightning protection system or through metal installations inside the building may be:

- avoided with the aid of low coupling impedance shielding of cables
- limited by means of surge protective devices (SPD).

Detailed information and requirements on the subject are reported in International Standards [12, 21].

10.8.2 Lightning equipotential bonding

Equipotentialisation is achieved by interconnecting the LPS with metal elements of the structure construction, with the metal installations, with the external conductive parts and with electrical, signal and telecommunication installations within the structure to be protected.

Methods of interconnection are:

- bonding conductors, where the electrical continuity is not provided by natural bonding
- surge protective device (SPD), where direct connections with bonding conductors are not allowed.

Lightning equipotential bonding connections shall be made as direct and straight as possible.

Lightning equipotential bonding to conducting parts of the structure at locations corresponding to ring conductors facilitates effective protection. When lightning equipotential bonding is established to conducting parts of the structure a part of the lightning current may flow into the structure and this effect should be taken into account. Therefore, lightning equipotential bonding at the level higher than the basement is only recommended if the required separation distance [11] can not be reached.

The SPD characteristics depend on the lightning current flowing along the relevant part of the external LPS. For external conductive parts, as well as for electrical, signal and telecommunication equipotential bonding, installations shall be performed at the entrance point into the structure.

Bonding conductors should withstand the part of the lightning current flowing through them. This current may be evaluated taking into account the conventional earth resistance of the earth termination system, the number of entering services (external conductive parts) bonded at the same point of entry and the number of conductors of each line entering into the structure, all connected in parallel. Details on the sharing of the current between different incoming services and formulae to evaluate the current flowing in each of them may be found in [21] and in [12].

If the electrical, signal and telecommunication conductors are screened or located in metal conduit, it is normally sufficient to bond only these screens and conduits. If the electrical, signal and telecommunication conductors are neither screened nor located in metal conduit, they shall be bonded *via* SPDs.

All the conductors of each line should be bonded directly or with an SPD.

10.8.3 Electrical insulation of the external LPS

Analysis of the elctromagnetic field caused by the flowing of lightning currents along the conductors of the protection system allows the assessment of rules for evaluating the spacing between air termination and protected structures in order to avoid side flash between them.

In order to avoid side flashes between the air termination or the down conductor on the one hand and the metal installations and electrical, signal and telecommunication installations internal to the structure to be protected on the other hand, a distance d between the parts shall be ensured not smaller than a separation distance s:

$$d > s \tag{10.13}$$

where the separation distance may be calculated with the following relation [11]:

$$s = k_i \frac{k_c}{k_m} l \quad \text{[m]} \tag{10.14}$$

where k_i, k_c, k_m depend, respectively, on the selected lightning protection level of LPS, the share of lightning current on the down conductors and the electrical insulation material (see [11] and [23] for more details) and l is the length, in metres, along the

air termination or the down conductor from the point where the separation distance is to be considered to the nearest equipotential bonding point.

10.9 Shielding

Any lightning strike into the building causes partial currents flowing through metal installations inside the building and induces voltages between the individual conductors of a cable and between these conductors and earth. These voltages may be dangerous for the instrumentation and control equipment.

The dangerous voltages can be avoided by protective measures such as installation of SPD or shielding. Possible shielding measures are:

- a conductive cable screen, capable of carrying the individual partial lightning current
- laying the cables in well closed conductive cable races
- laying the cables in a metal conduit.

10.10 Maintenance and inspection of LPS

The main objective of the inspections are to ascertain that all components of the LPS are in good condition and capable of performing their designed functions, and that there is no corrosion and any recently added services or constructions are incorporated into the LPS.

Inspections should be made as follows:

- during the construction of the structure, in order to check the embedded electrodes
- after the installation of the LPS
- periodically at such intervals as are determined with regard to the nature of the structure to be protected, the corrosion problems and the protection level
- after alterations or repairs, or when it is known that the structure has been struck by lightning.

During the periodic inspection, the deterioration and corrosion of air termination elements, conductors and connections and of earth electrodes must be particularly checked.

Regular inspections are among the fundamental conditions for a reliable maintenance of a LPS.

Further detailed information is reported in [23].

10.11 Annex A: parameters of lightning current

10.11.1 Lightning flashes to earth

Two basic types of lightning flash exist, downward flashes initiated by a downward leader from cloud to earth and upward flashes initiated by an upward leader from an

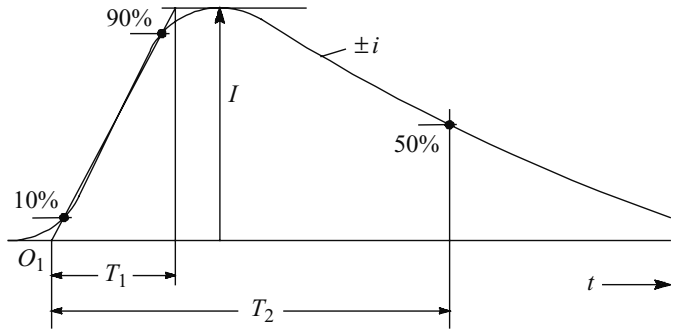

Figure 10.11 Definitions of short stroke parameters (typically $T_2 < 2\,ms$) [4,12]
O_1 = virtual origin
I = peak current
T_1 = front time
T_2 = time to half value

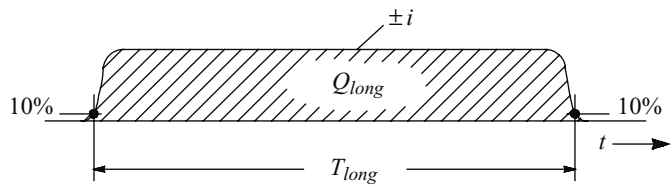

Figure 10.12 Definitions of long stroke parameters (typically $2\,ms < T_{long} < 1$ s) [4,12]
T_{long} = duration time
Q_{long} = long stroke charge

earthed structure to cloud. In flat territory and to lower structures mostly downward flashes occur, whereas for exposed and/or higher structures upward flashes become dominant. With the effective height the striking probability increases and the physical conditions change.

A lightning current consists of one or more different strokes, short strokes typically below 2 ms (Figure 10.11) and long strokes with more than 2 ms (Figure 10.12). Further differentiation of strokes comes from their polarity (positive or negative) and from their position during the flash (first, subsequent, superimposed). The possible components are shown in Figure 10.13 for downward flashes and in Figure 10.14 for upward flashes.

The additional component in upward flashes is the first long stroke without or with up to some ten superimposed short strokes. But all short stroke parameters of upward flashes are less than those of downward flashes. A higher long stroke charge of

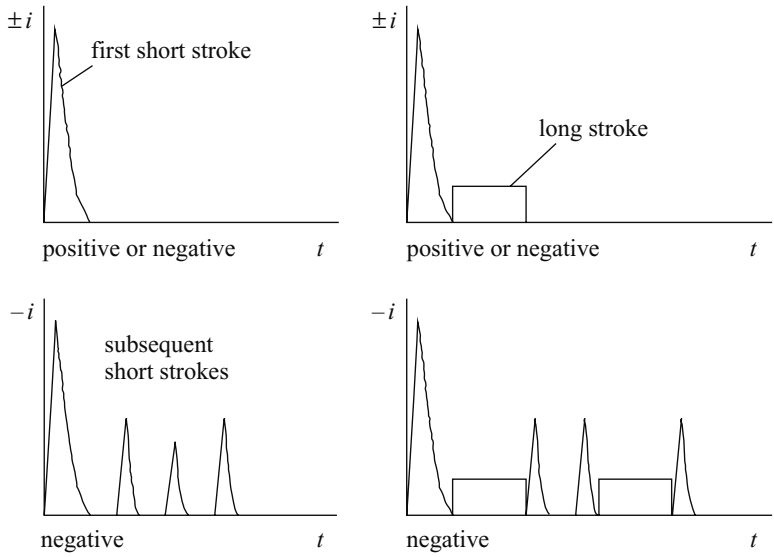

Figure 10.13 Possible components of downward flashes [4,12] (typical in flat territory and to lower structures)

upward flashes is not yet confirmed. Therefore, for lightning protection, the lightning parameters of upward flashes are considered to be covered by the maximum values taken from downward flashes. A more precise evaluation of lightning parameters and their height dependency with regard to downward and upward flashes is still under consideration in the scientific community.

10.11.2 Lightning current parameters

The lightning current parameters in this standard are based on the results of CIGRE given in Table 10.6. Their statistical distribution can be assumed to have a logarithmic normal distribution. The corresponding mean value μ and the dispersion $\sigma_{\log}$ is given in Table 10.7 and the distribution function is shown in Figure 10.15. On this basis the probability of occurrence of any value of each parameter can be determined (see Figure 10.15).

A polarity ratio of ten per cent positive and 90 per cent negative lightnings is assumed. The polarity ratio is a function of the territory. If no local information is available, the ratio given herein should be used.

For lightning protection level I the fixed maximum values in Table 10.3 shall not be exceeded with a probability of 99 per cent . According to the polarity ratio given above, values taken from positive flashes must have probabilities below ten per cent, those from negative flashes below one per cent.

Table 10.6 Tabulated values of lightning current parameters taken from CIGRE and fixed values for lightning protection level I [4]

Parameter	Units	Values			Fixed value for level I	Stroke type	Line in Figure 10.14
		95%	50%	5%			
I	kA	4(98%)	20(80%)	90	–	* first negative short	1A + 1B
		4.9	11.8	28.6	50	* subsequent negative short	2
		4.6	35	250	200	first positive short (single)	3
Q_{flash}	C	1.3	7.5	40	–	negative flash	4
		20	80	350	300	positive flash	5
Q_{short}	C	1.1	4.5	20	–	first negative short	6
		0.22	0.95	4	–	subsequent negative short	7
		2	16	150	100	first positive short (single)	8
W/R	kJ/Ω	6	55	550		first negative short	9
		0.55	6	52	–	subsequent negative short	10
		25	650	15.000	10.000	first positive short	11
di/dt_{max}	kA/μ s	9.1	24.3	65	–	* first negative short	12
		9.9	39.9	161.5	–	* subsequent negative short	13
		0.2	2.4	32	20	first positive short	14
$di/dt_{30/90\%}$	kA/μs	4.1	20.1	98.5	200	* subsequent negative short	15
Q_{long}	C				200	long	

Table 10.6 Continued

Parameter	Units	Values			Fixed value for level I	Stroke type	Line in Figure 10.14
		95%	50%	5%			
T_{long}	s				0.5	long	
Front duration	μs	1.8	5.5	18		first negative short	
		0.22	1.1	4.5	$T_1 = 0.25$	subsequent negative short	
		3.5	22	200	$T_1 = 10$	first positive short (single)	
Stroke duration	μs	30	75	200		first negative short	
		6.5	32	140	$T_2 = 100$	subsequent negative short	
		25	230	2.000	$T_2 = 350$	first positive short (single)	
Time interval	ms	7	33	150		multiple negative strokes	
Total flash duration	ms	0.15	13	1.100		negative flash (all)	
		31	180	900		negative flash (without single)	
		14	85	500		positive flash	

The values of $I = 4$ kA and $I = 20$ kA correspond to a probability of 98% and of 80%, respectively.

Table 10.7 Logarithmic normal distribution of lightning current parameters [4] mean μ and dispersion $\sigma_{\log}$ calculated from 95% and 5% values

Parameter	Units	Mean μ	Dispersion $\sigma_{\log}$	Fixed value for level I	Stroke type	Line in Figure 10.14
I	kA	(61.1)	0.576	–	* first negative short (80%)	1A
		33.3	0.263		* first negative short (80%)	1B
		11.8	0.233	50	* subsequent negative short	2
		33.9	0.527	200	first positive short (single)	3
Q_{flash}	C	7.21	0.452	–	negative flash	4
		83.7	0.378	300	positive flash	5
Q_{short}	C	4.69	0.383	–	first negative short	6
		0.938	0.383	–	subsequent negative short	7
		17.3	0.570	100	first positive short (single)	8
W/R	kJ/Ω	57.4	0.596		first negative short	9
		5.35	0.600	–	subsequent negative short	10
		612	0.844	10.000	first positive short	11

Table 10.7 Continued

Parameter	Units	Mean μ	Dispersion $\sigma_{\log}$	Fixed value for level I	Stroke type	Line in Figure 10.14
di/dt_{max}	kA/μs	24.3	0.260	–	* first negative short	12
		40.0	0.369	–	* subsequent negative short	13
		2.53	0.670	20	first positive short	14
$di/dt_{30/90\%}$	kA/μs	20.1	0.420	200	* subsequent negative short	15
Q_{long}	C			200	long	
T_{long}	s			0.5	long	
Front duration	μs	5.69	0.304		first negative short	
		0.995	0.398	$T_1 = 0.25$	subsequent negative short	
		26.5	0.534	$T_1 = 10$	first positive short (single)	
Stroke duration	μs	77.5	0.250		first negative short	
		30.2	0.405	$T_2 = 100$	subsequent negative short	
		224	0.578	$T_2 = 350$	first positive short (single)	
Time interval	ms	32.4	0.405		multiple negative strokes	
Total flash duration	ms	12.8	1.175		negative flash (all)	
		167	0.445		negative flash (without single)	
		83.7	0.472		positive flash	

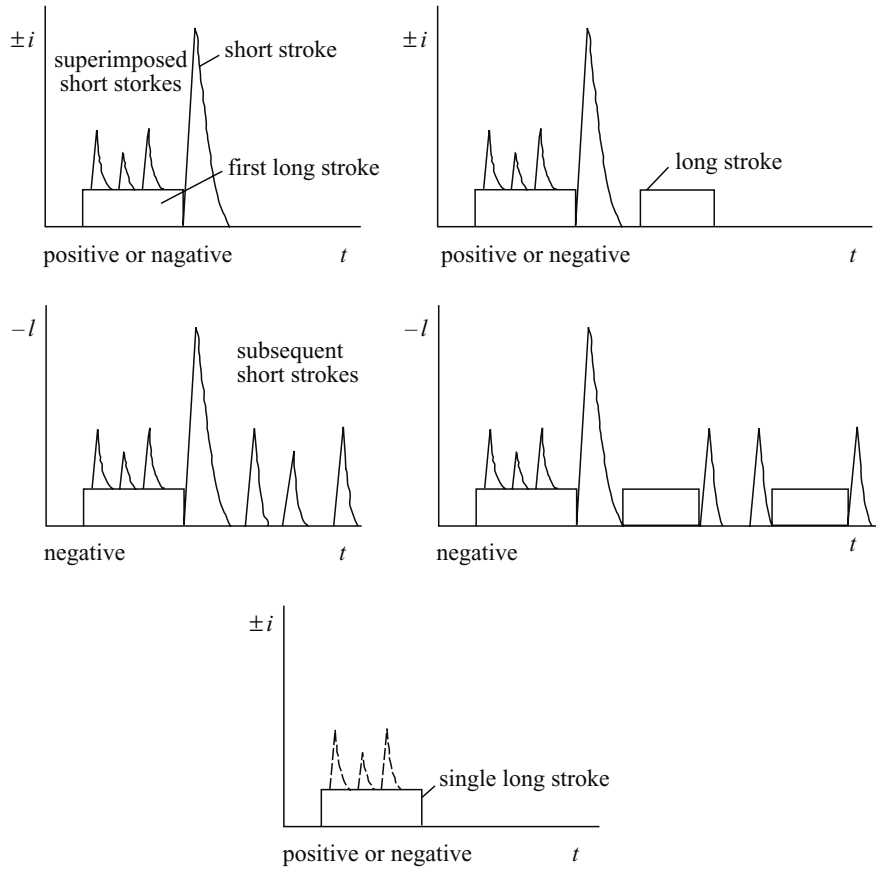

Figure 10.14 Possible components of upward flashes [4,12] (typical to exposed and/or higher structures)

The maximum values of current parameters relevant to protection level I are reduced to 75 per cent for level II and to 50 per cent for level III and IV (linear for I, Q and di/dt, but quadratic for W/R). The time parameters are unchanged.

The minimum values in Table 10.2 are used to determine the interception probability of air terminals.

10.11.3 Maximum lightning current parameters used for dimensioning lightning protection systems

The mechanical effects of lightning are related to the peak value of the current (I), and to the specific energy (W/R). The thermal effects are related to the specific energy (W/R) when resistive coupling is involved and to the charge (Q) when arcs develop to the installation. The dangerous sparking caused by inductive coupling is related to the steepness (di/dt) of the lightning current front.

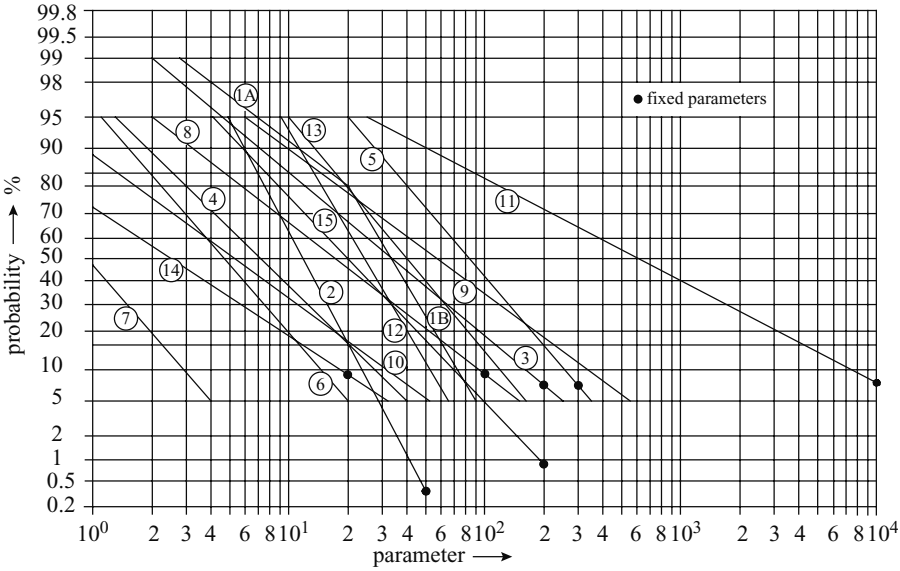

Figure 10.15 Cumulative frequency distribution of lightning current parameters (lines through 95% and 5% vaues) [4,12]. (The meaning of the number and black points are in Tables 10.6 and 10.7)

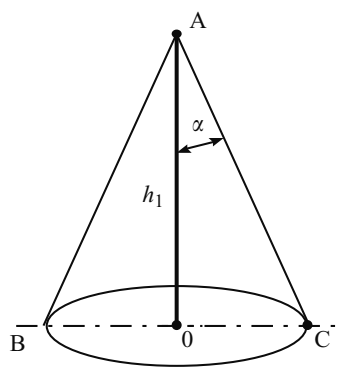

Figure 10.16 Volume protected by a vertical rod air termination [23]

Each of the single parameters (I, Q, W/R, di/dt) tends to dominate each failure mechanism. This is to be taken into account in establishing test procedures [4].

10.11.3.1 First short stroke and long stroke

The values I, Q, W/R related to mechanical and thermal effects are determined from positive flashes (because their ten per cent values are much higher than the

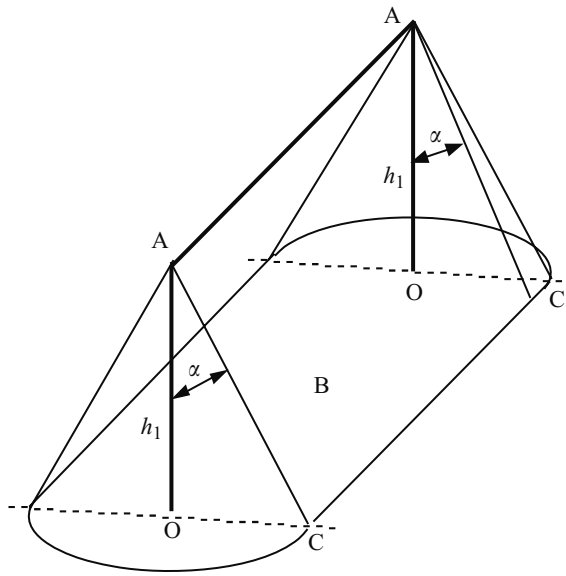

Figure 10.17 *Volume protected by a catenary wire air termination [23] A: tip of an air termination; B: reference plane; OC: radius of protected area; h_1: height of an air termination rod above the reference plane; α: protective angle according to Table 10.5*

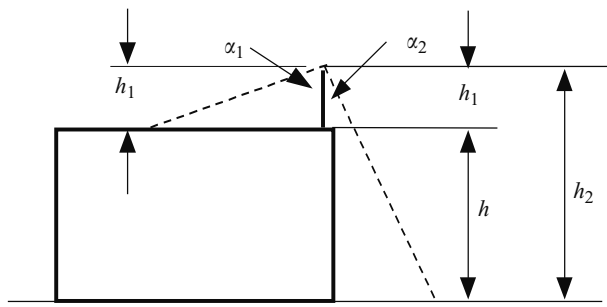

Figure 10.18 *Volumes protected by a vertical air termination rod [23] h_1 is the physical height of an air termination rod. The protective angle α_1 corresponds to the air termination height h_1, being the height above the roof surface to be protected (reference plane); the protective angle α_2 corresponds to the height $h_2 = h_1 + h$, being the soil reference plane; α_1 is related to h_1 and α_2 is related to h_2*

corresponding one per cent values of the negative flashes). From Figure 10.15 (lines 3, 5, 8, 11 and 14) the following values with probabilities below ten per cent can be taken: $I = 200\,\text{kA}$, $Q_{flash} = 300\,\text{C}$, $Q_{short} = 100\,\text{C}$, $W/R = 10.000\,\text{kJ}/\Omega$ and $di/dt = 20\,\text{kA}/\mu\text{s}$. For a first short stroke according to Figure 10.11 these values

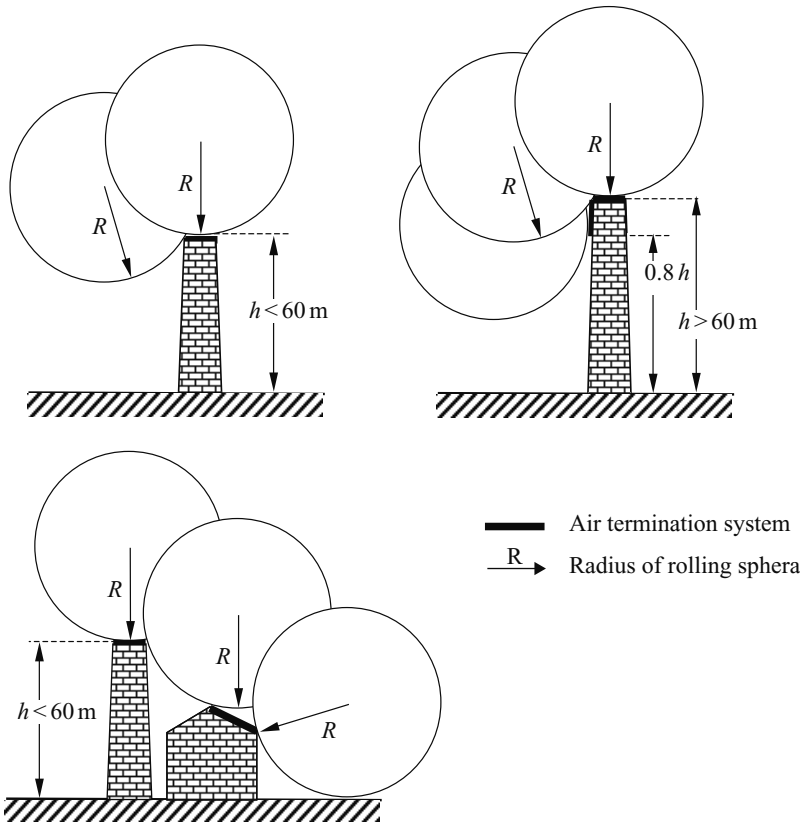

Figure 10.19 Design of an LPS air termination according to the rolling sphere method. The rolling sphere radius should comply with the selected lightning protection level (see Table 10.3)

give a first approximation for the front time:

$$T_1 = I/(di/dt) = 10\,\mu s \tag{10.15}$$

T_2 is of minor interest. For an exponentially decaying stroke current the following approximately applies ($T_1 \ll T_2$):

$$Q_{short} = (1/0.7) \cdot I \cdot T_2$$
$$W/R = (1/2) \cdot (1/0.7) \cdot I^2 \cdot T_2 \tag{10.16}$$

These formulas together with the values given above lead to a first approximation for the time to half value of $T_2 = 350\,\mu s$.

For the long stroke its charge can be approximately calculated from:

$$Q_{long} = Q_{flash} - Q_{short} = 200\,\mathrm{C} \tag{10.17}$$

Its duration time according to Figure 10.12 may be estimated from the flash duration time to $T_{long} = 0.5\,\mathrm{s}$.

10.11.3.2 Subsequent short stroke

The value di/dt related to the dangerous sparking caused by inductive coupling is determined from subsequent short strokes of negative flashes (because their one per cent values are much higher than the one per cent values from first negative strokes or the corresponding ten per cent values of the positive flashes). From Figure 10.15 (lines 2 and 15) the following values with probabilities below one per cent can be taken: $I = 50\,\mathrm{kA}$ and $di/dt = 200\,\mathrm{kA/\mu s}$.

For a subsequent short stroke according to Figure 10.11 these values give as a first approximation for its front time:

$$T_1 = I/(di/dt) = 0.25\,\mu\mathrm{s}. \tag{10.18}$$

Its time to half value may be estimated from stroke duration of negative subsequent short strokes: $T_2 = 100\,\mu\mathrm{s}$ (T_2 is of minor interest).

10.11.4 Minimum lightning current parameters used for interception efficiency of air terminals

Following the electrogeometric model the final jump distance (rolling sphere radius R) is correlated with the peak value of the first short stroke. According to the IEEE working group report [39] the relation is given as:

$$R = 10 \cdot I^{0.65} \tag{10.19}$$

where R is the rolling sphere radius (m) and I is the peak current (kA).

For a given rolling sphere radius R it can be assumed that all flashes with peak values higher than the corresponding minimum peak value I will be intercepted by the air terminations. Therefore, the probability for the peak values of first strokes from Figure 10.15 is assumed as interception probability. Taking into account the polarity ratio of ten per cent positive and 90 per cent negative flashes the total interception probability can be calculated.

10.12 Annex B: models for the evaluation of lightning exposure of structures and interception probability of air terminals

10.12.1 Electrogeometric model

The electrogeometric model (EGM) was first proposed in Europe and was later further developed in America, notably by Whitehead and his team.

The position of a downward leader approaching the grounded structure defines a distance from the structure top called the striking distance. This parameter is usually related to the charge in the downward leader and then to the peak value of the lightning current, taking into account the correlation between the integrated leader charge and the current [15].

Different relations have been proposed to express the relationship between striking distance and peak value of the lightning current. Figure 10.4 shows some curves according to different authors together with some available data [35]. The curves exhibit a large spread due to different assumptions made by the authors to take care of the physics of the phenomenon. The comparison with recorded data [35] of striking distance to tall structures leads to the conclusion that the following relation fits well the recorded points:

$$D_s = 6.7I^{0.8} \tag{10.20}$$

More recently, following the proposal of IEEE WG [39], the International Standard for lightning protection against direct strikes to the structure [7] accepted the following similar relation:

$$D_s = 10I^{0.65} \tag{10.21}$$

10.12.2 Improved electrogeometric model

In contrast to earlier approches, in which the striking distance is a function of current amplitude only, this model [16] provides a rational basis for taking account of the influence of structure height.

According to this model an attractive radius, defined as the maximum distance from the structure for which a downward leader having a defined charge is captured by the structure itself, may be evaluated as a function of downward leader charge. Consequently, a volume above the structure, within which leader interception is possible, can be evaluated on the basis of the attractive radius on the assumption that relative upward/downward leader approach velocity ratio be constant and equal to unity.

With the above assumption the impact of lightning to the structure is only possible when the tip of the downward leader reaches the volume above the structure defined by the attractive radius.

Application of the model over a broad range of structure heights and lightning current amplitudes allows us to derive the generalised curves. Regression through these curves allows us to estimate the structure attractive radius:

$$R = I^a 0.84\, h^{0.6} \tag{10.22}$$

where $a = 0.7\, h^{0.02}$.

From the model results relevant to structures with height ranging from 10 to 100 m, making reference to an average amplitude current of 35 kA, the following simplified formula is proposed:

$$R = 14\, h^{0.6} \tag{10.23}$$

10.12.3 Generalised leader inception model

A further step in the simulation of the lightning impact mechanism is the representation of positive leader initiation from earthed objects under the influence of a negative descending leader and of the subsequent propagation of the two channels.

According to this model the conditions may be evaluated both for the corona inception at the earthed object and mainly for continuous positive leader inception and propagation from the corona critical dimension, which is generated by the negative leader charge approaching earth.

An iterative procedure is applied to determine the attractive radius as a function of the lightning current and of the height of the structure. For a free standing structure of up to 60 m height the following simplified formula has been proposed [17] for a lightning current of 31 kA:

$$R = 24.6\,h^{0.4} \tag{10.24}$$

10.12.4 Leader progression model

A more detailed simulation of the lightning impact mechanism has been developed in 1990, and more recently (1996) refined, in which both the leader progression in time and space and the variation in time of the resulting electrical field can be considered. Detailed references of this dynamic model may be found in [19] and [20].

The model takes into account physical mechanisms investigated during the development of discharges in long air gaps and the investigations of the development of lightning channels. Of the involved phenomena, the model mainly takes into account the propagation of the downward negative channel and the inception and propagation of the upward positive leader from earthed structures.

A mathematical description of the phenomena requires a determination of the resulting electric field, repeated at different times, in order to simulate the charge in the cloud and the actual charge displaced by the leader channels during their progression.

This model allows us to simulate structures located in orographic conditions different from flat territory, such as valleys, hills and mountains with the presence of other structures in the vicinity.

Application of the model to different cases of structures and conductors together with considerations and comments on the model assumptions could be found in the report [20] prepared in the frame of CIGRE.

10.13 References

1 IEC 81/170/Q: 'Questionnaire-approval of new publications' plan', April 2001
2 BERGER, K., ANDERSON, R.B., and KRONINGER, H.: 'Parameters of lightning flashes', *Electra*, 1975, (41), pp.23–37
3 ANDERSON, R.B., and ERIKSSON, A.J.: 'Lightning parameters for engineering applications', *Electra*, 1980, (69), pp.65–101
4 IEC 62305-1/CD 2002: 'Protection of structures against lightning – Part 1: general principles' (according to the new publications' plan)

5 WG of Italian Electrotechnical Committee (CEI), TC81-Lightning Protection: 'Lightning protection of structures', Part I to Part III, *Energ. Elettr.*, 1984, (5), pp.185–214
6 WG of Italian Electrotechnical Committee (CEI), TC81-Lightning Protection: 'Lightning protection of structures', Part IV to Part VI, *Energ. Elett.*, 1985, (11), pp.447–475
7 FLISOWSKI, Z., and MAZZETTI, C.: 'A new approach to the complex assessment of the lightning hazard of buildings', *Bull. Pol. Acad. Tech. Sci.*, 1984, **32** (9–10), pp.571–581
8 MAZZETTI, C., POMPILI, M., and FLISOWSKI, Z.: 'Review of application problems of probabilistic approach to the lightning hazard assessment'. Proceedings of 23rd international conference on *Lightning protection* (ICLP), Florence, Italy, September 1996, paper 7.1, pp.707–712
9 FLISOWKI, Z., and MAZZETTI, C.: 'Risk assessment method for the protection of electronic systems against lightning overvoltages'. IV SIPDA, Sao Paolo, Brazil, May 1999
10 IEC 62305-2: Protection against lightning – Part 2: risk management. Draft IEC 81/214/CD, March 2003, produced by TC81/WG9 under revision of IEC 61662, TR 1995
11 IEC 61024-1: 'Protection of structures against lightning', Edn 1, 1990 (according to the new publications' plan: IEC 62305-3, Protection against lightning – Part 3: physical damages and life hazard). Draft IEC 81/215/CD, March 2003, produced by TC81/WG8
12 IEC 61312-1: 'Protection against LEMP – Part 1: general principles'. 1995 (according to the new publications' plan: IEC 62305-4, Protection against lightning, Part 4: Failure of electrical and electronic systems within structures). Draft IEC 81/214/CD, March 2003, produced by TC81/WG3
13 IEC 61663-2: 'Lightning protection of telecommunication lines – Part 2: lines using metallic conductors'. 2001
14 GOLDE, R.H.: 'Lightning vol. 1 and 2' (Academic Press, London 1977)
15 UMAN, M.A.: 'Lightning discharge' (Academic Press, 1987)
16 ERIKSSON, A.J.: 'The incidence of lightning strikes to power lines', *IEEE Trans. Power Deliv.*, 1987, **PWRD-2**, pp.859–870
17 RIZK, F.A.M.: 'Modelling of transmission line exposure to direct lightning strokes', *IEEE Trans. Power Deliv.*, 1990, **5** (4), pp.2009–2029
18 PETROV, N.I., and WATERS, R.T.: 'Determination of the striking distance of lightning to earthed structures', *Proc. Roy. Soc. A*, 1995, **450**, pp.589–601
19 BERNARDI, M., DELLERA, L., GARBAGNATI, E., and SARTORIO, G.: 'Leader progression model of lightning: updating of the model on the basis of recent test results'. Proceedings of 23rd ICLP, Florence, Italy, September 1996, paper 4.2, pp.399–407
20 GIGRE SC 33 WG 33.01 (TF03): 'Lightning exposures of structures and interception efficiency of air termination systems'. 1989
21 IEC 61312-3: 'Protection against LEMP – Part 3: requirements for surge protective device (SPD)'. 1998

22 MAZZETTI, C., D'ELIA, B., TOMASSINI, R., DI GREGORIO, G., KUCA, B., and FLISOWSKI, Z.: 'LEMP disturbances in the mains incoming to the structures'. Proceedings of international scientific conference on *Energy savings in electrical engineering*, Warsaw, May 2001, paper C-09, pp.65–69
23 IEC 61024-1-2: 'Protection of structures against lightning – Part 2: application guide B'. 1998
24 LIEW, A.C., and DARVENIZA, M.: 'Dynamic model of impulse characteristics of concentrated earths'. *Proc. Inst. Electr. Eng.*, 1974, **121**, (2)
25 VERMA, R., and MUKHEDKAR, D.: 'Impulse impedance of buried ground wire', *IEEE Trans. Power Appar. Syst.*, 1980, **PAS-99**, (5)
26 GUPTA, B.R., and THAPAR, B.: 'Impulse impedance of grounding grids', *IEEE Trans. Power Appar. Syst.*, 1980, **PAS-99**, (6)
27 MAZZETTI, C., and VECA, G.: 'Impulse behavior of ground electrodes'. IEEE PES winter meeting, New York, 1983, paper 83 WM142-7
28 VAINER, A.L.: 'Impulse characteristics of complex earth grids', Electrical Technology, USSR, Vol. I, 1966
29 KOSTALUK, R., LOBODA, M., and MUKHEDKAR, D.: 'Experimental study of transient ground impedances'. IEEE PES summer meeting, Portland, 1981, paper 81 SM 399-5
30 KOUTEYNIKONOFF, P.: 'Réponse impulsionelle des prises de terre aux courantes de foudre'. CIGRE symposium 22-81, Stockolm, 1981
31 OETTLÉ, E.E.: 'A new general estimation for predicting the impulse impedance of concentrated earth electrodes', *IEEE Trans. Power Deliv.*, 1988, **3**, (4), pp.2020–2029
32 CRISHOLM, W.A., and JANISCHEWSKYJ, W.A.: 'Lightning surge response of ground electrodes', *IEEE Trans. Power Deliv.*, 1989, **4**, (2), pp.1329–1337
33 POPOLANSKY, F.: 'Impulse characteristics of soil'. 20th ICLP, Interlaken, September 1990, paper 3.2
34 GILMAN, D.W., and WHITEHEAD, E.R.: 'The mechanism of lightning flashover on HV and EHV transmission lines', *Electra*, 1973, (27), pp.65–96
35 ERIKSSON, A.J.: 'Lightning and tall structures', *Trans. SAIEE*, 1978, pp.238–252
36 DAVIS, R.: 'Lightning flashovers on the British Grid', *Proc. Inst. Electr. Eng.*, 1963, pp.969–974
37 WAGNER, C.F.: 'The lightning stroke as related to trasmission line performance', *Electr. Eng.*, May–June, 1963
38 YOUNG, F.S., CLAYTON, J.M., and HILEMAN, A.R.: 'Shielding of transmission lines', *IEEE Trans. Power Appar. Syst.*, 1963, special supplement, p.132
39 IEEE WG report: 'Estimating lightning performance of transmission lines – updates to analytical models'. SM 453-PWRD 1992
40 POPLARSKY, F.: 'Relationship between the number of thunderstorm days and the lightning flash density registered by LFC in the world scale', *Proc. of 21st International Conference of Lightning Protection*, Berlin, Germany, paper 6.10
41 LEE, R.H.: 'Lightning protection of buildings', *IEEE Trans. on Industry Application*, 1979, **IA-15**, pp.237–240

Chapter 11

Electrical aspects of lightning strike to humans

Chris Andrews

11.1 Introduction

In assessing any lightning injury both in electrical and medical terms, and indeed in assessing any electrical injury, the investigator must find a cogent and plausible explanation for the current pathway and the magnitude of the current flowing. This must make sense in both electrical and physiological terms. There must be a concordance between this and the extant observations of injury, and proposed current size and mechanisms. Without this, the assessment of any injury is conjectural, inaccurate and poorly based. Current magnitude and pathway have, nonetheless, not been well characterised in lightning injury.

This Chapter is an attempt to provide a theoretical model of the currents flowing in lightning injury in several circumstances.

11.2 Strike mechanisms

In all lightning injuries one of several physical mechanisms operates, and conceivably combinations of these mechanisms. Direct strike occurs when an individual in the field is the direct point of attachment of a flash. When an individual is near a stricken object, and a streamer jumps from that object to the individual, then a side flash occurs. If the individual is in direct contact with the stricken object, then voltage division occurs, and current flows from the point of contact through the individual. This may be termed contact potential.

If an individual has points of contact with (nonideal) ground within the field of current passage away from the base of a flash then, by virtue of the distributed ground resistance, a potential is set up between the points of contact. Current therefore flows through the individual. For a human this may be of little consequence if the points

of contact are the feet. If, however, a four footed animal like a cow stands in such a configuration, current may be conducted between fore and hind limbs, and the thorax may be involved – with much greater damage. Shock by this mechanism is variously termed EPR shock, stride potential, or similar.

Finally, a fifth mechanism for injury has been proposed and also explains injury without direct contact of the individual with the lightning flash. As the stepped leader initially approaches ground, several answering leaders may be generated and extend towards the stepped leader. Such a leader may extend from the head, or other part, of an individual even though the lightning channel is ultimately formed elsewhere. The answering leader requires current passage through an individual and this may well be injurious [1,2,5].

For humans, direct strike is associated with the greatest injury, with stride potential being the least harmful. Touch potential and side flash may be thought of as variants of each other and of intermediate consequence.

The literature contains very little contemporary estimate of current pathways and magnitudes.

Blake-Pritchard [4] provided simplistic calculations. Other work (from Japanese researchers) has been aimed more at determining lethal levels of flash current and the relationship between the development of flashover and the lethality of a given flash. They have also shown that respiratory support may save life after cardiorespiratory arrest (see [3] also for support of this observation).

Ishikawa *et al*. [10] examined the lethal current level of a flash to live unanaesthetised rabbits using a multipulse technique. Their findings were that a threshold of approximately 62.6 J/kg existed beyond which death would occur. Further, their finding was that provided one stroke in a multistroke flash exceeded this level, then death would ensue. Specifically, there was no memory engendered for succeeding strokes, and no cumulative effect of multiple strokes was seen. The strokes were approximately 40 ms apart, three in number, and were applied directly to the animal's head *via* a needle. Energy input was examined, and no account was taken of synchrony with the cardiac cycle – especially the probability of transgressing the vulnerable window of late repolarisation. Nagai *et al*. [12] confirmed the order of the above energy level. Ishikawa *et al*. [9] drew attention to the fact that if artificial ventilation was instituted after death from a lightning strike, then survival was increased from 25 to 48 per cent.

Ohashi *et al*. [13] also draw attention to the protective effect of the development of external flashover in a human strike by survey of post mortem findings. Of 50 victims, nine had evidence of flashover and 41 showed no such evidence. Of the former, five survived, and of the latter only six survived. The division into groups was somewhat subjective, but nonetheless these results are impressive. If flashover occurs, it is protective. In an experimental determination they noted two separate groups of animals subjected to artificial shocks. In those developing early flashover (sooner than 20 μs from contact), the survival was markedly better than those developing later flashover. This bears obvious relation to energy dissipation internally and also duration of internal current passage.

In a different approach, Flisowski and Mazzetti [7], used an analytical technique to predict the mortality level from strikes given the probability distributions of

stroke current, local parameters and known fatal current levels for the human body.[1] Although the latter are an extrapolation of Dalziel's well known formula into regions of short impulses, the mortality level arrived at of 20–40 per cent is of the order of that seen in practice. The body model used, however, was simply resistive, and took no account of either reactive components, or the different nature of the skin from the internal milieux.

11.3 Experimental parallels

There are extreme experimental difficulties in verifying any of the above data on humans. It is unacceptable to subject human beings to shocks under laboratory conditions. This may be one reason why considerations of current pathways and magnitudes in humans have received so little attention, and modelling is a viable alternative.

An interesting side note, however, exists in the work of Darveniza [6] who examined the electrical properties of wood used in power reticulation structures. This biological material is markedly more homogeneous than the animal body, but nonetheless contains possible channels for internal breakdown that parallel the tissue planes and channel structures of the mammalian body.

Darveniza found that the breakdown path seen when a wooden structure was submitted to an impulse was either entirely internal, or entirely external, never both. Which pathway was seen in an individual case was dependent on a number of factors, of which two were particularly important, *viz.*, the moisture content of the wood (more moisture favouring the internal path), and the existence of an entry site (e.g. a bolt or the like) to the interior. In dry woods, moisture content less than 20 per cent, the pathway was invariably external. In wet woods, moisture content greater than 50 per cent, the pathway was invariably internal. In the intermediate range other factors needed to be considered, such as length of wood sample, types of electrode used, wet *versus* dry surface conditions, and associated hardware.

Using this information, the human body has some features favouring truly internal breakdown. These include high moisture content, relatively short length and significant portals of entry. The latter include the special sense orifices of the cranium. It has been suggested that these orifices represent more important portals of entry than previously thought [3]. Hence, also, their vulnerability to injury in their own right. Nonetheless, the body possesses properties disposing to external flashover. These include the likelihood of being externally wet by rain, having less in the way of attached hardware, such as bolts and screws, and being less homogeneous.

Darveniza notes that evidence of internal flashover in wood is often easily seen, as the internal pathway almost always follows wood pores. The arc is of fine diameter, typically a few millimetres, and indeed tends to reduce in diameter internally

[1] The levels of current which are fatal for the human body may be found from standard tables (IEC479). The level of fatal current actually involves an estimate of the current flowing in a given pathway, the proportion of this flowing through the heart and the time for which it flows. Fatal levels may be found from strength/duration curves derived for this purpose. For example, a current of 200 mA a.c. flowing for 20 ms produces no harmful effects, whereas a current of 200 mA flowing for 500 ms carries a probability of causing a fatal cardiac arrhythmia of more than 50 per cent

with ongoing flow compared with external arcs. In the body, evidence of internal breakdown is rarely found. The most likely medium for transmission within the body is *via* the vascular tree or other fluid channel with its ionic liquid content. If current is transmitted internally *via* these media, post-mortem evidence may not be present. Even so, such conduction is likely to be quite dangerous, leading directly to the heart.

11.4 Important factors

A model of current flow within humans must take into account and be consistent with certain observed phenomena.

First, the body impedance is known to a greater or lesser degree. IEC479 [8], among other documents, provides lengthy discussions of the calculation of body impedance for the intact human body. The influence of pathway, contact voltage, area of contact, frequency and so on, are all examined. Thus the impedance of a given body path can be estimated closely. This impedance structure must be respected in a lightning model. Ultimately it is possible that disruption of elements of this impedance may occur (due to mechanical forces, electrical breakdown, burns, electroporation or similar), however the evidence for this is equivocal.

Second, the model must allow for sufficient internal current to flow to provide large internal functional consequences – particularly that of cardiac asystole.

Third, it must allow for the development of flashover.

Fourth, it must also allow for the fact that internal injury or burn of a structural kind is not seen. Thus any internal current must be short lived.

In the light of these factors, three cases are considered – direct strike with no external flashover (this could occur in side flash or contact potential), direct strike with external flashover (such as might occur in direct strike) and EPR shock. At least the first two cases are shown to engender shocks of lethal magnitude.

11.5 Proposed shock mechanism

The common theme running through the models to be presented proposes a shock mechanism as follows. This is outlined for direct strike, as this mechanism contains the most detail of all facets.

It is hypothesised (and the models return results supporting these hypotheses) that the strike attaches to a superior part of the human anatomy. Current is then transmitted internally and reaches a large magnitude. During this internal current passage period there is no external current flashover and therefore no consideration of any plasma properties over the body surface. Also during this internal conduction period, skin capacitance charges and ultimately a threshold is passed where skin breaks down and internal current increases momentarily. Skin in this case is taken to include shoe soles and the like, and breakdown of the skin includes breakdown of any skin covering like a shoe sole. Voltage builds up between the attachment point and (nonideal) ground, until flashover occurs between the attachment point and ground. At this point, the internal current flow decreases dramatically.

From the model, the internal current passage flow is short, and therefore internal damage is not seen. It is also suggested that the majority of current flow is *via* ionic

fluid – blood, cerebrospinal fluid and similar. Muscle would seem to be next lowest in impedance, and this continues to higher and higher impedances up to bone. It is submitted that, contrary to popular belief, nerve tissue actually has a high impedance. Although axonal tissue may be saltatory and ionic, significant nerve tissue is highly inaccessible, being covered with multimembranous layered fatty myelin.

From the point of flashover, the model contains certain weaknesses. External flashover certainly may be modelled as an extremely low-impedance pathway between attachment and earth, and the model proposed operates in this way. Thus the total current and majority path are accounted for. However, as plasma exists over the skin surface after flashover, there will be some current passage into the body from this plasma due to its potential, and distributed skin impedance. This is however suggested to be low, as the potential of the plasma will be low and the skin impedance (intact) will be high.

11.6 Results

11.6.1 In the field strike

11.6.1.1 Body model

The model used for the body is shown in Figure 11.1 The components follow commonly accepted lines, and include a 1 kΩ internal resistance split between arms, torso and legs as the internal component. This is purely resistive. The components for skin resistivity are significantly larger than for the internal resistance, and consist of a parallel resistance and capacitance of 10 kΩ and 0.25 μF. When this body model is placed in circuit with the lightning current source a means of modelling external and skin breakdown is required. This is shown in Figure 11.2 where gaps G_1 to G_4 model the breakdown. G_4 represents external flashover, and G_1, G_2, and G_3, respectively model the cranial skin breakdown and the two foot skin breakdowns. The skin is assumed to breakdown at a voltage of 5 kV across the parallel combination, and body surface breakdown to occur at a gradient of 2.7 kV/cm or, for a 1.8 m adult, approximately 500 kV. These are standard accepted values.

11.6.1.2 Earth resistance component

Meliopoulos [11] has derived expressions for earth resistance applicable to these conditions. For an individual standing on a surface of earth resistance ρ Ωm, the resistance measured from single foot to true earth is given by:

$$R_e = \rho/8b$$

where ρ is the earth resistivity and b is the radius of the equivalent flat plate representing one foot. Thus he shows that $R_e = 3\,\rho$ approximately, and two feet in parallel is half that. In subsequent sections ρ is taken to be 100 Ωm.

11.6.1.3 Direct strike – no flashover

The two cases of direct strike are now considered.

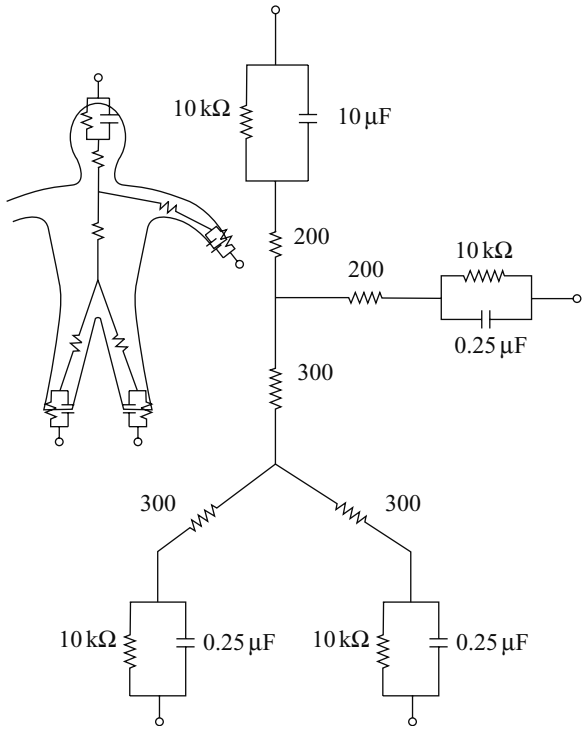

Figure 11.1 Body Model

The first is assumed to be direct strike with no external breakdown. The equivalent circuit is shown in Figure 11.2. An impulse of 5 kA using an 8/20 μs waveform is directly applied to the cranial skin and the sequence of events shown in Figure 11.3 are observed using this model.

Even though no external flashover is modelled to occur in this example, skin breakdown is highly likely and is programmed to occur at 5 kV. The sequence of events shows:

(i) Voltage is generated across the body (here represented by the cranial–earth voltage) by the applied current, and leads the current which, in the internal milieux, rises exponentially. Voltage across the foot and cranial skin elements slightly lag the current.

(ii) At 1.1 μs and 1.7 μs, respectively, breakdown of skin components occurs. This only has marginal impact on the internal current and cannot be distinguished on the scale of the Figure.

(iii) Ultimately a maximum value of internal current is reached. This is 5 kA, and is an obviously harmful current.

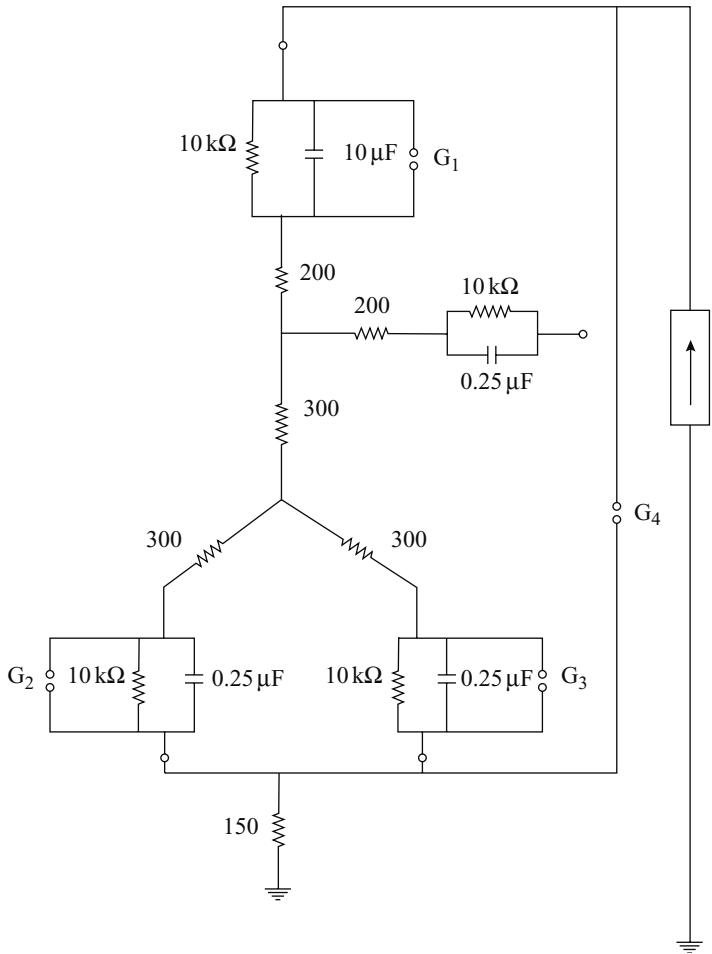

Figure 11.2 Equivalent circuit for direct strike in the field

(iv) By 100 μs the current wave has largely decayed and only a small component remains at 500 μs. During the decay, the internal current becomes negative as capacitive elements discharge.

This situation is obviously harmful and the degree of harm depends on the localisation of the breakdown channel, and the current density in the channel. It seems a reasonable worst case assumption that this be conducted directly to the heart *via* the blood vessels, and probably is transmitted *via* the aorta with a cross sectional area of around 7 cm^2. The current density is thus extremely large.

Dalziel's original work was not conducted at this brevity of impulse, but if we extrapolate as others have done, the lethal current at, say, 50 μs impulse duration

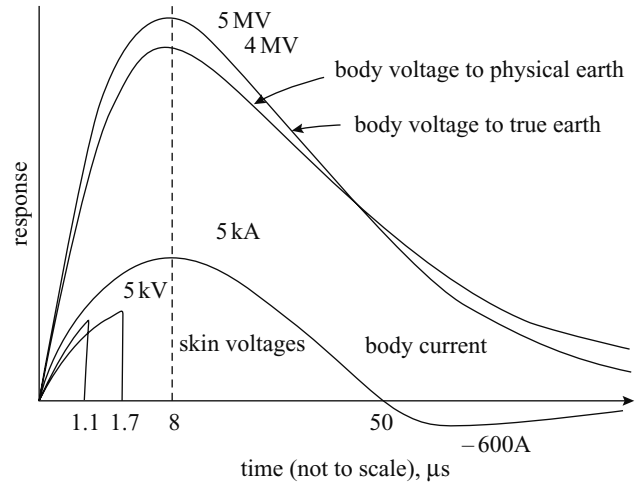

Figure 11.3 Sequence of events following direct strike in the field without the occurrence of flashover

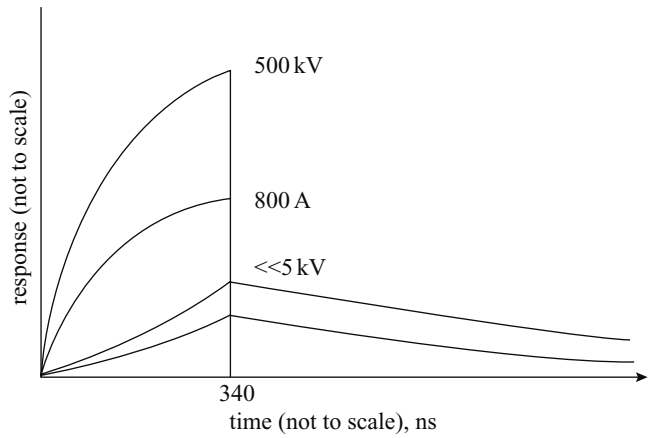

Figure 11.4 Sequence of events following direct strike in the field with the occurrence of flashover

is 16.4 A. Obviously this is greatly exceeded and this circumstance is supremely dangerous.

11.6.1.4 Direct strike with flashover

The second case under consideration is that where the circumstances are as above, but external flashover occurs. The equivalent circuit is the same as the above and the sequence of events is shown in Figure 11.4.

The voltage between the cranium and local ground rises exponentially until 500 kV is reached when external flashover occurs at approximately 340 ns after attachment. This is remarkably small. At this stage the body current has risen to approximately 800 A. At flashover the voltage and internal current drops dramatically to zero, and the vast majority of current is transmitted externally. The skin voltages now do not rise to 5 kV and so electrical breakdown does not occur. It is highly likely, however, that mechanical disruption of the skin surface occurs, and so skin resistance markedly decreases. Nonetheless the effect of this on body current is negligible.

Using Dalziel's criterion, the lethal current for a 340 ns impulse is 199 A, and this is certainly exceeded. Thus this circumstance also represents a highly dangerous situation. It is stressed that Dalziel's criterion was not derived at such short impulse times. Others have extrapolated to this level, however, and as the criterion is markedly exceeded it serves simply as a guide to lethality. This guide is also supported by the recent IEC 479–1 and 2 reports for shorter duration impulses, which also regard the above level as lethal [8].

11.6.1.5 Heating considerations

Other considerations have been proposed for the effects of lightning damage to tissue, including heating. It is instructive to calculate possible temperature rises given the above possible scenarios.

The internal current rises to approximately 800 A in 340 ns, and if as a first approximation this is considered linear, the energy input is approximately 33 J. If this is dissipated in the heart with a volume of about 200 mL, and the specific heat of water, then the temperature rise is around 0.04°C. If on the other hand no flashover occurs, the current is much larger and the energy absorption is around 188 kJ, and the cardiac temperature rise would be potentially 224°C which is obviously capable of producing thermal damage. Since damage of this magnitude is simply not seen, the worst case assumption that this dissipation occurs totally within the myocardium is not valid.

The situation for metal on the body surface is significant since it is claimed that heating of metal objects can cause contact burns. If a piece of metal is in the path of a 5 kA flashover, and is perhaps a piece of jewellery with a resistance of 1 Ω, then the energy absorbed will be of the order of 625 J (148.4 cal). If the metal weighs 100 g and is of material such as aluminium with a specific heat of .21 cal/gm/°C then the temperature rise will be 7°C. This is unlikely to cause thermal burns, although the metal may cause current concentrations and arcing to the skin beneath. This may explain the contact burns seen in the injury.

11.6.2 EPR mediated shock

The remaining case for consideration is EPR mediated shock. The equivalent circuit for this circumstance is shown in Figure 11.5.

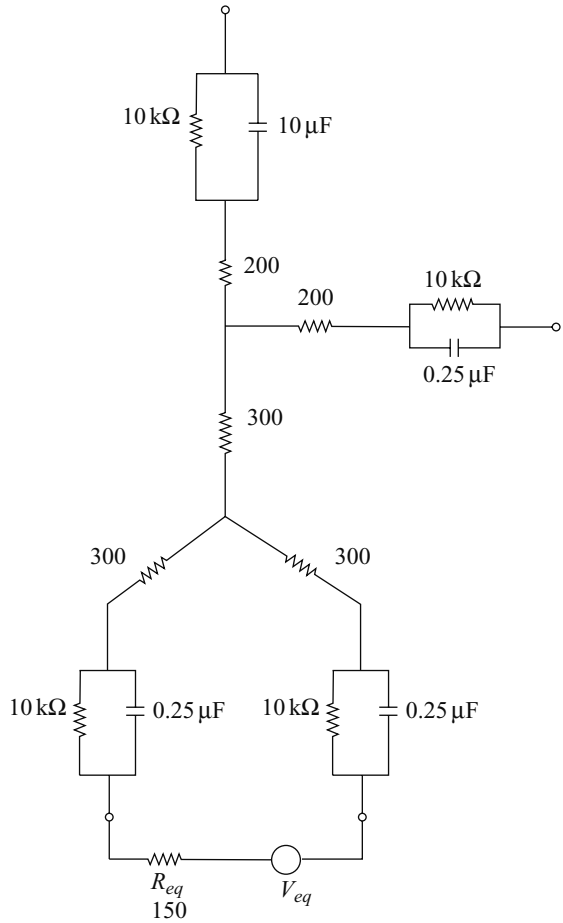

Figure 11.5 Equivalent circuit for EPR mediated in the field strike

The equivalent circuit for the applied voltage is that given by Meliopoulos [9]. The magnitude of the voltage source is given by:

$$V_{eq} = (\rho I/2\pi)(1/r_1 - 1/r_2)$$

where r_1 and r_2 are the distances of the body parts in contact with physical ground from the base of the lightning stroke. The other quantities are defined as before. R_{eq} is given by 1.5 ρ being two 3 ρ resistances in parallel. If we assume a 5 kA lightning stroke and a person 10 m distant with legs 1 m apart V_{eq} is 800 V, and is thus approximated as 1 kV in the model. If the person is 20 m from the base of the stroke then the voltage falls to 200 V, and it may be seen that EPR (in-the-field) is a relatively small effect.

When these parameters are introduced to the model, a current of approximately 1.05 A peak, flows through the legs. Modelled in this way the myocardium seems at no risk, however it must be remembered that the internal resistance is distributed rather than discrete in reality. Thus a small current will flow peripherally through the myocardium. The accepted factor applied due to a leg-to-leg current is less than 0.3, and so it is expected that less than 300 mA will flow. This is unlikely to be dangerous, on IEC and Dalziel criteria, given the small duration (45 μs) of the impulse. The effect for large animals, e.g. cattle, with legs up to 4 m apart, and direct transthoracic pathways, may well be dangerous.

11.6.3 Telephone-mediated strike

A research interest of the author's is that of lightning shock delivered to individuals involving the public telephone system. Similar modelling has been undertaken for this circumstance.

The ear in telephone-mediated lightning injury is at special risk and is, in fact, subject to two distinct insults, one electrical and one acoustic. This section aims to quantify the order of electrical trauma to which the hearing organ is subjected, and consequently to indicate the order of electrical insult to which the whole body is subjected. The most significant organ from the point of view of mortality is the heart. The entry of current through the ear can be transmitted *via* one of several mechanisms to the remainder of the body.

An equivalent circuit for the body under in-the-field conditions has already been developed, and the same body model is used in this section. The external connections, however, are slightly different. In normal operation, the telephone handset is pressed to the ear using one hand. Coupling to the handset therefore is dual. The coupling is capacitative and the capacitance is taken as 88 pF, experimentally determined by the author.

Two circumstances of shock bear examination. The first is direct surge application through the telephone line through handset and cranium to a return path *via* the feet, or possibly another part of the body touching an earthed structure. In this case, the applied surge is a voltage surge, and compared with in-the-field strike, of somewhat less power. Breakdown of the handset/head interface may still occur, but surface flashover of the body is not considered at all likely. Occasional breakdown of skin entry/exit sites may occur. Using the previous model the earth resistance is set up in exactly the same way. The applied impulse is taken as a 10 kV 1/50 μs voltage surge. Local measurement on lightning prone telephone lines indicates an upper limit of 5 kV unlikely to be exceeded, but 10 kV is taken as a worst case. The equivalent circuit and simulation result are shown in Figures 11.6 and 11.7.

The following may be seen. The 88 pF capacitor is modelled to breakdown at 5 kV, and prior to this body current is small, rising to a maximum of 700 mA. The handset coupling breaks down at approximately 1.5 μs and when this occurs body current rises dramatically to a maximum of approximately 12 A at 10 μs and then falls quickly to negligible values by 54 μs. The possibility exists for skin breakdown to occur, but the model indicates that the skin voltage only rises to about 600 V.

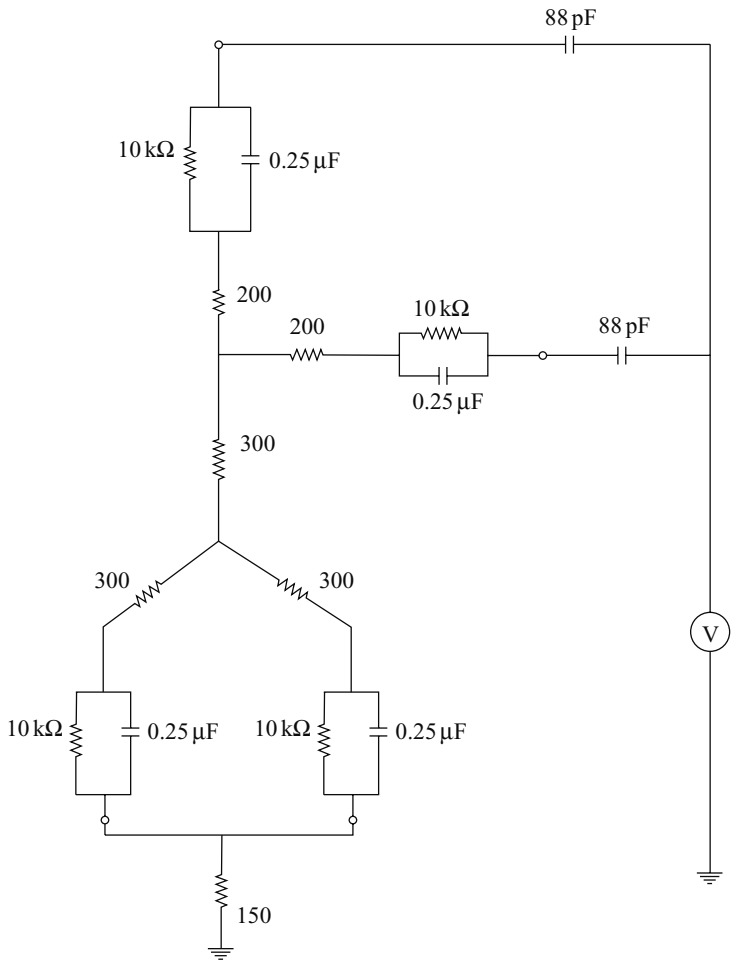

Figure 11.6 Equivalent circuit for telephone mediated lightning strike with the impulses transmitted directly by the telephone cable

Although this is sufficient to be very noticeable, it will not cause breakdown. IEC 479 indicates that impulse shocks lasting less than 100 µs are unlikely to cause fibrillation (probability less than five per cent) at values less than 7 A, and moderately likely (probability greater than 50 per cent) at currents above 12 A. Given that a 10 kV surge is uncommon, and that the majority are less than 5 kV, the risk of mortal injury is low. Indeed below 5 kV handset flashover may not occur. When it does, the spark will be local and form the capacitative spark often seen. Although unlikely to be fatal, such shocks are nonetheless highly perceivable, and unpleasant.

Estimates are that the majority of telephone-mediated shocks in the author's country (Australia) are mediated by local EPR causing current to be transmitted

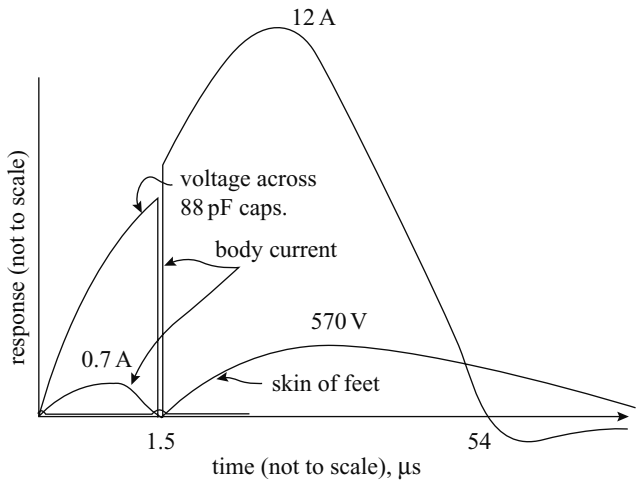

Figure 11.7 Body response for telephone mediated lightning strike with the impulses transmitted directly by the telephone cable

back to the remotely earthed telephone exchange. An equivalent circuit for such a circumstance is shown in Figure 11.8, using the same parameters as previously (a stroke 20 m away, and of 100 Ω m). A voltage impulse of 1 kV is applied to both feet in parallel, and the results of the simulation are shown in Figure 11.9. This is an appropriate level of impulse EPR given circumstances similar to these shown above. It may, however, underestimate the degree of the insult given modern construction of dwellings. It may be that power supply reticulation, or the structure itself is struck, and the impulse transmitted to a highly conductive floor structure, e.g. concrete slab. This would increase the EPR voltage markedly. The 1 kV impulse used could, however, be scaled easily.

The simulation shows that the voltage across the 88 pF capacitors rises rapidly as expected, but does not necessarily break down. Body current rises to around 72 mA, and this is unlikely to be injurious. Even with an order of magnitude scaling, the results still represent the least dangerous of the strike circumstances.

These results support the observation that no death has yet been seen in Australia from telephone-mediated lightning strike. If, however, high current strokes occur and circumstances conspire, such is not beyond possibility.

11.7 Experimental support

Experimental support for these models is hard to obtain, however one incidental observation may be important.

In other work [3], Australian sheep were subjected to cranial impulses, and flashover occurred. The impulses were multipulse. Tracings of the applied current

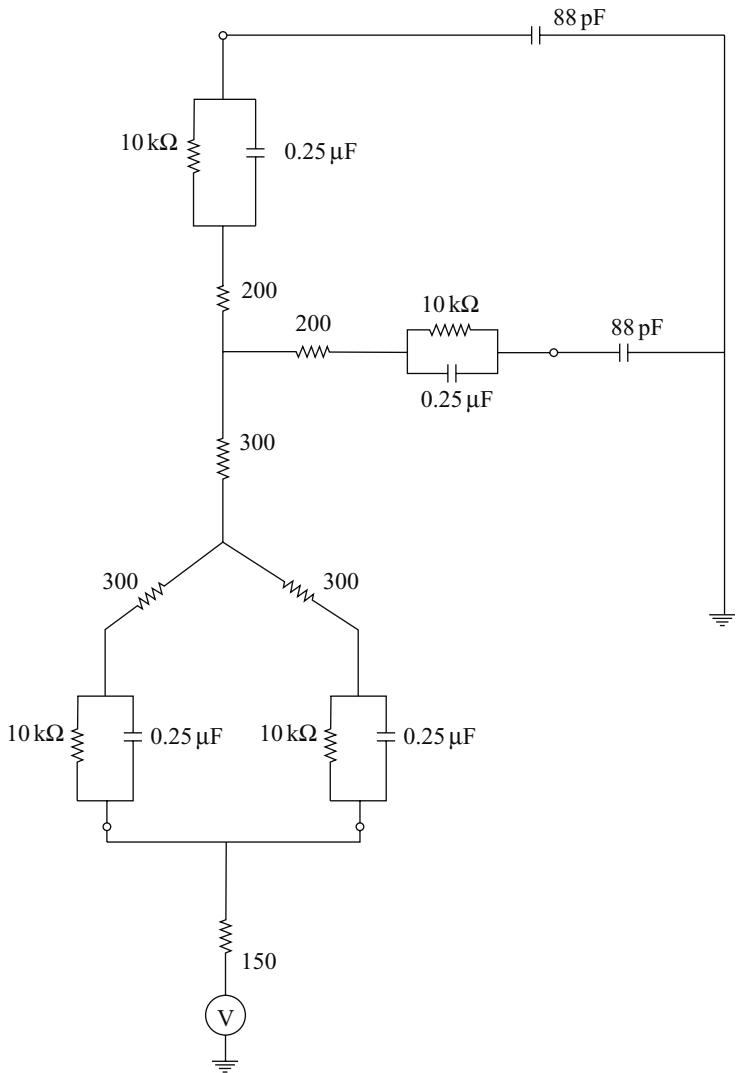

Figure 11.8 Equivalent circuit for telephone mediated lightning strike, with the impulse transmitted by EPR

pulse were obtained, and traces of the resulting cranium to hind quarter voltage were also obtained. These are shown in Figure 11.10. In all cases where flashover occurred, the voltage dropped dramatically at approximately 500 nS, this being a rough limit of measurement. The trace of a single impulse in Figure 11.10 shows the drop in voltage but also a short tail which represents the limitation of the proposed model with respect to the plasma sheet after flashover.

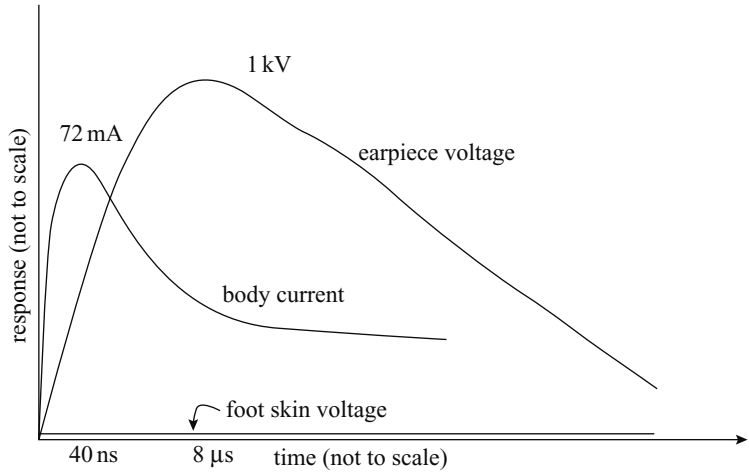

Figure 11.9 Body response for telephone mediated lightning strike, with the impulse transmitted by EPR

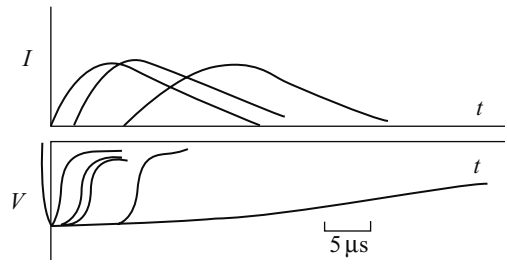

Figure 11.10 Voltage tracing – cranium to earth (upper trace – multipulse traced from polaroid; lower trace – single pulse)

11.8 Conclusion

In this segment models for in-the-field strike and telephone-mediated strike have been developed, and proposals regarding pathways have been made. An estimation of the magnitude and the time course of the insult has been given.

11.9 References

1 ANDERSON, R.B.: 'Does a fifth mechanism exist to explain lightning injuries', *IEEE Eng. Med. Biol.*, Jan–Feb 2001, p.105 *et seq*

2 ANDERSON, R.B., JANDRELL, I.R., and NEMATSWERANI, H.E.: 'The upward streamer mechanism versus step potentials as a cause of injuries from close lightning discharges', *Trans. SA Inst. Elec. Eng.*, March 2002, pp.33–43.
3 ANDREWS, C.J.: 'Structural changes after lightning strike, with special emphasis on special sense orifices as portals of entry', *Semin. Neurol.*, 1995, **15**(3), pp.296–303
4 BLAKE-PRITCHARD, E.A.: 'Changes in the central nervous system due to electrocution', *Lancet*, 1934, **1**, p.1163
5 COOPER, M.A.: 'A fifth mechanism of lightning injury', *Acad. Emerg. Med.*, Feb 2002, **9**, (2), p.1724.
6 DARVENIZA, M.: 'Electrical properties of wood and line design' (Univ. Qld. Press, 1980)
7 FLISOWSKI, Z. and MAZZETTI, C.: 'An approximate method of assessment of the electric shock hazard by lightning strike'. 18th international conference on lightning protections, Munich, VDE-Verlag GMbH, 1985, pp.449–453, paper 6.9
8 IEC Standard 479–1: 'Effects of current passing through the human body'. IEC, Geneva, 1984 *et seq*
9 ISHIKAWA, T., MIYAZAWA, T., and OHASHI, M., *et al*.: 'Experimental studies on the effect of artificial respiration after lightning accidents', *Res. Exp. Med. (Berl)*, 1981, **179**, 59–68
10 ISHIKAWA, T., OHASHI, M., KITIGAWA, N., NAGAI, Y., and MIYAZAWA, T.: 'Experimental study on the lethal threshold value of multiple successive voltage impulses to rabbits simulating multi-strike lightning flash', *Int, J. Biometeorol.*, 1985, **29** (2), pp.157–168
11 MELIOPOULOS, A.P., SAKIS: 'Power system grounding and transients' (Marcel Dekker, N.Y., 1990)
12 NAGAI, Y., ISHIKAWA, T., OHASHI, M., and KITIGAWA, N.: 'Study of lethal effects of multiple-stroke flash on Rabbits subjected to 3-successive voltage impulses simulating multiple-stroke flash (sic)', *Res. Lett. Atm. Phys.*, 1982, **2**, p.87
13 OHASHI, M., KITIGAWA, N., and ISHIKAWA, T.: 'Lightning injury caused by discharges accompanying flashovers – a clinical and experimental study of death and survival', *Burns*, **12** (7), 1986, pp.496–501

Index

The Lightning Flash

This unique book provides the reader with a thorough background in almost every aspect of lightning and its impact on electrical and electronic equipment. The contents range from basic discharge processes in air through transient electromagnetic field generation and interaction with overhead lines and underground cables, to lightning protection and testing techniques. This book is of value to anyone designing, installing or commissioning equipment which needs to be secured against lightning strikes, as well as being a sound introduction to research students working in the field.

Vernon Cooray is Full Professor in Electricity at the Division for Electricity and Lightning Research, The Angström Laboratory, Uppsala University, and is responsible for postgraduate studies in the field of Atmospheric Electrical Discharges. Professor Cooray is the Swedish member of CIGRE-WG33.01 (lightning location), CIGRE-WG33.02 (interaction of electromagnetic fields with power lines) and CIGRE-WG33.04 (soil ionisation) and is the chairman of the CIGRE-WG33.03 (lightning interception). He is also a member of the scientific committee of the International Conference on Lightning Protection. Professor Cooray has conducted experimental and theoretical research work in electromagntic compatibility, electromagnetic wave propagation, lightning physics, lightning protection and discharge physics, has authored and coauthored more than 150 scientific papers, and is the author of a popular book in Swedish (*Blixt ock Åska – Så fungerar naturens fyrverkeri*, Hallgren & Fallgren) on lightning.

The Institution of Engineering and Technology
www.theiet.org
0 85296 780 2
978-0-85296-780-5